AD-A274 452

PROCEEDINGS OF THE HIGH ENERGY DENSITY MATTER (HEDM) CONTRACTOR'S CONFERENCE HELD 6-8 JUNE 1993 IN WOODS HOLE, MA.

T.L. Thompson, Editor

S DTIC
ELECTE
DEC 15 1993
A

November 1993

Special Report

93-30276

93 12 14 012

PHILLIPS LABORATORY
Propulsion Directorate
AIR FORCE MATERIEL COMMAND
EDWARDS AIR FORCE BASE CA 93524-5000

NOTICE

When U.S. Government drawings, specifications, or other data are used for any purpose other than a definitely related Government procurement operation, the fact that the Government may have formulated, furnished, or in any way supplied the said drawings, specifications, or other data, is not to be regarded by implication or otherwise, or in any way licensing the holder or any other person or corporation, or conveying any rights or permission to manufacture, use or sell any patented invention that may be related thereto.
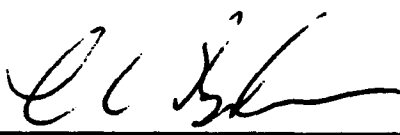
FOREWORD

This Conference Proceedings was compiled and edited by Capt Tim Thompson, OLAC Phillips Laboratory, Edwards AFB CA.

This report has been reviewed and is approved for release and distribution in accordance with the distribution statement on the cover and on the SF Form 298.

TIM L. THOMPSON, Capt, USAF
Editor

STEPHEN L. RODGERS
Chief, Emerging Technologies Branch

RANNEY G. ADAMS
Public Affairs Director

REPORT DOCUMENTATION PAGE

Public reporting burden for this collection of information is estimated to average 1 hour per response, including the time for reviewing instructions searching existing data sources gathering and maintaining the data needed, and completing and reviewing the collection of information. Send comments regarding this burden estimate or any other aspect of this collection of information, including suggestions for reducing this burden to Washington Headquarters Services, Directorate for Information Operations and Reports, 1215 Jefferson Davis Highway, Suite 1204, Arlington, VA 22202-4302, and to the Office of Management and Budget, Paperwork Reduction Project (0740-0188), Washington DC 20503.

1. AGENCY USE ONLY (LEAVE BLANK	2. REPORT DATE November 1993	3. REPORT TYPE AND DATES COVERED Special Report 92/05 to 92/06

4. TITLE AND SUBTITLE
PROCEEDINGS OF THE HIGH ENERGY DENSITY MATTER
(HEDM) CONTRACTOR'S CONFERENCE HELD 6-8 JUNE 1993 IN
WOODS HOLE, MA.

6. AUTHOR(S)

T.L. Thompson, Editor

5. FUNDING NUMBERS

C:

PE: 62302F

PR: 3058

TA: 00N2

7. PERFORMING ORGANIZATION NAME(S) AND ADDRESS(ES)

8. PERFORMING ORGANIZATION REPORT NUMBER

9. SPONSORING/MONITORING AGENCY NAME(S) AND ADDRESS(ES)

PHILLIPS LABORATORY (AFMC)
Propulsion Directorate
EDWARDS AFB, CA 93524-7680

10. SPONSORING/MONITORING AGENCY REPORT NUMBER

PL-TR-93-3041

11. SUPPLEMENTARY NOTES
EXTENDED ABSTRACTS FROM THE SEVENTH HIGH ENERGY DENSITY MATTER CONTRACTORS
CONFERENCE

12a. DISTRIBUTION/AVAILABILITY STATEMENT

APPROVED FOR PUBLIC RELEASE
DISTRIBUTION UNLIMITED

12b. DISTRIBUTION CODE

A

13. ABSTRACT (MAXIMUM 200 WORDS)

This report documents the information presented at the seventh annual High Energy Density Matter (HEDM) Contractors Conference held 6-8 June 1993 in Woods Hole, MA. This report contains the extended abstracts of the oral, workshop and poster presentations given by the Air Force funded contractors and by the in-house researchers from the Phillips Laboratory.

14. SUBJECT TERMS
HIDM; High Energy Density Matter; propellant; solid hydrogen; cryogenic matrices; energetic materials; potential energy surfaces.

15. NUMBER OF PAGES

16. PRICE CODE

17. SECURITY CLASSIFICATION OF REPORT Unclassified	18. SECURITY CLASSIFICATION OF THIS PAGE Unclassified	19. SECURITY CLASSIFICATION OF ABSTRACT Unclassified	20. LIMITATION OF ABSTRACT SAR

Table of Contents

Extended Abstracts from Poster Session

Introduction

The main purpose of the High Energy Density Matter (HEDM) program is to research and develop advanced high energy compounds containing increased energy densities (Energy to mass ratios) and greater specific impulses (thrust per weight flow rate of propellant) which will enable spacecraft to carry larger payloads. With these advanced propellants, future space-bound payloads could be possibly four times greater than they are today. Theoretical experimental research is carried out by in-house researchers at the Phillips Laboratory at Edwards Air Force Base (PL) and through Air Force funded contracts with numerous researchers in the academic and industrial communities.

The HEDM program is administered by a steering group made up of representatives from the Propulsion Directorate of the Phillips Laboratory and the Air Force Office of Scientific Research (AFOSR). A technical panel administered by the National Research Council (NRC) assists the steering group in ensuring the high technical content of the program.

Annual conferences, alternatively hosted by the AFOSR and the PL are arranged in order to allow in-house and contract researchers to report on their progress and new developments. The Seventh High Density Matter Contractors Conference was held 6 - 8 June 1993 in Woods Hole, Massachusetts. The conference consisted of an introductory and poster session on Sunday afternoon, Boron Chemistry and Parallel Computing Workshops on Sunday evening, oral presentations Monday and Tuesday, followed by HEDM Synthesis and Cryo-solids Workshops on Tuesday afternoon. This report documents the information presented at this conference and contains extended abstracts of the poster, workshop and oral presentations given at the conference.

The next High Energy Density Matter Conference is scheduled for June 1994.

Accesion For		
NTIS CRA&I	☑	
DTIC TAB	☐	
Unannounced	☐	
Justification		
By		
Distribution /		
Availability Codes		
Dist	Avail and / or Special	
A-1		

DTIC QUALITY INSPECTED 3

1

93 HEDM CONFERENCE AGENDA

Sunday, 6 June

11:00 am - 1:00pm	Registration/Lunch in Woods Hole Main House	
1:00 pm	Introductory Remarks, AFOSR plans	Michael Berman
1:15	PL plans/roadmap	Steve Rodgers
1:30	AF needs, mission, goals and opportunities	Maj Dave Lewis
2:00	NASA/JPL needs, mission, goals	Bob Frisbee
2:30 - 4:30	Formal Poster Session in Woods Hole Carriage House	
4:30	Dinner	
5:30 - 9:00 PM	Boron Chemistry Workshop Parallel Computing Workshop	

Monday, 7 June   Technical Session   in Main House

8:30 AM "Spectroscopy of Novel Metal Complexes,"
Michael Duncan, University of Georgia

9:00 "Photofragmentation of magnesium cluster ion-molecule complexes,"
Paul Kleiber, University of Iowa

9:30 "Spectroscopy and Bonding in the Excited States of B_2,"
Chris Brazier, University of Dayton Research Institute

10:00 Break

10:30 "Coupled Electronic-Nuclear Dynamics in Rare Gas Solids,"
Ara Apkarian, University of California - Irvine

11:00 "Vibrational dynamics in quantum clusters and solids,"
RB Gerber, University of California - Irvine

11:30 "Incipient condensed phase effects in the O_3/H_2O system: Chemical dynamics
in the gas phase and in small clusters,"
Michael Casassa, National Institute Standards and Technology

12:00 Lunch

1:30 PM "Experimental Spectroscopies of Polymeric Oxygen Molecules,"
Hanspeter Helm, SRI International

2:00 "The Dodecahedral N_{20} and P_{20} Molecules: Some Theoretical Predictions,"
Henry Schaefer, University of Georgia

2:30   "Theoretical/Experimental Investigations of the Structure and Dynamics of Highly Energetic Dication Species," Stephen Leone, Joint Institute for Laboratory Astrophysics, University of Colorado

3:00   Break

3:30   "In search of novel high energy density materials," Karl Christe, Rocketdyne

4:00   "Spectroscopy of gamma-ray irradiated para-H_2 crystals," Takeshi Oka, University of Chicago

4:30   "The remarkable phase line of orientational order in solid HD at high pressure," Isaac Silvera, Harvard University

5:00   Adjourn

6:30   Mixer

7:30   Clambake

Tuesday, 8 June   **Technical Session**

8:00 AM   "Trapping of light metal atoms in hydrogen matrices," Mario Fajardo, Phillips Laboratory

8:30   "Computer simulation of analytical studies of impurities in solid hydrogen," Greg Voth and Michael Klein, University of Pennsylvania

9:00   "The interaction of H_2 ($^1\Sigma_g$ +) with Li 2s ^2S and Li 2p ^2P," Daniel D. Konowalow, University of Dayton Research Institute

9:30   Break

10:00   "New Developments in Theory and Applications for High Energy Density Materials," Rod Bartlett, University of Florida

10:30   "Laser and fourier transform spectroscopy of novel propellant molecules," Peter Bernath, University of Waterloo

11:00   "Parallel Computing in Electronic Structure Theory," Mark Gordon, Iowa State University

11:30   "Geometrical isomerization and light metalloid molecule oxidation as a means of producing high impulse propellants," James Gole, Georgia Institute of Technology

12:00   Lunch

1:00 - 5:00 PM   Cryosolids workshop
Synthesis workshop

Air Force
High Energy Density Materials
Contractors Conference
Woods Hole Center of the
National Academy of Sciences
314 Quissett Avenue
Woods Hole, MA 02543-0086
June 6-8, 1993

Participants List

Nigel C. Adams
Department of Chemistry
University of Georgia
Athens, GA 30602

Angelo Alfano
University of Dayton Research Institute
OLAC PL/RKFE
Edwards AFB, CA 93524-7680

Millard H. Alexander
Department of Chemistry
University of Maryland
College Park, MD 20742

Lester Andrews
Department of Chemistry
University of Virginia
Charlottesville, VA 22901

V. Ara Apkarian
Department of Chemistry
University of California, Irvine
Irvine, CA 92717

Lucia M. Babcock
Department of Chemistry
University of Georgia
Athens, GA 30602

Rodney J. Bartlett
Quantum Theory Project
University of Florida
362 Williamson Hall
Gainesville, FL 32611-2085

Stephen C. Bates
Thoughtventions Unlimited
P. O. Box 1310
Glastonbury, CT 06032

Robert Behdadnia
Phillips Laboratory
OLAC PL/RKFE
Edwards AFB, CA 93524

David J. Benard
Rockwell International Science Center
1049 Camino Dos Rios
Thousand Oaks, CA 91360

Michael Berman
Air Force Office of Scientific Research
Bldg. 410, Room B217
Bolling AFB, DC 20332-6448

Peter F. Bernath
Department of Chemistry
University of Waterloo
Waterloo, Ontario, CANADA N2L 3GI

Jerry Boatz
Phillips Laboratory
OLAC PL/RKFE
Edwards AFB, CA 93524

Chris R. Brazier
University of Dayton Research Institute
Phillips Laboratory
OLAC PL/RKFE
Edwards AFB, CA 93524-7680

Leo Broline
Phillips Laboratory
OLAC PL/RKFE
Edwards AFB, CA 93524

Michael P. Casassa
National Institute of Standards
  and Technology
221 - B268
Gaithersburg, MD 20899

Jose Chirivella
California Institute of Technology
Propulsion Laboratory
4800 Oak Grove Dr. 241/205
Pasadena, CA 91109

Karl O. Christe
Rocketdyne
BA26 6633 Canoga Avenue
Canoga Park, CA 91309

Gilbert W. Collins
Lawrence Livermore National Laboratory
P. O. Box 808, L-482
Livermore, CA 94550

Michael Coolidge
FJSRL
2354 Vandenburg Dr. Suite 2A35
USAFA CO 80840

Robert A. Corbin
c/o Dr. John W. Kenney, III
Department of Physical Sciences
Station 33
Portales, NM 88130

Paul J. Dagdigian
Johns Hopkins University
Remsen Hall
34th & Charles Streets
Baltimore, MD 21218

Robert Damrauer
Department of Chemistry
University of Colorado
Campus Box 194
P. O. Box 173364
Denver, CO 80217-3364

David E. Daney
Cryogenic Engineering Laboratory
589 Left Fork Road
Boulder, CO 80302

Frederick L. Dryer
Department of Mechanical &
  Aero Engineering
Princeton University
D-36 Equad
Princeton, NJ 08544

Michael A. Duncan
Department of Chemistry
University of Georgia
Athens, GA 30602

Philip E. Eaton
Department of Chemistry
University of Chicago
Chicago, IL 60637

Richard D. Etters
Department of Physics
Colorado State University
Fort Collins, CO 80523

Mario Fajardo
Phillips Laboratory
OLAC PL/RKFE
Edwards AFB, CA 93524

Arthur Fontijn
Department of Chemical Engineering
Rensselaer Polytechnic Institute
Troy, NY 12180-3590

Robert L. Forward
Forward Unlimited
P. O. Box 2783
Malibu, CA 90265

Robert H. Frisbee
Jet Propulsion Lab (JPL)
4800 Oak Grove Drive
Mail Stop 125-224
Pasadena, CA 91109

Patrick E. Frye
Rocketdyne Div./Rockwell International
6633 Canoga Avenue
P. O. Box 7922
Canoga Park, CA 91309-7922

Bruce C. Garrett
Battelle Northwest
PSL Building
908 Battelle Boulevard
Richland, WA 99352

Robert B. Gerber
Department of Chemistry
University of California, Irvine
Irvine, CA 92717

Jeffrey W. Gilman
ENTHONE-OMI, Inc.
250 Weatherside Road
Cheshire, CT 06410

Judah M. Goldwater
Office of Naval Research
800 North Quincy Street, Room 704
Arlington, VA 22217-5660

James L. Gole
School of Physics
Georgia Institute of Technology
Atlanta, GA 30332

Mark S. Gordon
Department of Chemistry
Iowa State University
Ames, IA 50011

Tom W. Hawkins
Phillips Laboratory
OLAC PL/RKCP
Edwards AFB, CA 93523-5000

Hanspeter Helm
SRI International
333 Ravenswood Avenue, Bldg. PN085
Menlo Park, CA 94025

Marilyn Jacox
National Institute of Standards
  and Technology
Mail Stop B-268, Physics Bldg.
Gaithersburg, MD 20899

Kenneth C. Janda
Department of Chemistry
University of California, Irvine
Irvine, CA 92717-2025

Rajiv K. Kalia
Department of Physics and Astronomy
Louisiana State University
Nicholson Hall
Baton Rouge, LA 70803-4001

Daniel H. Katayama
Phillips Laboratory
GPID
29 Randolph Road
Hanscom AFB, MA 01731-3010

Paul D. Kleiber
Department of Physics and Astronomy
University of Iowa
Iowa City, IA 52242

Michael L. Klein
University of Pennsylvania
3231 Walnut Street
Philadelphia, PA 19104-6202

Daniel D. Konowalow
Phillips Laboratory
PL/RKFE
9 Antares Road
Edwards AFB, CA 93524-7680

Stephen R. Leone
University of Colorado/JILA
Boulder, CO 80309-0440

David W. Lewis
Phillips Laboratory
OLAC PL/RKFE
Edwards AFB, CA 93524

Joseph Lichtenhan
University of Dayton Research Institute
OLAC PL/RKFE
9 Antares Road
Edwards AFB, CA 93524

Michel Macler
Phillips Laboratory
OLAC PL/RKFE
Edwards AFB, CA 93524

Frank Magnotta
Lawrence Livermore National Laboratory
P. O. Box 808, MS L-278
Livermore, CA 94551

Alan P. Marchand
Department of Chemistry
University of North Texas
NT Station, Box 5068
Denton, TX 76203-0068

Humphrey J. Maris
Department of Physics
Brown University
Providence, RI 02912

Nikita Matsunaga
Iowa State University
Wilhelm Hall #402, ISU
Ames, IA 50011

H. Harvey Michels
Chemical Sciences Department
United Technologies Research Center
411 Silver Lane
East Hartford, CT 06108

John A. Montgomery
United Technologies Research Center
Silver Lane, MS-72
East Hartford, CT 06108

Robert A. Morris
Phillips Laboratory
PL/GPID
29 Randolph Road
Hanscom AFB, MA 01731-3010

Edmond Murad
Phillips Laboratory
PL/WSSI, 29 Randolph Rd
Hanscom AFB, MA 01731-3010

Donald S. McClure
Department of Chemistry
Princeton University
Washington Road
Princeton, NJ 08544

Timothy McKelvey
Phillips Laboratory
OLAC PL/RKFE
Edwards AFB, CA 93524

Kiet Nguyen
Iowa State University
Wilhelm Hall #402, ISU
Ames, IA 50011

Robert A. Nichols
Phillips Laboratory
OLAC PL/RKAS
Edwards AFB, CA 93523

Lewis H. Nosanow
Department of Physics
University of California, Irvine
P-2, Room 4129
Irvine, CA 92717-4575

Takeshi Oka
Department of Chemistry
University of Chicago
5735 S. Ellis
Chicago, IL 60637

Mitchio Okumura
California Institute of Technology
Chemistry 127-72
Pasadena, CA 91125

Stephen O'Neil
JILA
MS 440
University of Colorado
Boulder, CO

Joseph N. Pfahler
APD Cryogenics, Inc.
1833 Vultee Street
Allentown, PA 18103

Douglas J. Raber
National Research Council
2101 Constitution Avenue, N. W.
Washington, D. C. 20418

Michael J. Redmon
Hughes STX Corporation
4400 Forbes Blvd
Lanham, MD 20706

Eric E. Rice
Orbitec
402 Gammon Place, Suite 10
Madison, WI 53719

Michael C. Robel
U.S. Army RD&E Center
Kansas Street
Attn: SATNC-MA
Matick, MA 01760-5036

Steven Rodgers
Phillips Laboratory
OLAC PL/RKFE
Edwards AFB, CA 93524

Marcy E. Rosenkrantz
University of Dayton Research Institute
OLAC PL/RKFE
9 Antares Road
Edwards AFB, CA 93524-7680

Roberta Saxon
SRI International
333 Ravenswood Avenue, Bldg. PN093
Menlo Park, CA 94025

Richard J. Saykally
Department of Chemistry
University of California, Berkeley
Berkeley, CA 94708

Henry F. Schaefer, III
Center for Computational
    Quantum Chemistry
University of Georgia
Athens, GA 30602

George M. Seidel
Department of Physics
Brown University
Providence, RI 02912

Isaac F. Silvera
Department of Physics
Harvard University
Cambridge, MA 02138

Jack Simons
Department of Chemistry
University of Utah
Salt Lake City, UT 84112-1194

Alan Snelson
IIT Research Institute
10 West 35th Street
Chicago, IL 60616

William C. Stwalley
Department of Chemistry
University of Iowa
Iowa City, IA 52242

P. K. Swaminathan
CPI/APL
Applied Physics Laboratory
Johns Hopkins Road, Bldg. 24, Rm. W164
Laurel, MD 20723

Timothy Thompson
Phillips Laboratory
OLAC PL/RKFE
9 Antares Road
Edwards AFB, CA 93524

Albert Y. Tong
Department of Mechanical Engineering
University of Texas, Arlington
Arlington, TX 76019

Donald D. Tzeng
United Technologies/CSD
P. O. Box 49028
San Jose, CA 95161-9028

James J. Valentini
Department of Chemistry
Columbia University
Box 766 Havemeyer Hall
New York, NY 10027

Gregory A. Voth
Department of Chemistry
University of Pennsylvania
Philadelphia, PA 19104-6323

Albert F. Wagner
Chemical Division
Argonne National Laboratory
10243 Hickory Drive
Orland Park, IL 60562

John E. Walker
U.S. Army Natick RD&E Center
Kansas Street
Attn: SATNC-YSM
Natick, MA 01760-5020

David Weaver
Phillips Laboratory
OLAC PL/RKFA
Edwards AFB, CA 93524

Scott Weidman
National Research Council
2101 Constitution Avenue, N. W.
Washington, D. C. 20418

Eric Weitz
Department of Chemistry
Northwestern University
2145 Sheridan Road
Evanston, IL 60208

Carl Wieman
Department of Physics
University of Colorado
Box 390
Boulder, CO 80309-0390

Charles A. Wight
Department of Chemistry
University of Utah
2424 HEB
Salt Lake City, UT 84112

E. J. Wucherer
University of Dayton Research Institute
OLAC PL/RKFA
Edwards AFB, CA 93524

David R. Yarkony
Department of Chemistry
Johns Hopkins University
Baltimore, MD 21218

Richard A. Yetter
Department of Mechanical
   & Aero Engineering,
Princeton University
D-312 Equad
Princeton, NJ 08544

Mark A. Young
Department of Chemistry
University of Iowa
Iowa City, IA 52242

AIR FORCE NEEDS, MISSION, GOALS & OPPORTUNITIES
Presentation at HEDM Conference
Woods Hole, 1993
Major David Lewis
OL-AC PL/RKF
8 Draco Drive, Edwards AFB CA 93524-7230

Developing and transitioning technology is a consistent thread in the tapestry of
the Air Force (AF) vision; and the AF, Air Force Materiel Command (AFMC),
Space and Missiles Systems Center (SMC) and Phillips Laboratory (PL) Mission
Statements. The formal process for developing and validating requirements is
systems oriented (planes, rockets, etc) and leads to Mission Need Statements
(MNSs). Operational tasks derive from national strategy (Strategy To Tasks)
and needs derive from the inability to do operational tasks correctly or an
opportunity to do tasks better (Tasks To Needs). One AF need, documented in a
draft MNS, is Spacelifter; perhaps the most pertinent to HEDM. Spacelifter
quality characteristics are that it must not only be capable (right payload to right
orbit) but also available and responsive (launch when you need to), affordable,
and maintainable and supportable (See figure 1).

There is a process set forth in the new AFMC Technology Master Process for
transitioning technology to the user (technology push) which involves Technical
Planning Integrated Product Teams (TPIPTs). All stakeholders (labs, users,
developers, planners) decide which technologies feed which systems within a 20
year horizon. Figure 2 shows an example of this process. The user's (usually
the AF organization that is responsible for deploying the end item), the system
program office (SPO's--the AF organization responsible for developing the item),
the Air Logistic Center's (ALC's--the AF organization responsible for maintaining
and upgrading the end item) and industry identify needs and opportunities. The
AF laboratories (Phillips Laboratory is one of four AF "super laboratories"),
Universities and industry are responsible for identifying and developing the right
technologies. The AFMC Technology Master Process then provides for proper
planning, programming, execution, transition and transfer of these needs,
opportunities and technologies into the appropriate weapon system
infrastructure that is supportable from cradle to grave.

The TPIPTs are concerned with technologies which feed systems within a 20
year horizon. However, transition of fundamental technologies such as HEDM
do not show up within that 20 year event horizon. What are the needs for
HEDM? The answers to that depends on who are HEDM's customers? Though
there are many, I argue that the engineering research/development community
is the most near term and therefore the most immediately important. I assert the
quality characteristic by which you measure yourselves must go beyond the
classic measure of the research community of scholarly research and be
pertinent to the customer, the engineer. Herein lies an opportunity for a

11

paradigm shift; that is to build a bridge between the two camps. Indeed, it is imperative if HEDM is to succeed that the scientist determine what the engineer needs. Quality Function Deployment (QFD) is one tool for relating what the engineer wants, in the engineer's language, to how a scientist can deliver that in the scientist's language. Only then does HEDM have a chance of moving from world class research to the next generation rocket system.

OPERATIONAL SPACELIFT CHARACTERISTICS

ALL SPACELIFT SYSTEMS MUST BE:

CAPABLE: DELIVER ALL PAYLOADS TO MISSION ORBIT SAFELY, IN A TIMELY MANNER, RELIABLY, AND ACCURATELY

AVAILABLE AND RESPONSIVE: BE OPERATIONALLY READY TO DEPLOY, SUSTAIN, AND AUGMENT ON-ORBIT FORCE STRUCTURE AS NEEDED

AFFORDABLE: HAVE SIGNIFICANTLY LOWER OPERATING COSTS THAN CURRENT SYSTEMS

MAINTAINABLE AND SUPPORTABLE: USE STANDARD AF DATA COLLECTION, PROCESSING, AND PARTS PROVISIONING

13

Technology
Master Process

Plan
Program
Execute
Transition
Transfer

Identify
Needs
and
Opportunities

Identify
and do
the "Right"
Technologies

User's
SPO's
ALC's
Industry

Laboratories
Universities
Industry

WEAPON SYSTEM
INFRASTRUCTURE

Grave

Cradle

14
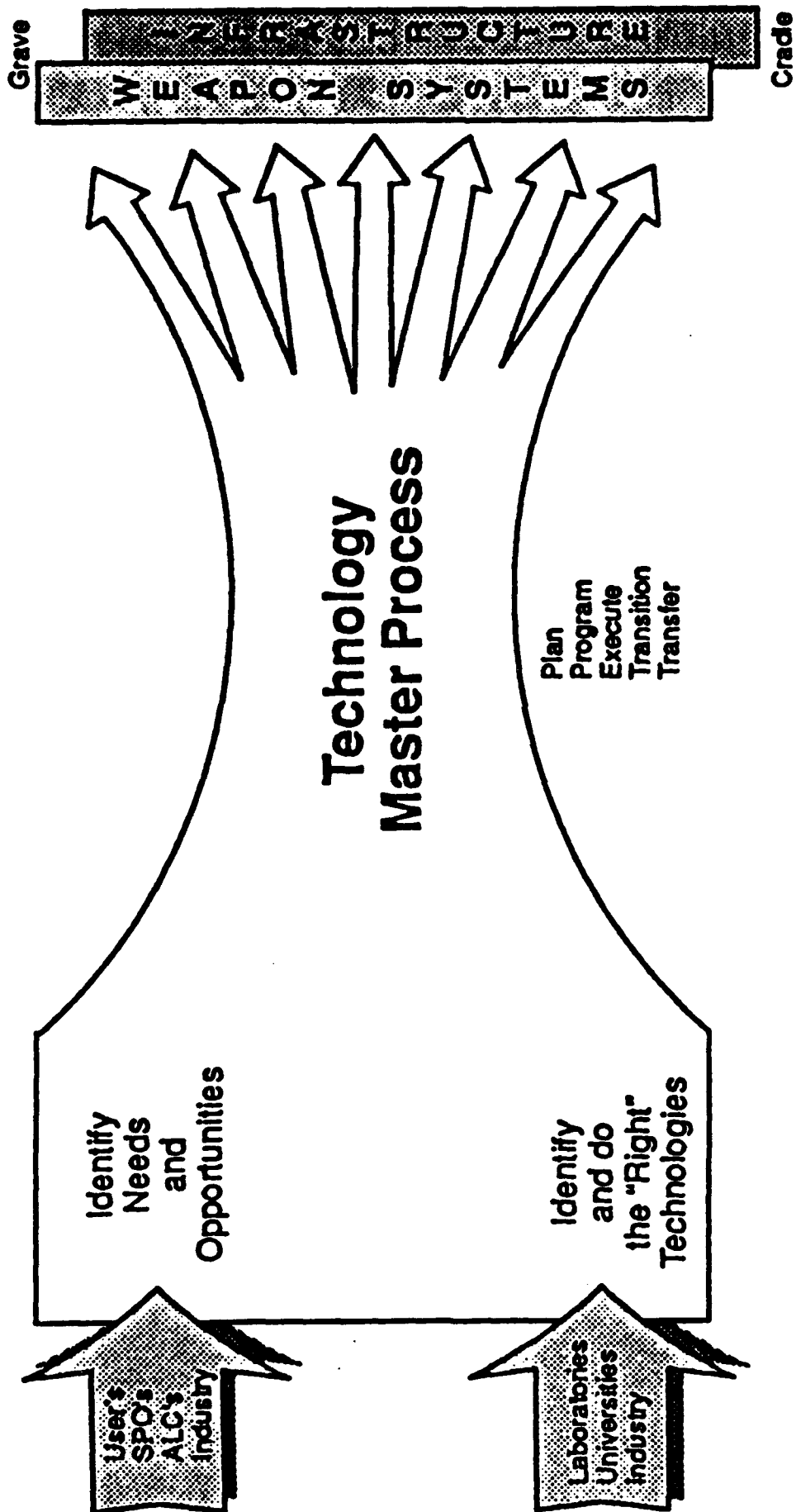
NASA HEDM Needs and Opportunities

Robert H. Frisbee
Jet Propulsion Laboratory
California Institute of Technology
Pasadena, California

This presentation discusses some of the general requirements that an advanced propulsion system must meet for application to NASA and civilian commercial missions, including those areas of commonality and difference between NASA and DoD requirements, and some examples of the types of benefits that could be realized from both near- and far-term HEDM propulsion concepts. Both NASA and DoD have generally similar requirements. The primary differences are in NASA's need for man-rating, high reliability, and for a long storage lifetime in space; by contrast, DoD's requirements include a need for high acceleration (for ballistic missile interceptors), rapid response time, and low vulnerability.

For all users, one of the most important requirements is the need to reduce the costs of access to space. For example, the cost of launching payloads into Earth orbit is comparable to that of the cost of gold on a $/kg basis. The potential for HEDM applications is in improving the vehicle performance by increasing the mass of the delivered payload for a given vehicle, or by improving performance such that a smaller and cheaper vehicle can be used.

HEDM applications could include relatively near-term chemical "additives" in existing propellants and vehicles for incremental improvements in performance, through far-term, totally new propellant combinations and vehicles for quantum improvements in performance. Note that near-term HEDM species used in existing systems could provide significant benefits to launch vehicles and upper stages and result in a potentially major impact to commercial users where launch costs are typically comparable to payload costs. For example, a near-term fuel or oxidizer HEDM compound added to the first-stage propellants (RP-1 and LOX) of the DELTA 7920 launch vehicle could increase the mass of payload delivered to low Earth orbit by 2 % for every 1 % increase in specific impulse. Far-term HEDM systems may enable ambitious space missions of the 21st century; for example, an advanced HEDM systems might give performance similar to that of a nuclear thermal propulsion (NTP) vehicle, but without the complexity of the nuclear power system. However, in order to realize these potential benefits, it will be necessary to develop HEDM systems that increase specific impulse without adversely impacting the vehicle "dry" mass, storage lifetime, response time, safety, cost, and so on, as well as meet any user-unique requirements (e.g., man-rating, etc.).

NASA HEDM NEEDS AND OPPORTUNITIES

Presented at the 1993 High-Energy Density Matter Contractors Meeting

Woods Hole MA

June 6, 1993

JPL

Robert H. Frisbee, Ph.D.
Propulsion and Chemical Systems Section

Jet Propulsion Laboratory
California Institute of Technology
Pasadena California

OUTLINE

JPL

- Introduction

- General Requirements

- NASA / DoD Areas of Common Interest

- Potential Benefits of HEDM

- Summary

JPL GENERAL REQUIREMENTS

- Generally Similar to DoD Requirements

  - Reduce Costs
    - Increase Payload Delivered, or
      Reduce Launch Costs

  - Improve Access to Space
    - More Frequent Launches
    - Launch More-or-Less On Demand

  - Improve Performance
    - Reduce Vehicle Size (Mass and Volume)
    - Increase Payload Mass
    - Increase Payload Injected Velocity
    - Increase System Operational Lifetimes

18

EXAMPLES OF COMMON REQUIREMENTS

AREA	COMMON	NASA-UNIQUE	DoD-UNIQUE
• All Missions	• Reduce costs • Improve performance	• Man-rated • Very high reliability	• Man-rated ? • Long storage time • Low vulnerability
• Launch Vehicles	• Low-to-moderate acceleration	• Somewhat on-demand (days) [SSF resupply] • Large (10-m dia.), heavy (>100 MT) payloads	• High accel. [SDI] • On-demand with very fast response (sec. - min.)
• Orbit Transfer (LEO/GEO) and Cis-Lunar Ops.	• Increase payload and ΔV, reduce trip time		• On-demand with moderate response (sec.[SDI] - hours)
• Lunar / Planetary		• Long storage time • Increase payload and ΔV, reduce trip time	

JPL LAUNCH VEHICLE COST A MAJOR DRIVER

PAYLOAD MASS TO 200 km CIRCULAR ORBIT (kg)

LAUNCH VEHICLE COST (FY'92 $ M)

20
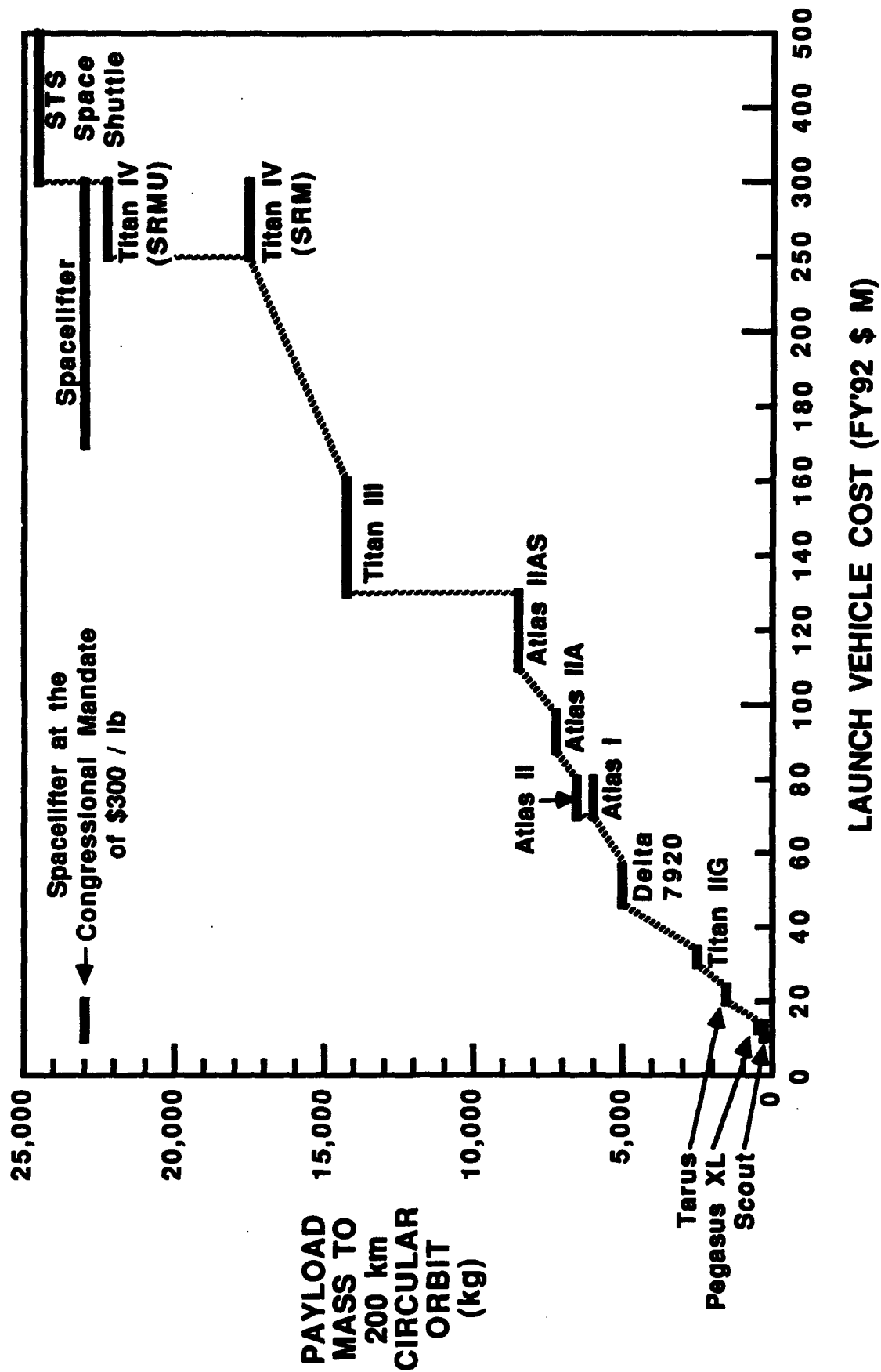
LAUNCH COSTS >$10M/MT ($10,000/kg) WITH EXISTING LAUNCH VEHICLES

JPL

PAYLOAD MASS TO 200 km CIRCULAR ORBIT (kg)

Spacelifter STS Space Shuttle
Titan IV (SRMU)
Titan IV (SRM)
Titan III
Atlas IIAS
Atlas IIA
Atlas II
Atlas I
Delta 7920
Titan IIG
Tarus
Pegasus XL   Scout

Spacelifter at the Congressional Mandate of $300 / lb

Gold at $ 400 / Troy Ounce
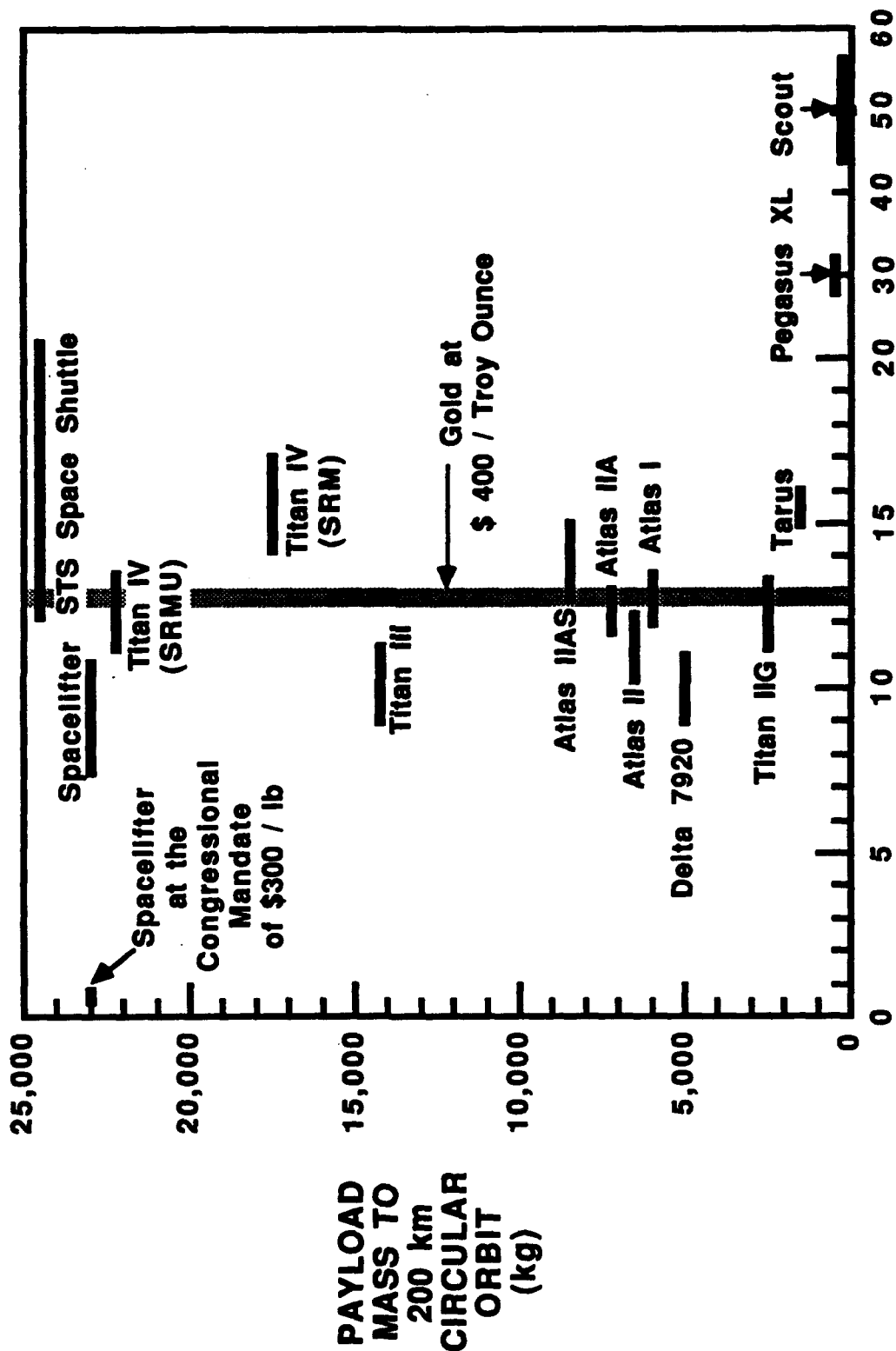
PAYLOAD LAUNCH COST (FY'92 $ M / METRIC TON OF PAYLOAD)
($ M / Metric Ton = $ 1,000 / kg = $ 454 / pound)

21

JPL

BENEFITS OF
ADVANCED PROPULSION

- Use advanced propulsion technology to reduce costs or to enable unique mission capabilities

  - Examples:

    - Increase payload delivered to reduce $ / kg

    - Provide unique capability by using advanced fission or fusion to enable 100-day round-trip manned Mars mission

- HEDM applications could include:

  - Near-term "additives" to existing propellants and vehicles for incremental improvements in performance

  - Far-term, totally new propellant combinations and vehicles for quantum improvements in performance

JPL — MODEST IMPROVEMENTS IN SPECIFIC IMPULSE CAN PROVIDE SIGNIFICANT SAVINGS

- Many of the near-term HEDM concepts can provide incremental improvements to Isp by acting as "additives" to existing propellants with minimal launch vehicle re-design

- Although not dramatic, even small improvements can result in significant savings by either reducing $/kg or by allowing the use of smaller, less expensive launch vehicles

EXAMPLE: DELTA 7920 DELIVERY TO LEO

VEHICLE	COST	PAYLOAD
Delta II 7920	$45-55M	5040 kg
Atlas I	$70-80M	5850 kg

PAYLOAD DELIVERED (kg): 5000, 5200, 5400, 5600

PERCENT INCREASE IN PAYLOAD: 0, 2, 4, 6, 8, 10

Baseline Delta II 7920

Stage 1 RP-1/LOX HEDM (+ 1 % Isp)

Stage 1 RP-1/LOX HEDM (+ 2 % Isp)

Stage 1 RP-1/LOX HEDM (+ 3 % Isp)

Stage 1 RP-1/LOX HEDM (+ 4 % Isp)

23
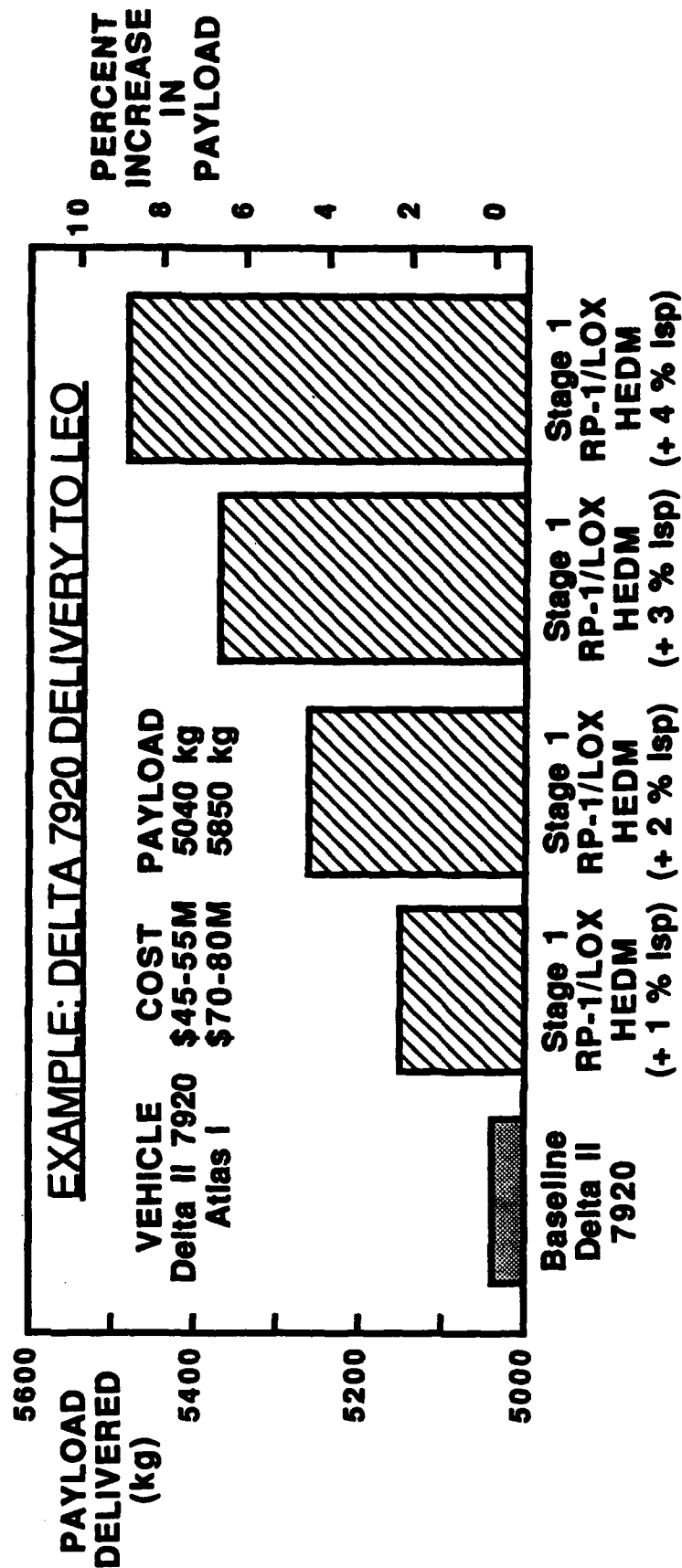
JPL   ADVANCED HEDM SYSTEMS CAN COMPETE DIRECTLY WITH NUCLEAR PROPULSION

- Advanced HEDM systems may give similar performance to nuclear thermal propulsion (NTP) but without the complexity of nuclear power

- High-density HEDM systems may allow the use of aerobraking (AB) to reduce mission ΔV - Can't aerobrake NTP vehicles due to large LH2 tanks and need for standoff distance from reactor

EXAMPLE: MARS CARGO MISSION

JPL

SUMMARY
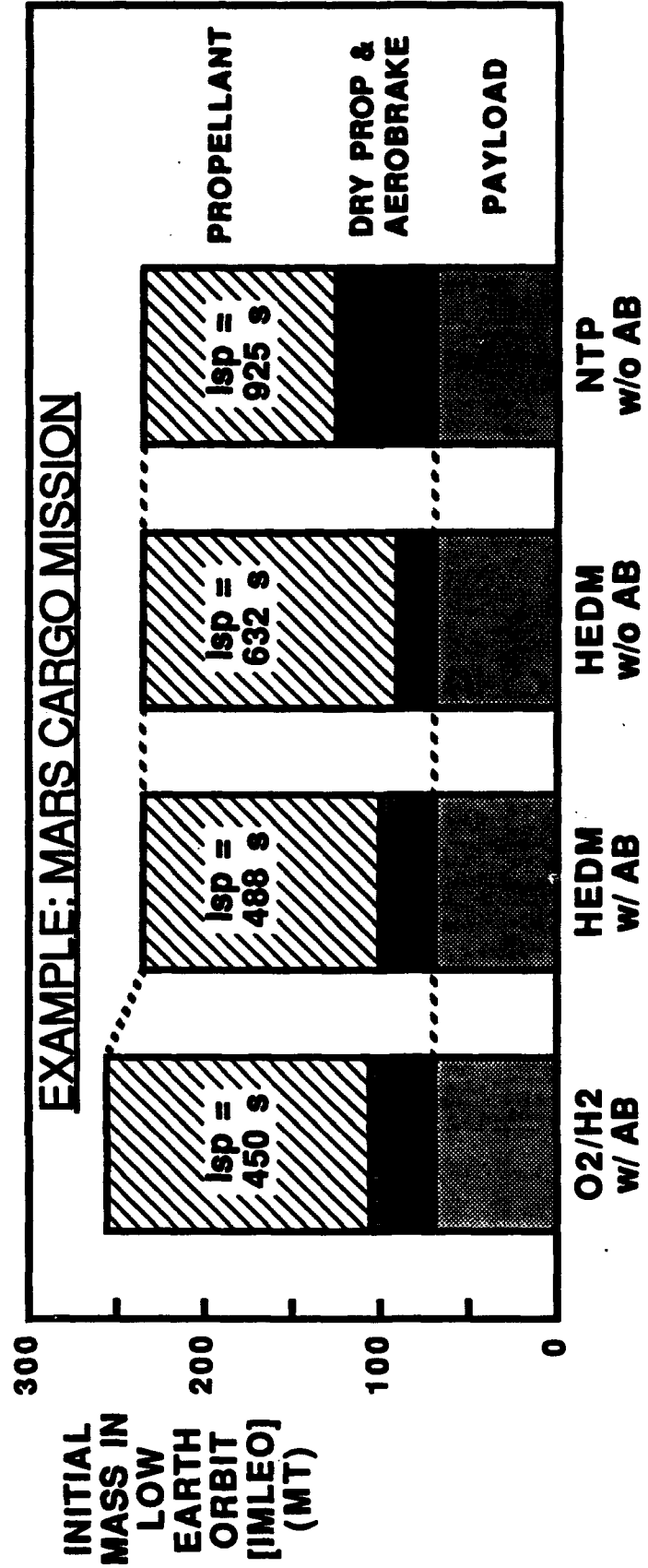
- NASA/Commercial and DoD general requirements similar

- Primary differences are:

  NASA: • Man-rating   DoD: • High accel. (SDI)
        • Reliability   • Fast response
        • Lifetime in space   • Low vulnerability

- Cost is a major driver to any operations in space

- Reduce cost by increasing payload delivered (less $/kg) or by using smaller launch vehicle

- Near-term HEDM "additives" used in existing systems can provide significant benefits to launch vehicles and upper stages

- Potential major impact to commercial users where launch costs are typically comparable to payload costs

- Advanced HEDM systems may enable ambitious space missions of the 21st century

- Ultimate goal is to develop HEDM systems that increase Isp without adversely impacting vehicle "dry" mass, storage lifetime, response time, safety, cost, etc.

Studies of Novel Metal Complexes:

Models of Metal-Seeded Energetic Materials

Michael A. Duncan

Department of Chemistry

University of Georgia

Athens, Georgia 30602

Light metals such as lithium, magnesium or aluminum are interesting as additives to pure component fuels to achieve advanced heterogeneous propellants. The high exoergicity of oxidation for metals such as these enhances propellant efficiency relative to the respective pure component systems. There is a significant interest, therefore, in the preparation of highly dispersed metal systems and in the fundamental chemical interactions in these systems. In our laboratory, fundamental interactions in highly dispersed metal systems are studied in the form of weakly bound metal complexes prepared and studied in the gas phase using molecular beam laser spectroscopy and mass spectroscopy methods.

Experiments over the last two years have focused on ion-molecule complexes containing the magnesium ion, Mg^+. Mg^+ has a simple electronic structure, and it has a strong electronic resonance line ($^2S \rightarrow {}^2P$) near 280 nm. Complexes containing Mg^+ condensed with small molecules are expected to absorb near this resonance line. However, the complexes will have characteristic spectral shifts and multiplet structure in their

electronic states depending on the details of the structure and bonding in the system. These details have been predicted with *ab initio* quantum chemistry calculations by Bauschlicher and coworkers. Therefore, calculations can be used to guide spectroscopic searches and to understand the spectra observed. The combined approach of theory and spectroscopy can provide considerable insight into the fundamental interactions in these systems, which will be useful in extrapolating to understand bulk condensed phased systems.

Initial experiments described at last year's contractor's meeting have examined complexes of Mg^+ with CO_2 and with H_2O. Both of these systems are observed to form ion-molecule complexes with reasonably strong bonding. As expected, vaporization of a magnesium sample in expansions containing these molecules produces an abundance of clusters. These clusters are mass selected and studied with laser photodissociation spectroscopy in a time-of-flight mass spectrometer system. The dissociation products are measured while the laser is tuned to obtain the photodissociation spectrum. Since last year we have completed the vibrational analysis in the two excited electronic states observed for the Mg^+-H_2O and Mg^+-D_2O complexes, and have identified all the vibrational modes in the system. We have also achieved partial rotational resolution in the analysis of the origin band of the lower $^2B_2$ electronic state. This analysis confirms that the complexes have the C_{2v} structure predicted by theory, and that the H-O-H angle is approximately 109°.

In other new work over the last year, we have tried to extend the study of magnesium ion complexes to additional systems with even weaker bonding. We have pursued new pulsed nozzle designs to achieve more extensive cooling in the complex systems, with the eventual goal of obtaining data for hydrogen complexes. As a result of these studies, we have been able to study some of the weakest bonded metal complexes yet investigated,

27

Mg^+-Ar and Mg^+-Kr. Both of these complexes have the same electronic state pattern we observed previously for the linear Mg^+-CO_2 complex. There is a $^2\Sigma^+$ ground state, and two excited states, $^2\Pi$ and $(2)^2\Sigma^+$, correlating to the Mg^+ (^2P) excited asymptote. We observe a highly structured spectrum for both complexes in the $X^2\Sigma^+\rightarrow^2\Pi$ transition. The photodissociation spectrum for Mg^+-Ar is shown in Figure 1. Vibrational frequencies and dissociation energies derived from these new spectra are given in Table 1, where they are compared to the data for the other magnesium complexes we have studied. Except for the Mg^+-D_2 complex recently reported by Stwalley and coworkers, the Mg^+-Ar spectrum is the most weakly bound metal ion system to be studied spectroscopically.

We have conducted similar photodissociation spectroscopy studies on the Mg^+-Kr complex. Its vibrational frequency is similar to that of the Mg^+-Ar complex, but its binding energy is greater, as expected based on its greater polarizability. The spin-orbit splitting value for the krypton complex is surprising, since it is greater than the value in the isolated Mg^+ ion (142 versus 92 cm^{-1}). In the other linear complexes which exhibit this spin-orbit splitting, its value is less than that in the isolated atom (i.e., Mg^+-CO_2:56 cm^{-1}; Mg^+-Ar:76 cm^{-1}).

In the magnesium ion complexes we have studied, the vibrational structure we measure is in the excited electronic state of the complex. However, theoretical calculations most often investigate the ground electronic state. We have therefore begun to develop a new spectroscopic technique which will probe the ground state of the metal complexes directly. Mass analyzed threshold ionization (MATI) is a newly discovered technique which is a variation of photoelectron spectroscopy. However, it is a "high resolution" technique, providing spectral bandwidths of a few cm^{-1}'s for typical spectra. MATI has been explored

28

for organic molecules and clusters, but it had not been demonstrated previously for a metal containing cluster or complex. We have now obtained the first example of a MATI spectrum for a metal complex in the form of Al-Ar. This spectrum is shown in Figure 2.

In the MATI experiment, ionization is achieved at threshold with a tunable dye laser. For Al-Ar, the ionization potential is about $5.8 \, eV$, which requires a tunable dye laser near $210 \, nm$. The MATI technique makes it possible to measure not only the initial appearance potential for the molecule, but also vibronic threshold in the corresponding cation. Excitation of the complex near the ionization potential populates highly excited Rydberg states of the neutral complex. These Rydberg states are available at each vibronic threshold in the system. A small DC electric field deflects ions formed directly by the laser. Highly excited neutral Rydbergs formed vanishingly close to a vibronic threshold are ionized by a time-delayed pulse electric field to form the MATI signal, which is then detected in the parent ion mass channel. There are many critical design parameters in the MATI experiment which affect the interpretation of the results. However, vibronic spectroscopy can be obtained with good resolution.

In the Al-Ar experiment, a short progression of lines is observed which are assigned to the Al^+-Ar stretching progression in its ground state. The frequency is $67 \, cm^{-1}$. The 1,1 sequence band allows determination of the frequency ($\Delta G_{1/2}$) for the Al-Ar neutral ground state ($39 \, cm^{-1}$). These data are the first ever for the ground state of a metal ion complex, and they compare favorably with theory, as indicated in Table 2.

Table 1. Spectroscopic constants of magnesium ion complexes studied with photodissociation spectroscopy.

Complex	$\omega_e'(Mg^+\text{-}L)$ (cm^{-1})		D_0'' (kcal/mol)		Structure
	Exp.	Theory[*]	Exp.	Theory[*]	
$Mg^+\text{-}CO_2$	382	359	14.7	16.4	Linear
$Mg^+\text{-}H_2O$	517	505	25.0	32.2	C_{2v}
$Mg^+\text{-}Ar$	272	-	3.6	3.25	Diatomic
$Mg^+\text{-}Kr$	258		5.8		Diatomic

[*] Bauschlicher and coworkers.

Table 2. Spectroscopic constants for Al-Ar and Al$^+$-Ar measured in MATI spectroscopy.

	This Work	Theory[a]	Prev. Exp.
Al-Ar			
ω_e'' (cm^{-1})	39 ($\Delta G_{1/2}$)	29	32[b]
D_0'' (cm^{-1})	-	121	122[c]
r_e'' (Å)	-	4.05	-
Al$^+$-Ar			
ω_e'' (cm^{-1})	67.4	76	-
D_0'' (cm^{-1})	-	921	982[c]
r_e'' (Å)	-	3.22	-

a Bauschlicher and coworkers.
b Hacket and coworkers.
c Morse and coworkers.

Figure 1.

^{24}MgAr$^+$

$^2\Sigma^+ \rightarrow ^2\Pi$

v′ 0 2 4 6 8 10 12 14

Intensity

Relative Frequency (cm^{-1})

0 600 1200 1800 2400 3000

Figure 2.

33
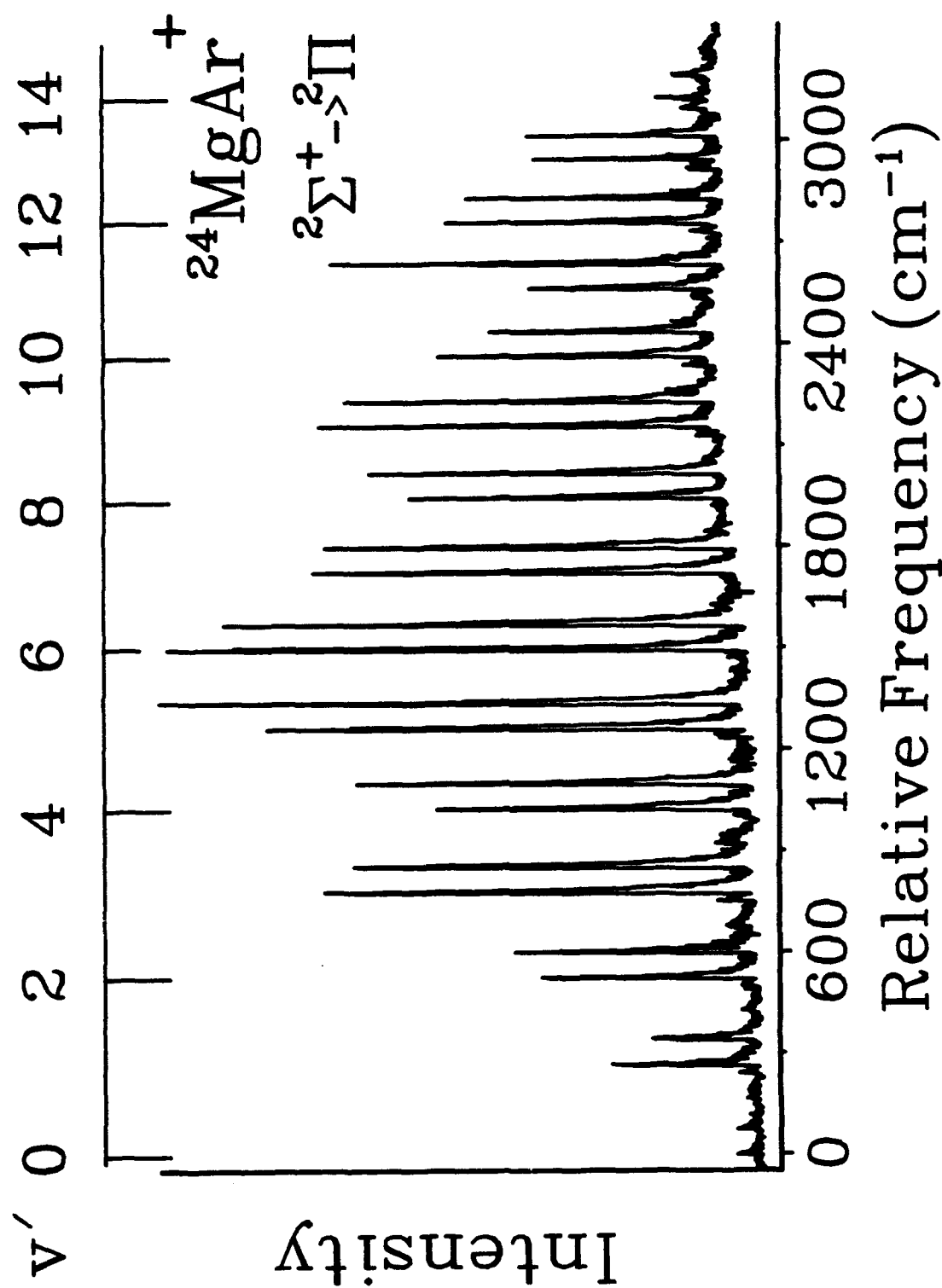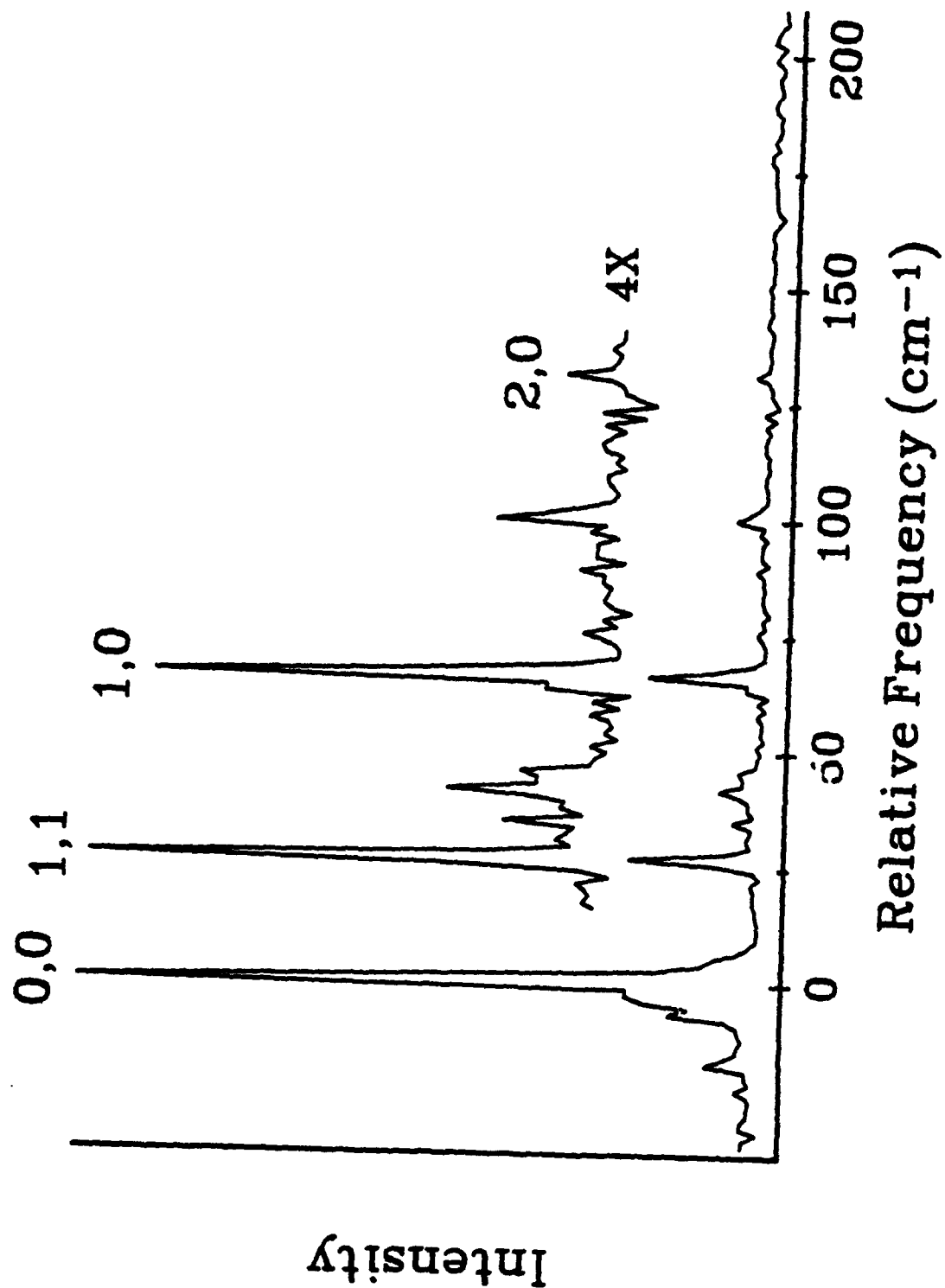
Photofragmentation of Magnesium Cluster Ion-Molecule Complexes

L. N. Ding, P. D. Kleiber, W. C. Stwalley, and M. A. Young

University of Iowa, Iowa City, Iowa 52242

Abstract

Magnesium cluster ion-molecule complexes (MgD_2^+, Mg_2^+, and $Mg_2CO_2^+$) are formed in a pulsed laser vaporization molecular beam source, mass selected and studied by laser photofragmentation spectroscopy in an angular reflectron-time-of-flight mass spectrometer. These spectroscopic techniques give information about the structure of the complex and the energy disposal dynamics including both reactive and nonreactive dissociation pathways. We describe recent results on three systems: (1) reactive fragmentation in MgD_2^+; (2) vector correlations in the photodissociation of Mg_2^+; and (3) photofragmentation dynamics in $Mg_2CO_2^+$.

I. Introduction

We report results from recent investigations of the photofragmentation of magnesium cluster ion-molecule complexes.[1-3] Cluster ions are formed in a laser vaporization source, mass selected, and studied by laser photodissociation spectroscopy in an angular reflectron time-of-flight mass spectrometer. These spectroscopic techniques give information about the structure and energy disposal dynamics in size selected molecular clusters. Ultimately, such studies on microscopic systems can form the basis for a more thorough understanding of the processes which govern electronic energy relaxation in the condensed phase.

Magnesium ions are selected as the core chromophore in our work for both theoretical and practical reasons. The relative simplicity of Mg^+ makes it possible to carry out high quality theoretical calculations. In addition, Mg_2^{++} has been suggested as a possible high energy density storage medium. The thrust of our work has been toward studies of complexes with a Mg_2^+ core. Here the core has significant internal structure which opens many additional interesting energy disposal pathways. In most cases the electronic transition dipole moment will be localized on the Mg_2^+ chromophore. It is then possible to excite states of different electronic symmetry, as well as vibrational and rotational degrees of freedom within the core, and to investigate these effects on the subsequent fragmentation dynamics. Following excitation of the complex, the dissociation may proceed through either breaking the (*intramolecular*) Mg-Mg bond, or the (*intermolecular*) Mg-ligand bond. The dissociation may be direct (as in cases where the laser accesses a purely repulsive electronic surface), or indirect (proceeding through electronic, vibrational, or rotational predissociation). In many cases reactive fragmentation channels may be accessible. It is also

possible to directly pump a purely repulsive electronic state of the Mg_2^+ core, driving the metal atom or atomic ion into the molecular adduct, and to study the subsequent chemistry under conditions of well-defined geometry, angular momentum, and energy. Caging of the Mg atom in the binary complex may be important in some systems. Examples of many of these processes will be given in the following discussion.

We describe below recent results from our spectroscopic studies on three systems:[1-3] reactive fragmentation in MgD_2^+; observation of vector correlations in the photodissociation of bare Mg_2^+; and caging and competitive branching in the photofragmentation of $Mg_2CO_2^+$.

II. Experimental

The experimental details have been given previously.[1-3] We use standard laser vaporization techniques to generate the magnesium cluster ion-molecule complexes. The supersonic expansion is initiated by a carrier gas pulse from a supersonic valve. The gas pulse flows over the Mg target rod, and through an extension channel where cooling and clustering occurs. In some experiments the extension channel is in thermal contact with a liquid nitrogen reservoir and is cooled to $\sim 100K$ to enhance the formation of weakly bound complexes.

The second harmonic of a pulsed Nd:YAG laser is focused onto the Mg target rod and timed to hit the rod near the middle of the carrier gas pulse. We use interchangeable source blocks and two different geometries have been tested: in the "longitudinal" source the vaporization laser counterpropagates through the gas flow channel to strike the Mg rod which is inserted directly into the flow channel;[4] the "transverse" source is of the standard Smalley-type design.[5]

Downstream from the nozzle the molecular beam passes through a skimmer into the extraction chamber. Ions are pulse extracted at right angles into a differentially pumped drift chamber which houses the reflectron assembly. The extraction and acceleration voltages are adjusted to achieve Wiley-McLaren space focusing conditions. Ions are mass selected with a pulsed mass gate focused into the reflectron.

A tunable, frequency-doubled pulsed dye laser is time delayed to "probe" the "target" parent ion at the turning point in the reflectron. Following fragmentation, parent and daughter ions are reaccelerated back into the flight tube and detected by a microchannel plate detector. A digital oscilloscope and gated integrators are used to monitor the mass spectrum. Two types of measurements are carried out. The time-of-flight mass spectrum can be measured at a fixed probe laser wavelength. Alternatively, the detection system may be gated to collect a selected daughter ion as a function of wavelength yielding a fragmentation "action" spectrum.

III. Results

A. Reactive Photofragmentation in MgD_2^+

We report studies of chemical reaction and photofragmentation of isolated MgD_2^+ ion-molecule complexes.[1] ($^{24}MgD_2^+$ was chosen over $^{24}MgH_2^+$ for reasons of experimental convenience in assigning the mass spectrum.) The photofragmentation process may be schematically described as;

$$MgD_2^+ + h\nu_1 \longrightarrow (MgD_2^+)^* \qquad \text{(excitation)}$$

followed by

$$(MgD_2^+)^* \longrightarrow MgD^+ + D \qquad \text{(reaction)} \qquad (1)$$

$$\longrightarrow Mg^+ + D_2 \qquad \text{(predissociation)} \qquad (2)$$

$$\longrightarrow Mg^+ + D_2 + h\nu_2 \qquad \text{(radiative dissociation)} \qquad (3)$$

$$\longrightarrow (Mg^+)^* + D_2 \qquad \text{(direct photodissociation)} . \qquad (4)$$
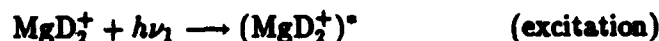
We have observed reproducible molecular absorption bands to the red of the $Mg^+(3^2S - 3^2P)$ resonance transition in the spectral region from $280\,nm - 315\,nm$. In this spectral range, $^{24}MgD^+$ is the only fragment daughter ion clearly observed corresponding to the reactive channel (1) above. Remarkably, the reactive action spectrum shows significant structure (Fig. 1). The spectrum consists of a broad continuum with overlapping sharp discrete resonances showing a clear vibrational progression, suggesting two reaction mechanisms: a direct (rapid) and an indirect (slow) pathway.

We tentatively assign the observed molecular spectrum to the perpendicular $1^2B_2, 1^2B_1 \leftarrow 1^2A_1$ electronic transitions in C_{2v} geometry. We assign the continuum background to the transition $1^2B_2 \leftarrow 1^2A_1$. Based on previous studies of reactions in other metal-atom-H_2 systems,[6] and on the ab initio calculations of Bauschlicher[7] on MgH_2^+, we propose that reaction on the $MgD_2^+(1^2B_2)$ surface can proceed directly and rapidly, probably through metal-ion insertion into a $D-Mg^+-D$ transition state.

Superimposed on this continuum background we can clearly identify a vibrational progression in the excited state with decreasing spacings from 489 to $314\,cm^{-1}$. The $\Delta G_{v'+1/2}$ values are quite consistent with the expected value ($\omega_e \simeq 588\,cm^{-1}$) for the $^2B_1$ state predicted in the theoretical ab initio calculations of Bauschlicher.[7] The observed anharmonicity yields an estimate for $\omega_e x_e \simeq 14\,cm^{-1}$.

There is also distinct substructure within each member of the progression; this can be plausibly assigned to K sub-band structure in the $1^2B_1 \leftarrow 1^2A_1$ perpendicular electronic excitation,

36

due to rotational transitions $K_{a''} = 0 \to K_{a'} = 1$ in ortho-, and $K_{a''} = 1 \to K_{a'} = 0, 2$ in para-MgD_2^+ respectively. These resonances exhibit widths of $\gtrsim 20\,cm^{-1}$. The observed widths put a lower limit on the lifetime of these states of $\sim 0.3\,ps$, corresponding to an intermediate state lifetime greater than ~ 3 vibrational periods. This indirect reaction mechanism may occur through weak-coupling of the 1^2B_1 state to the 1^2B_2 state.

Based on our tentative assignment of the K sub-band structure we can estimate values (A'' and A') for the a-axis rotational constants in the ground (1^2A_1) and excited (1^2B_1) states respectively. The a axis corresponds to the C_2 symmetry axis, i.e., to the axis of the minimum moment of inertia. The experimental values are $A'' = 34 \pm 4\,cm^{-1}$ and $A' = 32 \pm 4\,cm^{-1}$, both in reasonable agreement with the theoretical predictions of Bauschlicher[7] [$A'' = 30.0\,cm^{-1}$ and $A' = 29.3\,cm^{-1}$].

B. Vector Correlations in the Photodissociation of Mg_2^+

We have observed photodissociation of Mg_2^+ via the lowest repulsive $1^2\Sigma_g^+$ state. The process may be described as:

$$Mg_2^+(1^2\Sigma_u^+) + h\nu(\approx 630\,nm) \to Mg_2^{+*}(1^2\Sigma_g^+) \to Mg^+(3s\,^2S) + Mg(3s^2\,^1S) \qquad (5)$$
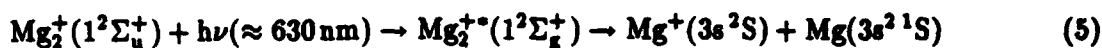
(Fig. 2). The photodissociation action spectrum consists of a broad structureless continuum ranging from 580 nm to 690 nm.

We have carried out spectral simulations based on the theoretical ab initio potential energy curves of Sodupe et al.[8] The calculated spectrum has an overall shape similar to the experimental profile but with the peak shifted $\sim 50\,nm$ to longer wavelengths. To obtain a better spectral fit, we slightly modified the repulsive wall of the $1^2\Sigma_g^+$ state; the adjusted repulsive potential is shown as the dashed curve in Fig. 2. With this change, we obtain the excellent agreement with the observed spectrum.

The observed Mg^+ daughter ion TOF spectrum is shown in Fig. 3 for two different orientations of the probe laser polarization with respect to the plane of the ion trajectory. The characteristic structure demonstrates a correlation between the laser polarization vector ($\hat{E}$), the transition dipole moment ($\hat{\mu}$), and the recoil velocity vector ($\hat{v}$).[9]

The photofragment angular probability distribution function, W, will be of the form

$$W(\theta, \chi) = \frac{1}{4\pi} \left[1 + \beta(\chi) P_2(\cos(\theta)) \right] \qquad (6)$$

where $\beta(\chi) = 2P_2(\cos(\chi))$. In Eq. (6), θ is the angle between the dissociation laser polarization vector ($\hat{E}$) and the recoil velocity vector ($\hat{v}$) of the daughter ions, and β is the anisotropy parameter (where χ is the angle between the transition dipole moment ($\hat{\mu}$) and the recoil velocity vector ($\hat{v}$)).

For this example the transition dipole is parallel to the internuclear axis ($\Sigma - \Sigma$, $\Delta\Lambda = 0$). Further, the dissociation will be fast relative to the time scale for molecular rotation. In this case the axial recoil approximation will be valid and β will take on the limiting value $\beta = +2$.

The resulting anisotropic velocity distribution will be apparent in the fragment ion flight time profile. We expect a splitting in the velocity distribution (i.e., the flight time distribution), which we indeed observe experimentally, as shown in the left-hand trace of Fig. 3(a). The distinct peaks in Fig. 3(a) essentially represent fragments with initial center of mass velocities either directly toward or directly away from the detector. The peak-to-peak time separation is related to the fragment recoil velocity, and hence the kinetic energy release.

Fitting the TOF spectrum enables us to determine the magnitude of the recoil velocity in the fragment center-of-mass frame, and to verify the value of the anisotropy parameter. We note that most of the flight time separation between the peaks occurs during the acceleration phase inside the reflectron assembly. The electric field is nearly constant over a well-defined length and simple kinematics arguments can be used to accurately relate the flight time to the recoil velocity and, hence, the recoil energy. The experimental TOF distribution is not as sharp, of course, as that predicted by the basic theory. The finite width of the experimental spectrum is due to the spatial and temporal spread of the parent ion packet, and the finite spatial overlap between the laser and the parent ion packet in the reflectron. These systematic effects can be taken into account by convoluting the predicted distribution with an apparatus function, chosen to be a Gaussian with an adjustable width. The simulated fit to the flight time distribution for a particular value of the wavelength is shown in the right-hand trace in Fig. 3(a). Also shown in Fig. 3(b) are the observed and simulated TOF distributions for the dissociation laser polarized perpendicular to the detector axis ($E \perp k$). This fitting procedure is carried out at several wavelengths. The calculated kinetic energy release varies across the photodissociation spectrum from $E \approx 4,100\,\mathrm{cm}^{-1}$ at $\lambda = 680\,\mathrm{nm}$ to $E \approx 7,100\,\mathrm{cm}^{-1}$ at $\lambda = 590\,\mathrm{nm}$.

From Fig. 2 it is clear that (neglecting the small amount of internal energy) the binding energy D_0'' for the $1\,^2\Sigma_u^+$ ground state can be related to the recoil energy E by

$$D_0'' = h\nu - E . \tag{7}$$

The binding energy thus calculated is fairly constant over the spectrum with a mean value of $D_0'' \approx 10,200\pm300\,\mathrm{cm}^{-1}$. Our experimental result is in good agreement with the theoretical ab initio results of both Durand et al.[11] ($D_0'' \simeq 9,600\,\mathrm{cm}^{-1}$) and Sodupe et al.[8] ($D_0'' \simeq 10,400\,\mathrm{cm}^{-1}$).

The maximum value of the observed anisotropy, $\beta = 2$, holds across much of the spectrum ($\lambda \leq 620\,\mathrm{nm}$, $\lambda \geq 660\,\mathrm{nm}$) and indicates a "clean" fragmentation process through channel (5). Remarkably, however, in the middle region of the spectrum ($\lambda \sim 620-660\,\mathrm{nm}$), the best fit

β differs significantly from the expected extreme value. This presumably indicates an alternate photodissociation channel.

Perhaps the most reasonable explanation for the competing channel involves photodissociation of bound metastable $Mg_2^+(1\,^2\Pi_u)$. If $Mg_2^+(1\,^2\Pi_u)$ is formed in the laser vaporization source it should be quite long-lived. If it survives into the reflectron, we may observe the photodissociation channel

$$Mg_2^+(1\,^2\Pi_u) + h\nu(\sim 640\,nm) \rightarrow Mg_2^+(2\,^2\Sigma_g^+ \text{ or } 1\,^2\Pi_g) \rightarrow Mg^+(3s\,^2S) + Mg^*(3p\,^3P) . \qquad (8)$$
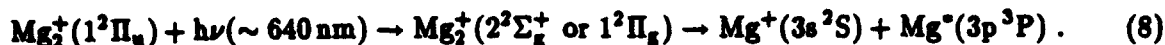
The $\Delta\Lambda = -1$ transition to the $2\,^2\Sigma_g^+$ state continuum could explain the apparent anomaly in the anisotropy parameter in this region.

C. Photofragmentation Dynamics of $Mg_2CO_2^+$

We report the photofragmentation spectroscopy of $Mg_2CO_2^+$ in the visible region of the spectrum ($425\,nm < \lambda < 725\,nm$).[3] Two molecular absorption bands are observed: a red band ranging from $\sim 630\,nm$ to $\sim 725\,nm$ (Fig. 4) and a green band ranging from $\sim 530\,nm$ to $\sim 568\,nm$ (Fig. 5). In each band both Mg^+ and Mg_2^+ daughter fragments are clearly observed, although with different action spectra. The photodissociation process may be schematically described as

$$Mg_2CO_2^+ + h\nu \longrightarrow (Mg_2CO_2)^{+*}$$

followed by,

$$(Mg_2CO_2)^{+*} \longrightarrow Mg^+ + Mg + CO_2 \text{ (or } MgCO_2, \text{ or } MgO + CO) \qquad (10)$$

$$(Mg_2CO_2)^{+*} \longrightarrow Mg_2^+ + CO_2 . \qquad (11)$$
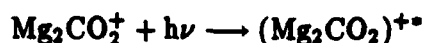
Based on the theoretical calculations of Sodupe et al.[8] we tentatively assign the red band as $1\,^2\Pi \longleftarrow 1\,^2\Sigma^+$, and the green band as $2\,^2\Sigma^+ \longleftarrow 1\,^2\Sigma^+$, in a linear $Mg_2CO_2^+$ complex.

In the red band, both the Mg^+ and Mg_2^+ fragment action spectra show a series of weak discrete peaks with spacings of approximately $35\,cm^{-1}$, superimposed on a strong, broad continuum. These results suggest two fragmentation mechanisms: a weak, slow (indirect), and a strong rapid (direct) pathway.

The red band transition, $1\,^2\Pi \longleftarrow 1\,^2\Sigma^+$, is to an excited state surface which correlates in bare Mg_2^+ to a deeply bound, metastable state (Fig. 2). Given this assignment we might explain the observed Mg_2^+ daughter ion as resulting from vibrational predissociation of the complex. Initial vibronic excitation in the Mg_2^+ chromophore could couple to the intermolecular $Mg_2^+ - CO_2$ bends and stretches, and, hence, break the intermolecular bond. However, the observed vibrational spacings are very low in frequency ($\sim 30-40\,cm^{-1}$), and show a negligible anharmonicity. This suggests that these resonance features are more likely due to the low frequency intermolecular vibrational

modes (probably the $Mg_2^+ - CO_2$ bend), rather than any of the higher frequency intramolecular modes.

The vibrational structure in both Mg^+ and Mg_2^+ channels is quite weak in comparison to the underlying continuum and was only apparent after extensive signal averaging (Fig. 4). This suggests the coupling from the bending mode to the dissociation coordinate (which presumably involves the $Mg_2^+ - CO_2$ stretch), may be weak and inefficient. This suggestion is supported by the resonance widths which give a lower limit on the complex lifetime of ~ 3 ps.

In both the Mg^+ and Mg_2^+ action spectra the dominant feature is the broad continuum, indicative of a rapid dissociation pathway. We believe the fragmentation may occur through electronic predissociation, perhaps on an inner wall $1^2\Pi - 1^2\Sigma^+$ surface crossing induced by the presence of the CO_2. This process must be accompanied by efficient E-V,R energy transfer or the fragments would be translationally hot. If sufficient energy is transferred to the CO_2 fragment, the Mg-Mg^+ products may relax into bound vibrational levels of the $Mg_2^+(1^2\Sigma_u^+)$ ground electronic state. The above discussion is speculative in nature, and is meant primarily to stimulate more detailed theoretical calculations of the relevant $Mg_2CO_2^+$ potential energy surfaces and the dynamics thereupon.

The green band (Fig. 5) has been assigned as the parallel transition $2^2\Sigma^+ \longleftarrow 1^2\Sigma^+$ in $Mg_2CO_2^+$, to an excited state surface which correlates with the purely repulsive $1^2\Sigma_g^+$ state of bare Mg_2^+. This agreement is consistent with the observation that the Mg^+ fragmentation channel dominates over the Mg_2^+ channel. The weak Mg_2^+ daughter ion signal can be rationalized as the result of caging[12] by the CO_2 partner in the complex, i.e., the Mg atom fragment impulsively transfers its kinetic energy to the CO_2 molecule before the fragments have separated appreciably. Note that the linear geometry of the $Mg_2CO_2^+$ complex[8] should enhance the caging. In many respects our green band results are similar to those of Lineberger and co-workers on the photodissociation of $X_2(CO_2)_n^-$ clusters ($X = Br,I$).[12] In both cases the photodissociation proceeds through a state which correlates with a purely repulsive electronic state of the active chromophore. However, in $X_2(CO_2)_n^-$, it was found that more than one CO_2 molecule was necessary to observe the cage effect. In our work the observation of Mg_2^+ from the parent $Mg_2CO_2^+$ implies that one CO_2 is sufficient to cause an observable caging. The observed difference in behavior may simply be a relative mass effect and reflect the efficiency of the energy transfer process. Both Br and I are significantly heavier than CO_2 while Mg is much lighter and therefore more easily "reflected". Also, the differences in the potential interactions of the halogen anions and the Mg^+ cation with CO_2 may play a role. Note also in Fig. 5 that the peak in the action spectrum for the Mg_2^+ fragment is redshifted relative to the corresponding peak in the Mg^+ action spectrum, suggesting that the caging is more effective with less excess photon energy. This observation is consistent with the conclusion drawn by Lineberger and co-workers that the caging mechanism operative in small clusters appears to be

controlled primarily by the photon energy, which correlates with the kinetic energy of the nascent atoms.

Acknowledgments

References

[1] L. N. Ding, M. A. Young, P. D. Kleiber, W. C. Stwalley, and A. M. Lyyra, J. Phys. Chem. 97, 2181 (1993).

[2] L. N. Ding, P. D. Kleiber, M. A. Young, W. C. Stwalley, and A. M. Lyyra, Phys. Rev. A (in press).

[3] L. N. Ding, M. A. Young, P. D. Kleiber, and W. C. Stwalley, Chem. Phys. Lett. (submitted).

[4] D. E. Lessen and P. J. Brucat, J. Phys. Chem. 90, 6296 (1989).

[5] T. G. Dietz, M. A. Duncan, D. E. Powers, and R. E. Smalley, J. Phys. Chem. 74, 6511 (1981).

[6] S. Bililign, P. D. Kleiber, W. R. Kearney, and K. M. Sando, J. Chem. Phys. 96, 213, 218 (1992); and references therein.

[7] C. W. Bauschlicher, Jr., Chem. Phys. Lett. 201, 11 (1993).

[8] M. Sodupe, C. W. Bauschlicher, Jr., and H. Partridge, Chem. Phys. Lett. 192, 185 (1992).

[9] P. L. Houston, J. Phys. Chem. 91, 5388 (1991).

[10] D. M. Szaflarski, R. van den Berg, and M. A. El-Sayed, J. Chem. Phys. 93, 6700 (1989).

[11] G. Durand, J. P. Daudey, and J. P. Malrieu, J. Physique 47, 1335 (1986).

[12] M. L. Alexander, N. E. Levinger, M. A. Johnson, D. R. Ray, and W. C. Lineberger, J. Chem. Phys. 88, 6200 (1988); J. M. Papanikolas, J. R. Gord, N. E. Levinger, D. R. Ray, V. Vorsa, and W. C. Lineberger, J. Chem. Phys. 95, 8028 (1991).
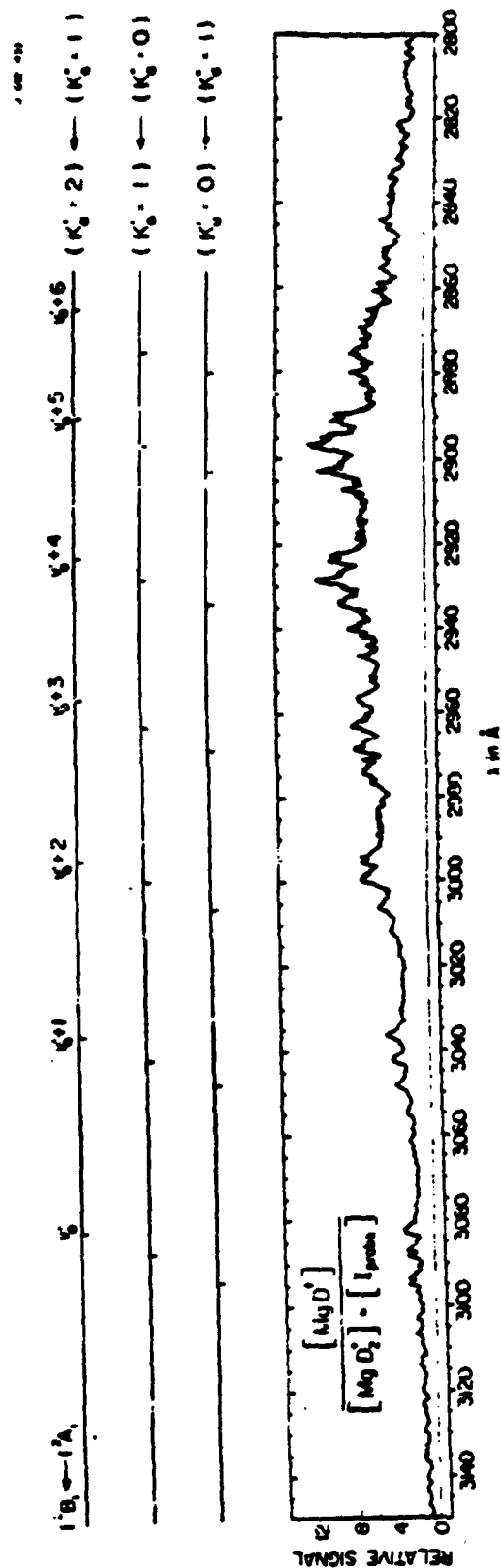
Fig. 1. Reactive action spectrum for MgD_2^+.
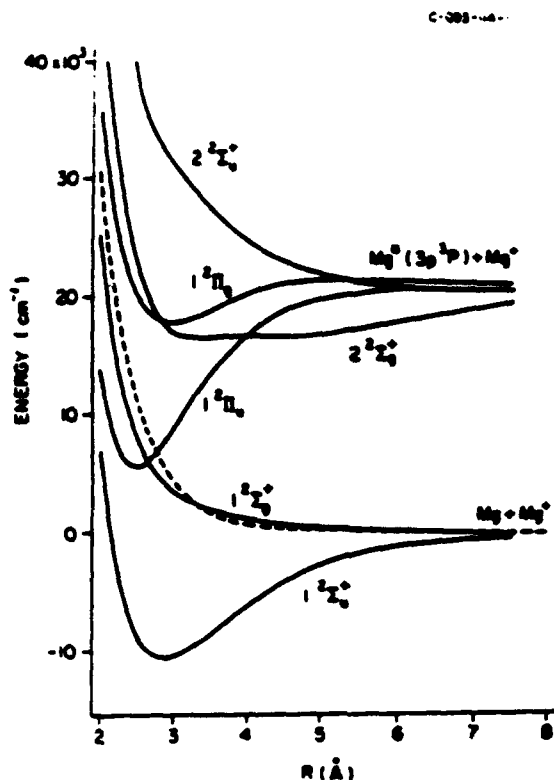
Fig. 2. Theoretical ab initio potential curves of Mg_2^+ taken from Ref. 7.
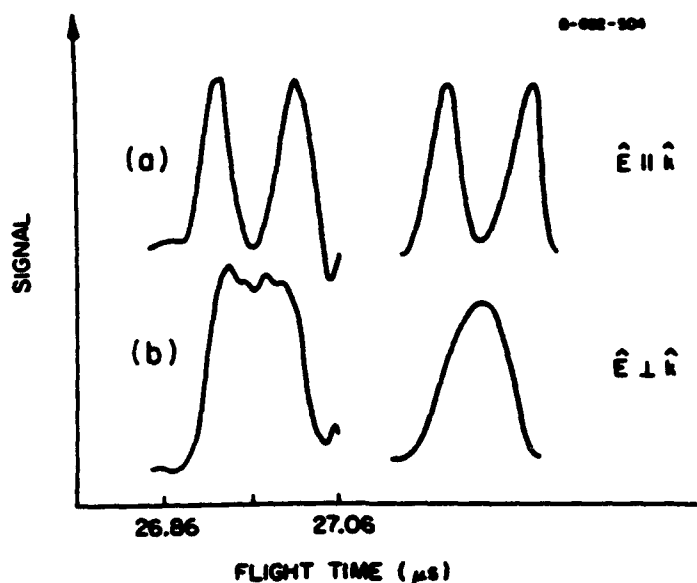
Fig. 3. (a) Experimental Mg^+ TOF spectrum (left), and the simulation (right) for E parallel to k.
(b) Experimental Mg^+ TOF spectrum (left), and the simulation (right) for E perpendicular to k. In each case the probe laser $\lambda = 618\,nm$.
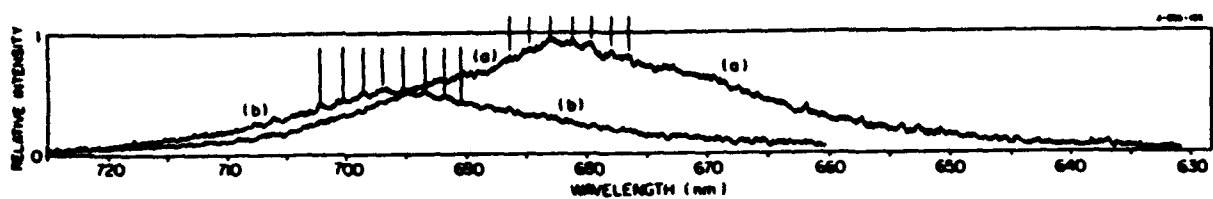
Fig. 4. Photodissociation action spectrum of $Mg_2CO_2^+$ in the red band leading to (a) Mg^+ and (b) Mg_2^+.
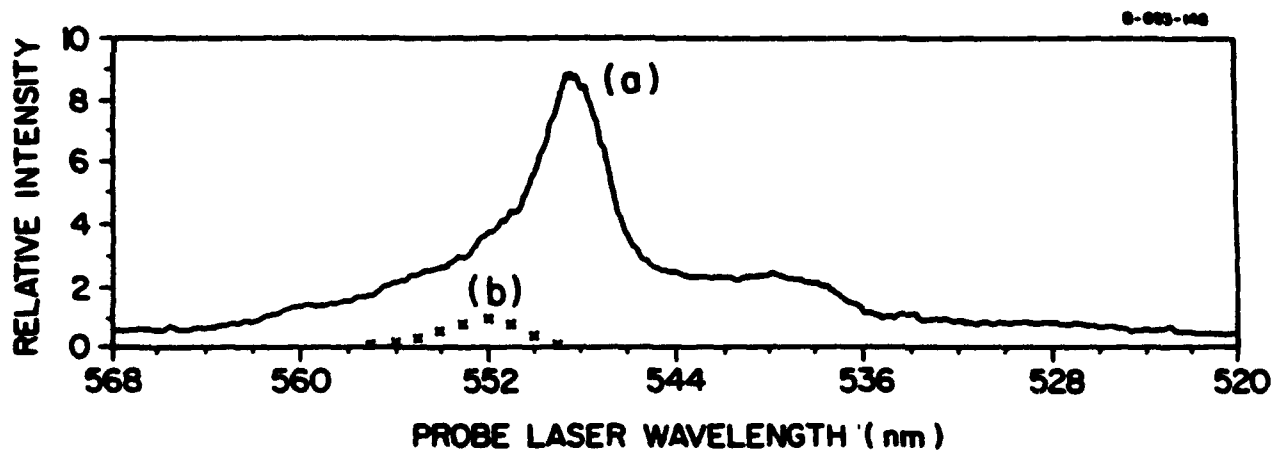
Fig. 5. Photodissociation action spectrum of $Mg_2CO_2^+$ in the green band leading to (a) Mg^+ and (b) Mg_2^+.

Spectroscopy and Bonding in the Excited States of B$_2$

C.R. Brazier, P.G. Carrick and M.E. Cordonnier

Propulsion Directorate
Phillips Laboratory /RKFE
Edwards AFB, CA 93524-7680

Boron chemistry continues to be of interest in the search for high performance propellants [1]. The large heat of combustion and the low atomic mass contribute to the interest in boron and boron-containing compounds as high energy density fuels [2]. The potential use of atomic boron isolated in cryogenic solid hydrogen as a rocket propellant [3] necessitates the continued study of small boron and boron/hydrogen molecules. In particular, B$_2$ is expected to be a major byproduct of boron atom deposition into solid hydrogen. In addition diatomic species may be less susceptible to reaction at the high doping densities required for a real fuel. Calculations for diatomic boron show a 100 sec improvement in I$_{sp}$ for 5 mole % of B$_2$ in solid H$_2$ compared to LOX/H$_2$ at optimum oxidizer concentration [3].

Experimental studies of the boron diatomic molecule extend back to 1940 with the observation by Douglas and Herzberg [4] of an electronic transition in the ultraviolet labeled $^3\Sigma_u^- - X^3\Sigma_g^-$. This was the only band system known until the beginning of the present study. In our initial survey of the visible and ultraviolet spectral emission from a Corona Excited Supersonic Expansion of diborane seeded in helium, we clearly identified three new electronic band systems in addition to the Douglas-Herzberg band. One system had previously been observed by Bredohl et al. [5] and assigned to transitions originating from v=0 of this $^3\Sigma_u^-$ state and terminating at high vibrational levels of the ground state. This assignment was clearly incorrect as the branches did not show the intensity alternation expected for a Σ-Σ transition of a homonuclear diatomic molecule. Observation of spin structure and a weak Q branch indicated that this was a $^3\Pi$-$^3\Pi$ transition, and by comparison with theoretical calculations [6] it was assigned as (2)$^3\Pi_g$-A$^3\Pi_u$. This result and an analysis of the two other new bands (2)$^3\Pi_u$-(1)$^3\Pi_g$ and (1)$^1\Delta_u$-b$^1\Delta_g$ were published recently [7].

The (2)$^3\Pi_g$-A$^3\Pi_u$ system showed clear evidence of perturbations which were hard to identify at the 1 cm^{-1} resolution of the 1.3 m monochromator/OMA system used to record the original spectra. High resolution spectra of this system were obtained using the

·1m FTS at Kitt Peak National Observatory. Additional spectra have been recorded recently using the monochromator system, leading to the identification of three more new band systems assigned as $(1)^3\Pi_g\text{-}A^3\Pi_u$, $(1)^1\Sigma_u^+\text{-}c^1\Sigma_g^+$ and $(1)^3\Delta_g\text{-}A^3\Pi_u$. Two other $\Pi\text{-}\Sigma$ systems have been identified but definitive assignments are not yet available. The discussion here will be limited to analysis of the high resolution data for the $(2)^3\Pi_g\text{-}A^3\Pi_u$ system and the three new bands assigned recently.

The $(2)^3\Pi_g\text{-}A^3\Pi_u$ System

The analysis of this system is described in detail in a forthcoming paper [8] and will only be described briefly here. The $(2)^3\Pi_g\text{-}A^3\Pi_u$ system consists of a clear progression of blue degraded bands with the 0-0 band readily identifiable. Additional bands coming from v'=0 were found up to 0-4 with the strongest band in the progression being 0-1. The 0-0 and 0-1 bands are shown in Fig. 1. An additional progression assigned to bands originating in v'=1 was observed weakly with the 1-0 and 1-3 components being the strongest. From this preliminary analysis, approximate vibrational frequencies (v"=800 cm^{-1}, v'=1200 cm^{-1}) were obtained.
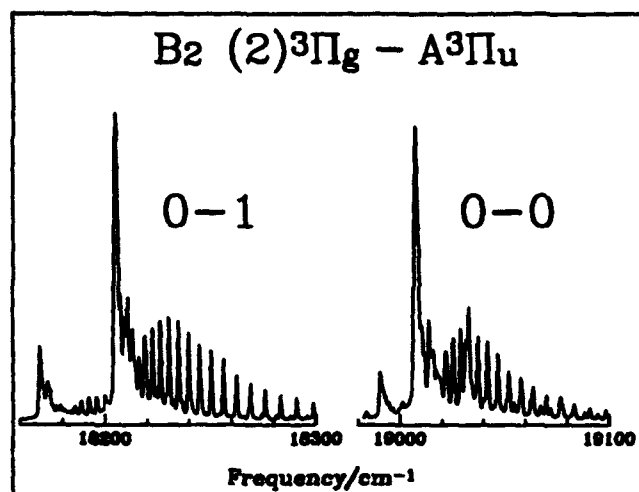
Figure 1

There are two naturally occurring isotopes of boron (^{11}B and ^{10}B) present in the ratio of 4:1. This results in three B_2 isotopomers $^{11}B_2$, $^{10}B^{11}B$ and $^{10}B_2$ in the ratio of 16:8:1. Unless the resolution and signal-to-noise are high the least abundant form is not observable, resulting in a ratio of 2:1 for the two main forms. The bands in Fig. 1 each show an extra feature to lower energy which can reasonably be assigned to the $^{10}B^{11}B$ isotopic form. From the approximate vibrational frequencies the $^{10}B^{11}B$ band should be shifted 3 cm^{-1} to higher energy for the 0-0 transition. However it is actually 16 cm^{-1} to lower energy, in addition the intensity is considerably less than half that of the main band. The most likely explanation for these effects is a perturbation in the upper state, as similar modifications are seen in all the bands coming from v'=0. The high resolution FTS data shown in Fig. 2 makes the form of the perturbation clear. The presence of two $^{10}B^{11}B$ bands separated by 40 cm^{-1} in each transition can clearly be seen. The v'=0 level, for the

Figure 2
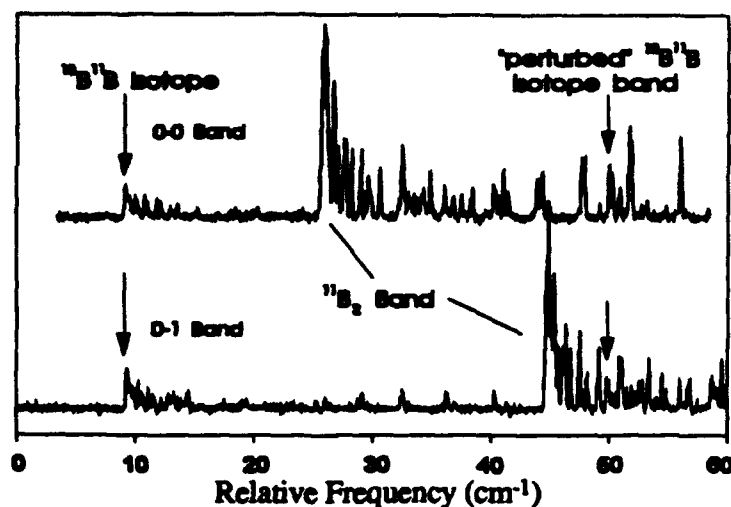
$^{10}B^{11}B$ isotopomer, of the $(2)^3\Pi_g$ state has been strongly perturbed by a vibrational level of another $^3\Pi_g$ state. The intensities of the two bands are about equal implying that the mixing of the two wavefunctions is almost 50-50 and therefore that the true positions of the two levels must be very close. Analysis of the high resolution data began with the strong 0-0 and 0-1 bands for the $^{11}B_2$ isotopomer. The well resolved high-J R branch lines could be assigned fairly easily but near the origin the structure became much more complicated as many satellite branches became strong. To gain an idea of which lines we were seeing near the origin, a spectral simulation program was developed, and a series of synthetic spectra generated using various values for the spin-orbit constants for the upper and lower states. A reasonable match to the observed spectrum was obtained using A"=3.7 cm^{-1} and A'=1.2 cm^{-1}. Using these initial trial constants most of the strong lines could be assigned. These lines were then fitted to a $^3\Pi$-$^3\Pi$ Hamiltonian and improved constants obtained. Eventually all of the lines could be assigned and the simulated spectrum showed a good match with the observed one. The analysis was then extended to the 1-0 and 1-3 bands and all of the data were fitted together. The data were

Table I Equilibrium Molecular Constants for $^{11}B_2$ (in cm^{-1})
$A^3\Pi_u$
$\omega_e = 817.9966(58)^a$ $\omega_e x_e = 7.4580(18)$ $B_e = 1.00681(17)$ $\alpha_e = 0.013167(23)$ $D_e = 5.73(35) \times 10^{-6}$ $A_e = 3.6034(53)$ $\lambda_e = -0.1160(40)$ $o_e = 0.2141(53)$ $p_e = 0.0063(10)$
$(2)^3\Pi_g$
$T_e = 18805.5630(69)$ $\omega_e = 1233.5336(81)$ $\omega_e x_e = 3.3^b$ $B_e = 1.16644(17)$ $\alpha_e = 0.00357(11)$ $D_e = 6.54(34) \times 10^{-6}$ $\beta_e = -3.08(36) \times 10^{-6}$ $A_e = 1.647(18)$ $\alpha_A = -0.213(28)$ $\gamma_e = 0.0057(11)$ $\alpha_\gamma = -0.0046(15)$ $o_e = 0.161(12)$ $\alpha_o = -0.133(17)$
[a] Values in parentheses represent one standard deviation error estimates from the final fit.   [b] Fixed at calculated value from Pekeris relation.

47

also fitted to Dunham expansions of the molecular parameters which are shown in Table I. This was very effective in the $A^3\Pi_u$ state which showed little vibrational variation but the $(2)^3\Pi_g$ state required two terms for every parameter. This is due to the same perturbation that strongly effects v=0 for the $^{10}B^{11}B$ isotopomer. The perturbing levels are further away for the $^{11}B_2$ isotopomer resulting in small changes in the effective molecular constants rather than a massive perturbation.

Initial assignments of the $^{10}B^{11}B$ bands, which are all split into two components due to a strong perturbation in the upper state, were made by using isotope relations to calculate the molecular constants and generate synthetic spectra. The upper state rotational constants and band origins were adjusted to produce a reasonable match to the observed bands, and then the line positions were fitted in the usual way with the lower state constants held fixed. Both upper state components could be fitted using a standard $^3\Pi$ Hamiltonian but the centrifugal distortion constants obtained were unusual, one state requiring a large positive value and the other a large negative value. This is indicative of the strong interaction between these two states. To obtain deperturbed constants for the $^{10}B^{11}B$ bands a coupling term was introduced between the two interacting $^3\Pi$ states. The constants for v=0 of the $(2)^3\Pi_g$ state were calculated from those for the $^{11}B_2$ isotopomer and held fixed while the constants for the perturbing state were allowed to vary. To reproduce the observed rotational structure an additional parameter describing the J dependence of the interaction between the two $^3\Pi$ states was needed in the effective Hamiltonian. The parameters for v=0 of the $(2)^3\Pi_g$ state, except the rotational constant, were held fixed and the observed lines could be reproduced to their estimated precision. The results of this fit are given in Table II.

Table II Constants from fit of interacting levels in 0-1 band for $^{10}B^{11}B$			
Constant	$A^3\Pi_u$ v=1	$(2)^3\Pi_g$ v=0	$(1)^3\Pi_g$ v=7
T	0	18195.77	18199.4374(64)
A	3.6055	1.5407	1.111(20)
λ	-0.1316	0	0
B	1.03596	1.21551(59)	1.16521
D	6.25×10^{-6}	5.61×10^{-6}	$19.0(14)\times10^{-6}$
γ	0	0.00366	0
o	0.2014	0.09318	0.053(13)
p	0.00653	0	0
H_{17} = 19.6598(33) H_{17D} = 0.013009(92)			

Although the $A^3\Pi_u$ potential is generally well behaved, there is clear evidence of a local perturbation in v=1 above N=8. As can be seen in Fig. 3 the lines exhibit irregularly varying spin structure as the successive components of the rotational levels are perturbed. The shifts are always less than the width of the blended lineshape and no extra lines could be found making a direct fit of the perturbation very difficult. The only state that lies low enough to be the cause of the perturbation is $a^5\Sigma_u^-$. Using the theoretically calculated electronic term energies and vibrational frequencies [6,9] the perturbing level can clearly be assigned as v=2 of the $a^5\Sigma_u^-$ state. Assuming this assignment and extrapolating back gives an equilibrium separation of about 1900 cm^{-1} for the $A^3\Pi_u$ and $a^5\Sigma_u^-$ states. This is in very close agreement with recent theoretical calculations of 1820 cm^{-1} [6], 2260 cm^{-1} [10], and 2340 cm^{-1} [9].
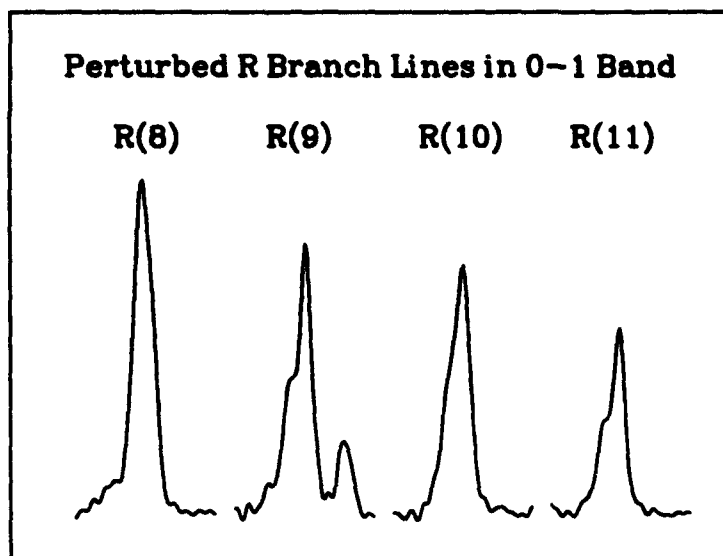
Perturbed R Branch Lines in 0-1 Band

R(8)   R(9)   R(10)   R(11)

Figure 3

The $(1)^3\Pi_g$-$A^3\Pi_u$ System

Towards the end of the analysis of the $(2)^3\Pi_g$-$A^3\Pi_u$ system, new observations of the weaker bands to the red of the main transitions were made in the hope of obtaining an improved vibrational analysis of the $A^3\Pi_u$ state. When looking at the 0-2 and 0-3 bands of the $(2)^3\Pi_g$-$A^3\Pi_u$ system several extra features were observed that actually became stronger than the main features in spectra recorded

Comparison of $(1)^3\Pi_g$ and $(2)^3\Pi_g$ Emission Intensities

Figure 4

very far out in the expansion. Fig. 4 shows the observed bands near the 0-2 region of the $(2)^3\Pi_g$-$A^3\Pi_u$ system. This new series of bands continues several thousand wavenumbers further to the red. The strongest features in this system were found to correspond to several unassigned bands which had been seen weakly in our earlier survey work. Improvements in the data collection efficiency meant that the new data were of much higher signal to noise and also were free from overlapping atomic and impurity bands. The structure in these bands was much more irregular than in the other B_2 bands, thus prompting earlier speculation that they might have been due to BH_2. Examination of the rotational and vibrational spacings in the new data has shown that the band system is definitely due to B_2 and that the lower state is $A^3\Pi_u$. As the bands are clearly Π-Π in character the upper state must be $(1)^3\Pi_g$ and the long progression of bands is due to emission from many excited vibrational levels.

The $(1)^3\Pi_g$ state was previously observed as the lower state in the $(2)^3\Pi_u$-$(1)^3\Pi_g$ system. Only the 0-0 band was seen in this system but the rotational analysis clearly indicated that near equilibrium the $(1)^3\Pi_g$ state is predominantl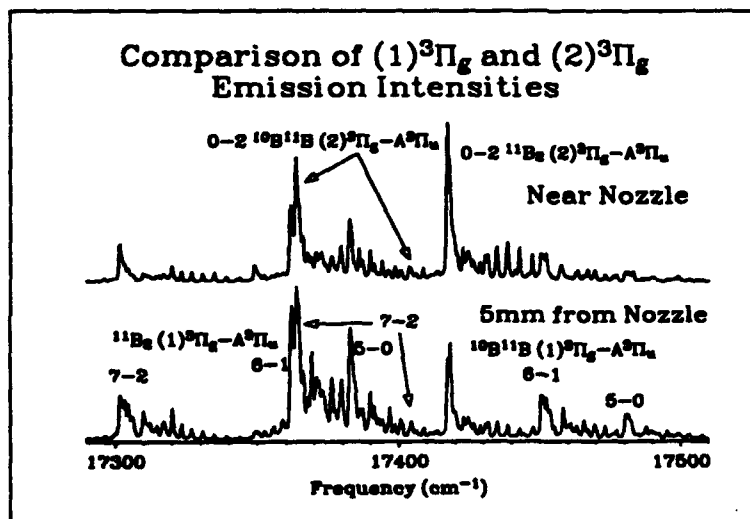y π^3 in character ($\sigma_g^2\sigma_u\pi_u^3$). This could be determined from the observed spin-orbit splitting of -4.43 cm^{-1} which is close to the expected value of $A=-\zeta/2=-5.35$ cm^{-1} for a π^3 configuration based on the boron atomic spin-orbit splitting of $\zeta=10.7$ cm^{-1}. The $A^3\Pi_u$ state has a fairly large positive spin-orbit splitting of 3.6 cm^{-1} and a dominant configuration of $\sigma_g^2\sigma_u^2\pi_u\sigma_g$ at the minimum [9]. As these two states differ by two orbitals, the electronic transition moment between them is expected to be small. The $(1)^3\Pi_g$ and $(2)^3\Pi_g$ states undergo a strong avoided crossing so that in the region of the crossing the dominant configuration is expected to change. The $(2)^3\Pi_g$ state has a spin-orbit splitting of 1.65 cm^{-1} near the minimum and the dominant configuration is $\sigma_g^2\sigma_u\pi_u\sigma_g^2$ [9]. The small size of the spin-orbit splitting indicates significant π^3 character near the minimum of $(2)^3\Pi_g$. Similarly the $(1)^3\Pi_g$ level observed in the perturbation with v=0 of $(2)^3\Pi_g$ has a small positive spin-orbit splitting of 1.1 cm^{-1} showing that the $(1)^3\Pi_g$ state undergoes a large change in electronic structure between the minimum and this level.

A preliminary analysis of some of the $(1)^3\Pi_g$-$A^3\Pi_u$ bands has been made. The results obtained so far are summarized in Table III. A vibrational

Table III Constants for $(1)^3\Pi_g$ (in cm^{-1})			
v	Energy[a]	A	B
0	?	-4.43	1.371
1			
2	15001.3	-3.64	1.321
3	16027.8	-2.85	1.288
4	16952.4	-2.00	1.240
5	17796.1	-0.83	1.182
6	18578.9	-0.32	1.145
7	19307.9	+0.22	1.110
[a]Energies are relative to $A^3\Pi_u$			

assignment of the observed levels was obtained by comparing the data for the $^{11}B_2$ and $^{10}B^{11}B$ isotopomers. The spacing of the vibrational levels is highly irregular due to the avoided crossing which results in a rather strange shaped potential curve. Based on this analysis the v=7 level is found to be responsible for the strong perturbation of v=0 of the $(2)^3\Pi_g$ state. Fig. 4 shows that the 7-2 band of the $(1)^3\Pi_g$-$A^3\Pi_u$ system has comparable strength with 0-2 of the $(2)^3\Pi_g$-$A^3\Pi_u$ system. As a result the intensities of the two bands resulting from the strong interaction between the upper state levels are combined as a sum and difference, giving one strong band and one very weak one. Once a full analysis of the observed levels has been performed it should be possible to directly fit all of the interactions between the $(1)^3\Pi_g$ and $(2)^3\Pi_g$ states. As the observed $(1)^3\Pi_g$ levels extend almost to the dissociation limit we may also be able to make an estimate of the dissociation energy to compare with theory.

The $(1)^1\Sigma_u^+$-$c^1\Sigma_g^+$ System

Analysis of this system near 34000 cm^{-1} is also still in progress. The analysis has been made more difficult by the presence of other band systems in the same region. This can be seen in Fig. 5 which shows the strong 0-0, 1-1 and 2-2 bands of the $(1)^1\Sigma_u^+$-$c^1\Sigma_g^+$ system. Part of a Π-Σ system overlaps the 2-2 band and in addition part of some other transition runs through the region between the 1-1 and 2-2 bands. Depending on the conditions of the discharge and where in the expansion the spectra are recorded these overlapping
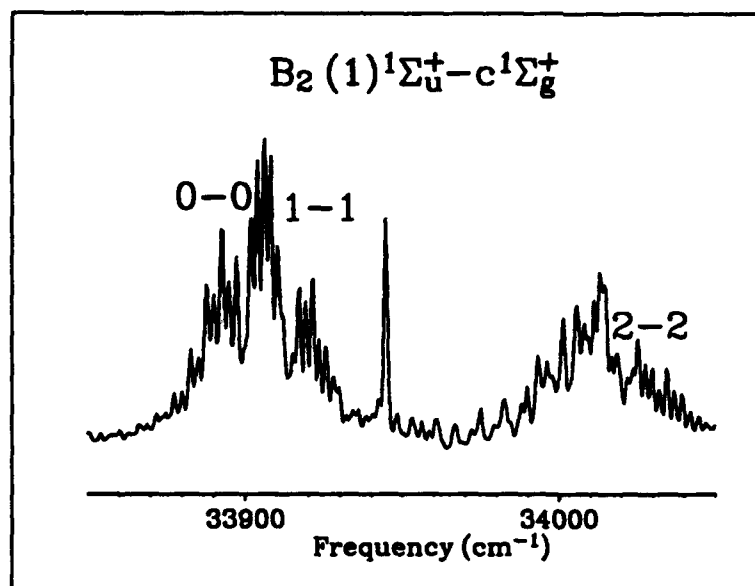
Figure 5

bands can become stronger than the $(1)^1\Sigma_u^+$-$c^1\Sigma_g^+$ system. Preliminary rotational constants match the theoretical predictions but the vibrational frequencies have not been determined so far.

Other Systems

A single band near 42000 cm^{-1} has been assigned as the 0-0 component of the $(1)^3\Delta_g$-$A^3\Pi_u$ transition by simulation of the spectrum and comparison with theory [6,9]. Several bands in the UV have been tentatively assigned to Π-Σ or Σ-Π transitions but assignments of the actual states involved have not yet been made.

Summary

A total of six new electronic transitions of the B_2 molecule have been observed in emission from a Corona Excited Supersonic Expansion source. By comparison with theory these transitions have been assigned to specific states within the extensive manifold of B_2 electronic states. Although many of the predicted states are still unknown we have observed all three states originating from the lowest $\sigma_g^2\sigma_u^2\pi_u^2$ configuration. In addition we have observed a perturbation between the $a^5\Sigma_u^-$ state and the $A^3\Pi_u$ state which provides a link to the low lying $a^5\Sigma_u^-$ state. It is hoped that analysis of the recently observed Σ-Π bands will provide a direct link between the ground $X^3\Sigma_g^-$ state and the $A^3\Pi_u$ state. A summary of the bands analyzed so far and their theoretically predicted positions is given in Table IV.

Table IV Band Origins for B_2 (in cm^{-1})				
Transition	ν_{00}	Theory[a]	Theory[b]	Theory[c]
$(2)^3\Pi_u$-$(1)^3\Pi_g$	18035.3	18474	18011	17770
$(2)^3\Pi_g$-$A^3\Pi_u$	19014.3	19700	19145	•••
$(1)^1\Delta_u$-$b^1\Delta_g$	29883.5	30345	31573	•••
$(2)^3\Sigma_u^-$-$X^3\Sigma_g^-$	30518.3	31035	29959	•••
$(1)^1\Sigma_u^+$-$c^1\Sigma_g^+$	33899.4	•••	35544	•••
$(1)^3\Delta_g$-$A^3\Pi_u$	~41946	42272	43075	•••
[a] Langhoff and Bauschlicher; [b] Hachey, Karna and Grein; [c] Bruna and Wright				

References

1. L. Pasternack, Comb. and Flame, **90**, 259 (1992).
2. N. Presser and A.T. Pritt, Jr., pp 7-16 in *Proceedings of the High Energy Density Materials Contractors Conference*, edited by W.J. Lauderdale and W.A. Sowell (USAF Astronautics Laboratory, Edwards AFB, CA 1987).

3. P.G. Carrick, submitted to J. Prop. and Power, (1993).

4. A.E. Douglas and G. Herzberg, Can. J. Res. 18, 165 (1940).

5. H. Bredohl, I. Dubois, and F. Mélen, J. Mol. Spec. 121, 128 (1987).

6. S.R. Langhoff and C.W. Bauschlicher, Jr., J. Chem. Phys. 95, 5882 (1991).

7. C.R. Brazier and P.G. Carrick, J. Chem. Phys. 96, 8684 (1992).

8. C.R. Brazier and P.G. Carrick, Submitted to J. Chem. Phys.

9. M. Hachey, S.P. Karna, and F. Grein, J. Phys. B, 25, 1119 (1992).

10. P.J. Bruna and J.S. Wright, J. Chem. Phys. 91, 1126 (1989); J. Phys. Chem. 94, 1774 (1990); J. Phys. B 23, 2197S (1990); J. Mol. Struct. (Theochem.) 210, 243 (1990).

Coupled Electronic-Nuclear Dynamics in Solids

A. Danilychev, R. Zadoyan, W. G. Lawrence and V. A. Apkarian
Department of Chemistry
University of California
Irvine, CA 92717.

Dynamics in many-body media always involves coupled motions of electronic and nuclear degrees of freedom. Born-Oppenheimer separation, which allows the construction of potentials by averaging over electronic degrees of freedom, in many cases is artificially imposed. This approximation is particularly problematic when open shell atoms, or radicals are involved in the dynamics. For any atom with electronic state other than $^1S_0$, deviation of the charge density from spherical symmetry, leads to anisotropic potentials, which cannot be treated as pairwise additive.[1] As a result, the nuclear dynamics cannot be understood without making explicit reference to the electronic degrees of freedom. In the limit of adiabatic following, which is appropriate for thermal motions in cryogenic media, simple and yet insightful treatments of spectroscopy and dynamics in these systems is possible. Detailed analysis of the problem will be given in the cases of atomic halogens, ^2P, and chalcogens, ^3P & ^1D, trapped in closed shell rare gas hosts. The methods will be delineated and used for the interpretation of experimental data on spectroscopy and thermal mobility. Examples will also be given from studies of electronic predissociation and photodissociation, in which case non-adiabatic dynamics needs to be treated.

It is worth emphasizing that in all of the HEDM applications involving the trapping and storage of radicals or atoms in condensed media, these themes will recur.

In what follows a detailed description of the treatment of interactions of halogen and oxygen atoms with many rare gas atoms will be given. The formulation is aimed at explaining observed atomic emission spectra in particular of I^* and $O(^1S)$, photomobility of atomic F, and the fascinating thermal mobility of O atoms in crystal Kr and Xe, where it is found that the thermal mobility of atomic O is characterized by migration lengths of order $\sim 1 \mu m$. The experimental evidence for this finding is discussed first.

O atoms are photogenerated in crystalline Kr and Xe by photodissociation of either O_2 or N_2O. The subsequent thermal induced recombination of O atoms is simultaneously followed by thermoluminescence from recombinant O_2, and

LIF from atomic O. The two yield identical results, they identify that the loss of O atoms is due to formation of O_2 and that this non geminate recombination even in samples as dilute as 1:100,000, follows first order kinetics. The latter implies that retrapping of a thermally activated O atom is less probable than the probability for it to find a second O atom. Given estimates of the initial O atom concentration, it can be conclude that the O atom motion is not diffusive, and that it involves travel lengths of order 1μm prior to scattering.

As the simplest prototype of open shell-closed shell interactions, consider a halogen atom, such I, trapped in a rare gas solid. For the processes of present interest, the interaction Hamiltonian for the system can be limited to:

$$H_{int} = V_{X-Rg}(r;R_1,R_2,...,R_n) + V_{Rg-Rg}(R_1,R_2,....,R_n) + H_{so}$$

in which r and R represent respectively the coordinates of the hole and the rare gas atoms, with origin on the halogen nucleus; H_{so} is the effective spin-orbit Hamiltonian. Given the large spin-orbit splitting in iodine, we expect H_{so} to be dominated by the hole-core coupling and only slightly modified by the lattice. Thus, the explicit dependence of H_{so} on {R_i} is initially ignored It is also assumed that the interactions between X and Rg do not effect Rg-Rg interactions. After expressing the angular dependence of V_{X-Rg} in Legendre polynomials, P_L:

$$V_{X-R_g}(r;R_1,R_2,...,R_n) = \sum_{k=1}^{n}\sum_{l=0}^{\infty} V_L(r,R_k)P_L(\vec{R}_k \cdot \vec{r})$$

the electronic eigenenergies can be obtained by diagonalizing the Hamiltonian in an appropriate basis. The limited basis set $|np>_X |ns>_{Rg}$, composed of the six ^2P functions on the halogen atom, and the single $^1S_0$ function on the rare gas atoms are adequate. In the decoupled basis, i.e. $|l\ m_l, s\ m_s>$, the individual matrix elements can be expressed as products of spherical harmonics:

$$V_{mm'} = \sum_{k}\sum_{L=0}^{\infty}\frac{4\pi}{2L+1}\langle Y_{lm'}|\sum_{M=-L}^{L} Y_{LM}|Y_{lm}\rangle V_L Y_{LM}^*(\vartheta_k,\varphi_k)$$

Since the basis is limited to l=1, the summation over L is limited to only two terms, L=0, 2. The radial functions, $V_0(R)$ and $V_2(R)$ are extracted from pair potentials. They are related to the diatomic Σ and Π interatomic potentials:

$$V_0 = \frac{1}{3}(V_\Sigma + 2V_\Pi); \quad V_2 = \frac{5}{3}(V_\Sigma - V_\Pi)$$

in the absence of spin-orbit coupling, H_{int} can be readily evaluated. Balling and Wright have given the explicit expressions for the $|l\ m_l>$ basis.[2] H_{so} can be directly included by moving to the $|Jm_J>$ basis, in which it is diagonal:

$$\langle Jm_J|H_{so}|J'm_J'\rangle = \begin{cases} \dfrac{2}{3}\Delta\delta_{J,J'}\delta_{m_J,m_J'}; & J = 1/2 \\[2mm] \dfrac{1}{3}\Delta\delta_{J,J'}\delta_{m_J,m_J'}; & J = 3/2 \end{cases}$$

$\Delta = 7606$ cm^{-1} in the case of iodine. The coupled basis set, $|Jm_J\rangle$, is constructed from the $|lm_l,sm_s\rangle$ functions by standard methods:

$$|Jm_J\rangle = \sum_{m_l,m_s} c(lsJ;m_l m_s m_J)|lm_l,sm_s\rangle$$

and the explicit matrix elements of H_{int} in this basis are obtained. This treatment is tantamount to assuming that the interaction potential is dominated by electrostatics — ignores core polarization, charge transfer, exchange or configuration interactions which may polarize the valence orbitals. These may seem drastic approximations, but in practice they are not.

Consider the potential energy surfaces for an I atom surrounded by an octahedral arrangement of Xe atoms, which is the situation for the relevant substitutional isolation sites. In the two-valued representation appropriate for an odd number of electrons, the spin-orbit coupled states belong to the two-fold degenerate $E_{1/2}$ and four-fold degenerate $G_{3/2}$ species.[3] Vibrations of E_g or T_{2g} modes will produce the Jahn-Teller splitting of the $G_{3/2}$ state, splitting it into $E_{1/2}$ and $E_{3/2}$ spin-doublets. This effect is shown in **figure 1**, along the $\nu_{2(E_g)}$ vibrational coordinate. In higher dimensions, the splitting results in conical intersections. At the center of the cell, where perfect cubic symmetry is experienced, the doubly degenerate $E_{1/2}$ excited state is separated from the four-fold degenerate $G_{3/2}$ ground state by the spin-orbit splitting, Δ. For any asymmetric motion, the degeneracy breaks and three states, each a degenerate Kramers pair, is obtained.

A statistical treatment is advanced for the simulation of $I^*\rightarrow I$ spectra. The formulation is based on the consideration that although at cryogenic temperatures, the system is in the high temperature limit with respect to all lattice modes, i.e. the thermal energy $\beta^{-1} = k_B T$ is large compared to the energy of motion on a given surface within the de Broglie wavelength $\hbar/(\mu k_B T)^{1/2}$ of the heavy atoms, specifically, for all R_i (but not r):

$$\beta\left(\frac{\hbar}{(\mu k_B T)^{1/2}}\nabla_{(R_i)}H_{int}\right) \ll 1$$

holds even at the lowest temperatures in these measurements (15K). Accordingly, the nuclear motions can be treated classically. The electronic coordinate on the halogen atom, r, which parametrically depends on {R_i} can be expected to follow the nuclear motions, therefore the I^* atom will remain on the adiabatic eigenenergy surface E_{III}. The relaxation from this surface to the lower surfaces, E_I or E_{II}, is by radiation. The spectral distribution of emission, say from E_{III} to E_I, can be given by the multi-dimensional reflection expression:

$$I(\omega) \propto Z^{-1} \int ... \int \frac{e^{-\beta E_{III}(r;R_1,R_2...R_n)}|\mu_{III,I}|^2 \omega^3 \delta[(E_{III} - E_I)/\hbar - \omega] \Pi_i d^3 R_i}{|\nabla_{(R_i)} V_I|}$$

In which Z is the classical partition function on the E_{III} surface; μ is the transition dipole moment which in principle depends on all coordinates; the integration and the gradient in the denominator, are over all classical coordinates. The expression has a simple insight, namely: the emission spectrum represents transitions between eigenstates, weighted by the probability of a configuration on the upper state, and the density of states on the lower surface for a particular configuration. Monte Carlo sampling is used for the actual simulations. The weighted configurations in phase space are generated by the standard Metropolis Algorithm, except at every step the 6X6 matrix is diagonalized, and the highest eigenenergy is used to judge the acceptance of a configuration. The densities of states are obtained from the gradient matrix, using the appropriate eigenvectors:

$$\left|\nabla_{(R_i)} V_I\right| = \left(\sum_i \left(\langle I|\frac{\partial}{\partial R_i} V_{tot}|I\rangle\right)^2\right)^{1/2}$$

in which | I> is the eigenvector of state I, at a particular classical configuration {R_i}. The force matrix is readily obtained.

Initial comparisons of the results of such simulations are in agreement with experiment. In the case of I^* the Δ is modified by 230 cm^{-1}. The observed doublet of bands in Xe are reproduced with respect to their widths, relative intensities and temperature dependences.

The treatment is extended in the case of two electron O atoms. Separate bases are used for interactions with $^3P(L=1)$, and $^1D(L=2)$ atoms. Evaluation of these eigensurfaces immediately show rather interesting features. We consider the surfaces relevant for the migration of interstitial defects. The ^3P surface is characterized by repulsion, trapping occurs in the largest cavities -- the O_h sites. These sites are connected through adjoining T_d sites. The potentials are subject
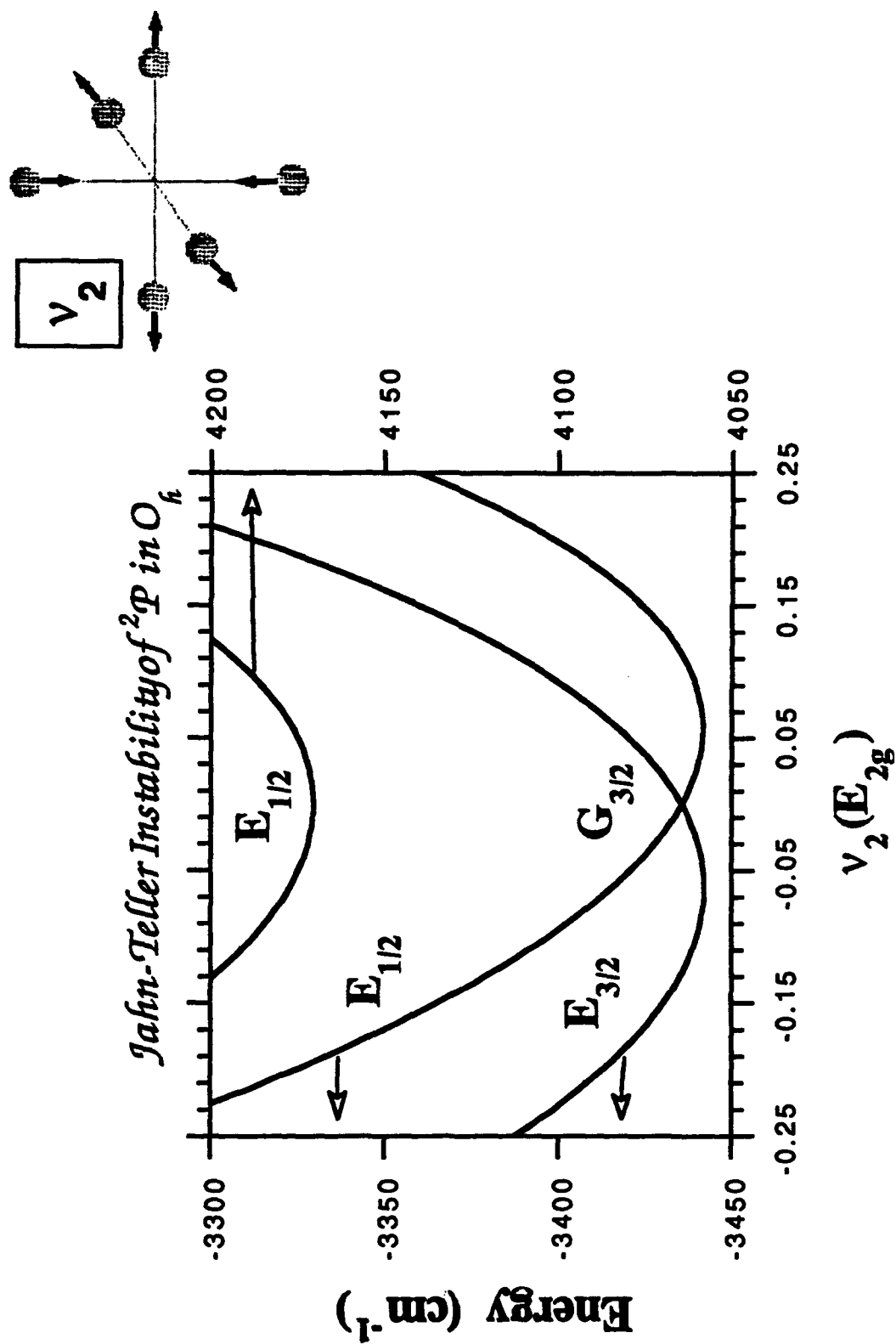
to large barriers, and involve large angle deflection. The connecting surface is given in **Figure 2**. Such a surface can only support diffusion, with extensive lattice realaxation -- passage over free energy barriers. The ^{1}D surface is charcterized by attractive interactions. The minima occur in the tightest sites -- between two rare gas atoms, forming Rg-O-Rg linear triatomics. In the case of Xe, if additional charge transfer contribution is incorporated these sites will become global minima, lower than the ^{3}P surface. The minimum energy surface connecting these sites occurs on the body faces. The connecting barriers are smaller than those on the ^{3}P surface, and can be navigated with little energy loss. Noting that crossing between ^{3}P and ^{1}D surfaces should be avoided through the $M_J = 0$ components, we present a difference surface, *the minimum energy surface, interconnecting two trap sites*, in **Figure 3**. Except for the octahedral minima, this surface is entirely dominated by the ^{1}D contribution.

Based on the features of these potentials we propose a mechanism for the observed long-range migration: thermal activation from ^{3}P to ^{1}D, and subsequent migration until either recombination or recrossing occurs. To attempt quantitative comparisons, the activation process and the dynamics of migration have to be treated by including lattice motions. However, all of the qualitative requirements to support the hypothesis are present in the static surfaces.

Orbital control dynamics should clearly be anticipated in reactive processes as well. To follow these in detail, experimental probes on relevant time scales are crucial. We have recently developed the tools to follow events with time resolution of ~100 fs. Relevant to the present theme is the observation of caging of I_2 on the $^3\Delta(I^*+I)$ surface. The geminate fragments remain on this surface for 15 ps in Ar, and 25 ps in Kr. The process is ascribed to orbital locking -- trapping in the Δ configuration, and detrapping after ~50 vibrational periods by a $\Delta\rightarrow\Pi$ flip.

References:

1.   W. E. Baylis, J. Phys. *B10*, 1477 (1977).

2.   L.C. Balling and J. J. Wright, J. Chem. Phys., *79*, 2941 (1983).

3.   G. Herzberg, "Electronic Spectra of Polyatomic Molecules", (Van Nostrand Reinhold, N.Y., 1966).

Jahn-Teller Instability of ^2P in O_h

ν_2

$\nu_2(E_{2g})$

Energy (cm^{-1})

$E_{1/2}$

$G_{3/2}$

$E_{1/2}$

$E_{3/2}$
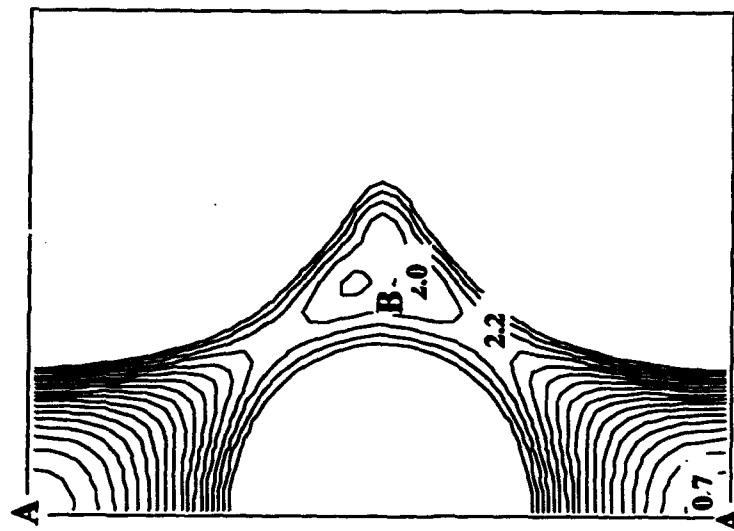
O(^{3}P)/Kr surface on [101] plane

Minimum energy path (r/a)

O(^{3}P) along min. energy path

O(^{1}D) minimum energy path (r/a)
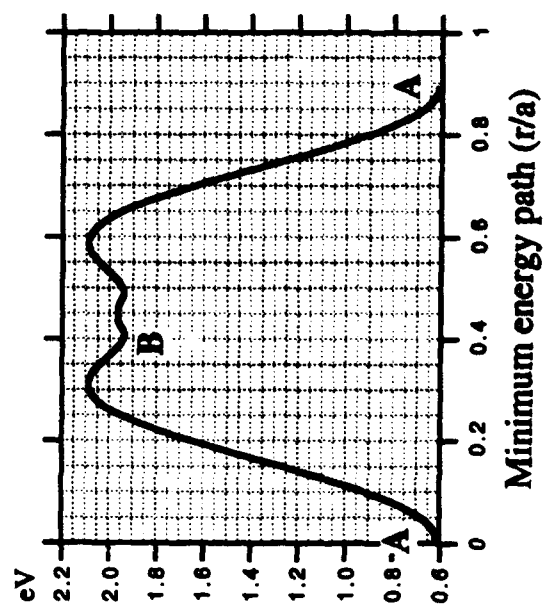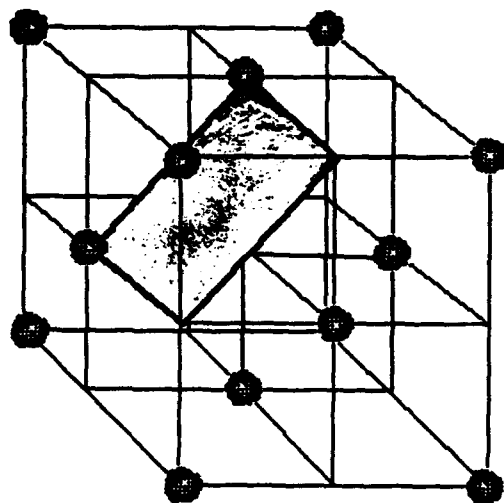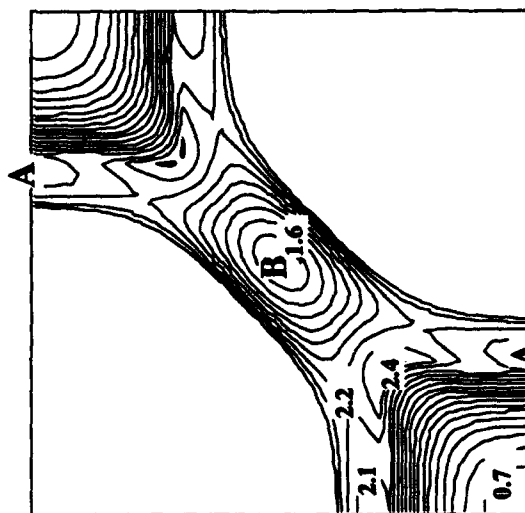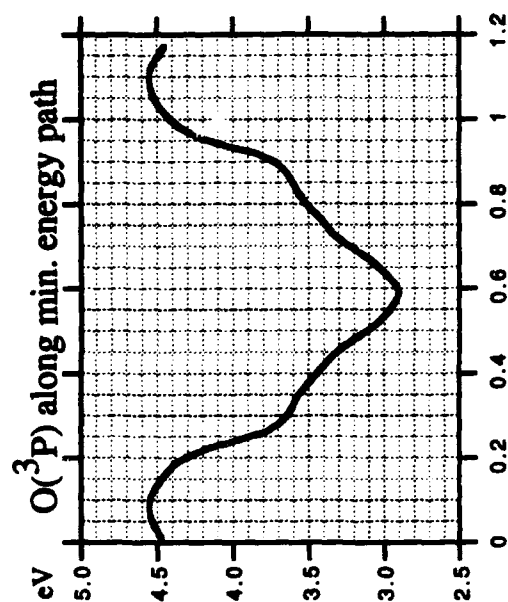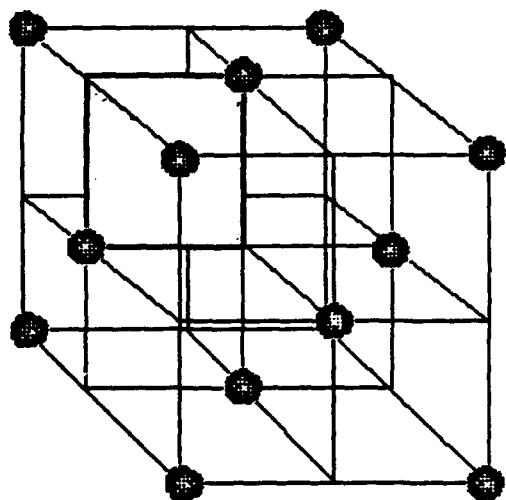
Surface of minimum energy path
[010] plane
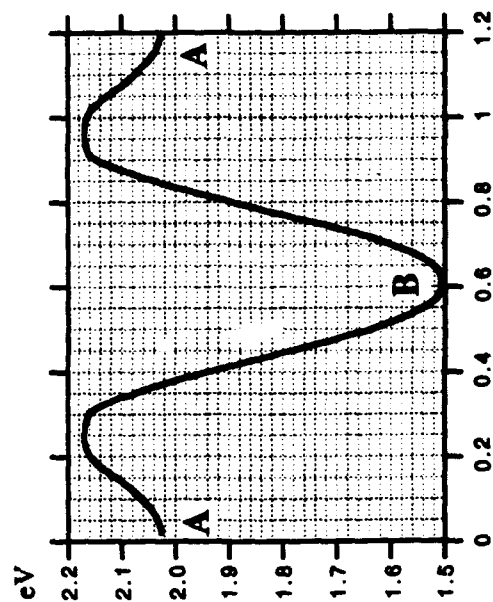
VIBRATIONAL DYNAMICS OF QUANTUM CLUSTERS AND SOLIDS

R.B. GERBER, Z. Li and A.B. McCoy
Department of Chemistry
University of California
Irvine, CA 92717

ABSTRACT:

This paper presents results of theoretical studies on the following topices: (1) The vib-rotational ground state wave functions of the clusters LiH_2(para); BH_2 (para); BH_2(ortho). (2) The time-dependent vibrational dynamics of quantum anharmonic solids and clusters, including collinear Ne clusters, one-dimensional models of solid H_2 and one dimensional solid H_2 doped with Li.

1. Vibrational ground states of LiH₂ and of BH₂

Diffusion Quantum Monte Carlo simulations were carried out to obtain the vibrotational ground states of LiH_2(para); BH_2(ortho); BH_2(para). For LiH_2 we used the potential surface calculated by D. Konowalow.(1) The BH_2 potential surface was provided by M. Alexander. (2) Fig. 1 shows the Li/H2 distance distribution in the LiH_2 cluster, and also the probability distribution for the orientation of the H_2 molecule within the cluster (θ being the angle between the H_2 axis and the atom-molecule distance vector). Fig. 2 shows the corresponding results for Bh_2(para) and BH_2(ortho). Both clusters are seen to be extremely floppy and delocalized, with a very broad atom-molecule distance distribution. The H_2 is essentially a free rotar in LiH_2, with almost spherically distributed H_2. The angular distribution for BH_2 shows considerably increased anisotropy especially for the ortho-case. These structures have important implications for the UV absorption lineshapes of these clusters, and indeed also for the UV absorption lineshapes of solid H_2 doped with Li or with B atoms. Consideration of these ground-state wave functions, with the excited state potentials for these systems, suggests an important role for the H_2 rotational mode in the photo excitation process.

2. Lattice vibrations of highly anharmonic quantum solids

Time-dependent quantum simulations were carried out for the vibrational dynamics of collinear Ne clusters;(3) of a one-dimensional of solid H_2, and of one dimensional solid H_2 doped with Li. The method used was based on the Time-Dependent Self Consistent Field (TDSCF) approximation.

The simulations carried out included up to 20 particles (with periodic boundary conditions in the case of the solids). Frequencies, phonon lifetimes, and time-correlation functions of the phonon wavefunctions were computed, and their proeprties analyzed. The results demonstrate the usefulness and power the new method for Quantum Molecular Dynamics simulations, developed in the framework of this project. Classical MD simulations were found to fail qualitatively for the systems studied.

Stretch projection of the ground state wavefunction for LiH2
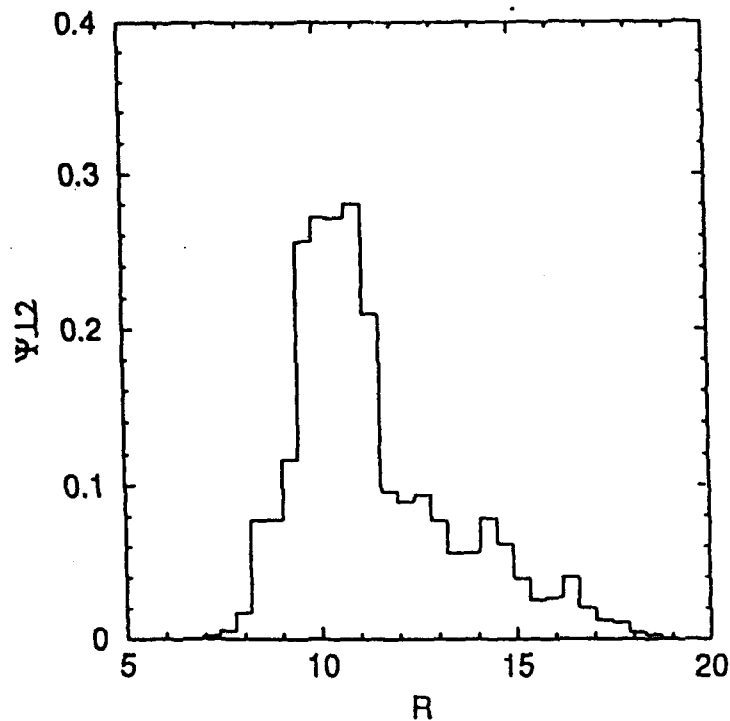
Bend projection of the ground state wavefunction for LiH2
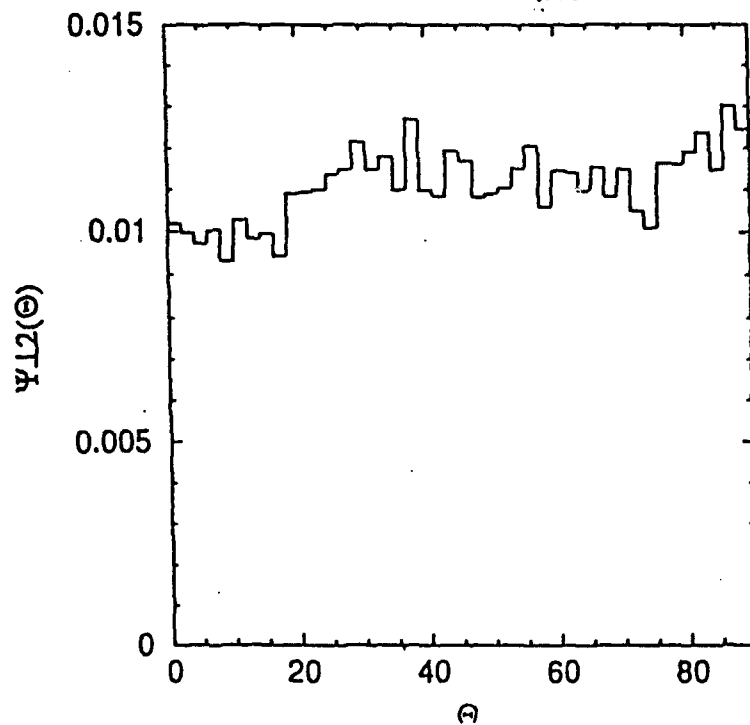
Fig. 1.
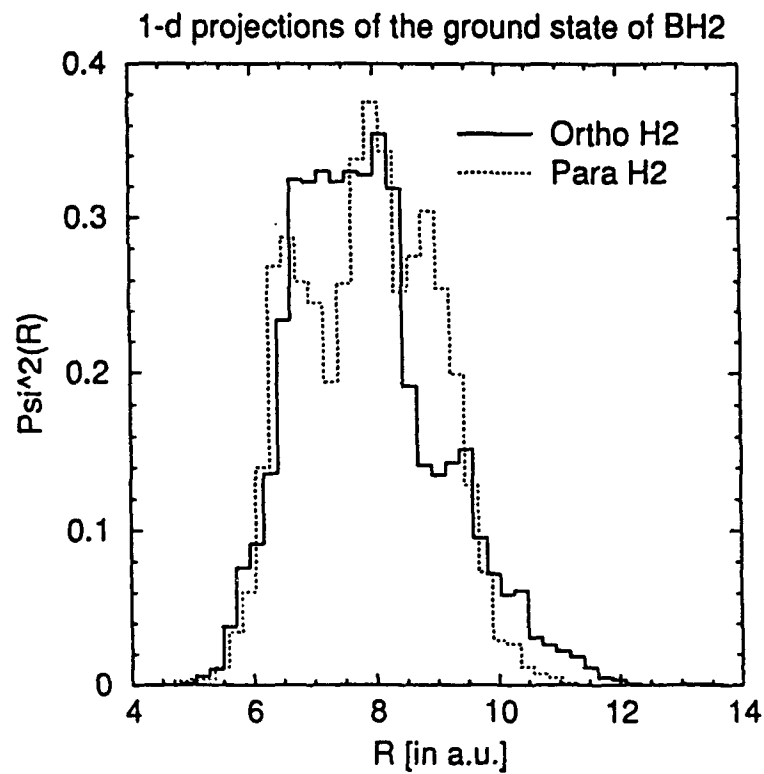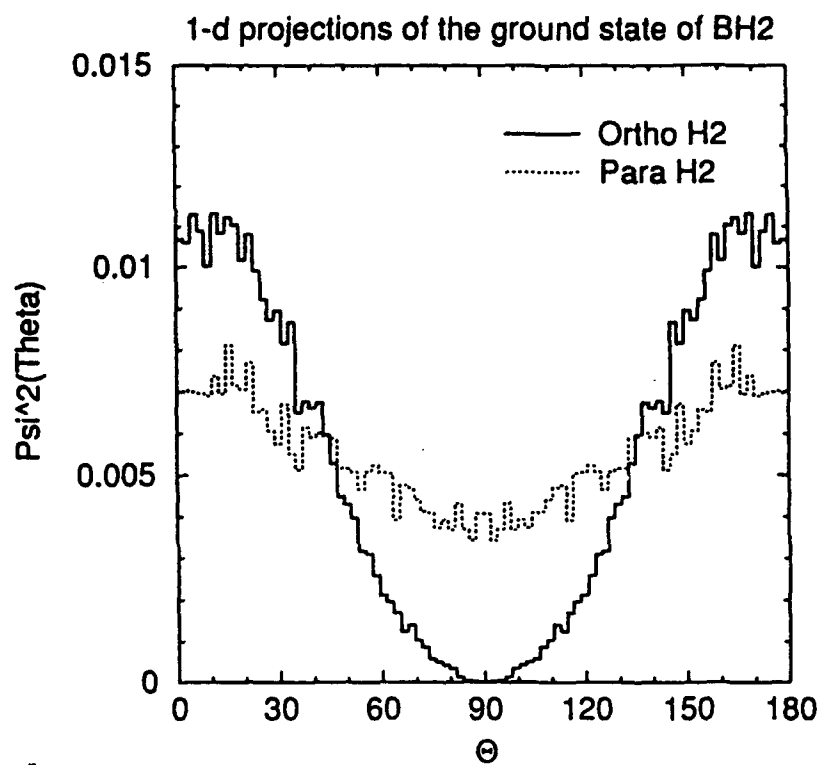
Fig. 2

References

(1)   D.D. Konwalow, private communication.
(2)   M.H. Alexander, to be published.
(3)   Z.Li and R.B. Gerber, J. Chem. Phys. (In press).

INCIPIENT CONDENSED PHASE EFFECTS IN THE O₃/H₂O SYSTEM: CHEMICAL DYNAMICS IN THE GAS PHASE AND IN SMALL CLUSTERS

David S. King, John C. Stephenson and Michael P. Casassa
Molecular Physics Division
National Institute of Standards and Technology
Gaithersburg, Maryland 20899

ABSTRACT

The dynamics of the 266nm-photoinitiated $^{16}O + H_2^{18}O \rightarrow ^{16}OH + ^{18}OH$ reaction were studied using $^{16}O_3 \cdot H_2^{18}O$ van der Waals dimers to pre-align the initial reagents. This complex presents a known equilibrium geometry and photolytic anisotropy that would predict a preference for initial trajectories of the "abstraction" archetype. Laser induced fluorescence probes show that "new"-^{16}OH and "old"-^{18}OH products are formed mainly in v=0, with a slight preference for the $\Pi(A')$ Λ-doublets, and average rotational energies of 900 and 760cm^{-1}, respectively. No significant vector correlations were observed. Sub-Doppler resolution experiments showed average kinetic energies for new-^{16}OH fragments about 20% higher than for old-^{18}OH fragments in the same rotational levels; increasing from values of ca. 500 cm^{-1} at low rotational levels, to ca. 1500 cm^{-1} at the highest rotational levels populated. These results are very different from those observed for the gas phase bimolecular $O(^1D) + H_2O \rightarrow 2OH$ reaction, photoinitiated in mixtures of O_3 and H_2O, and imply that the incipient condensed phase environment of the dimer results in a significant change in reaction path.

1. INTRODUCTION

The $O(^1D) + H_2O \rightarrow 2OH$ reaction has the intriguing property of producing two chemically identical OH fragments with distinctly different histories, and the nature of trajectories which produce products has been a topic of some interest. For example, there has been considerable speculation on whether the reaction conforms to the abstraction or insertion mechanistic archetypes.[1-5] In order to characterize the potential energy surfaces for this reaction, we have investigated the dynamics of the photoinitiated reaction of $^{16}O(^1D)$ and $H_2^{18}O$, occurring as a bimolecular reaction in $O_3 + H_2O$ mixtures, and triggered in $O_3 \cdot H_2O$ clusters. In these experiments, laser pulses (266nm) photolyze O_3 to produce $O(^1D) + O_2(a^1\Delta_g)$ with 90% quantum yield.[6] In the ensuing reaction,

$$^{16}O(^1D) + H_2^{18}O \rightarrow ^{16}OH + ^{18}OH + 118 \text{ kJ/mol}$$

the isotopic labelling enables us to distinguish between the newly formed ^{16}OH and the residual ^{18}OH fragment. The kinetic energy of the $O(^1D)$ atom provides an additional 22kJ/mol to the products of this exothermic reaction. Using laser induced fluorescence (LIF), we measured rotational, vibrational and fine-structure state distributions of the OH fragments. Fragment translational energies were measured using sub-Doppler LIF. The experiments have sufficient resolution to yield directly the correlations between energy states of the pairs of geminate OH products produced in the reaction. Generally, this type of information has only be inferred from statistical analyses of product state distributions.

Below we review our recent results for the photolytically triggered reaction in gaseous $O_3 + H_2O$ mixtures,[4,5] where the reaction proceeds via bimolecular collisions, and we present results for analogous measurements performed on $O_3 \cdot H_2O$ clusters. The gas phase results prove that the reaction is direct, and they suggest that there are no particular constraints on reactive geometries. They further show strong correlations between the velocities, scattering angles, and internal energy states of the fragments. The cluster reaction is initiated with reagents in close proximity with restricted orientations, and the dynamics of the cluster reaction are dramatically different than those of the bimolecular reaction. It is apparent that the

third body (O_2) produced by the reaction plays an active role, and carries away most of the available energy.

2. DYNAMICS OF THE BIMOLECULAR REACTION

The $O(^1D)+H_2O$ bimolecular reaction was studied under single-collision conditions in a low pressure flowing mixture of $^{16}O_3$ and $H_2^{18}O$ at room temperature, as previously described.[4] The $O(^1D)$ atoms were produced by 266nm photolysis of O_3, using pulses from a quadrupled, 10 ns Nd:YAG laser. The kinetic energy distribution of the resulting $O(^1D)$ atoms and their recoil anisotropy are well known, and these factors are incorporated into the analysis of our experiments. Product vibrational, rotational and fine-structure state populations were measured by LIF, using a YAG-pumped frequency-doubled dye laser, on the A–X OH (0,0) and (1,1) bands. The bandwidth of the probe light was approximately 0.4 cm^{-1} FWHM. Doppler profiles of the nascent OH products were also obtained using LIF, with the ca. 310 nm probe generated by doubling a pulse-amplified, single-frequency, continuous-wave dye laser. The probe bandwidth for Doppler measurements was about 0.0047 cm^{-1} (FWHM). Experiments were performed with various pump-probe-detection geometries and polarizations, in order to measure vector correlations among fragment motions and the photolysis electric vector. Pump and probe fluences were about 10mJ/cm^2 and 10-100mJ/cm^2, respectively. The LIF signal intensities were linear in pump and probe energy, and Doppler profiles were independent of pump and probe energy. Total pressures were maintained near 11 Pa (80 mtorr), and the pump-probe delay time was 10 nsec.

Figure 1 shows product rotation and vibration distributions produced following 266nm photolysis. These are similar to distributions reported using 248nm photolysis of O_3.[3] The "new"-^{16}OH product is formed with far more rotational and vibrational energy than the "old"-^{18}OH product. The "new" ^{16}OH is formed with vibrational populations in the ratio 0.39(v=0):0.29(v=1):0.3(v≥2). Gaussian rotational energy distributions peaked near N=12 give average rotational energies of $<E_{ROT}>$ =3440cm^{-1} and 2780cm^{-1} for ^{16}OH v=0 and v=1, respectively. The "old" ^{18}OH is much colder with vibrational populations 0.94(v=0):0.06(v=1) and a ^{18}OH v=0 Gaussian rotational energy distribution characterized by
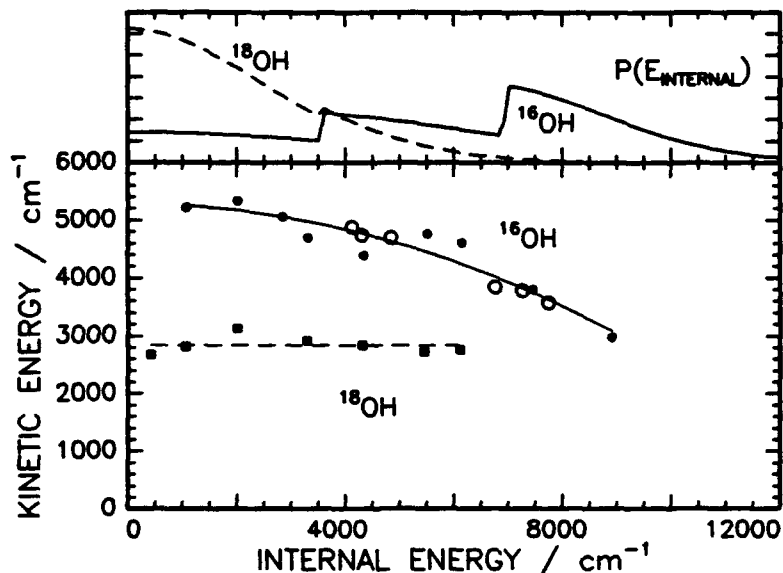

Figure 1. Upper panel- Internal energy distributions from Ref. 4. Discontinuities reflect different vibrational levels, e.g, ^{16}OH(v=0,1,2). Lower panel - LAB kinetic energies for the ^{16}OH (●, v=0; ○, v=1) and ^{18}OH (■, v=0) fragments of the $^{16}O(^1D)+ H_2^{18}O$ reaction, plotted against the product internal (vibrational plus rotational) energy, from Ref. 5.

$<E_{ROT}> = 1920 \text{cm}^{-1}$. The average vibrational energies are $<E_{VIB}> = 3120$ and 210 cm^{-1} for ^{16}OH and ^{18}OH, respectively. There is negligible rotational alignment of the ^{16}OH fragments, and the spin-orbit propensities are nearly statistical. The Λ-doublet populations exhibit a J-dependent $\Pi(A')\Pi/(A'')$ ratio for both isotopes, ranging from unity at low J to approximately 2 at high J. The vibrational population results suggest an abstraction or stripping process, possibly proceeding through an O--HOH transition state such as described in *ab initio* calculations.[7] The disparate product state distributions for the two isotopes could also result from an HOOH insertion intermediate (such as has been shown in O(^{1}D) reactions with alkanes[8], H_2,[9] and H_2S[10]) that dissociates rapidly compared to the intramolecular vibrational energy redistribution rate. On the other hand, the trend in Λ-doublet distributions conforms to expectations for a process that is statistical in a geometrical sense,[11] with no preferred reaction geometry. Thus the internal state distributions cannot be used to ascribe an archetype mechanism, e.g., abstraction or insertion, to this reaction. We suspect that both types of trajectories lead to products.

Much more detailed information can be obtained by examining the Doppler profiles of individual lines in the OH LIF spectra.[5] The velocities measured by the Doppler technique are laboratory-frame (LAB) velocities, which include contributions from the initial, center-of-mass velocity of the $O + H_2O$ reagents in the lab, and the recoil impulse from the reaction in the center-of-mass frame (CM). All of the observed Doppler profiles are well fit by Gaussian speed distributions. Small differences in Doppler widths were observed when comparing profiles obtained for different pump-probe geometries, or in a given geometry for P versus Q-type transitions. These differences reveal a small degree of laboratory recoil anisotropy, and a correlation between the laboratory velocity and the plane of rotation of the OH fragments. Therefore, Doppler profile measurements for most levels were made with pump electric and probe Poynting vectors set at the magic angle to avoid biases due to state- or fragment-dependent translational alignment. A single parameter is extracted from the Gaussian fits to the individual profiles. This is the average LAB kinetic energy, $<E_{KE}>$, for fragments in a specific rovibration level.

Figure 1 shows of $<E_{KE}>$ for ^{16}OH rotational levels in v=0 and 1 and for ^{18}OH rotational levels in v=0. Fragment levels for ^{16}OH v=2 and ^{18}OH v=1 are populated, but the LIF signals from these levels were too weak for Doppler analysis. For the ^{16}OH fragments with internal energies between 4000 and 8000 cm^{-1}, there are no significant differences between the kinetic energies measured for high-N rotational levels of v=0 and low-N levels of v=1 at a similar internal energy, implying that fragment kinetic energy is a function of internal energy, $E_{INTERNAL}$, and not quantum number. The rovibrational levels for which we have measured Doppler widths nearly span the range of internal energies produced by the reaction; the ^{18}OH data sample 98% of the range of $E_{INTERNAL}$ levels populated, while the new ^{16}OH data sample 83%.

For all rovibrational levels measured $<E_{KE}(^{16}OH)>$ significantly exceeds $<E_{KE}(^{18}OH)>$. This can only occur if the reaction is direct. Any mechanism involving a long-lived complex would accelerate both incipient OH groups to a common velocity (the CM velocity, V_{CM}) prior to fragmentation. Upon fragmentation, the CM recoil velocities of the isotopically distinguishable fragments would combine with V_{CM} to give average LAB speeds which would be the same, neglecting the ^{18}OH-^{16}OH mass difference. A more detailed picture of the reaction is obtained by transforming the measured laboratory velocities for the OH fragments into a pairs of coordinates in the CM. Each laboratory velocity can be associated with a range of recoil velocities and scattering angles in the CM. However, there is a unique correspondence of the measured average LAB speeds to the underlying average recoil energy $<E_{RECOIL}>$ in the CM, and the average scattering angle $<\chi>$ in the CM. (We measure $<\chi>$ from the initial O(^{1}D) atom velocity vector in the CM, and refer to scattering into the hemisphere with $\chi < 90°$ as forward scattering.) The uniqueness of the transformation is due to conservation of momentum in the CM, and to the observation that the LAB kinetic energy $<E_{KE}(^{18}OH)> = 2840 \text{cm}^{-1}$ is independent of $E_{INTERNAL}(^{18}OH)$. As a consequence, a pair of $<E_{RECOIL}>$ and $<\chi>$ values are uniquely associated with each value of $<E_{KE}(^{16}OH)>$ and with each $E_{INTERNAL}$ state of the fragments.
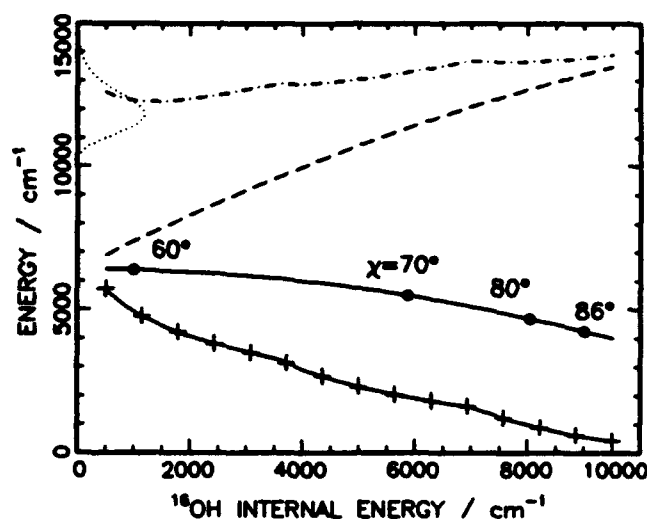
Figure 2. Energy correlations and average CM recoil angles as a function of the internal energy of the ^{16}OH fragment, from Ref. 5. Relative recoil kinetic energy, $<E_{RECOIL}>$ (————); partial sum of energies, $E_{INTERNAL}(^{16}OH) + <E_{RECOIL}>$ (– – –); $E_{INTERNAL}(^{18}OH)$ derived for anticorrelated pairing of $E_{INTERNAL}(^{18}OH)$ and $E_{INTERNAL}(^{16}OH)$ (–+–+–); resulting total energy release, $E_{INTERNAL}(^{16}OH) + <E_{RECOIL}> + E_{INTERNAL}(^{18}OH)$ (– · – ·). The distribution of available energy is shown as (·····), with energy as the ordinate.

Figure 2 shows $<\chi>$ and $<E_{RECOIL}>$ obtained from the LAB-to-CM transformation plotted as a function of $E_{INTERNAL}(^{16}OH)$. The solid curve shows the net CM $<E_{RECOIL}>$. Representative values of the CM scattering angle $<\chi>$ are indicated at filled points along this curve. Weighting the values of the internal-energy-dependent $<E_{RECOIL}>$ by the ^{16}OH population distribution gives an average CM kinetic energy release for the reaction of $<<E_{RECOIL}>> = 5200 cm^{-1}$. A similar weighting gives an average value of the CM scattering angle $<<\chi>> = 70°$. The new-^{16}OH fragments scatter preferentially in the forward direction, and the average CM scattering angle $<\chi>$ increases as the $E_{INTERNAL}(^{16}OH)$ of the correlated ^{16}OH-^{18}OH pair increases. The value of $<\chi> = 90°$, which is perhaps reached for the highest $E_{INTERNAL}(^{16}OH)$, could occur in a direct reaction, but could also arise if the reaction involved a long-lived complex. Except for this high-energy tail of the $E_{INTERNAL}(^{16}OH)$ distribution, the results clearly show the presence of significant scattering anisotropy in the CM, proving that the reaction proceeds in a direct fashion. Using the average initial relative velocity, $v = 2300 m/s$, and the impact parameter, $b = 1.7Å$, derived from the $O(^1D) + H_2O$ thermal rate constant,[1] the value of $<\chi> = 70°$ corresponds to a maximum collision complex lifetime of $\tau = b<\chi>/v = 90fs$.

The numerical transformation of the LAB velocities directly yields the correlations just described between fragment $E_{INTERNAL}$ and the CM scattering parameters $<E_{RECOIL}>$ and $<\chi>$. Interfragment energy correlations can also be derived. In fig. 2, the distribution of total available energy, $E_{AVAILABLE}$, is shown along the left-hand scale using a dotted curve. This incorporates the reaction exothermicity, the $O(^1D)$ recoil energy distribution,[12] and the reactant thermal energy distribution. The partial sum of energy released in producing ^{16}OH in a particular state, $E_{INTERNAL}(^{16}OH) + <E_{RECOIL}>$, is plotted against $E_{INTERNAL}(^{16}OH)$ using a dashed (– – –) curve . The difference between the available energy and this partial sum is the energy that must appear as internal energy of the geminate ^{18}OH. For the assumption of a strict anticorrelation of internal energy states (i.e., the highest $E_{INTERNAL}$ ^{16}OH states shown in fig. 1 are

69

produced with geminate ^{18}OH fragments in the lowest $E_{INTERNAL}$ states), the calculated total energy released, $E_{INTERNAL}(^{16}OH) + <E_{RBCOIL}> + E_{INTERNAL}(^{18}OH)$ is plotted in fig. 2 as the dash-dot (– · – ·) curve against $E_{INTERNAL}(^{16}OH)$. The values of the cofragment $E_{INTERNAL}(^{18}OH)$ were derived from the observed product state distribution (Fig. 1) and are plotted against $E_{INTERNAL}(^{16}OH)$ in Fig. 2 using (–+–+–). The total energy calculation is in good agreement with the available energy for all of the proposed ^{16}OH-^{18}OH pairings, indicating that the $E_{INTERNAL}$ distributions of geminate fragments are strongly anticorrelated.

These results provide for $O(^1D) + H_2O \rightarrow 2OH$ a level of dynamical detail that is unprecedented in the experimental description of bimolecular reactions that produce molecular products. We see that most "new" OH molecules are scattered in the forward direction. Those which have relatively little internal excitation are produced with geminate "old" OH fragments scattered in the opposite direction with high internal excitation. New OH molecules that are scattered at wider angles tend to have higher internal excitation and are paired with old OH fragments with low internal energy. On average, 27% of the available energy appears in OH product vibration, 34% appears in rotation, and 39% appears as translational energy. The results do not show that the reaction proceeds via a single abstraction/insertion mechanism, and both types of trajectories may be important. In any case, the results show that the dominant reaction processes are direct.

3. DYNAMICS OF THE CLUSTER REACTION

Since the $O(^1D) + H_2O \rightarrow 2OH$ bimolecular reaction is direct, we expect the dynamics of the reaction initiated in the $O_3 \cdot H_2O$ dimer to be affected by the restricted reaction geometries imposed by the cluster structure. The structure of $O_3 \cdot H_2O$ determined by Fourier transform microwave spectroscopy (FTMS)[13] is shown in fig. 3. Since the H_2O lies above the O_3 plane, and since in 266nm photolysis of O_3 the O^1D atoms are ejected along the O_3 b-axis[14] (out of the plane of the figure), the initial $O(^1D) + H_2O$ motion resembles a stripping trajectory. Therefore we supposed that the dynamics would comprise a subset of the correlated dynamics shown in fig. 2 for the unrestricted bimolecular reaction.
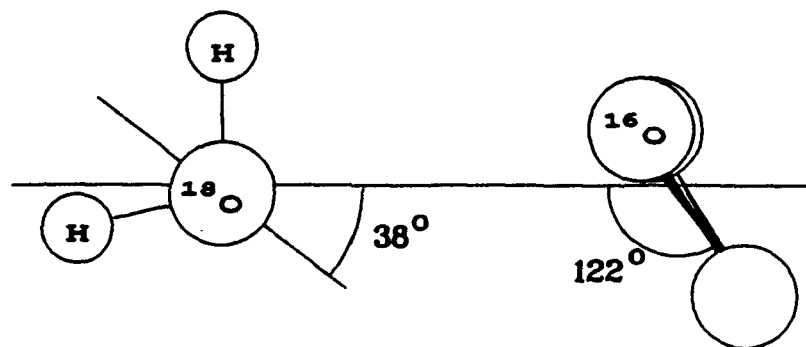
Figure 3. $O_3 \cdot H_2O$ dimer structure. The centers-of-mass separation is 2.96Å

$O_3 \cdot H_2O$ clusters were produced in a supersonic expansion of mixtures of $^{16}O_3$ and $H_2{}^{18}O$ in rare gases. The O_3 was diluted in Ar and Ne and stored in glass or stainless steel tanks. These mixtures were expanded through a 0.7mm diameter pulsed nozzle after passing over a temperature-controlled $H_2{}^{18}O$ reservoir. The laser and detection aspects of the cluster experiments were identical to those used for the gas phase bimolecular reaction studies. Generally, OH LIF signals were observed for both cluster-initiated and bimolecular reactions in the jet. The cluster and bimolecular components were readily distinguished by their dependencies on the time between photolysis and probe pulses. The cluster component appeared

instantaneously and was otherwise independent of pump-probe time delay from 10ns to 1μs. The bimolecular component increased linearly with time delay, and only became significant (i.e., commensurate with the cluster signal) with time delays of approximately 0.5μs.

It was more difficult to ascertain whether cluster signals arose from photolysis of the $O_3 \cdot H_2O$ dimer or from larger clusters. We used several procedures to optimize expansion conditions for $O_3 \cdot H_2O$ dimer production without significant interference from other clusters. Condensation in the jet was characterized by monitoring $O_3 \cdot H_2O$ microwave transitions using FTMS. This showed how the $O_3 \cdot H_2O$ concentration scaled with expansion conditions, and whether further clustering depleted the dimer concentration. (The absorption lines exhibited a central dip if larger clusters formed on the molecular beam axis at the expense of dimers.) We also measured how the OH LIF signal intensities scaled with expansion conditions. Interference from larger clusters was indicated by deviations from simple pressure scaling rules (i.e., $[O_3 \cdot H_2O] \propto P^2$) in the intensities of the LIF and FTMS signals. Finally, we measured the OH LIF Doppler widths as a function of expansion conditions. This was the most sensitive indicator of the presence of larger clusters, which caused a narrowing of Doppler profiles as the large-cluster concentrations became significant. We found that mixtures of 5%O_3/Ne P≤4atm and 2%O_3/Ar P≤1atm passed over 0°C $H_2^{18}O$ produced expansions in which $^{16}O_3 \cdot H_2^{18}O$ dimer signals predominated.

Figure 4 shows product state and kinetic energy results for the reaction observed in $^{16}O_3 \cdot H_2^{18}O$ clusters in the Ne expansion. Similar results were obtained for the Ar expansion. As can be seen by comparing this figure to figure 1, the rotational and vibrational distributions are dramatically colder in the cluster reaction than in the bimolecular reaction. The "new" ^{16}OH product is formed with vibrational populations in the ratio 0.81(v=0):0.19(v=1), giving $<E_{VIB}> \approx 680cm^{-1}$. The $\Pi(A')/\Pi(A'')$ ratios show a slight preference for the symmetric A-doublet states, but not as pronounced as for the gas phase reaction. The rotational energy distributions give $<E_{ROT}> = 900cm^{-1}$ and $930cm^{-1}$ for ^{16}OH v=0 and v=1, respectively. The "old" ^{18}OH is formed with $<E_{ROT}> = 760cm^{-1}$. Products of other cluster-initiated reactions[15] also show significantly colder internal energy distributions than their bimolecular analogs.
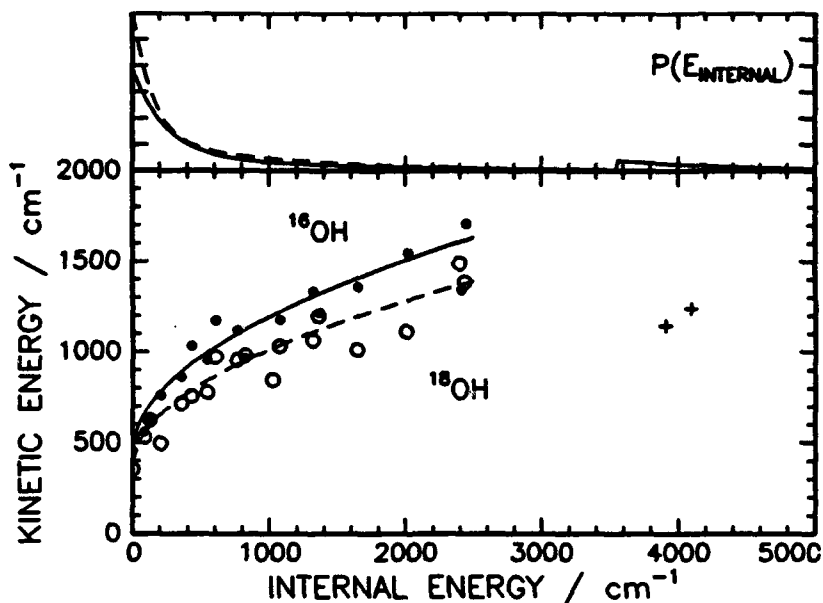
Figure 4. Upper panel- Internal energy distributions of the ^{16}OH (———) and ^{18}OH (— — —) products of the $^{16}O_3 \cdot H_2^{18}O$ cluster reaction. Discontinuities reflect different vibrational levels, e.g., ^{16}OH(v=0,1). Lower panel - LAB kinetic energies for the ^{16}OH (●, v=0; +, v=1) and ^{18}OH (○, v=0) fragments of the cluster reaction, plotted against the product internal energy.

71

Reference 15 cites several explanations based on the presence of the third body in the cluster reaction. In principle, the third body can carry additional kinetic energy, induce V,R→T transitions in the fragments, or effectively reduce the initial relative kinetic energy of the projectile atom and the target molecule (i.e., the "squeezed atom" effect).
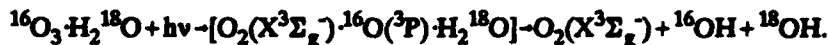
Kinetic energies of the OH products of the cluster reaction were measured using sub-Doppler LIF. Profiles measured with various pump-probe polarization geometries are well fit by Gaussian speed distributions, and show no rotational or recoil anisotropies. The results of measurements of profiles for most of the states with significant population are shown in figure 4. Comparison with figure 1 shows, for all states measured, that the kinetic energies of the cluster reaction products are significantly lower than those of the bimolecular reaction products. The average laboratory kinetic energy for ^{16}OH and ^{18}OH are $<E_{KE}> = 920cm^{-1}$ and $<E_{KE}> = 770cm^{-1}$, respectively. The average ^{16}OH-^{18}OH recoil energy is at most $<E_{RECOIL}> \leq 1690cm^{-1}$, formed in the limit of opposite OH momenta, and is far less than the $5200cm^{-1}$ value measured for the bimolecular process. This indicates that the incipient OH internal excitations are not simply quenched by V,R→T processes. Nor can the lowered internal energy of the OH fragments be ascribed to the "squeezed-atom" effect, since most of the available energy is generated by the reaction exothermicity, not from the initial relative kinetic energy of the $O(^1D) + H_2O$ reactants.

Most of the available energy in the cluster reaction must be drawn away by the O_2 fragment. The 266nm-initiated cluster reaction is presumed to be

$$^{16}O_3 \cdot H_2{}^{18}O + h\nu \rightarrow [O_2(a^1\Delta_g) \cdot {}^{16}O(^1D) \cdot H_2{}^{18}O] \rightarrow O_2(a^1\Delta_g) + {}^{16}OH + {}^{18}OH.$$
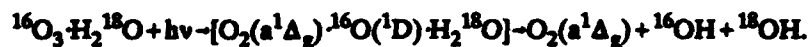
We would expect to find approximately $15200cm^{-1}$ of energy distributed among the three fragments. The average internal energy found in both OH fragments accounts for $2350cm^{-1}$ of this energy. The average kinetic energy sum for all three fragments is equal to $1690cm^{-1}$, in the limit of no $O_2(a^1\Delta_g)$ recoil, and is at most $3600cm^{-1}$ in the limit of maximum possible $O_2(a^1\Delta_g)$ momentum. (In this limit, the $O_2(a^1\Delta_g)$ momentum opposes parallel ^{16}OH and ^{18}OH momenta.) Therefore the $O_2(a^1\Delta_g)$ must carry at least $9200cm^{-1}$ as average internal energy, which is far greater than the $1400cm^{-1}$ internal energy seen in $O_2(a^1\Delta_g)$ produced by 266nm photolysis of isolated O_3.[12] This seems an unlikely result since in the gas phase excitation of OH products is caused by the $10000cm^{-1}$ exothermicity of the subordinate $^{16}O(^1D) + H_2{}^{18}O \rightarrow {}^{16}OH + {}^{18}OH$ reaction. How could the majority the energy (85%) generated in this way be transferred from both OH fragments to the internal of degrees of freedom the O_2 spectator?

Appealing alternatives for the cluster reaction mechanism are processes which involve $O(^3P)$ reactions, such as

$$^{16}O_3 \cdot H_2{}^{18}O + h\nu \rightarrow [O_2(X^3\Sigma_g^-) \cdot {}^{16}O(^3P) \cdot H_2{}^{18}O] \rightarrow O_2(X^3\Sigma_g^-) + {}^{16}OH + {}^{18}OH.$$

The subordinate cluster reaction, $^{16}O(^3P) + H_2{}^{18}O \rightarrow {}^{16}OH + {}^{18}OH$, is endothermic with an activation energy of 20kcal/mol, and a barrier to the reverse reaction of 0.6kcal/mol.[4,6] The dynamics of this subordinate process would not generate a significant amount of energy in the OH products, other than the initial energy supplied by the photolysis step. (The translational energy of the cluster products will be discussed below.) In the gas phase, $O_3 + h\nu \rightarrow O_2(X^3\Sigma_g^-) + O(^3P)$ photolysis occurs with 10% quantum yield at 266nm, and is a minor component ($\leq 5\%$) of the overall gas phase reaction producing OH. In the cluster, it is conceivable that the photochemistry of 266nm-excited O_3 is perturbed by the presence of the complexing H_2O to produce mainly $O(^3P) + O_2(X)$, and the $O(^1D)$ fragmentation becomes a minor channel. The branching in O_3 occurs at large separations,[12] so it is plausible that the H_2O causes such a perturbation. Like $O(^1D)$ production from 266nm-excited O_3, $O(^3P)$ emerges along the O_3 b-axis.[14] A geometry-induced preference for $^{16}O(^3P)$ reactions in $^{16}O_3 \cdot H_2{}^{18}O$ is consistent with the notion that $O(^3P)$ reacts by abstraction, while $O(^1D)$ reacts by insertion.

72

The subordinate $O_3 + h\nu \to O_2(X^3\Sigma_g^-) + O(^3P)$ reaction has been studied extensively in the gas phase.[14] We are unaware of measurements of the dynamics of the gas phase $O(^3P) + H_2O \to 2OH$ reaction, so here we resort to a *gedanken* gas phase experiment in order to compare the cluster results to gas phase expectations. In the gas phase, $O(^3P)$ is produced with a broad range of kinetic energies and about half of these O-atoms supply enough energy in the center-of-mass of $O \cdots H_2O$ collisions to overcome the barrier to OH production. Based on the $O(^3P)$ speed distributions in the literature, and assuming a 0.6kcal barrier to the $2OH \to O(^3P) + H_2O$ reaction, the gas phase reaction sequence would produce OH fragments with an average (total) excess energy of only $1900cm^{-1}$, which is far lower than the energy released in the $O(^1D)$ gas phase reaction, and relatively close to the energy actually seen in the $^{16}O_3 \cdot H_2^{18}O$ cluster products. At the same time, if the cluster reaction were simply a geometry-constrained version of the gas-phase $O(^3P)$ reaction, pairs of OH products with a combined average LAB kinetic energy of at least $6200cm^{-1}$ should be produced. This LAB kinetic energy, which is greater than observed, would be due to $^{18}OH \cdot ^{16}OH$ center-of-mass translation (not relative $^{18}OH \cdot ^{16}OH$ translation) impressed upon the fragments by the initial $O(^3P)$-atom recoil. Based on conservation of energy and momentum, the O_2 fragments produced from the cluster reaction must carry an average internal energy (electronic, vibrational, and rotational) of $18200 \pm 1300cm^{-1}$. In contrast, the $O_2(X)$ products associated with *reactive* $O(^3P) + H_2O$ gas phase trajectories contain on average only $c. 8000cm^{-1}$. Even if the $O(^3P)$ process occurs in the clusters, an additional effect must be operating to dispose of energy in the internal degrees of freedom of the O_2 fragment.

For the cluster reaction, figure 4 shows that $<E_{KE}>$ increases with $E_{INTERNAL}$ for both ^{16}OH and ^{18}OH. In contrast, photodissociation experiments which induce fragmentation of monoenergetic molecules generally produce fragments with $<E_{KE}>$ weakly dependent upon, or decreasing with $E_{INTERNAL}$. The behavior seen in figure 4 is reminiscent of the dynamics of laser-induced thermal desorption of molecules from surfaces, and of IR multiphoton dissociation. Both processes start with a distribution of energized molecules, and those with higher initial energy yield products with higher rotational and translational energy. This suggests by analogy that the energy content of the OH cluster products reflects a distribution of available energies. We speculate that the energy distribution in the O_2 portion of the cluster is somehow established before the $^{16}OH^{18}OH$ portion of the excited complex expels OH products, but these two components of the cluster process are not decoupled as they are in the gas phase reaction sequence.

The average LAB frame kinetic energy of the $^{16}OH(v=0)$ fragments of the cluster reaction is 1.19 times that of the $^{18}OH(v=0)$ products. The gas phase reaction results in a larger ratio of 1.66 for the LAB kinetic energies. The disparity in the gas phase LAB kinetic energies is a manifestation of pronounced recoil anisotropy in the $^{16}O(^1D) + H_2^{18}O$ center-of-mass frame, and shows that the gas phase reaction is direct. If the OH coproducts of the cluster reaction were formed with equal magnitude LAB momenta, the ^{16}OH products would exhibit kinetic energies a factor of 1.12 greater than their ^{18}OH partners. This prediction is within the experimental uncertainty of the ratio measured for the clusters. We conclude that the LAB momenta of the two fragments are essentially equal. They are certainly close to this limit, in stark contrast to the disparate LAB momenta observed in the gas phase reaction. This suggests that the cluster reaction proceeds in an indirect fashion, on a timescale slower than cluster motions which could reorient the inceptive OH velocities (*e.g.*, rotation of the excited complex, or intracluster motions such as internal rotations).

4. SUMMARY

The dynamics of the 226nm-photoinitiated $^{16}O + H_2^{18}O \to ^{16}OH + ^{18}OH$ reaction were studied using $^{16}O_3 \cdot H_2^{18}O$ van der Waals dimers to configure the initial reagents. This complex geometry and the O_3 photolytic anisotropy would bias the initial $O + H_2O$ motions in favor of trajectories of the "abstraction" archetype, in the absence of cluster perturbations on the O_3 photolysis. Sub-Doppler laser induced fluorescence probes show that "new"-^{16}OH and "old"-^{18}OH products are formed with far less rotational, vibrational, and kinetic energy than seen in the gas phase bimolecular $O(^1D) + H_2O \to 2OH$ reaction. The gas phase reaction products exhibit disparate energies, new-^{16}OH being "hotter" than old-^{18}OH, as well as

pronounced energy correlations and scattering anisotropy. The cluster products have none of these characteristics. Instead, the incipient condensed phase environment of the dimer results in a significant change in the reaction path; there is no evidence that the $O(^1D)+H_2O$ channel as it is understood in the gas phase, is involved in the cluster reaction. Our hypothesis is that analogs of $O(^3P)$ reactions occur in the $^{16}O_3 \cdot H_2^{18}O$ clusters. This is based on intuitive arguments, but could be tested if it were possible to examine the state of the O_2 cluster products, or if more were known about the dynamics of the gas phase $O(^3P)$ reaction. It is clear that the O_2 fragment of the cluster reaction plays a prominant role in the OH production dynamics, and receives in its internal degrees of freedom significantly more energy than seen in the gas phase reaction.

5. ACKNOWLEDGEMENTS

6. REFERENCES

1. F. J. Comes, K. -H. Gericke and J. Manz, J. Chem. Phys. 75, 2853-2863 (1981).

2. J. E. Butler, L. D. Talley, G. K. Smith and M. C. Lin, J. Chem. Phys. 74, 4501-4508 (1981).

3. C. B. Cleveland and J. R. Wiesenfeld, J. Chem. Phys. 96, 248-256 (1992).

4. D. G. Sauder, J. C. Stephenson, D. S. King and M. P. Casassa, J. Chem. Phys. 97, 952-961 (1992).

5. D. S. King, D. G. Sauder and M. P. Casassa, J. Chem. Phys. 97, 5919-5922 (1992).

6. D. L. Baulch et al, J. Phys. Chem. Ref Data 11, 327 (1982).

7. T. Fueno in Applied Quantum Chemistry, edited by V. H. Smith, Jr., H. F. Schaefer and K. Morokuma, pp. 33-34 (Reidel, 1986).

8. C. R. Park and J. R. Wiesenfeld, J. Chem. Phys. 95, 8166-8177 (1991); and references therein.

9. E. M. Goldfield and J. R. Wiesenfeld, J. Chem. Phys. 93, 1030-1040 (1990); and references therein.

10. N. Balucani, L. Beneventi, P. Casavecchia, D. Stranges and G. G. Volpi, J. Chem. Phys. 94, 8611-8617 (1991).

11. M. J. Bronikowski and R. N. Zare, Chem. Phys. Lett. 166, 5-10 (1990).

12. J. J. Valentini, D. P. Gerrity, D. L. Phillips, J.-C. Nieh and K. D. Tabor, J. Chem. Phys. 86, 6745-6756 (1987).

13. J. Z. Gillies, C. W. Gillies, R. D. Suenram, F. J. Lovas, T. Schmidt and D. Cremer, J. Mol. Spectrosc. 146, 493-512 (1991).

14. L. R. Carlson, Ph.D. thesis, University of California at Berkeley, 1979.

15. E. Böhmer, S. K. Shin, Y. Chen and C. Wittig, J. Chem. Phys. 97, 2536-2547 (1992): and references therein.

SPONTANEOUS DISSOCIATION OF EXCITED OXYGEN MOLECULES IN THE VICINITY OF A METAL SURFACE

P. C. Cosby, L. Hazell,[†] C. W. Walter,[‡] and H. Helm

Molecular Physics Laboratory
SRI International
Menlo Park, CA 94025

ABSTRACT

Dissociation of long-lived, electronically excited O_2 molecules is observed to occur as the molecules pass through a 300 μm wide metal slit. Spatial and temporal analysis of the correlated dissociation fragments is used to identify the dissociating O_2^* states and to determine the branching in dissociation to the $O(^1S) + O(^1D)$, $O(^1D) + O(^1D)$, $O(^1D) + O(^3P)$, and $O(^3P) + O(^3P)$ dissociation limits. Studies of this phenomenon as a function of electric field applied across the slit suggests that the dissociation is induced by Stark mixing of long-lived O_2 molecules that leads to predissociation by the valence continuum states. In the absence of an external electric field the mixing is induced by forces exerted on the molecule as a consequence of the image charges that the Rydberg molecule induces in the metal surface, when the molecule travels close to, but does not physically touch, the metal surface.

[†] Permanent Address: Institute of Physics, University of Aarhus, DK-8000 Aarhus C, Denmark.
[‡] Present Address: Department of Mathematics, Saint Mary's College of California, Moraga, CA 94575.

INTRODUCTION

Several recent papers have explored the influence of an external electric field on dynamic properties of molecular Rydberg states. These studies were concerned with two effects induced by the electric field: For one, the lowering of the ionization threshold leads to electric-field induced ionization. This effect has been studied for the molecules H_2, Li_2, Na_2, and H_3.[1-5] A second influence of the electric field derives from its effect of ℓ-mixing which can lead to selective predissociation of the molecular Rydberg. Such observations have been reported for the molecules H_2 [6-8] and H_3 [9]. The effect of ℓ-mixing may be interpreted in general terms by considering three electronic states: R_a, R_b, and C. Here R_a is a Rydberg state that is stable against dissociation at zero field and can couple to a Rydberg state of different parity, R_b, through the Stark effect. Predissociation of R_a can be "turned on" by an external electric field, provided a dissociative continuum state, C, is available which has a favorable coupling to R_b. While the intrinsic Stark matrix element merely couples ℓ with $\ell\pm1$, all ℓ values will tend to get mixed by the time that the electric field exceeds the critical value for mixing n-states[10].

In the present paper, we report observations of externally induced predissociation of O_2 Rydberg states when these molecules come close to, but do not touch, a metal surface. We attribute this process to forces exerted on the molecular Rydberg state by the image dipole, that is induced in the metal surface by the Rydberg dipole (core plus electron). We speculate that these forces induce ℓ-changes of an initially stable (long-lived) molecule, thereby opening a channel with good overlap to a dissociative continuum. This behavior is observed for excited states of the oxygen molecule that lie below the lowest ionization threshold, $v^+ = 0$ of $O_2^+(X^2\Pi_g)$, as well as for Rydberg states belonging to vibrationally excited levels that lie energetically in the autoionization continuum (but are stable on the time scale of microseconds before they approach the metal surface).

We investigate the vibrational dependence of the predissociation branching among the available dissociation limits of O_2, and we study the influence of an external electric field on this predissociation phenomenon.

EXPERIMENT

The apparatus used in the present investigation is essentially identical to that used in previous work[11-17] with one minor exception that will be detailed below. In brief, O_2^+ ions are produced by electron impact on O_2 gas and are extracted by a weak repeller field, accelerated, mass selected, and collimated into a beam with a specific kinetic energy E_0. Following a total flight distance of 250 cm from the ion source, the collimated O_2^+ beam passes through a cell containing Cs vapor (see Fig. 1). A small fraction (<<1%) of the O_2^+ beam is neutralized in the Cs vapor to produce O_2 molecules. Charged particles leaving the cell are swept out of the beam by an electric field applied 26 cm downstream from the cell. Neutral particles travel unimpeded from the cell to a slit assembly (50 cm). The slit, fabricated from razor blades with a nominal radius of curvature of order 1 µm, provides an opening of dimension 300 µm x 10 mm. All particles passing through the open area of the slit are collected by a 1.27 mm × 50 mm beam flag positioned 10 cm downstream from the slit. With the exception of the immediate vicinity of the Cs cell, all regions of the apparatus are maintained at a vacuum of 5×10^{-8} Torr or less. No contribution from collisional dissociation due to background gas is detected.

If a molecule dissociates in the region between the slit and the beam flag and its fragments escape collection by the beam flag, these fragments travel to a position-sensitive detector for correlated fragments. The detector explicitly measures the spatial $(R=R_1+R_2)$ and temporal (Δt) separations of the two correlated fragments produced by the dissociation of a single molecule of mass M, energy E_0, and velocity v $(E_0 = Mv_0^2/2)$ to define the center of mass translational energy (W) released in the dissociation:[11,18]

$$W = \frac{E_0}{4L^2} (R^2 + v_0^2\Delta t^2).$$ (1)

The combination of the narrow slit and the beam flag geometrically defines a range of distances from the detector, L, for which the two correlated fragments can be both produced and detected. The narrow slit (110.8 cm from the detector) defines the maximum value for L;[19] the beam flag (100.8 cm from the detector) defines the minimum value for L. The effect of an indeterminacy in L, $\Delta L \leq 10$ cm, is to produce a broadening in the correlation of the fragment temporal and spatial separations with W, in case

77
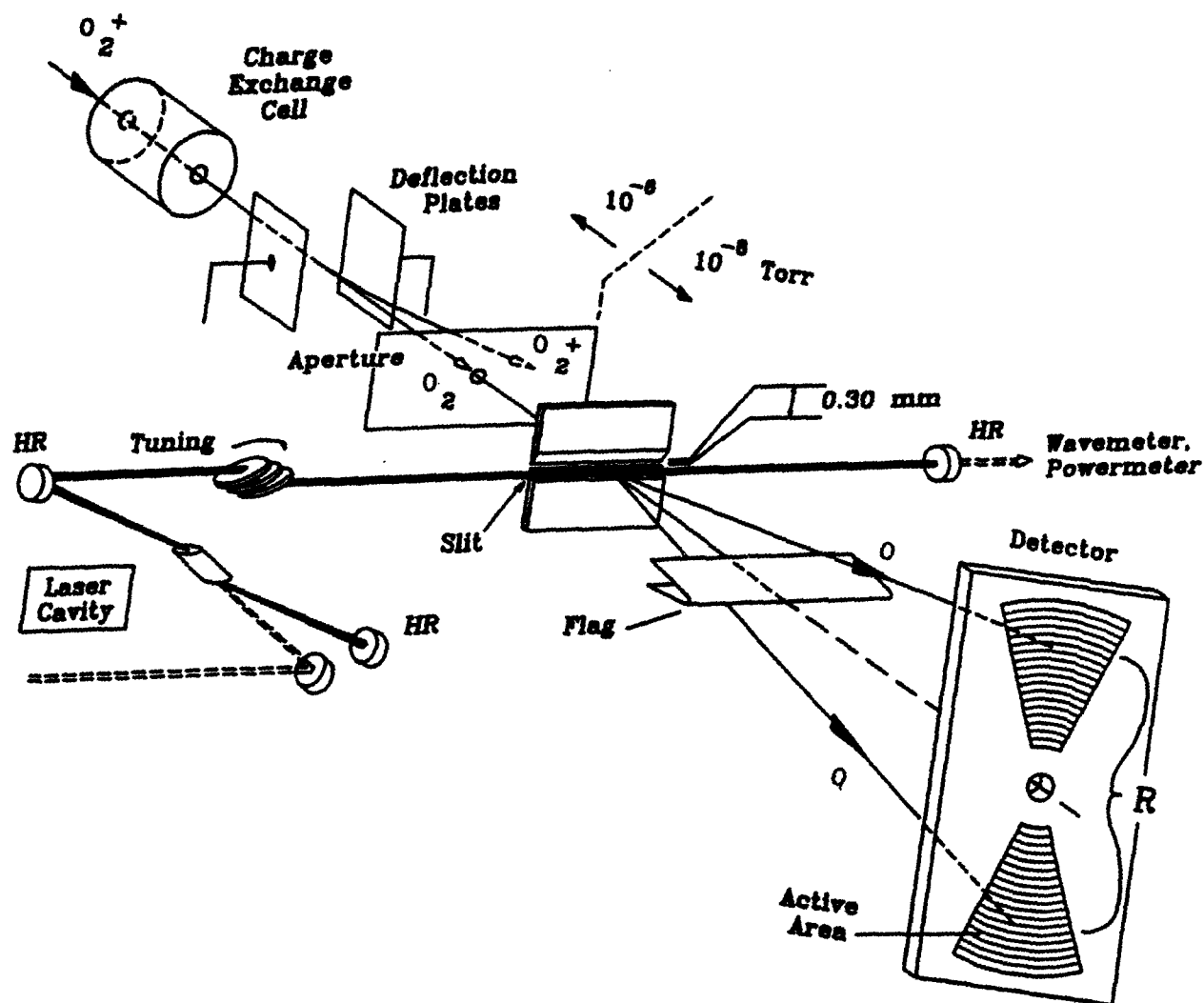
1. Schematic of fast beam apparatus to study dissociation of neutral molecules. Excited O_2 molecules, produced by neutralization of O_2^+ ($a^4\Pi_u$) in cesium vapor, are observed to dissociate at the slit assembly, both in the presence and absence of an applied electric field. The correlated neutral dissociation products are monitored on the position and time-sensitive detector.

dissociation occurs over this broad range of L values. Differentiating Eqn. (1), this broadening is

$$\Delta W/W = 2\Delta L/L. \qquad (2)$$

Thus ΔW is a constant proportional to the translational energy release. For unimolecular dissociation that occurs with equal probability over the full range of the interaction region ($\Delta L \sim 10$ cm), the resolution is quite poor with $\Delta W/W = 0.18$. On the other hand, prompt dissociation of a single molecular energy level prepared by photoexcitation within a ~2 mm laser beam diameter is found to yield $\Delta W = 0.025$ eV at $W = 1.7$ eV.

The state distribution in the precursor O_2^+ beam was selected by adjusting the ion source pressure and residence time in the source. The actual electronic, vibrational, and rotational populations of the O_2^+ ions at the time of charge-transfer neutralization was explicitly determined by Walter et al.[16] and by van der Zande et al.[20] Their results were confirmed in the present work for the specific experimental conditions employed here. Briefly, production of the O_2^+ beam at high O_2 source pressure and long source residence times produced an ion beam with >95% population in the first several vibrational levels of the $X^2\Pi_g$ state. Production of the beam at low source pressures and short residence times produced comparable populations in the $X^2\Pi_g$ state and the $a^4\Pi_u$ states, with the population of the latter extending to v>14. The $a^4\Pi_u$ state is the only electronic state of O_2^+ that is sufficiently long-lived to survive the >14 μs flight time between the ion source and the Cs charge transfer cell.

OBSERVATIONS

A weak dissociation signal of O_2 molecules produced by the reaction

$$O_2^+ + Cs \rightarrow O_2^* \qquad (3a)$$

is observed following passage of the molecules through the slit assembly:

$$O_2^* \rightarrow slit \rightarrow O + O + W, \qquad (3b)$$

where W is the released translational energy. The distribution of energy releases observed in this dissociation for a 5 keV beam of O_2^+ is shown in Figure 2. The spectrum in Fig. 2 is
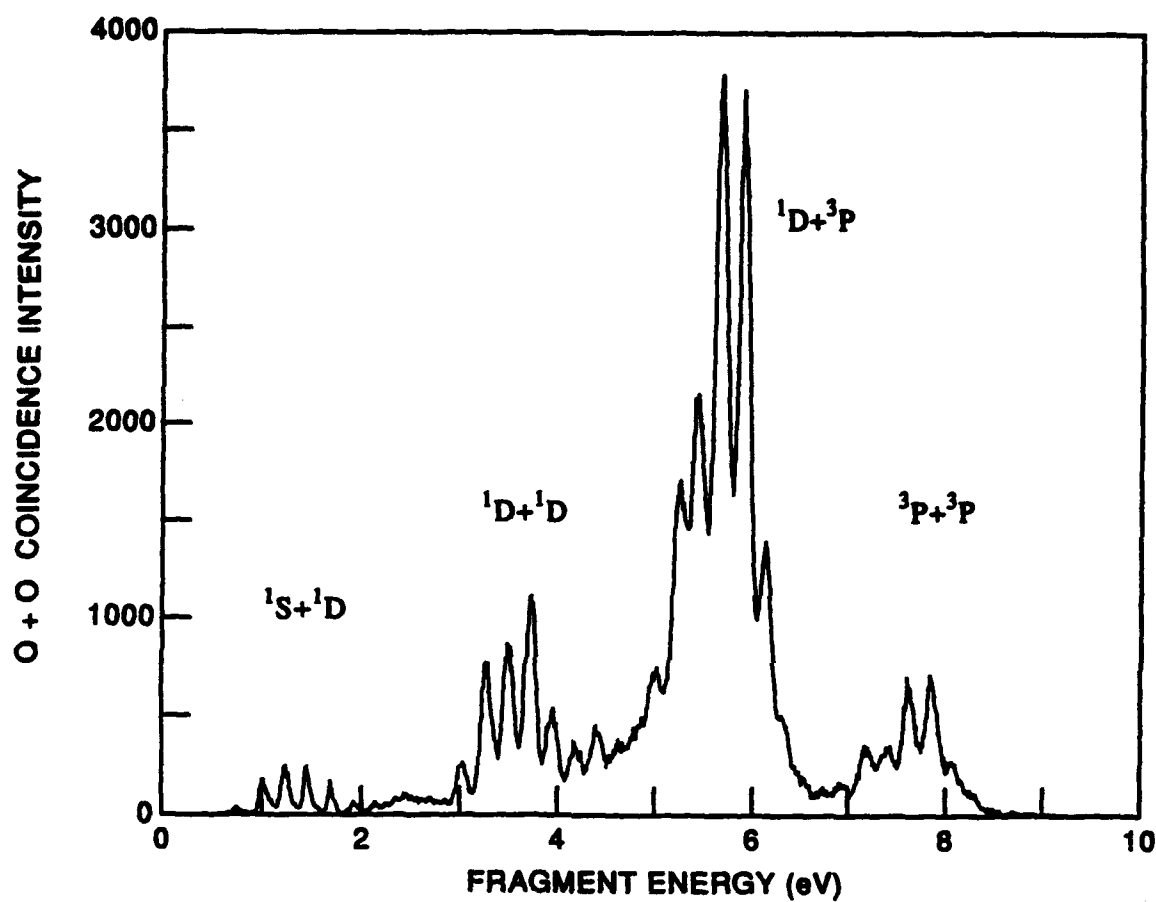
2. Measured energy release distribution for O + O atoms formed by dissociation of 5 keV O_2 at the slit in the absence of an applied electric field.

a histogram of the number of detected pairs of correlated fragments (fragment intensity) yielding [Eqn. (1)] a given value of energy release W in the range $0.5 \text{ eV} \leq W \leq 8.5 \text{ eV}$. The spectrum has been corrected for the variation of the collection efficiency with energy release.

The ratio of the fragment positions for each correlated dissociation pair relative to the center of the detector is found to be peaked at unity. This is consistent with the dissociation products being of equal mass, as expected for fragmentation from O_2 molecules. In addition, the degree of correlation in the spatial and temporal separations of the dissociation fragments proves that the signal does not arise from grazing collisions of the molecules with the surface of the slit.

It can be seen in Fig. 2 that the energy release peaks fall into four groups, each containing 6 or 7 peaks of significant intensity. The energy release values corresponding to the midpoint of each peak are given in Table I. Within the experimental uncertainty (± 10 meV), the spacings of the peaks within each group are identical and these spacings correspond to those[21,22] of the vibrational levels $v=0$-6 of the $O_2^+ \, X^2\Pi_g$ state. As discussed in the next section, the observed fragmentation arises from dissociation of near-degenerate (very high n) Rydberg states of O_2 on this core to produce four sets of O + O fragments with differing degrees of electronic excitation. For the purpose of referring to specific features in the spectra, we label each of the peaks within each group by consecutive vibrational numbers with $v=0$ being assigned to the peak at lowest W within each group. The four groups are labelled from low to high W as $O(^1S) + O(^1D)$, $O(^1D) + O(^1D)$, $O(^1D) + O(^3P)$, and $O(^3P) + O(^3P)$.

The spectrum in Figure 2 was recorded with the same potential (ground) applied to the two razor blades that form the slit assembly. However, dissociation is also observed with an electrostatic potential difference applied between the two razor blades. The effect of the potential difference on the fragment energy release spectrum is shown in Fig. 3 for the 3 keV beam. Each of the spectra in this figure is approximately normalized to the same beam flux and accumulation time to allow comparison. It can be seen in this figure that increasing the applied field affects the widths, relative intensities, and nominal values of the energy releases of the spectrum. In particular:

1. With the exception of the lowest group [$O(^1S) + O(^1D)$], the intensity of the $v=0$ peak increases with applied voltage whereas the intensities in $v > 0$ decrease rapidly. In the $O(^1S) + O(^1D)$ group, all peaks decrease in intensity with applied field with $v=0$ and $v=2$ exhibiting the smallest effect.

ELECTRIC FIELD DEPENDENCE
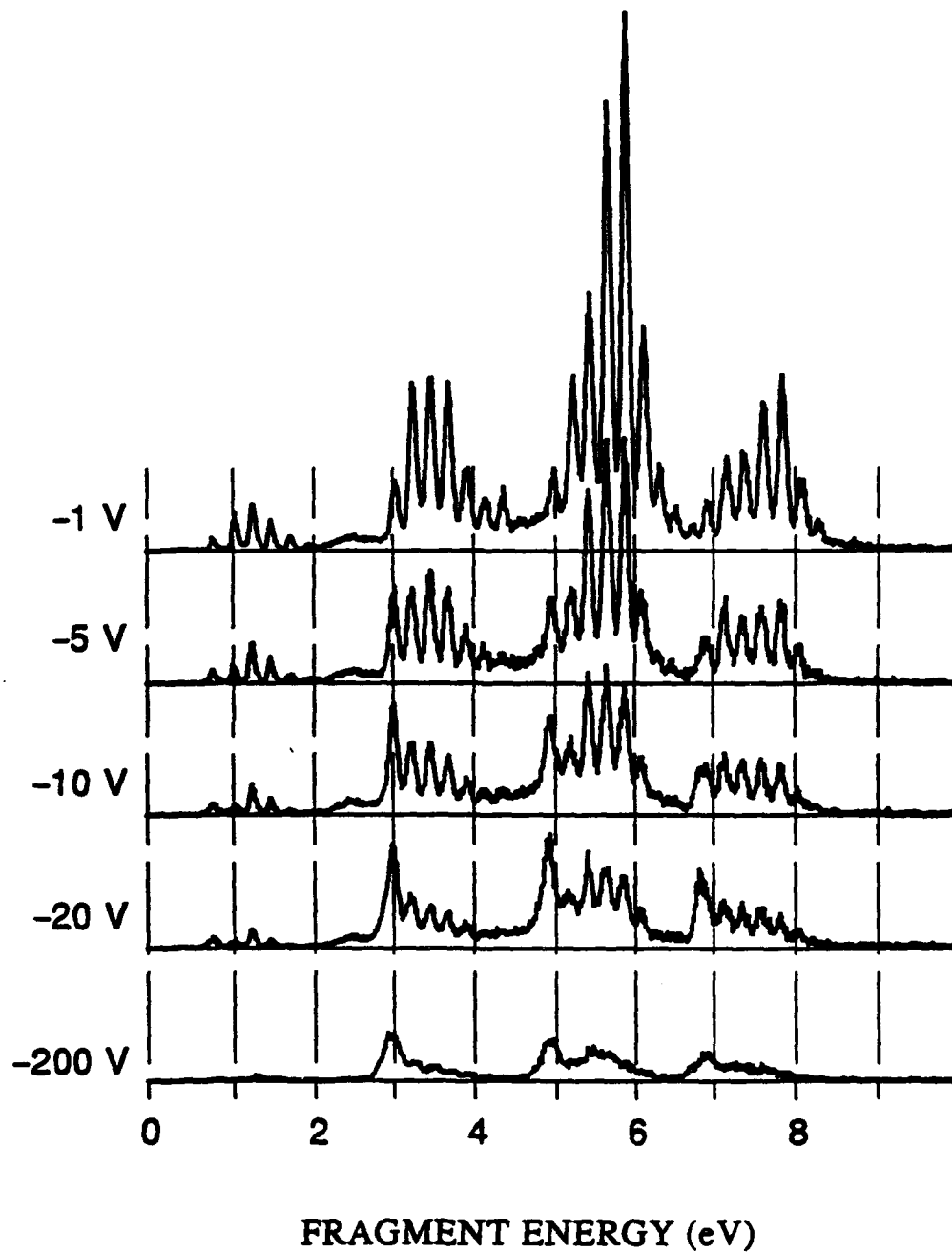
3. Dependence of the energy release distribution on the magnitude of the potential difference applied across the slit observed for a 3 keV O_2 beam.

2. The positions of the peaks within each group, as defined by the apparent W value at their Gaussian centroids, shift slightly to lower values of W with applied field.

3. With the exception of the lowest W group [$O(^1S) + O(^1D)$], the peaks corresponding to $v = 0$ appreciably broaden to lower W with applied field. This broadening will also influence the apparent midpoint of the $v=0$ peaks. Peaks $v > 0$ and all peaks in the $O(^1S) + O(^1D)$ group show no observable dependence of peak width on applied field.

4. The flux of detected dissociation fragments is found to scale directly with the concentration of O_2^+ $a^4\Pi_u$ in the precursor ion beam. The relative intensities of the vibrational peaks within each group are unaffected by the $a^4\Pi_u$ concentration.[23]

DISCUSSION

NATURE OF THE DISSOCIATING STATES

In molecular dissociation, the potential energy of the dissociating state (E_{tot}) is released as kinetic (translational, W) and potential (internal, E_{int}) energy of its dissociation products at infinite separation

$$E_{tot} = E_{int} + W. \qquad (4)$$

In the present experiment, the translational energy spectrum of the fragments specifically measures only the kinetic energy component, W. However, the possible internal energy states in the product atoms are relatively few and are widely separated in energy. The lowest dissociation limit of the O_2 molecule is to form ground state atoms:

$$O_2 \rightarrow O(^3P) + O(^3P) \qquad E_{int} \approx 0 \text{ eV}. \qquad (5a)$$

If we choose this as the reference of total energy (E_{tot}), the next higher limits lie at:

$$O_2 \rightarrow O(^1D) + O(^3P) \qquad E_{int} = 1.967 \text{ eV} \qquad (5b)$$
$$O_2 \rightarrow O(^1D) + O(^1D) \qquad E_{int} = 3.935 \text{ eV} \qquad (5c)$$
$$O_2 \rightarrow O(^1S) + O(^3P) \qquad E_{int} = 4.190 \text{ eV} \qquad (5d)$$
$$O_2 \rightarrow O(^1S) + O(^1D) \qquad E_{int} = 6.157 \text{ eV} \qquad (5e)$$
$$O_2 \rightarrow O(^1S) + O(^1S) \qquad E_{int} = 8.380 \text{ eV}, \qquad (5f)$$

where the atomic excitation energies are taken from Moore.[24] With this energy reference, the lowest energy levels of O_2 ($X^3\Sigma_g^-$, v=0,N=1,J=0) and O_2^+ ($X^2\Pi_{1/2}$, v=0) lie at -5.1167 eV and 6.954 eV, respectively, where the dissociation energy (D_0^0 = 5.1167 eV)[25] and the ionization potential (IP = 12.071 eV)[26] of O_2 provide the necessary connections between the neutral and ionic molecular levels and the atomic energy levels.

The separations among the four groups of peaks observed in the translational energy release spectrum of the O_2 molecule (see Fig. 2 and Table I) match the energy separations of the various O_2 dissociation limits, hence a unique assignment of the dissociation products can be made. Each of the groups contains at 6 or 7 discrete peaks spaced by roughly 0.23 eV. This corresponds to the vibrational spacing of the O_2^+ $X^2\Pi_g$ state, $\Delta G_{1/2} = \omega_e - 2\omega_e x_e = 0.2322$ eV. If we consider each of the peaks within a group to have a relative vibrational energy (G_v) equal to that of the $X^2\Pi_g$ state, then all of the observed peaks should be described by

$$E_{level} = W - G_v + E_{int}, \qquad (6)$$

where E_{int} is given by Eqn. (5). Assigning the vibrational numbering of the peaks as given in Table I, i.e. with the lowest member of each group assigned as v=0, and taking W_{obs} = W, the values of E_{level} for the four groups of peaks are found to be: 6.951±0.017 eV for $O(^1S) + O(^1D)$, 6.973±0.008 eV for $O(^1D) + O(^1D)$, 6.970±0.012 eV for $O(^1D) + O(^3P)$, and 6.953±0.008 eV for $O(^3P) + O(^3P)$. The four values are reasonably consistent and yield an energy for v=0 of the dissociating state of 6.963 ± 0.004 eV above ground state atoms. For comparison, the lowest level of the O_2^+ $X^2\Pi_g$(v=0) lies at 6.954 ± 0.001 eV.

Two features of the spectrum argue that the dominant contribution to the observed width of the translational energy peaks is due to the internal energy levels of the dissociating Rydberg molecules (rotational and fine-structure states) and to the presence of molecules in a range values of the principal quantum number n. One feature, obvious in the Gaussian fits, is that the peak envelopes tail toward higher energy release, such as would be expected for an ensemble of unresolved rotational levels. Secondly, the width of the peaks in the energy release spectrum are relatively broad ($\Delta W \sim 0.1$ eV in the narrowest spectra) in comparison with the intrinsic resolution of the apparatus ($\Delta W \sim 0.025$ eV), and are very nearly constant as a function of increasing energy release. In contrast, if fragments are produced over a range of distances spanning from the slit to the flag, as would occur for a unimolecular dissociation with microsecond lifetime, a broadening that is linearly dependent on energy release would result [as predicted in Eqn. (2)]. Since such a dependence is not observed here, the primary contribution to the observed peak widths

84

must arise from the molecular energies of the dissociating O_2 levels or atomic fine structure levels in the dissociation products.

Since the dissociating levels appear to describe a very high Rydberg state of O_2, an internal structure very nearly that of the O_2^+ $X^2\Pi_g$ state could be expected, i.e. a spin-orbit splitting of order 0.025 eV and a rotational manifold described by the rotational constants of the ion. Using an apparatus function characteristic of the present experimental arrangement, the experimental spectra were fit presuming the dissociation of 7 vibrational levels in a single Rydberg state of O_2 with internal energy levels exactly described by the O_2^+ $X^2\Pi_g$ molecular constants. We further presumed that both spin-orbit components have equal populations and dissociation rates, that the rotational population distribution in all vibrational levels can be characterized by a single Boltzmann temperature (T_{rot}), that ^3P_J dissociation products are produced in a statistical distribution, and that the dissociations occur within a region of length ΔL centered at the slit.

The resulting vibrational intensities from the fits are given in Table II. As described for the Gaussian fits, no evidence was found for the production of products in Reaction (5d). Both the 3 keV and 5 keV spectra were found to be well described by a single rotational temperature $T_{rot} = 630\pm50K$. This is comparable to the rotational temperature of $675\pm200K$ observed by Walter et al.[16] for the $C^3\Pi_u$ state of O_2 produced by charge transfer of $O_2^+(X^2\Pi_g)$ in Cs. Also, both spectra yielded the same value for the energy of the dissociating state, Eqn. (6), $E_{level} = 6.931 \pm 0.004$ eV, where the error refers only to the standard deviation in the fits. This value lies 31 meV below that estimated from the Gaussian fits. This was to be expected because now the energy refers to the lowest energy level rather than to the peak of a rotational and spin-orbit population distribution. In comparison to the energy of $O_2^+(X^2\Pi_g)$ at 6.954 eV, E_{level} lies 23 meV lower. This too is expected for a Rydberg state converging to this ion core. Of particular significance is that the 3 keV and 5 keV spectra could not be fit using a single value for ΔL, considering the participation of only a single Rydberg state in each case. Rather, values for ΔL of 4.2 $\pm$ 0.2 mm and 6.4 $\pm$ 0.2 mm had to be assumed for the 3 keV and 5 keV spectra, respectively. These would correspond to effective dissociation lifetimes of 31 ns and 37 ns, respectively.

Thus a single dissociating Rydberg state of O_2 cannot provide the proper description of the observed spectrum. However a consistent representation of the experimental spectrum is obtained if a series of Rydberg states is assumed to be present, that lie within a specific energy range and dissociate. This range is essentially equal to the difference in energy between E_{level} and the ionization energy of O_2, 0.023 eV,
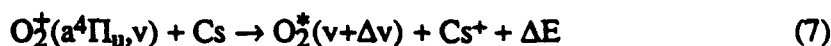
$O_2^+ (X^2\Pi_g)$
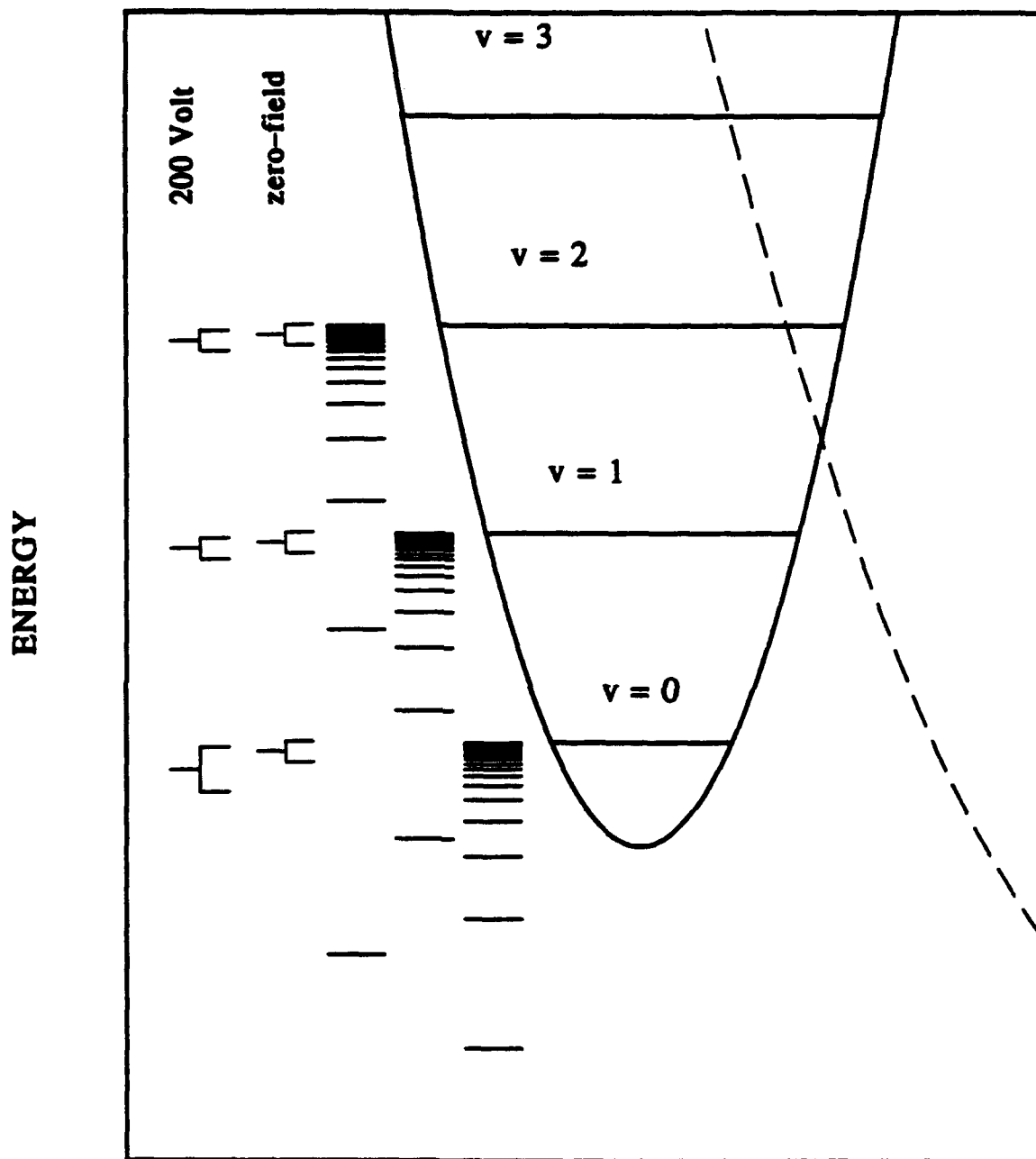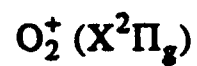
PREDISSOCIATION OF RYDBERG STATES OF O_2

4. Location of the excited states of O_2 that participate in the observed dissociation process, relative to the lowest vibrational levels of the molecular ion.

corresponding to a series of O_2 Rydberg states with effective quantum numbers in the range $24 \leq n \leq \infty$. This reasoning also implies that the dissociation lifetime is much smaller than 30 ns, that is the dissociation is confined into a narrow range of distances, L, in the vicinity of the slit. In Figure 4 we give an energy diagram that shows the location of the dissociating states relative to the lowest vibrational levels of the molecular ground state ion. The range of energies over which excited states participate in the dissociation process for zero field and for a potential difference of 200 V applied to the slit is indicated as well.

FORMATION OF THE DISSOCIATING STATES

The direct variation of dissociation fragment flux with the concentration of O_2^+ $a^4\Pi_u$ in the ion beam suggests that this state is the precursor of the dissociating O_2^* state that is formed by charge transfer in Cs vapor. The $a^4\Pi_u$ state lies 4.03 eV above the O_2^+ $X^2\Pi_g$ state or 4.05 eV above the range of Rydberg states that are observed here to dissociate. Given the 3.8939 eV ionization potential of Cs, the charge transfer reaction

$$O_2^+(a^4\Pi_u,v) + Cs \rightarrow O_2^*(v+\Delta v) + Cs^+ + \Delta E \tag{7}$$

is near resonant $(\Delta E \sim 0)$ for $\Delta v \sim 1$ if it is assumed that the O_2^* states are high Rydberg states of the ground state ion core. Thus, the energetics of the reaction strongly favor it.

Given the electron configurations[21] of the $O_2^+(a^4\Pi_u)$, $a^+ = ...(3\sigma_g)^2(1\pi_u)^3(1\pi_g)^2$, and O_2^+ $X^2\Pi_g$, $X^+ = ...(3\sigma_g)^2(1\pi_u)^4(1\pi_g)^1$, electron capture in Reaction (7) to form a $(n\ell)X^+$ Rydberg state must also involve the excitation of a core electron. Such a process is thought to be highly improbable. However, if we compare the observed flux of dissociation fragments in the present experiment with that produced by prompt dissociation at the Cs cell, the relative concentration of the O_2^* observed here to that of the $(3s\sigma_g)X^+$ states formed in Reaction (7) is only $\sim 10^{-6}$! Thus the reduced probability for a two electron process necessary to form $(n\ell)X^+$ states in Reaction (7) is consistent with the observed fragment flux.

DISSOCIATION PRODUCT BRANCHING

Figure 5 gives the relative flux of fragments at each of the four dissociation limits as a function of the vibrational quantum number of the dissociating state. The data shown represent the average between the results obtained at 3 keV and at 5 keV beam energies. It can be seen that the greatest flux of fragments is produced at the $O(^1D) + O(^3P)$ limit. The next higher product channel is the production of two ground state atoms, accounting for

Branching of $O_2^+(v) + e$
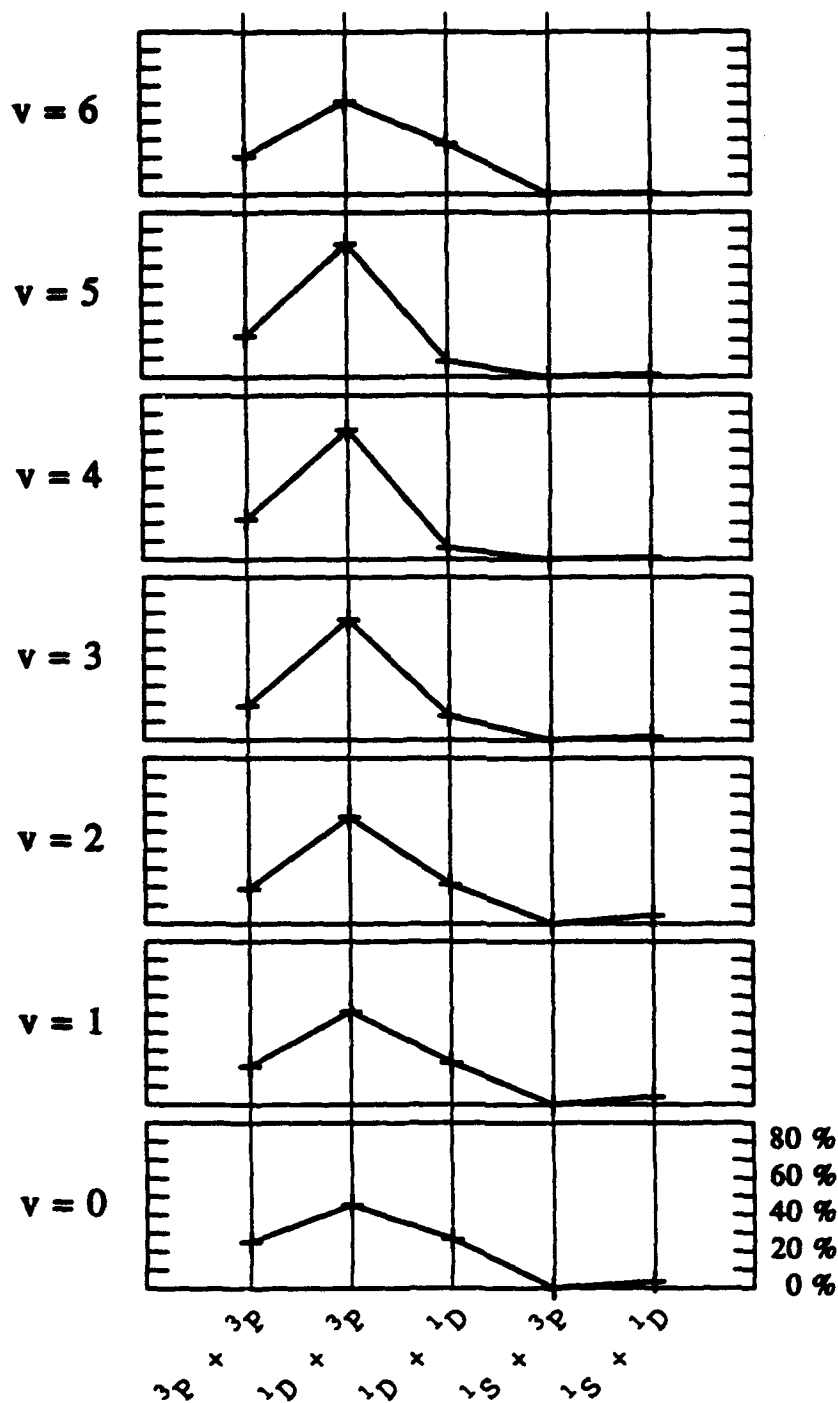
5. Measured branching of dissociation products that originate from Rydberg states belonging to the vibrational core states, v+ = 0 to 6, among the available dissociation limits of O_2.

roughly 20% of the fragments. Production of $O(^1D) + O(^1D)$ is also found to be highly probable. The highest energy dissociation channel $O(^1S) + O(^1D)$ is a relatively minor channel. No evidence is found in the experimental spectra for production of $O(^1S) + O(^3P)$ fragments. Such contributions would have to be less than 1% in the total product yield to escape detection.

DISSOCIATION MECHANISM

It is clear from our results that the process leading to dissociation of O_2^* must be confined to a narrow region in the vicinity of the the slit assembly. We propose that the following mechanisms are primarily responsible for the observed effects:

Let us assume that the charge transfer process leads to production of $(n\ell)X^+$ Rydberg states with a wide range of values of n and ℓ. Rydberg states with low values of ℓ generally have more efficient coupling to the valence continuum states. Hence, these lower ℓ members of the O_2^* ensemble of states will be removed from the beam during the transit period to the slit assembly by predissociation. Rydberg states with low values of n and ℓ can also be removed from the O_2^* ensemble by radiative decay to lower O_2 states.

Thus at the slit, only a small concentration of O_2^* will remain undissociated, and these will consist of high ℓ and high n Rydberg states that are relatively immune to predissociation and to radiative decay. At the slit, the O_2^* beam is subjected to one of several effects that can give rise to a Stark mixing of the $n\ell$ states, thereby admixing to all or some of the high ℓ quantum levels, components of lower ℓ states that are predissociated.

The high n Rydberg states are also subject to field-induced ionization. Here, the field can either lead to direct field ionization of Rydbergs with n greater than a critical value. This process will affect all vibrational levels of the O_2^*. In addition, the Stark mixing from the field can increase the rate of autoionization of Rydberg states with $v > 0$ (for $n > 7$ these levels lie in the ionization continuum). Since only neutral fragments are detected in the present experiments, the effect of O_2^* ionization is to remove it from contributing to the dissociation flux. This is evident for the dependence of the flux of dissociating molecules on the magnitude of the electric field applied across the slit as shown in Figure 3. The depletion of the dissociation signal due to field induced ionization and the origin of the dissociation signal due to an electric field related effect is further supported by the observations that the $v = 0$ peaks broaden to lower energy release with applied field, whereas $v > 0$ peaks do not perceptibly broaden, but only shift to lower values of energy release.

RELATIONSHIP TO DISSOCIATIVE RECOMBINATION

The variation of the predissociation branching with vibrational level reflects the availability of the different continuum states of O_2 to which the O_2^+ core can couple, as well as the dynamics of the dissociating system as it experiences the molecular continuum. In this sense, the dissociative process investigated here is related to the molecular dynamics involved in dissociative recombination (DR) of O_2^+ with electrons, both in the direct as well as in the indirect DR channel.[27] Therefore, as a corollary to our results, we can answer the important question of which final atomic states are produced when a specific vibrational level of superexcited oxygen molecule predissociates. This process is related to the dynamics of O_2^+ that undergoes dissociative recombination.

Previous investigations of dissociative recombination of O_2^+ were primarily concerned with the rate of formation of $O(^1S)$, the origin for the green atomic oxygen emission in the night sky.[28] Theory[29] predicts a yield of $O(^1S)$ (relative to a yield of 2 for all atoms) of 0.0024 for v=0, 0.051 for v=1, and 0.15 for v=2. This vibrational sensitivity is primarily a consequence of the location of the continuum state that is expected to contribute most strongly to the dissociative recombination reaction. Generally higher yields are deduced from satellite based observations,[30] which also predict an increase in the yield with vibrational quantum number. By comparison our experimental yields for $O(^1S)$ are 0.033, 0.041, 0.045, 0.018, 0.010, 0.015, and 0.007 for v increasing from v=0 to v=6, in marked disagreement with the strong vibrational dependence currently accepted from theoretical and experimental results. On the other hand our experimental yields for $O(^1D)$ are 0.73, 0.79, 0.83, 0.81, 0.78, 0.82, 0.78, for the vibrational levels v=0 to 6. Previous laboratory and satellite-based observations place this yield near unity.[30]

ACKNOWLEDGEMENT

90

REFERENCES

1. D. Eisel, and W. Demtröder, Chem. Phys. Lett. **88**, 481 (1982).

2. C. Bordas, P. Brevet, M. Broyer, J. Chevalyere, and P. Labastie, Europhys. Lett. **3**, 789 (1987).

3. E. Y. Xu, H. Helm, and R. Kachru, Phys. Rev. Lett. **59**, 1096 (1987)

4. C. R. Mahon, G. R. Janik, and T. F. Gallagher, Phys. Rev. A **41**, 3746 (1990).

5. C. Bordas and H. Helm, Phys. Rev. A **47**, 1209 (1993).

6. F. J. Comes, and U. Wenning, Chem. Phys. Lett. **5**, 195 (1970).

7. W. L. Glab and J. P. Hessler, Phys. Rev. Lett. **62**, 1472 (1988).

8. W. L. Glab and J. P. Hessler, Phys. Rev. A **42**, 5486 (1990).

9. C. Bordas and H. Helm, Phys. Rev A **43**, 3645 (1991).

10. C. Bordas and H. Helm, Phys. Rev A **45**, 387 (1992).

11. H. Helm and P. C. Cosby, J. Chem. Phys. **86**, 6813 (1987).

12. P. C. Cosby and H. Helm, Phys. Rev. Lett. **61**, 298 (1988).

13. P. C. Cosby and H. Helm, J. Chem. Phys. **90**, 1434 (1989).

14. H. Helm and P. C. Cosby, J. Chem. Phys. **90**, 4208 (1989).

15. C. Bordas, P. C. Cosby, and H. Helm, J. Chem. Phys. **93**, 6303 (1990).

16. C. W. Walter, P. C. Cosby, and J. R. Peterson, J. Chem. Phys. **98**, 2860 (1993).

17. P. C. Cosby, J. Chem. Phys. **98**, 7804 (1993).

18. D. P. de Bruijn and J. Los, Rev. Sci. Instrum. **53**, 1020 (1982).

19. This definition of the slit establishing the maximum value for L is only approximate because there is a short region upstream of the slit where both fragments from dissociation of a properly aligned O_2 molecule can both pass through the slit, escape collection by the flag, and arrive at an active area of the PSD-C. This upstream distance is 3.1 cm for production of fragments with a minimum separation at the detector and 0.45 cm for production of fragments with a maximum separation at the detector. In all cases, however, such events constitute only a small fraction of the dissociations produced in a randomly aligned beam and can be neglected for the purposes of the present discussion.

20. W. J. van der Zande, W. Koot, J. R. Peterson, and J. Los, Chem. Phys. 126, 169 (1989).

21. P. H. Krupenie, J. Phys. Chem. Ref. Data 1, 423 (1972).

22. R. R. Laher and F. R. Gilmore, J. Phys. Chem. Ref. Data 20, 685 (1991).

23. The population distribution in the $a^4\Pi_u$ state is observed to be unaffected by quenching.

24. C. E. Moore, Nat. Stand. Ref. Data Ser., Nat. Bur. Stand. (U.S.), 34 (1970).

25. P. C. Cosby and D. L. Huestis, J. Chem. Phys. 97, 6108 (1992).

26. K. P. Huber and G. Herzberg, *Molecular Spectra and Molecular Structure IV. Constants of Diatomic Molecules* (Van Nostrand Reinhold Co., N.Y., 1979).

27. J. N. Bardsley, J. Phys. B. 1, 349 (1968).

28. D. R. Bates, Planet. Space Sci. 38, 889 (1990).

29. S. L. Guberman and A. Giusti-Suzor, J. Chem. Phys. 95, 2602 (1991).

30. J.-H. Yee, V. J. Abreu, and W. B. Colwell, "Aeronomical Determinations of the Quantum Yields of $O(^1S)$ from Dissociative Recombination" in *Dissociative Recombination: Theory, Experiment, and Applications*, edited by J. B. A. Mitchell and S. L. Guberman (World Scientific, Singapore, 1989), p.286.

Table I. Observed translational energy releases (W_{obs}) of peaks in the O_2 dissociation spectrum. Peaks are fitted as Gaussians and W refers to the centroid of the Gaussian. The upper and lower entries for each vibrational level refer to data obtained with a 3 keV and 5 keV O_2 beam energy, respectively. The entries G_v are the relative vibrational energies of the O_2^+ $X^2\Pi_g$ state, taken from the constants of Ref. 22. Deviations, $W_{obs}-W_c$, are referenced to a calculated value for the translational energy release W_c that assumes a single dissociating state at the ionization limit (IP = 6.954 eV) with vibrational energies G_v.

v	$O(^1S) + O(^1D)$		$O(^1D) + O(^1D)$		$O(^1D) + O(^3P)$		$O(^3P) + O(^3P)$		G_v (eV)
	W_{obs} (eV)	$W_{obs}-W_c$ (meV)	W_{obs} (eV)	$W_{obs}-W_c$ (meV)	W_{obs} (eV)	$W_{obs}-W_c$ (meV)	W_{obs} (eV)	$W_{obs}-W_c$ (meV)	
0	0.790	-7	3.047	28	5.001	14	6.939	-15	0.
	0.761[a]	(-36)	3.027	8	5.029[a]	(42)	6.944	-11	
1	1.044	15	3.270	18	5.235	16	7.178	-8	0.2322
	1.027	-2	3.281	29	5.258	39	7.189	-3	
2	1.261	3	3.498	18	5.446	-1	7.408	-6	0.4604
	1.243	-14	3.505	25	5.449	2	7.417	3	
3	1.481	0	3.713	9	5.675	49	7.635	-4	0.6845
	1.457	-24	3.725	21	5.680	23	7.646	7	
4	1.727	26	3.931	8	5.901	10	7.861	2	0.9045
	1.700	-11	3.949	25	5.914	34	7.862	3	
5	1.964[a]	(46)	4.161	21	6.124	17	8.088	13	1.1206
	1.925	7	4.193[a]	(53)	6.141		8.043[a]	(-32)	

[a] Weak feature in the spectrum.

Table II. Observed intensities of the dissociation fragments for V_{slit} = -1V for the 3000 eV and 5000 eV O_2 beam energies. The intensities at each beam energy are given by I which is normalized to a total intensity of 100. The relative vibrational intensities at each dissociation limit are given by I_v.

Beam Energy (eV)	v	$O(^1S) + O(^1D)$		$O(^1D) + O(^1D)$		$O(^1D) + O(^3P)$		$O(^3P) + O(^3P)$		Normalization
		I	I_v	I	I_v	I	I_v	I	I_v	
3000	0	0.18	.06	2.08	.10	1.63	.03	1.32	.06	
	1	0.70	.21	4.49	.22	4.90	.09	2.67	.13	
	2	1.10	.34	5.18	.25	7.74	.14	2.74	.13	
	3	0.69	.21	4.54	.22	15.0	.27	4.94	.24	
	4	0.39	.12	2.07	.10	17.6	.32	5.79	.28	
	5	0.19	.06	1.0	.05	6.70	.12	2.36	.11	
	6	0.03	.01	1.0	.05	2.15	.04	0.82	.04	
	SUM	3.3		20.4		55.7		20.6		= 100.
5000	0	0.07	.05	0.34	.04	1.55	.02	0.64	.03	
	1	0.29	.22	1.20	.14	7.05	.10	2.36	.12	
	2	0.36	.28	1.78	.21	10.5	.15	2.38	.12	
	3	0.28	.22	2.54	.29	21.5	.30	5.26	.27	
	4	0.18	.14	1.19	.14	21.2	.30	6.16	.31	
	5	0.10	.07	0.69	.08	7.20	.10	2.20	.11	
	6	0.02	.02	0.88	.10	1.41	.02	0.61	.03	
	SUM	1.3		8.6		70.5		19.6		= 100.

93

The Dodecahedral N_{20} Molecule:

Some Theoretical Predictions

Henry F. Schaefer III
Center for Computational Quantum Chemistry
University of Georgia
Athens, Georgia 30602

The intense scientific and popular interest in the C_{60} molecule has naturally raised the question whether other important cluster species have been systematically overlooked. Our interest in this respect arises from a comparison with the dodecahedrane molecule $C_{20}H_{20}$, the subject of an intense organic synthesis quest that ended in 1982 with the work of Paquette. Isoelectronic with $C_{20}H_{20}$ would be the dodecahedral N_{20} molecule, which presumably would also display I_h symmetry.

Assuming that dodecahedral N_{20} can be synthesized, it is *not* expected to rival the remarkable stability of C_{60}. Assuming that the thirty equivalent nitrogen-nitrogen single bonds are unstrained, N_{20} would be bound by roughly

$$30 \times (40 \text{ kcal/mole}^3) = 1200 \text{ kcal/mole}$$

relative to twenty infinitely separated nitrogen atoms. For comparison ten nitrogen molecules (N_2) are bound by

$$10 \times (225 \text{ kcal/mole}^4) = 2250 \text{ kcal/mole}$$

relative to the same set of twenty nitrogen atoms. Thus our back-of-the-envelope calculation suggests that dodecahedral N_{20} will lie above separated N_2 molecules by roughly 105 kcal per mole of N_2 molecules. One concludes that N_{20} with its weak nitrogen-nitrogen single bonds would be a reasonable candidate for a high energy density material (HEDM).

To our knowledge, the only previous mention of N_{20} in the chemical literature is contained in the 1992 paper Chen, Lu, and Y a n g. These authors note that the N-N-N bond angles in dodecahedral N_{20} are exactly 108°, very close to the tetrahedral bond angle 109.47°, suggesting that N_{20} may be relatively unstrained. Chen, Lu, and Yang have applied the semi-empirical MINDO/3, MNDO, and AM1 methods to dodecahedral N_{20}. Unfortunately, the semi-empirical results are inconsonant, even with respect to the question of whether dodecahedral N_{20} lies senergetically above 10 N_2 (it obviously does; see discussion above). Moreover, for such a novel species as dodecahedral N_{20}, it is not a *priori* obvious which of these three semi-empirical methods will be most reliable.

In this research, the structure of dodecahedral N_{20} has been predicted using *ab initio* quantum mechanical methods. The minimum basis STO-3G set of Hehre, Stewart, and Pople was used in preliminary studies. This was followed by the N(9s5p/4s2p) double zeta (DZ) basis of Huzinaga and Dunning. The double zeta plus polarization (DZP) basis added a set of d functions on each nitrogen atom, with orbital exponent α_d (N) = 0.8. Finally, the Huzinaga-Dunning triple zeta plus double polarization (TZ2P) basis set, designated N(10s6p2d/5s3p2d), was used. In the TZ2P basis set of 480 contracted gaussian functions the polarization function orbital exponents were α_d (N) = 1.6, 0.4. In addition to the self-consistent field (SCF) method, used here with all basis sets, second-order perturbation theory (designated MP2 here) was used in conjunction with the DZP basis set. All computations were carried out using the TURBOMOLE programs of Ahlrichs and coworkers.

Table 1 shows the *ab initio* bond distances and dissociation energies for N_{20} and compares these with the semi-empirical results of Chen, Lu, and Yang. At the SCF level of theory, the N-N bond

distance appears to be reasonably converged with the DZP basis set. Extension from DZP to TZ2P decreases the SCF bond distance by only 0.001 Å.

The treatment of electron correlation effects using second order perturbation theory is seen to significantly increase the N-N single bond distances - by 0.065 Å to 1.503 Å. Given the tendency of the MP2 method to somewhat exaggerate correlation effects and the expected shortening of bonds with larger basis sets , we suggest a final N-N bond distance of about 1.48Å. Thus the MINDO/3 method is seen to be severely deficient, the MNDO method fair, and the AM1 method exemplary in their predictions of the N_{20} bond distances. This 1.48 Å bond distance is somewhat longer than the "normal" nitrogen-nitrogen single bond distance of 1.447 Å in hydrazine, H_2N - NH_2.

The *ab initio* binding energies of N_{20} relative to ten separated N_2 molecules are consistent with the back-of-the-envelope arguments given in the introduction to this paper. Expansion of the basis set favors 10 N_2 relative to N_{20}, due no doubt to the importance of polarization functions in describing the N_2 triple bond. However, second-order perturbation theory is more important for N_{20} than for 10 N_2. A reasonable final *ab initio* estimate for $\Delta E(N_{20} - 10\ N_2)$ is about 1000 kcal/mole, or 50 kcal per mole of nitrogen atoms. Thus N_{20} would be a very effective high energy density material if it could be readily synthesized. The highly constrained dodecahedral structure of this N_{20} isomer suggests that a substantial barrier to fragmentation may exist. As with the structural results, the *ab initio* energetic predictions confirm the reasonableness of the AM1 predictions but discredit the MINDO/3 and MNDO methods.

DZ SCF and DZP SCF vibrational frequencies for dodecahedral N_{20} were also predicted. All of the N_{20} vibrational frequencies are remotely distant from the isolated N_2 harmonic vibrational frequency, 2359 cm^{-1}. Unfortunately only the T_{1u} vibrational frequency among the fundamentals is allowed in the infrared. The IR intensity of the T_{1u} fundamental decreases drastically from the DZ SCF (13 km/mole) to the DZP SCF (0.4 km/mole) level of theory. Experience suggests that the DZ SCF results should not be taken very

seriously, as polarization functions are mandatory for reliable IR intensity predictions. Although the theoretical magnitude (0.4 km/mole) of the T_{1u} intensity is weak, the unusual simplicity of the expected IR spectrum may make detection of this feature near 770 cm^{-1} possible. The one A_g and three H_g fundamentals are Raman allowed, but this is unlikely to be the first experimental technique applied to dodecahedral N_{20}. To estimate the true fundamentals, the DZP SCF harmonic vibrational frequencies should be multiplied by a factor close to 0.9, as was done above to obtain the T_{1u} estimate of 770 cm^{-1}.

In summary, several properties of the hypothetical dodecahedral N_{20} molecule have been predicted. The most plausible experimental means for the initial detection of this remarkable species would appear to be mass spectrometry. This work also suggests the possibility of dodecahedral P_{20}, which will be thermodynamically far more stable relative to 10 P_2 (than N_{20} is to 10 N_2) due to the greater strength (~55 kcal/mole) of P-P single bonds and smaller dissociation energy (D_o = 116 kcal/mole) of P_2.

Table 1. Total and relative energies and bond distances for dodecahedral N_{20}.

	E(hartrees)	$\Delta E_e(N_{20} - 10N_2)$ kcal/mole	$r_e(N-N)$
MINDO/3	-	-406	1.347
MNDO	-	486	1.426
AM1	-	1095	1.484
Minimum Basis			
STO-3G SCF	-1074.28955	450	1.506
DZ SCF	-1087.18536	1002	1.486
DZP SCF	-1087.94298	1031	1.438
TZ2P SCF	-1088.08644	1107	1.437
DZP MP2	-1091.42677	924	1.503

Theoretical/Experimental Investigations of the Structure and Dynamics of Highly Energetic Dication Species

W. Carl Lineberger, Stephen R. Leone, and Stephen V. ONeil
Joint Institute for Laboratory Astrophysics
University of Colorado
Boulder, Colorado 80309-0440

Dication research at JILA continues along both experimental and theoretical explorations. Doubly charged molecular ions are novel species with unique energetic and bonding properties. As a class, they exhibit high energy content, long lifetimes against predissociation, and bonding partnerships for which there are no neutral analogs. A goal of this research is to understand the bonding and energy release of these species in chemical transformations.

Considerable focus of our recent work is on the reactions and interactions of dication species with rare gases, H_2, and O_2. In the laboratory, molecular dications are prepared by electron impact ionization and are mass selected. For reactive studies, the beam of ions is crossed with a pulsed jet of neutral reactants and the ion products are detected with a time-of-flight mass spectrometer. The results of these studies have shown some remarkable properties and trends, which are important in determining their stability, as enumerated below.

Theoretical investigations involve complete active space self consistent field (CAS-SCF) and multi-reference configuration interaction (MR-CI) techniques to investigate the stability of isolated dication species and to determine their reactivity with various collision partners.

We have shown that the CAS-SCF theoretical methods are only qualitatively correct for dications. The MR-CI method combined with the insights from the CAS-SCF are essential for accurate predictions. As an example, consider a calculation of the charge localization on the ion CF_2^{2+}. Experimentally, we have found this "core" ion to be a particularly stable species; it is readily formed in high yield by loss of neutral F atoms from CF_3^{2+} in collisions. At low levels of theory, the charge is almost completely on the carbon, but at the highest levels of theory there is +1.2 charge on the carbon and +0.4 on each of the fluorine atoms. Such a result is an invaluable aid to understanding the mechanisms of the observed reactions in which chemical bond breaking and forming occur. The core ion principal appears to be quite general, having also been observed experimentally, in the formation of SF_2^{2+}

species from collisions of SF_x^{2+} (x=3,4).

Detailed studies of reactivity have now been completed between CO^{2+}, COS^{2+}, CO_2^{2+}, CF^{2+}, CF_2^{2+}, CF_3^{2+}, SF_2^{2+}, SF_3^{2+}, and SF_4^{2+} with each of the rare gases, between CO_2^{2+}, CF^{2+}, CF_2^{2+}, CF_3^{2+}, SF_2^{2+}, SF_3^{2+}, and SF_4^{2+} with D_2 and between CF^{2+} and CF_2^{2+} with O_2. The reactions are studied at low enough collision energies that chemical bond transformations are observed, as well as charge transfer, collision-induced dissociation and neutral loss channels. New studies will involve the reactions of dications with hydrocarbon molecules.

A number of important principals have been elucidated from the reaction studies. Experimentally, it is found that collision-induced dissociation (or predissociation) of the dications does occur, especially with the lighter rare gases such as He and Ne. However, the cross sections for these processes are typically small, less than 1 Å^2. Charge transfer reactions have large cross sections, but charge transfer is restricted to those processes that are intrinsically exothermic, i.e. not including the collision energy. Essentially charge transfer does not occur if kinetic energy is required. This is explained by simple Landau Zener models of the collision process. In addition, the observed product states of charge transfer obey a rigorous Landau Zener formalism in which the potential curves must cross within an appropriate small range of distances in order for reaction to occur. Because of this mechanism, the reactions are remarkably specific in producing selected product species or states. Our MR-CI calculations for CO^{2+} with Ne confirm this analysis. We have also observed a first example of a double charge transfer process with a molecular dication in the reaction of CO^{2+} with Xe.

Surprisingly, we also detect major channels of bond breaking and forming in reactions of dication species with D_2 and O_2. For example, the reaction of CF_2^{2+} with D_2 forms DCF_2^+ in high yield, effectively competing with charge transfer, and the reaction of CO_2^{2+} with D_2 forms DCO^+ as one of the highest yield ion products. These results are surprising in light of the large charge transfer cross sections which are available in these systems. Evidently, the dications are able to get close enough together to induce chemical bond transformations, without immediate predissociation or charge transfer followed by separation of products. The evidence for neutral loss reactions and chemical bond breaking and forming represent general new classes of reactions involving multiply charged ions.

In the near future, our studies will also make use of ultrafast laser spectroscopic techniques to probe the dynamics of clustered species relevant to HEDM, and corresponding theoretical work will be initiated. An apparatus is being

developed to prepare mass selected oxygen cluster ions with specific dopant molecules embedded inside; the fragmentation of these cold cluster species and their stability and internal reactions will be investigated.

References

J. Senekowitsch, S. V. ONeil, H. -J. Werner, and P. J. Knowles, J. Chem. Phys. **93**, 562 (1990).

P. J. Miller, S. A. Rogers, J. Senekowitsch, S. V. ONeil, S. R. Leone, H. -J. Werner, and P. J. Knowles, Int. J. Mass Spectrom. Ion Proc. **100**, 505 (1990).

J. Senekowitsch, S. V. ONeil, H. -J. Werner, and P. J. Knowles, Chem. Phys. Lett. **175**, 548 (1990).

S. A. Rogers, P. J. Miller, S. R. Leone, and B. Brehm, Chem. Phys. Lett. **166**, 137 (1990).

J. Senekowitsch, S. V. ONeil, H. -J. Werner, and P. J. Knowles, J. Phys. B **24**, 1529 (1991).

G. Parlant, J. Senekowitsch, S. V. ONeil, and D. R. Yarkony, J. Chem. Phys. **94**, 7208 (1991).

J. Senekowitsch, S. V. ONeil, H. -J. Werner, and P. J. Knowles, J. Phys. Chem. **95**, 2125 (1991).

J. Senekowitsch and S. V. ONeil, J. Chem. Phys. **95**, 1847 (1991).

D. M. Szaflarski, A. S. Mullin, K. Yokoyama, M. N. F. Ashfold, and W. C. Lineberger, J. Phys. Chem. **95**, 2122 (1991).

J. Senekowitsch, S. V. ONeil, and W. Meyer, Theor. Chim. Acta **84**, 85 (1992).

A. S. Mullin, D. M. Szaflarski, K. Yokoyama, G. Gerber, and W. C. Lineberger, J. Chem. Phys. **96**, 7191 (1992).

S. A. Rogers, S. D. Price, and S. R. Leone, J. Chem. Phys. **98**, 280 (1993).

S. D. Price, S. A. Rogers, and S. R. Leone, J. Chem. Phys. (in press).

IN SEARCH OF NOVEL HIGH ENERGY DENSITY MATERIALS

Karl O. Christe and William W. Wilson

Rocketdyne Division of Rockwell International Corporation
Canoga Park, California 91309

The following areas were investigated during the past year and good progress toward novel high energy density materials was made: (i) nitrogen pentafluoride; (ii) azide chemistry; (iii) polynitrogen compounds; (iv) tetranitrohydrazine and trinitramine; (v) oxygen-fluorine exchange reactions; and (vi) chemistry at the limits of oxidation and coordination.

Nitrogen pentafluoride would be a promising space-storable oxidizer and its performance would exceed that of N_2F_4 by about 40 seconds. Since the energy difference between covalent NF_5 and either crystallinic or solvated $NF_4^+F^-$ is small,[1] the stability of NF_5 can be examined by studying the thermal stability of solvated NF_4^+ and F^- ions in a suitable solvent. The lowest melting, compatible solvent previously available was CH_3CN (mp -44°C). It was found that CHF_3 (mp -155°C) is also a compatible solvent. This allowed to examine the thermal stability of $NF_4^+F^-$ at much lower temperature. It was found that even at -142°C $NF_4^+F^-$ still decomposes to NF_3 and F_2 and, hence, is not stable at this temperature toward decomposition to NF_3 and F_2.

In the area of azide chemistry, a series of stable salts of protonated hydrazoic acid was discovered and their structures were determined by X-ray crystallography, vibrational spectroscopy, a

normal coordinate analysis and local density functional theory calculations. It was shown[2] that the $H_2N_3^+$ cation has the asymmetric, aminodiazonium structure, H_2NNN^+, and is analogous to that of the isoelectronic cyanamide molecule, except for its $-NH_2$ group being less pyramidal which results in a lower inversion energy barrier.

There has been recently considerable interest in polynitrogen compounds for possible use as halogen free propellants. Two potential candidates for which no previous references could be found in the literature and which synthetically might be more readily accessible are the triazidamine molecule, N_{10}, and the diazidamide anion, N_7^-. Ab initio calculations at the MP-2/6-31G* level were carried out by Harvey Michels and John Montgomery at UTC and show that these compounds are vibrationally stable and exhibit true energy minima. The heat of formation and the barrier to decomposition of N_{10} were calculated to be 303 kcal/mol and 10.8 kcal/mol, respectively, which makes the expected stability of N_{10} comparable to that of the known FN_3 molecule. Possible synthetic routes to these compounds involve the reactions of trimethylsilyl precursors with suitable halogen compounds.

In the area of nitramines, tetranitrohydrazine and trinitramine would be attractive replacements for N_2O_4 as halogen free, earth-storable oxidizers which would result in a performance improvement of about 15 sec. Screening reactions were carried out to study whether tetranitrohydrazine could be prepared by oxidative coupling of the dinitramide anion which was recently discovered by R. Schmidt at SRI. Cyclic voltametry of aqueous $N(NO_2)_2^-$ solutions at a pH of 4.3 showed an irreversible oxidation peak at 1.03 volt versus Ag/AgCl. This

indicates that $N(NO_2)_2^-$ is readily oxidized but that the resulting $N(NO_2)_2$ radical is short-lived in aqueous solution, and organic solvents will be needed for this coupling reaction. We have also explored the use of trimethylsilyl compounds as starting materials and studied the reaction of $N[Si(CH_3)_3]_3$ with FNO_2 in CH_3CN solution as a model. The desired products, $FSi(CH_3)_3$ and $O_2NN[Si(CH_3)_3]_2$ were observed, in addition to some $O_2NN(NO)_2$, but the product mixture was very complex and better isolation and separation methods will be needed.

Oxygen-fluorine exchange reactions are being studied as a potential route to novel oxidizers such as ClF_5O. We expect ClF_5O to be a highly stable molecule and to be the best earth-storable oxidizer with an I_{sp} improvement of about 10 seconds over ClF_5. A recent report[3] by Bougon that oxygen in OsO_4 can be exchanged for fluorine by the use of KrF_2 in anhydrous HF solution prompted us to repeat his experiment. It was found, however, that the reaction product was not $OsOF_6$, as reported by Bougon, but cis-OsO_2F_4 instead. To properly identify this novel Os(+VIII) compound, its structure was determined by electron diffraction, vibrational and NMR spectroscopy, and density functional theory calculations. Since the highest F atom fluxes, without simultaneous destruction of the desired product, can be generated in a hot wire reactor, such as reactor was designed and constructed. The hot wire reactor technology was pioneered[4] at the Kurchatov Institute in Russia and has primarily been used for the synthesis of KrF_2. The operating parameters of our reactor are presently being optimized using the KrF_2 reaction.

Excellent progress was made in the chemistry at the limits of coordination and oxidation. Our experimental work on the problems of heptacoordination is essentially complete and the results are in various stages of publication. Two papers on IF_7 and IF_6O^- have already been published[5,6] and two more on XeF_7^+ and TeF_7^- and $TeOF_6^{2-}$ have been accepted for publication. It is shown in these papers that all heptacoordinated main-group element compounds have highly fluxional, pentagonal bipyramidal structures with mainly covalent, short axial bonds and longer, semi-ionic equatorial bonds. The structures are governed by the geometry of the binding electrons of the central atom and not, as in the corresponding transition metal compounds, by repulsion effects.

References

1) K.O. Christe and W.W. Wilson, J. A. Chem. Soc., **14**, 9934 (1992), and references cited therein.

2) K.O. Christe, W.W. Wilson, D.A. Dixon, S.I. Khan, R. Bau, T. Metzenthin, and R. Lu, J. Am. Chem. Soc., **115**, 1836 (1993).

3) R. Bougon, J. Fluorine Chem., **53**, 419 (1991).

4) V.N. Bezmel'nitsyn, V.A. Legasov, and B.B. Chaivanov, Dok. Akad. Nauk. SSSR, **235**, 96 (1977).

5) K.O. Christe, E.C. Curtis, and D.A. Dixon, J. Am. Chem. Soc., **115**, 1520 (1993).

6) K.O. Christe, D.A. Dixon, A.R. Mahjoub, H.P.A. Mercier, J.C.P. Sanders, K. Seppelt, G.J. Schrobilgen, and W.W. Wilson, J. Am. Chem. Soc., **115**, 2696 (1993).

Charge Induced Spectrum in

γ-Ray Irradiated para-H_2 Crystals

Takamasa Momose,[*] Karen E. Kerr,

Charles M. Gabrys, David P. Weliky,

Robert M. Dickson, and Takeshi Oka

Department of Chemistry,

Department of Astronomy and Astrophysics,

and the Enrico Fermi Institute

The University of Chicago

Chicago, IL 60637

[*] Present address;   Department of Chemistry, Kyoto University, Kyoto, Japan

107

Abstract

A very sharp spectral line was observed in γ-ray irradiated para-H_2 crystals and assigned to the pure vibrational Raman type $Q_1(0)$ transition induced by the electric fields of charges in the ionized crystal. The integrated intensity of the spectrum gives the average distance between charges to be ~500Å and the charge density to be ~10^{16} cm^{-3}. The sharpness of the spectral line is ascribed to the $\Delta k = 0$ exciton momentum rule which holds approximately for the domains of microcrystals between charges. The induced spectrum is very stable and remains undiminished over many days and over temperature cycles. A sequence of events was inferred which lead to the localization of charges in the form of ion clusters $H_3^+(H_2)_n$ and $H^-(H_2)_n$.

The spectroscopic study of ionized solid hydrogen was initiated when Souers and his colleagues studied infrared spectra of isotopic solid hydrogens containing tritium and discovered new spectral features caused by the radioactivity.[1] Since then, extensive studies on the charge induced spectrum have been carried out by the groups of Lawrence Livermore, University of Guelph, and McMaster University using tritium[2] and 15 MeV proton beams.[3,4] Several induced features in the infrared[1-4] and ultraviolet[5] spectra of isotopic species have been interpreted on the basis of a variety of physical effects such as the Stark shift,[6,7] electron bubbles,[8,9] small polaron holes,[9] interference effects,[10] and ion clustering.[11] More recently Chan et. al. conducted similar experiments on para-H_2 crystals using 3 MeV electron bombardment.[12,13] Their results were complementary to those from previous infrared studies in that the broad near infrared absorption ascribed to electron bubbles[8,9] were not observed, but many new features ascribed to H_2 and ionized hydrogenic species were observed. In particular, a sharp induced spectral line at 4149.66 cm^{-1} appeared to be an excellent candidate for a high resolution spectroscopic study.[12,13]

In this paper we report our study of this line using the high resolution of laser spectroscopy.[14, 15] γ-ray irradiation is used for radiolysis because of its efficiency, ease of operation and capability to produce uniform ionization. Such radiolysis has been extensively used for solid hydrogen by Miyazaki and his colleagues. Their ESR experiments revealed interesting behaviors of hydrogen atoms in solid hydrogen.[16]

A crystal of nearly pure para H_2 (99.8% para, 0.2% ortho) was prepared in a manner similar to that reported earlier.[14,17] The crystal was grown at 7K in a cylindrical copper cell (1.7 cm in diameter, 10 cm long) by continuously flowing the converted hydrogen gas into the cell. The sample was then allowed to cool to 4.2K. The crystal container was irradiated with γ-rays from a ^{60}Co source at Argonne National Laboratory. The irradiation time was ~ 1 hour and the dose rate was ~ 1 M rad/hour which corresponds to ~ 3.5×10^{17} ionizations cm^{-3} in solid hydrogen. The crystal temperature was measured to be ~ 9K during the irradiation. Two hours after the completion of the irradiation, the infrared spectrum of the crystal was observed in low resolution (~ $0.1\ cm^{-1}$) using BOMEM DA-2 Fourie transform spectrometer and in high resolution using either a difference frequency laser system or a color center laser (~ 5 MHz). When using the difference frequency system, we also recorded the stimulated Raman gain spectrum[18] for which the Ar^+ and dye lasers provided the pump and probe radiations, respectively. The optical arrangement for the simultaneous observation is shown in Fig. 1.

A low resolution spectrum in the region of the Q_1 (0) and Q_1 (1) transitions before and after the γ-ray irradiation is shown in Fig. 2. The prominent sharp induced feature at 4149.66 cm^{-1} is the subject of this study. Other broader features observed in longer wavelength regions that have been ascribed to ionic clusters[13] will be discussed in a separate paper.

Under the high resolution of laser spectroscopy, the γ-ray induced spectral line was found to be extremely sharp (Δv ~ 80MHz hwhm) and intense. Three experiments have been conducted over a span of two months. Two examples of observed lines are

shown in Fig. 2. The intensity and the line shape varied depending on the run, the probed positions of the crystal, and the polarization of the laser field. However, the position of the strongest peak (4149.696 cm^{-1}) was found to be very close to the position of the simulated Raman spectrum of the unionized para-H_2 reported earlier.[18] This strongly suggested that this spectral line corresponds to the Q_1 (0) ($v = 1 \leftarrow 0$, $J = 0 \leftarrow 0$) pure vibrational transition obeying the exciton momentum selection rule $\Delta k = 0$, which is induced by the electric field of the charges within the crystal. The electric field induced spectrum, as predicted by Condon,[19] should obey the Raman type selection rules. The spectrum was taken near the wall of the container since the crystal is opaque towards the center. In such regions the intensity of the induced feature is maximum when the electric field of the radiation is normal to the wall. The intensity is much less when the field is parallel to the wall indicating the uniformity of the charge induced electric field.

Condon's formula gives the relation between the observed transmission $I(v)/I_0(v)$ and the average electric field E as

$$\frac{1}{\ell}\int \ln \frac{I_0(v)}{I(v)} dv = \int \gamma(v) dv = \frac{8\pi^3 v}{9hc} n(\alpha_{01} E)^2, \qquad (1)$$

where $\gamma(v)$ is the absorption coefficient (cm^{-1}), α_{01} (0.170×10^{-24} cm^3) is the matrix element of the isotropic polarizability α^{20}, and n (2.61×10^{22} cm^{-3}) is the number density of H_2. The observed values of $I(v)/I_0(v) = 0.6 \sim 0.65$ and the widths of $160 \sim 900$ MHz give the induced transition dipole moment of $\mu = \alpha_{01} E = 0.4 \sim 1 \times 10^{-5}$ Debye and the average electric field of $7 \sim 20 kV$/cm. This field corresponds to the average distance between positive and negative changes of ~ 500Å or ~ 130 R_0 (the intermolecular distance $R_0 = 3.795$Å). The Stark *shift* of the spectral line is negligible at this field ($\Delta v < 0.1$ MHz).

One surprising aspect of our observation is the sharpness of the induced line, even if we include the accompanying structure. In a para-H_2 crystal, the vibrational excitation (vibron) hops around the crystal sites with a frequency of $\varepsilon' \sim 11$ GH$_z$ (0.36 cm^{-1}) and

forms a Bloch State[21, 22] with a width of ~ 3.5 cm^{-1} (the strongest broad feature in Fig. 2). The sharpness of the Raman type spectral line results from the excition (vibron) momentum selection rule $\Delta k = 0$ which locates the spectral line at the lowest end of the vibron band 7.23 ε' below the origin. In order for this selection rule to hold rigorously, all molecules must have the same transition moment and the crystal must be perfect. Obviously both of these conditions are violated in the ionized crystal, but the observed sharpness of the feature indicates that they are still approximately satisfied. While a proof of this has to await detailed theoretical treatments, the following semi quantitative argument may be given to justify our interpretation. In the charge impregnated crystal, molecules that are close to a charge experience large electric fields and their spectral lines are shifted many cm^{-1} without forming a sharp fracture.[7] However, the Stark Shift $\Delta v = -(\alpha_1 - \alpha_0)e^2/2hR^4$ decreases rapidly as the distance R from charge to molecule increases ($\alpha_1 - \alpha_0 = 7.0 \times 10^{-26}$ cm^3 is the difference of the isotropic polarizability between the $v = 1$ and 0 states).[20] At $R = 15$ R_0, the shift is calculated to be 12 MHz well within the width of the observed line. Although the electric field is inhomogeneous, there exists domains of microcrystals within a length of ~100 R_0 containing ~ 10^6 molecules for which the electric field and thus the transition probability are comparable. The violation of the $\Delta k = 0$ because of the finite size of the microcrystal and the resulting energy uncertainty may be estimated from the excition dispersion relation,

$$E_k = -7.23\varepsilon' + \frac{\hbar^2 k^2}{2M} \tag{2}$$

where $M = \hbar^2/2\varepsilon' R_0^2 \sim 3.2$ a.m.u. is the effective mass of the vibron.[21] The finite size of the microcrystal with $R \sim 100$ R_0 gives the momentum uncertainty of $\hbar\Delta k \sim \hbar/R$ which translates to the energy uncertainty at $k \sim 0$ of $\Delta E = \hbar^2/2MR^2 \sim 1$ MHz, smaller than the line width. Thus the microcrystal is sufficiently large to form Bloch state and satisfy the approximate $\Delta k = 0$ rule.

The charge induced signal is very stable. It lasts several days without a sign of decrease. When the crystal temperature was varied from 4.2 K to near the triple point the

111

position of the induced spectrum moved ~3 GHz towards higher frequency due to the expansion of the crystal and the resulting lowering of the vibron hopping rate ϵ'. When the temperature was lowered back to 4.2 K the intensity of the signal was approximately equal to that before the heating indicating the amazing stability of the charge distribution. When the crystal was melted above the triple point, the feature disappeared.

Based on these observations, it is inferred that the following sequence of events occur in the crystal. First the 1.17 MeV and 1.33 MeV γ-rays ionize H_2 through Compton scattering. The cross section for this process can be estimated accurately[23] to be 2.2×10^{-25} cm^2 and thus the mean free path of γ-ray in solid H_2 is ~1m while it is ~2cm in the Cu container. The scattered electrons have energies of a fraction of MeV and they initiate cascades of ionizations which stop after a few mm.[24] Altogether approximately 3.5×10^{17} cm^{-3} of ionizations occur in the crystal. The ion density is higher near the wall of the container because of the higher rate of Compton scattering in Cu. This and the absorption of electrons by Cu causes the observed alignment of the electric field normal to the wall. The electron bombardment also generates copious amounts of hydrogen atoms which move through the crystal and settle in substitutional sites as shown by Miyazaki et. al.[25] The observed charge density of ~1×10^{16} cm^{-3} indicates that most of the electrons recombine with positive ions but approximately 3% get stabilized and localized in the crystal. We believe that they are localized on hydrogen atoms in the form of H$^-$. H$^-$ attracts surrounding H_2 and is stabilized in the form of ion clusters H$^-$(H$_2$)$_n$. While such cluster ions are thermodynamically unstable when zero point vibrations are taken into account[26] and have never been observed in gaseous phase, they have a binding energy of several kcal/mol.[26, 27] The H_2^+ ions react with neighboring H_2 to form H_3^+ and H[11]. The latter takes much of the exothermicity of 1.7 eV and flies apart. The stable H_3^+ attracts neighboring H_2 and is stabilized in the form of ion cluster H_3^+(H$_2$)$_n$.[28] The long lifetime of the charge induced signal demonstrates that, once stabilized, the positive and negative cluster ions remain localized.

112

We believe that this intense and well defined spectrum with its long life time may be used to monitor production, annihilation, and transfer of charges in the crystal.

References

1. P. C. Souers, E. M. Fearon, P. E. Roberts, R. J. Tsugawa, J. D. Poll, and J. L. Hunt, Phys. Lett. 77A, 277 (1980).

2. J. L. Hunt and J. D. Poll, NATO ASI Ser. B, 127, 395 (1985) and references therein.

3. R. L. Brooks, M. A. Selen, J. L. Hunt, J. R. MacDonald, J. D. Poll, and J. C. Waddingotn, Phys. Rev. Lett. 51, 1077 (1983).

4. J. J. Miller, R. L. Brooks, J. L. Hunt and J. D. Poll, Can. J. Phys. 66, 1025 (1988) and references therein..

5. J. A. Forest, J. L. Hunt, and R. L. Brooks, Can. J. Phys. 68, 1247 (1990).

6. J. D. Poll and J. L. Hunt, Can. J. Phys. 63, 84 (1985)

7. J. J. Miller, J. D. Poll, and J. L. Hunt, Can. J. Phys. 69, 606 (1991).

8. J . H. Richardson, S. B. Deutscher, P. C. Souers, R. J. Tsugawa, and E. M. Fearon, Chem. Phys. Lett. 82, 26 (1981).

9. R. L. Brooks, S. K. Bose, J. L. Hunt, J. R. MacDonald, J. D. Poll and J. C. Waddington, Phys. Rev. B32, 2478 (1985).

10. R. L. Brooks, J. L. Hunt, J. R. MacDonald, J. D. Poll, and J. C. Waddingotn, Can. J. Phys. 63, 937 (1985).

11. S. K. Bose and J. D. Poll, Can. J. Phys. 65, 67 (1987).

12. M.-C. Chan, Ph.D. Thesis, The University of Chicago (1991).

13. M.-C. Chan, M. Okumura, and T. Oka, manuscript in preparation.

14. M. Okumura, M.-C. Chan, and T. Oka, Phys. Rev. Lett. 62, 32 (1989)

15. M.-C. Chan, M. Okumura, C. M. Gabrys, L. W. Xu, B. D. Rehfuss, and T. Oka, Phys. Rev. Lett. 66, 2060 (1991).

16. T. Miyazaki, S. Kitamura, H. Morikita, and K. Fueki, J. Phys. Chem. 96, 10331 (1992) and references therein.

17. M.-C. Chan, S. S. Lee, M. Okumura, and T. Oka, J. Chem. Phys. 95, 88 (1991).

18. T. Momose, D. P. Weliky, and T. Oka, J. Mol. Spectrosc. 153, 760 (1992).

19. E. U. Condon, Phys. Rev. 41, 759 (1932).

20. W. Kolos and L. W. Wolniewicz, J. Chem. Phys. 46, 1426 (1967).

21. J. Van Kranendonk, Solid Hydrogen, Theory of the Properties of Solid H_2, HD and D_2, Plenum Press, New York (1983).

22. S. K. Bose and J. D. Poll, Can. J. Phys. **68**, 159 (1990).

23. W. Heitler, **The Quantum Theory of Radiation**, Oxford University Press, London (1960).

24. M. Inokuti, Rev. Mod. Phys. **43**, 297 (1971).

25. T. Miyazaki, H. Morikita, K. Fueki, and T. Hiraku, Chem. Phys. Lett. **182**, 35 (1991).

26. R. A. Kendall, J. Simmons, M. Gutowski, G. Chalasinski, J. Phys. Chem. **93**, 621 (1989).

27. A. M. Sapse, M. T. Rayez-Meaume, J. C. Rayez, and L. J. Massa, Nature **278**, 332 (1979).

28. Y Yamaguchi, J. F. Gaw, R. B. Remington and H. F. Schaefer III, J. Chem. Phys. **86**, 5072 (1987).

115

Figure Captions

Figure 1.

Apparatus for the simultaneous spectroscopy of the infrared and Raman transitions. The nonlinearity of $LiNbO_3$ is used for the former and that of solid H_2 is used for the latter. D.M. stands for dichroic mirror.

Figure 2.

Low resolution (~ 0.1 cm^{-1}) spectrum of para-H_2 crystal before and after the γ-ray irradiation using a BOMEM DA-2 FTIR spectrometer. Arrow shows the sharp induced feature which is the subject of this paper.

Figure 3.

Two typical examples of the γ-ray induced spectral line under high resolution. Trace A was recorded by the difference frequency system. The position of the absorption maximum agrees well with that of the $Q_1(0)$ Raman line of unionized crystal. The structure accompanying the strongest line has not been understood but is likely caused by crystal imperfections. Trace β was recorded by a color center laser on a different run of the γ-ray radiolysis. Both traces were recorded at the positions of the crystals close to the wall. Upper traces are for laser electric field normal at the wall while the lower traces are for parallel.
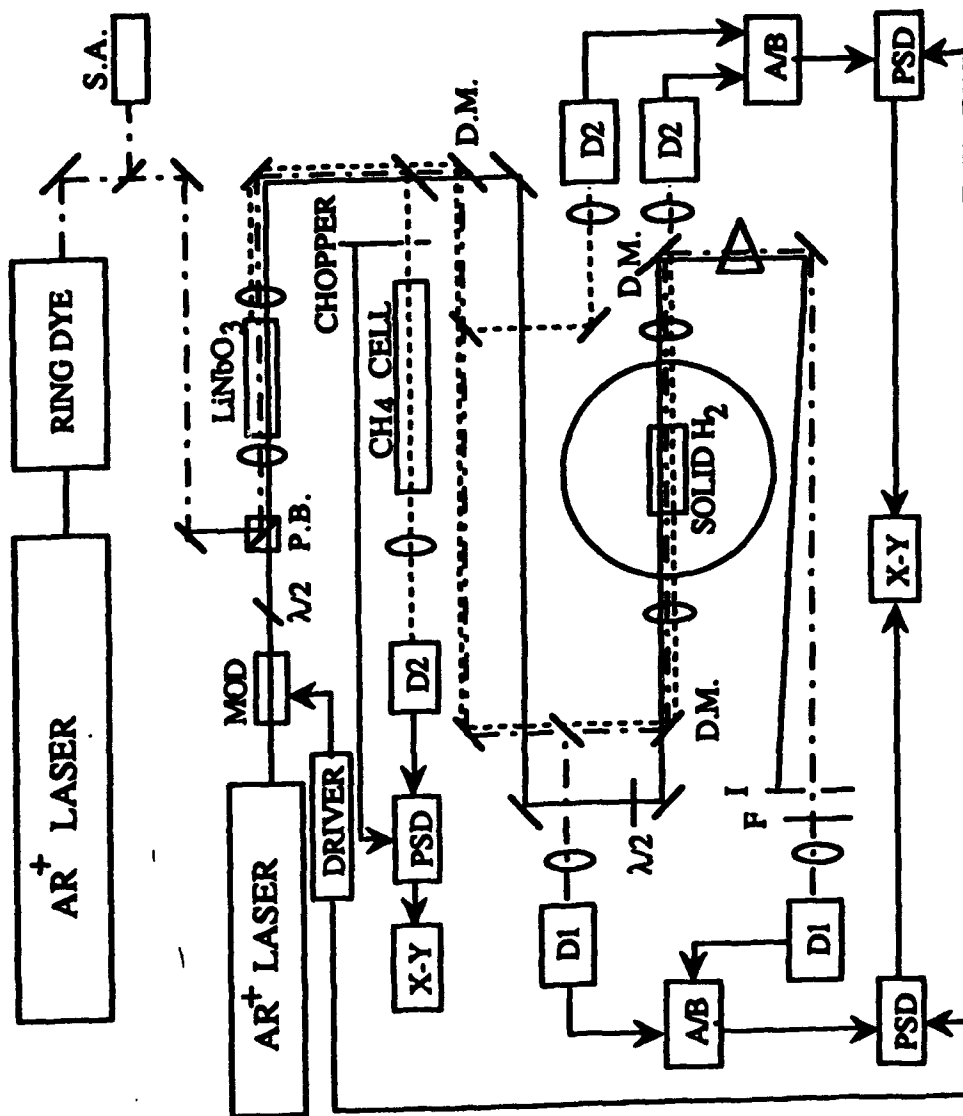
Fig 1

117

Fig. 2

TRANSMITTANCE

A

1500MHz

B

150MHz

Fig 3

119
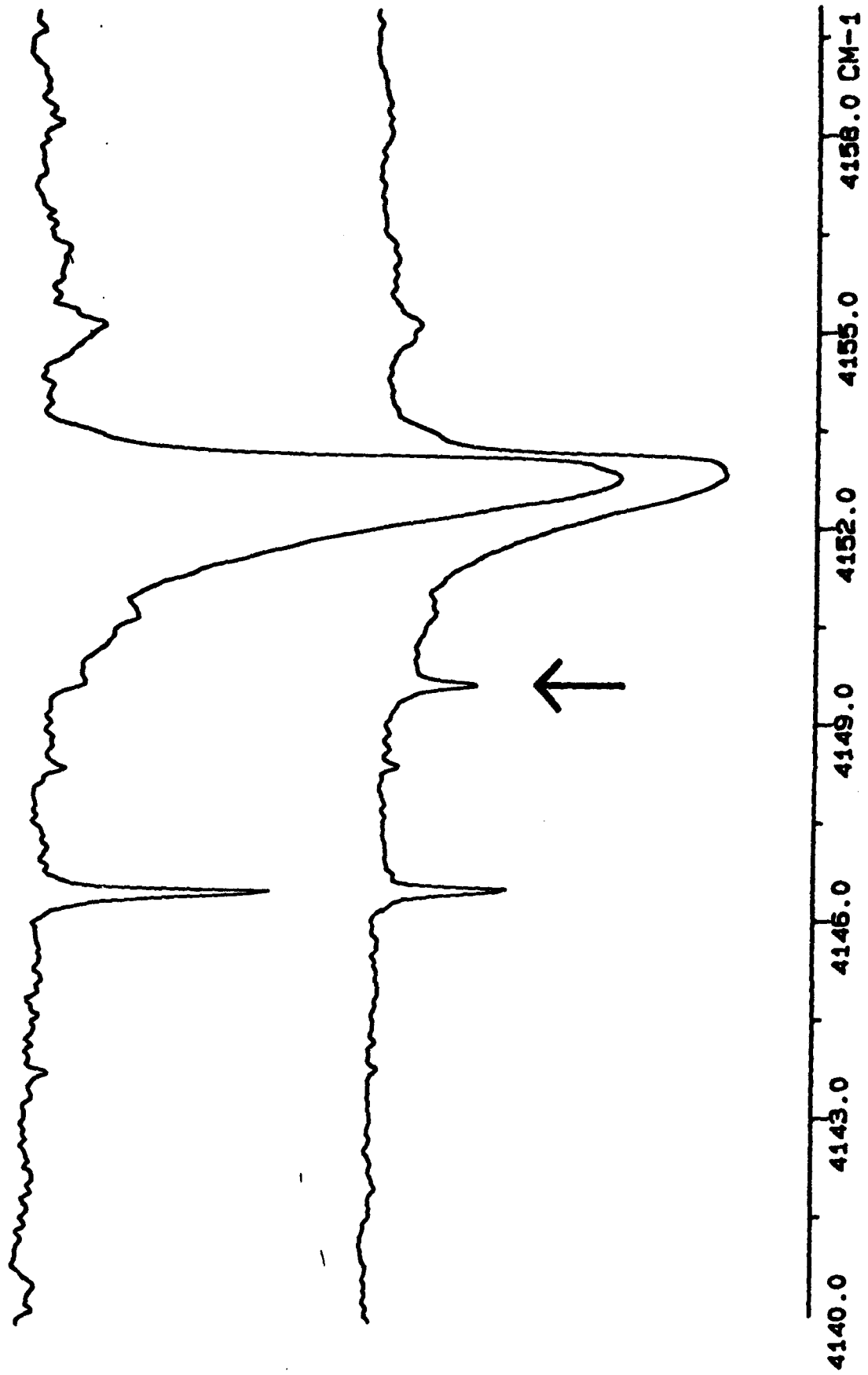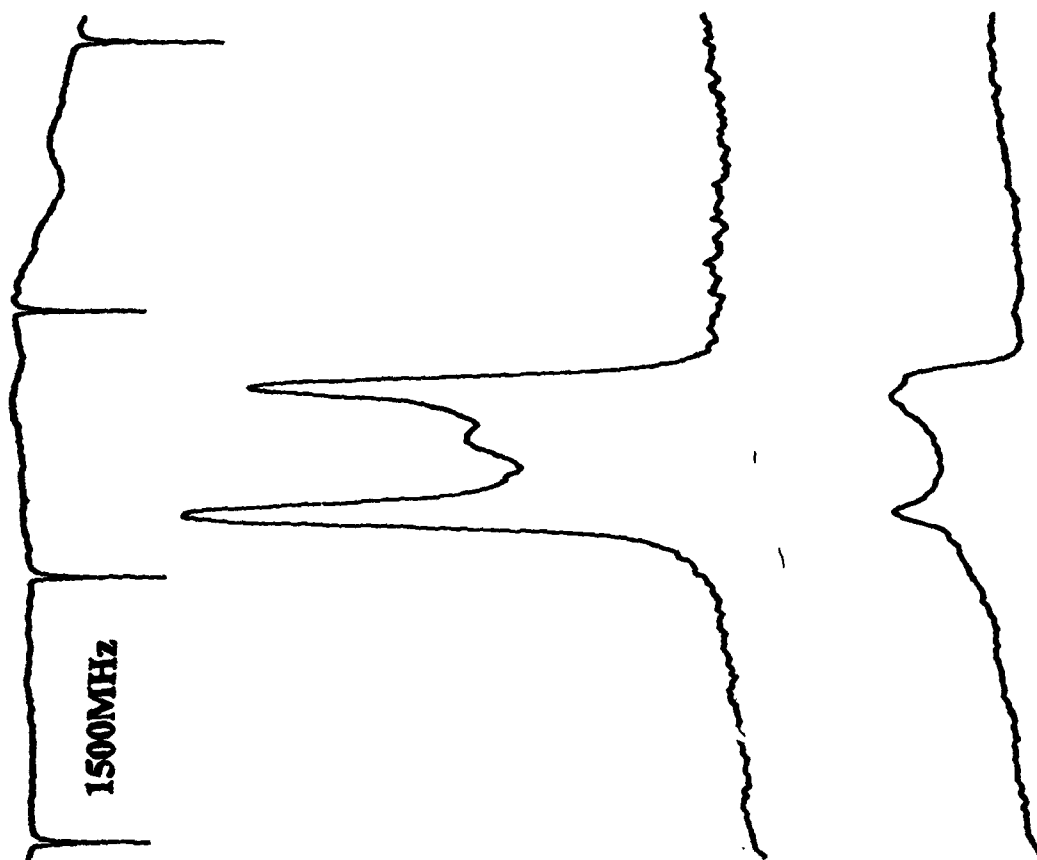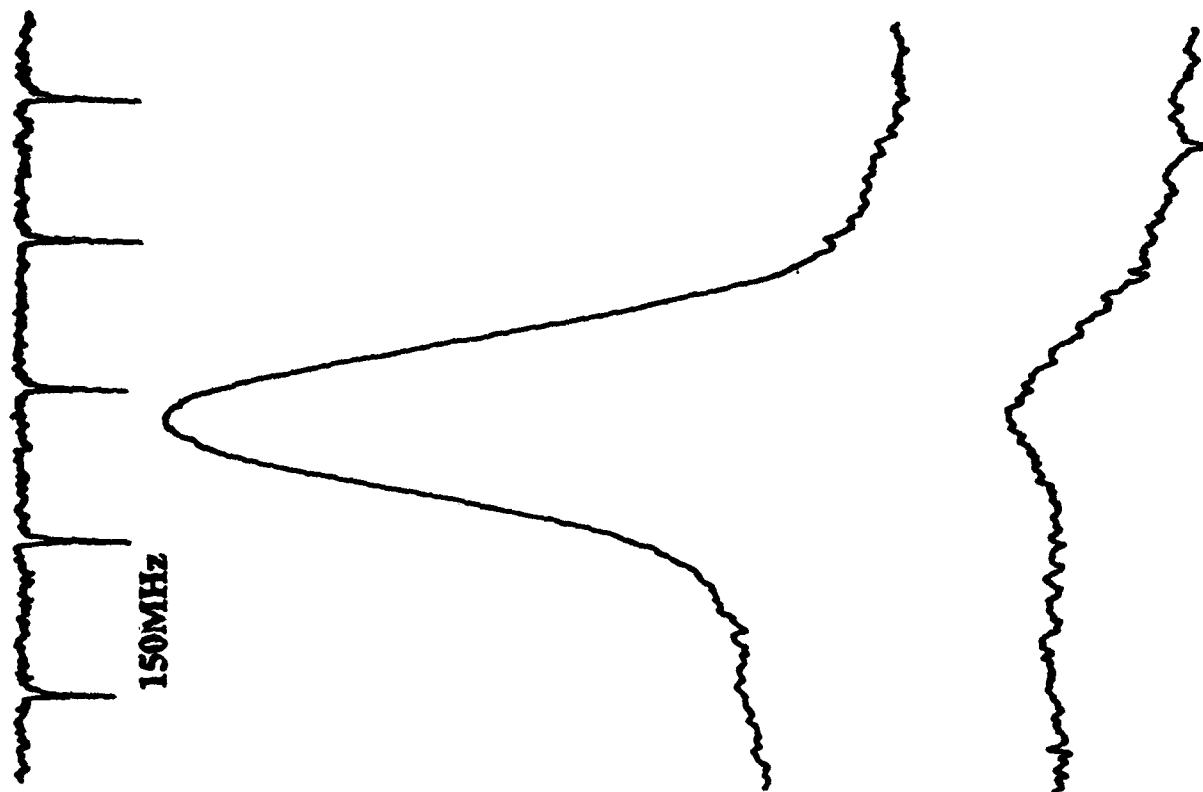
The Remarkable Phase Line of Orientational Order in Solid HD at High Pressure*

Isaac F. Silvera

Lyman Laboratory of Physics, Harvard University, Cambridge, MA

We have studied molecular HD as a function of pressure to 120 GPa and to liquid helium temperatures. Using Raman scattering, both the rotons and vibrons were observed. From changes in the frequencies or lineshapes we traced out the critical line for orientational order. This phase line has an unusual reentrant behavior so that as temperature is increased the crystal goes from a state of being unordered to order to disorder, very much unlike the analog transition in hydrogen or deuterium. We explain the unusual behavior in terms of the thermal population of both even and odd rotational states.

In the quest for metallic hydrogen it has been recognized that the orientational order of the molecules plays a crucial role as the critical pressure for metallization should depend on the order [1]. It is thus crucial to understand orientational order of hydrogen and its isotopes at high pressure. HD is different from the homonuclear diatomic hydrogen isotopes in that the nuclei are not identical and identical particle properties of quantum mechanics such as the ortho-para classification do not apply. At low pressure the orientational distributions of the molecules are well described by the free rotor rotational states, the spherical harmonics with rotational quantum numbers J, M_J. As a result the even and odd rotational states are generally in thermodynamic equilibrium. This is in contrast with H_2 or D_2 where the relaxation (or conversion) between even and odd rotational states is strongly forbidden, so that the ortho-para concentrations are locked in with time constants for change of order hours to days (ortho hydrogen and para deuterium have odd rotational states, whereas para hydrogen and ortho deuterium have even states). Due to the large rotational energies at low temperatures the only important states that can be thermally populated are $J=0$ and 1. Pure $J=1$ solids have an orientational order transition at a few degrees Kelvin, whereas the $J=0$ species do not order as they are in spherically symmetric states.

At very high pressures para-H_2 and ortho-D_2 (described by $J=0$ states at low pressure) also order as the molecular states are distorted when the anisotropic interactions become of the order of the splitting between rotational states; in this case J is no longer a good quantum number. This is called the broken symmetry phase (BSP) transition and has been observed in both hydrogen and deuterium at pressures of 110 GPa [2]and 28 GPa [3], respectively. The transition is a quantum transition occurring at $T=0$ K; the critical temperature increases with increasing pressure as the anisotropic interactions grow; however we note that as T increases the ortho-para concentration remains fixed because conversion is slow.

We have studied the BSP transition in HD and find the critical pressure P_c at $T=0K$ to be just under 70 GPa. Our measurements were carried out in a diamond anvil cell (DAC) from liquid helium temperatures and higher and terminated at a pressure of 120 GPa due to catastrophic failure of the diamond anvils. The DAC was placed into a cryostat and HD gas was cryogenically loaded in the liquid state into the DAC and pressurized to form solid HD. The DAC, cryostat and cryogenic loading technique are described elsewhere [4]. Using Raman scattering we have observed Raman active vibrons and roton modes. From changes or discontinuities in the observed properties of these modes we were able to determine the critical line for orientational order.

The pressure dependence of the transition temperature has the unexpected
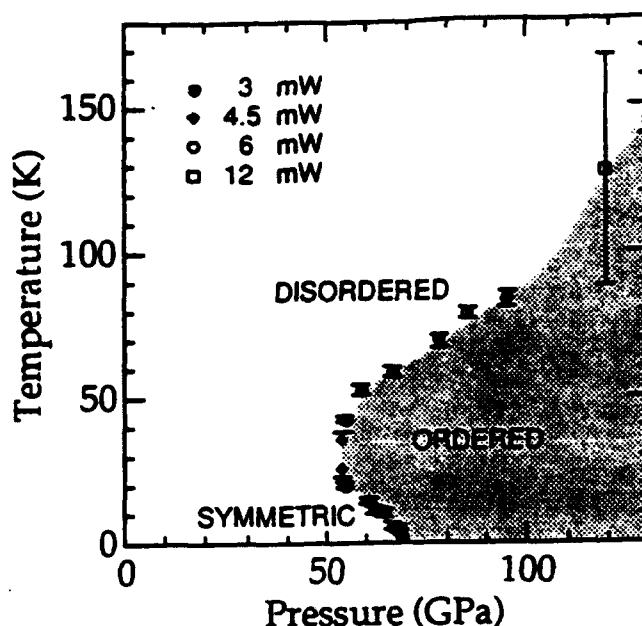
Figure 1. A temperature-pressure plot showing the phase diagram of solid HD with the line for orientational order . The symbols show the laser power that was used for making measurements in different parts of the phase diagram.

and unusual behavior that the critical temperature increases as the pressure is decreased from P_C and then rises with increasing pressure, so that the phase line is in the shape of a boomerang, as shown in figure 1. Restated, for a range of pressures below P_C, as the temperature is increased at fixed pressure, HD goes from a symmetric or disordered phase to an ordered phase and then at higher temperature to a disordered phase. This reentrant behavior can be understood in terms of the populating of the molecules into the J=1 states with increasing temperature.

In order to understand this transition we appeal to a qualitative understanding of orientational order (in hydrogen) as a function of ortho-para concentration. For pure ortho, the concentration of J=1 molecules is C=1 and the transition temperature at zero pressure is 3.8K. Silvera and Jochemsen [5] found that T_C increased rapidly as pressure increased and essentially followed the increase in the strength of the anisotropic interaction which at low pressure is mainly due to electric quadrupole (EQ) quadrupole interactions. Thus, one expects a rapidly rising phase line in a plot of T vs P. Now at a given density, as the ortho molecules are replaced with para molecules the interaction is diluted as ortho molecules bare EQ moments and the para molecules do not. Thus, at zero-pressure, the critical temperature falls off with decreasing C and goes to zero at C_{crit}=0.56, the percolation concentration [6]. In a study for pressures less than 1 GPa, it was found that the critical concentration decreases with increasing pressure [5]. In fact we know that this must be the case, since for P=110 GPa, C_{crit}=0. We note that if the anisotropic interactions remained pure EQQ and para molecules were inert and did not participate in the anisotropic interactions, then the critical concentration would be a geometric quantity and would be independent of density.

With the above description it is clear that there must be a phase line for every ortho concentration and that these must be bounded by the ones for C=1 and C=0. We can now understand the behavior for HD. At T=0 K, C=0 and we observe that BSP transition at 69 GPa. However, as the temperature is raised, J=1 states are thermally populated so that C increases. As a result, the critical pressure actually decreases because the larger C the lower the critical pressure for ordering. For a given pressure below the critical pressure for C=1, as

temperature is increased, the solid goes from the symmetric unordered state into an ordered state; with still increasing temperature, eventually the system disorders. However, at sufficiently low pressure the combination of interaction strength and J=1 concentration will be insufficient to result in orientational order. Thus, it is now clear how the transition line does not reach down to zero pressure and we can understand the strange reentrant phase line of HD with the shape of a boomerang.

References

1. I.F. Silvera. *NATO ARW on Frontiers of High Pressure Research*. 1. Plenum Press, New York, pg. 101 (1991).
2. H.E. Lorenzana, I.F. Silvera, and K.A. Goettel, Phys. Rev. Lett. **64**, 1939 (1990).
3. I.F. Silvera and R.J. Wijngaarden, Phys. Rev. Lett. **47**, 39 (1981).
4. I.F. Silvera and R.J. Wijngaarden, Rev. Sci. Instrum. **56**, 121 (1985).
5. I.F. Silvera and R. Jochemsen, Phys. Rev. Lett. **43**, 337 (1979).
6. J.F. Jarvis, H. Meyer, and D. Ramm, Phys. Rev. **178**, 1461 (1969).

Trapping of Light Metal Atoms in Hydrogen Matrices

Mario E. Fajardo, Simon Tam, and
Michel Macler (NRC Research Associate)

Emerging Technologies Branch, Propulsion Directorate, Phillips Laboratory
(OLAC PL/RKFE Bldg. 8451, Edwards AFB, CA 93524-7680)

ABSTRACT

We report on the progress of our experiments on the trapping of light metal atoms and small clusters in cryogenic rare gas and hydrogen matrices. A major disappointment has been our inability to improve on our preliminary data demonstrating the trapping of B and Al atoms in solid hydrogen, as reported at last year's contractors' conference. We believe that this situation is due to our failure to reproduce the necessary matrix deposition conditions in our new experimental apparatus. We are presently in the process of systematically varying the experimental parameters (*e.g.*: deposition substrate temperature, matrix host gas flow rate, ablation laser fluence and repetition rate, experimental geometry, etc.) in order to optimize the generation of isolated B and Al atoms. We are also investigating the possibility that the original data were due to some matrix contaminant, or other spurious cause.

Nonetheless, we have been able to make some progress on the understanding of the spectroscopy of matrix isolated B atoms. Careful inspection of our extensive data from B/Ne and B/Ar matrices has prompted us to consider the possibility that the accepted literature assignments may be incorrect. We are building a case for the reassignment of the B atom matrix absorptions, observed in the 200 to 220 nm region, to the $2s^22p(^2P) \rightarrow 2s2p^2(^2D)$ transition, instead of the generally accepted $2s^22p(^2P) \rightarrow 2s^23s(^2S)$ transition. This reassignment would better explain the observed spectral splittings and matrix dependent shifts, however at the expense of accepting the absence of the $(^2P) \rightarrow (^2S)$ "Rydberg" transition in these spectra.

We have also just recently completed very preliminary infrared absorption experiments on B/H_2, B/D_2, Al/H_2, and Al/D_2 matrices which indicate the formation of metal hydride products. These experiments, along with our measurements of the properties of laser ablated B and Al plumes in a separate apparatus, suggest that alternative metal atom sources may be required to reduce the loss of metal atoms due to reactions with the hydrogen matrix host.

EXPERIMENTAL

The experimental techniques have been reported previously[1,2] and will be described here only briefly. Rare gas solids doped with boron or aluminum impurities were prepared in a closed cycle cryostat by co-condensing a slow flow of the rare gas, along with the products of a laser ablated boron or aluminum plume, onto a thin sapphire window cooled to 10 K. Similar solid hydrogen or deuterium matrices were prepared in a liquid helium (lHe) transfer, and in a lHe bath cryostat, at substrate temperatures between 2 and 5 K. The ablated plume was generated by focusing the output of a XeCl excimer laser (308 nm) onto a rotating disk of the target material; typical incident laser intensities were of order 10^8 W/cm^2. The rate of deposition of the matrix gas was monitored by back reflection interference using a HeNe laser. UV/vis transmission spectra of the matrices were obtained using a 50 W deuterium lamp, a 10 W quartz-halogen lamp, and an optical multichannel analyzer (OMA) equipped with an unintensified silicon photodiode array. Simultaneous UV/vis and infrared (4700 to 750 cm^{-1} region) absorption spectra of samples deposited on a cooled BaF$_2$ substrate were obtained by incorporating into the setup a Fourier Transform infrared (FTIR) spectrometer operated at 0.5 cm^{-1} resolution.

RESULTS AND DISCUSSION

Figure 1 shows the transmission spectrum of an as-deposited B/Ar matrix at T = 10 K. The peaks near 208 and 213 nm have been previously assigned to isolated B atoms[4-6]; in particular to the $2s^22p(^2P)\rightarrow2s^23s(^2S)$ transition[4] which appears near 249.7 nm in the gas phase[7]. The appearance of two peaks "is not understood,"[4] but was presumed to be due to trapping of B atoms in two distinct sets of sites in the Ar matrices. However, the insert to figure 1 shows a strong linear correlation between the integrated intensities of the 208 and 213 nm peaks, in data taken from 37 spectra of five differently prepared and annealed samples. We interpret this positive correlation to mean that both absorptions originate from B atoms in a single type of trapping site. Furthermore, theoretical simulations of the optical absorption lineshape for the $(^2P)\rightarrow(^2S)$ B atom transition in solid Ar failed to reproduce the observed doublet structure[8]. Thus, we propose that the B atom matrix absorptions, observed in the 200 to 220 nm region, be reassigned to the $2s^22p(^2P)\rightarrow2s2p^2(^2D)$ transition which appears near 209.0 nm in the gas phase[7]. This assignment would explain the presence of multiple absorption peaks as due to the splitting of the degeneracy of the ^2D excited state by the matrix environment. We do not, however, as yet understand the fate of the $2s^22p(^2P)\rightarrow2s^23s(^2S)$ transition, and are examining the literature of Rydberg transitions in matrices for possible explanations.

124

Figure 2 shows the transmission spectrum of an as-deposited B/H_2 matrix at T = 3 K, obtained using our new lHe bath cryostat. The weak absorptions near 209 and 216 nm correspond to the B atom absorption features reported at last year's contractors' conference (then at 211 and 218 nm). We have improved our optical setup since obtaining those preliminary results, in particular we can now record and correctly wavelength calibrate UV absorption spectra to about 185 nm. Unfortunately, the spectrum in figure 2 represents our best UV absorption data of the B/H_2 system, obtained from our new experimental apparatus in over a dozen deposition attempts. We have not yet learned how to deposit matrices to reliably produce these purported B atom absorptions, *and again caution the reader to treat these results as preliminary* and still subject to skepticism. We are currently re-evaluating our experimental techniques, and are considering the use of alternate B atom sources (*vide infra*).

Figure 3 shows absorption spectra of as deposited Al/D_2 (traces a and b, peaks near 328 nm) and Al/H_2 (traces c and d, peaks near 331 nm) matrices. We believe these features may correspond to the 338 nm absorption observed in Al/Ar matrices[9-12] and previously assigned to the Al atom 3p→4s transition ($\lambda_{gas} \approx 394$ nm). Our confidence in these aluminum atom experiments is higher than in our B/H_2 experiments; we will soon perform laser induced fluorescence experiments on these samples and measure the emission decay lifetime as an additional check of our assignment to an Al atom transition.

We have previously discussed in detail our model of the matrix deposition process, and the supposed atomic isolation advantages of laser ablation metal atom sources[1-3]. However, the implantation of fast (typically 1 to 20 eV kinetic energy[13-16]) metal atoms into H_2 and D_2 matrices raises the possibility of reactions between the molecular host and the fast metal atoms. In order to check this possibility, we performed infrared (IR) absorption experiments on B/H_2, B/D_2, Al/H_2, and Al/D_2 matrices deposited by the laser ablation technique. Figure 4a shows a portion of the IR absorption spectrum of a B/H_2 matrix, figure 4b shows the corresponding H⇒D isotopically shifted region in a B/D_2 matrix. We assign the two sharp peaks in each spectrum to the v_{17} vibration of the four major isotopomers of $^{(10,11)}B_2^{(1,2)}H_6$, based on the known gas phase spectrum[17], and calculated[18] intensities and isotopic shifts. The broad feature just to the red of these peaks survives warmups to temperatures which cause the complete sublimation of the host matrix gas, hence we assign this feature to some B_xH_y polymeric material. We also observed several absorption features in our aluminum experiments, however our analysis of this data is very tentative and is based on an incomplete examination of the literature of aluminum hydrides[19-22], oxides, and hydroxides. We summarize all of our IR data and assignments below in Table I.

CONCLUSIONS AND FUTURE DIRECTIONS

We believe that we may have successfully isolated B and Al atoms in solid H_2 and D_2 matrices, however we are still seeking conclusive evidence for this claim. Future experiments along this track will include LIF of Al doped matrices, as well as the use of a thermal B atom source in hopes of reducing the extent of reactions between the B atoms and the host matrix gas molecules. We have detected metal hydride reaction products in our matrices via IR absorption and will continue to pursue this diagnostic technique during future matrix deposition experiments.

REFERENCES

1. M.E. Fajardo, P.G. Carrick, and J.W. Kenney III, J. Chem. Phys. 94, 5812 (1991).

2. M.E. Fajardo, J. Chem. Phys. 98, 110 (1993).

3. M.E. Fajardo, S. Tam, and M. Macler in Proceedings of the High Energy Density Matter (HEDM) Conference, edited by M.R. Berman, (USAFOSR, Bolling AFB, DC, 1992).

4. W.R.M. Graham and W. Weltner, Jr., J. Chem. Phys. 65, 1516 (1976).

5. G.H. Jeong and K.J. Klaubunde, J. Am. Chem. Soc. 108, 7103 (1986).

6. G.H. Jeong, R. Boucher, and K.J. Klabunde, J. Am. Chem. Soc. 112, 3332 (1990).

7. H.G. Kuhn, Atomic Spectra, (Academic Press, New York 1969).

8. J.A. Boatz and M.E. Fajardo, "Monte Carlo Simulations of the Structures and Optical Absorption and Emission Spectra of Na/Ar and B/Ar Solids," these proceedings.

9. J.H. Ammeter and D.C. Schlosnagle, J. Chem. Phys. 59, 4784 (1973).

10. R. Grinter and D.R. Stern, J. Mol. Struct. 80, 147 (1982).

11. H. Abe and D.M. Kolb, Ber. Bunsenges. Phys. Chem. 87, 523 (1983).

12. R. Grinter and R.J. Singer, Chem. Phys. 113, 87 (1987).

13. J.F. Friichtenicht, Rev. Sci. Instrum. 45, 51 (1974).

14. H. Kang and J.L. Beauchamp, J. Phys. Chem. 89, 3364 (1985).

15. M. Macler and M.E. Fajardo, Mat. Res. Soc. Symp. Proc. 285, 105 (1993).

16. M. Macler and M.E. Fajardo, "Modification of Nascent Energy Distributions of Laser Ablated Species Using Transverse Magnetic Fields," these proceedings.

17. W.C. Price, J. Chem. Phys. 16, 894 (1948).

18. J.F. Stanton, R.J. Bartlett, and W.N. Lipscomb, Chem. Phys. Lett. 138, 525 (1987).

19. R.B. Wright, J.K. Bates, and D.M. Gruen, Inorg. Chem. 17, 2275 (1978).

20. J.M. Parnis and G.A. Ozin, J. Phys. Chem. 93, 1215 (1989).

21. J.A. Pople, B.T. Luke, M.J. Frisch, and J.S. Binkley, J. Phys. Chem. 89, 2198 (1985).

22. M. Shen and H.F. Schaefer, J. Chem. Phys. 96, 2868 (1992).

TABLE I: Infrared absorption bands observed in as deposited B/H_2, B/D_2, Al/H_2, and Al/D_2 matrices produced by laser ablation of the metals. Peak intensity and lineshape annotations: s=strong, m=medium, w=weak, br=broad, blue=blue shoulder, site=trapping site splittings. Note: no M_xO_y or $M_xO_yH_z$ species included in analysis of band assignments.

matrix	band positions (cm^{-1})	assignments
B/H_2	2604w, 2510w, 1169.7m	B_2H_6 ν_8, ν_{16}, ν_{18}
	1598.4s, 1596.2s	B_2H_6 ν_{17} isotopomers (overlapped by H_2O)
	1589s,br	B_xH_y
B/D_2	3285w,br, 3165m,br	D_2 $S_{1\leftarrow0}(1)$ and $S_{1\leftarrow0}(0)$
	2343.7m	CO_2
	1988w, 1842m,br	B_2D_6 ν_8, ν_{16}
	1970w,br, 1766w	?
	1597.1m	H_2O
	1197.3s, 1194.0s	B_2D_6 ν_{17} isotopomers
	1190s,br	B_xD_y
Al/H_2	4503w,br, 4152w,br	H_2 $S_{1\leftarrow0}(0)$ and $Q_{1\leftarrow0}(0)$
	2344.8w	CO_2
	1889m, 1884.3s	? site
	1825m, 1822.0s, 1790w, 1787.8m	AlH_2 ν_3, ν_1 (?) site pairs
	1611.0s, 1599.9s	AlH (?) site
	1838w,br, 1409w, 1268w	?
Al/D_2	3735w, 1597.0m	H_2O
	3286m,br, 3166m,br	D_2 $S_{1\leftarrow0}(1)$ and $S_{1\leftarrow0}(0)$
	3055w,br, 2985w, 2772m	?
	2343.7m,blue	CO_2 + aggregates
	1604w, 1597.0m	H_2O
	1404w, 1379w, 1371w	?
	1337.6m, 1293w	AlD_2 ν_3, ν_1 (?)
	1173.5w, 1163.5m	AlD (?) site
	1034w, 896w, 879w	?

Figure 1
B/Ar transmission spectrum, T=10K
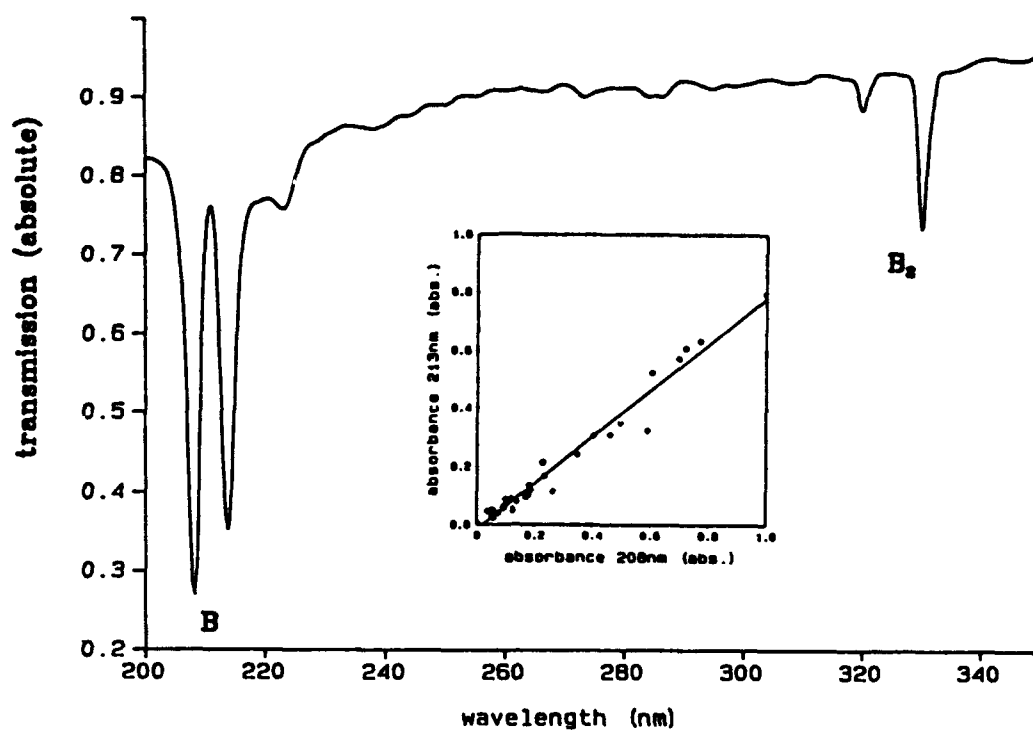
Figure 2 B/H2 raw data
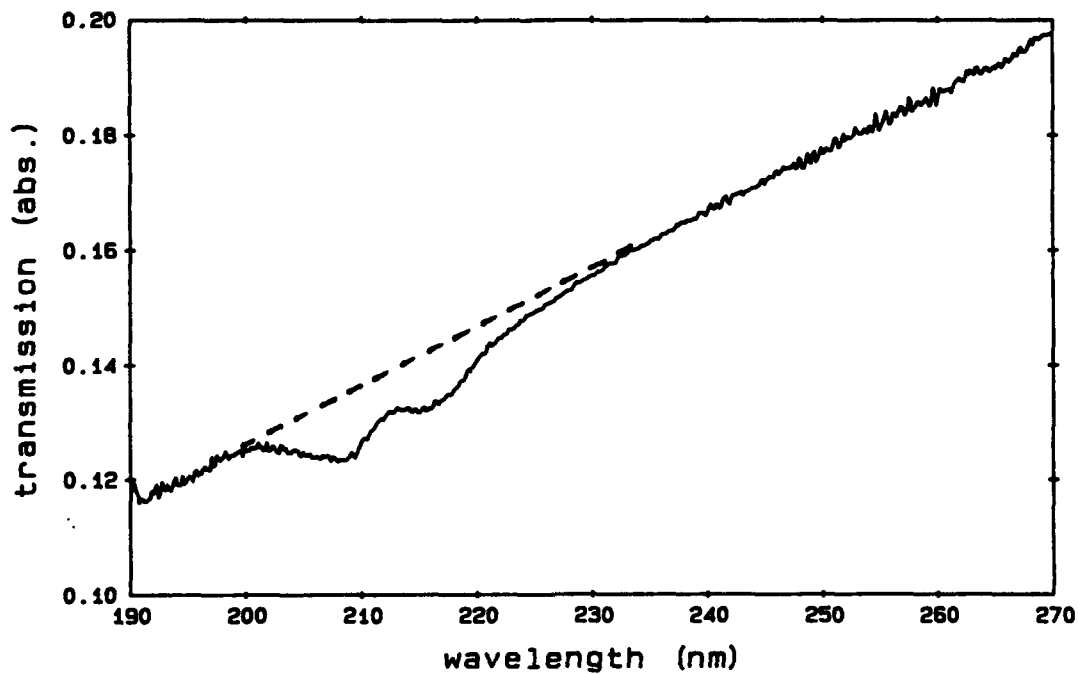
Figure 4
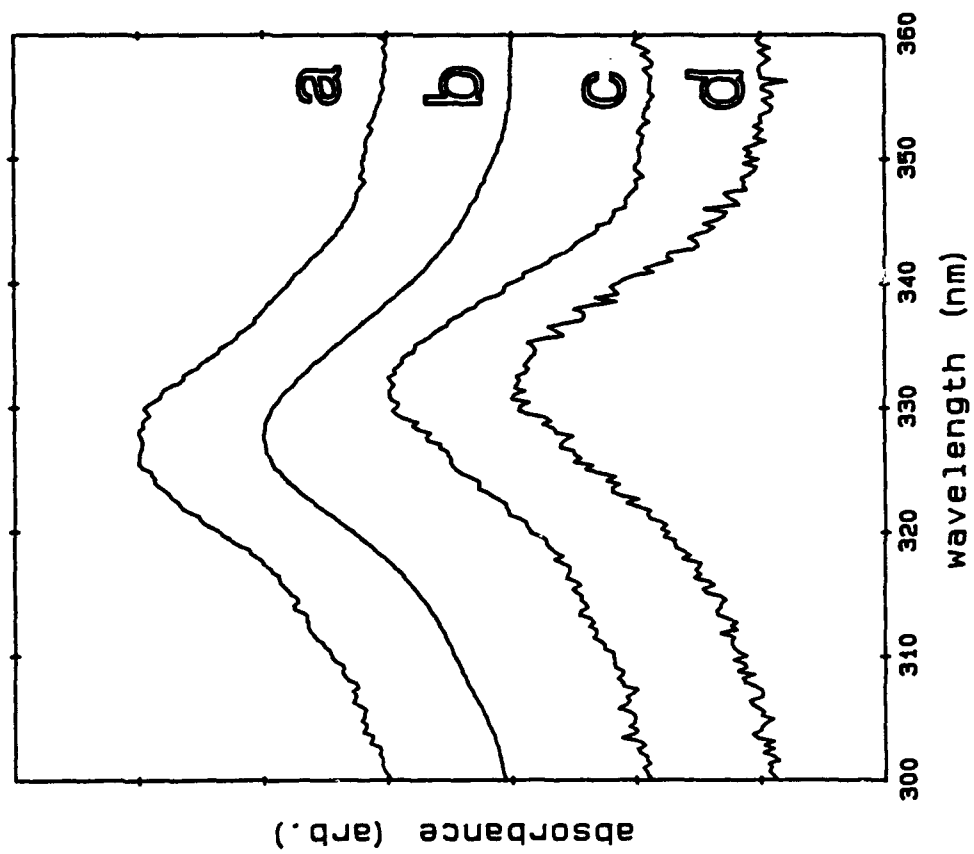
Figure 3
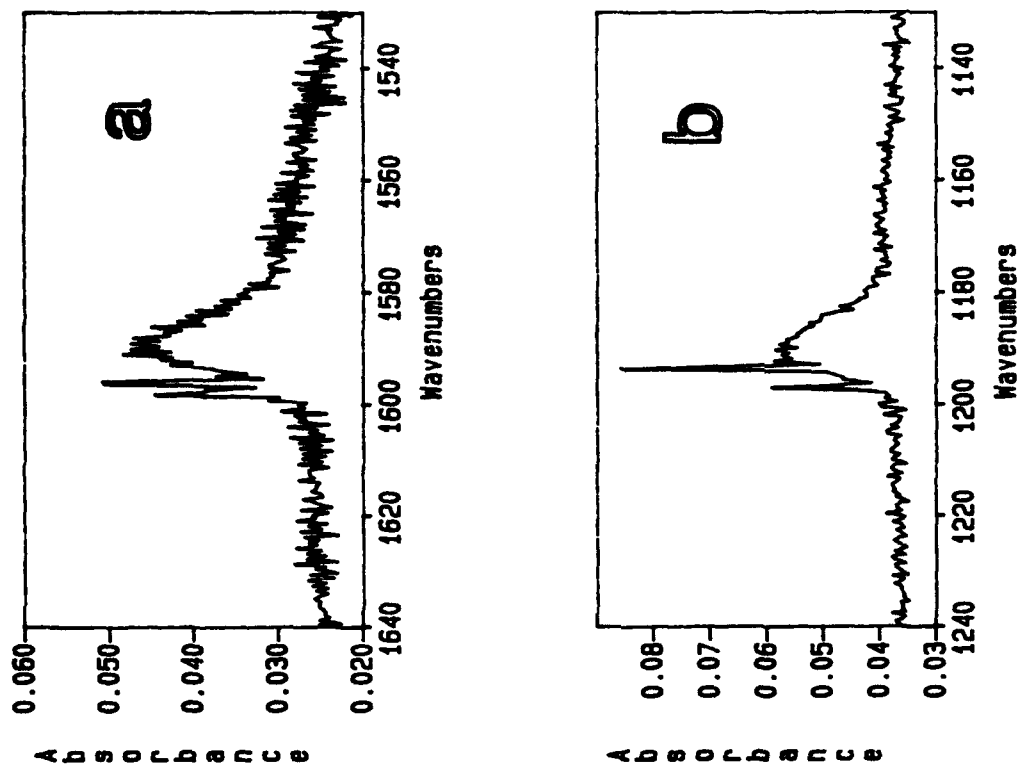
Nature of the trapping sites and the electronic spectrum of lithium atoms in the quantum solids *para*-hydrogen and *ortho*-deuterium*

Daphna Scharf, Glenn J. Martyna, Daohui Li,
Gregory A. Voth and Michael L. Klein

Department of Chemistry, University of Pennsylvania,
Philadelphia, PA 19104-6323

Abstract

Quantum mechanical studies of a lithium impurity in solid *para*-hydrogen and *ortho*-deuterium have been performed using the path integral formulation of statistical mechanics. Since an isolated lithium atom is much larger than the host molecules, trapping sites consisting of from one to six vacancies have been investigated. Interestingly, all of the sites are comparable in energy. This is due to the large compressibility of *para*-hydrogen and *ortho*-deuterium solids, which permits the lattice to relax to comfortably accommodate the impurity. The inhomogeneously broadened dipole spectrum of the lithium impurity in the various sites was calculated using the Radial Fast Fourier Transform Lanczos method and compared to experiments by Fajardo [J. Chem. Phys. **98**, 110 (1993)]. Based on the present calculations, lithium atoms appear to occupy preferentially a three-vacancy trapping site in *para*-hydrogen while in *ortho*-deuterium a four-vacancy trapping site seems to be favored. Complementary variational Einstein model calculations predict that the four-vacancy trapping site is favorable in both *para*-hydrogen and in *ortho*-deuterium.

---

1 Introduction

Recent experiments [1, 2] have demonstrated that a low concentration of lithium atoms can be metastably trapped in both solid H_2 and D_2 in the temperature range $T < 5K$. This is of interest because the ability of hydrogen to act as a rocket fuel might be significantly enhanced if small quantities of such light impurities are introduced into the system[3]. In order to better understand the properties of such metastable quantum "alloys", it is important to first characterize the trapping site/sites of individual lithium atoms in this solid matrix.

Previous experimental studies of impurities in host matrices have focused on both mixed rare gas systems and metallic impurities in otherwise neat rare gases [4, 5, 6]. Unfortunately, experimental measurements alone are insufficient to uniquely determine the trapping site/sites. For example, the electronic spectra of the lithium impurities in *para*-hydrogen and *ortho*-deuterium have been measured. The spectra consist of a doublet and a "shoulder" which is located at higher energy than the main peak [1, 2]. This information, at best, indicates the rough symmetry of the site. In order to more precisely determine the nature of the site, it is necessary to predict the spectral line-shifts and line shapes of the impurity on the basis of theoretical calculations. This approach has been successfully used to interpret the older experimental work mentioned above [4, 7, 8, 9, 10, 11, 12].

In this paper, the microscopic model of the lithium-*para*-hydrogen/ *ortho*-deuterium system developed elsewhere [13] is applied to the present problem. The results of quantum mechanical Constant Pressure Path Integral Monte Carlo (CP-PIMC) calculations are presented for a single lithium impurity in solid *para*-hydrogen/*ortho*-deuterium lattices in sites with different numbers of bound vacancies, n_v. Structural and energetic comparisons are made to a quantum Einstein model [14]. The resulting configurations from the Monte Carlo runs are, then, used to calculate the electronic spectra of lithium atoms

in the various sites. A comparison with experiment [1, 2] suggests that a three-vacancy site is the dominant structure observed in the *para*-hydrogen system while a four-vacancy site is appropriate to the *ortho*-deuterium system. Complementary calculations are performed using a variational quantum Einstein model for selected trapping sites. Based on free energy considerations it is shown that the Einstein model favors the four-vacancy site in both *para*-hydrogen and in *ortho*-deuterium.

2 Electronic Spectrum

Inhomogeneously broadened dipole spectra of an isolated lithium atom trapped in various vacancy sites (see Fig. 1) in solid *para*-hydrogen/*ortho*-deuterium have been calculated. This was accomplished by taking equilibrium configurations from the CP-PIMC runs, replacing the lithium atom by an electron and a lithium ion and determining the electronic states using the Radial Fast Fourier Lanczos Method described elsewhere [13]. This approach accounts for the zero-point motion and thermal effects present in the system [13].

In Fig. 2, dipole spectra of isolated lithium atoms in solid *para*-hydrogen are presented and compared to experiment. For small n_v, the first peak is shifted well to the blue compared to experiment. We notice a split first peak for $n_v = 1, 2$ and 4 in Fig. 2(a) and (b). The calculated splitting, which seems to be reproducible, is not seen in the experimental spectrum. For the larger vacancy sizes studied, $n_v = 5$ and 6, the dipole spectrum resembles that obtained in the liquid at $T = 14K$. The spectral widths for $n_v = 5$ and 6 are narrower than those of the smaller trapping sites. Based on the overall shape and width, the three vacancy trapping site seems to give the best correlation with the experiments [2]. However, the high energy tail of the experimental spectrum is absent in all the calculations. The "average" energy of this tail region suggests that it may in fact be caused by a rotational Franck-Condon transition; such effects have been neglected in our simulation.
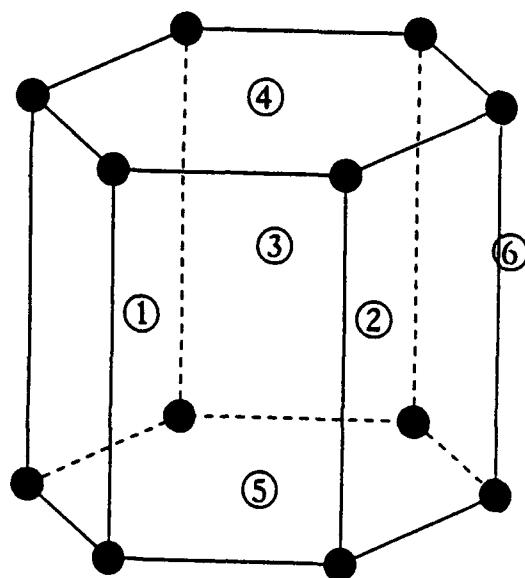
Fig. 1: A schematic representation of possible trapping sites for a lithium atom an ideal HCP lattice. The trapping sites are constructed by removing the desired number of molecules, labeled 1 to 6, and placing the lithium atom in a lattice site ($n_v = 1$) or at an interstitial site ($n_v = 2 - 6$). For example, for $n_v = 2$ the midpoint between lattice points 1 and 2 was used and for $n_v = 3$, the center of the triangle formed by removing the molecules 1, 2 and 3.
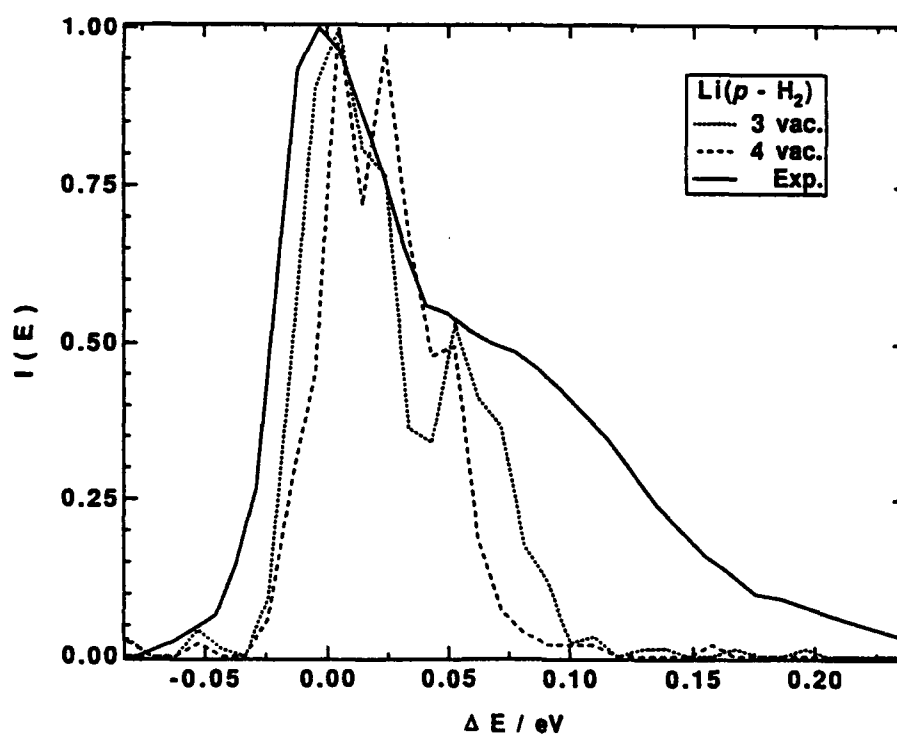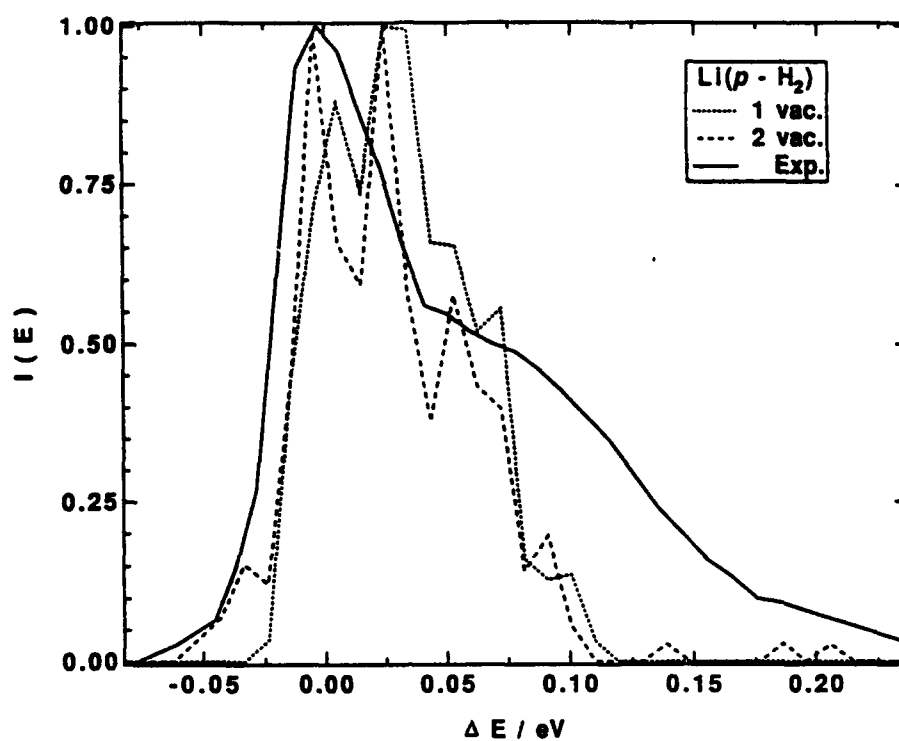
Fig. 2 (a) and (b)
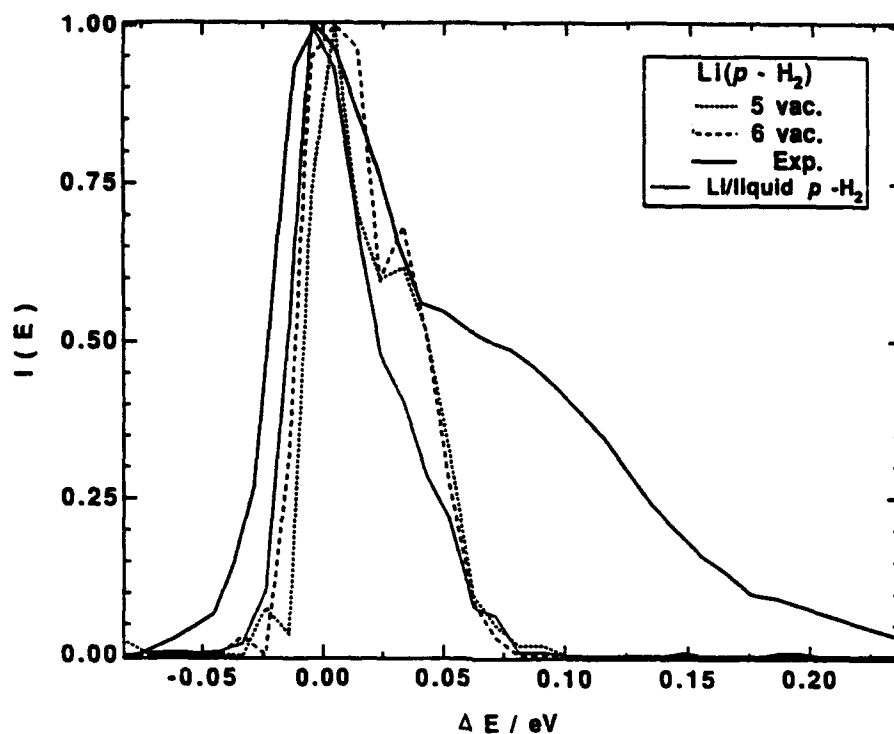
Fig. 2: The dipole spectrum of a lithium atom in solid *para*-hydrogen at $T = 4K$ and $P_{ext} = 0$ compared to experiment (bold curve) from Ref. [1]: (a) $n_v = 1$ (dotted) and $n_v = 2$ (dashed) (b) $n_v = 3$ (dotted) and $n_v = 4$ (dashed) (c) $n_v = 5$ (dotted), $n_v = 6$ (dashed) and the spectrum in the low temperature liquid (T=14K).

In Fig. 3 the analogous dipole spectra for a lithium impurity in solid *ortho*-deuterium are presented. The $n_v = 3$ site has the second peak/shoulder shifted to the blue and an incorrect peak-to-peak ratio, in comparison with experiment. The $n_v = 5$ site has a split first peak, which renders it less favorable. The four-vacancy trapping site seems to give the best agreement with the experimental results [2].

3   Conclusion

Constant Pressure Path Integral Monte Carlo calculations have been perform for a single lithium impurity in solid *para*-hydrogen and solid *ortho*-deuterium for a variety of different trapping sites. The large compressibility of *para*-hydrogen/*ortho*-deuterium solids allows the lattice to easily deform to accommodate the large lithium impurity. Thus, the impurity is found to be relatively stable even in a substitutional site. The electronic spectrum of the lithium atom was calculated for a variety of trapping environments. A three-vacancy trapping site was found give the best agreement with the experimental spectrum in solid *para*-hydrogen, while a four-vacancy trapping site is suggested for solid *ortho*-deuterium. This is in slight disagreement with the Einstein model which predicts $n_v = 4$ as a favorable site in both *para*-hydrogen and *ortho*-deuterium, based on free energy considerations. The possibility of an isotope effect on the nature of the trapping site is not surprising. In going from *para*-hydrogen to *ortho*-deuterium the energy per particle increases by about fifty percent and the volume per particle decreases by about ten percent. Accordingly, the lithium atom should need to displace more *ortho*-deuterium molecules than *para*-hydrogen molecules to form an optimal trapping site.

136
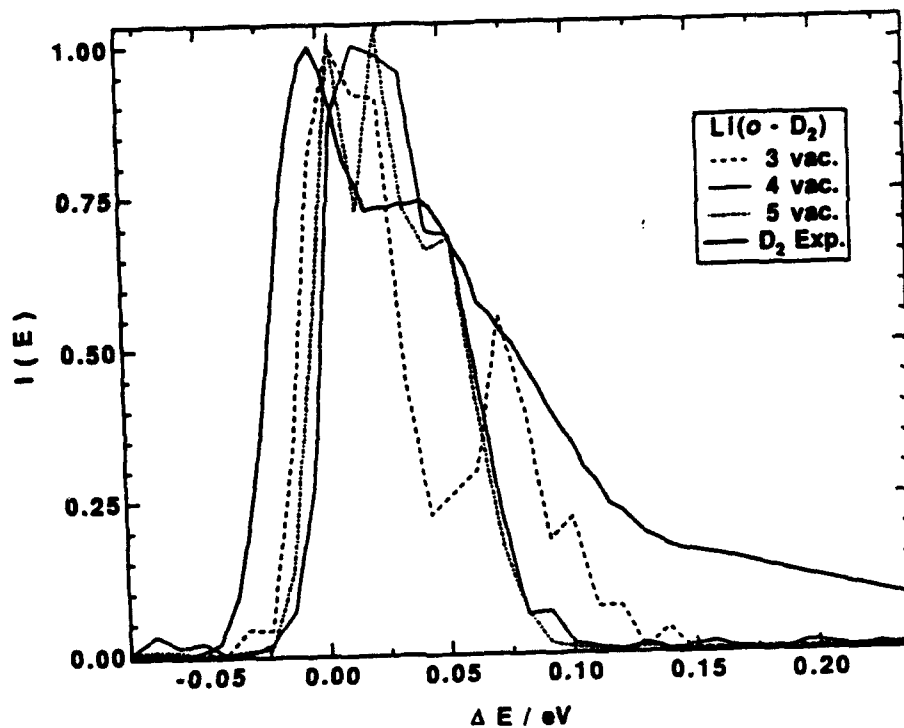
Fig. 3: The dipole spectrum of a lithium atom in solid *ortho*-deuterium, at $T = 4K$ and $P_{ext} = 0$, compared to experiment (bold curve) from Ref. [1]. $n_v = 3$ (dashed), $n_v = 4$ (dotted) and $n_v = 6$ (dash-dotted).

4   Acknowledgements

References

[1] M. E. Fajardo. In M. E. Cordonnier, editor, *Proceedings of the High
    Energy Density Matter Conference.* USAF Phillips Laboratory, Edwards
    AFB, CA., (1991).

[2] M. E. Fajardo. *J. Chem. Phys.*, 98:110, (1993).

[3] M. E. Cordonnier, editor. See e.g. the discussion in *Proceedings of the
    High Energy Density Matter Conference.* USAF Phillips Laboratory, Ed-
    wards AFB, CA., (1991).

[4] N. Schwentner, E. E. Koch, and J. Jortner. *Electronic Excitations in
    Condensed Rare Gases.* Springer Verlag, Berlin, (1985).

[5] L. C. Balling and J. J. Wright. *J. Chem. Phys.*, 81:675, (1984).

[6] M. E. Fajardo and. G. Carrick and J. W. Kenney III. *J. Chem. Phys.*,
    94:5812, (1991).

[7] S. Ossicini and F. Forstman. *J. Chem. Phys.*, 75:2076, (1981).

The interaction of H_2 ($^1\Sigma_g^+$) with Li 2s ^{2}S and Li 2p ^{2}P

Daniel D. Konowalow

The University of Dayton Research Institute
Air Force Phillips Laboratory
Edwards AFB, CA 93524-7680

Specific Impulse calculations [1] suggest that the incorporation of about 15 mol% in solid H_2 could lead to an I_{sp} increase of some 17% over the value for undoped H_2 burned with liquid oxygen. Fajardo has shown that Li can be trapped and stored in cryogenic H_2 for hours [2]. Even though the concentration of atoms achieved thus far is much less than the optimum loading, these experiments suggest that the LiH_2 system warrants further investigation

This study is directed toward the understanding of the structure and spectra of Li atoms trapped in a matrix of ground state H_2 molecules. I present the potential surfaces for the molecular states corresponding to the interaction of a ground state H_2 with either a ground ^{2}S Li atom or the first excited ^{2}P Li atom and the transition electric dipole moment function for transitions connecting the ground and excited molecular states. In addition, I present the (diagonal) dipole moment for the ground van der Waals state as a guide for its observation by IR spectroscopy

The interaction surfaces were obtained from three electron in six orbital (3/6) multireference configuration interaction (MRCI) calculations. The CI is based on a state-averaged MC which incorporates all the states emanating from the lowest two Li + H_2 asymptotes. These calculations utilize a spherical Gaussian basis comprising 9s,8p,2d,1f functions on Li; 5s,3p on H; and 1s,3p,2d,1f on the H_2 bond center for a total of 112 spherical basis functions. Preliminary studies were carried out with a truncated 71-function basis which contained only the s and p functions enumerated above. The full basis describes rather accurately a Li atom with the valence electron in any of the orbitals 2s, 3s, 4s, 2p, 3p, 4p, 3d, 4d, 4f and is similar to a basis which optimizes the dipole, quadrupole and octupole polarizabilities of the ground state atom. The hydrogen basis is a compromise between that providing good CI energies and that needed to obtain optimum polarizabilities through the sixth rank for ground state H_2 The polarizabilities of the excited state atoms are presumably not nearly so well described as are those of the ground state atom. Thus, the 112-member basis is designed to afford a reasonable description of dispersion effects (particularly those involving the ground state atom) as well as ordinary correlation effects.

Table 1 lists the depth and position of the potential minimum for the various states of LiH_2 for three values of the H-H spacing which correspond *approximately* to the equilibrium internuclear separation [r(H-H) = 1.4 a_0], the left-hand classical turning point [r(H-H) = 1.2054 a_0] of the ground vibrational motion, and the right-hand classical turning point [r(H-H) = 1.7234 a_0] . I report these characteristic constants for five values of the Jacobi angle ranging between 0° and 90° by increments of 22.5^o. For simplicity, I label the states of LiH_2 according to their identity in C_{2v} symmetry. The A_1 states in C_{2v} correspond to A' in C_s symmetry and Σ in $C_{\infty v}$. The states B_1 and B_2 become A' and A" in C_s and the doubly degenerate Π state in $C_{\infty v}$.

Let us examine the angular dependence of the relatively strongly bound B states. Clearly, the C_{2v} geometry is energetically highly favored-- most dramatically so for the B_2 state whose energy is lowered substantially by an interaction between the p_z orbital on Li with the σ_u orbital on H_2 which becomes more and more favorable as the H_2 rotates from the $C_{\infty v}$ (0°) position to the C_{2v} (90°) position. (z is along the bond axis of H_2.) This enhanced binding is very sensitive to the degree of stretch of the H_2 bond. The interaction is most favorable when the H_2 bond is stretched most since it is then that the σ_u orbital comprises its highest proportion of the H_2 wavefunction. By contrast, in $C_{\infty v}$ symmetry, the Π state is most strongly bound when the H-H bond contracts toward its left-hand turning point. That is presumably due to a favorable interaction between the p_π orbital on Li and the correlating π orbital on H_2 which becomes relatively more important as the H-H separation decreases.

Figure 1 shows that when H_2 is stretched to its right-hand turning point limit [r(H-H) = 1.7234 a_0], the $1A_1$ and B_2 states cross at short interfragment separations in C_{2v} geometry. This has implications for the quenching of the Li fluorescence (which I do not explore further here) and for the possibility that the B_2 state could be a chemically bound excited state (CBES) of the sort that was investigated in some detail by others earlier in the life of the HEDM program. Since the crossing lies to the left of the minimum in the B_2 state, it appears that this will not provide a suitable energy storage situation. A careful optimization of the geometry of the B_2 state yielded the C_{2v} structuure with r(H-H) = 1.579 a_0, R(Li-H_2) = 3.147 a_0. At that geometry the $1A_1$ state lies 3524 cm^{-1} below the B_2 state, thus verifying the thought that the B_2 state of LiH_2 is not a suitable CBES.

Although this study was not designed to describe the long-range interactions with ultimate accuracy, various van der Waals features appear to have at least a qualitatively correct dependence on orientation. The $1A_1$ state is more attractive in $C_{\infty v}$ than C_{2v} , and is more attractive as the bond stretches from its left-hand to its right-hand turning point. This is in consonance with the facts that the dipole polarizability of ground state H_2 is substantially larger along the bond direction than perpendicular to it, and that the polarizability increases with bond stretch [3]. So the ground state curves are the sort one expects for binding due only to the dispersion type interactions. The excited states have, in addition to dispersion effects, electrostatic

effects due to the quadrupolar nature of the H_2 molecule and the ^2P Li atom. Evidently, the $2A_1$ interaction is so attractive since it benefits from an attractive quadrupole- quadrupole interaction in the $C_{\infty v}$ orientation. As the H_2 rotates to the C_{2v} symmetry, its quadrupole is now oriented in such a way that the electrostatic interaction with ^2P Li becomes repulsive. At large separations, the doubly degenerate $C_{\infty v}$ Π state is repulsive (as is shown in Fig. 2) due to the repulsive quadrupole-quadrupole interaction in the linear orientation. As the H_2 rotates, the states split and become more deeply bound due both to the diminuation of the unfavorable electrostastic interaction and the growing importance of the favorable H_2 σ_u-Li p_z interaction as discussed above. Figures 2 and 3 show the van der Waals region for the $C_{\infty v}$ and C_{2v} symmetries, respectively. WARNING! the curves are shown as binding energy curves; remember that the asymptote for the $1A_1$ state lies about 14904 cm^{-1} *below* that for the excited states.

The sensitivity of the Li-H_2 interaction energies to the H_2 orientation carries over to the diagonal and transition dipole moments which involve the ground van der Waals state. Figure 4 shows that the diagonal dipole moment of the ground state is small in absolute magnitude and also oppposite in sign for the extreme orientation angles (0° and 90°). I have not yet calculated the diagonal dipole moments at intermediate angles, but I presume that they will be intermediate between the values I've already calculated. The upshot is I expect that the IR spectrum to be of very low intensity and to be difficult to sort out in any case. The *transition* dipole moments are, by contrast, very near the very high atomic resonance transition value over the entire van der Waals region. The Franck-Condon factors (FCF) for the B_1 (or B_2) - $1A_1$ transition look quite good, while the $2A_1$ - $1A_1$ transition is of the (barely) bound-free sort. Thus only the former transition looks promising. However, in $C_{\infty v}$ the corresponding Π-Σ transition which involves the repulsive Π state is another bound-free transition. It is clear that the observation and interpretation of the Li-H_2 system presents formidable challenges.

References

[1] S. L. Rodgers, unpublished calculations, 1988.
[2] M. E. Fajardo, J. Chem. Phys. **98**, 110 (1993).
[3] W. Meyer, Chem. Phys. **17**, 27 (1976).

Table 1. Characteristic constants for the 3/6 MRCI 112 basis potential curves, (assuming H_2 to be a single rigid particle) for three values of r(H-H).

A. r(H-H) = 1.2054 a_0

angle Θ	R_e (Li-H_2) /a_0				D_e /cm^{-1}			
	$1A_1$	B_2	B_1	$2A_1$	$1A_1$	B_2	B_1	$2A_1$
0.0	9.86	4.213	4.213	12.79	10.40	699.7	699.7	18.87
22.5	—	4.047	4.135	—	—	1083.2	865.4	—
45.0	—	3.694	3.893	—	—	2186.6	1338.9	—
67.5	—	3.410	3.670	—	—	3534.2	1907.4	—
90.0	10.56	3.297	3.584	repuls	7.46	4169.0	2174.6	repuls

B. r(H-H) = 1.4 a_0

angle Θ	R_e (Li-H_2) /a_0				D_e /cm^{-1}			
	$1A_1$	B_2	B_1	$21A_1$	$1A_1$	B_2	B_1	$2A_1$
0.0	9.67	4.391	4.391	—	14.99	656.9	656.9	27.33
22.5	—	4.123	4.258	—	—	1198.3	852.8	—
45.0	10.11	3.691	3.970	—	11.85	2746.7	1411.6	—
67.5	—	3.358	3.701	—	—	4646.9	2106.1	—
90.0	10.02	3.228	3.578	repuls	9.68	5553.2	2441.2	repuls

C. r(H-H) = 1.7234 a_0

angle Θ	R_e (Li-H_2) /a_0				D_e /cm^{-1}			
	$1A_1$	B_2	B_1	$2A_1$	$1A_1$	B_2	B_1	$2A_1$
0.0	9.33	4.627	4.627	10.67	27.20	623.3	623.3	57.82
22.5	—	4.169	4.456	—	—	1719.4	853.6	—
45.0	—	3.659	4.104	—	—	4345.0	1532.9	—
67.5	—	3.268	3.749	—	—	7350.7	2414.1	—
90.0	9.75	3.092	3.604	repuls	13.70	8912.0	2856.7	repuls

LiH$_2$ 90.0deg (rhtp)

144

145

Ground state diagonal dipole moment
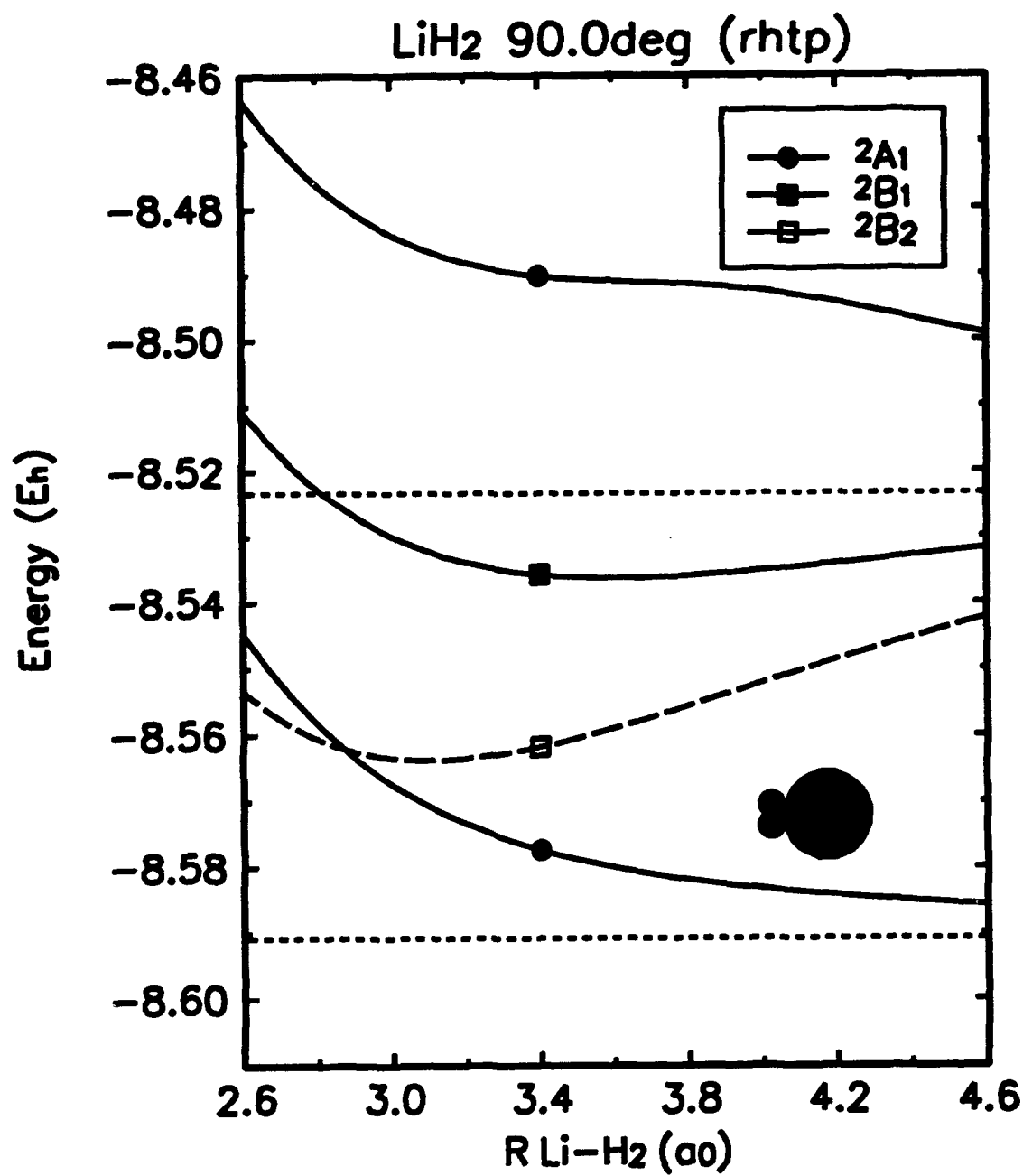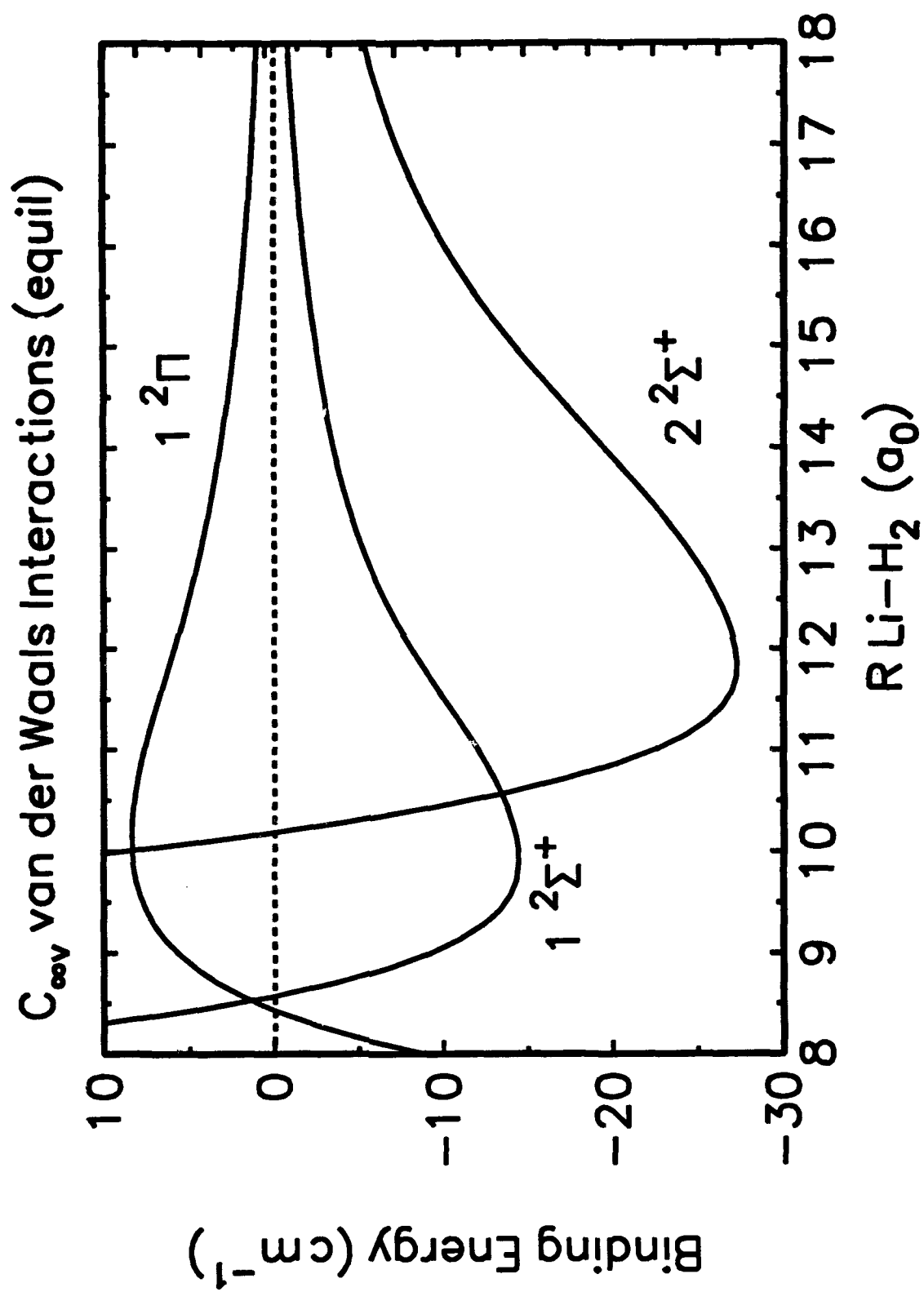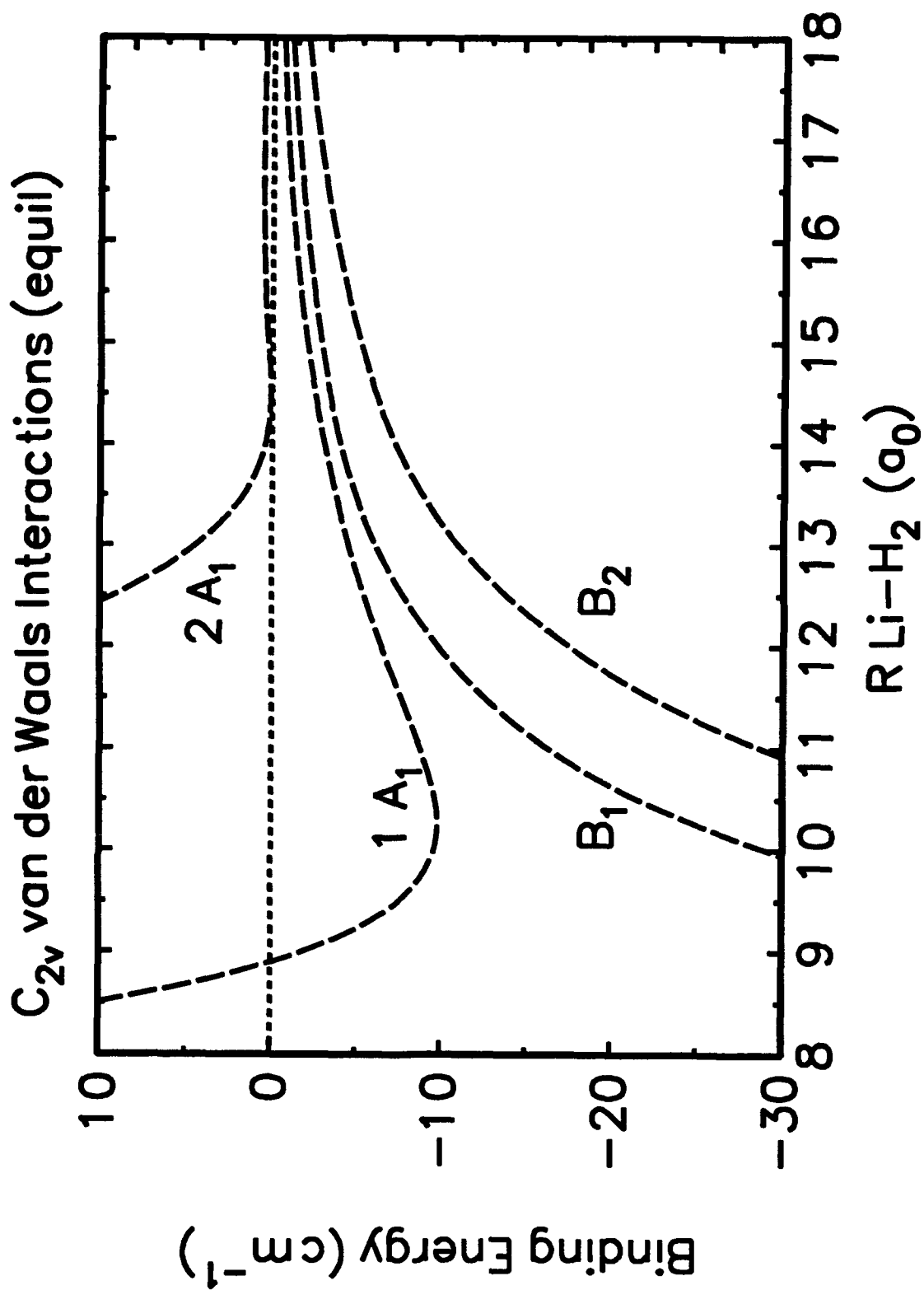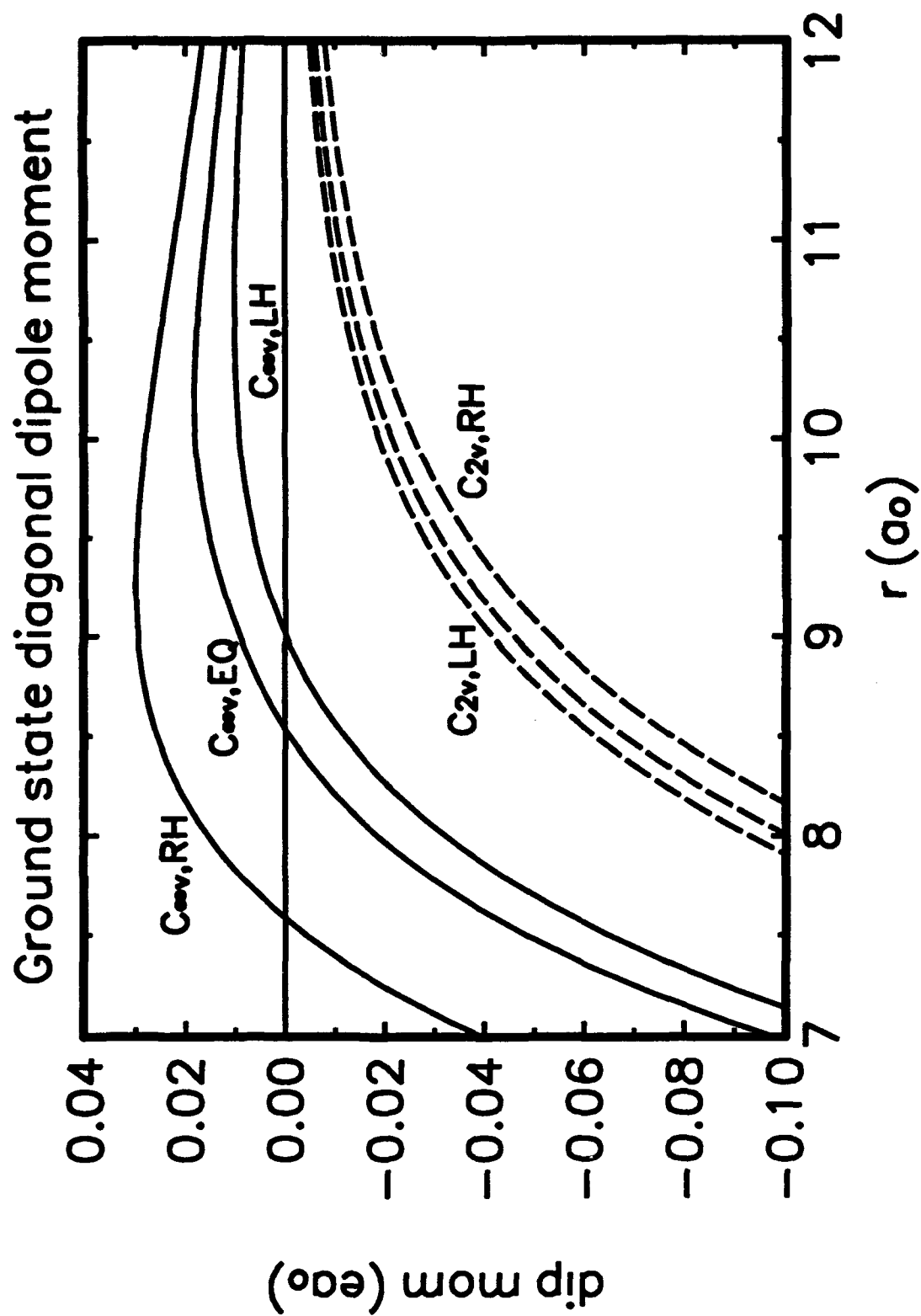
EXTENDED ABSTRACT FOR
HIGH ENERGY DENSITY
MATERIALS (HEDM) CONFERENCE

Rodney J. Bartlett

Quantum Theory Project
University of Florida
Gainesville, Florida 32611

OBJECTIVES OF HEDM EFFORT

- Identification of potential metastable molecules as viable high energy density materials.

    —N_4, N_8, N_5H, HCNBH, N_5–N_5, $LiBe(BH_4)_3$, etc.

- Theoretical spectroscopic characterization of boron oxides and related systems.

    —Boron combustion kinetics models are severely hindered by a need for "better molecular parameters for HBO, B_2O_3 and BO_2."

- Electronic spectra signature of atoms in cryogenic matrices.

    —Equation-of-motion coupled-cluster (EOM–CC) methods. NEW METHOD! ACES II.

- Migration in cryogenic solids.

    —ROHF–CC/MBPT methods and analytical gradient techniques. NEW METHOD! ACES II.

*R.C. Brown, C.E. Kolb, R.A. Yetter, F.L. Dryer, H.R. Rabitz, Final Reports 1987, 1991.

METASTABLE MOLECULES

- Metastability occurs when a molecule has a potential energy surface like
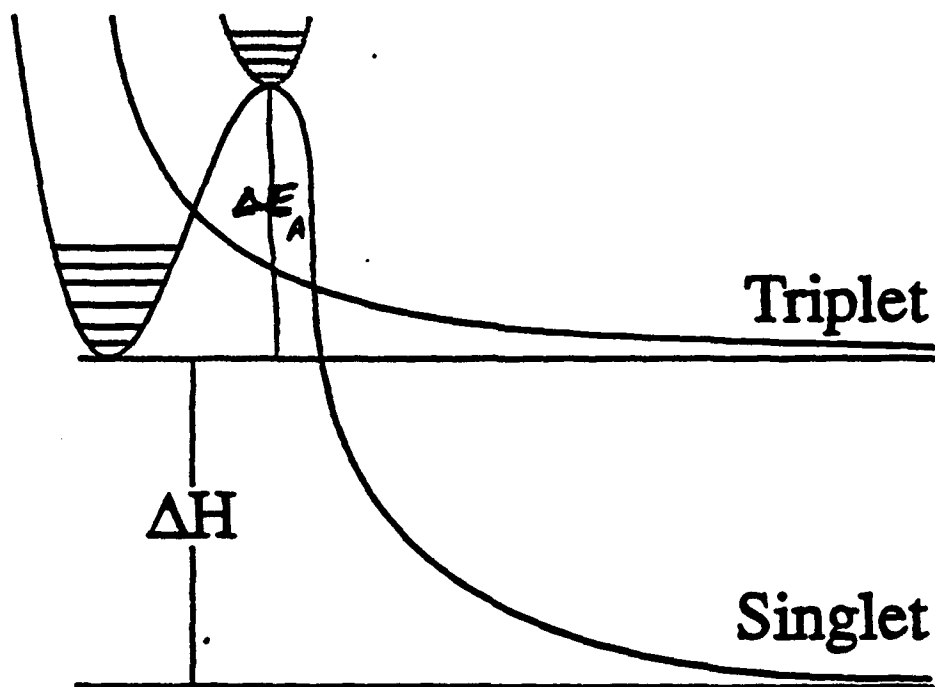
Provided the barrier, ΔE_A, to dissociation is sufficiently high, and provided that there are no alternative dissociation pathways like the triple surface shown, the metastable molecule should have a sufficient lifetime to store an amount of energy, ΔH.

- In chemistry there is a whole world of metastable molecules that is largely unexplored, since such molecules are not readily amendable to experimental observation.

- Alternatively, high level, correlated *ab initio* quantum chemical methods offer a microscope that probes the potential existence of metastable species.

Chemistry of Nitrogen Metastable Species

Molecules previously considered include:
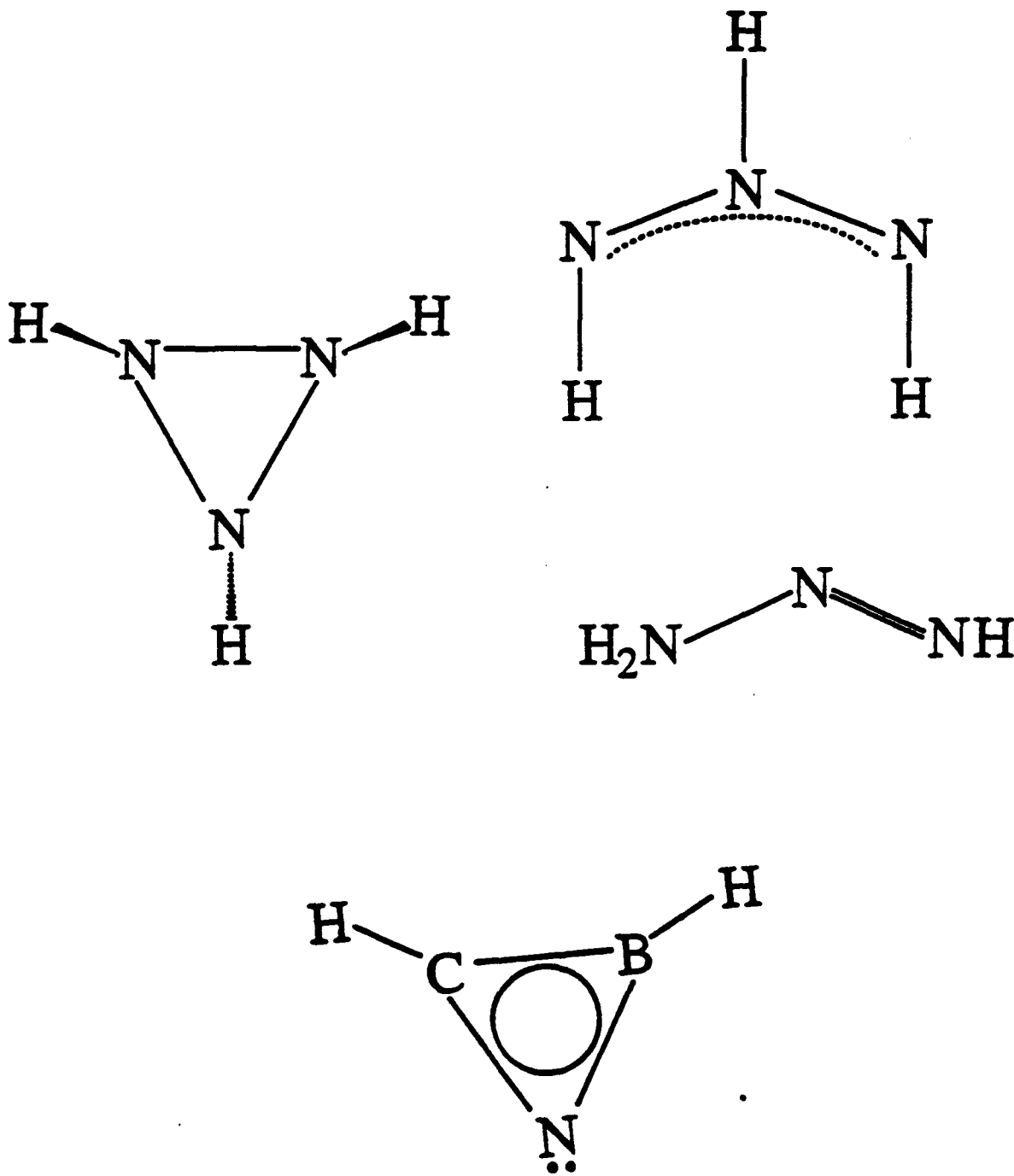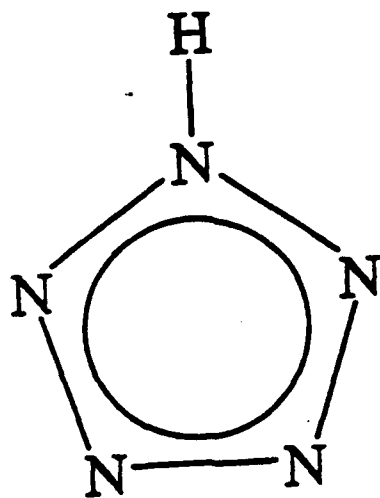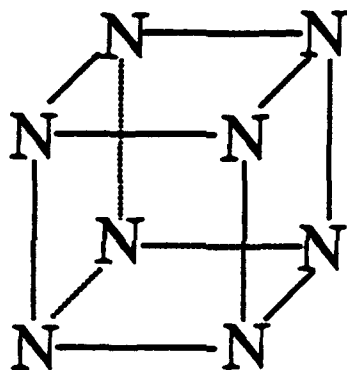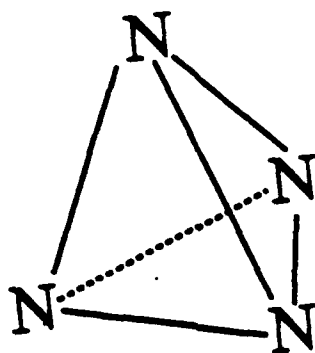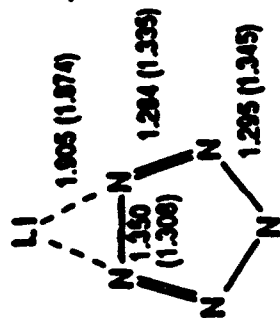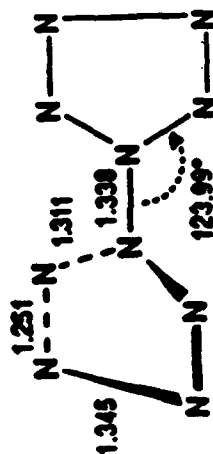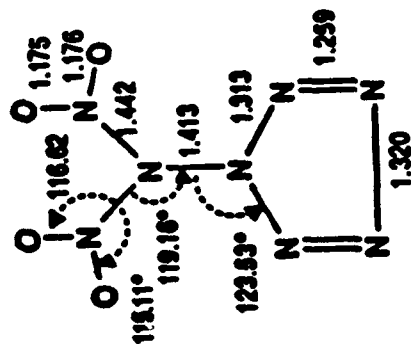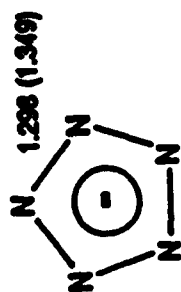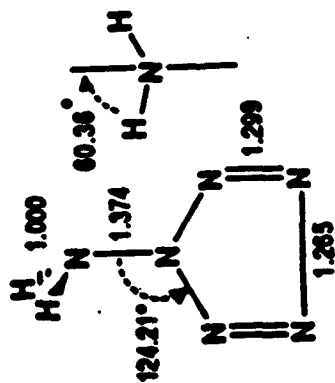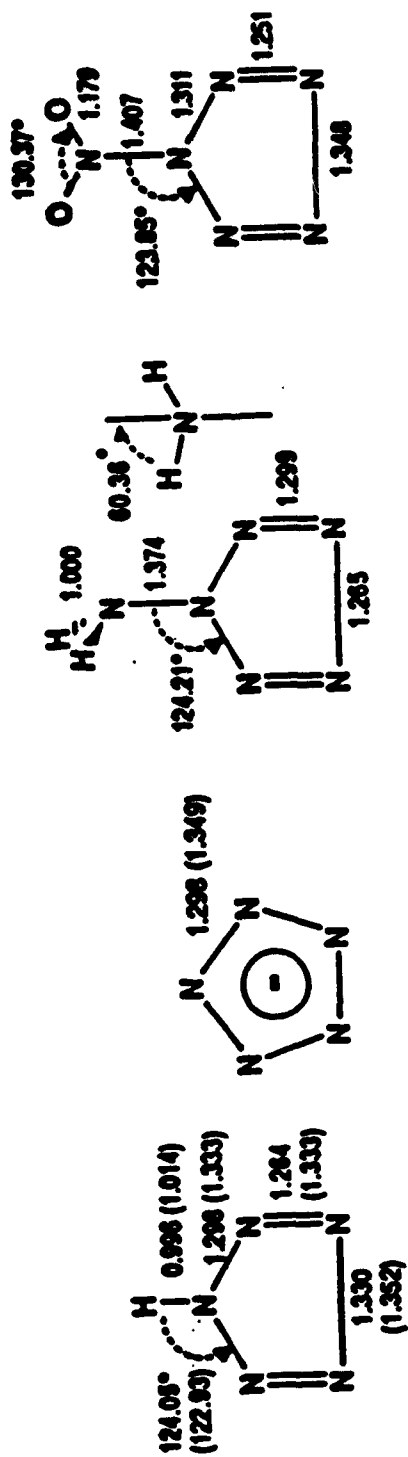
SCF angles and bond lengths (MBPT(2) structures in parenthesis)

None of these molecules are known experimentally, although some like pentazole have known derivatives.

We have found all of the above to be local minima on their potential energy surfaces at the correlated level, implying their likely existence. Furthermore, in most we present prediction of vibrational spectra including electron correlation which will facilitate their potential identification in matrix isolation experiments.

From computed heats of formation at high level CC/MBPT correlated levels, we have made estimates of Isp's. They are shown in the following table.

Specific Impulse of Several Molecular Systems (in seconds)

	SCF	CCSD + T(CCSD)
$H_2 + O_2$	456 (467)*	
$N_2H_4 + N_2O_4$	324	
$N_3H_3 + O_2$	SCF	CCSD + T(CCSD)
triazine	351	347
triimide	382	365
triaziridine	399	390
Monopropellants		
$N_4(T_d)$	520*	489*
$N_8(O_h)$	559*	531 *
HN_5	343*	303*
$H_2N - N_5$	351*	317*

*The formula $265\sqrt{\Delta H/M}$ was ___

153

More information about the above molecules can be obtained in the following publications:

1. D.H. Magers, E.A. Salter, R.J. Bartlett, C. Salter, B. Andes Hess, Jr., and L.J. Schaad, "Do Stable Isomers of N_3H_3 Exist?" Am. Chem. Soc. 110, 3435 (1988).

2. W.J. Lauderdale, J.F. Stanton and R.J. Bartlett, "Stability and Energetics of Metastable Molecules: Tetraazatetrahedrane (N_4), Hexaazabenzene (N_6), and Octaazacubane (N_8)," J. Phys. Chem. 96, 1173 (1992).

3. I. Cernusak, S. Beck and R.J. Bartlett, "Potential Energy Surface of Borazirene (HCNBH)," J. Phys. Chem. 96, 10284 (1992).

4. K. Ferris and R.J. Bartlett, "Hydogen Pentazole: Does It Exist?" J. Am. Chem. Soc. 114, 8302 (1992).

NEW BORON–NITROGEN MOLECULES

Iminoboranes are a new class of molecules first synthesized in 1975, of the general form $RB \equiv NR$, which involve two-coordinate boron atoms with nitrogen atoms of coordination number 4, 5 or 6. Because of the high energy content of B and N containing species, iminoboranes would appear to be a potential source of new energetic materials. Now more than 50 iminoboranes have been synthesized and characterized.[1]

In our search for metastable energetic materials we have considered isovalent analogs of the known aromatic species cyclopropenyl cation and benzene, where we replace a $C_3H_3^+$ group by HBNCH and C_6H_6 by the dimer to give the molecule in Figure 1a.[2] This molecule is not planar like benzene, but assumes a boat form with the two B–H bonds being out of the plane.

We have determined the molecule to have a high heat of formation, $\Delta H_f^0 = 109.6$ kcal/mol, from which an Isp could be estimated.

The potential for making high energy polymer materials has also been investigated. Cis and trans forms are shown in Figures 1b and 1c. The energy difference between the boat and trans form is 12.5 kcal/mol. By adding extra HCN–BH units to the terminal B–H bonds, an extended polymeric structure can be envisioned.

In Figure 2a, 2b, and 2c are shown the predicted vibrational spectra for the three isomers in Figure 1. These should be accurate enough to use for identification of the synthesized molecules.
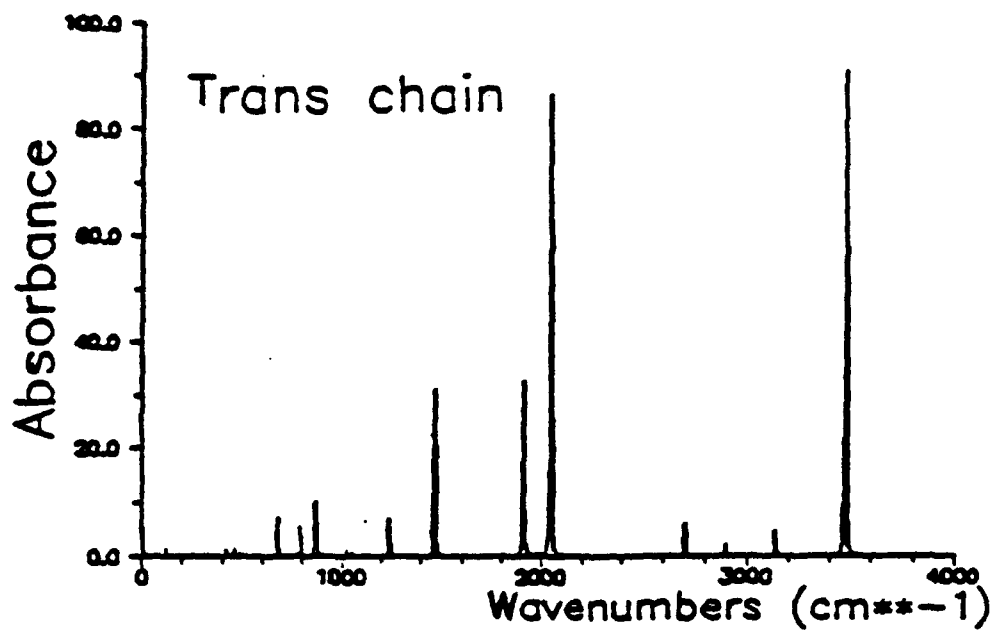
[1] P. Paetzold, Pure and Appl. Chem. 63, 345 (1991). P. Paetzold, Adv. Inorg. Chem. 31, 123 (1987); H. Nöth, Angerv. Chem. Int. Ed. Engl. 27, 1603 (1988).

[2] L. Cemmak, M. Urban, P. Erd and R.J. Bartlett, J. Am. Chem. Soc. 114, 10955 (1992).

Figure 1
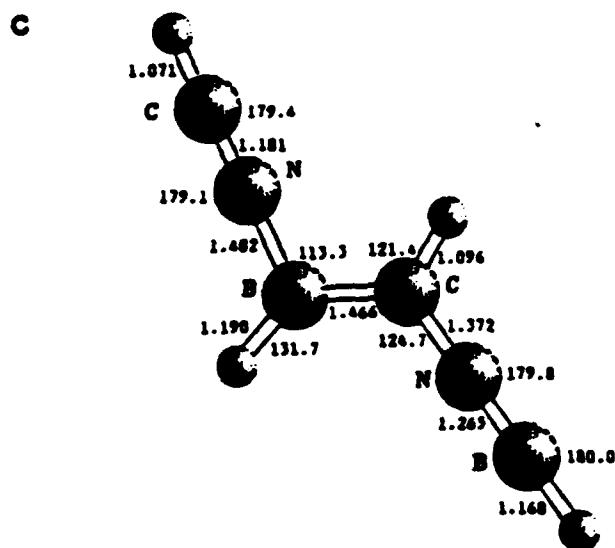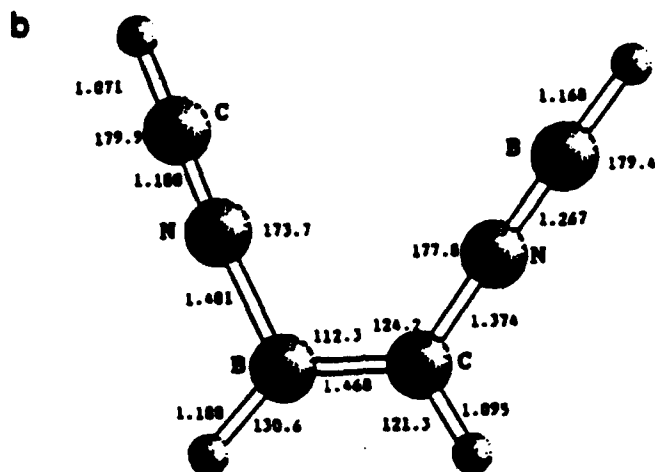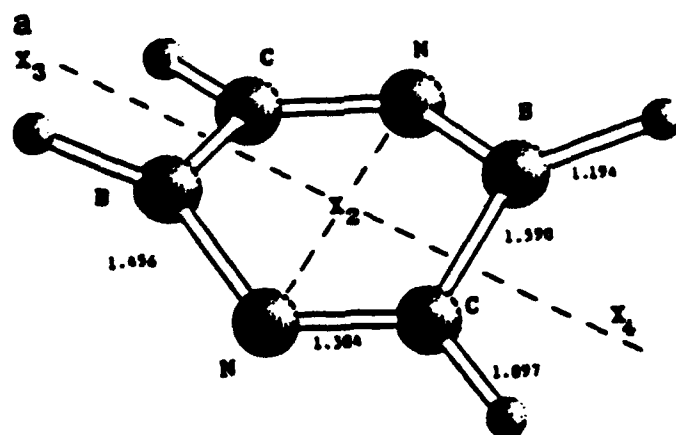
Three MBPT(2)/DZP optimized structures of $C_2H_4B_2N_2$. (a) Boat (C_2). Bond angles (deg): $CNX_2 = 63.5$; $BNX_2 = 56.1$; $HCN = 119.1$; $HBN = 120.7$; $X_3X_2N = 90.0$. Dihedral angles (deg): $CNX_2X_3(X_4) = 172.4$; $BNX_2X_4(X_3) = 156.0$; $HCNX_2 = -158.1$; $HBNX_2 = -144.9$. X_2 is the NN distance midpoint; X_3, X_2, and X_4 are collinear. (b) Cis (C_s). (c) Trans (C_s).

Trans chain

Cis chain

Boat

157
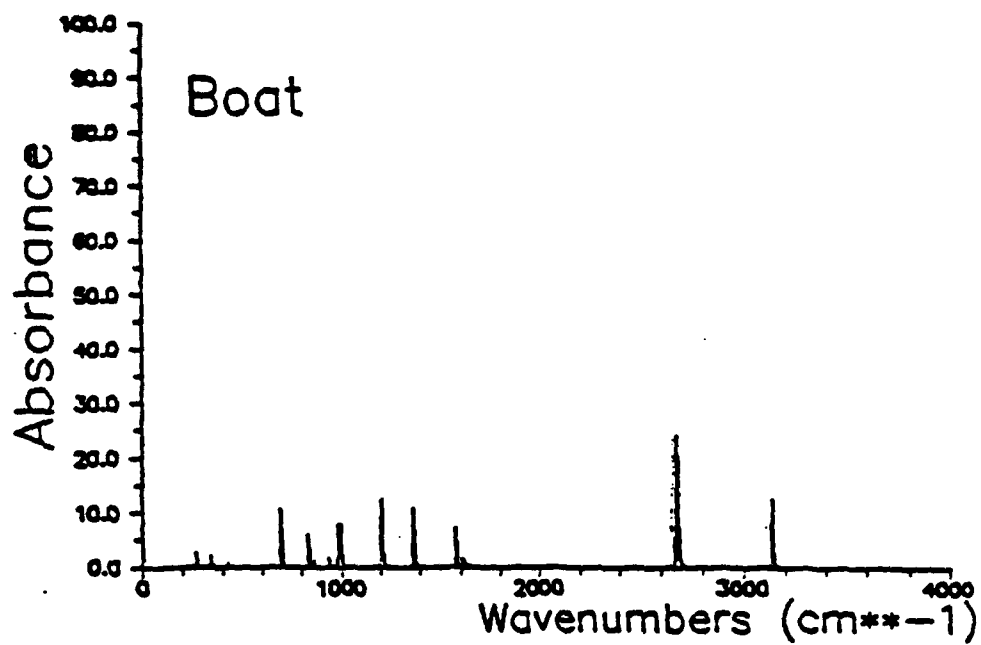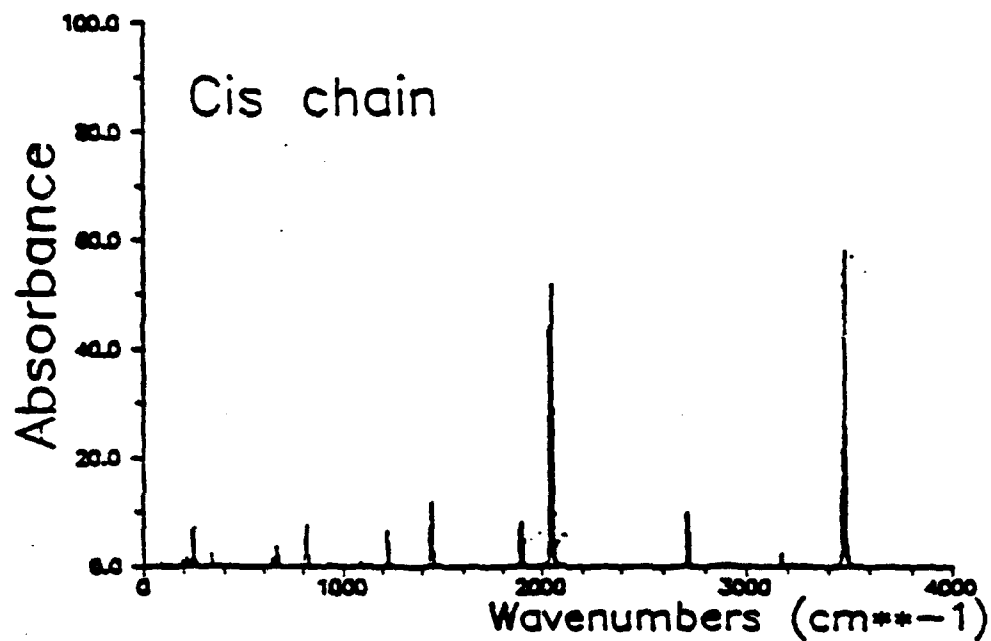
Laser and Fourier Transform Spectroscopy
of Novel Propellant Molecules

Peter Bernath
Department of Chemistry
University of Waterloo
Waterloo, Ontario, Canada N2L 3G1

and

Department of Chemistry
University of Arizona
Tucson, Arizona 85721 USA

A variety of molecules important as potential advanced propellants were studied by high resolution Fourier transform emission spectroscopy.

A. Jet Spectroscopy: Swan system of C_2.

The C_2 molecule is a common constituent of flames and is made during the combustion of conventional propellants. The green color often observed in flames is due to the Swan system of C_2. In addition, C atoms and C_2 molecules are possible advanced propellants if they can be trapped in solid hydrogen.

The $d^3\Pi_g$-$a^3\Pi_u$ Swan system of C_2 was produced in a jet-cooled corona excited supersonic expansion of diazoacetonitrile in He[1]. The C_2 emission was observed in a series of experiments on the CCN^2 and the $CN^{3,4}$ molecules. The C_2 emission was detected at 0.025 cm^{-1} resolution with the McMath Fourier transform spectrometer at Kitt Peak.

As was observed in our CN work[3,4], the electronic emission of C_2 was vibrationally hot but rotationally cool (~90K). The spectrum of C_2 was also produced in a conventional hollow cathode discharge with an Al_4C_3/Cu cathode. The remarkable simplification provided by jet-cooling is illustrated in Figure 1. The top panel is the 0-0 band of the Swan system of C_2 from

Figure 1

159
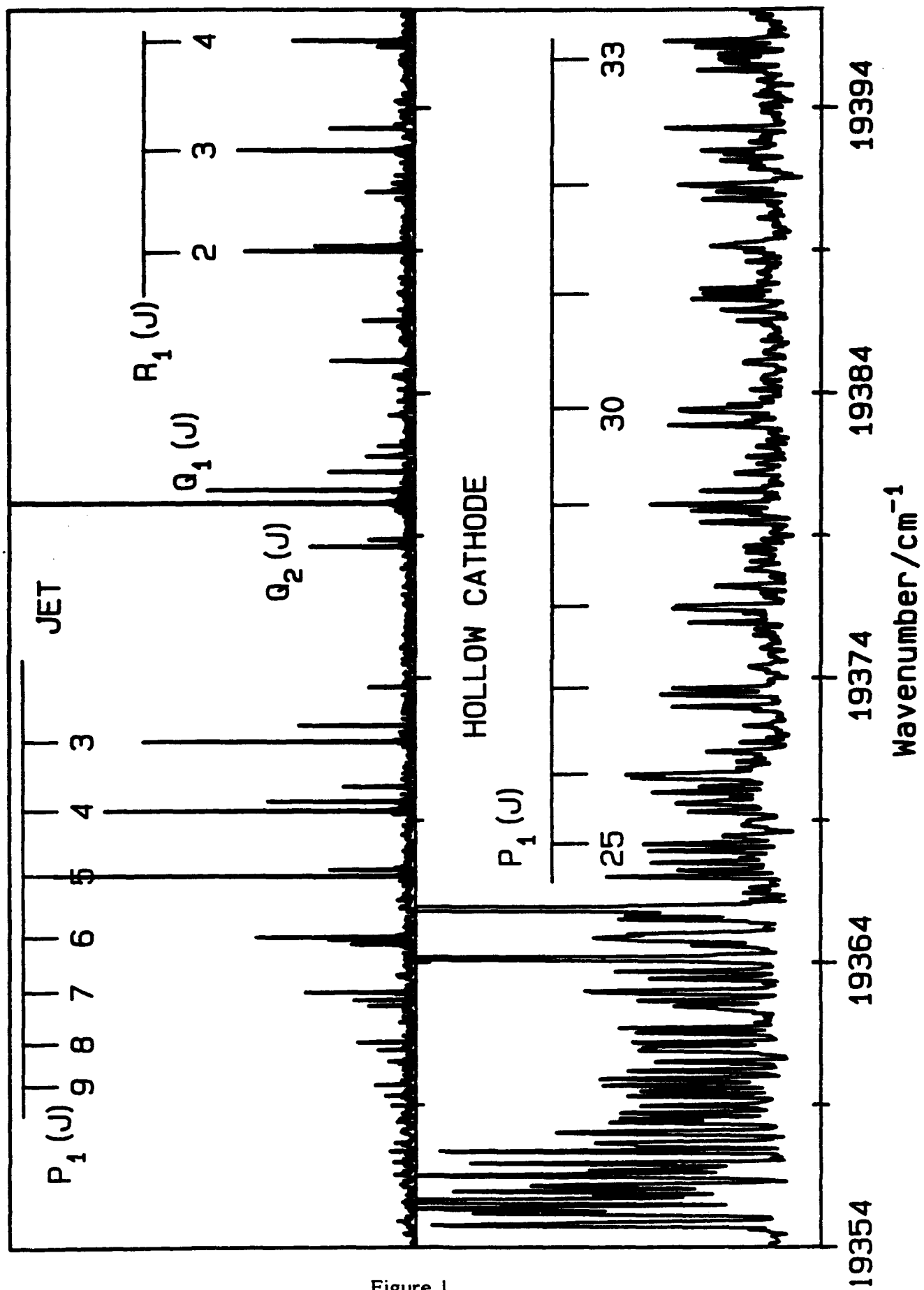
the jet emission source while the lower panel is the corresponding near room temperature spectrum recorded with the hollow cathode source.

The cold spectrum in the jet source (Figure 1) allows the low-J lines of many vibrational bands to be easily assigned. We analysed the vibrational levels with $v' = 0$-3 in the excited $d^3\Pi_g$ state and $v'' = 0$-4 in the lower $a^3\Pi_u$ state.[1] The line positions from the jet source were augmented with our hollow cathode data as well as some laser and Fourier transform data from the literature. A greatly improved set of spectroscopic constants were derived for the $d^3\Pi_g$ and $a^3\Pi_u$ states of C_2.

B. Vibration-Rotation Emission Spectroscopy: AlCl, HCl, AlH, AlD, GaH, GaD, InH and InD.

One promising scheme for boosting the performance of the hydrogen/oxygen propellant system is to trap light metal atoms or metal hydrides in solid hydrogen. We are exploring the chemical interaction of light metals such as aluminum with hydrogen at high temperatures by Fourier transform emission spectroscopy. We find high resolution emission spectroscopy to be a very sensitive diagnostic tool for high temperature chemistry.

In order to trap a metal atom in solid hydrogen, it first must be vaporized probably in the presence of hydrogen gas. Our gas phase studies are, therefore, the first steps in any practical trapping scheme.

Aluminum powder is currently used in conventional solid propellants and Al atoms are a very favorable additive to solid hydrogen. Aluminum liquid and aluminum vapors are very corrosive, but we have found that a carbon liner protects the alumina furnace tube at high temperatures. At 1550°C aluminum and hydrogen react to give AlH in the gas phase (Figure 2), with no evidence for the formation of AlH_2 or AlH_3. The remarkably strong AlH emission allowed the line positions to be measured with a precision of ±0.0001 cm^{-1} (in the most

Fig. 3 - Overview Emission Spectrum Of AlH

Figure 2

161
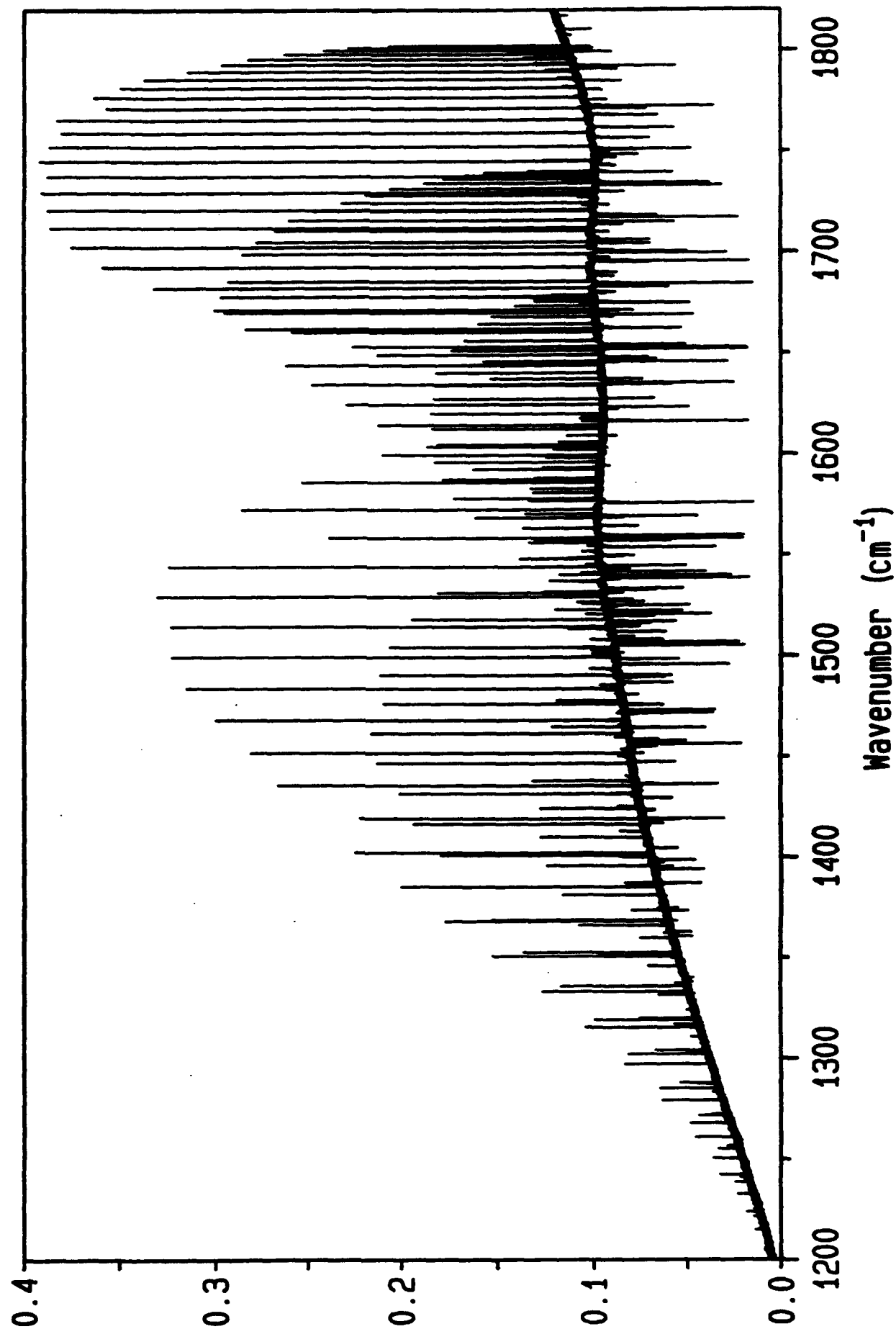
favourable cases) with our Bruker IFS 120 spectrometer at Waterloo. This precision is unprecedented for an unstable molecule such as AlH. Similar experiments were carried out on AlD as well as GaH, GaD, InH and InD. These molecules were measured to test our new data reduction methods (see below).

The long wavelength limits of our emission technique were explored by recording the vibration-rotation spectrum of AlCl and the pure rotational spectrum of hot HCl at 20 microns. Both HCl and AlCl are observed in the plumes of rockets burning aluminized solid propellants with an ammonium perchlorate oxidizer.

C. "New" Data Reduction Techniques.

We typically measure thousands of line positions for a molecule, but we would like to represent these data in a more compact form. Spectroscopists traditionally fit their data to polynomials to extract spectroscopic constants. However, the most physically meaningful quantity is the potential energy curve. With accurate potential energy curves (and dipole moment functions) all spectra could be calculated. Moreover the potential energy curves are the key ingredients for any simulation of the physical properties in a condensed state.

We are directly fitting the experimental data to the eigenvalues of the Schrödinger equation ("inverse perturbation approach"). The Schrödinger equation is solved numerically using a parameterized modified-Morse potential energy function of the form[5]

$$V(r) = D_e \, (1 + e^{-\beta(r)})^2 / (1 - e^{-\beta(\infty)})^2$$

with $\qquad \beta(r) = z(\beta_0 + \beta_1 z + \beta z^2 + ...)$ and $\quad z = (r - r_e)/(r+r_e)$.

Corrections for Born-Oppenheimer breakdown are made by adding mass-dependent terms to V(r). This approach is a modification of one proposed by Coxon. The potential energy function obtained for AlH and AlD is drawn in Figure 3.

Born–Oppenheimer Potential
AlH

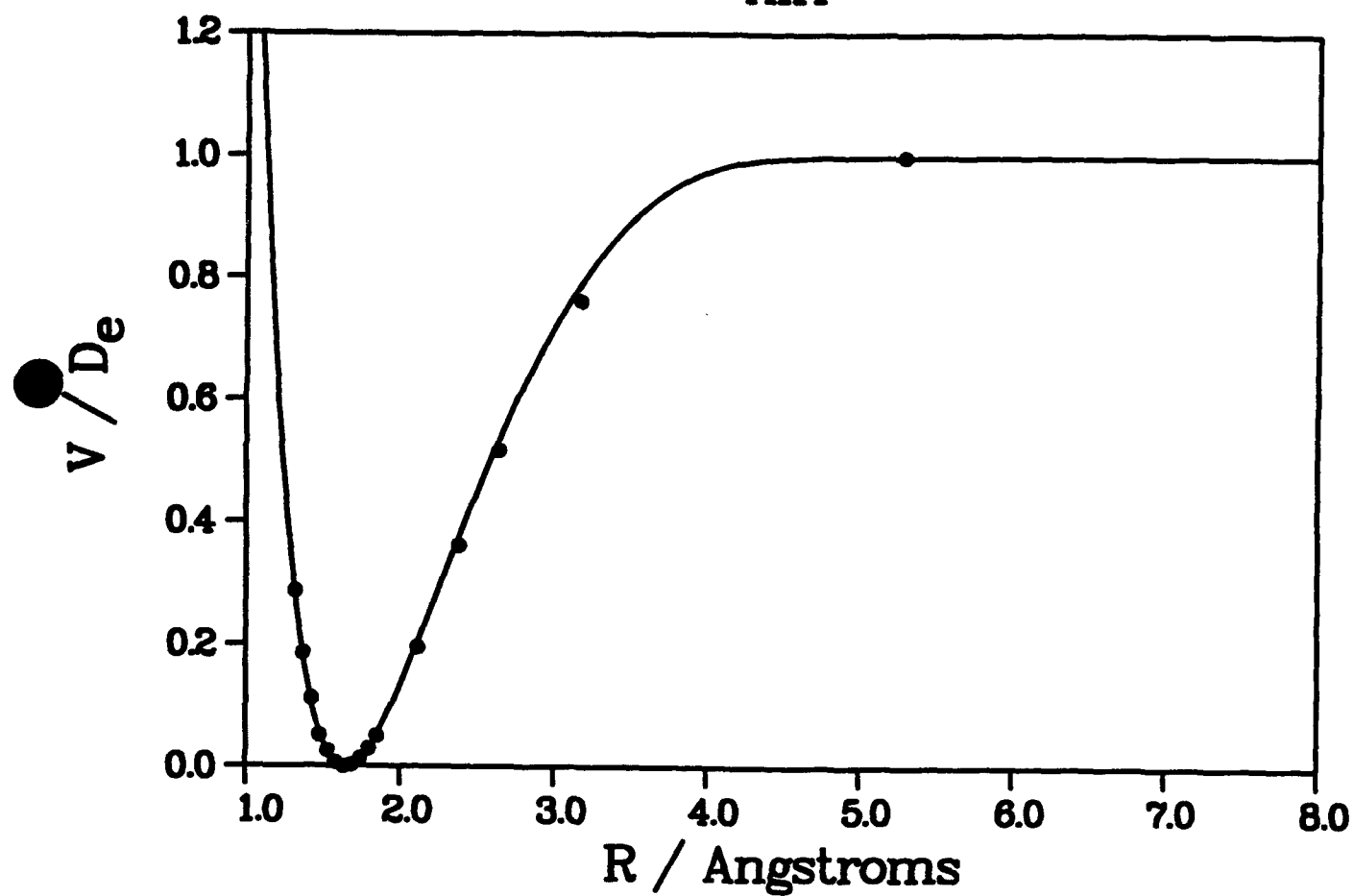
Figure 3

The advantage of our approach is that the potential energy function, V(r), is quantitatively correct for the lower half of the curve (Figure 3) where we have spectroscopic data and is qualitatively correct for the upper half of the curve. For comparison we have plotted the points of a high level *ab initio* calculation in Figure 3. Notice the excellent agreement between our extrapolated curve at high v and the *ab initio* points. Our approach is also capable of incorporating all the available information and represents the "best" potential curve.

References

1. C.V.V. Prasad and P.F. Bernath, *Ap. J.*, submitted.

2. N. Oliphant, A. Lee, P.F. Bernath and C.R. Brazier, *J. Chem. Phys.* **92**, 2244 (1990).

3. C.V.V. Prasad, P.F. Bernath, C. Frum and R. Engleman, *J. Mol. Spectrosc.* **151**, 459 (1992).

4. C.V.V. Prasad and P.F. Bernath, *J. Mol. Spectrosc.* **156**, 327 (1992).

5. H. Hedderich, M. Dulick and P.F. Bernath, *J. Chem. Phys.*, submitted.

ELECTRONIC STRUCTURE CALCULATIONS WITH PARALLEL COMPUTING

MARK S. GORDON, THERESA L. WINDUS AND MICHAEL W. SCHMIDT

DEPARTMENT OF CHEMISTRY

IOWA STATE UNIVERSITY

AMES, IOWA 50011

There has been a flurry of activity in the past two years in the development of parallel codes for electronic structure calculations. This effort has been considerably enhanced by the efforts of the Argonne theoretical chemistry group, most notably Robert Harrison, who have developed a message passing code (TCGMSG) that is particularly well suited to electronic structure calculations. This development has facilitated the conversion of a major part of the electronic structure program GAMESS to parallel.

The core of GAMESS calculates electronic wave functions for atoms and molecules at several levels of theory. The simplest of these, the restricted Hartree-Fock (RHF) wave function, applies only for closed shell species, in which all electrons are paired. Most molecules in their ground electronic states and lowest energy isomers are closed shell species, for which RHF wave functions are applicable. Open shell species can be described with restricted open shell Hartree-Fock (ROHF) wave functions, in which the unpaired electrons are described by singly occupied orbitals. The remaining electrons are again entered into orbitals in alpha-beta spin pairs, as in the RHF wave functions. An alternative to the ROHF description of open shells is the unrestricted Hartree-Fock (UHF) wave function, in which all alpha and beta electrons are placed in separate orbitals.

While Hartree-Fock wave functions are often a reasonable starting point for treating molecular structures, this level of theory is rarely sufficient for the prediction of reaction energetics. For accurate prediction of energetics, one must add correlation corrections into the wave function. In GAMESS, there are several methods for doing this. The simplest improvement in the wave function, particularly well suited for the treatment of diradicals, is the two configuration (TC) self-consistent field (SCF) method (equivalently, the generalized valence bond (GVB) method). Here, the two electrons in the highest occupied molecular orbital (HOMO) are allowed to occupy the lowest unoccupied (correlating) molecular orbital (LUMO) as well. This is simple version of the more general multi-configurational (MC) SCF method, in which several occupied and unoccupied orbitals are correlated. MCSCF wave functions are necessary when several bonds and lone pairs are involved in a chemical reaction. The occupied and unoccupied orbitals used in an MCSCF wave function are collectively referred to as the "active space". Once the MCSCF calculation has been completed, one normally does a configuration interaction (CI) calculation, in which all single and double excitations from ALL of the MCSCF configurations are included. This is frequently referred to as second order (SO) CI. All of the methods described so far are variational methods. An alternative approach to incorporating correlation is perturbation theory. Second order Moller-Plesset perturbation theory (MP2) is include in GAMESS, for closed shell (RMP2) and open shell (UMP2, ROMP2) wave functions.

In order to predict geometries of stationary points on a potential energy surface (PES), one requires the gradient of the energy. The gradient is also essential for the calculation of minimum energy paths (MEP's) for chemical reactions. GAMESS currently has the ability to calculate analytic gradients for RHF, UHF, ROHF, TCSCF, and MCSCF wave functions. The second derivatives of the energy are also important to characterize the nature of stationary points (e.g., as minima, transition states) and for the prediction of frequencies. Analytic hessians are available in GAMESS for RHF, ROHF, and TCSCF wave functions. Of course, numerical hessians are available for all wave functions for which analytic gradients can be calculated.

At the present time, the calculation of energies, wave functions, gradients and associated properties can be performed in parallel for RHF, ROHF, UHF, and TCSCF (GVB) levels of theory. As noted above, this means geometry optimizations and reaction path following can be done in parallel. The remaining wave function types, MCSCF, CI, and MP2, as well as analytic hessians, have a common bottleneck - the transformation of the two-electron integrals from the molecular orbital (MO) to the atomic orbital (AO) basis. There are several possible alternative approaches to performing this transformation in parallel. These include direct or semi-direct methods, in which the two-electron integrals are calculated partially or entirely in the AO basis, distributing the calculation of different parts of the transformation and integral calculation to several nodes, and the use of a series of two-by-two rotations. The first two of these are under development in our laboratory, while the third is being developed by Iowa State colleagues Klaus Ruedenberg and Steven Elbert.

Because of the portability of both GAMESS and TCGMSG, parallel GAMESS is available on several hardware platforms. It runs across several (equivalent or inequivalent) workstations, as well as on Intel, Connection, and Kendall Square massively parallel computers. In general, we find that the code scales with nearly 100% efficiency using 1-16 nodes and at approximately 80% efficiency up to 64 nodes. Recent calculations on the prismane structure of borazine can serve as a specific example. A 6-311G(2d,2p) calculation on this molecule requires 204 basis functions. This is a fairly modest test case by current standards. Nonetheless, as shown in the Table, this RHF calculation scales quite well through 32 processors, and a non-trivial speedup is obtained even upon going from 128 to 256 nodes. Note that the orbital guess part of the code is a pretty trivial part of the total calculation when p = 8 nodes. In contrast, the initial guess part of the calculation is nearly 50% of the time required for the two-electron integrals when the number of nodes is increased to 256. This serves to emphasize the point that one should scale the size of the calculation as the number of nodes is increased.

The parallel version of GAMESS has been used in several applications of interest to the HEDM program. Since these are reported in separate abstracts in this document, the reader is referred to the reports on high energy prismane structures and on isomers of the nitric oxide dimer.

B$_3$N$_3$H$_6$-Prismane   *C$_s$* **Symmetry**

RHF/6-311G(2d,2p)//RHF/SBK(d)   **204 basis functions**

p=	8	16	32	64	128	256
1e· int.	3.84	3.23	3.27	3.12	2.95	3.08
orb. guess	191.18	190.15	195.89	197.18	192.06	188.27
2e· int + RHF	4027.72	2151.85	1234.92	771.37	518.30	401.90
property	40.69	37.32	43.09	42.53	37.27	39.29
1e· grad	10.83	5.74	6.94	6.80	3.39	3.22
2e· grad	1542.77	776.94	394.46	201.96	104.66	56.46
total	5822.18	3170.10	1883.65	1228.42	863.56	697.05

GEOMETRICAL ISOMERIZATION AND LIGHT METALLOID MOLECULE OXIDATION AS A MEANS OF PRODUCING HIGH IMPULSE PROPELLANTS

James L. Gole
School of Physics, Georgia Institute of Technology
Atlanta, Georgia 30332

Geometric Isomers of the Halogen Oxides, FO_x (x=1,2)

Previously,[1] we have discussed the isomeric forms of the halogen dioxides, FO_2 and ClO_2, and the potential use of the fluorine dioxide isomers as high energy density materials. The $FOO(^2A'')$ radical[2] corresponds to a moderately reactive ground state while OFO represents a highly excited local minimum on the FO_2 potential surface. The specific enthalpies of reaction of these conformers with $H_2(\ell)$ and several boron based metalloid molecules (Table I) considerably exceed that inherent to the benchmark "Lox-hydrogen" conversion (12.56 MJ/kg).

FOO represents an unusually stable radical which can be generated in the gas phase through the thermal decomposition of O_2AsF_6[3] or O_2BF_4[3]. While the corresponding OFO isomer has not been observed, its OClO counterpart is well studied.[4] Quantum chemical calculations suggest that OFO lies ~ 110 kcal/mole higher in energy than FOO[2], thus accounting for the dominant formation of the FOO radical in fluorine-oxygen mixtures. While the OFO radical is thermo-dynamically unstable relative to the peroxy radical, there is no reason to believe that OFO would not be kinetically stable if prepared photochemi-cally[2,5] or by an appropriate synthetic route such as that applied to the synthesis of OClO.[5]

If the OFO radical can be produced and subsequently stabilized, this isomer as well as its more stable isomeric conformer and the OF radical, may provide important starting materials (Table I) for use in high specific impulse reactive encounters. The maintenance and stabilization of the OFO radical, in particular, should best be accomplished in a low temperature matrix environment. In order to create a useful propellant, the matrix host material must be a potential fuel component such as H_2, O_2, or molecular boron. It will be most feasible to examine the trapping of OFO in solid O_2 or highly doped boron matrices; however, this should be prefaced by initial studies carried out in solid argon to reduce chemical complexity.

OFO in argon might be produced via photoisomerization[1] or dissociation/recombination channels. FOO ($\nu_{0-0} = 1494$ cm^{-1},[2] $\nu_{0-F} = 584$ cm^{-1},[2]), generated by thermal decomposition,[3] when exposed to pulsed excimer laser radiation at several wavelengths (e.g., 193, 222, or 248 nm) may access states with workable branching ratios to form OFO.[1] While it is probable that dissociative and predissociative states will be excited, the complete dissociation of the molecule should be prevented by the matrix cage. The photolysis products may recombine with the possibility of trapping in the OFO local minimum. The formation of OFO should be monitored by the observation of new absorption bands near 400 and 600 cm^{-1}.[1]

It may also be possible to generate OFO in the gas phase through photolysis of O_2F/Ar mixtures during condensation or through the deposition of the products from a microwave discharge in $O_2/F_2/Ar$ mixtures. The gas phase generation of OFO is desireable even if photoisomerization is effective in

Table I

Comparative Reaction Specific Enthalpies (MJ/kg) and Specific Impulses

For Select Halogen Oxide and Boron Molecule Reactions

Reactants	Reaction	Specific Enthalpy (MJ/kg)	I_{sp} (seconds) Ideal	(0.8 H)
$FOO,H_2(l)$	$5/2H_2(l) + FOO(g) \rightarrow HF(g) + 2H_2O(g)$	14.07	541	484
$OFO,H_2(l)$	$5/2H_2(l) + OFO(g) \rightarrow HF(g) + 2H_2O(g)$	22.36	682	610
B_2,FOO	$3/2B_2(g) + FOO(g) \rightarrow BF(g) + 2BO(g)$	16.26	582	520
B_2,OFO	$3/2B_2(g) + OFO(g) \rightarrow BF(g) + 2BO(g)$	21.71	672	601
B_3,FOO	$B_3(g) + FOO(g) \rightarrow BF(g) + 2BO(g)$	12.29	506	452
B_3,FOO	$B_3(g) + OFO(g) \rightarrow BF(g) + 2BO(g)$	17.81	609	544
B_2,OF	$B_2(g) + OF(g) \rightarrow BF(g) + BO(g)$	18.18	615	550
BH,OF	$BH(g) + OF(g) \rightarrow BF(g) + BO(g)$	17.16	597	534
HB_2,FOO	$HB_2(g) + FOO(g) \rightarrow BF(g) + 2BO(g)$	> 13.38 (17.31[a])	527	472
HB_2,OFO	$HB_2(g) + OFO(g) \rightarrow BF(g) + 2BO(g)$	> 19.65 (23.58[a])	639	572
B_3H,OF	$B_3H(g) + 2OF(g) \rightarrow HF(g) + 2BO(g)+BF(g)$	12.79	516	461
B_3H^b,OF	$B_3H^*(g) + 2OF(g) \rightarrow HF(g) + 2BO(g)+BF(g)$	13.58	531	475
Al_2,FOO	$3/2Al_2(g) + FOO(g) \rightarrow AlF(g) + 2AlO(g)$	6.65	372	
Al_2,OFO	$3/2Al_2(g) + OFO(g) \rightarrow AlF(g) + 2AlO(g)$	10.16	460	

a. Upper bound based on a dissociative B-B bond (see text for discussion).
b. Bridged isomer.

argon (or a heavily boron doped argon matrix) for a very different circumstance will certainly pervade in an O_2 matrix. Because solid O_2 absorbs strongly in the uv region, at best, in-situ generation of OFO would only be effective near the surface of an O_2F/O_2 matrix. In addition, O_2F photochemistry would be substantially modified by its intimate contact with O_2 (or for that matter molecular boron) in a matrix. If gas phase methods for generating OFO can be demonstrated, it will be possible to apply them to the trapping of OFO in O_2 or moderately dilute boron molecule based matrices, determining the long term stability of OFO/O_2 or OFO/B_x solids and the upper limit to the mole fraction of OFO that can be stabilized.

Boron Molecule Based - Fluorine Oxide Combustion Processes

Boron oxidation reactions are capable of producing among the highest volumetric energy densities based largely on substantial specific enthalpies. Given this backdrop, and a knowledge of the multicentered oxidation chemistry

which small metal or metalloid molecules can undergo,[6] it is appropriate that one investigate the nature of the reactions of small boron molecules as they react to form the oxides and fluorides.

Detailed studies of boron (and for that matter, aluminum) molecule reactions have not been undertaken. Although previous studies of potential boron fuels have emphasized particle ignition, it has also been recognized that as much as half of the potential energy content of boron rocket fuels must be released in gas phase oxidation processes. Thus previous research efforts have addressed both the heterogeneous and homogeneous boron combustion regimes, the latter experiments prejudicing the chemistry to compounds containing a single boron atom.[7-9] This impressive work neglects the extremely important bridge between the heterogeneous chemistry of boron particle ignition and the homogeneous chemistry associated with the gas phase oxidation of compounds containing a single boron atom. Thus, an approach to study the oxidation chemistry of small boron molecules identifies a virtually unexplored and potentially bridging middle region lying at the interface of hetero- and homogeneous boron combustion chemistry.

Small boron molecules, B_2 and B_3, and the boron clustered hydrides of these stable but highly reactive species can be generated in significant concentration using at least two established cluster generating techniques. High flux boron flows can be agglomerated to form intense continuous sources of small boron molecules[10] or produced using pulsed laser vaporization-supersonic expansion from boron rods. The boron cluster hydrides, B_xH_y ($x=2,3$, $y \leq 2$) might be formed by seeding hydrogen into one or the other of these configurations[11] or via in-situ synthesis as hydrogen donating constituencies are entrained and flow over boron at the elevated temperatures[12] commensurate with a significant hydride vapor pressure. Once formed, these molecules and their reactions can be interrogated using a combination of chemiluminescence,[13] laser induced fluorescence (single and multiphoton),[14] and mass spectroscopy (photoionization and electron impact quadrupole or time-of-flight).

Energetics of Boron Molecule Reactions

Given the ability to form copious quantities of small boron molecules and their respective clustered hydrides, we consider the specific enthalpies associated with their multicentered reaction in Table I. There is already significant information to make these assessments. The bond energy of boron dimer, B_2, is a respectable but moderate 69 kcal/mole[15] vs. the very strong BO (191 kcal/mole)[2,16] and BF (181 kcal/mole)[17] bond energies. Although the B_3 bond strength, 114 kcal/mole, which appears to have been accurately calculated by Hernandez and Simons,[18] considerably exceeds that of B_2, it is still well below that of the oxide and fluoride.

Hernandez and Simons[19] have determined the structures in Figure 1 for B_3H. The first of these structures represents a global minimum and the latter, a bridged isomer, corresponds to a local minimum, approximately 20 kcal/mole higher in energy, which possesses distinct vibrational frequencies relative to that of the ground state. The B-H bond strength for the global minimum, 87 kcal/mole, should be compared with the bond strength of diatomic BH (78-82 kcal/mole).[20] The B-H bond strength of the local minimum bridged conformer decreases to 69 kcal/mole.

Recently, Michaels[21] has investigated the B_2H molecule, finding a lowest energy C_{2v} structure corresponding to a saddle point and leading to BH+B. In other words the HB_2 molecule is unstable with respect to dissociation of the
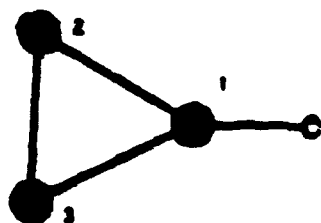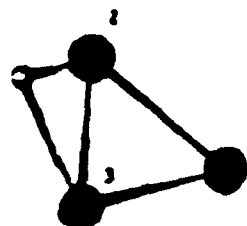
Fig.1

$r_{12} = 1.43 Å$ $\angle 123 = 58.9°$

$r_{23} = 1.53 Å$ $r = 8.95 Å$

$r_{00} = 1.18 Å$ $\theta_e(B-0) = 87$ kcal/mol

$\nu_{00} = 987, 1223, 2083$ cm^{-1}

$\nu_{00} = 745, 823$ cm^{-1}

(a) $\nu_{00} = 647$ cm^{-1}

$r_{13} = 1.58 Å$ $\angle 213 = 58.7°$

$r_{23} = 1.54 Å$ $\angle 803 = 69.7°$

$r_{00} = 1.35 Å$ $r = 1.42 Å$

$\theta_e(B-0) = 69$ kcal/mol

$\nu_{00} = 281, 1068, 1271, 2138$ cm^{-1}

(b) $\nu_{00} = 767, 1152$ cm^{-1}

(a) B_3H (σ-bonded) global minimum properties. (b) B_3H (π-bonded) local minimum properties. (Reference 19)

B-B bond (via the asymmetric stretch). This seems surprising in view of the B_2 and BH bond strengths and the molecular electronic structure of HAB molecules[22]; however, it suggests (1) that an approaching H atom will greatly destabilize a B_2 bond, (2) that the specific enthalpies estimated in Table I for the reactions of HB_2 with FOO and OFO represent stringent lower bounds,[23] and (3) that the HB_2 radical, stabilized in a rare gas matrix might represent an outstanding candidate for a high specific enthalpy reaction.

The boron (or aluminum) based reactant species which we consider in Table I, with the exception of HB_2, are sufficiently stable so that they should be maintained for extended periods if formed in the gas phase and/or deposited in rare gas matrices. For the process

$$3/2\ B_{2(g)} + FO_{2(g)}{}^{22} \rightarrow BF_{(g)} + 2BO_{(g)} \tag{1}$$
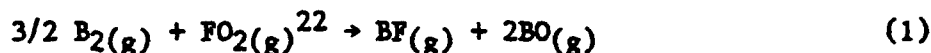
the specific enthalpy is between 15.57 and 16.26 MJ/kg for the peroxy radical. These values increase to between 21.07 and 21.71 MJ/kg for the symmetric form of the FO_2 radical. The process (1) should be contrasted to the reaction combination

$$B_{3(g)} + FO_{2(g)} \rightarrow BF_{(g)} + 2BO_{(g)} \tag{2}$$

for which the specific enthalpy ranges are 11.59 - 12.29 and 17.12 - 17.81 MJ/kg for the peroxy and symmetric isomer respectively.

For the multicentered process involving boron dimers and OF radicals (see previous)

$$B_{2(g)} + OF_{(g)}{}^{24} \rightarrow BF_{(g)} + BO_{(g)} \tag{3}$$

169
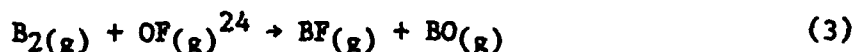
the specific enthalpy is between 17.67 and 18.18 MJ/kg whereas the multicentered process

$$BH(g) + OF(g) \rightarrow HF(g) + BO(g) \qquad (4)$$

has a specific enthalpy ranging between 16.54 and 17.16 MJ/kg. We evaluate processes (3) and (4) on the basis of an OF bond energy of 55 kcal/mole.[25] This estimate of the OF bond energy is based largely on its ready production from the photolysis of O_2 - F_2 mixtures in rare gas matrices or F_2 in an oxygen matrix.[25] The radical is stable for extended periods in these matrices.

The specific enthalpies associated with the reaction of the higher boron clustered hydrides are significant but do decrease relative to those for processes (1) - (4). We consider also the HB_2 - FO_2 systems and the B_3H - OF system in Table I and, for comparison, we include select reactions of Al_2 and Al_3. Again, note that the evaluated enthalpies for the HB_2 based reactions would appear to[21] represent stringent lower bounds.[23]

The results of the analyses in Table I suggest that several processes involving the oxidation of small boron clusters and their hydrides have specific enthalpies which significantly exceed that of Lox-hydrogen. Further, this table focuses on the reaction of ground state boron based species and does not begin to address the possible formation of long-lived metastable boron molecule reactants whose comparable oxidation will produce even higher specific enthalpies. With the plethora of excited states characterizing both the B_2[26] and B_3[18] molecules, several of which possess differing multiplicities from that of the ground electronic state, the possibility of forming a metastable reactant should be a future consideration.

In order to approach a study of certain of the reactions outlined in Table I, it will be necessary to examine the photophysics of the B_3 molecule. Fortunately, we can follow the lead of Hernandez and Simons who have evaluated the ground and several excited states of B_3, compiling the overview diagram of Fig. 2. They find that the ground electronic state of B_3 is a $^2A_1'$ (D_{3h}) equilateral triangle configuration. Electric dipole allowed transitions to three states of $^2A_2''$ and $^2E'$ symmetry, whose vertical excitation energies lie between 7000 and 27000 cm^{-1} above the ground state, and vibronically allowed transitions to $^2E''$ states whose vertical excitation energies lie approximately 26,000 and 40,000 cm^{-1} above the ground state are summarized in Table II. This table demonstrates that a significant component of the low-lying electronic states in the B_3 molecule should be accessible to pump-probe experiments using Nd:YAG and excimer pumped dye lasers. Local harmonic vibrational frequencies have been determined for these states. The lowest excited $^2E'$ (2 $^2A_1$, 1 $^2B_2$) and $^2E''$ (1 $^2A_2$, 2 $^2B_1$) states undergo a first order Jahn Teller distortion with a low barrier to pseudo-rotation. Hernandez and Simons[18] have calculated geometries, energies, and vibrational frequencies for the minima and saddle points associated with these Jahn-Teller split states. They note that the low barrier to pseudorotation should facilitate the observation of clearly discernable features in the vibrationally resolved spectra for transitions involving these states. A study of this B_3 photophysics will certainly complement the elegant work of Carrick and Brazier[27] now underway at the Phillips Laboratory as well as providing a basis for the study of several of the reactions outlined in Table I.
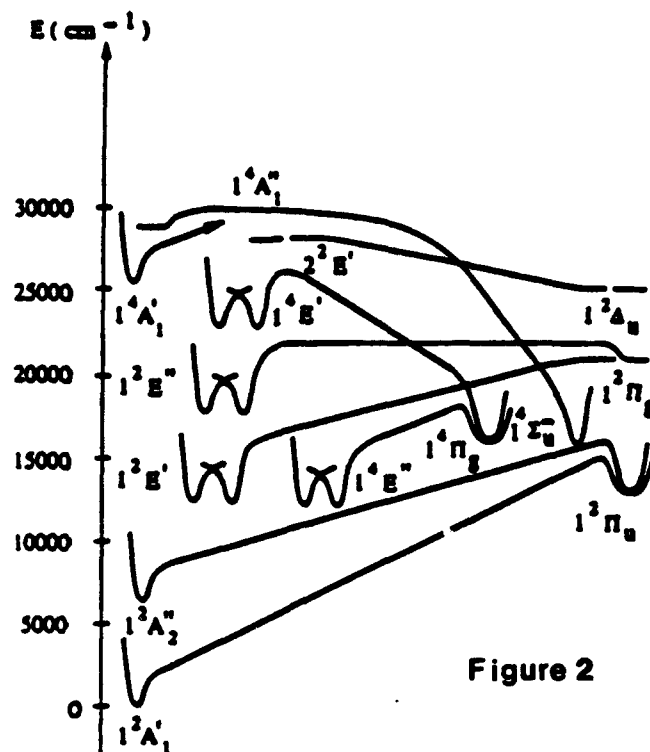
Figure 2

Overview picture of the low-lying states in B_3. The different curves represent states that have been geometrically optimized. The horizontal lines represent states for which electronic energies are known but whose geometry has not been optimized.

Table II

Lowest Few Vertical Excitation Energies

Calculated by Hernandez and Simons for B_3

Transition Type	State[a]	T_e (cm^{-1})[b]
	$1\,^2A'_1$ ($1\,^2A_1$)	0
Dipole allowed	$1\,^2A_2"$ ($1\,^2B_1$)	7 082
Dipole allowed	$1\,^2E'$ ($2\,^2A_1$, $1\,^2B_2$)	15 085
Dipole allowed	$2\,^2E'$ ($3\,^2A_1$, $2\,^2B_2$)	27 308
Vibronically allowed	$1\,^2E"$ ($1\,^2A_2$, $2\,^2B_1$)	26 594
Vibronically allowed	$2\,^2E"$ ($2\,^2A_2$, $3\,^2B_1$)	38 918

[a]D_{3h} and C_{2v} labels are used for each state to facilitate comparison with Fig. 2.

[b]The $^2E'$ excitation energies were obtained as configuration interaction (CI) eigenvalues in the CASSCF optimization of the $1\,^2A_1'$ state (both symmetries appear as A_1 in C_{2v} symmetry). Similarly, the $^2E"$ excitation energies were obtained as CI roots in the CASSCF optimization of the $1\,^2A_2"$ state (both symmetries appear as B_1 in C_{2v} symmetry).

Heterovalent Isomerization in the BOH ↔ HBO System

In contrast to the combination of one of the Group IIIA metals Al-Tl, oxygen, and hydrogen which produces the resulting structure of a typical monovalent metal hydroxide, MOH, the combination of boron, oxygen, and hydrogen atoms forms a most stable linear structure, $H - B = O$, in which boron, now trivalent, is not the terminal atom but the central atom. The ground state HBO structure is thought to lie between 40 and 50 kcal/mole lower in energy than the corresponding metalloid hydroxide, BOH, which thus represents a local minimum on the $B + O + H$ potential surface. The substantial energy increment separating the BOH and HBO structures, the significant changes (decrease) in bond angle which can accompany the lowest energy transitions in these "HAB - HBA" molecules, and the bonding trends associated with the Group IIIA elements suggest that one might take advantage of a photochemical isomerization process in which BOH, formed in a kinetically controlled environment, is converted to HBO, liberating considerable energy. Gurvich et al.[28] and more recently Michaels[21] have assessed the isomerization process and the appropriate nature of the barrier to hydrogen migration on the lowest $^1A'$ surface as one converts BOH to HBO. Further, Michaels has now examined the lowest lying $^3A'$, $^3A''$, and $^1A'$ excited surfaces. The results obtained by Gurvich et al.[28] and Michaels[21] are in good agreement with the calculations of previous workers summarized in Table III. The only spectroscopic work on the system comes from Lory and Porter[29] who have studied four isotopes of the matrix isolated HBO radical deducing the data summarized in Table IV.

TABLE III: Equilibrium Geometries for Boron Based HXY Species

	R_{H-X}, Å	R_{H-Y}, Å
HBO	1.154[a], 1.165[b]	1.202[a], 1.192[b]
lit. values	1.179[c], 1.153[d], 1.157[e]	1.177[c], 1.199[d], 1.205[e]
BOH	0.937[a], 0.947[b]	1.275[a], 1.297[b]
lit. values	0.936[d], 0.950[e]	1.298[d], 1.295[e]

a. J. Tyrrell, J. Phys. Chem. **83**, 2906 (1979).
b. T. S. Zyubina, O. P. Charkin, and L. V. Gurvich, Zh. Strukt. Khim. **20**, 3 (1979).
c. C. Thompson and B. J. Wishart, Theor. Chim. Acta. **35**, 267 (1974).
d. N. L. Summers and J. Tyrrell, J. Am. Chem. Soc. **99**, 3960 (1977).
e. P. Botschwina, Chem. Phys. **28**, 231 (1978).

TABLE IV: Frequencies (cm^{-1}) Observed for HBO in an Argon Matrix

	Isotopic species			
	$H^{11}BO$	$H^{10}BO$	$D^{11}BO$	$D^{10}BO$
1	(2849)[a]	(2784)[a]	2259	2303
2	754	764	606	617
3	1817	1855	1648	1663

Product Rule Calculations for HBO

Vibration Species	Isotope pair X/X'	$(\nu_1\nu_3)/(\nu_1'\nu_3')$ Obsd	Calcd	ν_2/ν_2' Obsd	Calcd
Σ^+	$D^{10}BO/D^{11}BO$	1.029	1.031		
Σ	$H^{10}BO/H^{11}BO$			1.013	1.013
Σ	$H^{11}BO/D^{11}BO$			1.244	1.243
Σ	$D^{10}BO/D^{11}BO$			1.018	1.019

a. Calculated

A simple description of the isomerization process BOH ↔ HBO can be obtained within the framework of the valence states model. Because the boron atom must undergo a promotion of the type $2s^2 2p \rightarrow 2s2p^2$ in the course of rearrangement and the corresponding excitation energy of an electron from the 2s to the 2p level, estimated from atomic spectra, is fairly large ($\sim$ 80-90 kcal/mole), the path for migration of hydrogen from oxygen to boron is expected to show a high potential barrier associated with the promotion of the boron atom. This picture is confirmed by <u>ab-initio</u> calculation.

Gurvich et al.[28] in studying the BOH ↔ HBO rearrangement, have generated the minimum energy path diagram depicted in Fig. 3, now closely confirmed by Michaels.[21] In the figure, the lowest energy configuration (a) corresponds to the linear HBO structure with a formally "trivalent" boron atom and optimum

Fig.3
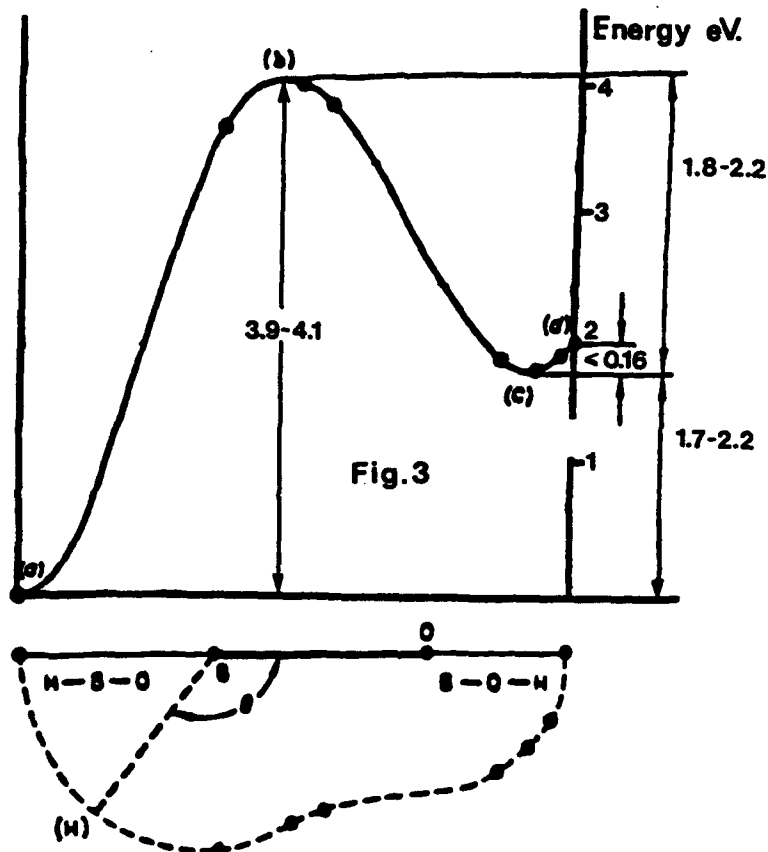
Cross section of potential energy curves showing the minimum energy path for the rearrangement BOH → HBO.

bond distances, R_{B-O} = 1.192, R_{B-H} = 1.165 Å (Michaels: 1.185, 1.167 Å). The hydrogen migration has a high potential barrier, requiring formation of the cyclic structure (b)
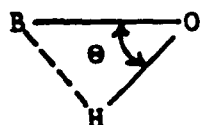
Cyclic structure

with optimized structural parameters $\theta_{BOH} \sim 53°$, $R_{B-O} \approx 1.26$ A, and $R_{OH} \approx$ 1.419 Å. (Michaels 57°, 1.218, 1.413 Å). The optimized BOH structure corresponds to configuration (c) with $\theta_{BOH} \sim 125°$, $R_{B-O} \sim 1.30$ Å, $R_{OH} \sim 0.95$ Å

(Michaels 121.4°, 1.300, 0.95) at an energy appreciably above ground state HBO. However, the BOH molecule is quite floppy as the calculated barrier to the linear configuration (d) is less than 4 kcal/mole. Calculated energy increments are indicated in Figure 3.

The height of the potential barrier for the rearrangement BOH ↔ HBO measured from the excitation energy of the configuration (c) lies between 40 and 50 kcal/mole, comparable to the 40 kcal/mole barrier determined for the transformation HNC → HCN.[30] However, for BOH, the configuration (c) is much less favorable ($\sim$ 40-50 kcal/mole) than that for ground state HBO (config. (a)) whereas the difference in energy of the HNC and HCN structures is only 9.5 kcal/mole. It is most significant that in both systems, the potential barrier to isomerization is large, presenting a significant obstacle to interconversion. Once formed, either isomer can be stable for an extended period. If these barriers are overcome in a photochemical process, it should be possible to convert the energy increments, corresponding to the sum of the photon energy and the relative isomeric stability, both of which are quite significant for the BOH ↔ HBO interconversion.

The potential for using the BOH ↔ HBO interconversion process as a photochemically induced energy source results, in part, because of the floppy nature of the BOH molecule, and, in part, because of the plausible existence of routes to initiate the cyclic interconversion process via substantial decreases in bond angle which accompany optical pumping using photons within the far visible or ultraviolet regions. We require a minimum of 40 kcal/mole for interconversion of BOH to HBO.

We suggest that (1) excited electronic states of the BOH molecule which lead to a substantial decrease in bond angle may well be available to absorb a photon in the visible or near ultraviolet and (2) that the resulting excitation in the HBO product might well be extractable in the form of a significant and usable energy.

Michaels has calculated portions of the ground $^1A'$ as well as the a $^3A'$, b $^3A''$, and A $^1A'$ excited state surfaces. The a $^3A'$, b $^3A''$, and A $^1A'$ excited states, with calculated excitation energies of 2.37, 3.01 and 5.86 eV.[21] respectively, bear a close analogy to the manifold of states in the isoelectronic BF molecule whose a $^3\Pi$ and A $^1\Pi$ states lie at $\sim$ 3.61 and 6.34 eV. respectively.

While the a $^3A'$ - X $^1A'$ transition is forbidden to first order, the system should be possessed of a small (but useable) oscillator strength due to intensity borrowing from the allowed, higher lying A $^1A'$ - X $^1A'$ system ($f_{calculated} = 0.28^{21}$). Indeed, the analogous a $^3\Pi$ - X $^1\Sigma^+$ intercombination band system of BF is readily observed in "single collision" chemiluminescence (Fig. 4) when boron atoms react with F_2 (or ClF). The $^3\Pi_1$ - X $^1\Sigma^+$ component of the observed fluorescence results from an intensity borrowing involving the A $^1\Pi_1$ state at 6.34 eV. whereas the $^3\Pi_0$ - X $^1\Sigma_0^+$ intercombination transitions borrow intensity from the B $^1\Sigma_0^+$ state at 7.85 eV. The observation of the intercombination band systems in BF, the floppy nature of the BOH radical, and the lone pair orbitals on the boron atom, suggest that transitions in the visible or ultraviolet, based on a small but useable oscillator strength for the BOH a $^3A'$ - X $^1A'$ transition, will be accessible, resulting in a substantial decrease in bond angle and thus promoting formation of the cyclic (BOH, HBO) conformation.[31] Michaels[21] recent calculations confirm this possibility.

At the UHF/6-31G* level of description, Michaels finds that the intriguing low-lying a $^3A'$ excited state appears to exhibit two minima. The first of these minima (Fig. 5) corresponds to a BOH angle, θ, of 114.2°
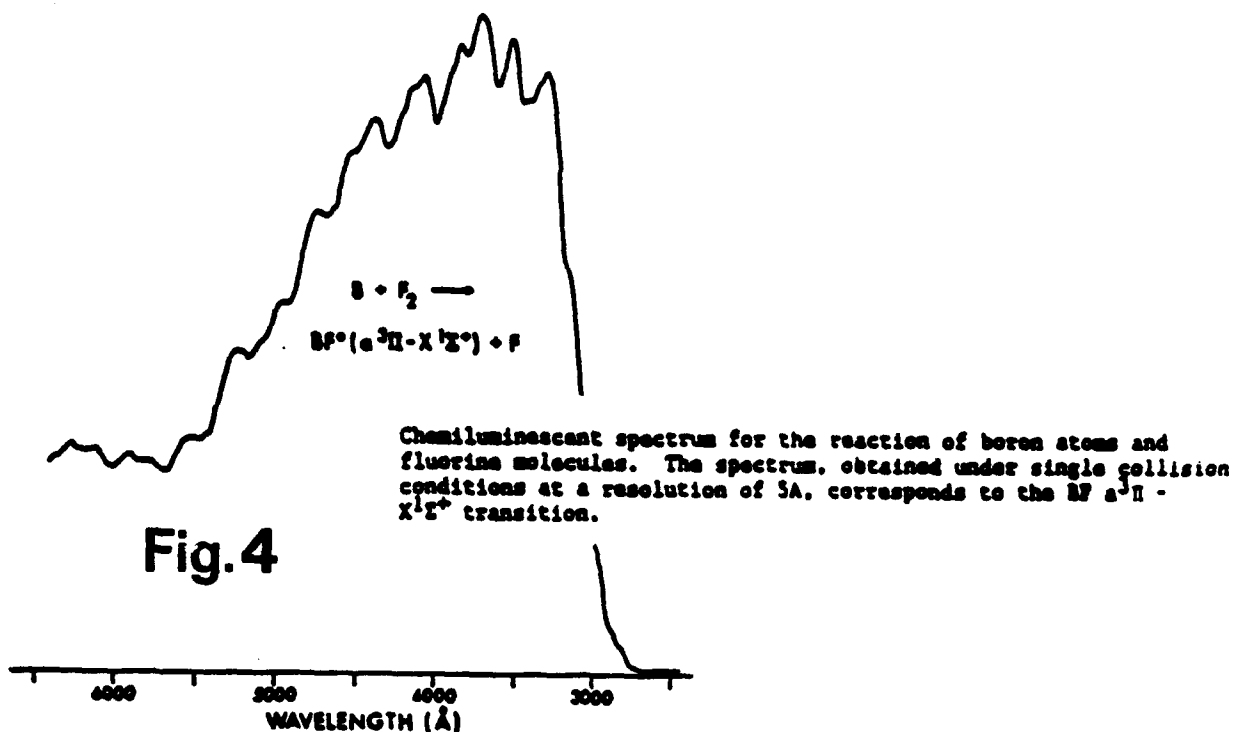
B + F₂ ⟶

BF°(a³Π-X¹Σ°) + F

Chemiluminescent spectrum for the reaction of boron atoms and fluorine molecules. The spectrum, obtained under single collision conditions at a resolution of 5A, corresponds to the BF a³Π - X¹Σ⁺ transition.

Fig.4

WAVELENGTH (Å)

whereas a second lower energy minimum corresponds to $\theta \sim 29.8°$. In contrast to the floppy ground electronic state, the first minimum of the $^3A'$ state is a substantial 0.91 eV. lower in energy than the linear configuration. Further, the calculated second minimum, although separated from the first by a substantial barrier associated with the $^3A'$ transition state ($\theta \sim 63.7°$), lies an additional 0.66 eV. lower in energy. If we pump from a nearly linear configuration of the ground electronic state to the $^3A'$ state with photons of energy ~ 2.75 eV., the resulting excitation should produce a substantial decrease in bond angle as the BOH molecule finds itself initially ~ 0.91 eV. above the outer minimum of the $^3A'$ potential. If calculations at a higher level of sophistication indicate a lower $^3A'$ transition state energy (Fig. 5), it is apparent that the molecule can easily bend to an angle close to $\theta \approx 53-57°$. Thus, with a photon at the fringes of the visible region, it appears feasible to accomplish the BOH ↔ HBO interconversion.

Can BOH be made and what are the consequences of its photochemical conversion to HBO? We assume that HBO is at least 40 kcal/mole more stable than BOH and must be reached through a cyclic intermediate which is > 50 kcal/mole higher in energy than BOH. The process

$$BOH + h\nu \rightarrow BOH^* \rightarrow HBO$$
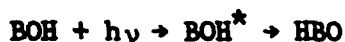
will therefore release in excess of 90 kcal/mole, corresponding to a specific enthalpy in excess of 3.33 kcal/gram or 13.93 MJ/kg.

It should be possible to produce the BOH radical using a number of chemical routes. At temperatures approaching 1000°C, the BOH and BOD radicals can be produced (in-situ synthesis) by passing H_2O (D_2O) over boron in a flow system.[32] This approach must be applied with some care, however, for at temperatures in excess of 1200°C, it will likely lead to substantial HBO production. It should also be possible to form the BOH radical through the reaction of an intense boron atom beam[33] with water vapor or dilute hydrogen

175
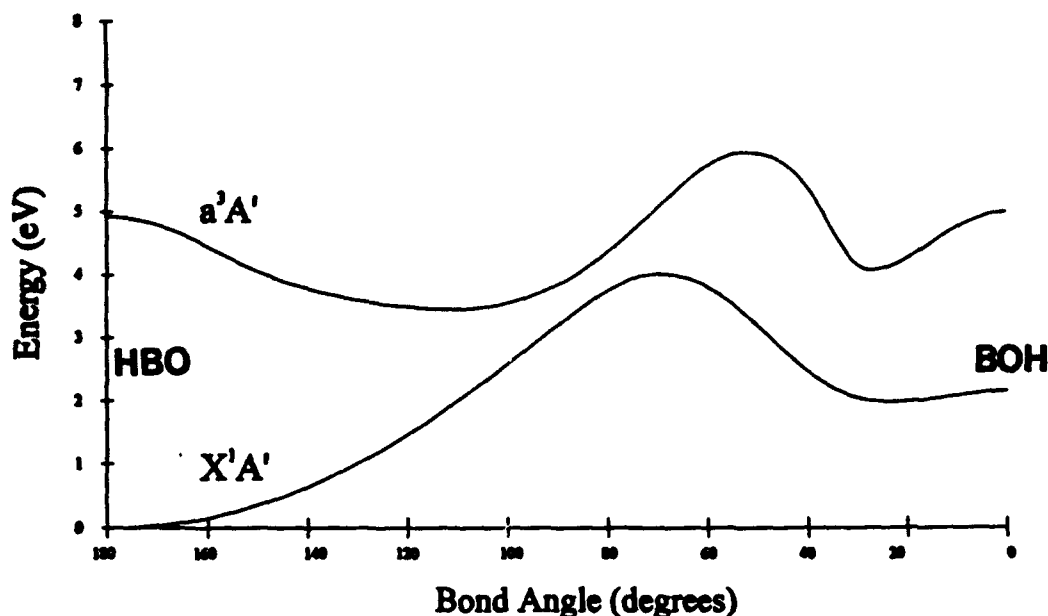
Figure 5: Calculated portions of the X $^1A'$ and a $^3A'$ surfaces of HBO, BOH as a function of bond angle minimized to the R_{B-O} and R_{B-H} bond distances for individual angles after Michaels[21] (see also Fig. 3).

peroxide. The action of sodium hydroxide on boron at temperatures between 500 and 800°C can also produce the radical, albeit in a much more deleterious environment.

Lory and Porter obtained the HBO radical (Table IV) as one of the photolysis products of $H_2B_2O_3$ illuminated by either a low pressure Xenon lamp (LiF window) with radiation of wavelength 1480 ± 10Å or a medium pressure mercury lamp @ 1849Å. These authors not only identified HBO but also B_2O_3 as the product of the photolysis of $H_2B_2O_3$. Lory and Porter identified at least one product channel in addition to those leading to HBO and B_2O_3. They observed a band at 3367 cm^{-1} which, on the basis of deuteration, could most reasonably be assigned to a hydrogen bonded OH stretching vibration. Further, they observed bands between 1380 and 1440 cm^{-1} which they suggested might be associated with a hydrogen bonded complex formed by the intramolecular transfer of H atoms from boron to oxygen sites. It is striking that the, BOH isoelectronic, BF ground state vibrational frequency is 1378.2 cm^{-1}. It would be reasonable to suggest that BOH or a hydrated BOH is produced as a matrix trapped vacuum ultraviolet photolysis product of $H_2B_2O_3$. We might ask why this BOH constituency was not converted to HBO in the photolysis process. We suggest that the photolysis wavelengths employed in the Lory and Porter study (1458 and 1849Å) are at too high an energy and encompass too narrow a range to access regions of the BOH excited state potential which are readily amenable to a considerable bond angle decrease, rearrangement, and formation of the cyclic structure (analog of a V-N transition in HBO). It would be interesting to discern whether photolysis in the ultraviolet after the vacuum uv photolysis of $H_2B_2O_3$ will lead to the conversion of the "BOH" constituency to HBO.

Given the formation of the BOH radical via the multiplicity of synthetic techniques which we have outlined, it will be desireable to characterize the radical in the gas phase, studying its absorptions in the ultraviolet and infrared regions.[34] The electronic spectroscopy can be accomplished with a Nd:YAG pumped dye laser system operative in the visible and ultraviolet wavelength regions (550 ≥ λ ≥ 250 nm).[34] In coincidence, it will be

appropriate to deposit BOH formed via in-situ synthesis[32] into a matrix environment, again establishing the range of optical excitation required to induce the isomerization BOH → HBO, determining the concentration of BOH radicals which can be achieved as well as the efficiency of the isomerization process with increasing concentration. It should also be possible to monitor the formation of the BOH radical by observing its infrared spectrum which we suggest will be characterized by infrared bands in the regions close to 1380 and 3370 cm^{-1} (B-OH and O-H stretch) as well as a bending frequency in the range 800-900 cm^{-1}. The interconversion of the BOH radical to HBO should be characterized by developing HBO infrared absorptions which, in a matrix environment, will be identical to those summarized in Table IV and which should be similar in the gas phase. The HBO frequencies are certainly quite distinct from those of BOH and therefore the interconversion process should be readily assessed using conventional IR absorption spectroscopy.

References

1. J. L. Gole and M. J. Heaven, "Impulsive Halogen Dioxide Reactions", in Proceedings of the High Energy Density Matter (HEDM) Conference, April 12-15, Edwards Air Force Base, Lancaster, California, pg. 145.

2. R. W. Fessenden and R. H. Schuler, J. Chem. Phys. 44, 434 (1966). P. N. Noble and G. C. Pimentel, J. Chem. Phys. 44, 3541 (1966); M. E. Jacox, J. Mol. Spectrosc. 84, 74 (1980). A. Arkell, J. Am. Chem. Soc. 87, 4057 (1965). P. O. Chegodaev, V. I. Tupikov, and E. G. Stukov, Russian J. Phys. Chem. 47, 746 (1973). J. L. Gole and D. A. Dixon, work in progress.

3. See for example, R. D. Coombe, A. T. Pritt, Jr., and D. Pilipovich, in Electronic Transition Lasers II, edited by Wilson, Suchard, Steinfield, M.I.T. Press, 1978 and the work of J. N. Kieth, I. J. Solomon, I. Sheft, H. H. Hyman, Inorg. Chem. 7, 230 (1968).

4. See for example, M. G. K. Killai and R. F. Curl, J. Chem. Phys. 37, 2921 (1962); R. F. Curl, R. F. Heidelberg, and J. L. Kinsey, Phys. Rev. 125, 1993 (1962); R. F. Curl, J. Chem. Phys. 37, 779 (1962). See E. C. Richard and V. Vaida, J. Chem. Phys. 94, 153 (1991), and references therein. ibid. 94, 163 (1991).

5. See for example, discussion and references in J. L. Gole, J. Phys. Chem. 84, 1333 (1980).

6. T. C. Devore and J. L. Gole, "Oxidation of Small Metal Clusters", Proceedings of the Sixth International Conference on High Temperature Materials, High Temperature Science 27, 49 (1989). J. L. Gole, "Toward the Modeling of the Oxidation of Small Metal and Metalloid Molecules", in "Gas Phase Metal Reactions", edited by A. Fontijn, Elsevier, North Holland, Elsevier Science Publishers, (1992), pp. 573-604. J. L. Gole, "The Unique Nature of Metal Cluster Oxidation", in Proceedings of the International Symposium on the Physics and Chemistry of Finite Systems: From Clusters to Crystals, Kluwer Academic Publishers, NATO ASI Series C: Mathematical and Physical Sciences, Vol. 274 (1992) pg. 1025.

7. W. A. Parker, A. H. Clark and M. Vanpee, <u>Heterogeneous Combustion</u>, Progress in Astronautics and Aeronautics <u>15</u>, 327 (1964).

8. W. J. Miller, "Boron Combustion Product Chemistry", AeroChem TP - 349, October 1976.

9. D. Boyer and W. Wooster, Calspan Co., Private Communications to A. Fontijn, September 1982.

10. T. C. Devore, R. Woodward and J. L. Gole, Chem. Phys. <u>92</u>, 1404 (1988).

11. M. McQuaid, J. R. Woodward, and J. L. Gole, J. Phys. Chem. <u>92</u>, 252 (1988). M. McQuaid, K. Morris, and J. L. Gole, J. Am. Chem. Soc. <u>110</u>, 5280 (1988).

12. J. L. Gole, R. H. Hauge, J. L. Margrave, and J. W. Hastie, J. Molec. Spectroscopy <u>43</u>, 441 (1972).

13. See for example, D. R. Preuss and J. L. Gole, J. Chem. Phys. <u>66</u>, 2994 (1977); J. L. Gole and D. R. Preuss, J. Chem. Phys. <u>66</u>, 3000 (1977); L. H. Dubois and J. L. Gole, J. Chem. Phys. <u>66</u>, 779 (1977). D. M. Lindsay and J. L. Gole, J. Chem. Phys. <u>66</u>, 3886 (1977); J. L. Gole and S. A. Pace, J. Phys. Chem. <u>65</u>, 2651 (1981); J. L. Gole, Ann. Rev. Phys. Chem. <u>27</u>, 525 (1976).

14. H. Wang and J. L. Gole, "A Chemiluminescent and Laser Induced Fluorescent Probe of a New Low-Lying A'Ω1 State of Gaseous AgF", submitted to J. Mol. Spectros. H. Wang and J. L. Gole, "Laser Induced Fluorescence Study and Radiative Lifetimes of the Low-Lying Electronic States of Gaseous AgF", J. Chem. Phys., in press.

15. A. G. Gaydon, <u>Dissociation Energies and Spectra of Diatomic Molecules</u>, Chapman and Hall Ltd. 1968.

16. J. Berkowitz, J. Chem. Phys. <u>30</u>, 858 (1959), A. Lagerqvist and K. Wigartz, Ark. Fys. <u>13</u>, 379 (1958), A. W. Searcy, Univ. of Cal. Rad. Lab. Rep. U.C.R.L. 1404 (1951).

17. D. L. Hildenbrand and E. Murad, J. Chem. Phys. <u>43</u>, 1400 (1965). See also R. F. Barrow, Trans. Faraday Soc. <u>56</u>, 952 (1960) and reference 15.

18. R. Hernandez and Jack Simons, J. Chem. Phys. <u>94</u>, 2961 (1991).

19. R. Hernandez and Jack Simons, J. Chem. Phys. <u>96</u>, 8251 (1992).

20. A. C. Hurley, Proc. Roy. Soc. <u>261</u>, 237 (1961).

21. H. Michaels, private communication.

22. A. D. Walsh, J. Chem. Soc. 2283 (1953).

23. The values given in Table I correspond to a B-H bond strength of 75 kcal/mole for a linear HB_2 radical.

24. R. W. Fessenden and R. H. Schuler, J. Chem. Phys. <u>44</u>, 434 (1966), P. N. Noble and G. C. Pimental, J. Chem. Phys. <u>44</u>, 3541 (1966).

25. The dissociation energy used in these calculations, 55 kcal/mole, represents an upper bound based on A. Arkell, R. R. Reinhand, and L. P. Larson, J.A.C.S. <u>87</u>, 1016 (1965). Also Lester Andrews, private communication. See also reference 15.

26. M. Dupuis and B. Liu, J. Chem. Phys. <u>68</u>, 2902 (1978). See also C. R. Bender and E. R. Davidson, J. Chem. Phys. <u>46</u>, 3313 (1967).

27. P. G. Carrick and C. R. Brazier, "Isp Calculations of Diatomics and Observation of Several New Electronic Transitions of the B_2 Molecule", in Proceedings of the HEDM Conference, 12-15 April 1992, pg. 8 and private communication.

28. T. S. Zyubina, O. P. Charkin, and L. V. Gurvich, Zh. Strukt. Khim. <u>20</u>, 3 (1979).

29. E. R. Lory and R. F. Porter, J.A.C.S. <u>93</u>, 6301 (1971).

30. P. K. Pearson and H. F. Schaefer III, J. Chem. Phys. <u>62</u>, 350 (1975).

31. These transitions, as they access excited electronic states with a substantially smaller minimum energy bond angle than the near linear ground electronic state, must, by the Franck-Condon principle, involve optical pumping to vibrationally excited levels in the bending mode of the excited electronic state. This process allows the excited state molecule to bend to a considerably smaller bond angle than that of the equilibrium ground state geometry, thus enhancing the probability for forming the cyclic conformation.

32. See for example, R. H. Hauge and J. L. Margrave, private communication. R. Klick and P. L. Timms, Chem. Comm. <u>3</u>, 18 (1967). J. L. Gole, R. H. Hauge, J. L. Margrave, and J. W. Hastie, J. Molec. Spectroscopy <u>43</u>, 441 (1972). E. F. Pearson and R. V. McCormick, J. Chem. Phys. <u>58</u>, 1619 (1973).

33. G. J. Green and J. L. Gole, Chem. Phys. Lett. <u>69</u>, 45 (1980). A. Hanner and J. L. Gole, J. Chem. Phys. <u>73</u>, 5025 (1980). S. A. Pace and J. L. Gole, J. Phys. Chem. <u>85</u>, 2651 (1981).

34. J. L. Gole, G. J. Green, S. A. Pace, and J. L. Gole, J. Chem. Phys. <u>76</u>, 2247 (1982). J. R. Woodward, S. H. Cobb, and J. L. Gole, J. Phys. Chem. <u>92</u>, 1404 (1988); W. H. Crumley, J. S. Hayden, and J. L. Gole, J. Chem. Phys. <u>84</u>, 5250 (1986). S. H. Cobb, J. R. Woodward, and J. L. Gole, Chem. Phys. Lett. <u>156</u>, 197 (1989), <u>143</u>, 205 (1988). H. Wang and J. L. Gole, "A Chemiluminescent and Laser Induced Fluorescent Probe of a New Low-Lying A'Ω1 State of Gaseous AgF", submitted to J. Mol. Spectros. H. Wang and J. L. Gole, "Laser Induced Fluorescence Study and Radiative Lifetimes of the Low-Lying Electronic States of Gaseous AgF", J. Chem. Phys., in press.

Characterization of van der Waals Complexes
of the Boron Atom

Paul J. Dagdigian and Eunsook Hwang
Department of Chemistry, The Johns Hopkins University
Baltimore, MD 21218

Millard H. Alexander
Department of Chemistry, University of Maryland
College Park MD 20742

Introduction

The study of the nonbonding van der Waals interaction between metal and rare gas atoms continues to be of great interest. In part, this interest follows from a desire to understand atomic interactions for both ground and electronically excited systems in a wide variety of chemical systems. In addition, the elucidation of such interactions will facilitate an understanding the structure and dynamics of cryogenic media containing isolated metal atoms, as well as an understanding of gas-phase collision dynamics.

Boron is the lightest member of the group 13 elements, and little is known about its nonbonding interactions with stable molecules. We present here the results of a combined experimental and theoretical study of the BAr van der Waals complex, in particular the B $^2\Sigma^+ - X\,^2\Pi_{1/2}$ electronic transition of the ^{11,10}BAr isotopomers, which correlates with the boron atomic $3s\,^2S - 2p\,^2P$ transition.[1] Rotational and vibrational analyses have been carried out to derive information on the low-lying electronic states. Information on the repulsive portions of the $X\,^2\Pi$ and $A\,^2\Sigma^+$ states, both of which correlate with the B($2p\,^2P$) + Ar asymptote, has also been obtained from analysis of bound–free emission spectra from various excited $B\,^2\Sigma^+$ vibrational levels. In conjunction with these experiments, *ab initio* calculations of the B + Ar interaction, in the $X\,^2\Pi$, $A\,^2\Sigma^+$, and $B\,^2\Sigma^+$ states, were performed. In order to obtain accurate interaction energies, multireference, internally contracted, configuration-interaction calculations were carried out. The information derived on theses states from experiment and theory agree reasonably well.

Experiments

Boron atoms were produced by 193 nm photolysis of diborane diluted in a He/Ar mixture, and the van der Waals complex was formed in the supersonic expansion. A set of 4 rotationally resolved bands of the (v',0) progression of the $B\,^2\Sigma^+ - X\,^2\Pi_{1/2}$ electronic transition of the ^{11,10}BAr isotopomers was observed and analyzed. The low rotational temperature of the beam prevented observation of spin-orbit excited levels. The upper state

vibrational quantum numbers were assigned from the observed isotope splittings. Additionally, two higher v' rotationally unresolved bands were observed. The large line widths in these bands indicate that the upper levels are quasibound levels which are predissociating through a barrier. Vibrational and rotational constants were derived from fits to the observed transition wavenumbers. It was found that the $X\,^2\Pi_{1/2}$ state had a significant Λ doubling, because of the presence of the low-lying $A\,^2\Sigma^+$ state, and it was possible to determine the parameter p_0''. Table 1 presents the spectroscopic parameters obtained from this analysis of the rotationally resolved bands. The intensity of the lowest wavenumber member ($v' = 4$) of the (v',0) progression was too weak to allow high-resolution scans and hence determination of the upper state rotational constant.

Table 1. Spectroscopic constants (in cm^{-1}) derived for the bound states of $^{11,10}BAr$.

State	Level	Parameter	^{11}BAr	^{10}BAr
$X\,^2\Pi$	$v'' = 0$	B_0''	0.1503(5)	0.1617(6)
		p_0''	–0.0269(13)	–0.0302(17)
$B\,^2\Sigma^+$	$v' = 5$	B_v'	0.2906(5)	0.3113(5)
	$v' = 6$	B_v'	0.2721(5)	0.2881(4)
	$v' = 7$	B_v'	0.2476(4)	0.2582(5)

Derived constants for $^{11}BAr(B\,^2\Sigma^+)$:

ω_e = 208.5(20) $\qquad$ B_e = 0.4178(16)

$\omega_e x_e$ = 8.04(16) $\qquad$ α_e = 0.02267(23)

Also included in Table 1 are the derived values of the parameters ω_e, $\omega_e x_e$, B_e, and α_e for ^{11}BAr from a fit to all the term values and rotational constants for the $^{11,10}BAr(B\,^2\Sigma^+)$ isotopomers. These data were employed to derive an RKR potential for the lower portion of the $B\,^2\Sigma^+$ potential energy curve, which will be presented below when it is compared with the theoretical calculations. From the derived value of B_e, we estimate the equilibrium internuclear separation to be 2.162(5) Å. In addition to 4 bound vibrational levels, we also observed features (assigned as $v' = 8$ and 9) with large line widths, indicating that these levels are quasibound. From the vibrational parameters, we estimate that the first such level ($v' = 8$) lies 1186(6) cm^{-1} above the bottom of the $B\,^2\Sigma^+$ well. With an estimate of the $X\,^2\Pi$ dissociation energy, we can compare the energy of this level

with that of the B($3s$ ^2S) + Ar asymptote. Employed our *ab initio* estimate for D_0'' (given below), we find that the v' = 8 level of [11]BAr lies 112 cm^{-1} *above* the atomic asymptote. The next lower state (v' = 7), whose rotational lines do not show appreciable broadening, is also found to lie above the atomic asymptote (by 38 cm^{-1}). This indicates that the excited electronic state has a *barrier*. Such a barriers at long range have been inferred in HgAr[2] and HgNe[3] from observation of bound–free double resonance spectra.

We have also taken dispersed fluorescence spectra for excitation of several [11]BAr(B $^2\Sigma^+$) vibrational levels. Because of the large difference in the equilibrium internuclear separation between the X $^2\Pi$ and B $^2\Sigma^+$ states, this emission occurs mainly to the repulsive wall of the lower state, as well as to the A $^2\Sigma^+$ state. Thus, comparison of the experimental emission with simulated spectra calculated using the *ab initio* potential energy curves will provide an independent test of the validity of the calculations, especially of the repulsive portions.

Emission spectra were taken for excitation of [11]BAr(B $^2\Sigma^+$) v' = 5–8 levels. Figure 1 presents the spectrum for v' = 6. The spectra are similar for v' = 5 and 7, except that the maxima occur at larger (smaller) wavenumber shifts for smaller (larger) v'. The undulatory behavior of the spectra reflect interferences between the upper state vibrational and lower state continuum wave functions. The spectrum for v' = 8 is dominated by the B $3s$ ^2S – $3p$ ^2P atomic transition since predissociation of the excited BAr state yields B($3s$ ^2S) atoms.
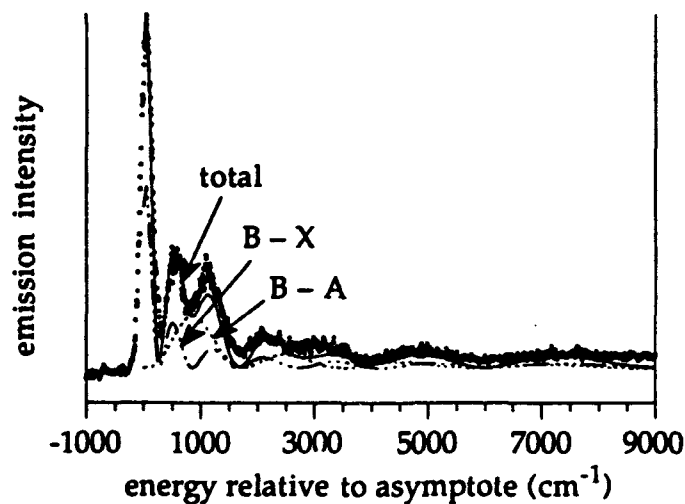
Figure 1. Dispersed emission spectrum for excitation of the v' = 6 level of [11]BAr. The experimental spectrum is compared with a simulated spectra, as described in detail in the text.

Theoretical Calculations

The *ab initio* determination of the B + Ar potential energy curves were carried out with a *spdfg* Gaussion basis set built Dunning's recent correlation-consistent valence

quadruple zeta basis.[4] For the Ar atom, the primitive basis ($16s11p3d2f1g$) was contracted to (6/5/3/2/1), while for B the (12/6/3/2/1) primitive basis was contracted to (5/4/3/2). The final basis consisted of 164 contracted Gaussian functions. For each atom, one additional diffuse s, p, d, f, and g function was added. Complete active space self-consistent field (CASSCF) calculations with 3 electrons in 4 active orbitals ($2s$ and $2p$ of B) were performed. State averaging was employed to obtain a single set of CASSCF orbitals for the $X\,^2\Pi_x$, $X\,^2\Pi_y$, and $A\,^2\Sigma^+$ states. Subsequently multireference, internally contracted, configuration-interaction (MR–CI) calculations were carried out. The effect of higher order excitations was estimated by the multireference version of the Davidson (D) correction or the multireference averaged coupled-pair functional method (MR–ACPF) of Gadnitz and Ahlrichs. Additionally, correlated electron pair (CEPA–1) calculations were carried out. For calculations on the $B\,^2\Sigma^+$ state, two additional diffuse functions were added on the B atom. The CASSCF active space was expended to include the $3s$ orbital on B. All calculations were performed with the MOLPRO suite of *ab initio* programs.[5] Counterpoise and self-consistency corrections were made.

Figure 2 presents the calculated potential energy curves for the low-lying $X\,^2\Pi$ and $A\,^2\Sigma^+$ states. The $X\,^2\Pi$ state is found to have a well with dissociation energy $D_e = 94.7$ cm^{-1}. The dissociation energy of the ^{11}BAr zero-point level is $D_0 = 75.1$ cm^{-1}. The A $^2\Sigma^+$ state is found to have a shallow well at long range but is primarily repulsive. The calculated potential curves for the $B\,^2\Sigma^+$ state are compared with the experimental RKR curve in Fig. 3. It can be seen that calculated curves reveal a barrier in this excited state, as anticipated by the experimental results. It can also be seen from Fig. 3 that binding in the B $^2\Sigma^+$ state is achieved only after the inclusion of higher-order excitations (triple and
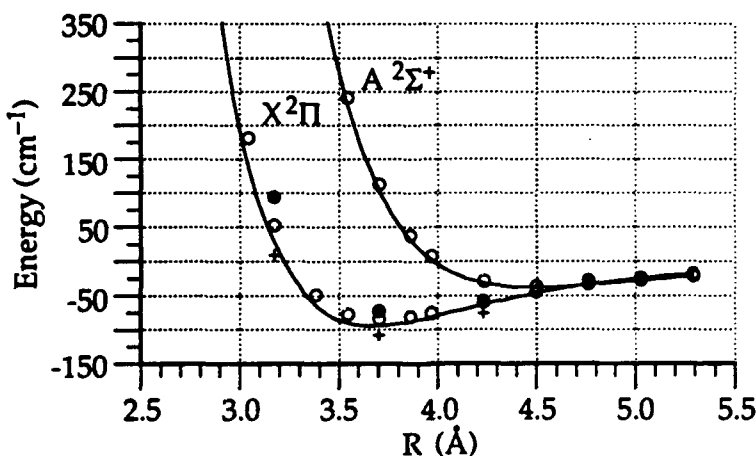
Figure 2. Calculated MR–ACPF interaction energies for the $X\,^2\Pi$ and $A\,^2\Sigma^+$ of BAr. The corresponding CEPA, MR–CI, and MR–CI(D) values for the $X\,^2\Pi$ state are indicated by open circles, filled circles, and crosses, respectively.
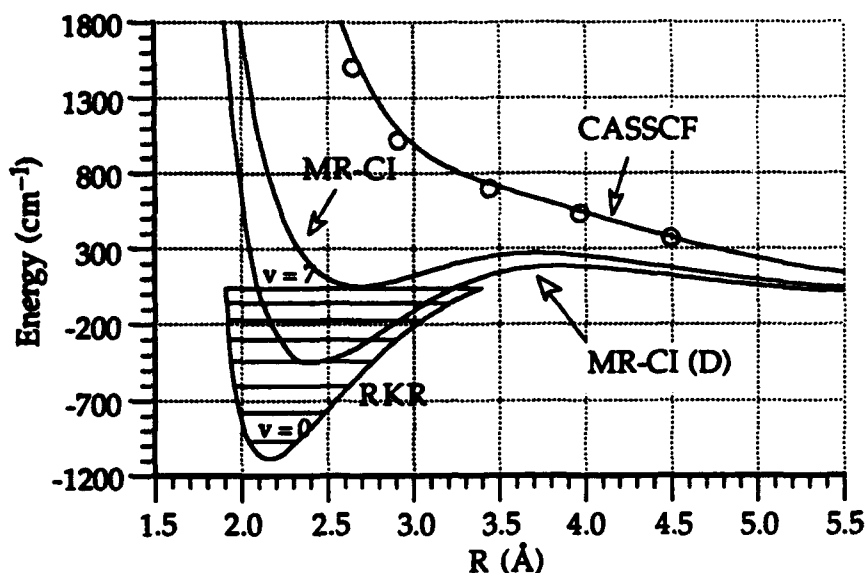
Figure 3. Calculated CASSCF, MR–CI, and MR–CI(D) interaction energies for the $B\ ^2\Sigma^+$ of BAr. The open circles represent the results of CASSCF calculations in which the orbitals were optimized solely for the $B\ ^2\Sigma^+$ state. Also shown is the RKR curve for the $B\ ^2\Sigma^+$ state assuming that $v' = 7$ level lies 38 cm^{-1} above the atomic asymptote (see text).

quadruple excitations) in the molecular wave functions. This suggests that the well in the this state does not admit a simple chemical explanation but reflects a subtle interplay between electron correlation and the polarization of the B–Ar charge distribution.

Discussion

It is of interest to compare the information obtained on the BAr potential energy curves from the experimental and theoretical portions of this study. For the $X\ ^2\Pi$ state, the *ab initio* calculations predict a slightly longer average internuclear separation than that inferred from the experiments. From the experimental value of B_0'', we calculate an average separation $R_0 = [\ <R^{-2}>_{v=0}\ ]^{-1/2} = 3.606(7)$ Å, while the theoretical prediction is 3.703 Å. Since the theoretical calculations do not provide a complete description of the electron correlation, we anticipate that the *ab initio* estimate of the well depth in the $X\ ^2\Pi$ state will b e10-20% too low, and the corresponding value of R_e slightly too large. The latter is consistent with this comparison with experiment. The Λ doubling parameter p_0'' provides information on the average separation of the $X\ ^2\Pi$ and $A\ ^2\Sigma^+$ states. A theoretical modeling of this parameter yields the result $p_0'' = -0.0295$ cm^{-1}, in reasonable agreement with the experimental value given in Table 1.

There is a considerable discrepancy between the *ab initio* estimate of the $B\ ^2\Sigma^+$ well depth (455 cm^{-1}) and the experimental estimate ($\sim$1100 cm^{-1}). The well was uncovered in the calculations only after inclusion of higher-order excitations in the CI wave

function. Perhaps a fuller variational treatment of these excitations would yield a deeper well in better agreement with experiment. Both the experiments and the calculations reveal the presence of a barrier at long range. We have derived an experimentally based estimate of the height of the barrier by comparing calculated Lorentzian widths of the $v' = 8$ and 9 resonances using a combination of the experimental RKR potential and a scaled long-range *ab initio* potential with widths estimated from the experimental spectra. The experimental line widths are found to be consistent with a barrier height of 141 cm^{-1}.

We have also modeled the bound free emission spectra for the radiative decay of B $^2\Sigma^+$ excited vibrational levels, using the hybrid B $^2\Sigma^+$ state potential derived above. In simulating these spectra, the $B - X$ and $B - A$ emission must both be included and weighted properly. Accordingly, the $B - X$ and $B - A$ dipole transition moments were calculated. These were found to be approximately equal, as expected in the atomic limit, except at short range. In order to get good agreement with the experimental spectra, we found that the lower X $^2\Pi$ and A $^2\Sigma^+$ potentials had to be shifted inward by 0.2 Å, as shown in Fig. 1. This inadequacy in the potentials is consistent with the differences found between the experimental and theoretical estimates of R_0 for the ^{11}BAr X $^2\Pi$ $v' = 0$ vibrational level.

In conclusion, we believe that the present paper shows the power of a joint theoretical and experimental investigation. Although the *ab initio* estimate of the X $^2\Pi$ and B $^2\Sigma^+$ well depths are low and the estimates of the equilibrium bond distances too large, the calculations gave considerable insight into the character of the molecular wave functions. The experimental results have provided a critical calibration of the accuracy of these calculations of the non-bonding interactions of the boron atom.

1.   E. Hwang, Y.-L Huang, P. J. Dagdigian, J. Chem. Phys. **98**, 8484 (1993).

2.   M.-C. Duval, O. Benoist-d'Azy, W. H. Breckenridge, C. Jouvet, and B. Soep, J. Chem. Phys. **85**, 6324 (1986).

3.   M. Okunsihi, K. Yamanouchi, K. Onda, and S. Tsuchiya, J. Chem. Phys. **98**, 2675 (1993).

4.   T. H. Dunning, J. Chem. Phys. **90**, 1007 (1989).

5.   MOLPRO is a package of *ab initio* programs written by H.-J. Werner and P. J. Knowles, with contributions from J. Almlöf, R. Amos, S. Elbert, W. Meyer, E. A. Reinsch, R. Pitzer, and A. Stone.

PARTICULATE BORON COMBUSTION:
KINETIC MODELING AND SENSITIVITY ANALYSIS

R.C. Brown and C.E. Kolb
Aerodyne Research, Inc.
Billerica, MA

R.A. Yetter, B.-Y. Cho and F.L. Dryer
Department of Mechanical and Aerospace Engineering
Princeton University
Princeton, NJ

H. Rabitz
Department of Chemistry
Princeton University
Princeton, NJ

It has been known for some time that elemetal boron has great potential as a high energy density fuel for aeronautical and aerospace applications. Slurries of solid boron particles in hydrocarbon jet fuels have long been investigated for air breathing propulsion applications, while particulate boron has also been considered as a replacement for aluminum as a fuel component in solid rocket propellants. Examples of the latter are new formulations of fluoroamino/nitroamino/B(s) mixtures which are also of high interest in advanced underwater explosive concepts and solid rocket ignition systems.

The combustion of solid particulate boron is a complex, multiphase process which includes: (1) heterogeneous ignition and volatization of boron oxide or boron flouride surface species, (2) homogeneous (gas phase) and heterogeneous (gas/surface) oxidation and (3) (in a hydrocarbon environment) homogeneous/heterogeneous condensation leading to liquid or solid B_2O_3. This presentation will review the chemistry of boron oxidation with emphasis on efforts to model the gas phase and gas–surface reactions governing the first two stages of boron combustion. Both B/H/O/C and B/H/O/C/F combustion systems will be discussed. Flourine significantly changes the dominant reaction pathways and increases gas phase reaction and heat release rates. These differences will be discussed in relation to the potential advantages in propulsion systems.

THE AUTHOR DID NOT PROVIDE AN EXTENDED ABSTRACT

THEORETICAL STUDIES OF BORON COMPOUNDS*

Roberta P. Saxon
Molecular Physics Laboratory, SRI International
Menlo Park, California 94025

This theoretical research program was originally based on the premise that species which show promise as high energy density materials may exhibit novel bonding mechanisms which distinguish them from conventional stable molecules. The goal of the program was to theoretically evaluate compounds composed of first row-atoms that might serve as the basis of new propulsion schemes. The particular classes of molecules under scrutiny were: (1) electron deficient compounds, certain compounds of B and Be which do not have sufficient valence electrons to distribute two per chemical bond, and (2) mixed metal clusters of the form $Li_nB_mH_k$. As the HEDM program, in general, and this research program, in particular, evolved, emphasis has shifted from seeking new metastable compounds to serve as high energy fuels by themselves to improving on conventional liquid hydrogen/liquid oxygen systems by devising a way to incorporate appropriate additives into solid hydrogen.

The boron atom has been identified as a promising additive to sH_2. The combustion energy of B is second only to that of Be, among the first row atoms[1] and model calculations by Carrick[2] have predicted addition of 5 mole percent of boron atoms to sH_2 would results in an increase in theoretical I_{sp} of 80 seconds or 21% over LH_2/LO_2. In studying the effects of additives, one needs knowledge of all possible compounds of boron and hydrogen. We review here the calculations on the BH_4 radical completed under this program and report on the calculations of the previously unexplored excited states and correlation diagram for BH_2.

STRUCTURE AND ENERGY OF THE BH_4 RADICAL

In this work, geometries of BH_4, the dissociation products $BH_2 + H_2$ and $BH_3 + H$, and the possible transition state for the addition reaction of BH_2 and H_2 were optimized at the MCSCF level with a B(4s3p2d)H(4s2p) basis set. As illustrated in Table 1, the minimum geometry for BH_4 is predicted to have C_{2v} symmetry with one pair of short B-H bonds and one pair of longer B-H bonds. The structure may be described qualitatively as a BH_2 molecule to which a stretched H_2 has been added in the perpendicular plane. Analysis of the wavefunction indicates that of the seven valence electrons, four are contained in the $B-H_a$ and $B-H_b$ bonds while there are only three electrons contained in the longer $B-H_c$, $B-H_d$ bonds. Comparison with calculations[3] of the C_{2v} symmetry bidentate form of the ionic compound $LiBH_4$ is also given in Table 1. In this form, the metal ion lies in the H_c-B-H_d plane. The principal observation is that the longer bonds in $LiBH_4$ are shorter than in BH_4 due to the additional electron in the H_cBH_d moiety as compared with the radical.

Table 1.

BH$_4$ GEOMETRY

CAM-1089-2
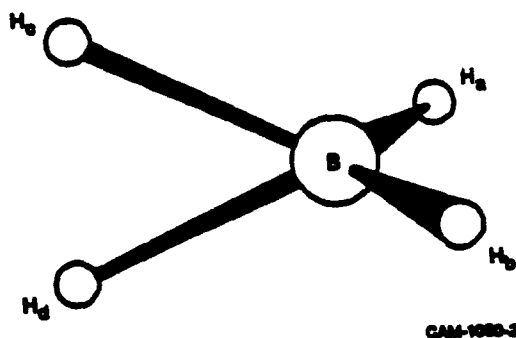
	BH$_4$[a]	LiBH$_4$[b]
B-H$_a$	1.201 Å	1.200 Å
B-H$_c$	1.315 Å	1.253 Å
<H$_a$-B-H$_b$	131.7 °	115.2 °
<H$_c$-B-H$_d$	44.4 °	109.1 °
H$_c$-H$_d$	0.994 Å	2.041 Å

[a]MCSCF/TZP (this work)
[b]Ramondo, et al., Ref. 3.

Harmonic frequencies for BH$_4$ and LiBH$_4$ are listed in Table 2, which includes a qualitative description of the modes. Normal modes of BH$_4$ corresponding to the BH$_2$ symmetric and asymmetric stretches (a$_1$ and b$_2$ symmetries respectively) can be easily identified. Considering the other hydrogens, H$_c$ and H$_d$, together with the central atom as a BH$_2$ unit, the corresponding modes may also be noted with reduced frequencies, as expected from the longer bond lengths.

Table 2.

CALCULATED HARMONIC FREQUENCIES
(cm^{-1})

	BD$_4$[a]	BH$_4$[a]		LiBH$_4$[b]
a$_1$	1832	2534	BH$_2$ sym stretch	2570
	1520	2086	BH$_2$ (long) sym stretch	2133
	1003	1413	scissors (in phase)	1500
	751	996	scissors (out of phase)	1261
b$_1$	1396	1962	BH$_2$ (long) asym stretch	2059
	497	634	rock	1170
b$_2$	1999	2656	BH$_2$ asym stretch	2612
	783	1053	twist	1342
a$_2$	628	888	twist	1244

BH$_2$: 2456 sym stretch
2636 asym stretch
1022 bend

[a]MCSCF/TZP (this work).
[b]Ramondo, et al., Ref. 3.

188

Relative energies for the BH_4 system determined from multireference single- and double-excitation CI calculations using MCSCF molecular orbitals are reported in Table 3. The electronic energy of the BH_4 minimum is predicted to lie 19.23 kcal/mol below $BH_3 + H$ and 20.10 kcal/mol below $BH_2 + H_2$. Including our calculated zero point energies, the BH_4 species is bound by 14.83 and 14.55 kcal/mol, respectively, with respect to $BH_3 + H$ and $BH_2 + H_2$. Values for the heat of formation of BH_4 and dissociation limits at 0 K and 298 K are also listed in Table 3. We have chosen to base these numbers at 0 K on a value of 22 kcal/mol for $\Delta H_f^o(BH_3)$, taken from experimental[4] and theoretical[5] work, and the standard value of 51.6 kcal/mol for H. Corrections to 298 K were made following the procedure given by Pople et al.[5] Note that while the value in the JANAF compilation[6] for $\Delta H_f^o(BH_3)$ of 26.4 kcal/mol is reasonably similar to the 22 kcal/mol value adopted here, the JANAF tables give an incorrect value for $\Delta H_f^o(BH_2)$ of 48.3 kcal/mol as compared with 73.3 kcal/mol calculated in this work.

Table 3.

BH_4 SYSTEM HEATS OF FORMATION
(kcal/mol)

	Relative Energy/ZP	ΔH_f^o	ΔH_f^{298}
BH_4	-14.83	58.5	56.6
$BH_3 + H$	0.0	73.6	73.2
$BH_3 + H_2$	-0.28	73.3	73.4
BH_2			
JANAF entry[a]		48.3	

[a]JANAF thermochemical Tables, Third Edition, J. Phys. Chem. Ref. Data 14, 51 (1985).

Full details of our calculations[7] of BH_4 are given in a paper that will appear in the Journal of Physical Chemistry late in 1993.

EXCITED STATES OF BH_2

Accurate predictions of the I_{sp} resulting from boron atoms or small molecules containing boron as additives to solid hydrogen requires accurate heats of formation. As part of the gas phase spectroscopic experimental program at the Phillips Laboratory, Carrick and Brazier have been investigating the spectrum of the B_2 molecule produced by corona discharge of diborane in helium.[1,8] It was originally hypothesized that unidentified lines in that investigation around 7000 Å could be due to BH_2, although it was later shown[8] that they can be attributed to B_2. While the two lowest states of BH_2, the $X\,^2A_1$ and $A\,^2B_1$, have been characterized experimentally[9] and theoretically[10] we were unable to find any previous knowledge of the higher-lying excited states of BH_2. Therefore, we have theoretically predicted the excited state spectrum of the BH_2 molecule.

The principal results of our investigation are presented graphically in the correlation diagram in Figure 1. In constructing this diagram, the heat of formation determined in our study of
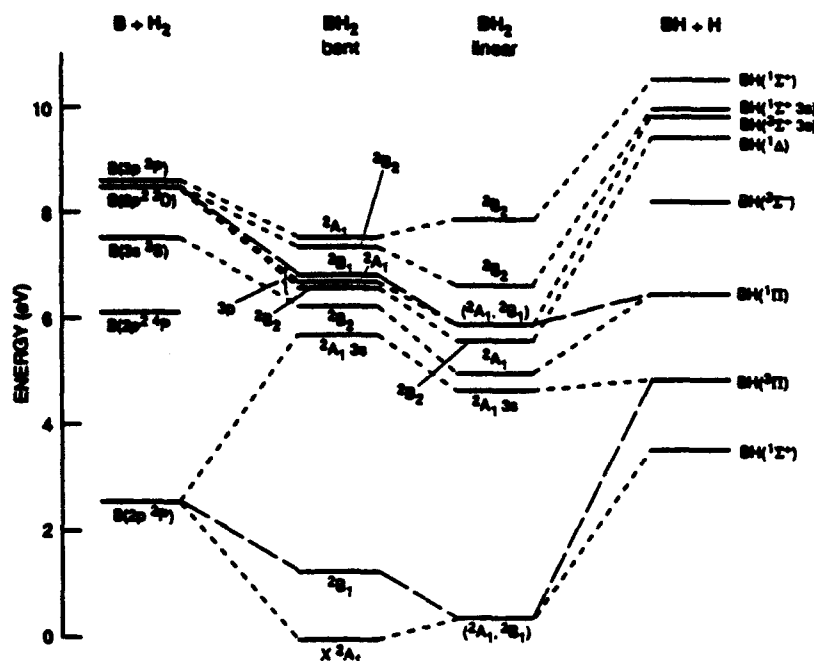
Figure 1. Correlation diagram for BH2. States are connected adiabatically in Cs symmetry. Bent geometry: Calculated equilibrium geometry of the X²A₁ state (R=1.206Å, θ = 127°). Linear geometry: R=1.206Å; BH asymptote: R=1.206Å. Energies from second order CI calculations.

BH₄ was used along with tabulated atomic levels and BH molecular excitation energies calculated in this work. The adiabatic correlations have been drawn in planar, Cs symmetry. The energetics give the BH₂ ground state bound by 83.6 kcal/mol (3.62 eV) with respect to BH + H including zero point energy and by 57.7 kcal/mol (2.57 eV) with respect to BH + H.

The energies displayed here were determined by Second Order CI (SOCI) calculations using state-averaged MCSCF orbitals with the basis set from our study of BH₄ extended by two 3s and two 3p diffuse functions on boron and one diffuse s and p on hydrogen. In each molecular symmetry, the active space in the MCSCF calculation was extended by the appropriate number to accommodate the B 3s and 3p Rydberg orbitals of that symmetry. The energies labeled BH_2 bent in Figure 1 have been plotted at the BH_2 ground state geometry (BH bond length = 1.206 A and bond angle = 127). At this geometry, the 3s Rydberg state lies 5.72 eV above the ground state and the three components of the 3p state lie between 6.61 and 6.84 eV. However, the underlying BH_2^+ ion has a linear geometry. One would therefore expect the Rydberg states to have a strong dependence on bond angle. This effect is illustrated in Figure 2 where the excited states are shown adiabatically in C_{2v} symmetry as a function of bond angle. The excitation energies at the linear geometry (R(BH) = 1.206 Å, θ = 180°) are also shown in Figure 1. All of the Rydberg states are predicted to have a linear equilibrium geometry as are the valence excited states with the exception of the third $^2B_2$, the highest state plotted.

The possible transitions that could be observed experimentally in emission have been estimated from calculations of the transition moment at the linear geometry. The crude estimate of the band oscillator strength, $f=2/3\Delta E <r>^2$ was used along with the standard relationship between oscillator strength and Einstein A coefficient. For the calculations of the transition moment, the wavefunctions were recomputed in a common orbital set. The allowed vertical transitions with significant strength are displayed in Figure 3 where the wavelength in nm and Einstein A value in sec⁻¹ are shown. Although the 3s Rydberg state is likely to be predissociated, the rich excited state structure of BH_2 should lead to emissions that may be observed experimentally.
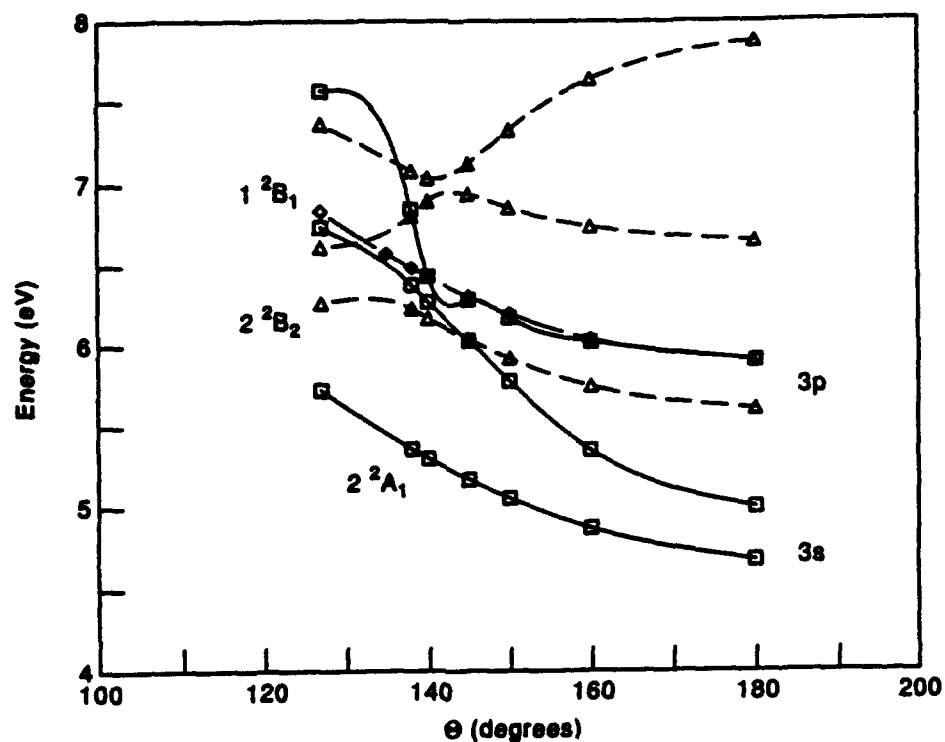
Figure 2. BH₂ excited states as function of bond angle for R(BH)=1.206Å. States are connected adiabatically in C_{2v} symmetry. Energes from second order CI calculations.
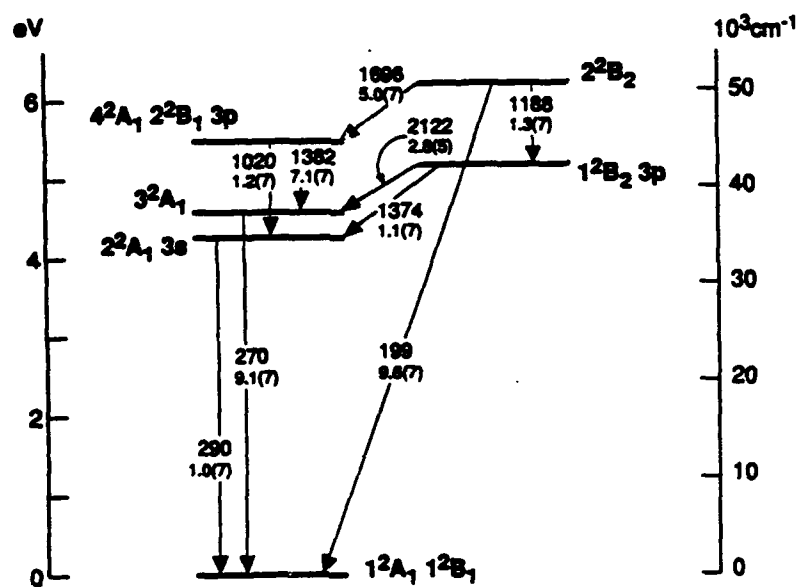
Figure 3. Vertical transitions in emission for linear BH₂(R=1.206Å, θ=180°). Transitions labeled by wavelength in nm (top line) and A value in sec⁻¹ (lower line), estimated as described in the text.

191

References

1. P. G. Carrick and C. R. Brazier, in *Proceedings of the HEDM Conference*, November, 1992.
2. P. G. Carrick, "Specific Impulse Calculations of High Energy Density Solid Cryogenic Rocket Propellants 1: Atoms in Solid Hydrogen," Report PL-TR-93-3014 (1993).
3. F. Ramondo, L. Bencivenni, and V. Di Martino, Chem. Phys. **158**, 41 (1991).
4. B. Ruscic, C. A. Mayhew, and J. Berkowitz, J. Chem. Phys. **88**, 5580 (1988).
5. L. A. Curtiss and J. A. Pople, J. Chem. Phys. **89**, 614 (1988).
6. JANAF Thermochemical Tables, 3rd Edition, J. Phys. Chem. Ref. Data **14**, 51 (1985).
7. R. P. Saxon, "Theoretical Investigation of the Structure and Stability of the BH_4 Radical," J. Phys. Chem., to be published (1993).
8. C. R. Brazier, P. G. Carrick, and M. E. Cordonnier, presented at the HEDM conference (1993).

Potential Energy Surfaces for the B···H_2 van der Waals Molecule and Studies of the B···(p-H_2)$_n$ Complexes

Millard H. Alexander and Aliki Vegiri

Department of Chemistry and Biochemistry, University of Maryland

College Park, MD 20742

Motivated by the ongoing experimental work on reactions of electronically excited B with H_2,[1] and on the spectroscopy of B in molecular hydrogen matrices,[2] we have undertaken the *ab initio* determination of the potential energy surfaces which are accessed by the approach to H_2 of B in its ground ($2s^2 2p$ ^2P) electronic state.

The complicating, and challenging, feature of the B···H_2 system, as compared to the interaction of an S-state atom [Li($2s$) or Mg($3s^2$)] with H_2, is the additional complexity introduced by the threefold degeneracy of the $2p$ orbital. In this respect, the B···H_2 system is analogous to the interaction of H_2 with ground-state F($2s^2 2p^5$ ^2P)[3] or C($2s^2 2p^2$ ^3P)[4] or with electronically excited Na($3p$ ^2P),[5,6] Be($2s2p$ ^3P)[7] or Mg($3s3p$ $^{1,3}P$).[8,9] Particular study has been made of transformations from an electronically *adiabatic* potential surfaces to an electronically *diabatic* representation.[5,6,10]

In general, the interaction of an atom in a P electronic state with H_2 can be attractive if a singly filled p orbital lies parallel to the H_2 molecule and is thus able to interact with the unfilled σ^* antibonding H_2 orbital. On the other hand, the interaction will likely be repulsive if a singly or doubly filled p orbital points directly toward the H_2 molecule.

The BH_2 molecule is a well characterized species with a bent structure[11] (H–B–H angle 131°, BH distance 1.18 Å, molecular symmetry $^2A_1$). The B–H_2 binding energy is substantial (349 ± 65 kJ/mol).[12] Notwithstanding, in contrast to the interaction of C(^3P) and Be*(^3P) with H_2, there is a significant barrier to molecular formation. since the H_2 molecule must be significantly stretched before insertion of the B atom can occur. To demonstrate this we carried out a series of CASSCF)[13] calculations at a total of 1160 points. Approach of B to H_2 on all three potential energy surfaces ($1^2A'$, $2^2A'$, $1^2A''$) is

193

initially sufficiently repulsive that molecule formation would not be possible for thermal velocities.

Consequently, approach of the $B(2s^2 2p\,{}^2P)$ atom to H_2 can lead only to a weakly-bound van der Waals adduct. Multi-reference singles and doubles CI calculations of the three $B - H_2$ PES's were carried out at 99 geometries with the augmented correlation-consistent valence-triple-zeta (avtz) basis of Dunning and co-workers[14, 15] (92 contracted functions) with the Davidson correction for higher order excitations. Application of the standard counterpoise correction can be done unambiguously only after transformation to a diabatic basis, which will be discussed below.

Contour plots of the three adiabatic PES's are shown in Fig. 1, as a function of the usual Jacobi coordinates R (the distance between B and the center of the H_2 molecule) and θ (the angle between $\bar{R}$ and the H_2 bond). The $1A'$ potential energy surface is lowest in energy, with the minimum in perpendicular geometry ($^2B_2$ symmetry) at a $B-H_2$ distance of 3.11 Å, and a dissociation energy D_e of 121 cm^{-1}. The $1A''$ potential energy surface, corresponding to the out-of-plane orientation of the B $2p$ orbital, also has a minimum in perpendicular geometry ($^2B_1$ symmetry) at a $B-H_2$ distance of 3.35 Å, and a dissociation energy D_e of 68 cm^{-1}. The higher potential energy surface of A' symmetry ($2A'$) is repulsive in perpendicular geometry, but has an attractive well in collinear geometry (Σ symmetry) at a $B-H_2$ distance of 3.93 Å, and a dissociation energy D_e of 75 cm^{-1}.

Asymptotically, one can choose the three degenerate states of the B atom to correspond to a nominal orientation of the B $2p$ orbital along $\bar{R}$ (P_z), perpendicular to $\bar{R}$ but still in the triatomic plane (P_x), and, finally, perpendicular both to $\bar{R}$ and to the triatomic plane (P_y). As the B atom approaches the H_2 molecule, the lowest two adiabatic states of A' symmetry can represent a 2×2 orthogonal transformation of the two, asymptotically degenerate, diabatic states of A' symmetry (P_x and P_z). This transformation can be represented by a single transformation angle $\gamma(R,\theta)$, as follows:

$$\begin{bmatrix} 1A' \\ 2A' \end{bmatrix} = \begin{bmatrix} \cos\gamma & \sin\gamma \\ -\sin\gamma & \cos\gamma \end{bmatrix} \begin{bmatrix} P_x \\ P_z \end{bmatrix}. \tag{1}$$

Physically, the angle γ as representing an orthogonal *rotation* of the pair of in-plane orbitals p_x and p_z. The magnitude of this rotation depends on the position of the H_2 molecule. For perpendicular, C_{2v}, geometry the A_1 state always lies above the B_1 state so that the rotation angle in Eq. (5) is always $0°$. For linear geometry the angle γ is $90°$ at long range, where the Σ state (p_z) lies below the Π state (p_x), but switches to $0°$ at shorter range, where the Π state crosses below the Σ state.

For the van der Waals interaction of an atom with a single p electron outside a closed shell and a closed shell molecule, where the interaction is expected to be weak and no bonds are formed, it is physically reasonable to anticipate that the electronic orbital angular momentum L of the B atom will be little quenched by the presence of the H_2 molecule. This is the so-called "pure precession" approximation common in diatomic molecular spectroscopy.[16, 17] In this limit, transformation to an approximate diabatic representation, in which the three states correspond, nominally, to the three body-frame orientations of the B $2p$ orbital, can be achieved easily by determination of the matrix elements of the electronic orbital angular momentum L, as proposed originally for the $F+H_2$ system by Rebentrost and Lester.[10] More accurately, this angle could be determined from the fundamental derivative relationship,

$$\partial \gamma(R,\theta) \,/\, \partial q \,=\, <1A' \,|\, \partial/\partial q \,|\, 2A'> \,, \qquad (2)$$

where q designates any nuclear coordinate.

In the diabatic representation the *three* adiabatic potential energy surfaces ($V_{1A'}$, $V_{2A'}$, and $V_{1A''}$) become replaced by *four* potential energy functions: three diagonal terms (V_{xx}, V_{zz}, and V_{yy}) and one off-diagonal term (V_{xz}). Obviously, the V_{xx} and V_{yy} interaction potentials are identical for collinear geometry, where they correspond to the energies of the two degenerate components of a Π electronic state. Additionally, in collinear, as well as perpendicular (C_{2v}) geometry, the transformation angle is either $0°$ or $90°$, so that there is no mixing of the P_x and P_z states, only a possible energy reordering. Thus the off-diagonal potential energy function V_{xz} vanishes for collinear and perpendicular geometries. Figure 2 displays contour plots of the variation with the $B\cdots H_2$ angle of the V_{zz}, V_{xx}, and V_{xz} approximate *diabatic* PEF's. The dependence on the Jacobi angle θ of

each of the diabatic PEF's can be described in terms of an expansion in regular or associated Legendre polynomials.

In principle, with the approximate diabatic potential energy functions determined above, one could determine the wavefunction, and concomitantly, the energy levels for the $B(2s2p\ ^2P)\cdots H_2$ van der Waals molecule. A simplification occurs if one constrains molecular hydrogen to the lowest ($j = 0$) rotational level of p-H_2. In this case the H_2 can be considered a spherical atom, and the $B(2s2p\ ^2P)\cdots H_2$ system becomes equivalent to the interaction of an atom in a ^2P electronic state with a spherical, closed-shell partner.[18, 19] The V_Σ and V_Π potentials which describe the interaction between the atom and spherical partner when the p orbital is pointed, respectively, along and perpendicular to the internuclear axis, are displayed in Fig. 3.
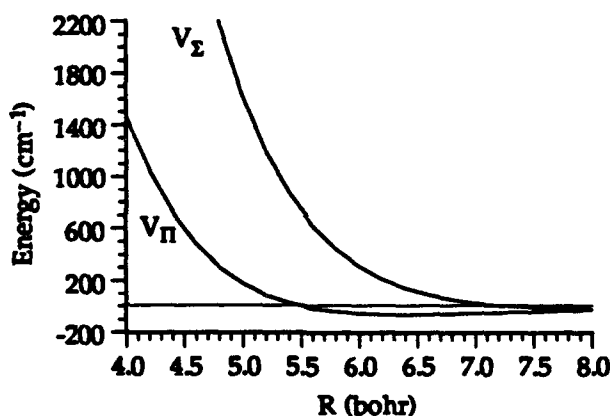
Fig. 3. Interaction potentials [$V_\Pi(R)$ and $V_\Sigma(R)$] for the states of Π and Σ^+ symmetry which characterize the interaction of a spherical H_2 molecule ($j = 0$) with a B ^2P atom.

The lowest energy level(s) of a $B\cdots p$-H_2 van der Waals molecule in the $J_t = 1/2$ rotational level can be determined by solution of a one-dimensional Schroedinger equation governed by the lower root of the diagonalization of the 2×2 Hamiltonian involving V_Σ and V_Π. In fact, the zero point energy is so large that there exists only *one* bound vibrational level in this potential with a dissociation energy of 25.4 cm^{-1}. The corresponding wavefunction is very broad, due to the light reduced mass of the B-H_2 system. The expectation value of the B-H_2 distance is $< R > = 7.61$ bohr, considerably larger than the location of the minimum in the potential ($R_e = 6.41$ bohr, see Fig. 3). A

measure of the width of the wavefunction is given by $< (R - < R >)^2 >^{1/2} = 1.07$ bohr). The upper root of the same 2×2 Hamiltonian, which resembles closely the $V_\Sigma(R)$ potential, also supports one bound state, with, however, a much smaller dissociation energy ($D_0 = 4.6$ cm^{-1}). The wavefunction, also shown in Fig. 9, is even broader than that for the nominally Π state ($< R > = 9.96$ bohr, $< (R - < R >)^2 >^{1/2} = 1.75$ bohr).

To simulate the structure and energetics of clusters of a single B atom with multiple spherical hydrogen molecules, we have used the diffusion Monte-Carlo (DMC) method.[20, 21] The interaction between individual p-H$_2$ molecules is described as

$$V(R) = cos^2 \beta \, V_\Pi(R) + sin^2 \beta \, V_\Sigma(R) \, , \qquad (3)$$

where β is the angle between the vector connecting the B atom with the ith p-H$_2$ molecule and an arbitrary, but fixed, orientation specifying the orientation of the $2p$ orbital. The H$_2$ – H$_2$ potential used was that of Buck et $al.$[22] Calculations were carried out for clusters involving up to 6 spherical H$_2$ units.

The keys results of these DMC calculations are that the B atom tends to sit in the geometric middle with the H$_2$ molecules situated in a volume lying between two conical surfaces excluding the p-orbital of the B atom, as shown in the following figure.
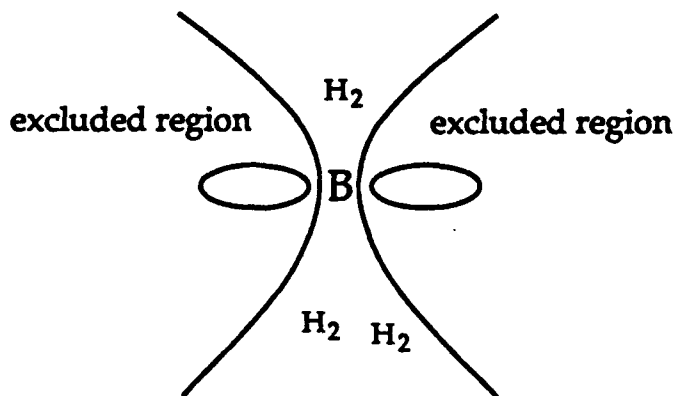
References

1. X. Yang and P. J. Dagdigian, J. Phys. Chem. **XX**, YYYY (1993).
2. M. E. Fajardo and S. Tam, private communication, 1993.
3. F. Rebentrost and W. A. Lester Jr., J. Chem. Phys. **63**, 3737 (1975).
4. T. H. Dunning Jr. and L. B. Harding in *Theory of Chemical Reaction Dynamics*, edited by M. Baer (CRC Press, Inc., Boca Raton, FL, U.S.A., 1985), p. 1.
5. P. Botschwina, W. Meyer, I. V. Hertel, and W. Reiland, J. Chem. Phys. **75**, 5438 (1981).
6. D. R. Yarkony, J. Chem. Phys. **84**, 3206 (1986).
7. R. A. Poirier, M. R. Peterson, and M. Menziger, J. Chem. Phys. **78**, 4592 (1983).
8. N. Adams, W. H. Breckenridge, and J. Simons, Chem. Phys. **56**, 327 (1981).
9. M. Rosenkranz, to be published.
10. F. Rebentrost and W. A. Lester Jr., J. Chem. Phys. **64**, 3879 (1976).
11. G. Herzberg, *Molecular Spectra and Molecular Structure III. Electronic Spectra and Electronic Structure of Polyatomic Molecules*, (D. Van Nostrand, Princeton, 1967).
12. M. W. Chase Jr., C. A. Davies, J. R. Downey Jr., D. J. Frurip, R. A. McDonald, and A. N. Syverud, J. Phys. Chem. Ref. Data **14**, Supplement 1 (1985).
13. P. J. Knowles and H.-J. Werner, Chem. Phys. Lett. **115**, 259 (1985).
14. T. H. Dunning Jr., J. Chem. Phys. **90**, 1007 (1989).
15. R. A. Kendall, T. H. Dunning Jr., and R. J. Harrison, J. Chem. Phys. **96**, 6796 (1992).
16. J. T. Hougen, Natl. Bur. Stand. (U. S.) Monogr. 115 (1970).
17. H. Lefebvre-Brion and R. W. Field, *Perturbations in the Spectra of Diatomic Molecules*, (Academic, New York, 1986).
18. R. H. G. Reid, J. Phys. B **6**, 2018 (1973).
19. F. H. Mies, Phys. Rev. A **7**, 942 (1973).
20. J. B. Anderson, J. Chem. Phys. **63**, 1499 (1975).
21. M. A. Suhm and R. O. Watts, Phys. Repts. **204**, 293 (1991).
22. U. Buck, F. Huisken, A. Kohlhase, D. Otten, and J. Schaefer, J. Chem. Phys. **78**, (1983).
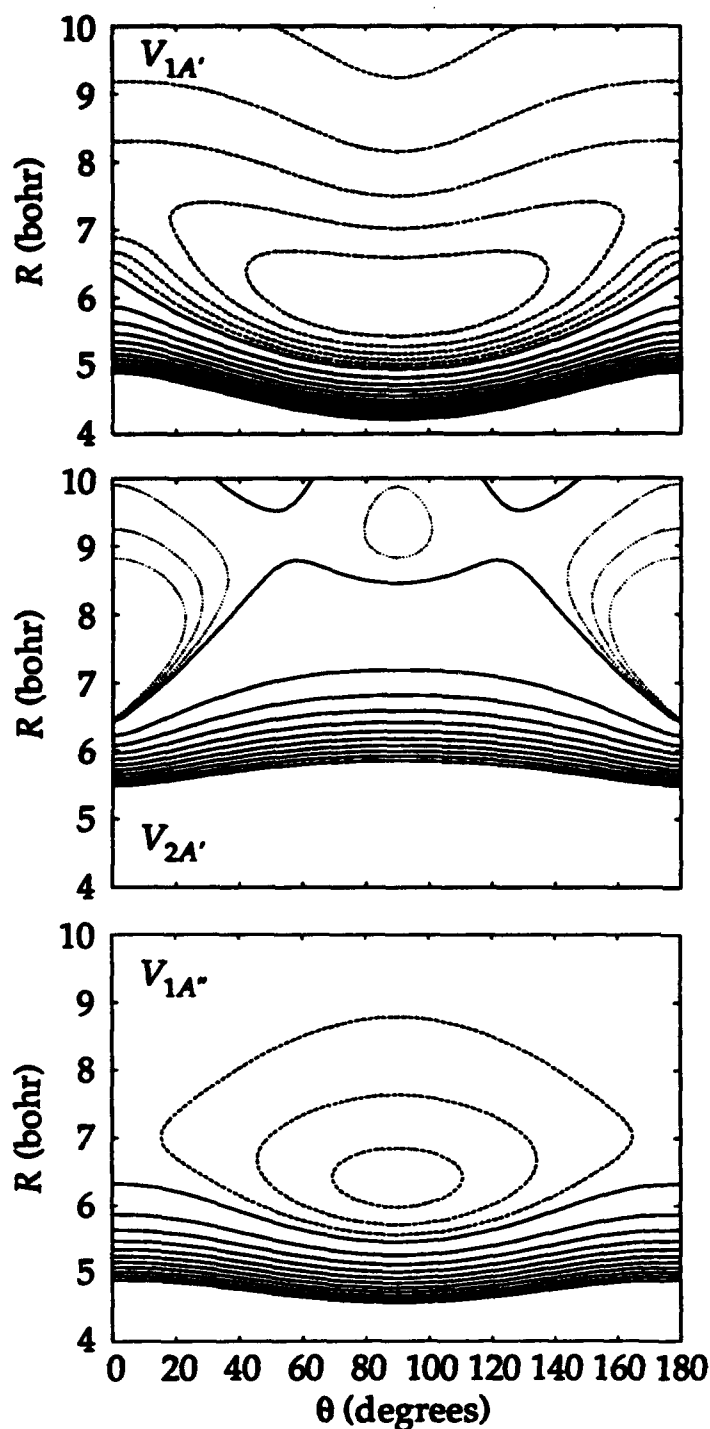
Fig. 1 Contour plots of the lowest three B···H₂ adiabatic PES's as determined by MR-ACPF calculations. The solid contours indicate positive interaction energies ranging upwards from 0 in steps of 50 cm⁻¹. The dashed contours (in the contour plots of the 1A' and 1A" PES's) indicate negative interaction energies ranging down from – 20 cm⁻¹ in steps of 20 cm⁻¹. The dotted contours (in the contour plot of the 2A' PES) indicate negative interaction energies ranging down from – 2 cm⁻¹ in steps of 2 cm⁻¹.
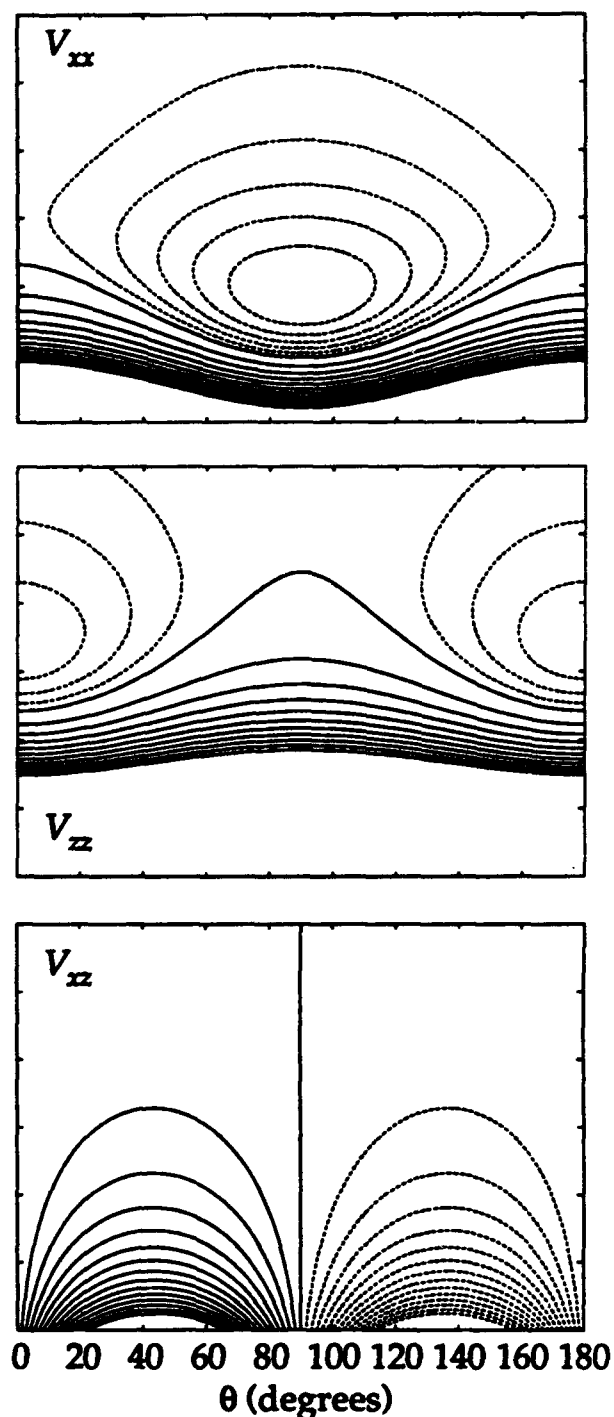
Fig. 2 Contour plots of the V_{xx}, V_{zz} and V_{xz} B···H₂ approximate *diabatic* PES's as determined by MR-CI calculations. The V_{xx} and V_{zz} PES's correspond to the interaction energy for approach of the B atom with the 2p orbital pointing, respectively along R and perpendicular to R but in the BH2 plane. The V_{xz} PEF represents the off-diagonal electrostatic coupling between these two states of A' symmetry. The solid contours indicate positive interaction energies ranging upwards from 0 in steps of 50 cm–1. The dashed contours indicate negative interaction energies. In the case of the V_{xx} and V_{zz} PEF's these range down from – 20 cm⁻¹ in steps of 20 cm⁻¹, and, in the case of the V_{xz} PEF, down from – 50 cm⁻¹ in steps of 50 cm⁻¹.

199

NOVEL BORON HYDRIDE DONORS FOR VISIBLE WAVELENGTH CHEMICAL LASERS

D.J. Benard
Rockwell International Science Center
P.O. Box 1085 - Mail Stop: A9
Thousand Oaks, CA 91358
805/373-4278

EXTENDED ABSTRACT

The use of molecules with high energy content is central to the development of visible wavelength chemical lasers in our laboratory. The systems under investigation and development rely on dissociation of fluorine azide (FN_3) as the principal source of electronically excited metastable NF^* molecules which power the laser by energy transfer to a suitable emitting species. This generator scheme is capable of achieving record ($\geq 3 \times 10^{16}/cm^3$) concentrations of NF^* with near unit conversion efficiency because (1) the N_2 byproducts do not significantly quench or react with NF^* and (2) the conversion is initiated by rapid temperature jump, rather than by a slower mixing process, which allows the FN_3 to fully dissociate before the NF^* is destroyed by self-annihilation reactions that occur at rates near 3×10^{-12} cm^3/s. In practice, the conversion process is most easily initiated by passing a M = 2 shock wave through 50 torr of 1% FN_3 in He and reflecting the shock off a backwall at normal incidence. The NF^* then appears suddenly behind the reflected shock after a characteristic time delay of ~ 50 µs. Under these conditions, the shock only serves to initiate very slow decomposition of the FN_3 during the induction period, which leads to rapid autocatalytic decomposition once a small but critical concentration of NF^* is achieved. Since the gas behind the reflected shock is static, the time profile of the NF^* inside the laser cavity (adjacent to the reflecting backwall) is that of a "delayed avalanche." Weak lasing on the BiF(A-X, 1-4) band at 470 nm has already been achieved by seeding trace amounts of $Bi(CH_3)_3$ into the shocked gas mixture. The NF/BiF system, however, has very low gain and is inefficient because quenching of the NF^* by the organometallic donor (and its byproducts) limits the active BiF concentration to a value that is too small for the transfer reaction to compete effectively with self-annihilation of the metastable species.

Recent experiments in our laboratory have shown that energy transfer from NF* to BH excites the BH(A-X) band which emits most strongly at 433 nm on the $0 \rightarrow 0$ transition. The mechanism of excitation appears to be sequential production of the $a^3\Pi$ and $A^1\Pi$ states by resonant transfer from NF*, with the latter step determining the overall rate of $\sim 3 \times 10^{-11}$ cm^3/s. Consideration of these findings and the radiative rates (cross sections) of BH suggest that an efficient high gain laser can be obtained at 482 nm on the $0 \rightarrow 1$ transition, if a target BH concentration of $\sim 3 \times 10^{15}/cm^3$ is achieved and the BH(X, v = 1) level is rapidly thermalized. Production of BH from B_2H_6 or $BH_3:CO$ has a low yield, but appears to be a scalable process as (amazingly) neither the FN_3 nor NF* are significantly reacted by these donors. Yields approaching unity have been achieved (at very low concentration) by the reaction of discharged F_2 with $BH_3:CO$, but this approach did not scale to the desired BH concentration (in a slow flow reactor) due to secondary three body reactions. Work is underway to extend this approach to a fast flow reactor which should suppress the undesired side effects.

An even more interesting approach, however, is the possible identification of an energetic RBH type molecule that can dissociate to yield free BH radicals. For such a molecule to be useful, it must possess a vapor pressure of at least 0.1 torr at 300°K and must be stable for at least 10 seconds under these conditions. The byproduct R must also be a weak quencher of NF* and the dissociation time of the molecule under the conditions of NF* generation must be on the order of 1 μs. The likely mechanism of dissociation will be transfer of vibrational energy from N_2 molecules formed as a byproduct of the FN_3 decomposition. Consideration of these requirements suggest that a small, highly strained, ring molecule such as HBN_2 or one of its analogs, with a barrier height of ~ 0.5 eV, would be optimum. Since little is known about these molecules (experimentally), ab initic calculations are of great value as are identification of potential synthetic routes for their production.

In summary, the HEDM community with its focus on energetic molecules, boron chemistry and ab initio calculations is well positioned to provide a donor system that will enable a major breakthrough in energy transfer chemical lasers that operate at visible wavelength. This work is supported by the Innovative Science and Technology Office of the Strategic Defense Initiative Organization.

PULSED LASER EVAPORATION OF REFRACTORY MATERIALS FOR MATRIX INFRARED SPECTROSCOPIC STUDIES

Lester Andrews
Department of Chemistry
University of Virginia
Charlottesville, VA 22901

ABSTRACT

A technique for evaporating refractory materials with pulsed 1064 nm radiation for the purpose of infrared spectroscopic study of new molecular species in solid argon has been developed. Three types of substrates have been employed: (a) metals such as B, Al, Ga, and Be, which give hot atoms for reaction with small molecules such as O_2, (b) oxides like Al_2O_3 and Ga_2O_3, which evaporate and decompose to give the small stable metal oxide intermediates, and (c) mixed substrates such as B/C and Al/C, which evaporate and react to give new transient binary species. The product species are identified through isotopic substitution, vibrational analysis, photolysis and annealing behavior and comparison to isotopic spectra from high level ab initio calculations.

INTRODUCTION

Pulsed-laser evaporation is a unique method of evaporating solids, particularly refractory materials, for spectroscopic study of the atoms and molecules so produced.[1-3] One advantage of this method is that the evaporated atoms can be hyperthermal depending on the laser focus.[4,5] The following discussion will present several examples of new molecular species produced by reactions or trapping of the vapor from pulsed-laser ablation in cryogenic matrices. In several cases the excess kinetic energy of the ablated atoms was essential for their reaction.

EXPERIMENTAL

The apparatus used for pulsed-laser matrix infrared experiments has been described elsewhere.[3,6] Figure 1 shows the arrangement of the components. Briefly the 1064 nm fundamental of a Nd-YAG laser in Q-switched mode with 10 ns pulse width was focussed with a 10-cm focal length lens through a hole in the cryogenic window onto a rotating target. Typically, laser energy of 10-100 mJ/pulse produced laser tracks approximately 0.1 nm wide on the target. Although laser focus in these experiments was not perfect, instantaneous laser power was on the order of $1\text{-}10 \times 10^9$ W/cm^2, and an emission plume was always observed. This is 1-2 orders of magnitude larger than the instantaneous laser power used by Wang, et al. to measure hyperthermal velocities for laser-ablated Al atoms.[4] It must be concluded that some of the atoms ablated in these experiments are hyperthermal.

Fourier-transform infrared spectra were recorded for the samples deposited on the CsI window held at 11K. Samples were subjected to photolysis and thermal cycling, and more spectra were recorded.
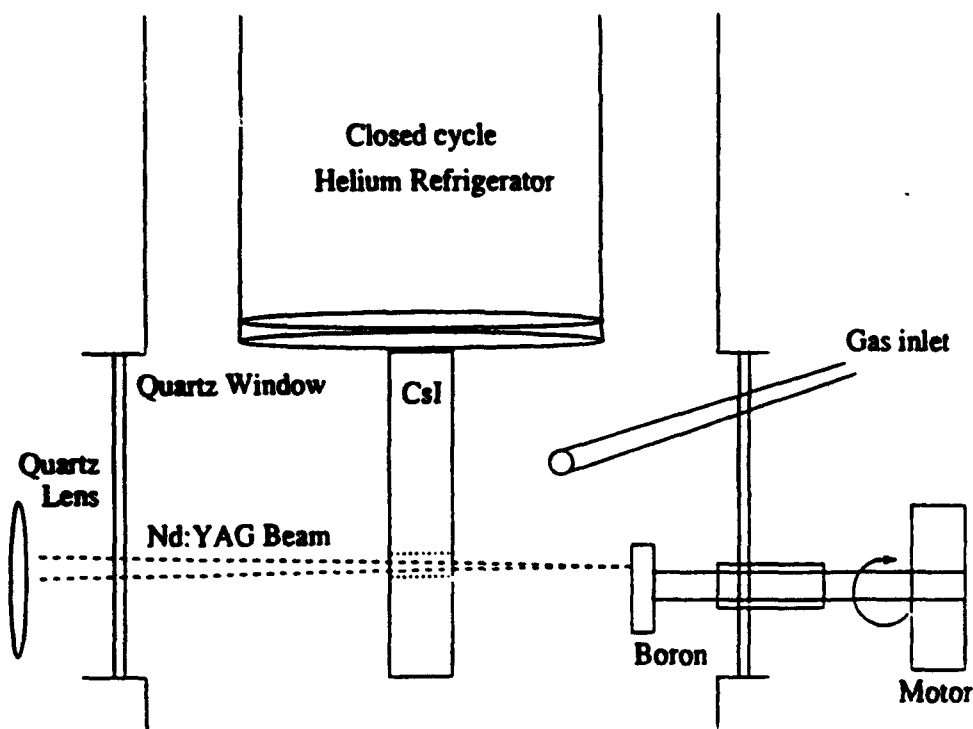
Figure 1. Schematic diagram of apparatus for laser-ablation matrix-isolation experiments.

RESULTS AND DISCUSSION

Infrared spectra will be presented and discussed for different chemical systems.

B+O_2

The spectrum in Figure 2(a) was recorded after deposition of natural isotopic boron atoms with Ar/$^{16}O_2$ = 200/1 sample using an Ar/B ratio near 1000/1. Strong reaction product bands were observed for $^{11}BO_2$ at 1274.6, 1282.8 and 1299.3 cm^{-1} and $^{10}BO_2$ at 1322.3, 1331.0 and 1347.6 cm^{-1} with the expected 4:1 isotopic intensity ratio for a single boron atom species. Clearly atomic boron is inserting in molecular O_2 to give the linear OBO molecule observed in the gas phase at 1278.26 and 1326.08 cm^{-1}.[7] The 3 argon matrix bands are due to different trapping sites. Note the increase of the lower frequency site on annealing to 25K (Figure 2(b)), and the increase of all sites

on photolysis (Figure 2(c)). The growth of BO_2 was observed on annealing to 15K in other experiments.[3] Clearly atomic B inserts into molecular O_2 without activation energy.
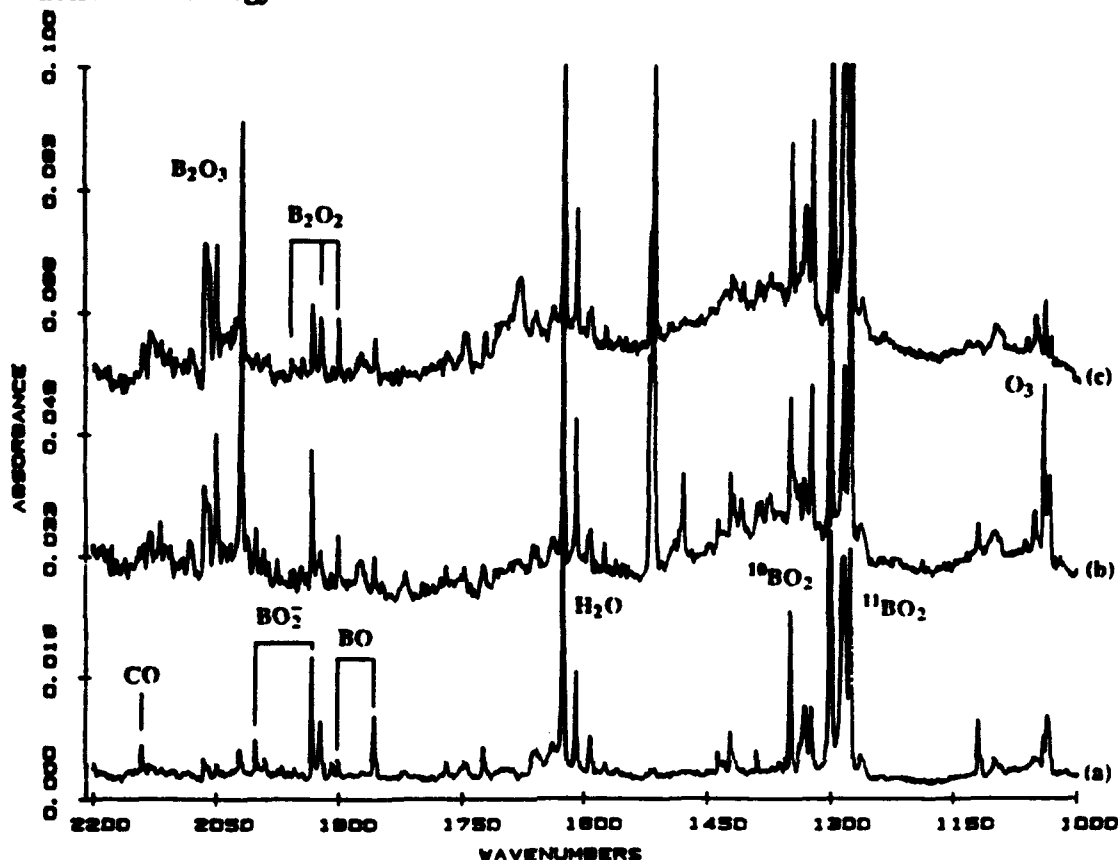
Figure 2. Infrared spectra of natural isotopic B atoms codeposited with O_2 in excess argon at 11±1 K. (a) Ar/O_2 = 200/1, 30 mJ/pulse laser energy, Ar/B – 1000/1, (b) after annealing to 25±1 K, and (c) after irradiation with full light of medium pressure mercury arc for 30 min.

Weaker reaction product bands were observed for BO at 1854.7 and 1907.6 cm^{-1} and BO_2^- at 1931.0 and 2000.0 cm^{-1}. The ^{11}BO matrix fundamental is slightly red shifted from the gas-phase 1862.1 cm^{-1} fundamental,[8] and the $^{11}BO_2^-$ band is near those for metaborate salts in alkali halide lattices.[9]

Experiments were also done with enriched ^{11}B, ^{10}B, $^{18}O_2$ and $^{16}O_2$, $^{16,18}O_2$, $^{18}O_2$ mixtures. The boron isotopic absorptions from natural isotopic material were confirmed. The mixed oxygen isotopic experiment gave a doublet for BO, showing one O atom, and 1:2:1 triplets for BO_2 and BO_2^-, showing 2 equivalent O atoms in these species. Finally, isotopic frequency ratios were appropriate for BO diatomic and the linear OBO and (OBO)$^-$ species.

Annealing allows for the diffusion and reaction of small molecules as well as atoms. Note the increase in B_2O_2 and B_2O_3 at the expense of BO (Figure 2(b)). The weak bands at 1420.5 and 1436.0 cm^{-1} with ^nB exhibited a ^{10}B counterpart at 1449.5 cm^{-1} in ^{10}B experiments. In higher yield ^nB experiments, these bands form a 16:8:1 relative intensity isotopic triplet, which identifies a new species with 2 equivalent B atoms, namely BOB, a linear molecule[11] analogous to AlOAl, which will be identified in the next section.

The small yield of BO relative to BO_2 demonstrates that most of the energetic BO_2 species formed by the highly exothermic insertion reaction are relaxed and stabilized by the matrix. In contrast the gas phase reaction gives only BO.[10] Finally, the small yield of BO_2^- relative to BO_2 shows that ionization processes play only a minor role in these experiments.

$Al+O_2$ and Al_2O_3

Matrix infrared experiments with pulsed laser evaporated Al atoms and O_2 give a very strong cyclic AlO_2 band at 496.3 cm^{-1}, a weaker Al_2O band at 992.8 cm^{-1}, and sharp weaker bands at 1129.5, 1176.3-1169.2, and 1211.2 cm^{-1}.[5] Similar laser ablation of polycrystalline Al_2O_3 gave the strong cyclic-AlO_2 band, a substantially increased Al_2O band, and the same 1129.5, 1176.3-1169.2, and 1211.2 cm^{-1} bands.[5] Clearly the $Al+O_2$ reaction gives the same molecular products as Al_2O_3 ablation-decomposition. Photolysis decreased the cyclic-AlO_2 band and increased the sharp 1129.5 cm^{-1} absorption. Annealing in dilute reagent concentration experiments increased cyclic-AlO_2 and the sharp 1211.2 cm^{-1} band but decreased the sharp 1129.5 and 1176.3-1169.3 cm^{-1} bands.

The laser-ablation work reaffirms the Moscow group[12] identification of cyclic-AlO_2 and assigns the 1129.5, 1176.3-1169.2 and 1211.2 cm^{-1} bands to linear OAlO, OAlOAl and OAlOAlO. First, Al atom concentration studies using different laser powers show that the 1129.5 and 496.3 cm^{-1} absorbers contain less aluminum than Al_2O and hence are monoaluminum species. Mixed oxygen isotopic experiments reveal a sharp 1:2:1 triplet for the 1129.5 cm^{-1} band, a triplet for the 1176.3-1169.2 cm^{-1} pair, and a sharp 1:2:1:1:2:1 sextet for the 1211.2 cm^{-1} band. The $^{16}O/^{18}O$ frequency ratio for the 1129.5 cm^{-1} band identifies the v_3 (antisymmetric) stretching mode of linear OAlO. The 1176.3 and 1211.2 cm^{-1} bands are assigned to the strongest antisymmetric O-Al-O stretching modes of linear OAlOAl and OAlOAlO based on agreement between ab initio calculated (MP2/DZP) and observed isotopic spectra.[5,13]

The $Al+O_2$ addition reaction proceeds on annealing in solid argon, and thus requires no activation energy. In contrast the $Al+O_2$ insertion reaction was not observed on annealing, but was favored in pulsed laser experiments[5] compared to thermal evaporation studies,[12] and was initiated by photolysis. We conclude that the $Al+O_2$ insertion reaction requires activation energy.

Several comparisons of Al and B oxides are of interest. Boron is more reactive with O_2, the B+O_2 insertion reaction proceeds on annealing whereas the Al+O_2 insertion reaction does not. The BO dimer species is OBBO whereas the AlO dimer species favored is OAlOAl. Finally, OBOBO is bent whereas the OAlOAlO molecule is linear.[3,5]

Ga+O_2 and Ga_2O_3

Similar experiments were performed with gallium. A sharp new 3:2 gallium isotopic doublet was observed at 912.7-908.6 cm^{-1} in addition to the 381 cm^{-1} band assigned previously to cyclic-GaO_2.[14,15] The new doublet increased on photolysis and decreased on annealing whereas the reverse behavior was found for cyclic-GaO_2. Mixed oxygen isotopic data reveals a triplet of doublets for the new band showing 2 equivalent oxygen atoms. The 3:2 natural gallium isotopic doublet demonstrates the presence of a single Ga atom in the new species. Laser ablation of Ga_2O_3 gave the new doublet as well as Ga_2O.[14] The gallium and oxygen isotopic ratios are appropriate for the ν_3 vibration of a linear OGaO molecule, analogous to OAlO and OBO.

The new linear OGaO molecule was not observed with thermal Ga atoms and O_2, but linear OGaO was observed with pulsed-laser evaporated Ga atoms and on photolysis of Ga+O_2 samples. Hence, we conclude that activation energy is necessary for the Ga+O_2 insertion reaction, but not for the Ga+O_2 addition reaction.

Be+O_2

Beryllium is a hazardous material due to the toxicity of its oxide; hence, laser ablation provides an efficient method of evaporation to give Be atoms for reactions with O_2. The Be+O_2 matrix system produced a strong broad band at 1573 cm^{-1} and sharp new product bands at 1413.2, 1131.4, 866.8 and 522.7 cm^{-1}.[16] Reactions with $^{18}O_2$ gave product bands and 16/18 ratios of 1.0187, 1.0120, 1.0199, 1.0204 and 1.0199, respectively. The 16/18 ratio for the 1413.2 band is near the harmonic value (1.0125) calculated for linear O-Be-O. Near agreement with the MBPT(2) calculated value (1422.5 cm^{-1}) using the 6-311G* basis set in the ACES II program system[17] confirms the assignment to the linear O-Be-O molecule analogous to O-B-O. The 16/18 ratios for the last three bands are near the harmonic diatomic value (1.0207), which are expected for the infrared allowed modes of rhombic $(BeO)_2$. Again, agreement with MBPT(2) calculated values (1140.5, 873.1 and 513.4 cm^{-1}) is excellent and confirms the identification of rhombic $(BeO)_2$. Note that the favored structure of B_2O_2 is linear with a B-B bond.[3] Finally, the 1573 cm^{-1} band is believed to be due to a $(BeO)_x$ cluster species.

B/C Pellets

In order to prepare new boron carbide molecular species, pellets (13 mm dia x 2 mm th) were pressed (10 tons) from mixtures of boron and graphite powder. Pellets with B/C mole ratios ranging from 1/1 to 5/1 were laser ablated into a condensing argon stream. Carbon clusters were produced and identified from their matrix infrared spectra as were traces of boron oxides.[18] The intensities of carbon cluster bands and the cluster size decreased with increasing B/C ratio while a new 4:1 boron isotopic doublet increased at 1194.6 and 1232.5 cm^{-1}; a pellet prepared from ^{10}B gave the 1232.5 cm^{-1} band.[19]

The new 4:1 boron isotopic doublet indicates that a new BC$_x$ species has been formed. Unfortunately, carbon-13 could not be incorporated into the pellet to determine the number of carbon atoms, but the boron isotopic shift provides useful information. The boron 10/11 isotopic frequency ratio 1235.5/1194.6 = 1.03173 shows more boron dependence than the harmonic diatomic BC ratio (1.02562). The B-C vibration of linear B-C≡C· is expected to exhibit an isotopic ratio near the diatomic molecule. On the other hand B vibrating between two C atoms in the v_3 (antisymmetric) stretching mode of open C-B-C or B against C$_2$ in the v_2 (symmetric) stretching mode of acute triangular B-C$_2$ would show more B isotopic dependence than an isolated B-C vibration. The boron isotopic shifts are compatible with assignment to v_3 of open C-B-C with a valence angle near 130° or to v_2 of a triangular B-C$_2$ molecule with an apex angle near 50°. This species has probably been observed in ESR matrix studies.[20]

Coupled cluster and complete active space calculations[19] predict the global minimum BC$_2$ structure to be an asymmetric triangle; however, the vibrationally averaged structure will be an isosceles triangle with a strong symmetric B-C$_2$ stretching fundamental near 1200 cm^{-1}. The calculated boron 10/11 frequency ratio (1.0333) is in excellent agreement with the observed ratio and confirms assignment of the 1194.6 cm^{-1} band to the B-C$_2$ ring.

Al/C Pellets

Similar laser ablation studies were done with Al/C pellets. New bands were observed at 629.8 and 605.3 cm^{-1} with a 613 cm^{-1} shoulder. Annealing to 20 and 30 K had little effect on the 629.8 cm^{-1} band but markedly increased the 605.3 cm^{-1} band at the expense of the shoulder. A mixed Al/^{12}C/^{13}C pellet gave sharp bands at 629.8, 612.9, 605.2, 596.8, and 589.0 cm^{-1}. Annealing increased the latter triplet.[21]

The 629.8-612.9 cm^{-1} doublet is clearly due to a single carbon atom species. The carbon 12/13 ratio 629.8/612.9 = 1.02757 is in excellent agreement with the harmonic diatomic ratio (1.02774) which confirms assignment of the 629.8 cm^{-1} band to diatomic AlC. Calculations (CASSCF and MRCI levels of

theory)[22] predict a 629 cm^{-1} fundamental for the $^4\Sigma^-$ ground state of AlC in strong support of the matrix assignment.

The 605.2, 596.8 and 589.0 cm^{-1} triplet is due to a species with 2 equivalent carbon atoms. Triangular AlC$_2$, which has been characterized by ESR spectroscopy,[23] is immediately suggested. The growth of AlC$_2$ on annealing requires the presence of Al atoms and C$_2$ in the matrix from the ablation process and their reaction without activation energy. The carbon 12/13 ratio 605.2/589.0 = 1.02716 is slightly smaller than the AlC diatomic ratio, which is consistent with more Al participation in the normal mode, as expected for the ν_2 (symmetric) Al-C$_2$ vibration of the isosceles triangular species. Ab initio electronic structure calculations (SCF)[24] predict a 735 cm^{-1} ν_2 fundamental for AlC$_2$; proper scaling puts the calculated and observed frequencies in good agreement and supports the matrix infrared identification of cyclic AlC$_2$.

CONCLUSIONS

The pulsed-laser ablation studies presented here show that a pulse of atoms can be evaporated from the surface of solid materials. Many of these atoms are hyperthermal and can undergo chemical reactions that require activation energy. Although the surface temperature at the laser focal point is very high, the volume element heated is very small, and no adverse heating effects were noticed for a 11±1 K cryogenic sample collecting window 3 cm from the target. The pulsed laser can also be used to evaporate and decompose refractory materials such as alumina into stable small molecules. Binary composite materials such as B/C and Al/C as pulsed-laser targets produce atoms and small molecules of both materials as reactants to make new molecules.

ACKNOWLEDGMENTS

REFERENCES

1.   L. B. Knight, Jr., B. W. Gregory, S. T. Corbranchi, D. Feller, and E. R. Davidson, *J. Am. Chem. Soc.* 108, 3521 (1987).
2.   K. J. Klabunde, R. Boucher, and G. H. Jeong, *J. Am. Chem. Soc.* 112, 3332 (1990).
3.   T. R. Burkholder and L. Andrews, *J. Chem. Phys.* 95, 8697 (1991).

4. A. P. Salzberg, D. I. Santiago, F. Asmar, D. N. Sandoval, and B. R. Weiner, *Chem Phys. Letts.* 180, 161 (1991); H. Wang, A. P. Salzberg, B. R. Weiner, *Appl. Phys. Letts.* 59, 935 (1991).

5. L. Andrews, T. R. Burkholder, and J. T. Yustein, *J. Phys. Chem.* 96, 10182 (1992).

6. P. Hassanzadeh and L. Andrews, *J. Phys. Chem.* 96, 9177 (1992).

7. A. Maki, J. B. Burkholder, A. Sirha, and C. J. Howard, *J. Mol. Spectrosc.* 130, 238 (1988).

8. K. P. Huber and G. Herzberg, Constants of Diatomic Molecules (Van Nostrand, Princeton, 1979).

9. R. Teghil, B. Janis, and L. Bencivenni, *Inorg. Chim. Acta* 88, 115 (1984).

10. A. W. Hanner and J. L. Gole, *J. Chem. Phys.* 73, 5025 (1980); M. A. A. Clyne and M. C. Heaven, *Chem. Phys.* 51, 299 (1980).

11. L. Andrews and T. R. Burkholder, *J. Phys. Chem.* 95, 8554 (1991).

12. I. L. Rozhanskii, G. V. Chertihin, L. V. Serebrennikov, and V. F. Shevel'kov, *Russ. J. Phys. Chem.* 62, 1215 (1988).

13. Y. Hannachi and L. Andrews, to be published.

14. T. R. Burkholder, J. T. Yustein, and L. Andrews, *J. Phys. Chem.* 96, 10189 (1992).

15. M. J. Zehe, D. A. Lynch, Jr., B. J. Kelsall, and K. D. Carlson, *J. Phys. Chem.* 83, 656 (1979).

16. C. A. Thompson and L. Andrews, to be published.

17. J. F. Stanton, J. Gauss, J. D. Watts, W. J. Lauderdale, and R. J. Bartlett, ACES II, Quantum Theory Project, University of Florida, Gainesville, Florida, 1992.

18. J. Szczepanski, R. Pellow, and M. Vala, *Z. Naturforsch.* 47a, 595 (1992).

19. J. M. L. Martin, P. R. Taylor, J. T. Yustein, T. R. Burkholder, and L. Andrews, *J. Chem. Phys.*, to be published.

20. L. G. Knight, Jr., S. T. Corbranchi, J. T. Petty, E. Earl, D. Feller, and E. R. Davidson, *J. Chem. Phys.* 90, 690 (1989).

21. G. V. Chertihin, and L. Andrews, to be published.

22. C. W. Bauschlicher, Jr., S. R. Langhoff, and L. G. M. Petterson, *J. Chem. Phys.* 89, 5747 (1988).

23. L. B. Knight, Jr., S. T. Corbranchi, J. O. Herlong, and C. A. Arrington, *J. Chem. Phys.* 92 5856 (1990).

24. J. R. Flores and A. Largo, *Chem. Phys.* 140, 19 (1990).

ATOMISTIC SIMULATIONS OF CONDENSED-PHASE MATERIALS ON PARALLEL ARCHITECTURES

Rajiv K. Kalia, Aiichiro Nakano, and Priya Vashishta

Concurrent Computing Laboratory for Materials Simulations
Department of Physics and Astronomy
Department of Computer Science
Louisiana State University, Baton Rouge, LA 70803-4001

Recent advances in microprocessor technology, increased density of memory chips, and sophisticated high-bandwidth communications have led to the development of truly affordable high-performance parallel computers. Coupled with recent developments in algorithms and simulation techniques, parallel computer architectures offer the necessary compute power to carry out realistic simulations for condensed-phase systems. In the past few years, our research has focused on the application of advanced numerical methods, parallel and distributed computing techniques and tools, and scientific visualization to condensed-phase simulations. The simulations have been carried out on the following parallel computer architectures in our *Concurrent Computing Laboratory for Materials Simulations* (CCLMS):

- MasPar 1208B - a SIMD (Single Instruction Multiple Data) machine with 8,192 processors;
- Intel iPSC/860 - an 8-node distributed-memory MIMD (Multiple Instructions Multiple Data) machine;
- Intel iWarp - a 64-cell MIMD machine with message-passing and systolic communications;
- Silicon Graphics IRIS 4D/380VGX Power Center for real-time visualization.

Recently the Louisiana Board of Regents awarded us $850,000 to acquire a 56-node Intel Paragon machine. Plans are in place to connect these machines by FDDI (Fiber Distributed Data Interface) to form a distributed multiparallel processing network so that different parts of a large-scale simulation can run concurrently on different architectures along with real-time visualization.

The research effort of the CCLMS focuses on molecular dynamics (MD) and quantum molecular dynamics (QMD) simulations of the following systems:

- Embedded atoms and molecules in crystalline and porous materials;
- Glasses, ceramics, and nanophase materials;
- Electron transport and optical response of nanodevices.

This extended abstract briefly describes our recent work on parallel algorithms for MD simulations to investigate structural transformations in densified and porous silica, an implementation of the QMD approach on SIMD machines, and the development of a parallel dynamical-simulated-annealing approach to simulate the condensed phase of the ozone-oxygen system.

Parallel Molecular Dynamics Algorithms

Molecular-dynamics approach has played a key role in our understanding of classical and quantum microscopic processes in physical systems [1]. In the MD approach, one obtains the phase-space trajectories of particles from the numerical solution of Newton's equations. The MD approach has considerable inherent parallelism and it maps well on MIMD machines.

Domain decomposition is the most appropriate scheme to implement MD simulations on distributed-memory MIMD machines [2]. In this case, the total system is divided into subsystems which are geometrically mapped onto processors. The relevant data for all the particles whose coordinates fall within the boundaries of a given subsystem are stored on the processor for that subsystem.

The forces and potential energy are computed with the multiple-time-step (MTS) approach and the linked-cell list scheme [1]. The MTS approach exploits the fact that the force experienced by a particle can be separated into a rapidly varying primary component and a slowly varying secondary component. The primary interaction arises from nearest neighbors, whereas the secondary forces are due to other particles within the range of the interparticle interaction. The primary contributions to potential energy and forces are computed with the aid of a neighbor list constructed at regular time intervals with use of the linked-cell list method.

The secondary forces vary slowly in time and are therefore calculated with the Taylor series expansion. They consist of intranode and internode contributions. The former can be calculated straightforwardly with the linked-list scheme. Internode contributions require data motion (positions, velocities, etc.) for particles on neighboring nodes. The message-passing strategy we have used is as follows: First the data from node 0 is sent to node 1, data from node 1 to node 2, ..., and data from node p-1 (p is the number of processors) to node 0 synchronously. Then using the linked-cell list method the contributions to secondary forces, potential energy, and their time derivatives are calculated. Node 0 sends back the calculated contributions to node p-1 while receiving the contributions calculated at node 1. Similar message-passing of calculated contributions takes place synchronously at other nodes as well. Next node 0 receives data from node p-2, node 1 from node p-1, ..., and node p-1 from node p-3. The contributions to forces, potential energy, and their time derivatives are calculated synchronously and the results are sent back to the nodes from which the data had been received. This procedure is continued until all the necessary interactions have been computed.

The performance of the domain-decomposition algorithm for MTS-MD simulations was evaluated on our 8-node Intel iPSC/860 system. The execution time scales linearly with the size of the system and it is inversely proportional to the number of processors for a fixed subsystem size per processor. For applications described below, the parallel efficiency, η ($= t_1/(p^*t_p)$) where t_p is the execution time on p processors and t_1 is the execution time on a single processor), is estimated to be 0.97 and the algorithm sustains good load balancing.

Recently, we have also implemented MD simulations involving the Ewald summation for Coulomb interaction on distributed-memory MIMD machines [3]. The parallel algorithm we have designed reduces the computational complexity from $O(N^{3/2})$ to $O(N)$. This is achieved by ensuring that both the real-space and Fourier-space contributions scale linearly with the size of the system for a desired level of precision.

Structural Transformations in Densified and Porous Systems

The parallel MD approach has been used to determine novel structural transformations in highly densified and porous condensed phases of silica glasses. Silica (SiO_2) is one of the most interesting materials because of its numerous polymorphs. Over the years, many attempts have been made to investigate structures and dynamics of crystalline and glassy states of SiO_2 at high pressures. Recent in-situ high-pressure x-ray diffraction experiments reveal significant changes in the short-range and medium-range order in SiO_2 glasses [4].

Molecular-dynamics simulations for silica glasses are based on an effective interatomic potential consisting of two- and three-body terms. The two-body potential includes long-range Coulomb interaction due to charge-transfer effects, charge-dipole interaction due to large electronic polarizability of O^{2-} ions, and steric repulsion between ions. The three-body covalent potentials for Si-O-Si and O-Si-O interactions include the effects of bond bending and stretching.

Our high-pressure MD simulations [5] cover a wide range of mass density, from 2.20 g/cm^3 (normal density) to 4.28 g/cm^3. At normal density, silica glasses are corner-sharing networks of $Si(O_{1/2})_4$ tetrahedra, see Fig. 1 (a). The medium-range order in the normal-density glass is manifested in the form of a first sharp diffraction peak (FSDP) at 1.6 Å^{-1} in the static structure factor, S(q). This peak reflects the connectivity of tetrahedra over distances in the range of 4-8 Å. With an increase in the density, the height of the FSDP decreases, its width increases, and its position shifts to higher values of q. (Elastic compression cannot account for the observed shift in the position of the FSDP.) In addition, a new peak appears when the density is increased by 20%. Located at 2.85 Å^{-1}, the peak grows under pressure with only a slight shift in its position. The simulation results for the effect of pressure on S(q) are in good agreement with high-pressure x-ray measurements [4].

Pair-distribution functions and bond-angle distributions provide strong evidence for an interesting structural phase transition in the highly densified silica glass at 4.28 g/cm^3. The Si-O pair-distribution functions reveal that the nearest-neighbor coordination of Si increases from 4 to 5.8 as the density of the system increases from 2.2 to 4.28 g/cm^3. Furthermore, the density increase causes significant changes in O-Si-O and Si-O-Si bond-angle distributions. At normal density, the former has a single peak at 109°. When the glass density reaches 4.28 g/cm^3, the O-Si-O distribution develops broad peaks around 90° and 180°. The Si-O-Si bond-angle distribution for the normal density SiO_2 glass has a peak at 142° with a FWHM of 26°. (Both of these results are in excellent agreement with NMR measurements.) With densification to 4.28 g/cm^3, the distribution exhibits broad peaks around 95° and 128°. These results for pair-distribution functions and bond-angle distributions provide strong evidence for corner-sharing and edge-sharing $Si(O_{1/3})_6$ octahedra at 4.28 g/cm^3, see Fig. 1 (b).
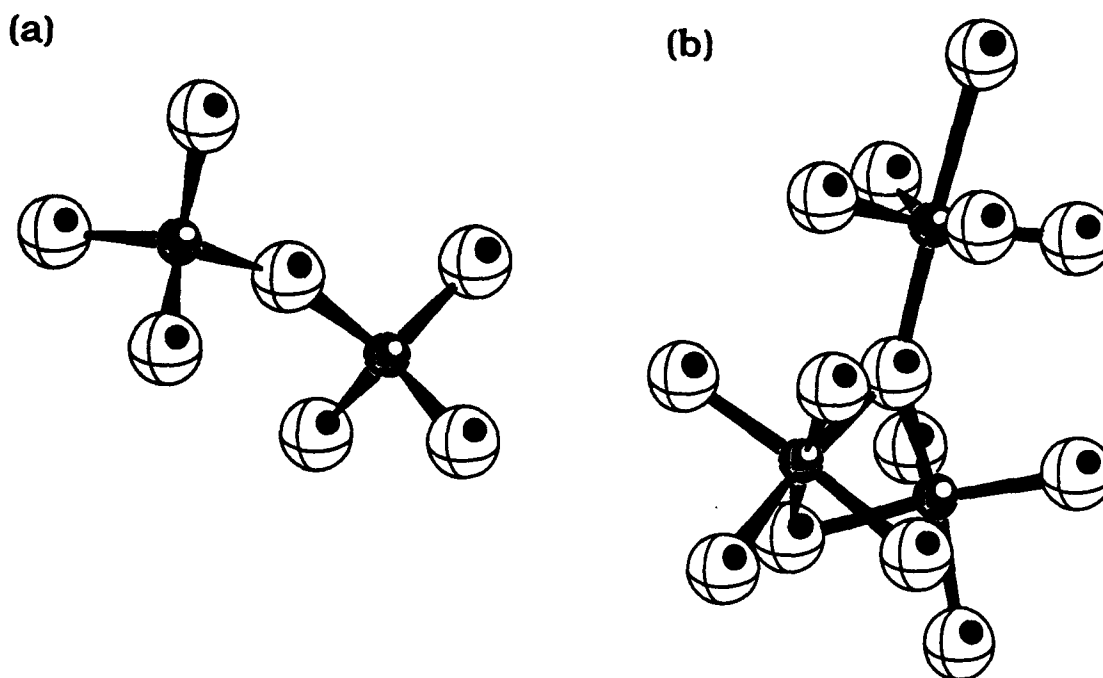
Figure 1:   a) Corner-sharing $Si(O_{1/2})_4$ tetrahedra in the normal-density glass; b) corner-sharing and edge-sharing $Si(O_{1/3})_6$ octahedra in the highly densified silica glass.

Recently, we have also investigated structural correlations in porous silica. This environmentally

safe material with a large thermal resistance and high optical transmission is an excellent alternative to CFC foamed plastic in thermal insulation of refrigerators and a highly desirable material for passive solar energy collection devices. Efforts are also being made to produce optical switching devices by embedding semiconducting microclusters in the pores of aerogel silica.

Our MD simulations for porous silica cover a wide range of densities, from 2.2 to 0.1 g/cm^3 [6]. The simulated systems are large enough (41,472 particles; the lowest density system is a cube with an edge of 240 Å) to cover the entire range of structural correlations. In Fig. 2a, we show pair-distribution functions, g(r), on a logarithmic scale at several densities. Superimposed on the peaks in g(r) is a power-law decay from which one can determine the fractal dimension, d_f, of the silica network: $d_f = 3+dlog[g(r)]/dlog(r)$. Figure 2b shows density variations of fractal dimensions at T = 300 K (open circles) and 1000 K (solid circles).

One of the most important characteristics of porous glasses is the pore statistics. The pore-size distribution is determined as follows: The system is divided into cubic cells of volume l^3. The number of pores of size l is the number of empty cells which are isolated and do not share any face with other empty cells. The pore-size distribution changes from Gaussian to a power law when the density is lowered across the tensile limit of the silica glass, see Fig. 2c.
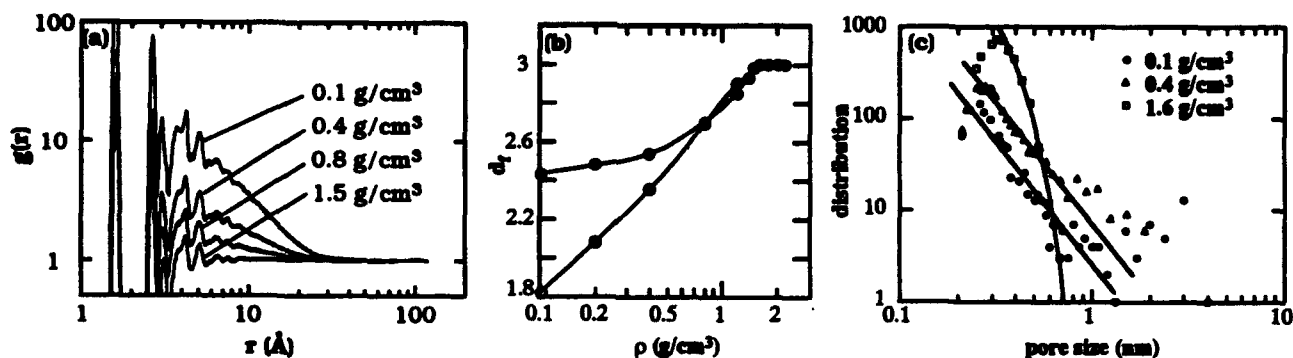
Figure 2: (a) Pair-distribution functions, g(r), of porous silica; (b) density dependences of fractal dimensions; and (c) pore-size distributions at various densities.

Quantum Molecular Dynamics on Parallel Machines

Quantum molecular dynamics simulates the dynamics of coupled electron-ion systems by combining the MD approach with numerical solutions of the time-dependent Kohn-Sham equations

in the density-functional formalism. In addition to the MD algorithm, the QMD simulation requires [7]:

(1)   Solution of parabolic partial differential equations (PDEs) (the time-dependent Kohn-Sham equation);
(2)   Solution of elliptic PDEs (the Poisson equation);
(3)   Optimization of electronic structures and atomic configurations.

Parallel algorithms for these components involve:

(1)   Space-Splitting (SS) Schrödinger solver;
(2)   Simulated-Annealing (SA) and parallel multigrid Poisson solvers;
(3)   Conjugate-Gradient (CG) optimization with use of second derivatives.

The SS Schrödinger solver relies on the decomposition of a tridiagonal matrix into block diagonal matrices each of which can be manipulated analytically. The SA method is applicable when successive calls to a Poisson solver is highly correlated, as is the case in most dynamical simulations. The Poisson equation can then be replaced by a hyperbolic PDE which is computationally less demanding. Both algorithms (1) and (2) are scalable (parallel time complexity is independent of the number of grid points) and local (only nearest-neighbor communications are needed). Applied to energy minimizations of MD configurations, algorithm (3) speeds up the conventional CG by a factor of 13. For first-principles electronic-energy minimizations based on the self-interaction-corrected local-spin-density (SIC-LSD) approximation, a single-iteration CG algorithm has been developed which significantly speeds up conventional SIC calculations using doubly-nested iterations.

The QMD algorithms (1)-(3) have been implemented on the SIMD architecture (8,192-node MasPar 1208B) and the shared-memory MIMD machine (8-processor Silicon Graphics 4D/380 VGX) in our *Concurrent Computing Laboratory for Materials Simulations*. Both the SS-Schrödinger and SA-Poisson solvers are significantly faster than conventional algorithms and achieve more than 60 % of the theoretical peak speed of the MasPar. On the Silicon Graphics, high and sometimes superlinear speedup (parallel efficiency 0.83 ~ 1.08) is observed.

Future Work: Dynamical Simulated Annealing for Ozone-Oxygen System
Density functional theory (DFT) has proved remarkably successful in developing an understanding of electronic properties such as binding energies, interatomic distances and crystal structures. A few years ago, electronic-structure calculations in DFT were combined with MD simulations to include electronic effects in the motion of ions at finite temperatures [8]. This so called dynamical-simulated-annealing (DSA) approach utilizes the MD technique to perform simultaneously the electronic energy minimization and the integration of Newton's equations of motion to obtain ionic

trajectories. In this scheme, the electronic effects are explicitly present and therefore the need for effective interparticle interactions is obviated. The distinct advantage of the DSA approach is that it allows electronic-structure calculations for any arbitrary atomic configuration, thereby making it possible to simulate disordered materials at finite temperatures.

The bottleneck in the DSA technique results from the expansion of electronic orbitals into a plane-wave basis set. In many physical situations, electronic orbitals are localized in space and hence the plane-wave representation requires an enormous number of terms. A new family of functions called wavelets provides an optimal representation for localized functions, thereby significantly reducing the computational cost of these simulations. Parallel algorithms are being designed to implement the DSA approach on distributed-memory MIMD machines.

The parallel DSA approach will be used to determine the thermodynamic properties, positional and orientational correlation functions, and translational and rotational dynamics of molecules in ozone-oxygen mixtures. The simulations will employ an ultrasoft pseudopotential developed recently for oxygen [9]. Its application to electronic-structure calculations for O_2 and O_3 molecules provides reliable results for energetics and structures of these molecules. The knowledge of a reliable pseudopotential makes it feasible to carry out DSA simulations for condensed phases of ozone-oxygen mixtures. Highly accurate results for the ground-state properties will be calculated with the Green's Function Monte Carlo approach.

References

1. M. P. Allen and D. J. Tildesley, *Computer Simulation of Liquids*, (Oxford University Press, Oxford, 1990).
2. R. K. Kalia, S. W. de Leeuw, A. Nakano, D. L. Greenwell, and P. Vashishta, Supercomputing, in press.
3. R. K. Kalia, S. W. de Leeuw, A. Nakano, and P. Vashishta, Comp. Phys. Commun. 74, 316 (1993).
4. C. Meade, R. J. Hemley, and H. K. Mao, Phys. Rev. Lett. 69, 1387 (1992).
5. W. Jin, R. K. Kalia, P. Vashishta, and J. P. Rino, to be published.
6. A. Nakano, L. Bi, R. K. Kalia, and P. Vashishta, Phys. Rev. Lett. 71, 85 (1993).
7. A. Nakano, P. Vashishta, and R. K. Kalia, SIAM J. Sci. Comput., submitted.
8. R. Car and M. Parrinello, Phys. Rev. Lett. 55, 2471 (1985).
9. D. Vanderbilt, Phys. Rev. B 41, 7892 (1990).

Bond-Stretch Isomerism in Strained Organosilicon Compounds

Jerry A. Boatz

Phillips Laboratory

OLAC PL/RKFE

9 Antares Road

Edwards AFB, CA 93524-76R0

and

Mark S. Gordon

Ames Laboratory - USDOE

Iowa State University

Ames, IA 50011

ABSTRACT

The existence of bond-stretch isomers (isomers which differ primarily
in the length of the bridgehead bond) of tetrasilabicyclobutane, Si_4H_6,
recently has been predicted using ab initio electronic structure methods of
quantum chemistry. At the GVB/3-21G* level of theory, the "short bond"
isomer is predicted to be less stable than the "long bond" isomer.
Although the parent compound has not yet been experimentally observed, the
X-ray crystal structure of a heavily-substituted derivative is known. This
derivative compound apparently does not exist in two bond stretch forms;
rather, only the short bond isomer is observed. The present work is an
attempt to resolve the differences between the theoretical predictions for
the parent Si_4H_6 molecule and the experimental observations of the
derivative compound. In particular, a systematic study of how various
substituents affect the relative stabilities of the two bond-stretch
isomers is presented. The rather large size of many of the molecules of
interest in this study requires the use of massively parallel computers.

I. Introduction

Highly strained compounds with large positive heats of formation may
be useful as additives to rocket propellants as a means of improving

217

performance. Examples of such compounds include derivatives of cubane and quadricyclane. Compounds such as these can lead to increases in specific impulse (I_{sp}) of several seconds.

Another type of molecule which might be capable of boosting the performance of conventional propellants is tetrasilabicyclo[1.1.0]butane (Si_4H_6), the silicon analog of bicyclo[1.1.0]butane. Preliminary I_{sp} calculations show that when Si_4H_6 is used as an additive to RP1, an increase in specific impulse of up to ten seconds over pure RP1 can be obtained. This is due in part to the high heat of formation of Si_4H_6, which ab initio calculations predict to be $\Delta H^0_{f,298}$ = 93 kcal/mol.[1] Another contributing factor is the overwhelming thermodynamic stability of SiO_2, one of the combustion products.

Previous theoretical calculations[2] predict the existence of two Si_4H_6 "bond stretch" isomers. These isomers differ primarily in the distance between the bridgehead silicons. The "short bond" isomer is a closed shell species with the length of the bridgehead bond only slightly longer than a typical Si-Si single bond. The "long bond" isomer is essentially a singlet diradical species in which the bridge bond is broken and the unpaired electrons on the bridgehead silicons are singlet coupled. What differentiates the latter from other diradical species is that it is approximately 10 kcal/mol more stable than its closed shell counterpart (i.e., the short bond isomer.)

Si_4H_6 has not been experimentally detected, but the X-ray crystal structure of the 1,3-di-tert-butyl-2,2,4,4-tetrakis-(2,6-diethylphenyl) derivative is known.[3] In this derivative, only the short bond isomer is observed. This observation suggests that substituents may have a dramatic effect on the relative energies of the bond stretch isomers of silicon-based bicyclobutanes. The present work is a systematic study of how various bridgehead substituents affect the relative energies of the short and long bond isomers of tetrasilabicyclobutane derivatives. In particular, the effects of replacing the bridgehead hydrogens in Si_4H_6 with methyl and tert-butyl groups is examined in this study. (Note that tert-butyl groups are present at the bridgehead positions in the experimentally observed derivative.[3])

218

II. Theoretical Methods

The geometries and energies of the 1,3-dimethyl and 1,3-di-*tert*-butyl derivatives of tetrasilabicyclobutane were calculated at the generalized valence bond[4] (GVB) level of theory using the 3-21G* basis set[5] (denoted as GVB/3-21G*.) The bonding (σ) and antibonding (σ^*) orbitals of the Si-Si bridge bond comprised the GVB pair.[6] The geometry of each molecule was fully optimized within the confines of the molecular point group symmetry. All stationary points were verified as local minima or transition states by diagonalizing the matrices of energy second derivatives; i.e., the hessian matrices.

All calculations were performed using the *ab initio* electronic structure program GAMESS.[7] For the calculation of energies, geometries, and hessians for the di-*tert*-butyl derivatives, the newly developed parallel capabilities of GAMESS[8] were utilized on both the massively parallel Touchstone Delta computer located at Caltech and on a local cluster of high performance IBM Risc/6000 workstations.

III. Results and Discussion

For ease of discussion, the short and long bond isomers of the parent compound, Si_4H_6, will be referred to as 1S and 1L, respectively. Likewise, the corresponding isomers of the 1,3-dimethyl (1,3-di-*tert*-butyl) derivative will be denoted as 2S and 2L (3S and 3L), respectively.

Table 1 shows the relative energies of the bond stretch isomers as a function of bridgehead substituent. (A negative relative energy means that the long bond structure is the more thermodynamically stable isomer.) For the parent compound, the long bond isomer is lower in energy than the short bond structure by nearly 10 kcal/mol. Replacement of the bridgehead hydrogens with methyl groups decreases the energetic preference of the long bond isomer to approximately 2 kcal/mol. *Tert*-butyl groups at the bridgehead positions actually reverse the order of relative stability, leading to at least a 3 kcal/mol energy preference for the short bond isomer (*vide infra*.)

Based solely on steric interactions between the bridgehead groups, one might expect the relative stability of the long bond isomer to increase as the bulkiness of the bridgehead substituents increases. Since the distance between the bridgehead silicon atoms in the long bond isomer is greater than in the short bond counterpart, it seems reasonable that there should be less steric crowding at the bridgehead positions in the long bond structure. However, the data in Table 1 show just the opposite trend in relative stability. This counterintuitive effect can be understood by examining in more detail the bond stretch geometries of the parent compound, which are shown in Figure 1.[9] While the bridgehead Si-Si internuclear distance is indeed larger in 1L than in 1S (2.91 Å vs 2.38 Å), the bridgehead hydrogen atoms in 1L are nearly 2 Å closer together than they are in 1S! The reason for this is immediately apparent in Figure 1: the bridgehead H-Si-Si angle is markedly smaller in 1L than in 1S. Therefore, the preference for a small bridgehead angle in the long bond isomer suggests that its relative stability will decrease as the size of the bridgehead groups increases. This is consistent with the data in Table 1.

Further evidence for increased steric crowding in the long bond isomers is found by examining the point group symmetries of the bond stretch local minima, which are summarized in Table 2.[10] For the parent compound, both bond stretch isomers are C_{2v}. In the dimethyl derivative, the short bond isomer (2S) is also C_{2v}, with the methyl groups in an eclipsed conformation (see Figure 2.[11]) However, in the long bond structure 2L, the C_{2v} conformation is no longer a local minimum but rather has one imaginary vibrational frequency, whose associated normal mode describes internal rotations of the methyl groups about the Si-C bonds. This is a result of the more severe steric crowding in the long bond isomer, which precludes an eclipsed conformation of the methyl groups. Consequently, 2L has a reduced degree of symmetry (C_s) in which the methyl groups are in a staggered arrangement.

In the di-tert-butyl derivative, the bridgehead substituents are sufficiently bulky that neither bond stretch isomer retains a C_{2v}-symmetric eclipsed conformation.[12] Furthermore, for both isomers the less-constrained C_s conformations with staggered arrangements of tert-butyl groups each have

220

a single imaginary frequency. However, for 3S the imaginary frequency of the C_s structure is small (approximately 61i cm^{-1}) so that the true 3S local minimum is anticipated to be very similar in geometry and energy to the C_s conformation, shown in Figure 3.[11] For 3L, a further distortion of the tert-butyl groups from C_s to C_2 is required to reach a local minimum (see Figure 3.)

IV. Conclusions

This theoretical study has predicted the existence of bond stretch isomers for the 1,3-dimethyl and 1,3-di-*tert*-butyl derivatives of tetrasilabicyclo[1.1.0]butane, at the GVB/3-21G* level of theory. For the dimethyl derivative, the long bond isomer 2L is more stable than 2S by 2 kcal/mol. However, the order of relative stability is reversed in the di-*tert*-butyl derivative. In this case, the short bond structure 3S is more stable than 3L by at least 3 kcal/mol. The predicted energetic preference for the short bond isomer is consistent with the X-ray crystal structure of the 1,3-di-*tert*-butyl-2,2,4,4-*tetrakis*-(2,6-diethylphenyl) derivative, where only the short bond isomer is observed.

This study has also shown that the relative energies of the bond stretch isomers of tetrasilabicyclo[1.1.0]butane systems are sensitive to the size of the bridgehead substituents. Because of the more severe steric crowding present in the long bond isomer, bulky groups tend to decrease its stability relative to the closed shell short bond structure.

Finally, the ability to perform *ab initio* electronic structure calculations on massively parallel computers such as the Touchstone Delta system enables the theoretical study of large molecules (such as 1,3-di-*tert*-butyltetrasilabicyclo[1.1.0]butane) which are beyond the capabilities of conventional computers.

References

1. J.A. Boatz and M.S. Gordon, *J. Phys. Chem.* 94, 7331(1990).

2. J.A. Boatz and M.S. Gordon, *J. Phys. Chem.* 93, 2888(1989), and references therein.

3. R. Jones, D.J. Williams, Y. Kabe, and S. Masamune, *Angew. Chem. Int. Ed. Engl.* 25, 173(1986).

4. a) W.A. Goddard III, T.H. Dunning, W.J. Hunt, and P.J. Hay, *Acc. Chem. Res.* 6, 368(1973).
   b) F.W. Bobrowicz and W.A. Goddard III, *Modern Theoretical Chemistry*; Vol. 3, H.F. Schaefer III, ed., Plenum Press, New York: 1977.

5. a) J.S. Binkley, J.A. Pople, and W.J. Hehre, *J. Am. Chem. Soc.* 102, 939(1980).
   b) W.J. Pietro, M.M. Francl, W.J. Hehre, D.J. DeFrees, J.A. Pople, and J.S. Binkley, *J. Am. Chem. Soc.* 104, 5039(1982).
   c) M.S. Gordon, *Chem. Phys. Lett.* 76, 163(1980).

6. This wavefunction is also known as a two-configuration self-consistent field (TCSCF) or a two-electron, two-orbital multiconfigurational SCF ([2e,2o] MCSCF) wavefunction.

7. M. Dupuis, D. Spangler, and J.J. Wendoloski, NRCC Software Catalog, 1980, 1, Program QG01.; M.W. Schmidt, J.A. Boatz, K.K. Baldridge, S. Koseki, M.S. Gordon, S.T. Elbert, and B. Lam, *Quantum Chemistry Program Exchange Bulletin* 7, 115(1987).; M.W. Schmidt, K.K. Baldridge, J.A. Boatz, J.H. Jensen, S. Koseki, M.S. Gordon, K.A. Nguyen, T.L. Windus, S.T. Elbert, *Quantum Chemistry Exchange Bulletin*, 10, 52(1990).

8. M.W. Schmidt, K.K. Baldridge, J.A. Boatz, S.T. Elbert, M.S. Gordon, J.H. Jensen, S. Koseki, N. Matsunaga, K.A. Nguyen, S. Su, and T.L. Windus, *J. Comp. Chem.*, in press.

9. Distances shown in Figure 1 are in Å. 1S and 1L denote the short and long bond isomers, respectively. The shaded (open) circles denote silicon (hydrogen) atoms.

10. The numbers in parentheses indicate the number of imaginary vibrational frequencies.

11. In Figures 2 and 3, two views of each local minimum are shown. The picture on the left is a "side" view, with the bridgehead silicon atoms lying in the plane of the page. The picture on the right is a "top" view, in which the bridgehead groups are closest to the viewer. The darkly (lightly) shaded circles denote silicon (carbon) atoms and the open circles denote hydrogen atoms.

12. Although the C_{2v} geometry and hessian of 3L have not been calculated, it seems reasonable to expect this conformation to be rather high in energy relative to its lower-symmetry conformations. Therefore, we assume that the C_{2v} conformation of 3L will have at least one imaginary vibrational frequency.

Table 1. Relative Energies of Bond Stretch Isomers.[a]
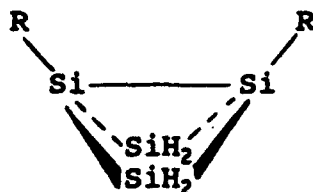
R	E(LB)-E(SB) (kcal/mol)	# Basis Functions
H	-9.6	88
CH_3	-1.9	114
$C(CH_3)_3$	≥ 3.2	192

[a] "E(LB)-E(SB)" denotes the difference in energies of the short and long bond isomers.

Table 2. Point Group Symmetries of Bond Stretch Isomers.[a]

R	SB	LB
H	C_{2v} (0)	C_{2v} (0)
CH_3	C_{2v} (0) C_s (1)	C_{2v} (1) C_s (0)
$C(CH_3)_3$	C_{2v} (1) C_s (1)[c]	C_{2v} (?)[b] C_s (1) C_2 (0)

[a] "SB" and "LB" denote the short and long bond isomers, respectively. The numbers in parentheses indicate the number of imaginary vibrational frequencies.

[b] See footnote 12.

[c] See text.

Figure 1

Figure 2

2S

2S

2L

2L

225
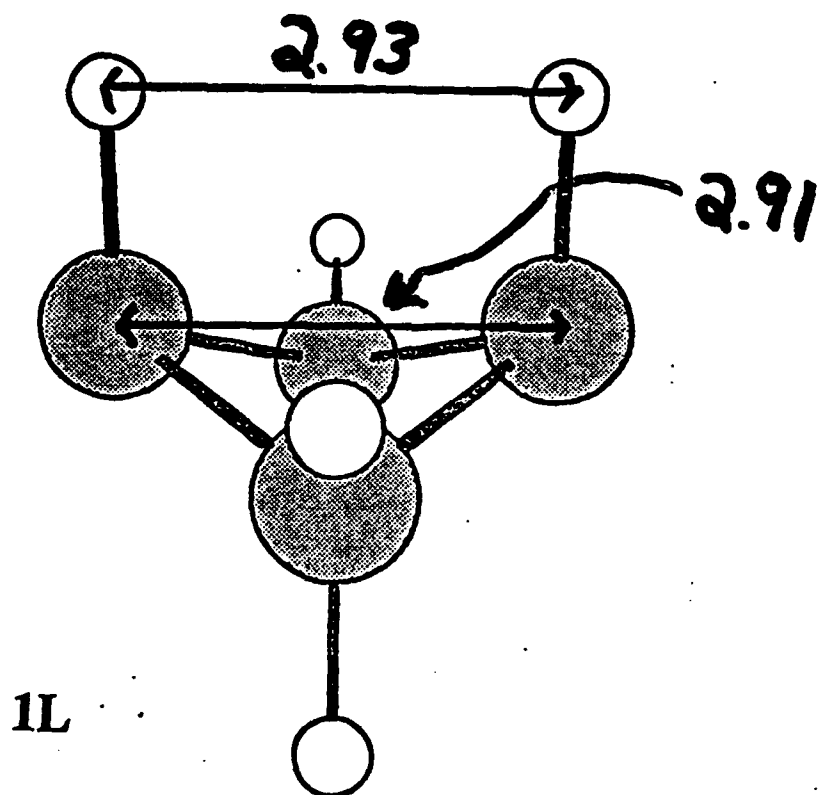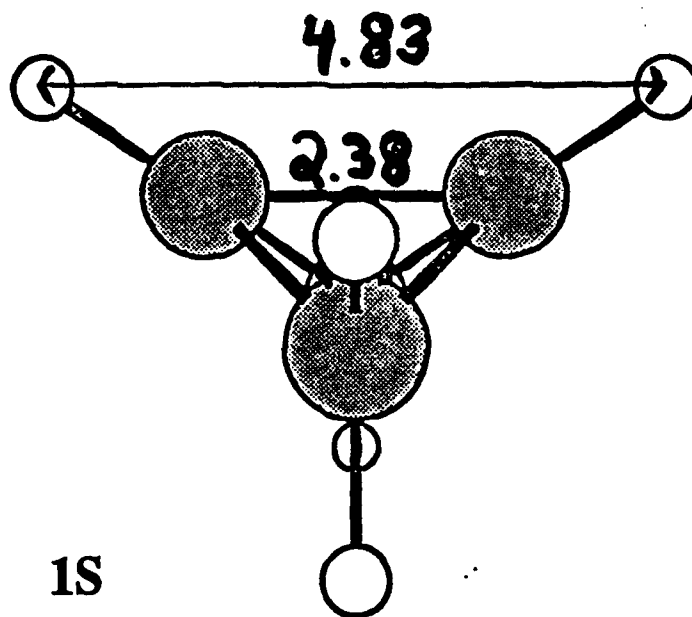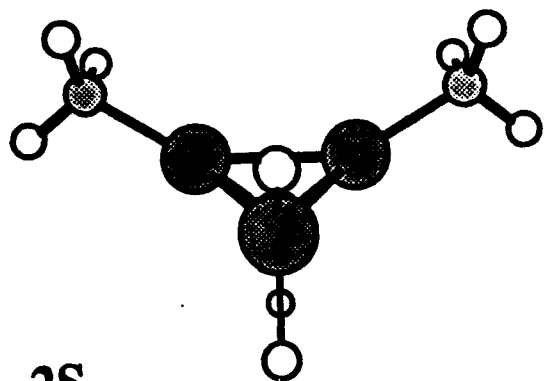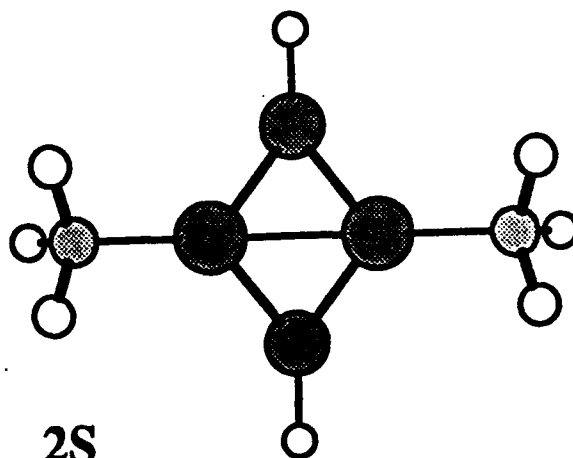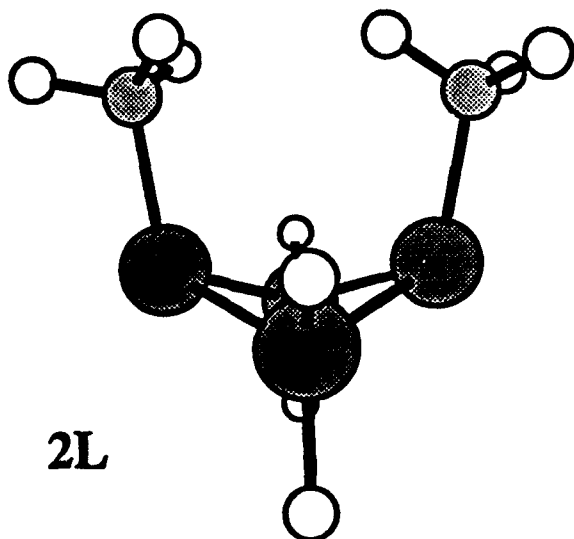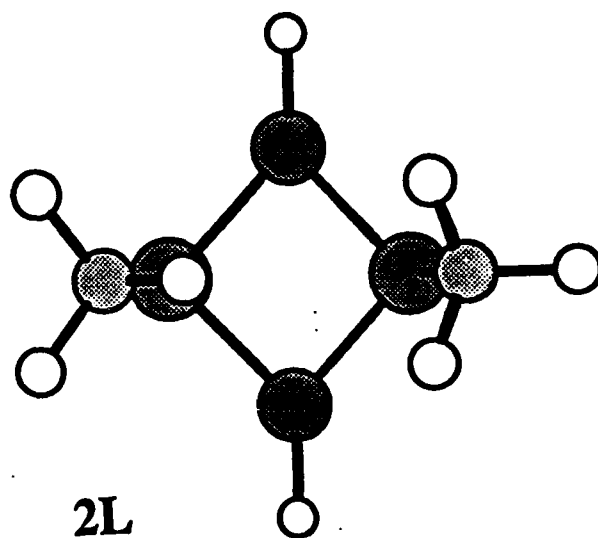
Figure 3
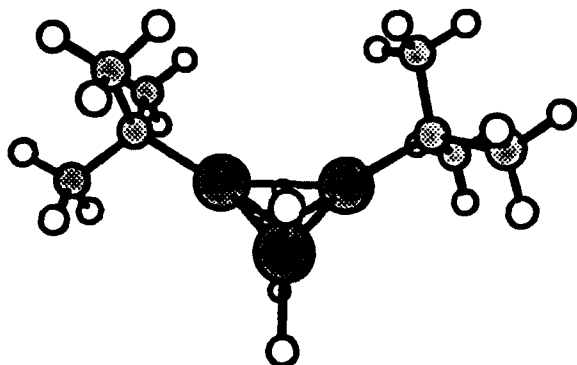
3S
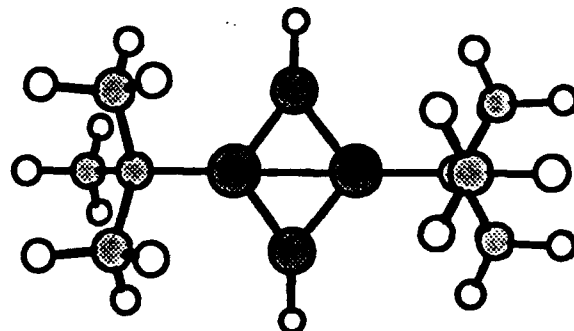
3S
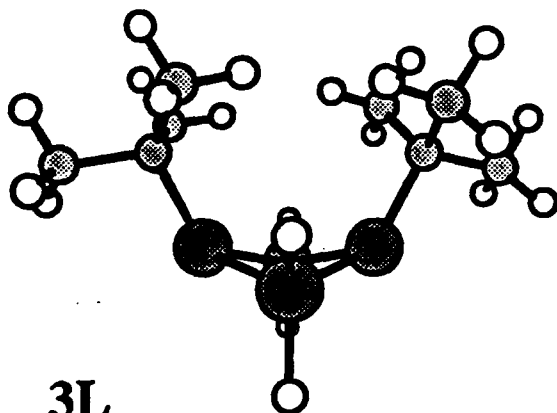
3L
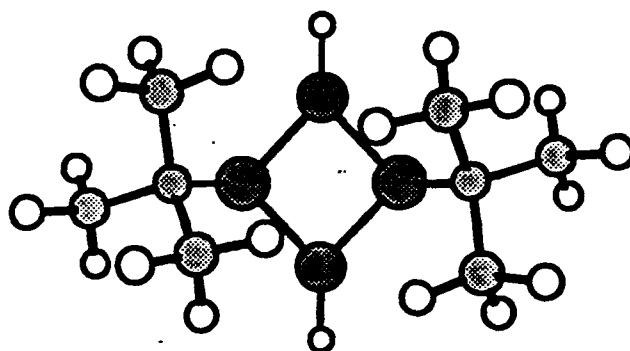
3L

1993 Air Force High Energy Density Matter (HEDM)

Contractors Conference

Woods Hole, MA
6-8 June, 1993

SYNTHESIS OF NEW ENERGETIC MATERIALS

Principal Investigator: Dr. Alan P. Marchand

Department of Chemistry, University of North Texas
NT Station, Box 5068, Denton, Texas 76203-0068

OBJECTIVE OF THE STUDY

To synthesize new high energy - high density polycarbocyclic bridged hydrocarbon systems.

Compounds of this type are of intense current interest to U. S. Military agencies as a promising new class of fuels for volume-limited applications

CRITERIA FOR SELECTION OF TARGET

MOLECULES FOR SYNTHESIS

(i) Compact Structures. The goal is to maximize density in order to achieve maximum net volumetric heat of combustion. Polycarbocyclic hydrocarbons, C_nH_m, are sought which maximize the ration n/m.

(ii) High Strain Energy Content, as evidenced by high, positive heat of formation. Polycyclic "cage" molecules are of particular interest in this connection.

(iii) Amenable to Relatively Large-Scale Laboratory Synthesis. Quantities of 100-500 grams are needed for testing and evaluation of fuel properties.

(iv) Liquids (or Low-Melting Solids) at Room Temperature. Alternatively, if the fuels are high-melting solids, they should be highly soluble in existing liquid fuel formulations (e.g., JP-10, RJ-6, etc.)

High Density Missile Fuels Research

Heptacyclo[$6.6.0.0^{2,6}.0^{3,13}.0^{4,11}.0^{5,9}.0^{10,14}$]
Tetradecane (HCTD)

$C_{14}H_{16}$

Pentacyclo[$5.4.0.0^{2,6}.0^{3,10}.0^{5,9}$]undecane
(PCUD)

$C_{11}H_{14}$
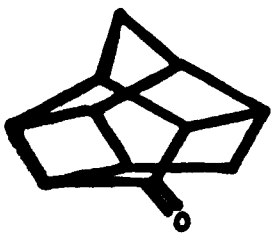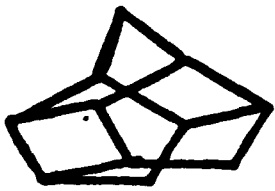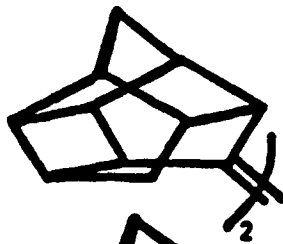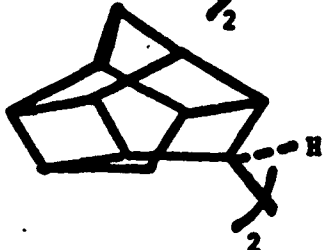
HIGH DENSITY MISSILE FUELS RESEARCH

COMPOUND	FORMULA	MP (°C)	DENSITY (g/cc)	ΔH_c (kcal/gm)	ΔH_c (kcal/cc)	%ΔH_c ABOVE HTPB
CYCLOPENTADIENE OLIGOMERS (CPDO)	$(C_5H_6)_n$	>200	1.13	8.65	13.90	15
BINOR S	$C_{14}H_{18}$	65	1.23	8.78	12.04	27
DIAMANTANE	$C_{14}H_{20}$	≈200	1.21	9.75	11.80	25
HTPB	$C_4H_6O_{0.05}$	0	0.93	10.16	9.46	0
HCTD	$C_{14}H_{18}$		1.26	9.52	11.90	(27)
PCUD	$C_{11}H_{14}$		1.23	10.00	12.30	(30)
PCUD DIONE	$C_{11}H_{10}O_2$		1.38	7.583	10.464	11

Table I. Calculated standard heats of formation and densities of cage hydrocarbons and cage ketones

Compound	Formula	ΔH_f° (kcal/mol)[a]	Density (g-cm^{-3})[b]
	$C_{11}H_{10}O_2$	-24.40	1.44 (observed, 1.38)
	$C_{11}H_{12}O$	+ 1.51	1.34
	$C_{11}H_{14}$	+27.42	1.23
	$C_{22}H_{24}$	+97.54	1.29
	$C_{22}H_{26}$	+67.76	1.26

[a] Calculated values. Method used for calculation of ΔH_f° values: Report on "Study of Pure Explosive Compounds. Part II. Correlation of Thermal Quantities with Explosive Properties"; Office of the Chief of Ordnance, Contract No. W-19-020-6436, Report No. C-57625, 2 April 1947.

[b] Calculated values. Method used for calculation of densities: J. R. Stine, "Prediction of Crystal Densities of Organic Explosives by Group Additivity", Los Alamos National Laboratory, Report No. LA-8920, August, 1981.

232
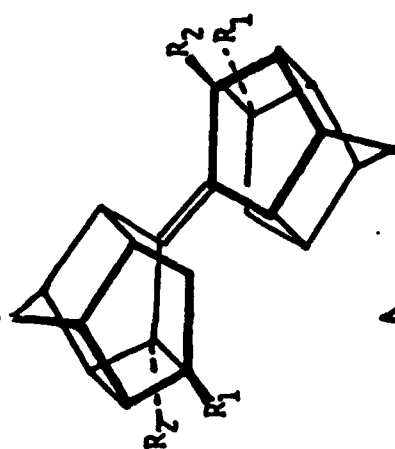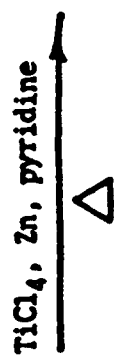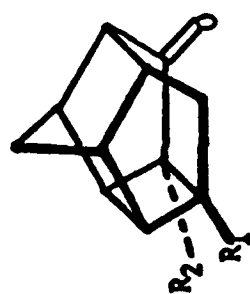
"S-shaped", anti
ACHIRAL (POINT SYMMETRY)
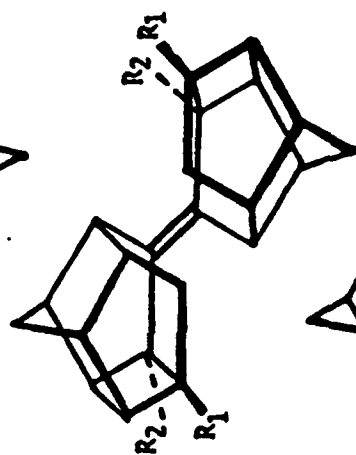
"C-shaped", anti
CHIRAL (C_2 AXIS)
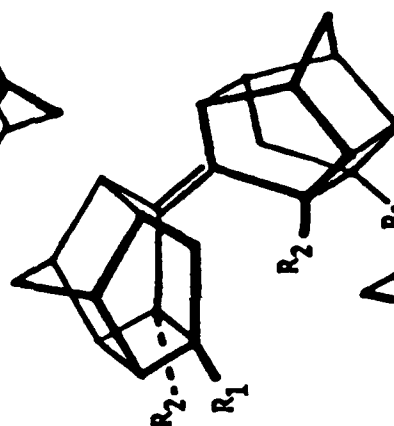
"S-shaped", syn
CHIRAL (C_2 AXIS)
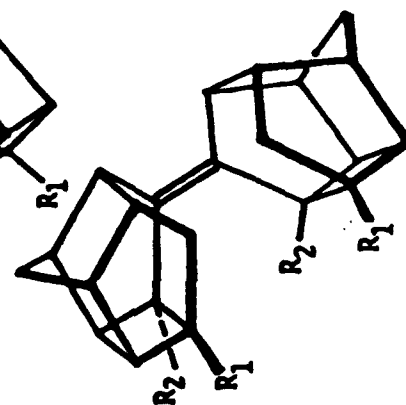
"C-shaped", syn
ACHIRAL (MESO)

$\xrightarrow[\triangle]{\text{TiCl}_4, \text{Zn, pyridine}}$

$R_1 = R_2 = H$

PCU ALKENE DIMERS: MM2 STERIC ENERGIES

COMPOUND	CONFIGURATION	TOTAL E_{steric} (kcal/mol)
	S-shaped, *anti*	130.9919
	C-shaped, *anti*	130.9815
	S-shaped, *syn*	130.8548
	C-shaped, *syn*	131.0292
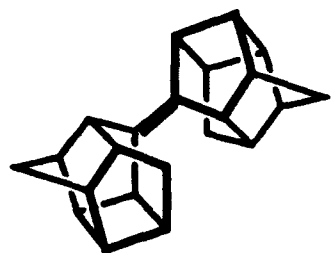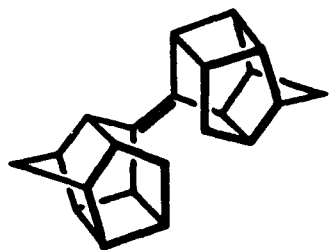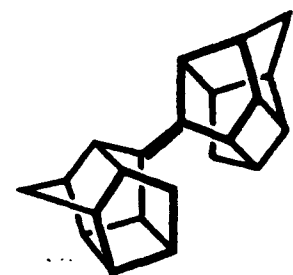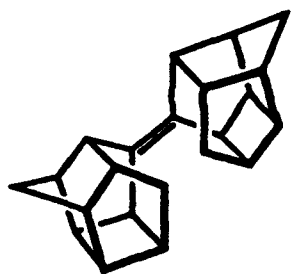
Structure of a Novel $C_{22}H_{24}$ Cage Dimer

By Judith L. Flippen-Anderson, Richard Gilardi and Clifford George

Laboratory for the Structure of Matter, Naval Research Laboratory, Washington, DC 20375, USA

and Alan P. Marchand, Pei-wen Jin and Mahendra N. Deshpande

Department of Chemistry, North Texas State University, Box 5068, Denton, Texas 87203, USA

Abstract. 8,11'-Bipentacyclo[5.4.0.0^{2,6}.0^{3,10}.0^{5,9}]-undecanylidene, $C_{22}H_{24}$, $M_r = 288 \cdot 43$, triclinic, $P\bar{1}$, $a = 6 \cdot 613$ (2), $b = 10 \cdot 809$ (3), $c = 10 \cdot 883$ (2) Å, $\alpha = 97 \cdot 52$ (2), $\beta = 99 \cdot 85$ (1), $\gamma = 99 \cdot 32$ (2)°, $V = 746 \cdot 2$ (2) Å^3, $Z = 2$, $D_x = 1 \cdot 284$ Mg m^{-3}, λ(Mo $K\alpha$) $= 0 \cdot 71073$ Å, $\mu = 0 \cdot 07$ mm^{-1}, $F(000) = 312$, $T = 295$ K, final $R = 0 \cdot 048$, $wR = 0 \cdot 048$ for 1118 observed reflections. The molecule, which has an unusually high density for a hydrocarbon, consists of two cage moieties which are related by an approximate twofold axis along the C(11)–C(11') double bond. There are no intermolecular approaches less than van der Waals separations; the high density is probably due to compression of the cage C atoms ensuing from the small bond angles. For example, the internal ring angles at C(11) and C(11'), both sp^2 C atoms, are only 102·6 (2) and 102·2 (2)°, respectively.
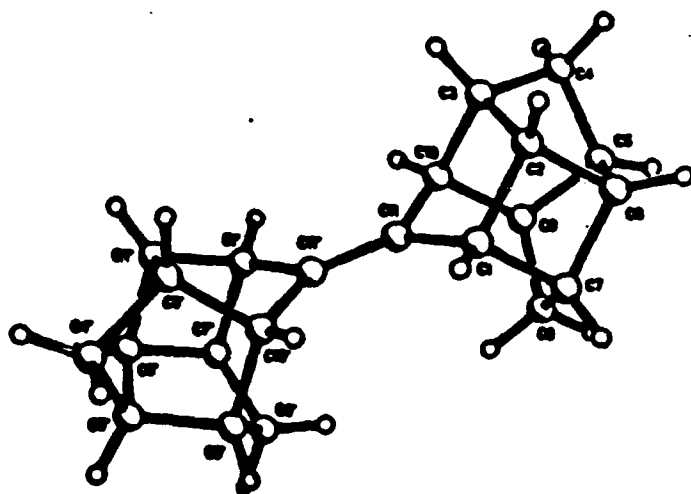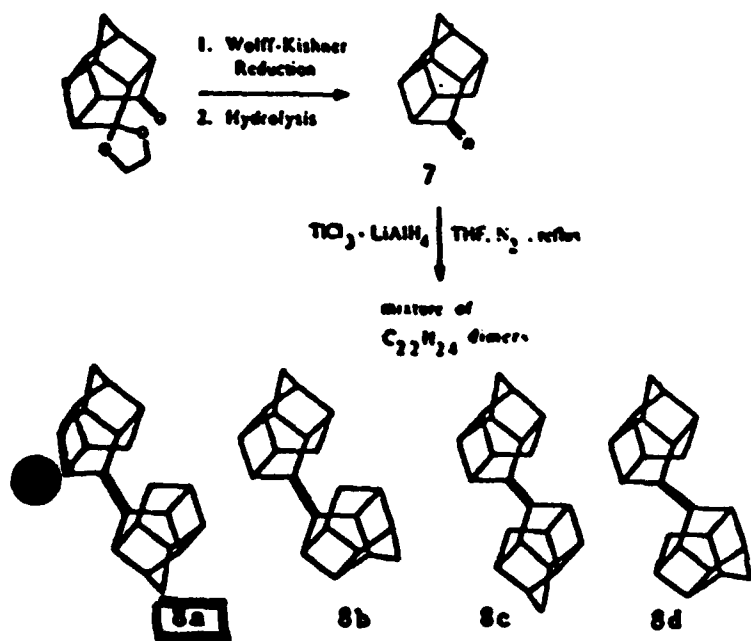
Fig. 1. Results of the X-ray study on 8a

SYNTHESIS OF METHYLATED PCU ALKENE DIMERS

(60 : 40)

1a + 1b

hv, Pyrex

EtOAc, 16 h
(84%)

2a + 2b

HOCH₂CH₂OH, TsOH

benzene, Dean-Stark apparatus
(96%)

3 (mixture of isomers)

Wolff-Kishner

reduction

4 (mixture of isomers)

10% aqueous HCl

THF, 25 °C, 15 h
(80%)

5 (mixture of isomers)

TiCl₄, Zn

pyridine, THF
reflux 22 h

6 (mixture of isomers, 73%)   7 (mixture of isomers, 19%)
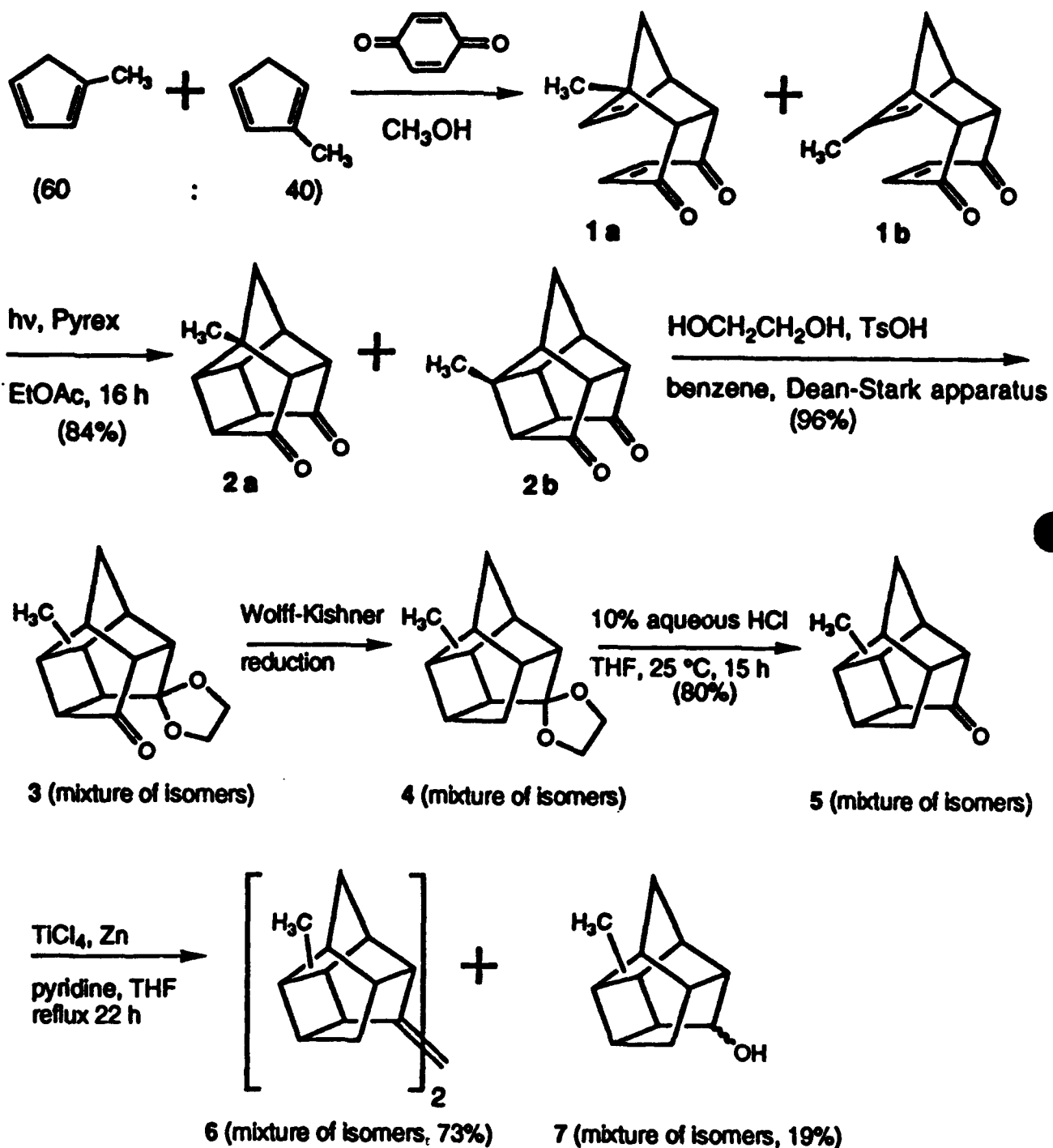
ISOLATION AND CHARACTERIZATION OF AN ISOMERICALLY PURE METHYLATED PCU ALKENE DIMER

The mixture of isomeric alkene dimers obtained via Ti(0)-promoted reductive dimerization of methylated PCU-8-ones was purified via column chromatography followed by fractional recrystallization. This purification procedure afforded an isomerically pure methylated PCU alkene dimer, **6a**, whose structure has been elucidated via X-ray crystallographic methods. A structure drawing of this compound appears below. The crystal density of **6a**, calculated from the X-ray derived unit cell parameters, is <u>1.286 g-cm^{-3}</u>.
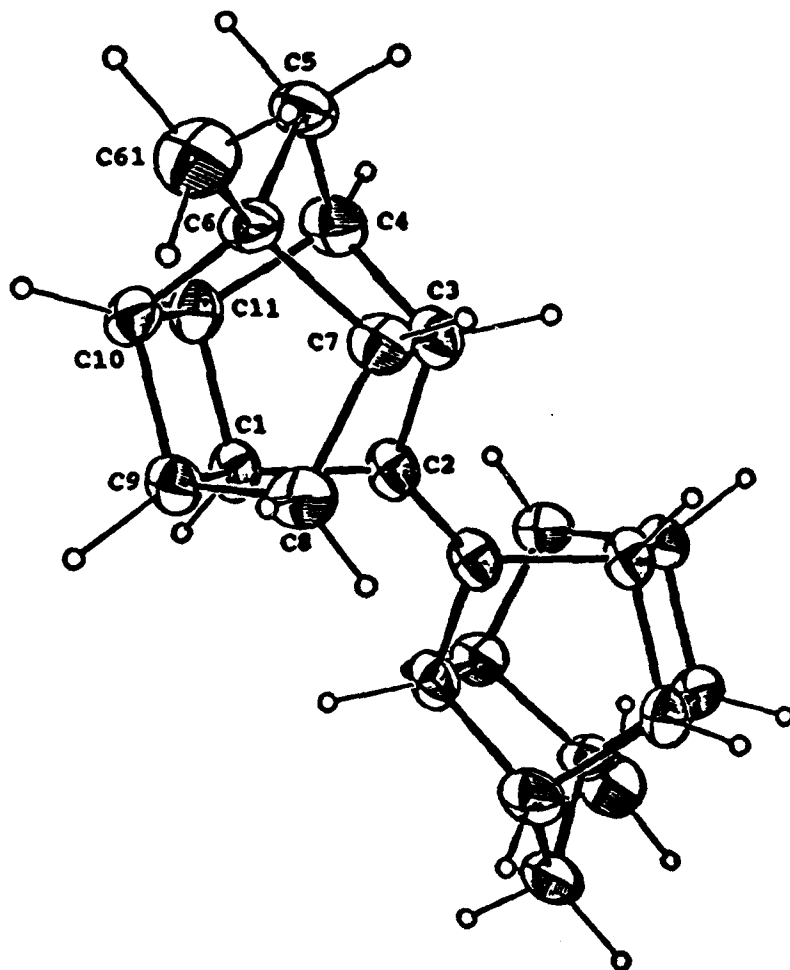
Structure drawing of **6a**

237

1993 HEDM Contractors Conference

Structures of Three Methylated PCU Alkene Dimers
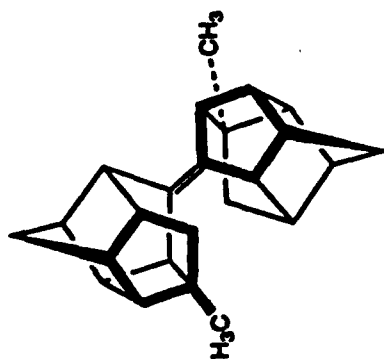
$D_c = 1.261$ g-cm^{-3}
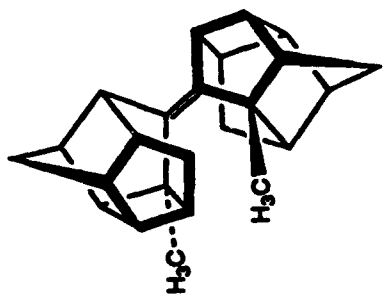
$D_c = 1.251$ g-cm^{-3}
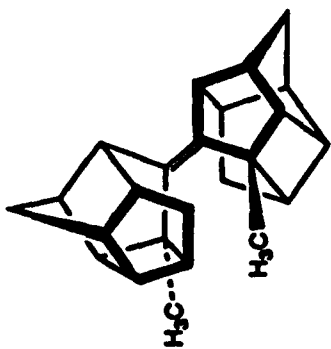
$D_c = 1.212$ g-cm^{-3}
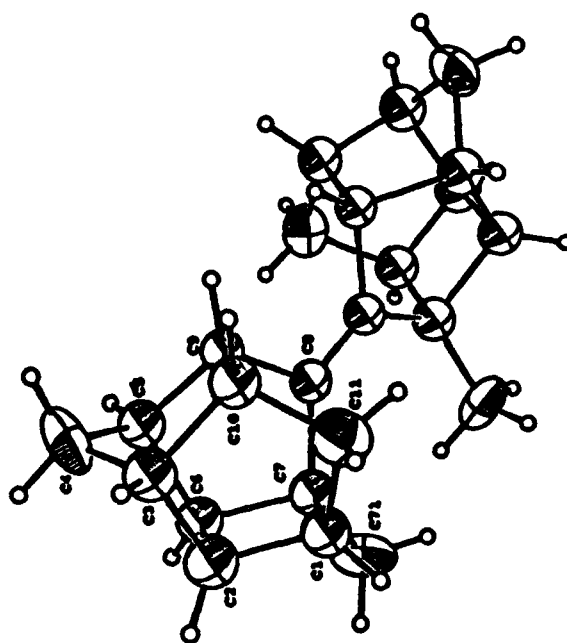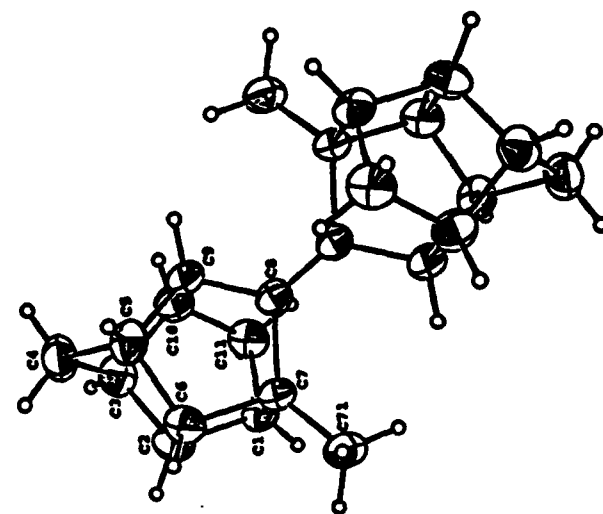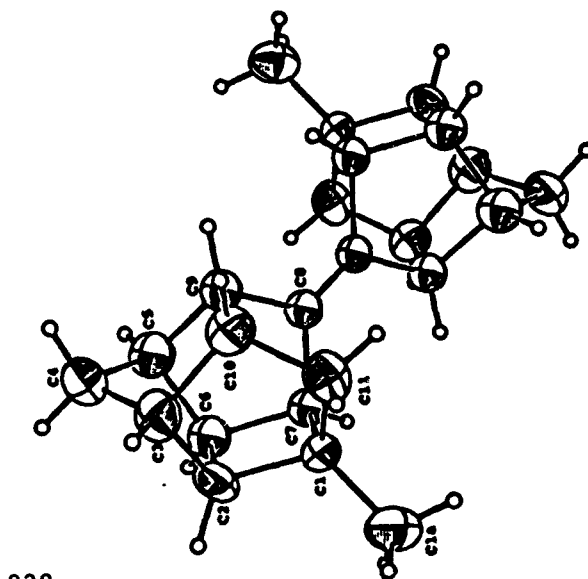
Synthesis and Reactions of *meso-* and *dl-D₃*-Trishomocubylidene-*D₃*-trishomocubane

Alan P. Marchand,*,[1] G. Madhusudhan Reddy,[1] Mahendra N. Deshpande,[1]
William H. Watson,*,[2] Ante Nagl,[2] Oh Seuk Lee,[1] and Eiji Osawa*,[3]

*Contribution from the Department of Chemistry, University of North Texas,
Denton, Texas 76203-5068, the Department of Chemistry, Texas Christian University,
Fort Worth, Texas 76129, and the Department of Chemistry, Faculty of Science, Hokkaido
University, Sapporo 060, Japan. Received April 26, 1989.
Revised Manuscript Received December 2, 1989*

Scheme I
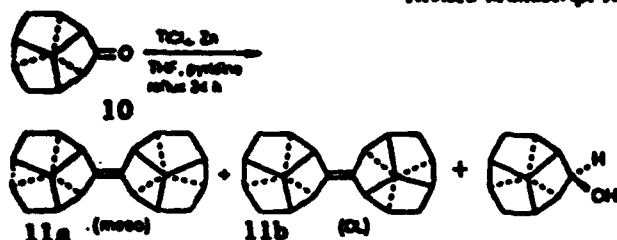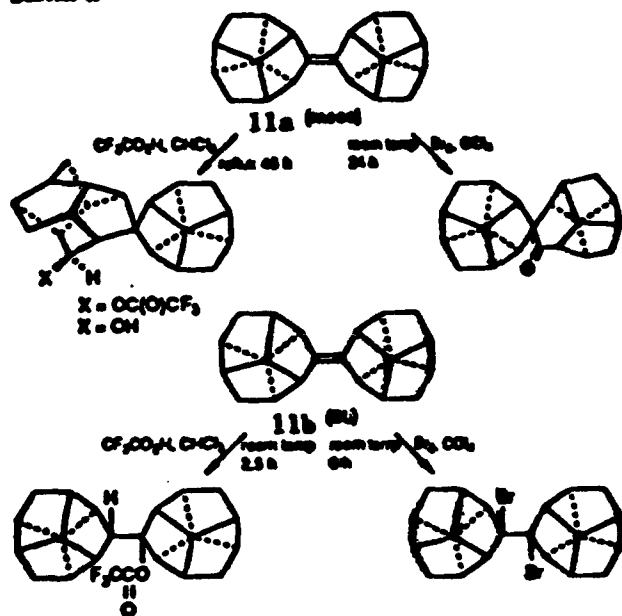
Scheme II
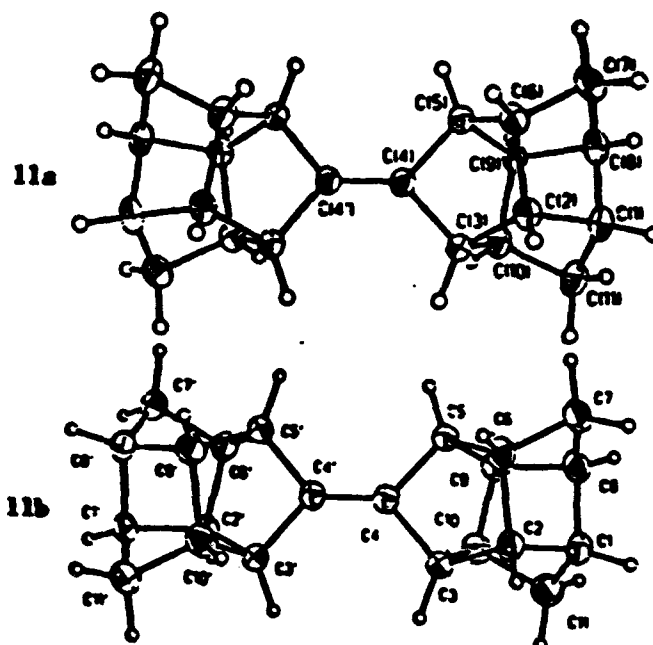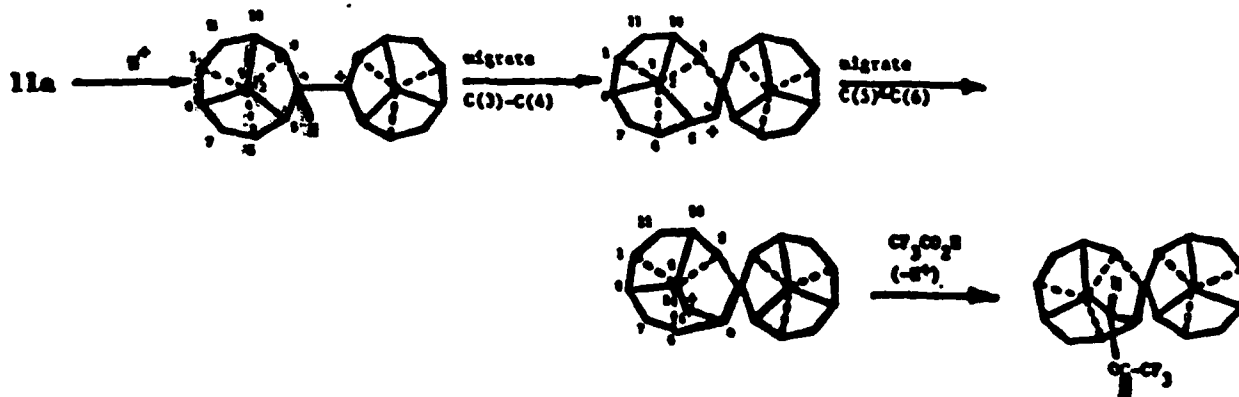
Figure 1. (Top) structure drawing of 11a; (bottom) structure drawing of 11b

Scheme III
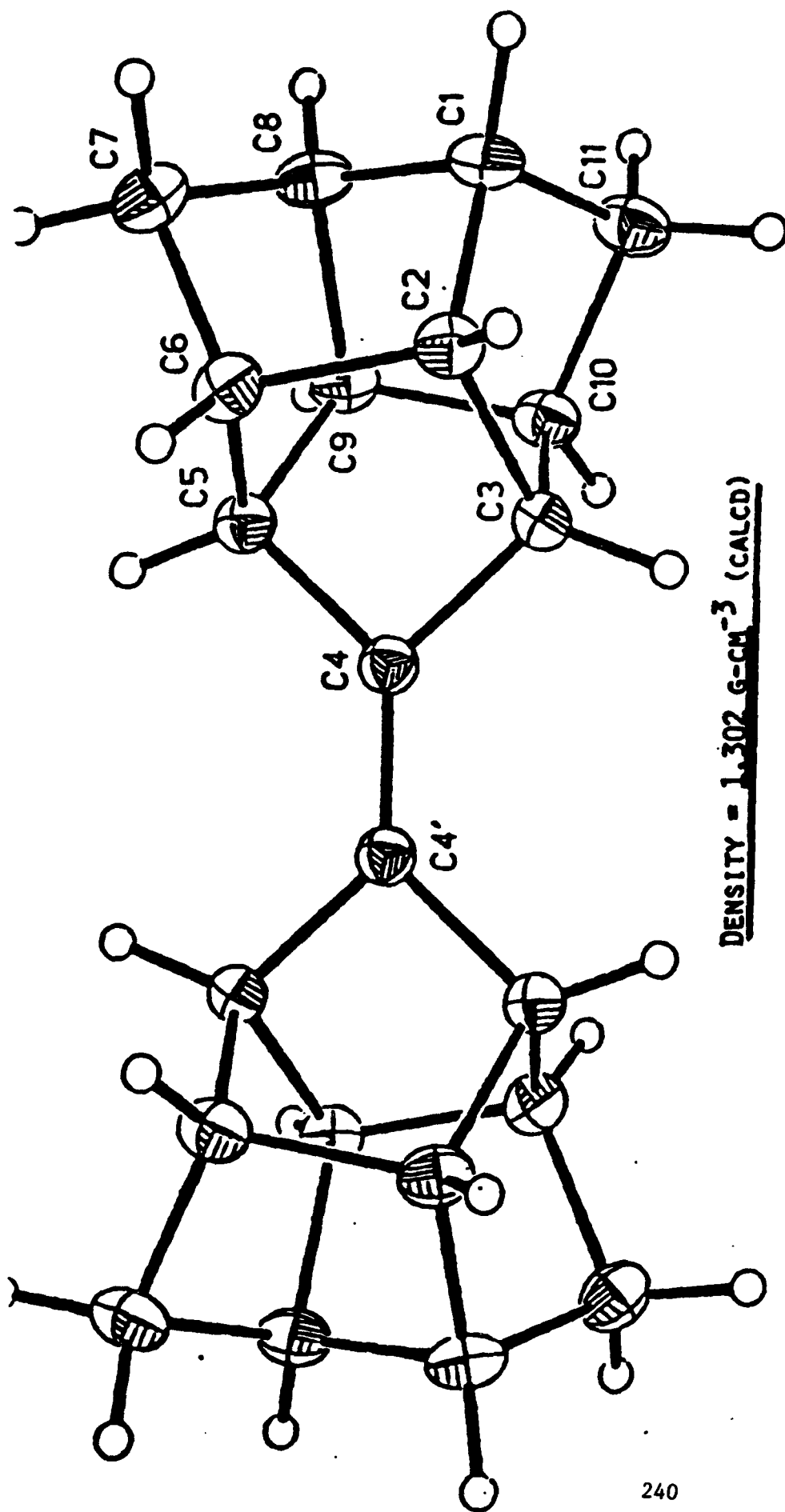
DENSITY = 1.302 G-CM^{-3} (CALCD)

7B (D,L)

7A (MESO)

+

$\xrightarrow[\text{REFLUX 24 H (65\%)}]{\text{TiCl}_4\text{-Zn, THF} \atop \text{PYRIDINE, N}_2}$

6
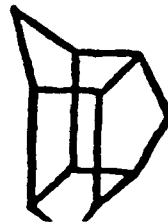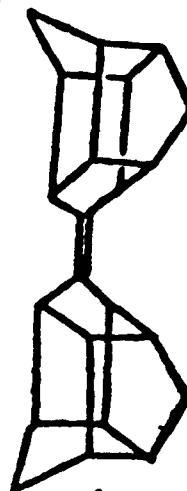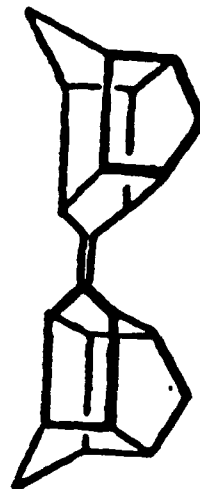
THE MESO ISOMER (7A) WAS ISOLATED VIA CAREFUL FRACTIONAL RECRYSTALLIZATION OF THE PRODUCT MIXTURE FROM LIGROIN. THE MATERIAL THEREBY OBTAINED DISPLAYED MP 246 °C.

SYNTHESIS: A. P. MARCHAND, M. N. DESHPANDE, AND G. MADHUSUDHAN REDDY, UNIVERSITY OF NORTH TEXAS

X-RAY CRYSTALLOGRAPHY: WILLIAM H. WATSON AND ANTE NAGL, DEPARTMENT OF CHEMISTRY, TEXAS CHRISTIAN UNIVERSITY, FORT WORTH, TEXAS 76129
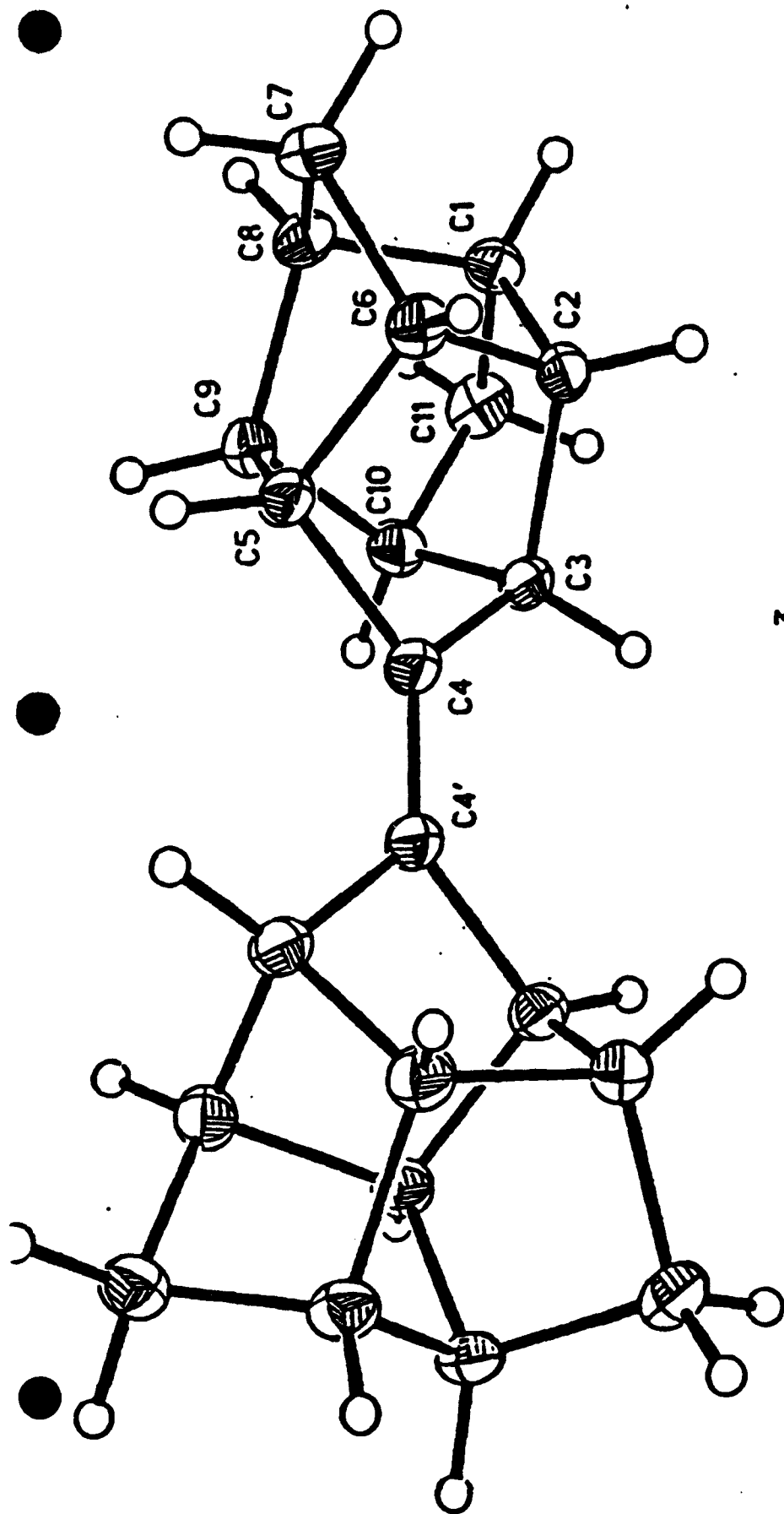
DENSITY = 1.269 $g-cm^{-3}$ (CALCD)

WE HAVE ALSO ISOLATED THE D,L DIMER, 7B, MP 186 °C (RECRYSTALLIZED FROM HEXANE-ETHER).
THE D,L ISOMER CRYSTALLIZES IN SPACE GROUP PĪ (TRICLINIC); IT IS SIGNIFICANTLY LESS DENSE
THAN THE CORRESPONDING MESO ISOMER (SPACE GROUP C2/C, MONOCLINIC, DENSITY = 1.302 $g-cm^{-3}$).

SYNTHESIS: A. P. MARCHAND, M. N. DESHPANDE, AND G. MADHUSUDHAN REDDY, UNIVERSITY OF NORTH TEXAS
X-RAY CRYSTALLOGRAPHY: WILLIAM H. WATSON AND ANTE NAGL, DEPARTMENT OF CHEMISTRY
TEXAS CHRISTIAN UNIVERSITY, FORT WORTH, TEXAS 76129

ATOMIZATION AND RADIATION PROPERTIES OF *MESO-* AND *D,L*-TRISHOMOCUBYLIDENETRISHOMOCUBANES

meso- and d,l-D_3-Trishomocubylidene-D_3-trishomocubane have been synthesized via Ti(0) promoted reductive dimerization of D_3-trishomocubanone:
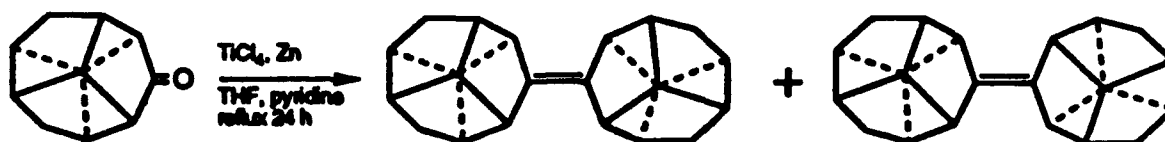
Reference: Marchand, A. P., et al. *J. Am. Chem. Soc.* 1990, *112*, 3521.

Atomization and radiation properties of a mixture of these $C_{22}H_{24}$ alkene dimers have been studied by Sojka and Gore (1992).

ATOMIZATION AND RADIATION PROPERTIES OF MESO-

AND D,L-TRISHOMOCUBYLIDENETRISHOMOCUBANES

CONCLUSIONS:

Temperature dependence of $C_{22}H_{24}$/RJ-4 mixture viscosities: Increase in $C_{22}H_{24}$ loading leads to an increase in the mixture viscosity. However, the increase in mixing viscosity with increased loading becomes negligible as the temperature approaches 50 °C.

Since fuel temperatures in gas turbine atomizers usually exceed 100 °C, this observation suggests that such fuel mixtures will have viscosities almost equal to that of the solvent (RJ-4) and therefore should form roughly equivalent mean drop size sprays.

Reference: Sojka, P. E.; Gore, J. P. *Atomization and Radiation Properties of High Energy-High Density Fuel Components,* AIAA 92-3378.

ATOMIZATION AND RADIATION PROPERTIES OF HIGH

ENERGY-HIGH DENSITY FUELS

CONCLUSIONS (contd.)

2. Measured radiation heat flux from RJ-4, JP-10, and toluene:

RJ-4 and JP-10 were chosen for study as representatives of fuel currently being burned in cruise missile gas turbines. Toluene was chosen as representative of proposed high energy-high density fuel mixtures due to a sooting tendency that is comparable to that of dihydrobenzvalene.

Plots of radiative heat flux vs. radial distance reveal that the heat flux levels for the JP-10 flames are roughly twice as great as compared to those for the RJ-4 flames, while the corresponding heat flux levels for the toluene flames are ca. *10 times greater* than the corresponding levels for JP-10 flames.

Thus, flame radiation data demonstrate an order of magnitude increase in radiation heat flux when a fuel with high carbon/hydrogen ratio is substituted for currently used gas turbine fuels.

The radiation data suggest that combustor wall cooling may be required in gas turbines which employ high energy-high density fuels.

Reference: Sojka, P. E.; Gore, J. P. *Atomization and Radiation Properties of High Energy-High Density Fuel Components*, AIAA 92-3378.

Large-Scale Synthesis of PCU Alkene Dimers, 6a-6d

endo-Tricyclo[6.2.1.0^{2,7}]undeca-4,9-diene-3,6-dione (1). *p*-Benzoquinone (415 g, 3.84 mol) and MeOH (2 L) were placed in a 4 L beaker, and the resulting suspension was cooled externally (ice-water bath) to 0 - 5 °C. To this cooled suspension was added dropwise with vigorous stirring freshly cracked cyclopentadiene (265 g, 4.02 mol) at such a rate, that the temperature of the reaction mixture did not exceed 10 °C The mixture was then allowed to stand at 0 - 5 °C for 19 h, at which time the mother liquor was decanted and the product was collected via suction filtration. The product was thoroughly air dried for 24 h and then recrystallized batchwise from hexane. The product, 1 (431 g, 65%), was thereby obtained as a yellow microcrystalline solid, which is suitable for use in the next (intramolecular photocylization) step. *Note:* It important to remove unreacted *p*-benzo-quinone from the product, as this material has been found to interfere with the subsequent intramolecular [2 + 2] photocyclization of the Diels-Alder adduct.

Pentacyclo[5.4.0.0^{2,6}.0^{3,10}.0^{5,9}]undecane-8,11-dione (2). A solution of 1 (431 g, 2.39 mol) in acetone (3 L) in a 4 L beaker was irradiated with a 450 W medium pressure Hg lamp until starting material could no longer be detected by thin layer chromatographic analysis of the reaction mixture. (*DANGER:* Acetone may ignite if the vapors come into contact with the hot lamp). The reaction mixture was concentrated in vacuo, thereby affording an almost colorless product, which can be employed in the next synthetic step without further purification.

Pentacyclo[5.4.0.0^{2,6}.0^{3,10}.0^{5,9}]undecane-8,11-dione Mono(ethylene acetal) (3). A mixture of diketone 2 (900 g, 5.2 mol), ethylene glycol (400 mL), toluene (*ca.* 2 L) and *p*-TsOH (30 g, 0.16 mol) was placed in a 5 L three-neck boiling flask which had been fitted with a Dean-Stark apparatus. The reaction mixture was refluxed and stirred magnetically. Water was distilled azeotropically from the reaction mixture and removed periodically by draining the Dean-Stark trap. The reaction was complete after *ca.* 4 h. The flask was then stoppered and cooled to room temperature by application of an external ice-water bath. Solid K$_2$CO$_3$ (33 g, 0.24 mol) was added with stirring, followed by addition of water (300 mL). The resulting mixture was shaken, and the two phases were allowed to separate slowly while standing overnight at room temperature. (*NOTE:* Avoid overly vigorous shaking, as a tight emulsion can result.) The aqueous layer was extracted with toluene (1 x 100 mL) and the combined organic layers were washed with brine (2 x 200 ml), dried (MgSO$_4$) and concentrated in vacuo (15 Torr.) until the recovery of toluene was completed. The hot residue was poured into a tared baker or plastic container, where it crystallized upon cooling. The resulting brown solid,(*ca.* 100%) is sufficiently pure to be used in the subsequent reaction

Pentacyclo[5.4.0.0^{2,6}.0^{3,10}.0^{5,9}]undecan-8-one Mono-(ethylene acetal) (4). A mixture of 4 (1500 g, 6.88 mol), diethylene glycol (6 L) and hydrazine hydrate (2.5 L) was placed in a 12 L three-necked flask, and the reaction mixture was refluxed with mechanical stirring for a minimum of 3 h (5-6 h may be better). The reaction mixture then was allowed to cool slowly (overnight) to room temperature. The refulx condenser then was replaced by a distillation apparatus, and volatiles were removed by distillation (internal temperature of the reaction mixture: 160 °C). After 1 L of distillate had been collected, heating was discontinued, and solid K$_2$CO$_3$ (700 g) was added portionwise with stirring to the hot reaction mixture at such a rate that mechanical stirring could be mantained smoothly and gas evolution did not become too violent. (The added K$_2$CO$_3$ should almost completely dissolve in the hot reaction mixture.) Heating then was re-

sumed, and distillation of volatile materials was continued (*ca.* 1.3 L) until the internal temperature of the reaction mixture reached 220 °C. This temperature then was maintained for a minimum of 3.5 h (4 or 5 h may be better). (*NOTE:* Once the Wolff-Kishner reduction has been initiated, the reaction should *not* be interrupted until the conclusion of the final period of heating at 220 °C.) The reaction mixture then was cooled to room temperature, and volatiles were removed by batchwise distillation in vacuo (15 Torr.) from a 2 L flask (boiling range *ca.* 140-170 °C). At the beginning of the distillation, an azeotropic mixture of diethylene glycol and product was collected in the distillate. However, as the distillation progresses, the distillate became clear. The residue was discarded. The combined distillates were placed in a separatory funnel. The upper layer was collected, and then water (500 mL) was added. The resulting mixture was extracted with CH_2Cl_2 (2 x 100 mL), and the combined extracts were added to the lower layer. The resulting solution was washed with water (1 x 100 mL), dried (Na_2SO_4), and concentrated in vacuo (15 Torr, 40 °C). The residue, a colorless oil, was used without further purification in the next step.

Pentacyclo[5.4.0.0^{2,6}.0^{3,10}.0^{5,9}]undecan-8-one (5). To the crude 4 obtained from the preceding reaction was added THF (600 mL), water (600 mL) and concentrated aqueous HCl (80 mL), and the resulting mixture was stirred at room temperature for 18 h. The layers then were separated, and the upper layer was extracted with CH_2Cl_2 (2 x 150 mL). The combined organic layers were washed sequentially with water (300 mL) and saturated aqueous $NaHCO_3$(300 mL), dried (Na_2SO_4), filtered, and concentrated in vacuo (15 Torr, 40 °C). The residue (solid + oil) was collected by suction filtration. A colorless solid (235 g) was thereby obtained. Toluene (100 mL) was added to the filtrate, and the resulting mixture was concentrated in vacuo. The residue again was collected by suction filtration. An additional 196 g of almost colorless product was thereby obtained. The total yield of 5 was 431 g (39% yield for two synthetic steps).

Titanium-promoted Dimerization of 5. Into a 12 L three-necked, argon-filled flask equipped with an argon bubbler and mechanical stirrer was added reagent grade THF (8 L, precooled to 0 °C) from a freshly opened bottle. Then, TiCl$_4$ (480 g, 2.53 mol) was added dropwise with stirring (without external cooling). To the resulting warm yellow mixture was added powdered Zn (340 g, 5.20 mol), and the reaction mixture then was refluxed for 3 h. To the resulting hot reaction mixture was added a dropwise with stirring a solution of 5 (169 g, 1.06 mol) in pyridine (240 mL), and the resulting mixture was refluxed for 43 h. At the conclusion of the reflux period, the heating source was removed, and the reaction mixture was allowed to stand at room temperature for 24 h. A mixture of water (300 mL), ice (300 mL), and concentrated aqueous HCl (50 mL) was added slowly with stirring to the reaction mixture. The resulting black mass was poured over ice (5 kg) and then allowed to stand overnight in an open vessel. The reaction mixture then was extracted with hexane (2 x 200 mL), and the combined extracts were washed with water (1 x 100 mL), filtered and concentrated in vacuo (15 Torr). The residue was triturated with ac   ▪ (250 mL). The resulting colorless precipitate was collected by suction filtration and air-dried. A mixture of isomeric alkene dimers, 6a-6c, was thereby obtained as a colorless solid (78 g, 51%), mp 174-188 °C. An additional 10 g (7%) of 6a-6c could be obtained from the mother liquor.

RESEARCH PLANS FOR FY93

LARGE-SCALE PREPARATION

OF PCU ALKENE DIMER

Attempt at Ti(0)-promoted Reductive Coupling of
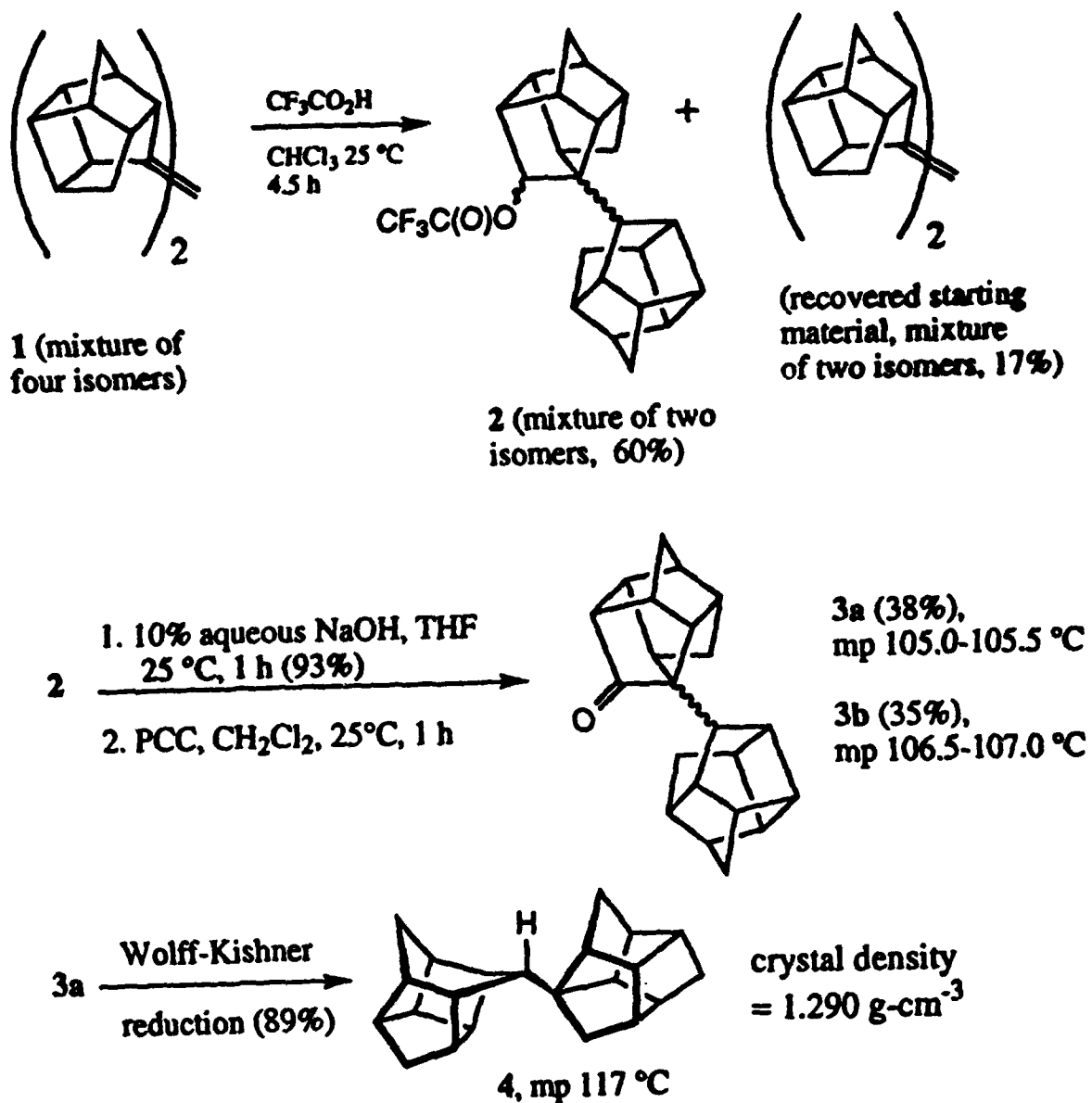Pentacyclo[5.4.0.0^{2,6}.0^{3,10}.0^{5,9}]undecan-8-one

TiCl$_4$, pyridine, Zn

ultrasound, heat

(mixture of isomers)

RESEARCH PLANS FOR FY93

LARGE-SCALE PREPARATION

OF PCU ALKENE DIMER

Attempt at Ti(0)-promoted Reductive Coupling of Pentacyclo[5.4.0.0^{2,6}.0^{3,10}.0^{5,9}]undecan-8-one

Modification of McMurray C=O Coupling

R = H, Me (mixture of isomers)
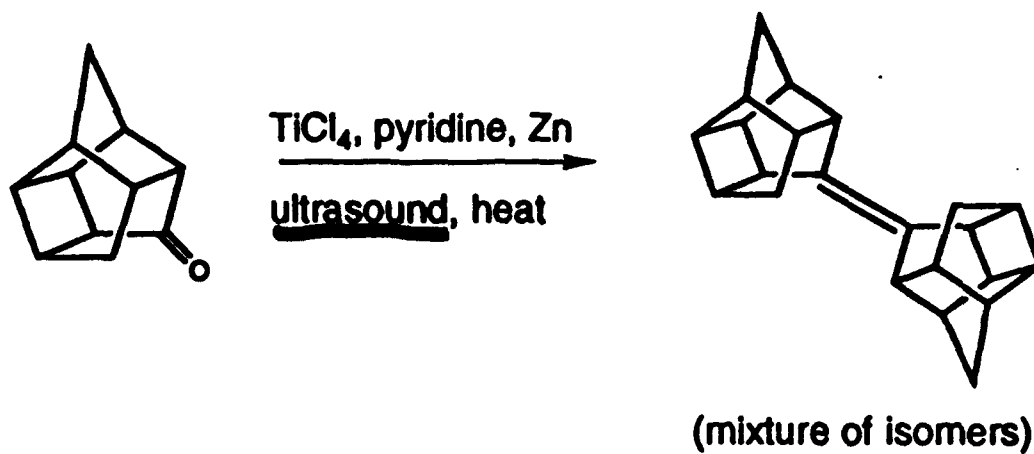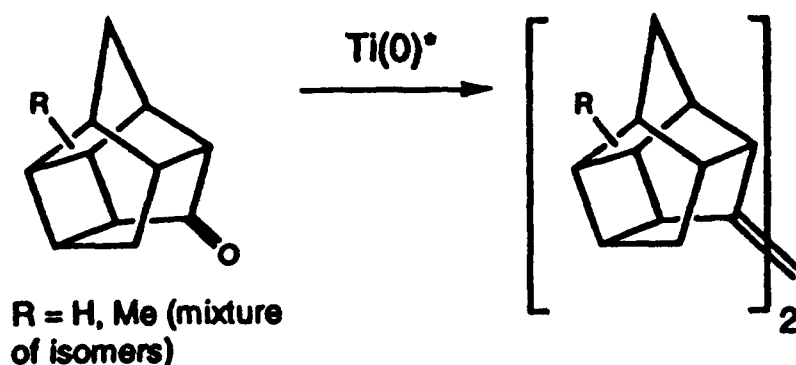
*Ti(0) is prepared *in situ* via reaction of TiCl$_4$ with _activated Zn_ in pyridine-THF solvent.

Preparation of activated Zinc:

1. A mixture of Zn powder and 1,2-dibromoethane in THF is heated under argon at 40-50 °C for *ca.* 15 min.

2. The reaction mixture is concentrated *in vacuo*, and the residue is dried *in vacuo* at 100 °C for 1 h. The resulting activated Zn is then used to reduce TiCl$_4$ to Ti(0) in the usual manner.

3. When this procedure was applied to reduction of PCU-8-one (R = H, 50 gram scale), the corresponding PCU alkene dimer could be obtained in **42% yield.**

RESEARCH PLANS FOR FY93

LARGE-SCALE PREPARATION

OF PCU ALKENE DIMER

Attempt at Ti(0)-promoted Reductive Coupling of
Pentacyclo[5.4.0.0^{2,6}.0^{3,10}.0^{5,9}]undecan-8-one

Modification of McMurray C=O Coupling

R = H, Me (mixture
of isomers)
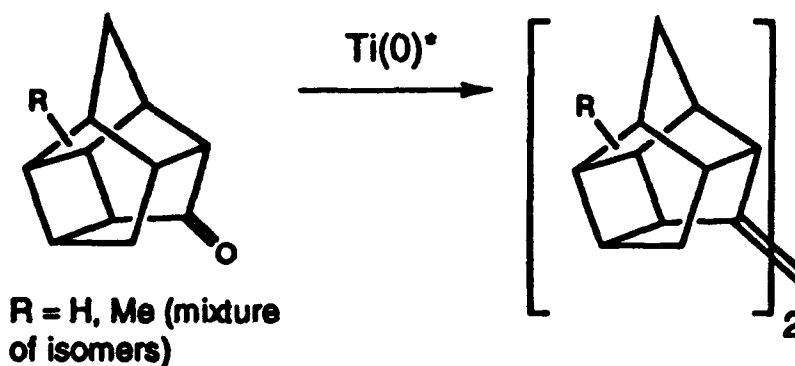
*Ti(0) is prepared *in situ* via reaction of TiCl$_4$ with Mg (2
equivalents) in dry THF (-70 °C to +25 °C).

Reference:

Betschart, C.; Seebach, D. *Helv. Chim Acta* **1987**, *70*, 2215.

Synthesis of a Novel C$_{22}$H$_{26}$ Hydrocarbon

1 (mixture of four isomers)

CF$_3$CO$_2$H

CHCl$_3$, 25 °C
4.5 h

CF$_3$C(O)O

2 (mixture of two isomers, 60%)

(recovered starting material, mixture of two isomers, 17%)

2

1. 10% aqueous NaOH, THF
25 °C, 1 h (93%)

2. PCC, CH$_2$Cl$_2$, 25°C, 1 h

3a (38%),
mp 105.0-105.5 °C

3b (35%),
mp 106.5-107.0 °C

3a

Wolff-Kishner

reduction (89%)

crystal density
= 1.290 g-cm^{-3}

4, mp 117 °C

Synthesis: Dr. M. N. Deshpande
X-ray Structure: Prof. W. H. Watson
Dr. Ram P. Kashyap

Synthesis of a Novel $C_{22}H_{26}$ Hydrocarbon
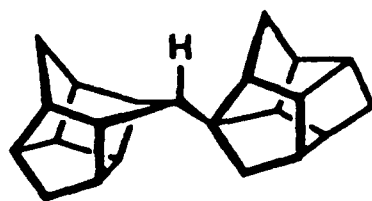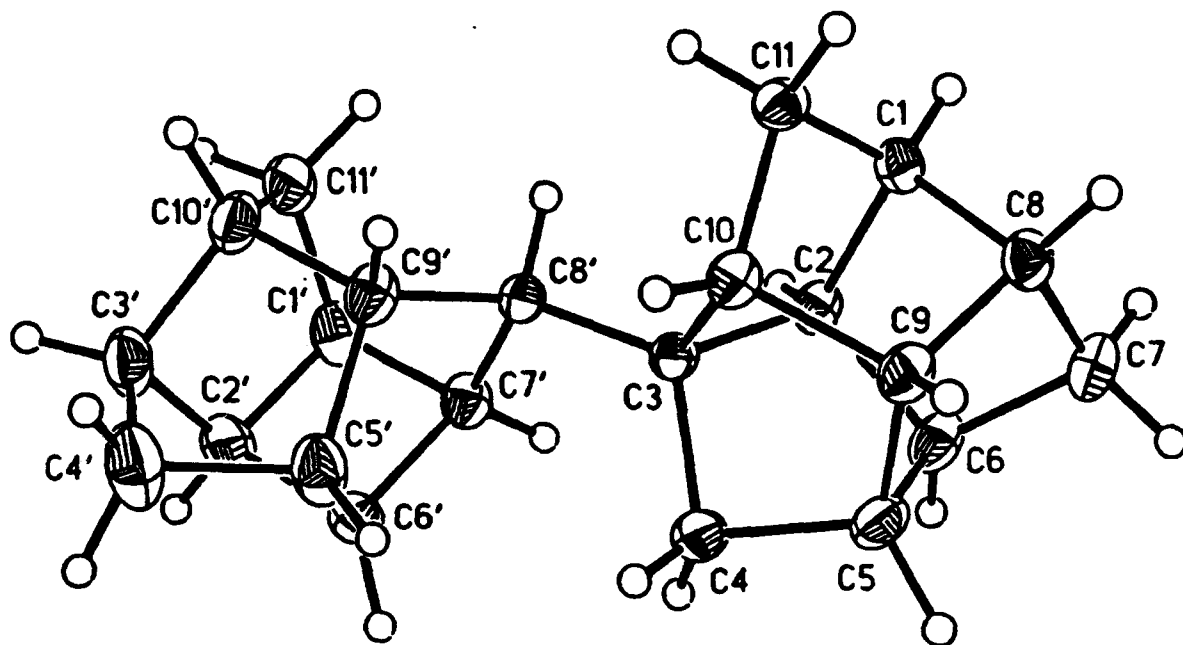
crystal density
= 1.290 g-cm^{-3}

mp 117 °C

Synthesis: Dr. M. N. Deshpande

X-ray Structure: Prof. W. H. Watson
Dr. Ram P. Kashyap

RESEARCH PLANS FOR FY93

LARGE-SCALE PREPARATION

OF PCU ALKENE DIMER

Attempt to promote Crank-Eastwood pinacol
bis-dehydroxylation:

(mixture of isomers)
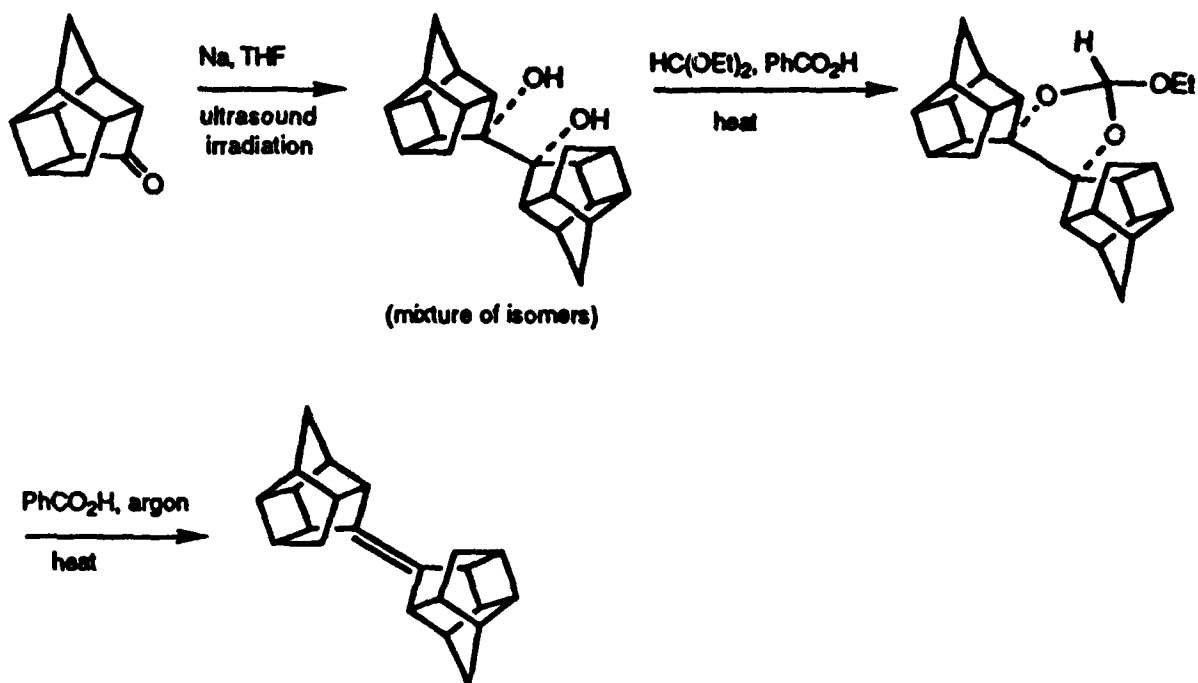
References:

Crank, G.; Eastwood, F. W. *Aust. J. Chem.* **1964**, *17*, 1392;
Josan, J. S.; Eastwood, F. W., *Aust. J. Chem.* **1968**, *21*, 2013.

Marchand, A. P.; Vidyasagar, V.; Watson, W. H.; Nagl, A.;
Kashyap, R. P. *J. Org. Chem.* **1991**, *56*, 282.

RESEARCH PLANS FOR FY93

Pinacol Condensation of PCU-8-one

Pinacol condensation of PCU-8-one is expected to afford a mixture of isomeric *vic*-diols. Acid-promoted rearrangement of this diol mixture should produce the corresponding mixture of spiropolycyclic cage ketones. Wolff-Kishner Reduction of the carbonyl group in these "pinacolones" is expected to provide an isomeric mixture of the corresponding polycyclic cage hydrocarbons. These spirocyclic hydrocarbons are of interest as a potential new class of high energy-high density fuels.
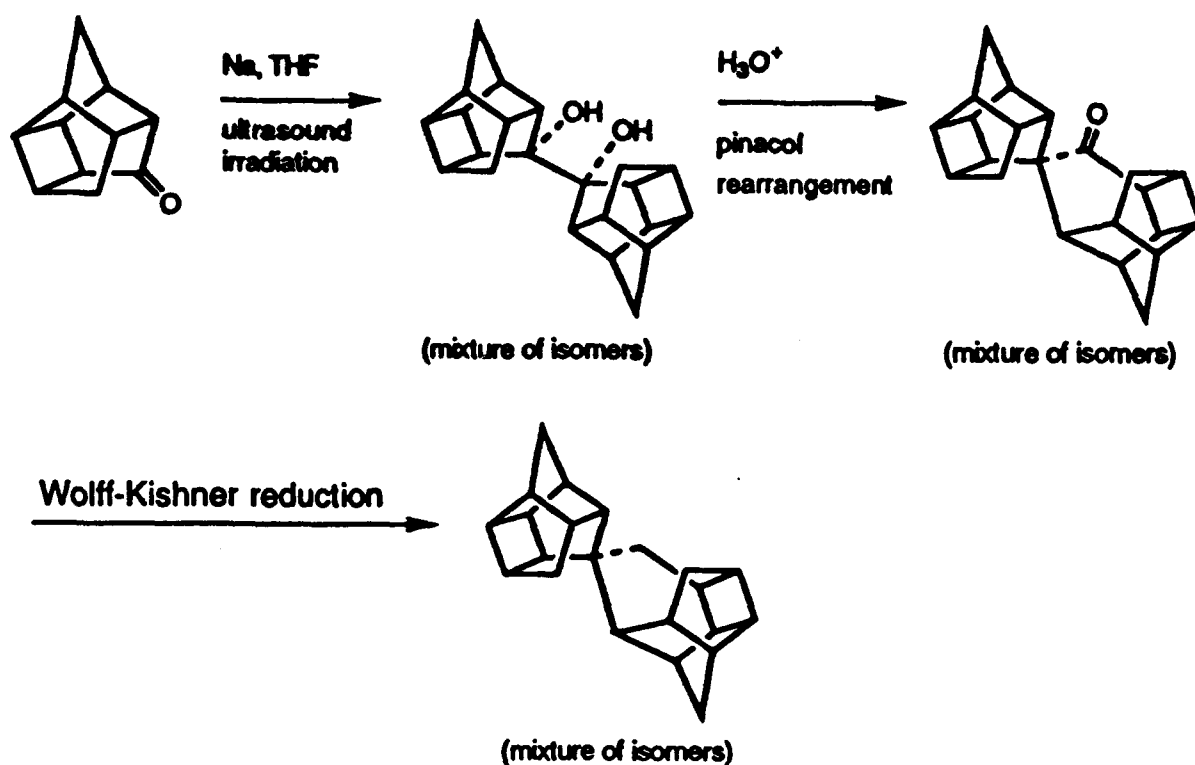
(mixture of isomers)   (mixture of isomers)

(mixture of isomers)

Na, dry THF

argon, sonicate
30 minutes, 25 °C

(mixture of isomeric pinacols
obtained via Na-promoted reductive
dimerization of PCU-8-one)

**MIXTURE OF
PINACOLS**

1. Fractional recrystallization from
CH₂Cl₂-hexane (to obtain a single,
pure isomer, mp 231-232 °C)

2. SOCl₂, pyridine, 0 °C
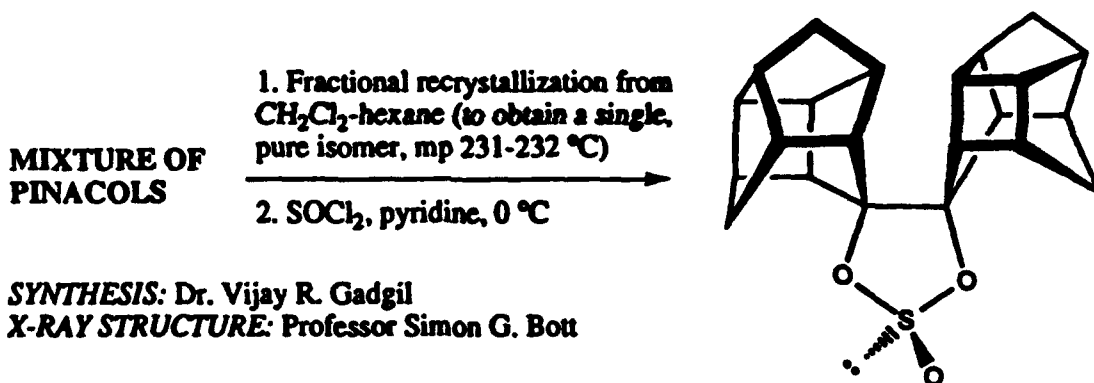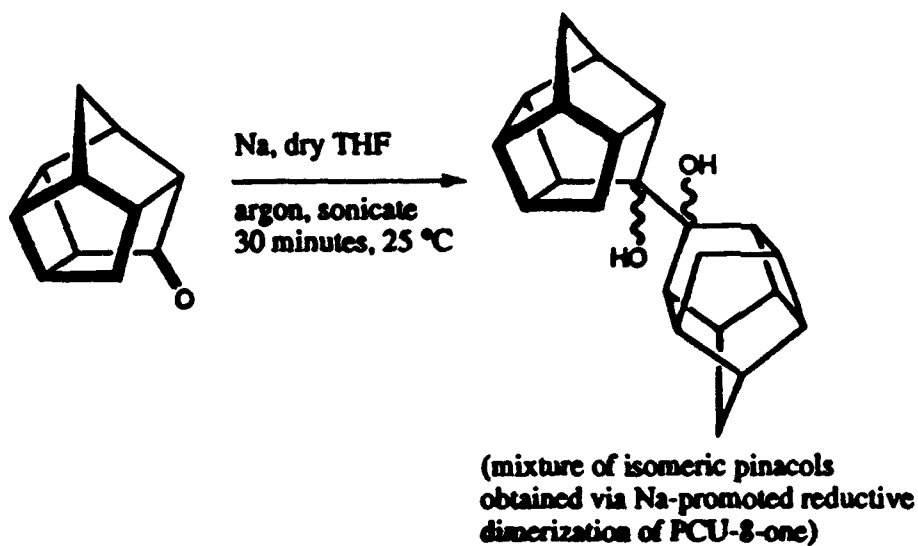
SYNTHESIS: Dr. Vijay R. Gadgil
X-RAY STRUCTURE: Professor Simon G. Bott
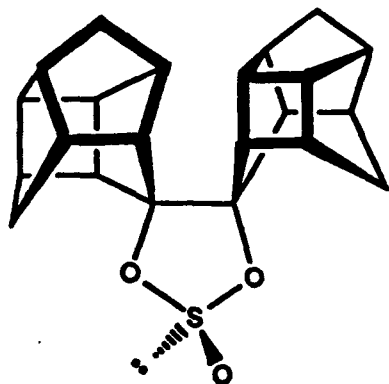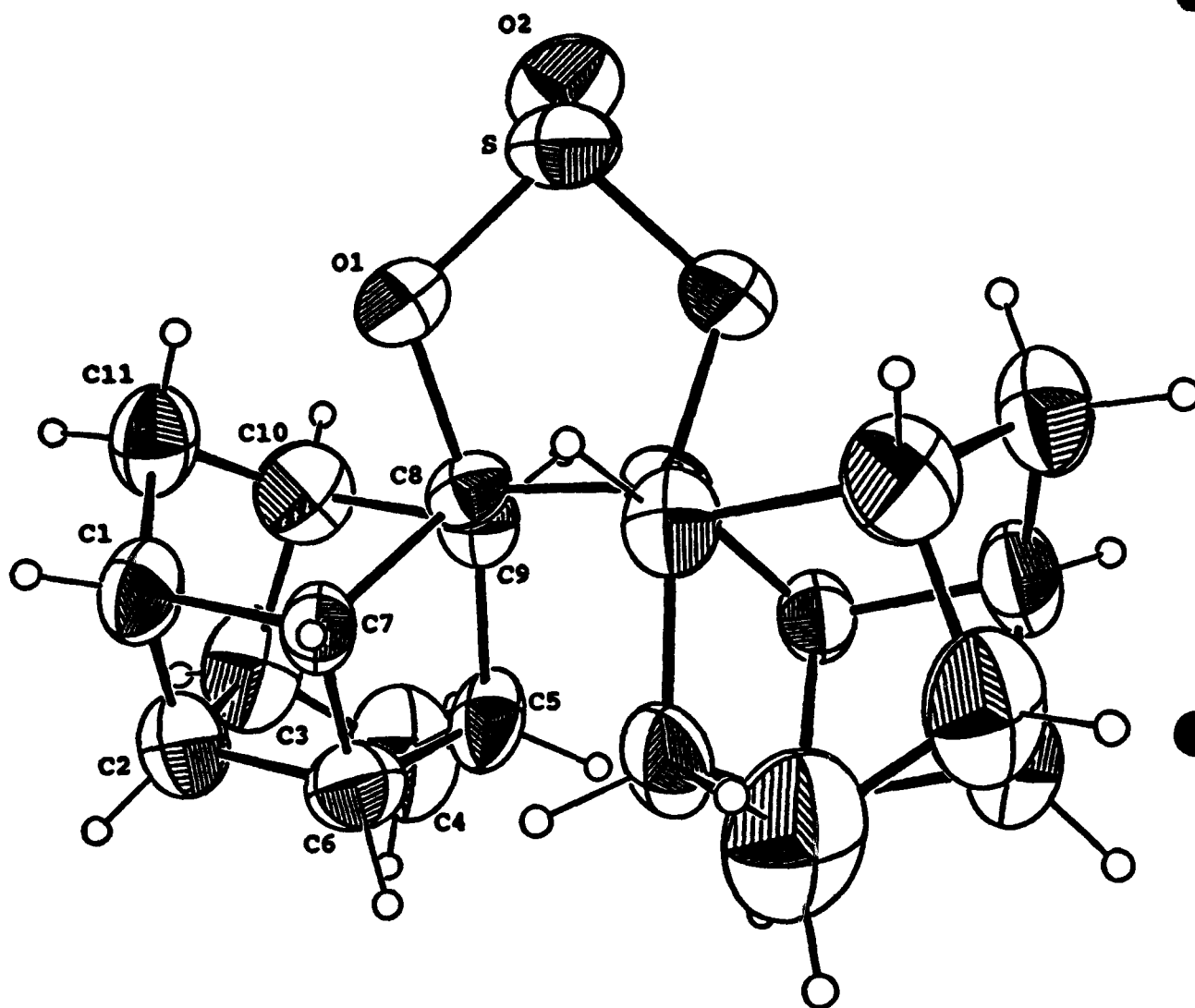
Synthesis: Dr. Vijay R. Gadgil

X-Ray Structure: Prof. Simon G. Bott

Na, dry THF

argon, sonicate
30 minutes, 25 °C

(mixture of isomeric pinacols
obtained via Na-promoted reductive
dimerization of PCU-8-one)
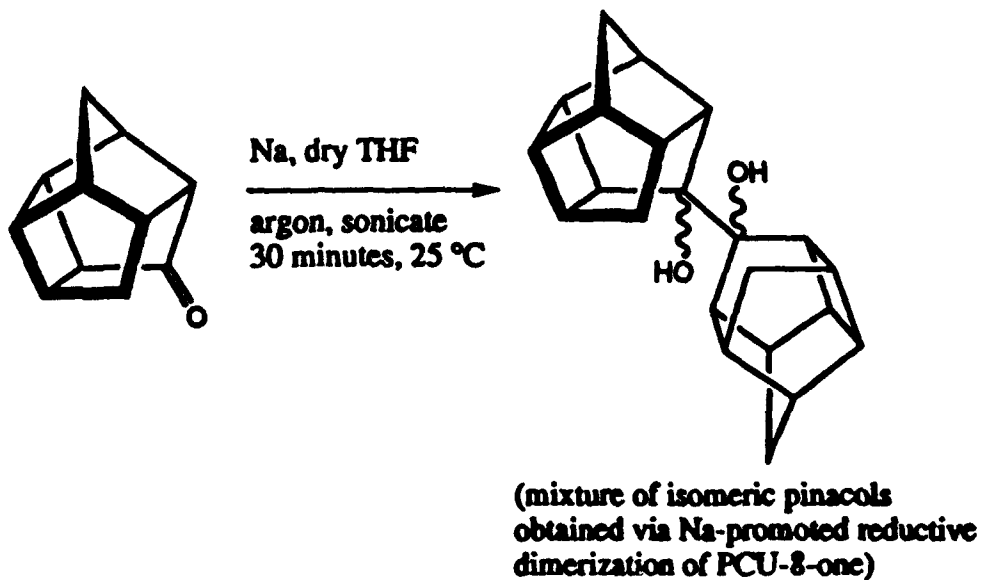
**MIXTURE OF
PINACOLS**

Fractional recrystallization from
EtOAc-hexane (to obtain a single,
pure isomer, mp 226-227 °C)
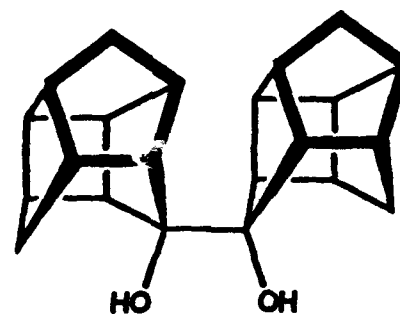
meso-pinacol

SYNTHESIS: Mr. Zenghui Liu
X-RAY STRUCTURE: Professor Simon G. Bott

Pinacol rearrangement might proceed with migration
of either (or both) bond (a) or bond (b):
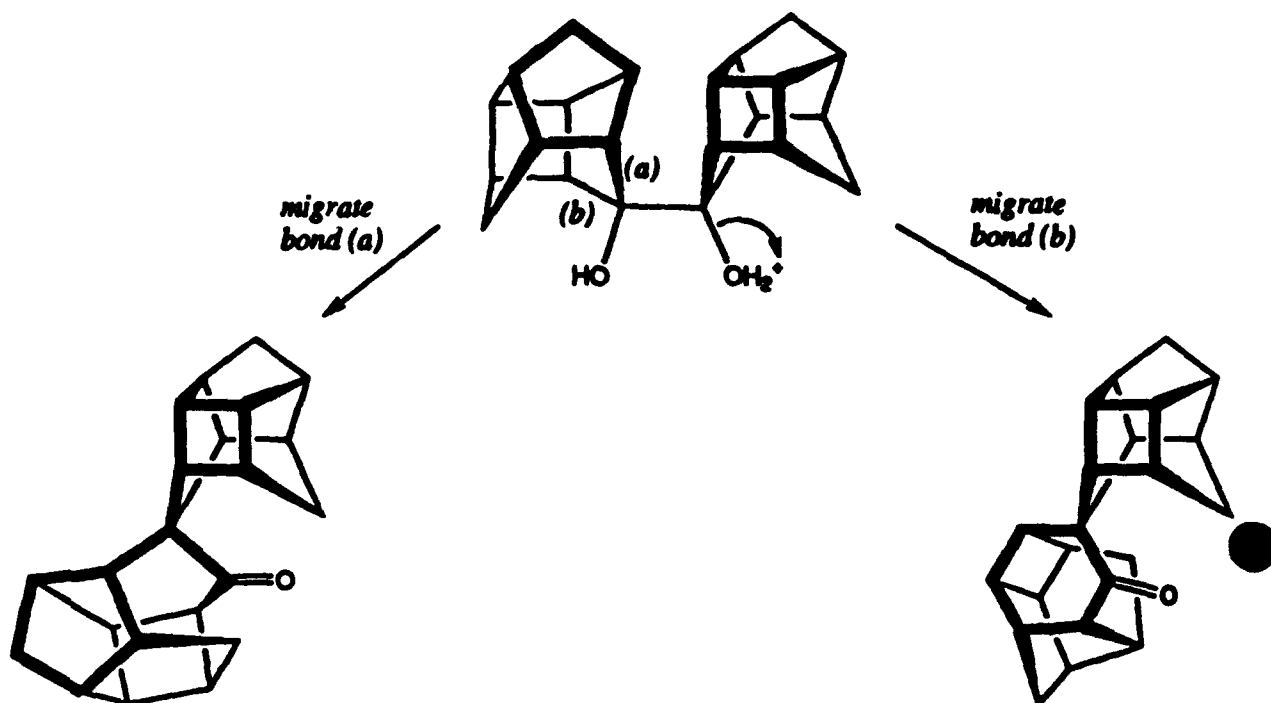
Result: This acid promoted pinacol rearrangement proceeds
quantitatively to afford a single product ketone.

Dr. Vijay R. Gadgil

RESEARCH PLANS FOR FY93

Ti(0)-promoted reductive dimerization of HCTD-7-one

HCTD alkene dimer
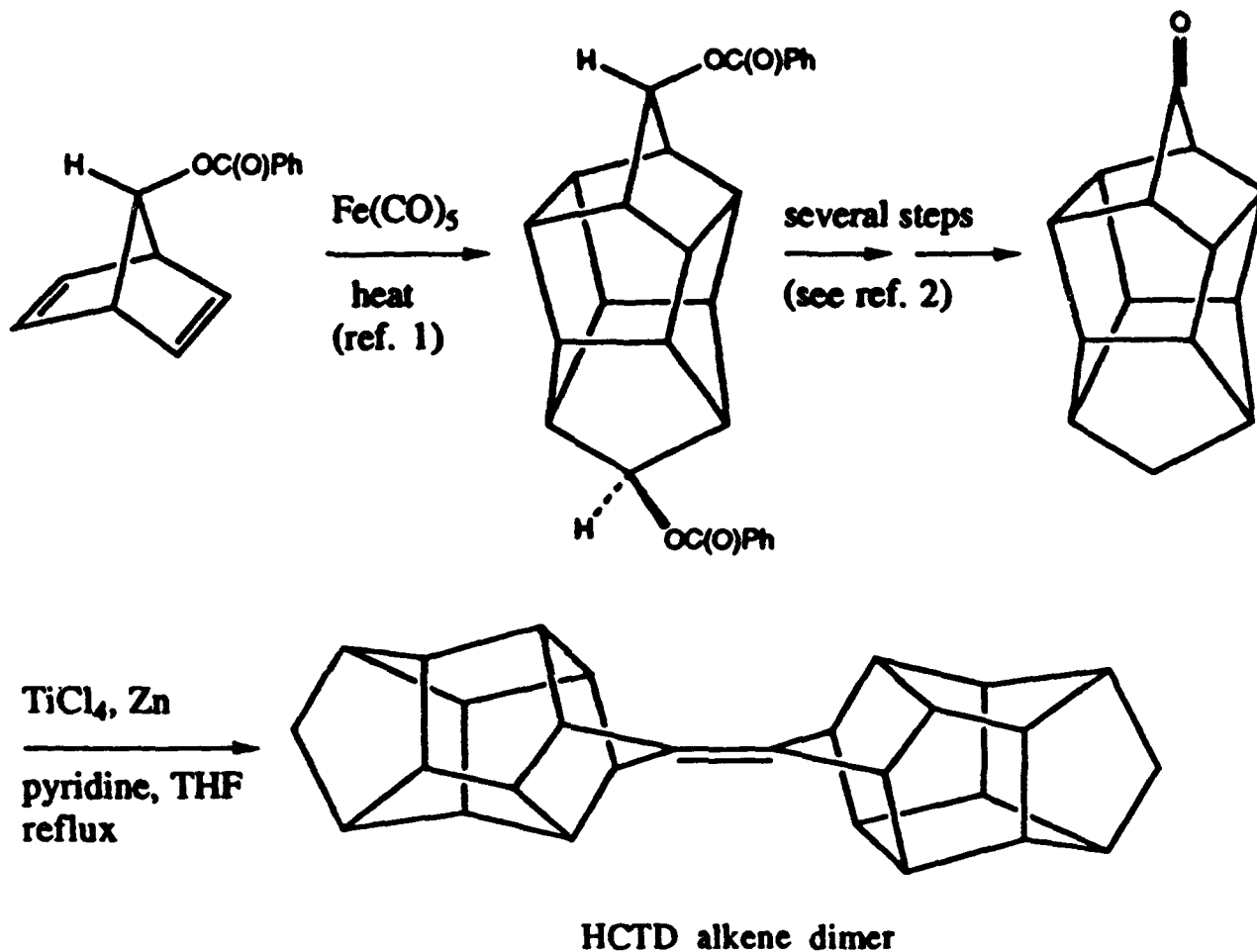
References:

1. Marchand, A. P.; Earlywine, A. D.; Heeg, M. J. *J. Org. Chem.* **1986, *51*,** 4096.

2. Albert, B.; Elsässer, D.; Martin, H.-D.; Mayer, B.; Chow, T. J.; Marchand, A. P.; Ren, C.-T.; Paddon-Row, M. N. *Chem. Ber.* **1991, *124*,** 2871.

Etc. (Higher Oligomers)

2a (n = 1)

2b (n = 1)

3a (n = 1)

3b (n = 1)

3a (n = 1)

1. Li, NH$_3$ (reductive dechlori-
nation, with concomitant
reduction of C=O to CHOH

2. PCC, CH$_2$Cl$_2$
(oxidation of CHOH to C=O)
3. Wolff-Kishner Reduction

[C$_{22}$H$_{24}$, (n = 1) A doubly
caged high density hydro-
carbon system]

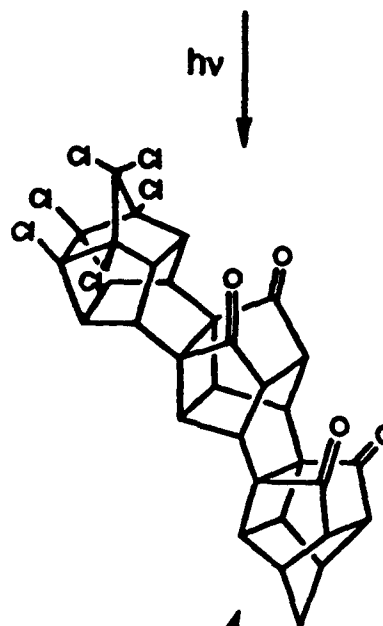Diene + Dienophile → (toluene, reflux 20 h) Two [4 + 2] cycloadducts, product ratio 3: 1
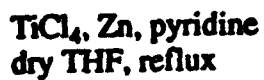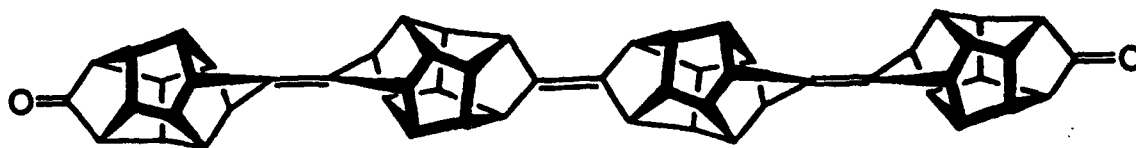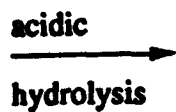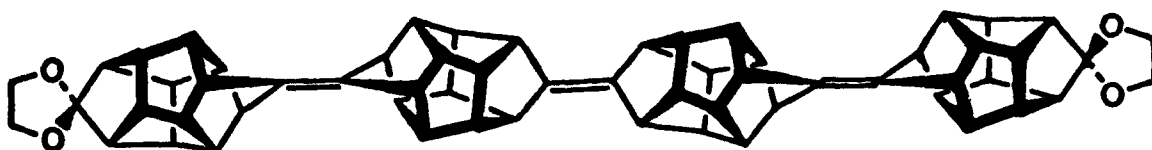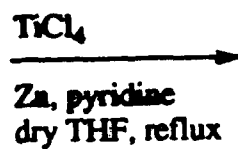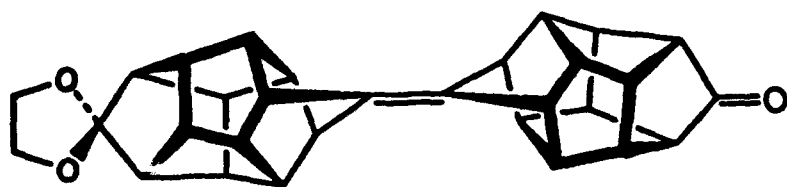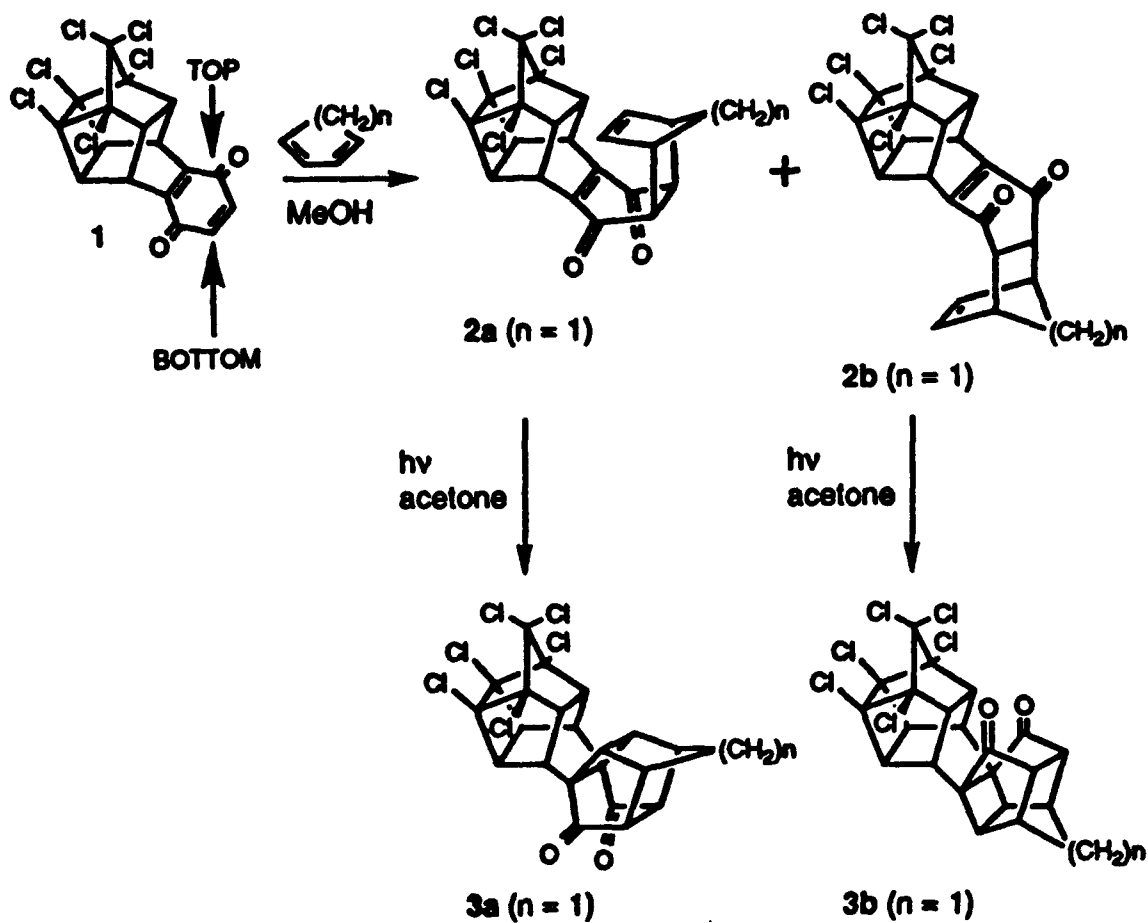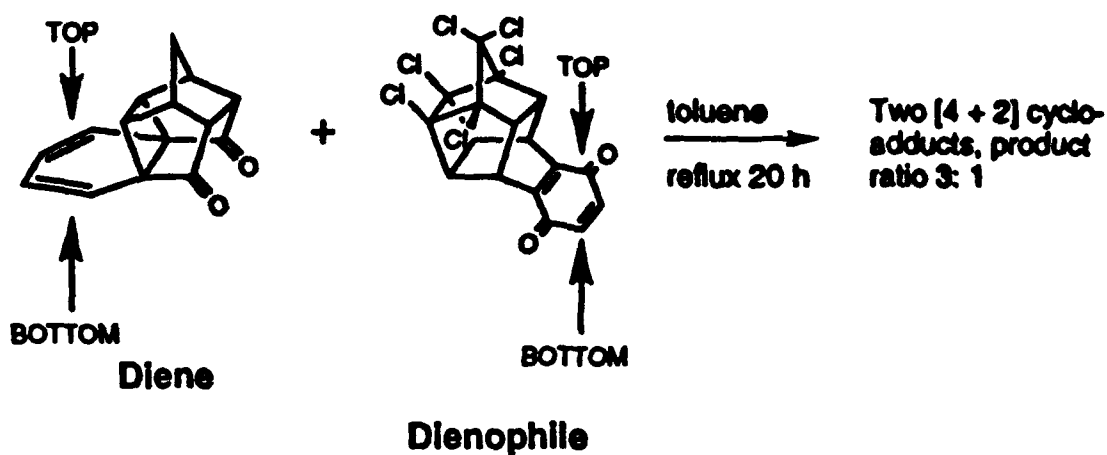
Probable structures of the two Diels-Alder [4 + 2] cycloadducts:
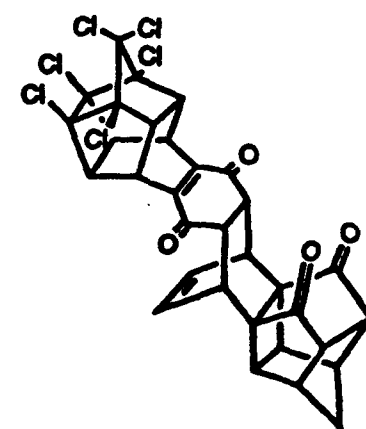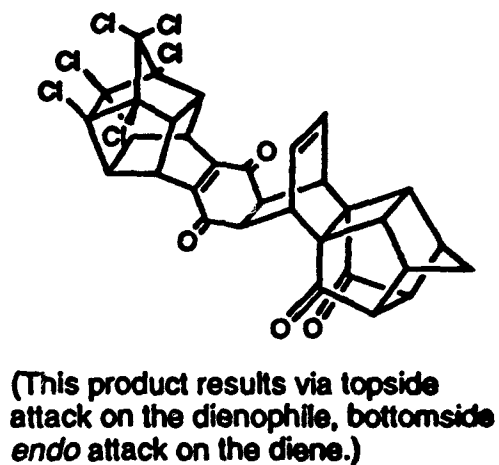
(This product results via topside attack on the dienophile, bottomside *endo* attack on the diene.)

(This product results via bottomside attack on the dienophile, bottomside *endo* attack on the diene.)

Mixture of two Diels-
Alder cycloadducts
(yellow solid)

→ diffuse room light →

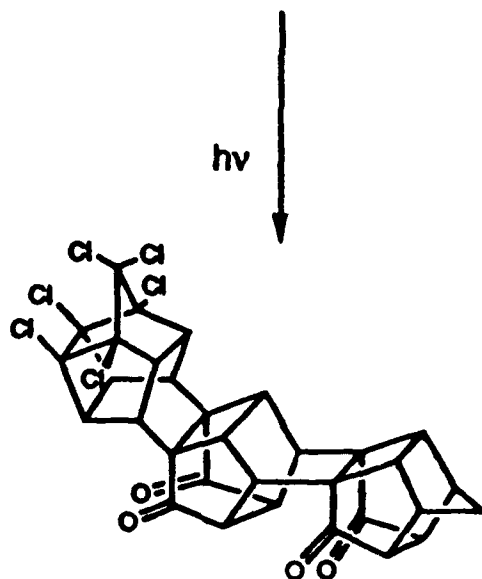Mixture of two [2 + 2]
photocycloadducts
(colorless solid)

Probable structures of the two [2 + 2] photocycloadducts:

(This product results via topside
attack on the dienophile, bottomside
endo attack on the diene.)

(This product results via bottomside
attack on the dienophile, bottomside
endo attack on the diene.)

hv

hv

(triply-caged products)

SYNTHESIS OF NEW ENERGETIC MATERIALS

Principal Investigator: Dr. Alan P. Marchand

*Department of Chemistry, University of North Texas
NT Station, Box 5068, Denton, Texas 76203-0068*

ACKNOWLEDGMENTS

Recent Progress with the HEDM Microthruster

Bob Nichols
Phillips Laboratory

THE AUTHOR DID NOT PRESENT AN EXTENDED ABSTRACT

Chlorine-Free Energetic Oxidizers

H. H. Michels and J. A. Montgomery, Jr.
United Technologies Research Center
East Hartford, CT 06108
and
Donald D. Tzeng
United Technologies Chemical Systems
San Jose, CA 95150

ABSTRACT

Nitramines, which exhibit one or more covalently bonded N-NO$_2$ groups, constitute one class of chlorine-free compounds with a high energy content. When formulated with conventional binders such as hydroxy-terminated polybutadiene (HTPB) or polyethylene glycol (PEG), solid composites based on nitramines exhibit performance characteristics (I$_{sp}$) superior to those obtained from existing formulations based on ammonium perchlorate.

We have carried out extensive *ab initio* calculations to characterize the structure and properties of the new inorganic class of dinitramides. The simplest compound HN(NO$_2$)$_2$ exists both as a secondary amine structure and as a remarkably strong oxyacid. The structures of several salts of the dinitramide anion have been examined, along with predictions of their thermochemistry. These studies have led to the prediction of several new nitramide oxidizers. We find a stable trinitramide molecule, N(NO$_2$)$_3$, with heat of formation estimated to be +59 kcal/mol. Studies of the N-NO$_2$ bond strength in this compound indicate that the thermal stability of trinitramide should be similar or slightly greater than that of dinitrogen pentoxide, N$_2$O$_5$. Calculations have been performed on a second N$_4$O$_6$ structure. This isomer has a tetrahedral (point group T$_d$) cage structure closely resembling that of the well-known hydrocarbon adamantane. Our calculations indicate that this structure is vibrationally stable at the RHF/6-31G* and MP2/6-31G* levels of theory. The calculated energy (including zero-point correction) of the T$_d$ structure of N$_4$O$_6$ is +150 kcal/mol above the C$_3$ (trinitramide) isomer, and its estimated heat of formation is +209 kcal/mol.

Several possible routes leading to the synthesis of trinitramide (TNA), tetranitrohydrazine and the other energetic oxidizers are being explored. The performance improvement available from the use of TNA in place of AP in solid propellant formulations offers a challenge for its successful synthesis.


Discussion

There has been growing interest recently in the development of chlorine-free oxidizers for use in advanced propellant formulations. Nitramines, which contain one or more covalently bonded $N-NO_2$ groups, constitute a promising class of chlorine-free energetic molecules. Examples of such compounds are the well-known explosives RDX and HMX[1,2], and the recently synthesized hydrogen and ammonium dinitramide.[3-5] Although there are many possible compounds of the form $RR'NNO_2$ and $RN(NO_2)_2$, there is only one possible trinitramide, $N(NO_2)_3$. There has been speculation concerning the existence of trinitramide, but very few results have actually been reported to date.

Ab initio calculations were performed on pyramidal (C_3) and planar (D_{3h}) structures of $N(NO_2)_3$. Full geometry optimizations and harmonic vibrational frequency calculations were performed on both planar and pyramidal structures at the RHF/6-31G* level of theory. An additional MP2/6-31G* geometry optimization and harmonic vibrational frequency calculation was performed on the pyramidal structure. Thermochemical calculations include vibrational zero-point effects, estimated from the RHF/6-31G* vibrational frequencies scaled by 0.8929. A summary of the calculated results is given in Tables 1 and 2. The C_3 structure is shown in Figure 1.

As in ammonia, nitrogen trifluoride, and trimethylene, our calculations show that trinitramide is pyramidal, not planar. At the RHF/6-31G* level, the planar structure is 24 kcal/mol higher in energy than the pyramidal ground state. The calculated vibrational frequencies (see Table 2) for the pyramidal structure are all real, indicating this structure is a true minimum. Three of the RHF/6-31G* vibrational frequencies found for the planar trinitramide structure are imaginary, indicating that it is not a stable minimum or a transition state, and therefore no further calculations were performed on this structure.

The heat of formation of trinitramide, can be estimated from the heat of reaction for

$$NH_3 + 3\,HNO_3 \rightarrow N(NO_2)_3 + 3\,H_2O \tag{1}$$
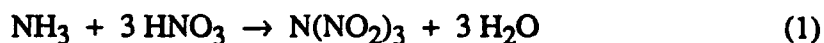
or, alternatively, from

$$3\,NH_2NO_2 \rightarrow N(NO_2)_3 + 2\,NH_3 \tag{2}.$$
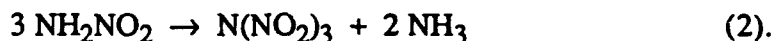
We average the MP2/6-31G* heats of formation calculated from the two reactions to obtain our final estimate, $\Delta H_f^0(N_4O_6) = 59.0$ kcal/mol. Analogous calculations[5] of the heat of formation of nitric acid give an error of 1.7 kcal/mol. Our estimated error in the calculated heat of formation of trinitramide is ± 5 kcal/mol.

As suggested earlier, the stability of trinitramide is determined by the strength of the long N-N bond. Using our calculated heat of formation of trinitramide, we find the heat of

reaction for:

$$N(NO_2)_3 \rightarrow N + 3\,NO_2 \tag{3}$$
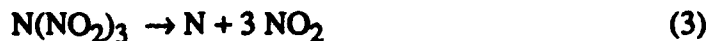
to be 78 kcal/mol, estimate the N-N bond strength as 1/3 of that, or 26 kcal/mol. Alternatively, if we estimate a value of 100 kcal/mol for the N_H bond strength in $HN(NO_2)_2$, then from our previously reported[5] heat of formation (28.4 kcal/mol) of $HN(NO_2)_2$, and the experimental heat of formation of NO_2 (8.6 kcal/mol)[6], we find the heat of formation of the $N(NO_2)_2$ radical to be 76 kcal/mol. We may now directly calculate $D_0(NO_2\text{-}N(NO_2)_2)$ from

$$N(NO_2)_3 \rightarrow N(NO_2)_2 + NO_2 \tag{4}$$

and obtain a value of 26 kcal/mol, in agreement with the average bond strength. The enthalpy of dissociation into ions, via

$$N(NO_2)_3 \rightarrow N(NO_2)_2^- + NO_2^+, \tag{5}$$

is estimated as 135 kcal/mol from the ionization potential of NO_2 (9.75 eV)[7] and our previous estimate of the electron affinity of $N(NO_2)_2$ (5.0 eV)[5]. From experimental thermochemical data,[7] the O-NO_2 bond strength in N_2O_5 is estimated to be 20-23 kcal/mol. Comparing this value with our estimated N-N bond strength, we conclude that the thermal stability of trinitramide should be similar to or slightly greater than that of dinitrogen pentoxide.

Calculations have been performed on a second structure of N_4O_6. This isomer has a tetrahedral (point group T_d) cage structure closely resembling that of the well-known compounds adamantane and hexamethylenetetramine (see Figure 2). Our calculations indicate that this structure is vibrationally stable at the RHF/6-31G* and MP2/6-31G* levels of theory. The RHF/6-31G* N-O bond distance is 1.37 Å, which increases to 1.43 Å at MP2/6-31G*. The calculated MP2/6-31G* energy (including zero-point correction) of the T_d structure of N_4O_6 is 150 kcal/mol above the C_3 (trinitramide) isomer, and its estimated heat of formation is 209 kcal/mol.

Because of its high symmetry, there are no obvious low energy decomposition paths for this compound. Based on the close resemblance to the diamond-like adamantane, we conjecture that the N_4O_6 T_d cage structure is relatively unstrained.

Synthesis Routes

The predicted stability of trinitramide, its high performance as an oxidizer, and chlorine-free composition make this compound a top priority synthesis target. The dinitramide anion may provide us with the most direct entry to the desired trinitramide

(TNA) structure. Possible synthesis routes for TNA, based on using dinitramides as a starting material, are illustrated in Figure 3. As with ADN, several other starting routes appear possible.

Beyond trinitramide, $N(NO_2)_3$, we also are interested in other energetic chlorine-free oxidizers such as tetranitrohydrazine, $(NO_2)_2N-N(NO_2)_2$ and dinitrodiazene, $(NO_2)N=N(NO_2)$. All of these molecules belong to a class of compounds called Solid Oxygenated Air since they contain only oxygen and nitrogen with oxygen/nitrogen ratios higher than that of air. Possible synthesis routes are illustrated in Figure 4. Similar to the synthesis of N-nitroacylamide, 1,2-diacetylhydrazine can be converted to 1,2-dinitrodiacetylhydrazine which can possibly be further nitrated to tetranitrohydrazine. Azodicarboxylate and related compounds may provide a starting point for the synthesis of dinitrodiazene. Electrolytic oxidation of the dintramide anion is also under consideration for the synthesis of tetranitrohydrazine.

Performance Characteristics

The density of trinitramide is estimated as 2.15 g/cm^3 by Cady's method.[8] Based on the density and heat of formation calculated above, we have carried out a performance evaluation of trinitramide as an oxidizer in a solid propellant formulation. In Figure 4, the theoretical I_{sp} of trinitramide with HTPB as binder is compared to the performance of a conventional AP-HTPB system. The challenge for successful synthesis of TNA is clearly evident.

References

[1] G. F. Adams, and R. W. Shaw, Jr., Annu. Rev. Phys. Chem. 43 (1992) 311.

[2] S. N. Bulusu, editor: Chemistry and Physics of Energetic Materials, Kluwer, London, 1990.

[3] R. J. Schmitt and J. C. Bottero, private communication.

[4] R. J. Schmitt, M. Krempp and V. M. Bierbaum, Int. J. Mass. Spect. 117 (1992) 621.

[5] H. H. Michels, and J. A. Montgomery, Jr., J. Phys. Chem. 97 (1993) XXXX.

[6] D. D. Wagman, W. H. Evans, V. B. Parker, R. H. Schumm, I. Halow, S. M. Bailey, K. L. Churney, R. L. Nuttal, J. Phys. Chem. Ref. Data, 11, Suppl. 2 (1982).

[7]   S. G. Lias, J. E. Bartmess, J. F. Liebman, J. L. Holmes, R. D. Levin, W. G. Mallard, J. Phys. Chem. Ref. Data, 17, Suppl.1. (1988).

[8]   H. H. Cady, "Estimation of the Density of Organic Explosives from Their Structural Formulas," Report LA-7760-MS, Univ. of Cal., LANL (1979).

HEDM93paper.5/93

Table 1. Calculated Energies (hartrees) and Geometries (angstroms and degrees) of Trinitramide.

	Level	Energy [a]	N-N	N-O_1	N-O_2	N-N-N	N-N-O_1	N-N-O_2	N-N-N-O_1	N-N-N-O_2
C_3	RHF/6-31G*	-666.44582 (0)	1.4444	1.1713	1.1757	110.9	112.6	116.7	-70.8	110.4
C_3	MP2/6-31G*	-668.26537 (0)	1.5453	1.2191	1.2209	105.2	111.0	117.4	-76.0	105.2
D_{3h}	RHF/6-31G*	-666.40519 (3)	1.4663	1.1698	1.1698	120.0	116.2	116.2	0.0	180.0

[a] The number of imaginary vibrational frequencies is indicated in parenthesis.

Table 2. Calculated Vibrational Frequencies (cm^{-1}) and Intensities (km/mol) of Trinitramide.

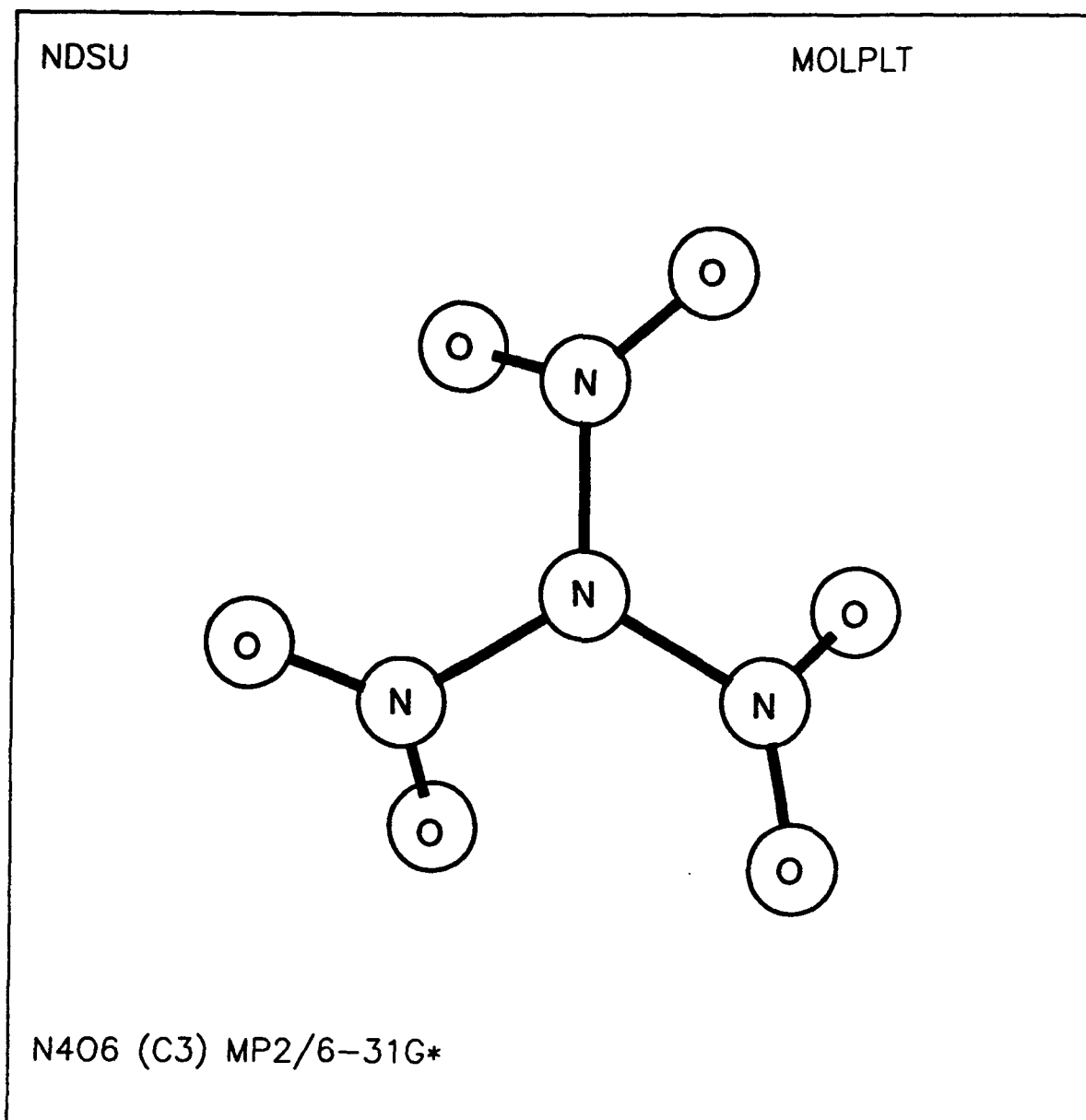|			
C_3	RHF/6-31G*	A	127(0.6), 241(5.0), 444(0.0), 651(4.7), 937(10.3), 997(9.3), 1641(31.5), 1934(869.1)
		E	53(0.1), 249(3.7), 508(2.3), 801(8.7), 908(155.5), 1155(79.3), 1537(290.8), 1979(550.1)
C_3	MP2/6-31G*	A	96(0.1), 217(2.1), 325(0.1), 521(0.2), 796(12.1), 835(6.0), 1350(14.3), 1912(90.5)
		E	43(0.1), 197(4.2), 321(58.0), 605(59.7), 748(172.1), 800(70.9), 1263(180.6), 1921(58.9)

Figure 1. Trinitramide Molecule

NDSU MOLPLT

N4O6 (C3) MP2/6-31G*
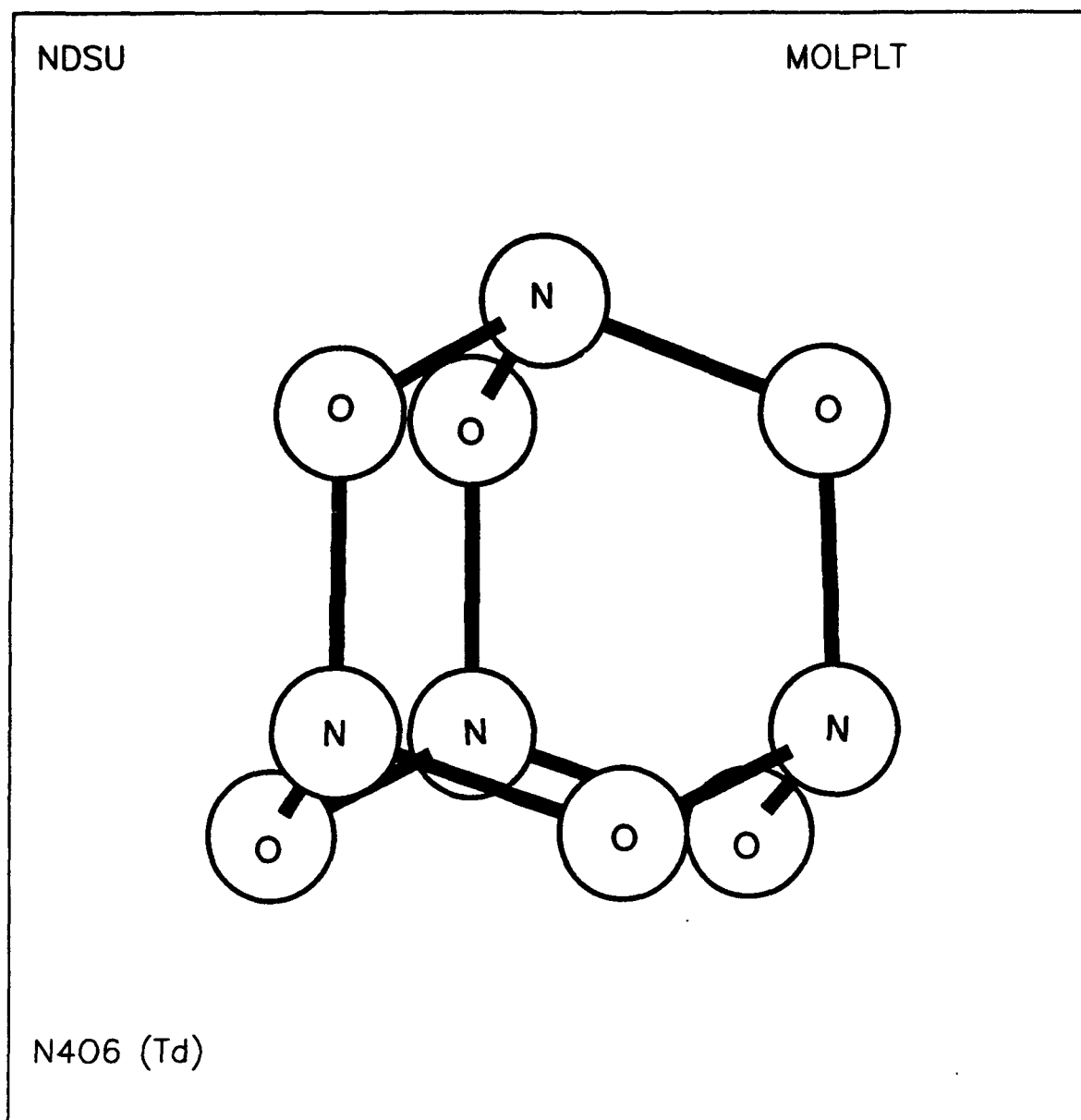
Figure 2. N_4O_6 (Adamantane-like) Molecule

NDSU

MOLPLT

N4O6 (Td)

Figure 3. Proposed Routes for the Synthesis of Trinitramide

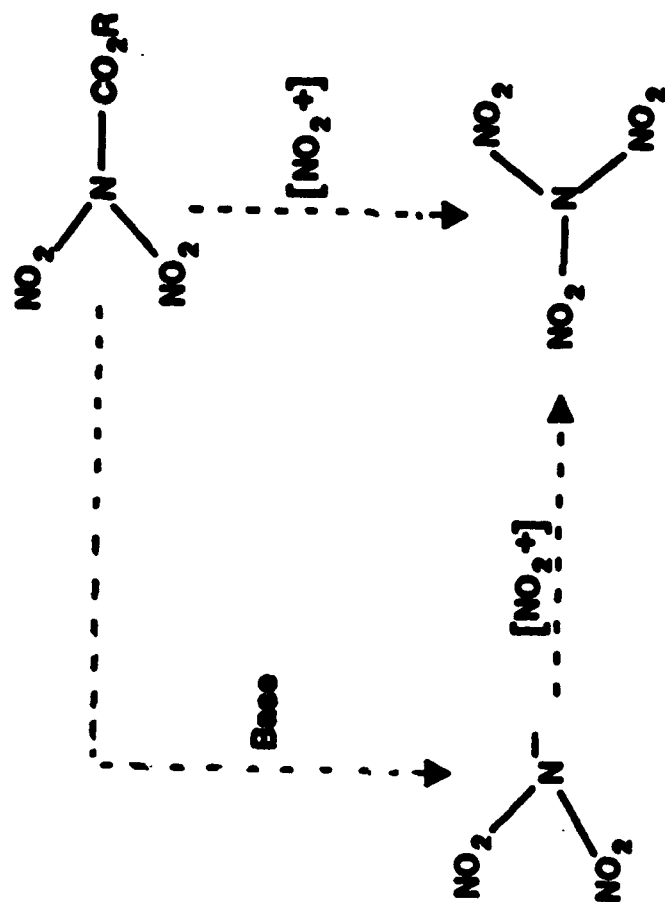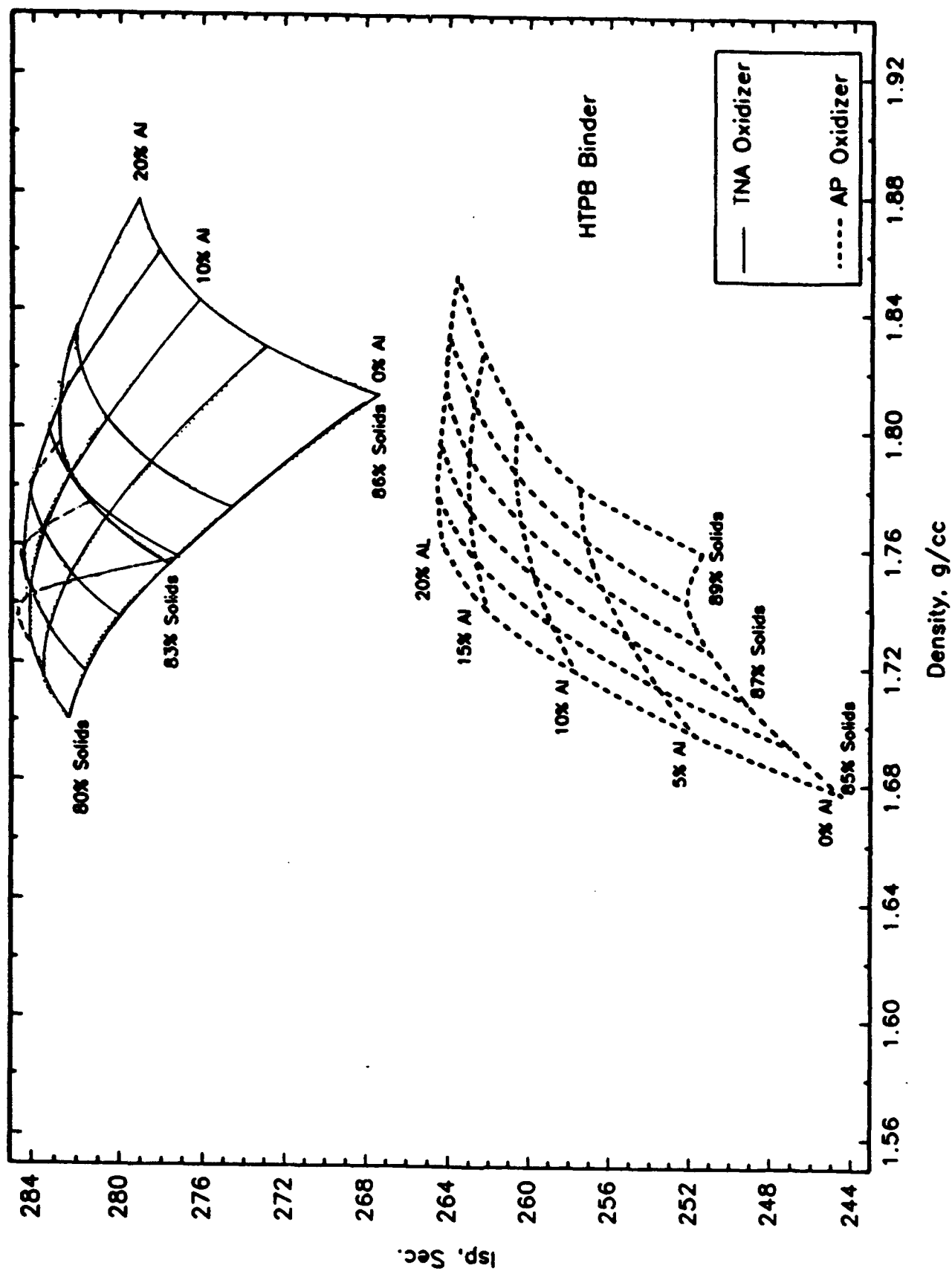Figure 4. Synthesis Routes to Tetranitrohydrazine and Dinitrodiazene

Figure 5. Comparison of Theoretical Performance (I_{sp}) with AP and TNA as Oxidizers

Cubanes and Azacubanes: New Generations of Fuels and Propellants

Professor Philip E. Eaton
Department of Chemistry, The University of Chicago
*5735 S. Ellis Ave, Chicago, IL 60637 USA*

Cubane is the most highly strained, kinetically stable system available in quantity. Kilogram amounts can be made commercially. Cubane has, in combination, the highest energy and highest density of any known stable organic compound.
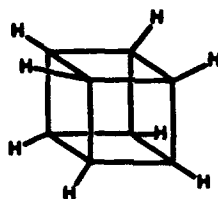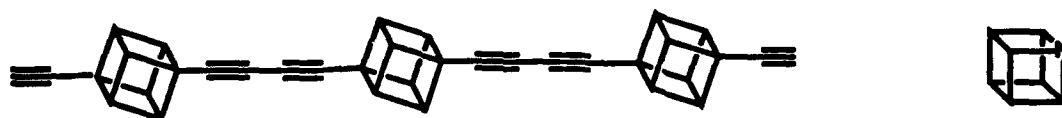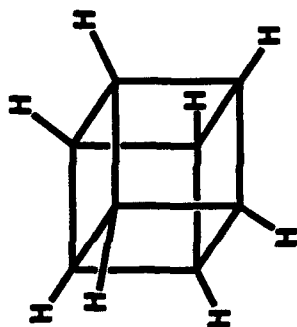

CUBANE

vapor pressure	1.1 Torr at 25°C
solubility	18 wt-% in hydrocarbons
melting point	130-131°C (easily depressed)
stability	inert to light, water, air
decomposition	>220° (very slow)
density	1.29 g/cm^3
heat of formation (gas)	+149 kcal/mole
strain energy	+166 kcal/mole
ΔHc	204,450 BTU/gal

Cubane as an air-breathing fuel offers an advantage of approximately 50% by volume over RJ-4 and much more over RP-1. Special methodology has been developed for the preparation of a wide range of cubanes. Such substitution can provide cubanes having remarkable explosive or propellant power. 1,3,5,7-Tetranitrocubane has already been demonstrated to be a superior explosive. It is now possible to tailor cubanes to produce exceptional fuel components; for example, many kinds of high-energy cubane polymers can readily be made:
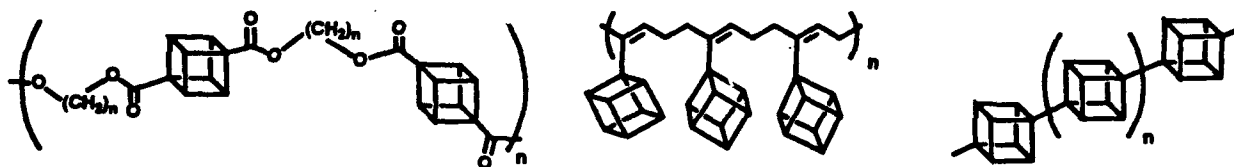

Cubyl acetylenes and azacubanes can be derived from cubanes. These will provide yet more powerful substances.

CUBANE

vapor pressure	1.1 Torr at 25°C
solubility	18 wt-% in hydrocarbons
melting point	130-131°C (easily depressed)
stability	inert to light, water, air
decomposition	>220° (very slow)
density	1.29 g/cm^3
heat of formation	+149 kcal/mole
strain energy	+166 kcal/mole
ΔHc	204,450 BTU/gal

OCTANITROCUBANE

$C_8(NO_2)_8 \longrightarrow 8CO_2 + 4N_2$
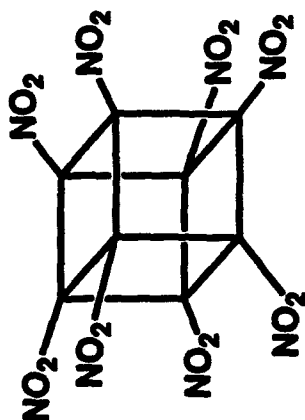
VOLUME EXPANSION   ca. 750 fold

ENERGY RELEASE   ca. 830 kcal/mole

281

CUBANE HAS THE HIGHEST ENERGY CONTENT OF ANY AVAILABLE STABLE HYDROCARBON BY WEIGHT OR VOLUME

CUBANE COMPARED TO RJ-4 AS AN AIR-BREATHING FUEL

cmpd	formula	density		ΔH_f		ΔH_c		%increase	
		g/cc	lb/in³	kcal/m	cal/g	cal/g	cal/cc	by weight	by volume
RJ-4	$C_{12}H_{20}$	0.92	0.0332	-32.5	-198.0	10,114	9,305	-	-
cubane	C_8H_8	1.29	0.0468	+124.0 (+137.6)	+1190.6 (+1321.6)	10,517 (11,674)	13,567 (15,059)	4.2 (4.7)	45.8 (50.8)

(using new estimate of cubane's heat of formation)

fantastic

density 1.728 g/cm³
decomposition >185 °C
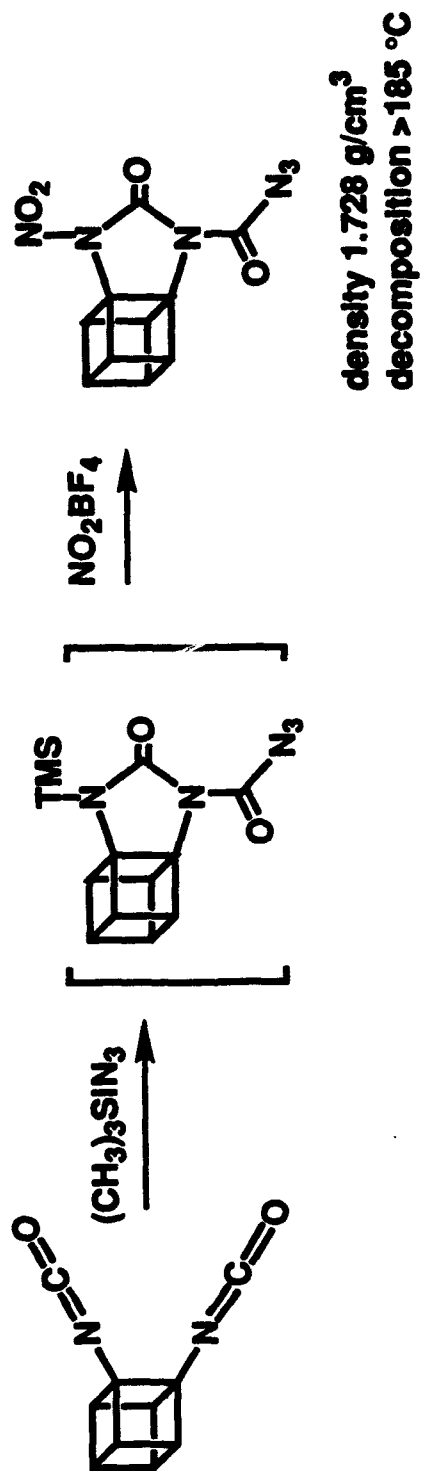
CUBANE POLYMERS

e.g., the polyester
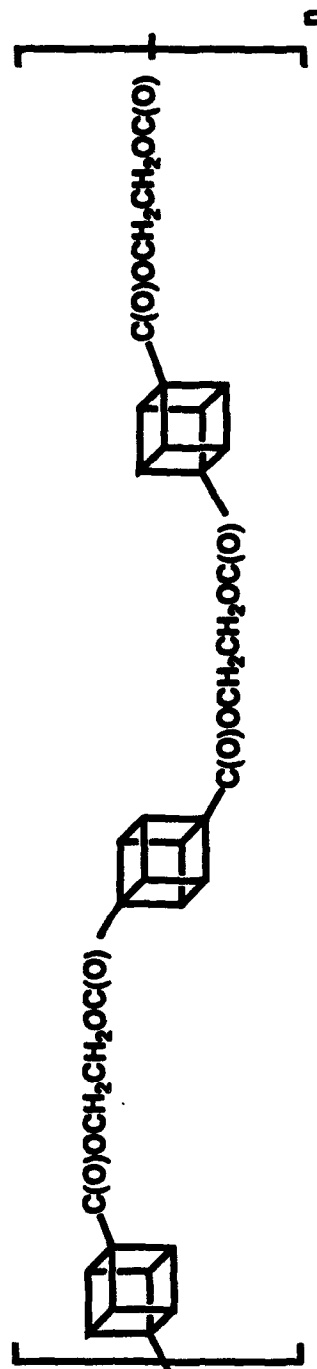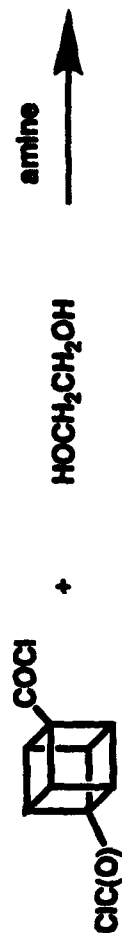
CUBANE-DERIVED RECORD SETTERS
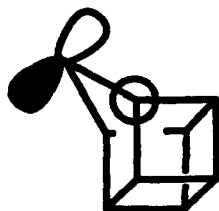
1,9-HOMOCUBENE
the most twisted olefin

CUBENE
the most highly pyramidalized olefin
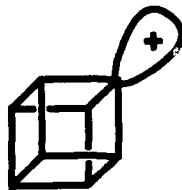
CUBYL CARBENIUM ION
the least likely cation
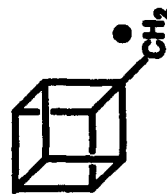
CUBYL CARBINYL RADICAL
the fastest rearranging alkyl radical

1,4-CUBADIYL
the wierdest intermediate around nowadays

1,4-CUBADIYL
A KEY PRECURSOR

CH₃LI

METHYLCUBANE

CYCLOPROPYLCUBANE
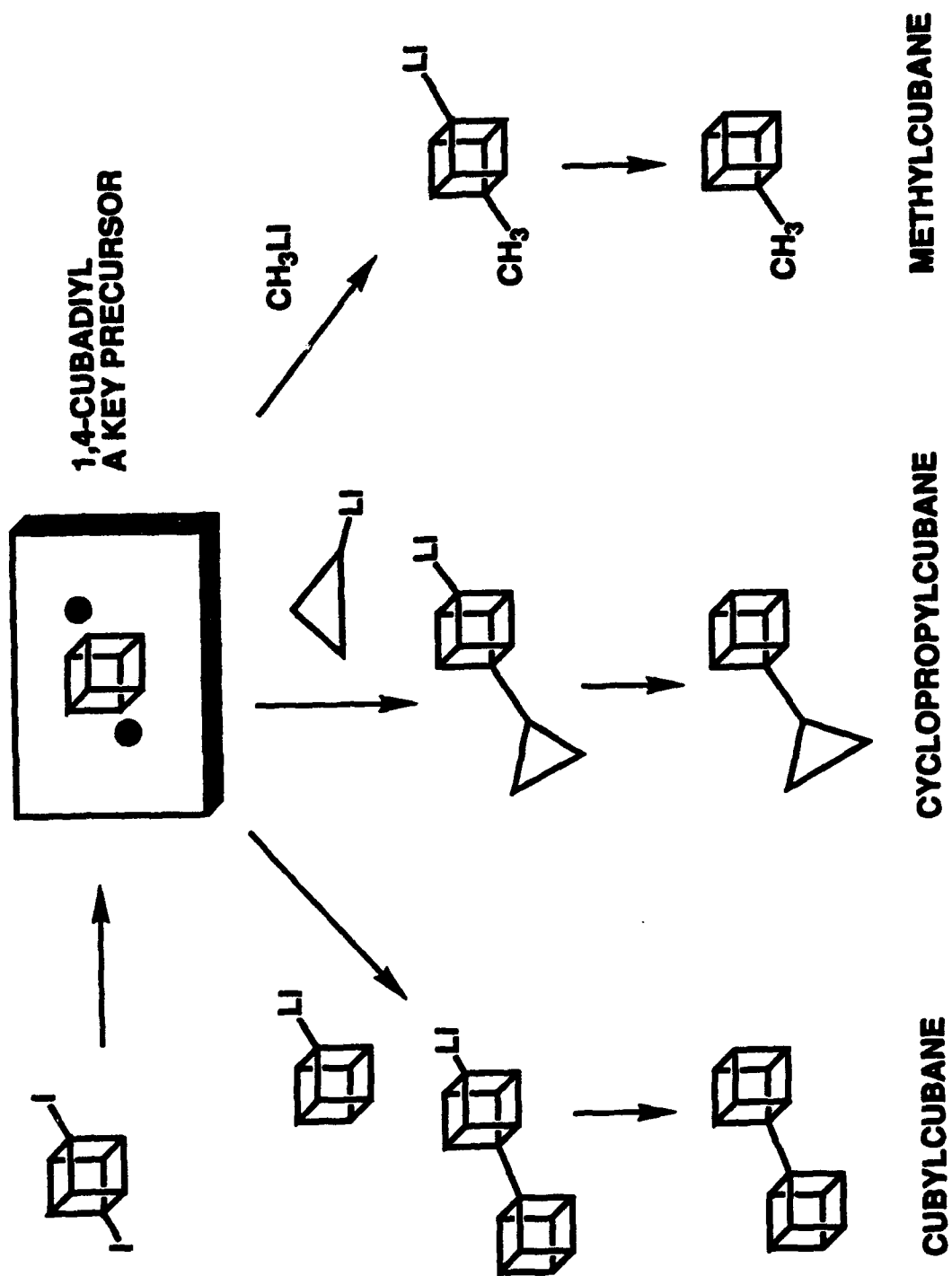
CUBYLCUBANE

POLYMERS WITH PENDANT CUBANES
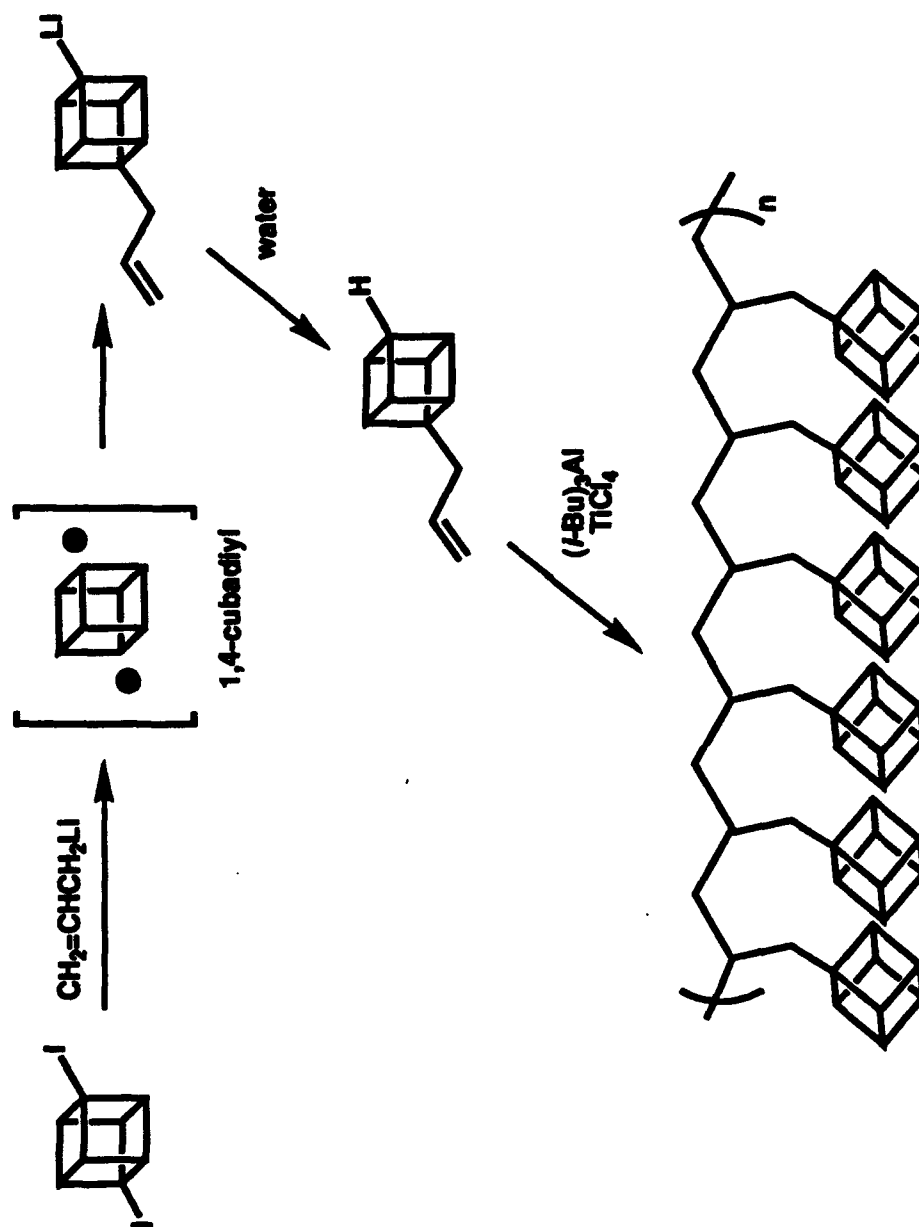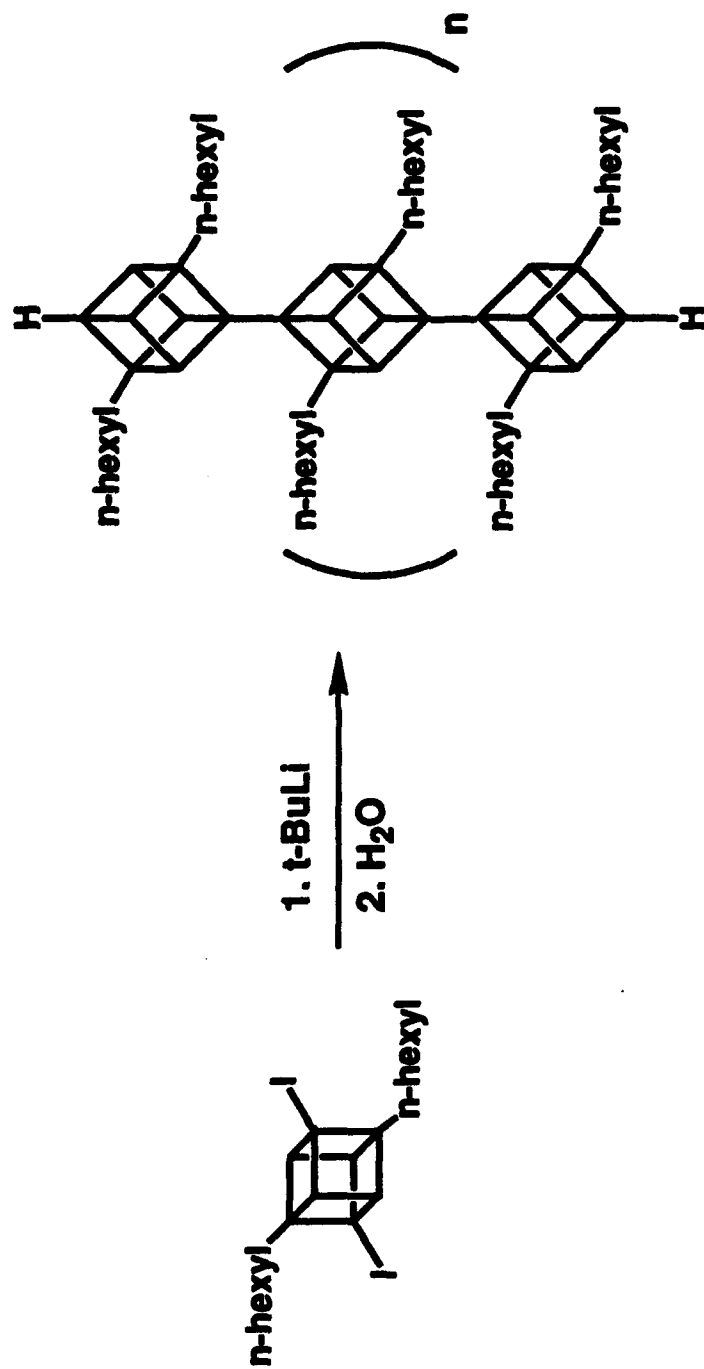
ALKYNYLCUBANE RODS
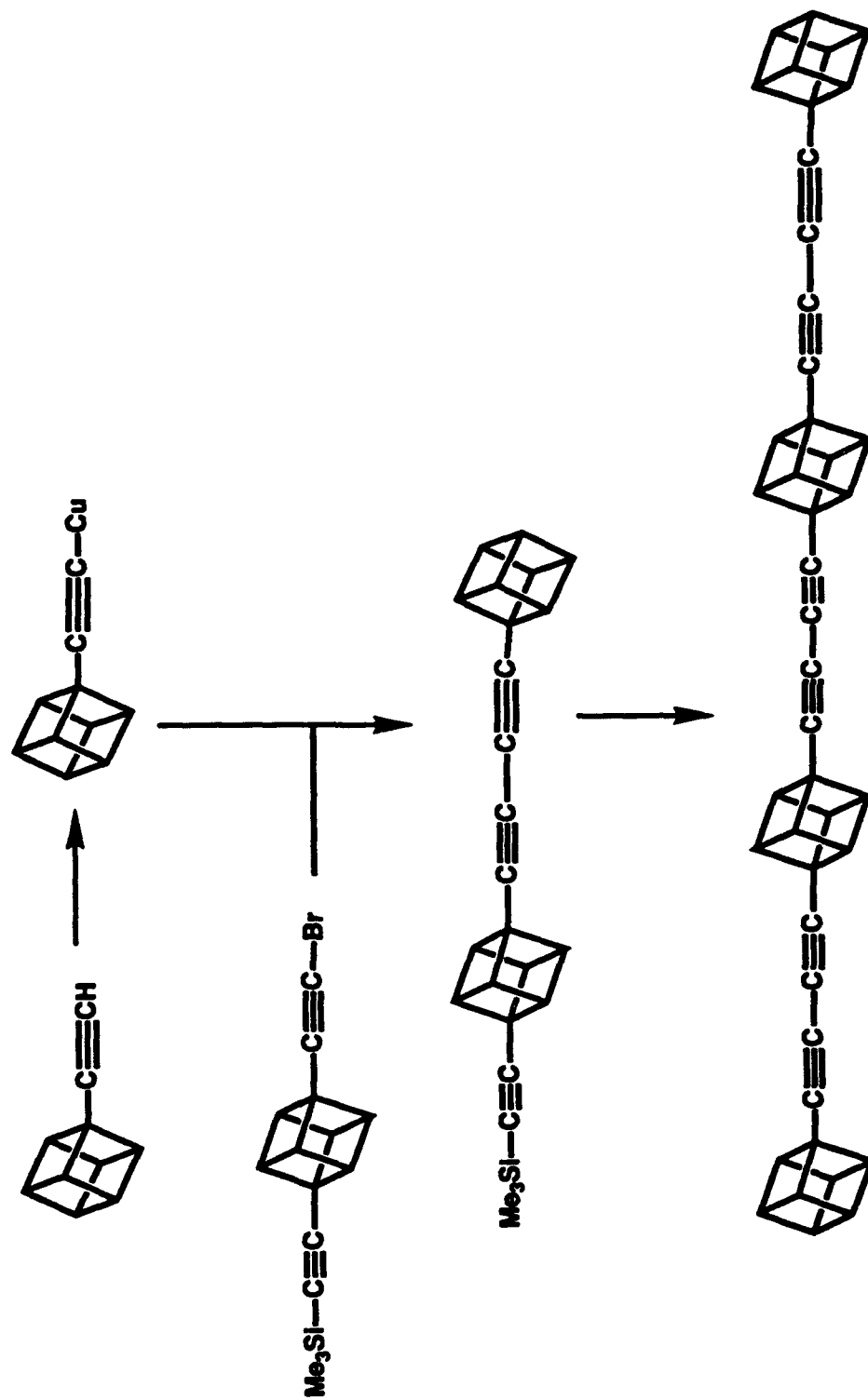
AZACUBANE
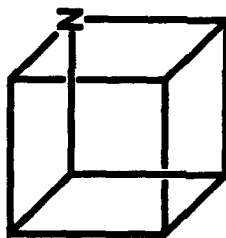
azacubane
strain energy > 200 kcal/mole
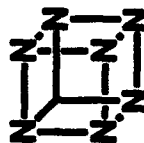
"dense nitrogen"

THE AZA DANCE

9-azahomocubane

a 1-azahomocubane

a 2-azahomocubane

AZACUBANE

291

5 stages
> 25% overall

CUBANE-1,4-DICARBOXYLIC ACID
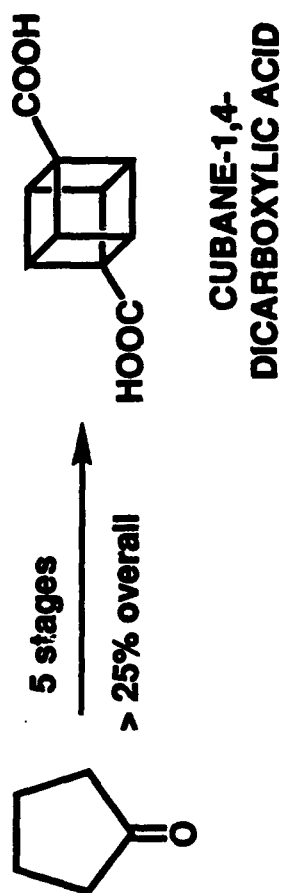
MULTI-KILO PILOT PLANT PRODUCTION
ALREADY ON-LINE

REPRESENTATIVE VALENCE SATISFIED (CH)ₙ OLIGOMERS
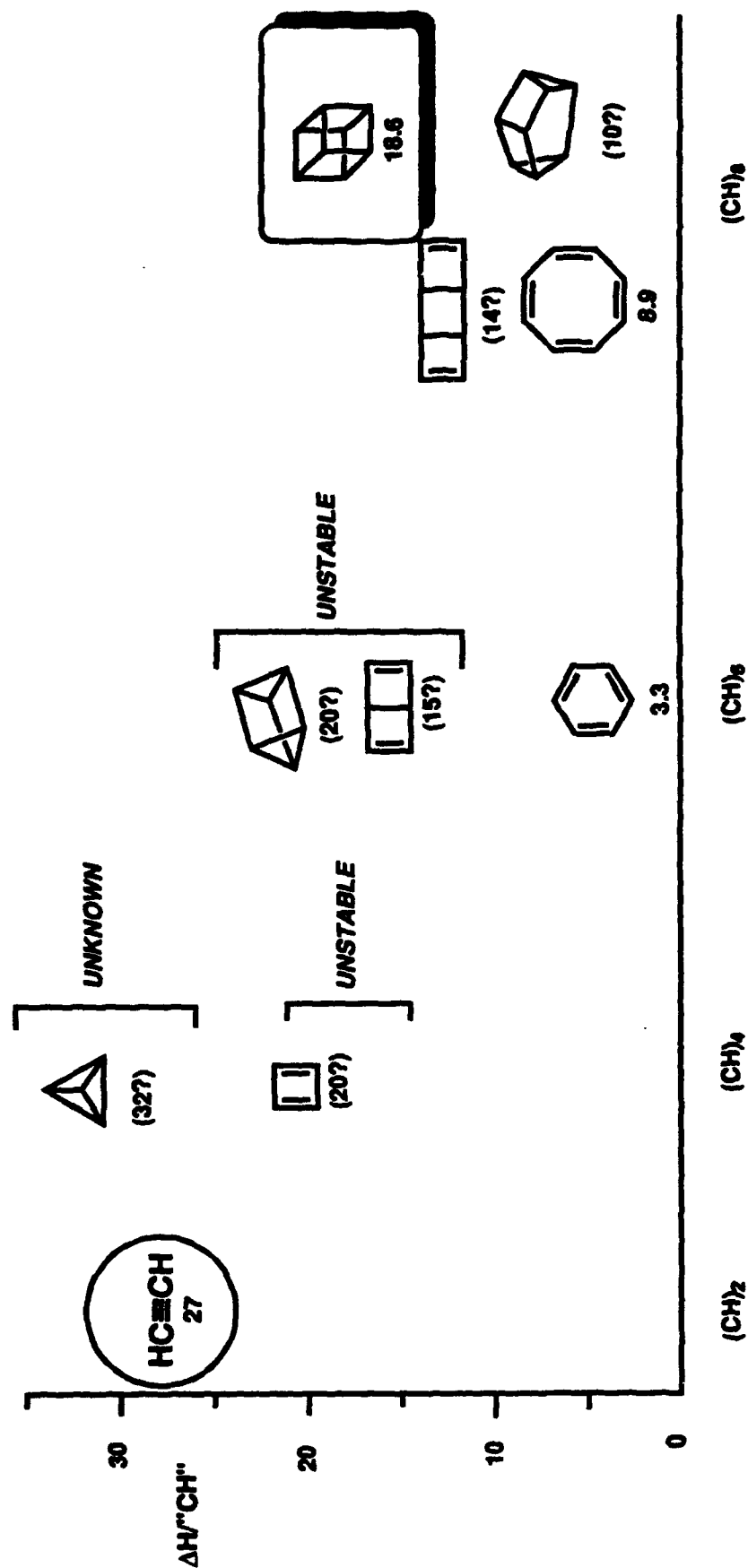
CONCLUSIONS: 1. CUBANE IS THE FIRST STABLE STOP BELOW ACETYLENE
2. CONVERSION IS APPROXIMATELY 68 KCAL/MOL EXOTHERMIC

UNIVERSITY OF CHICAGO

293

GOAL: AN ECONOMICALLY REASONABLE SYNTHESIS OF CUBANE

$$HC\equiv CH \xrightarrow{X4}$$

PROBLEM: FIND OUT HOW TO DO IT

PRESENT APPROACH: "EXOTEMPLATING" WITHIN MOLECULAR SIEVES

A PROPOSAL FOR OPTICAL SPECTROSCOPY AND PHOTOCHEMISTRY OF ATOMS IN SOLID H_2

William C. Stwalley* and John Bahns*

Departments of Chemistry and of Physics and Astronomy and

Center for Laser Science and Engineering,

University of Iowa

Iowa City, Iowa 52242

and

James R. Gaines

Department of Physics and Astronomy

University of Hawaii at Manoa

Honolulu, Hawaii 96822

ABSTRACT

Ultraviolet (UV) and vacuum ultraviolet (VUV) optical spectroscopic techniques for measuring the atomic and molecular hydrogen concentrations and for making "remote" measurements of the temperature in solid molecular hydrogen are proposed. Photochemical techniques for generating atomic hydrogen in pure solid hydrogen are also proposed. This combination of techniques should provide detailed understanding of the simplest and most quantum mechanical molecular solid as well as the fundamental limits on atomic concentrations in solid molecular hydrogen. They should also be particularly valuable in characterizing a complex cryogenic environment (e.g. inertial confinement fusion pellet containing T_2 or D-T where the tritium beta decay produces atoms or a solid molecular hydrogen fuel pellet doped with atoms (or small molecules)).

* Address after 8/16/93:   Dept. of Physics, University of Connecticut, Storrs, CT   06269-3046

BACKGROUND

There has been a re-awakened interest in solid molecular hydrogen because of the role it plays in new technological applications. Two such areas of interest are: (i) the production and storage of high energy density materials for rocket propulsion; and (ii) the use as a fuel (for suitable mixtures of the isotopes D and T) for inertial confinement fusion (ICF) experiments. Because of past research on pure, crystalline, solid hydrogen, there already exists a wealth of data including magnetic resonance, microwave, infrared and Raman spectroscopy but the new applications will probably be based on amorphous hydrogen and will require still more data-base development that must include: a new method to determine the atomic hydrogen concentration in the solid, a method to characterize to amorphous solids, and a "remote" method to determine the temperature of the solid when it is in the form of a film on a substrate or in a capsule. We are proposing a systematic research program that will address these needed diagnostic techniques while providing fundamental scientific results of high interest.

For instance, one mode of storing energy in solid hydrogen is to produce atoms of hydrogen (H in $H_2(s)$) that can release 4.5 eV when they recombine in pairs. This high energy density material holds promise for rocket propulsion, but its utility will depend on the amount of atomic hydrogen that can be stored. To date, atomic hydrogen concentrations in the range of 1-2 % may have been produced in solid T_2 where a single beta decay of a tritium nucleus produces of the order of 1000 atoms but there is no reliable method for measuring this concentration, non-destructively. The time honored method of determining the atomic hydrogen concentration, namely electron paramagnetic resonance (EPR), has recently been found to be unreliable above 0.1%, because the measurements apparently are not sensitive to a majority of the H atoms present. Concentrations above 1% will be the region of interest for high energy density materials. Moreover, the heavily radiation-damaged solid is probably not crystalline and not well characterized either. The optical spectroscopy diagnostics proposed below will provide a new method for determining the atomic hydrogen concentration "in situ" and also address the characterization of amorphous hydrogen solids with respect to crystalline hydrogen.

The cryogenic pellets used for inertial confinement fusion contain a solid mixture (D-T) of D_2, DT, and T_2 molecules in roughly the proportions 25% D_2, 50% DT, and 25% T_2. Before implosion, the encapsulated sample must be in the form of a spherically symmetric solid with a gaseous region in the center. It is important to be able to determine the capsule

temperature and the ratio of D to T in the solid and the gas, from a remote location, without any electrical leads attached to the sample. The beta decay of the tritium nucleus makes it possible to do this. However, the decay also produces many atoms, ions, and electrons as well as damage and defects and thus the solid D-T mixture is complex and poorly characterized. The optical spectroscopic diagnostics discussed below should significantly improve this characterization of D-T and provide a method for determining the temperature from a remote location.

In addition to proposing new, optical diagnostic techniques for characterizing amorphous hydrogen samples and for measuring the atomic hydrogen concentration, we are proposing a novel photochemical method for producing H atoms in solid hydrogen. These new methods have the important advantage that they would produce the atoms homogeneously over the sample volume as opposed to electron bombardment where the atoms would most likely be produced in only a very small portion of the sample making it difficult to achieve the maximum possible atom concentration.

It is worth noting that solid hydrogen comes in six chemically stable variants (p-H_2, o-D_2, p-T_2, HD, HT, DT, all in rotational level J=0) and three metastable variants (o-H_2, p-D_2, o-T_2, all in level J=1), where p = para and o = ortho. Of course, arbitrary mixtures of these nine variants are also possible (normal H_2(s) formed from room temperature gas is 1/4 p-H_2 and 3/4 o-H_2). Not only is the H_2(s) the simplest molecular solid, but it is also the most quantum mechanical and the number of variants greatly adds to the richness of its description and the interest in its fundamental understanding.

PROPOSED PROGRAM

Optical Diagnostics

Optical spectroscopy in H_2(s) should be possible below the band gap of ~17 eV, corresponding to a photon of 137,000 cm^{-1} (wavelength λ = 731 Å). In particular, H, H_2, and metal atoms should retain a clear relationship (slight shifts and broadenings) to their isolated gas phase spectra in an H_2(s) matrix, as long as λ > 731 Å. Below 11 eV (~110 nm), H_2(s) (and D_2(s)) are virtually transparent (Inoue et al., Sol. St. Commun. 30, 627 (1979) and Gedanken et al, J. Chem. Phys. 59, 2752 (1973)). In the intervening 11 - 17 eV region, there is significant B-X (and other) absorption (showing vibrational structure in low resolution).

The optical diagnostic techniques of potential interest for this proposal include the following:

1. Single photon (vacuum ultraviolet (VUV)) absorption, followed by visible/near infrared or VUV photon emission.

2. Two Photon (ultraviolet (UV)) absorption followed by visible/near infrared (or "forbidden" VUV) emission.

Other longer wavelength optical techniques, which do not involve electronic excitation, have been extensively applied to H_2, but will only be mentioned briefly here:

3. Spontaneous or stimulated Raman scattering using a visible or UV pump beam and observing the Stokes beam at $v_{pump} - v_{H_2}$.

4. Coherent antistokes (or Stokes) Raman scattering using two visible or UV pump beams with $v_{pump2} - v_{pump1} = v_{H_2}$ and $v_{pump2} > v_{pump1}$ and observing the antistokes beam at $v_{pump2} + v_{H_2}$ (or the Stokes beam at $v_{pump1} - v_{H_2}$).

5. Single photon (infrared) "forbidden" absorption, measured e.g. by beam attenuation, intracavity or photoacoustic techniques.

We discuss the first two techniques (VUV and UV electronic spectroscopy) in order below. Figure 1 shows an example of VUV one-photon excitation of the $B^1\Sigma_u^+$ v'=0 state, followed by UV emission to the $X^1\Sigma_g^+$ v"=6 state; and of UV two-photon excitation of the E,F $^1\Sigma_g^+$ v'=0 state, followed by IR emission to the $B^1\Sigma_u^+$ v=0 state.

Tunable laser/nonlinear optical sources are available throughout the infrared, visible, and ultraviolet regions of the electromagnetic spectrum; many such sources will soon be available in the University of Connecticut Laser Facility (see attachment). Of particular importance for this proposal is generation of ultraviolet photons near 2000 Å (which can be carried out with commercial instrumentation) and more importantly generation of vacuum ultraviolet photons near 1000 Å by e.g. third harmonic generation of frequency doubled pulsed dye lasers (near 3000 Å). Pulse energies in the µJ - nJ range are expected for 1300 - 700 Å, and in the mJ - µJ range for 2600 - 1400 Å.

Single VUV Photon Absorption

Atomic hydrogen spectroscopy is well known. For example, ultraviolet H(1s) → H(3p) excitation (Lyman β) at 1025 Å will produce H(3p) → H(2s) visible red (Balmer α) emission at 6563 Å (as well as re-emission of 1025 Å radiation), with the radiative transition probabilities of each step being known precisely. While the light at 1025 Å will be radiatively trapped and will not be significantly transmitted by optical windows, optical fibers, etc., the red light will not be radiatively trapped (there is a negligible population of the 2s state of atomic H) and will be

easily transmitted and detected. Such measurements will establish the absolute concentration of H in solid H_2 (there are no overlapping H_2 molecular lines in standard tabulations). L_α and L_β emission following "white light" excitation i.e. synchrotron radiation in the 400 - 3000 Å region) has been detected for H/H_2 deposited in Ne(s). No such experiments have been carried out for H in H_2(s), but detectable emission is expected.

In addition, under many conditions the rate equation for atomic hydrogen concentration n,

$$\frac{dn}{dt} = K - (2\alpha)n^2$$

where K is the production rate (H atoms/cm^3-s) and 2α is the two-body recombination rate constant (cm^3/H atom-s). In the steady state, for a constant production term such as the beta decay of the tritium nucleus where the half-life is twelve years, this has the solution

$$n_{ss} = \sqrt{\frac{K}{2\alpha}}$$

where α is strongly temperature dependent. {A form $2\alpha = (2\alpha_0)\exp(-E_a/kT)$ is often assumed}. Thus, once calibrated, a determination of n_{ss} is equivalent to a temperature measurement and can be made at a location remote from the sample.

The H_2(s) matrix itself can also be probed using vacuum ultraviolet photons. Near 1000 Å, the ground $X^1\Sigma_g^+$ electronic state of H_2 absorbs light at specific, precisely known, wavelengths to form specific upper levels. For para-H_2 (J"= 0 plus a few PPM of J"= 2, all v" = 0), the absorption is to J' = 1 (plus a few PPM to J' = 3) in several possible v' levels in each of the $B^1\Sigma_u^+$, $C^1\Pi_u$, $B'^1\Sigma_u^+$, and $D^1\Pi_u$ states of H_2. For ortho-H_2, the absorption is to J' = 0 and 2 in the same v' and electronic states. Because of the linewidths of these absorptions, however, it will be difficult to separate para (J"=0) versus ortho (J"=1) absorption (or J"=2 versus J"=0 for temperature determination).

The excitation can be detected in two convenient ways: for higher levels, e.g. various v' levels of $B'^1\Sigma_u^+$, well-known near infrared and visible emission lines occur to various v" levels of the E,F $^1\Sigma_g^+$ state; while, for all levels, well-known ultraviolet emission lines occur, often at much longer wavelengths (out to about 1700 Å for B → X emission) which are readily transmitted and detected. In either detection scheme, one can determine H_2 concentration absolutely, as well as possibly the relative para and ortho composition. Since only parts per million of para-H_2 (J" = 2) are present, it may be difficult to establish the temperature from the molecular spectroscopy. It is expected that the lineshapes (and also the lineshifts) of

the molecular lines (as well as the atomic lines described above) will be sensitive to the method of preparation and crystallinity of the $H_2(s)$ sample. Single crystal $H_2(s)$ (especially pure p-$H_2(s)$) is predicted to have relatively sharp absorption and emission lines (each of which can be readily detected). Amorphous $H_2(s)$ should have broader lines.

It should be noted that high concentrations of electronically excited H_2 could in principle cause problems, such as ionization. However, the light sources in the 1000 Å region are weak and not expected to generate high concentrations of electronically excited H_2. The sources, though weak, are more than adequate for the fluorescence-detected spectroscopy proposed here.

High concentrations of H atoms in $H_2(s)$ may also cause complications, as found in the EPR experiments. First of all, interactions between H atoms will give rise to resonance broadening of the atomic excitation line (L_β at 1025 Å). Shifts and broadening of the order of 1000 cm^{-1} should occur for nearest neighbor atoms (Gaussian line broadening and shifts should be significantly smaller). Nevertheless, the fluorescence quantum yield should remain near unity and if the $H_2(s)$ lattice spectrum is well-understood, a quantitative measure of the total H atom concentration should still be obtainable at high density. An accurate theory of resonance line broadening could be worked out from known potential energy curves and transition moments and tested on H in Ne(s) if necessary. Note that lineshapes of L_α and L_β emission in Ne(s) are available [W. Böhmer et al., Chem. Phys. 49, 225 (1980)].

A further complication could occur from H + H_2 interactions. In particular, the electronically excited atom could in principle transfer electronic energy to H_2 molecules of the lattice and/or chemically react with H_2 molecules of the lattice. Such channels would add to the complexity of the analysis, but should already be observable at low H atom concentrations (< 0.1 %). Moreover, both electronic energy transfer and chemical reaction, if they occur to a significant extent, could be expected to be highly selective, each producing only a few quantum states at most, each with characteristic emission lines. Moreover, the importance of these channels should vary dramatically with isotopic composition and nuclear spin state. The H(2p) state cannot transfer energy, but all higher p states can. The probability of chemical reaction is apparently not known.

Two UV Photon Absorption

Two photon excitation of atomic hydrogen is well known. For example, H(1s) → H(3s) excitation at 2050 Å will produce H(3s) → H(2p) visible red (Balmer α) emission at 6563 Å. Since 2050 Å light is considerably easier to generate than 1025 Å light, this UV diagnostic

300

technique may turn out to be superior to the VUV excitation discussed above.

Two photon excitation of H_2 is also well known. Figure 2 shows work by Young at Iowa on UV two photon excitation of H_2 (in a dilute molecular beam) from $X^1\Sigma_g^+$ v"=0,J"=0, 1 and 2 to E,F $^1\Sigma_g^+$ v'=0,J'=0, 1 and 2, respectively, at ~2020 Å using ionization detection. Alternatively, near infrared emission (e.g. E,F $^1\Sigma_g^+$ v'=0,J'=0 $\rightarrow$ B$^1\Sigma_u^+$ v"=0,J"=1) at ~1.1 μm can be readily detected.

It is worth noting that such two UV photon excitation lines should be much sharper than the corresponding single VUV photon excitation lines. This is because the strong resonance broadening and resonant energy transfer, which presumably dominate the broadening observed in B-X VUV absorption (so that vibrational but not rotational structure is seen), cannot occur in the two UV photon case since the E-X dipole matrix element is identically zero. Particularly for cases such as pure p-H_2(s) and o-D_2(s) (or better yet, trace amounts of p-H_2 in o-D_2(s)), the two photon lines should be extremely sharp (<1 cm^{-1}). Remarkably sharp lines have previously been observed in rovibrational and pure rotational spectra by Patel et al. and especially by Oka et al. Such sharp lines would be ideal for diagnostics of concentration, temperature and crystal quality.

Production of H atoms in the solid

The light sources used for spectroscopy can also be used to carry out photochemistry. The weak VUV sources near 1000 Å, however, are marginal for such studies. Nevertheless, a photon at $\lambda \leq$ 844.45 Å can photodissociate H_2 through the B$^1\Sigma_u^+$ state in the gas phase. This is rather close to the H_2(s) band gap at ~ 731 Å, but probably photodissociation of $H_2 \rightarrow$ 2H can also be carried out in the solid. By remaining close to threshold, one can directly and homogeneously produce "cold" atoms (kinetic energies of $\leq$ 1 K). Such mild photodissociation is to be contrasted with the significant radiation damage in production of H atoms by beta decay of tritium and other production techniques such as electron bombardment. Direct study of such atom production with the accompanying atomic and molecular spectroscopy diagnostics may establish fundamental limits on H atom storage in H_2(s). Moreover, pump/probe experiments to follow the time dependence of the H atom concentration would be feasible.

Another improved high energy density material is metal-doped H_2(s), where "metal" is used loosely to include B and C as well as Li, Be, Na, Mg, and Al. Such atoms give significant improvements in energy storage compared to pure H_2(s).

Visible and ultraviolet photochemistry for H production becomes possible based on these metal atoms at much longer wavelengths (with much more readily available photons) than for pure $H_2(s)$.

For example, for Li, the processes

(1) $\quad\quad\quad$ $Li + h\nu_{3233 \text{ Å}} \rightarrow Li(3p)$

(2) $\quad\quad\quad$ $Li(3p) + H_2 \rightarrow LiH + H$

(3) $\quad\quad\quad$ $LiH + h\nu_{2840 \text{ Å}} \rightarrow Li(2p) + H$

(4) $\quad\quad\quad$ $Li(2p) \rightarrow Li + h\nu_{6701 \text{ Å}}$

occur in the gas phase (although process 2 has not yet been observed, similar processes have been observed for Na, K, and Cs whenever they are energetically possible). They should all occur in $H_2(s)$, although the optical wavelengths should be slightly shifted.

Adding equations (1) through (4), one obtains

$$H_2 + h\nu_{3233 \text{ Å}} + h\nu_{2840 \text{ Å}} \xrightarrow{Li} 2H + h\nu_{6701 \text{ Å}}$$

This corresponds to a photocatalytic scheme by which H_2 and 2 UV photons generate 2 H atoms (and an unimportant red photon). Note that Li, the photocatalyst, is neither produced nor consumed overall. Hence, hundreds or thousands of H atoms can potentially be produced from a single Li atom. Similar considerations apply for all the "metal" atoms listed above, all at wavelengths which are easier to generate than the 844.45 Å wavelength required for pure $H_2(s)$.

PLAN OF RESEARCH

Thus we propose to combine the cryogenic and solid hydrogen expertise at Hawaii with the optical spectroscopic and laser expertise at Connecticut to study the above techniques. In the first year we would optimize tunable light sources near 1000 Å and near 2000 Å and test them on H_2 in the gas phase at Connecticut, while an optically accessible H_2 cryogenic system would be constructed at Hawaii. In the second year, we would irradiate with UV and VUV photons the Hawaii cryogenic system at Connecticut, emphasizing molecular spectroscopy and its relation to $H_2(s)$ crystallinity. In the third year, we would attempt photodissociation of H_2 just below the $H_2(s)$ bandgap, and study the resulting atomic spectroscopy. In the fourth and fifth years, we would study using atomic and molecular spectroscopic diagnostics, the photocatalytic production of H in $H_2(s)$ doped with various "metal" atoms.

The goal of these studies would be to establish the fundamental limits on atomic hydrogen concentrations in $H_2(s)$ (both pure and metal-doped) as well as to develop powerful spectroscopic techniques for characterization of cryogenic solids and better understanding of the broadening and shift of sharp spectroscopic lines by a solid matrix. This work would also complement existing theoretical and experimental work on hydrogen clusters and cryogenic hydrogen. Although it is not discussed here in detail, the effect of pressure on $H_2(s)$ is large and the appropriate spectroscopy would be an exciting extension of this proposal.
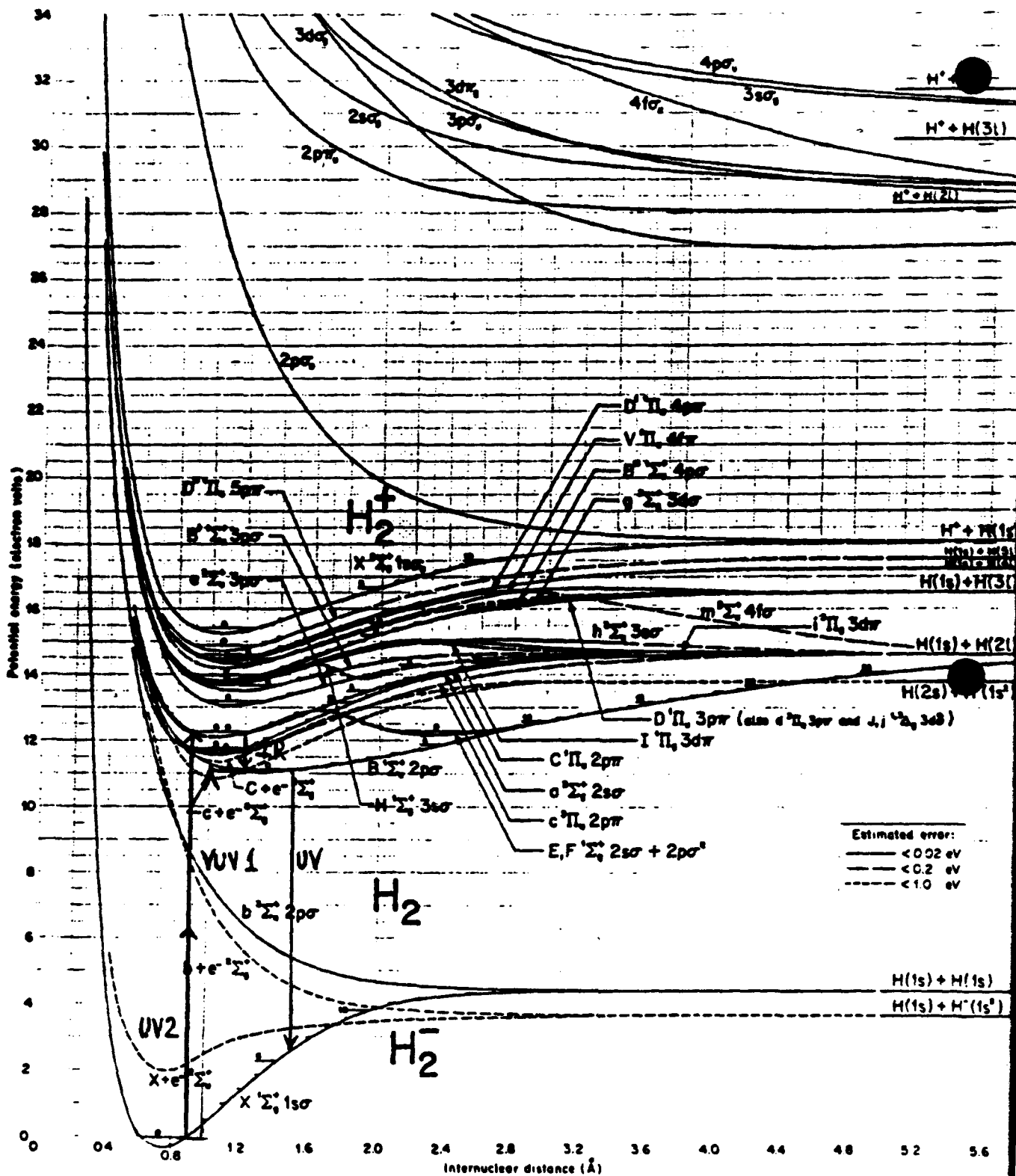
FIG. 1 Potential-Energy Curves for H_2, H_2^-, and H_2^+
A large-scale pullout of this drawing appears at the front of this issue
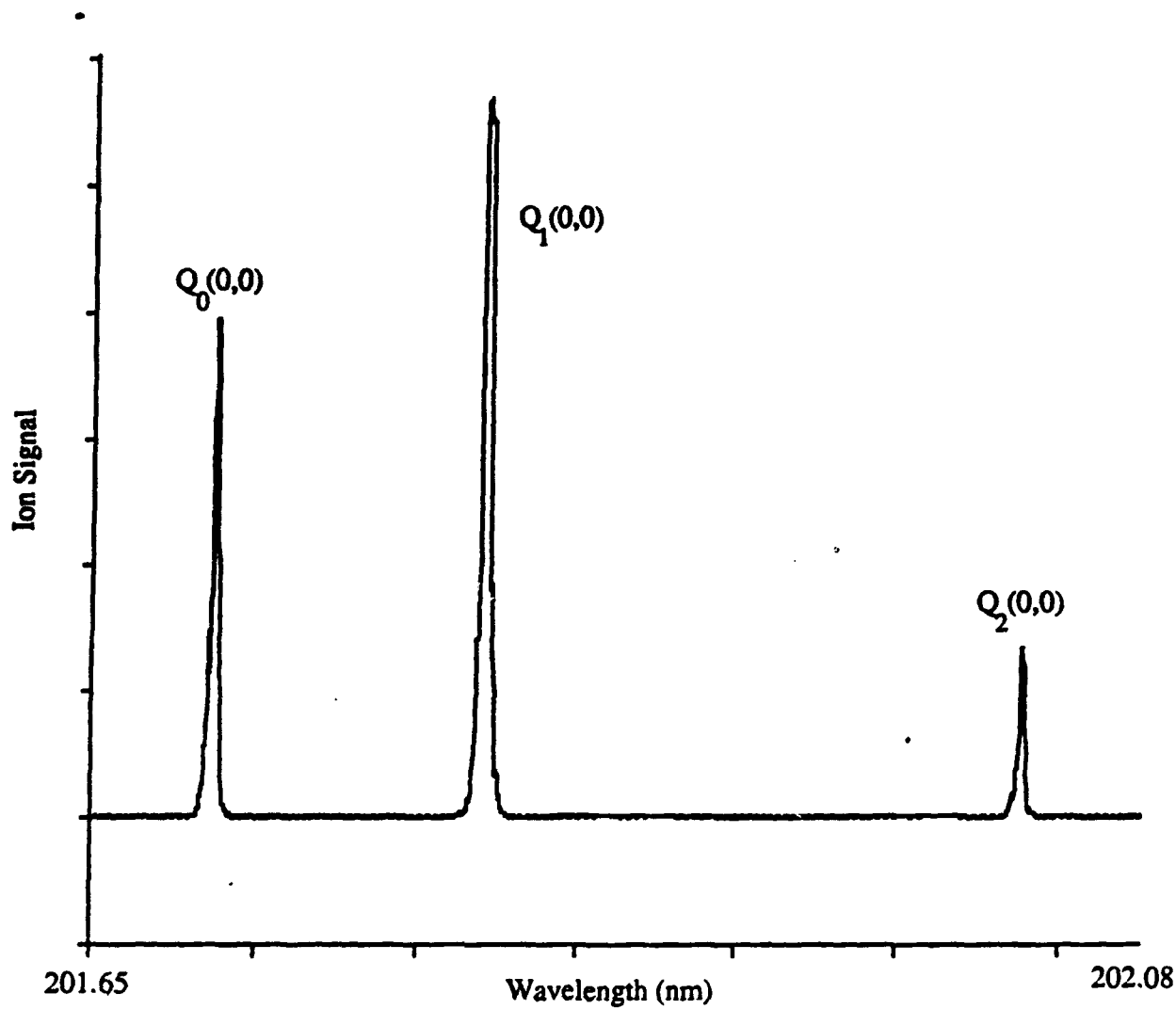In general $1s\sigma$ has been omitted from state designations in order to save space

FIGURE 2. (2+1) REMPI spectrum of the E, F $^1\Sigma_g^+$ state in H_2 with VUV laser radiation generated by sum frequency generation in a BBO crystal. Hydrogen was seeded 10% in a helium expansion and laser pulse energy was ≈ 100 μJ.

M. A. Young, University of Iowa, private communication (1992).

The University of Connecticut Laser Facility

Institute of Materials Science

William C. Stwalley
Director

P001, 007A
Physics Bldg.

The University of Connecticut

2152 Hillside Road

Storrs, CT 06269-3046

(203) 486-2924

Fax: (203) 486-3346

E-Mail
stwalley@uconnvm
.uconn.edu

The University of Connecticut Laser Facility is one of a very small number of laser user facilities. It is being established (effective 9/1/93) through the Institute of Materials Science to support the research efforts of University investigators in all fields involving lasers. However, off-campus users from industry, government, and other educational institutions are also welcome.

While the facility supports the work of others, it also houses the *important research of the facility's staff* in the development of new lasers and of new laser techniques, e.g. in high-resolution spectroscopy.

Fundamental photophysics and photochemistry studies using lasers constitute an important part of the facility's research. Topics of current interest include all optical multiple resonance spectroscopy, laser-induced ionization and plasma formation, laser diagnostics of plasmas and combustion systems, single and multiphoton photodissociation, diffuse emission bands, spectra of metal dimers and clusters, ultra-sensitive detection, laser photochemical reactions, and coherent laser Raman spectroscopies.

Other areas of interest include materials processing (cutting, drilling, welding, inscribing), optical image processing, use of laser and fiber optic sensors, and novel laser pumping schemes.

The Connecticut Laser Facility offers a wide variety of modern lasers and laser-related instrumentation. (See listing below.)

The facility occupies two nearby laboratories in the Physics Building: A new cw laser laboratory (1000 ft^2) and a new pulsed laser laboratory (2000 ft^2).

STAFF AND STAFF SERVICES

William C. Stwalley, Professor of Physics and Chemistry and Head of the Department of Physics, is Director of the Connecticut Laser Facility. Current personnel include Dr. John Bahns, research associate, who is responsible for assisting users and maintaining instrumentation; and Rod Miller, research assistant, who is responsible for handling inquiries, data bases, graphics, accounts and other duties. Educational activities include workshops, open houses and seminars.

SERVICES PROVIDED

The principal service provided by the facility is laser irradiation by one or more of the lasers noted below. Additional support is available in the following areas:

- Consulting on experimental design
- Use of supplementary equipment (optical, electronic, high vacuum, etc.)
- Assistance in performing experiments (and in analysis and reporting of results)

It should be noted that these services are available not only for the research areas cited, but also in other areas of laser application. The laser is a tremendously versatile device and innovative applications of lasers in areas not currently being explored in the facility are particularly welcome.

FEES

Facility users from within the University of Connecticut are charged $60/hour for laser time for any one of the laser systems, including research scientist time. Off-campus users are charged $90/hour for these services. Limited funds are available to defray the costs of demonstration or proof-of-principle experiments for which no funding is yet available. In addition, there is no charge for initial consultation to discuss and define possible experiments to be performed.

PROCEDURES FOR POTENTIAL USERS

Despite fairly heavy use of the laser systems, short experiments requiring only a few hours often can be scheduled within a week. An extended experiment is more difficult to schedule on short notice. Long-term, heavy use of a particular system is not normally possible; those with such potential uses may wish to perform demonstration experiments and then purchase, rent or lease a laser system elsewhere. Proprietary rights of users will be protected given advance notice. However, the Laser Facility staff expects to share in developments in which it has made a significant intellectual contribution.

MAJOR INSTRUMENTATION

I. CW Lasers (P007A)

A. Three Coherent 899-29 continuously scannable single mode tunable ring laser systems (pumped by I.B., C. or D.; 100 mW-6 W (3W single mode) at wavelengths in the visible or near infrared (400-900 nm))

B. Coherent Innova 200-25/7 UV argon ion laser (25 W visible or 7 W ultraviolet with single mode accessory for 10 blue-green and 9 near ultraviolet lines)

C. Coherent CR-3000 K krypton laser

(3 W total with single mode accessories for 5 blue-green, 3 violet, 3 near ultraviolet, 1 yellow, 2 red and 3 near infrared lines)

D. Coherent CR-18 argon ion laser (18 W with single mode accessories for 10 blue-green and 6 near ultraviolet lines)

E. Coherent CR-6 argon ion laser (6 W for 10 blue-green lines)

F. Coherent CR-2 argon ion laser (2 W at many of the visible lines mentioned in I.A.)

G. Custom Allied Corp. Alexandrite laser (up to 3 W tunable from 700 to 820 nm in the near infrared)

II. Pulsed Lasers (P001)

A. Lambda Physik EMG 102SE excimer laser (≤ 100 pulses/sec, $\sim 10^{-8}$ sec pulses), ≤ 250 mJ/pulse (KrF); excimer emission at 157, 193, 222, 249, 308 and 353 nm

B. Plasma Kinetics 351 CVL copper vapor laser with average output power of 30 W at 5.7 kHz

C. LASAG KLS-321 Nd:YAG materials processing laser. 20 J/pulse at 1.06 μm. Pulse length variable from 0.2 to 20 ms. Repetition rate 1-100 Hz. Maximum power 300 W.

D. A nanosecond tunable solid-state laser system will be ordered during the coming months and will be described in an update of this handout.

III. Support Equipment

A variety of support equipment is available including small lasers (HeNe, diode), spectrometers, detectors, and data acquisition systems in the infrared, visible and ultraviolet; optics; electronics; vacuum systems (e.g. time of flight mass spectrometer); and cryogenic systems.

307

PROPULSION SYSTEM DESIGN CONCEPT USING FREE RADICAL HEDM TECHNOLOGY

JOSE E. CHIRIVELLA

JET PROPULSION LABORATORY
CALIFORNIA INSTITUTE OF TECHNOLOGY
PASADENA, CA

PREPARED FOR

PROPULSION SYSTEM DESIGN CONCEPT USING FREE RADICAL HIGH-ENERGY DENSITY MATTER (HEDM) TECHNOLOGY

J.E. Chirivella
Jet Propulsion Laboratory, Pasadena, CA

1. INTRODUCTION.

Desirable Characteristics of a Free Radical HEDM Propellant System.

Free radical HEDM propellant technology makes use of high-energy molecular/atomic systems that are enriched with free radicals to obtain high performance in rocket propulsion. The high specific impulse that can potentially be obtained from such propellants makes the HEDM concept attractive for applications involving both spacecraft and launch vehicles. This high performance is derived primarily from the high heat of reaction of HEDM propellants that results in high combustion temperature T_0. If one assumes 100% combustion efficiency, c^* can be adopted as a figure of merit for the propellant system

$$c^* = \frac{\sqrt{g \gamma R T_0}}{\gamma \sqrt{2 \left[(\gamma+1)\right]^{(\gamma+1)/(\gamma-1)}}} \tag{1}$$

where R is the gas constant, and γ the gas specific heat ratio. As can be seen from Eq. 1, for a value of T_0, performance is favored by those HEDM systems that result in low molecular weight of the exhaust products, but in order to maximize c^* the exhaust composition has to be somewhat compromised to retain an acceptable value for the gas specific heat ratio.

The free radicals in the propellants must be sufficiently stable for long-term storage without excessively degrading their initial high energy density, i.e., concentration. This latter requirement is perhaps the highest challenge which may be encountered when developing free radical HEDM propellants. Applications of HEDM to propel launch vehicles (LV) can be somewhat more forgiving in this sense, given that the propellants need to be stabilized only for a few days, from fabrication to utilization. Applications to space vehicles (SV), on the other hand, often require storage periods of months, if not years. HEDM application to boosters requires also high propellant densities, otherwise the installation of large-volume tanks would be necessary. This would result in excessive launch vehicle cross sections, and translate into high drag losses during the lower portion of the ascending trajectory.

An important feature that these HEDM propellant systems may offer

in certain rocket configurations is the potential for very high burn rates, which means high thrust, that is, high acceleration. This latter characteristic is most desirable when selecting propulsion systems for high speed interceptors.

Current techniques to prepare free radicals HEDM propellants invariably invoke the trapping of free radicals in a low temperature crystal matrix. The trapped free radicals consist of atoms and/or atom clusters that are stabilized (prevented from undergoing recombination) by keeping the temperature low and/or the pressure high (Mbar range?). The alternative of stabilizing HEDM propellants by keeping them at high pressure, is hampered by the large increase in tank mass that can be tolerated. One possibility that has not been explored yet, however, is the use of additives for increasing free radical stabilities at temperatures and concentrations that would otherwise be prohibitively high. Exploratory performance calculations have fixed the minimum concentration of free radicals at levels of 5-10% for a cost effective but practical HEDM implementation.

To keep performance high, the HEDM solid matrix must be at least one of the major propellants, and this leaves only SO_2 and SH_2 as the most likely matrices to trap free radicals (the concern for toxicity and environmental impact has eliminated other candidates such as fluorine, nitrogen oxides, etc). In general, the lower the matrix temperature can be kept, the higher the energy densities which might be achieved by doping the matrix, and the higher the stability of the free radicals.

As a final note, the propellants must be environmentally sound, must be made available on short-term notice, and their fabrication has to be kept at reasonable cost. One cannot lose track either of the on-board equipment required for their storage, feed, and injection into the combustion chamber. It has been a experience in propulsion that higher specific impulse comes always accompanied by an increase in propulsion system dry mass. The various electrical propulsion systems proposed and developed are a good example, and HEDM technology is not expected to be an exception. A summary of desired characteristics of HEDM propellants is presented in Table 1.

Objective

The objective of this study is to explore conceptual designs and configurations of propulsion systems which employ free radical HEDM propellant technology. Only those designs that can be implemented by invoking readily (and/or on short-term basis) available technologies have been considered. Along these lines, while some esoteric concepts may be entertained, emphasis is given to those concepts that, if not exploiting the full potentials of HEDM, do result in a vehicle that exhibits performance superior to what is nowadays attained with chemical propulsion. Furthermore, present liquid propulsion systems powered with cryogenic propellants cannot be readily adapted to HEDM. The propellants need to be further

EXHAUST PROPERTIES

o High Combustion Temperature
o Low Molecular Weight
o Composition to Yield an Acceptable Gas Specific Heat Ratio

PROPELLANT TRAPPING MATRICES

o High Density
o Low Cost
o Environmentally Sound
o Safe
o Most Likely Candidates
   - Fuel: SH_2
   - Oxidizer: SO_2

o Best Trapping Results Are Obtained at Low Temperatures
   (a Few K) and High Pressures (a Few Mbar)

o For Certain Applications, High Burn Rates are Desired

FREE RADICALS

o Need to be Stable for Long-term Storage at Concentrations
   Sufficiently High for the Propellant to Exhibit HEDM
   Performance

o Required Stability Must Be Met at Temperatures Near or Above
   the Helium Lambda Point

o Required Stability May be Achieved by the Use of Additives

o The Stability Should Be Obtained at Pressures Not Exceeding
   the Propellant Tank Limits

o Propellant must be Available on Short-Term Basis

HEDM PROPELLANT UTILIZATION

o Storage System Must Be Kept Simple and Light

o Feed System and Injection Devices Cannot Increase the
   Propulsion System Dry Mass

Table 1. Desired Characteristics of Free Radical HEDM Propellants

cooled to solidify them into free radical trapping matrices.

The designs thus conceived could serve as a test bed of future free radical HEDM proposals, and can be also adopted to identify the type of technologies that must be demonstrated for the implementation of free radical HEDM technology in launch vehicles.

2.   DESIGN APPROACH.

Design Drivers.

Because of the short term technology readiness that we have scoped for our study, we will limit our review to SO_2 and/or SH_2 as the only viable candidate matrices for free radical HEDM applications.

When defining the matrix domain, one may think of a polycrystalline solid conglomerate or a slurry of condensate in a liquid. One can thus have the basic matrix dispersed as a solid conglomerate of hydrogen (SH_2) or oxygen (SO_2), or a slush of hydrogen (SLH_2) or oxygen (SLO_2). We will see later that there is no strong interest in SLO_2, but there are important reasons to consider a slush of solid hydrogen in liquid helium (SH_2/LHe).

The selection of SO_2 makes the implementation of a HEDM propellant a much more feasible proposition, given that it does not call for LHe temperature technology. The drawback is that the free radicals that can be trapped with sufficient stability within these matrices may not offer the attractive energy densities that have been quoted in HEDM studies. In addition, the HEDM community has focused their research around SH_2 matrices, and the only information available on free radicals trapped in SO_2 revolved around the allotropic forms of oxygen. At this time, the performance, stability, and/or existence of the higher energy forms are still speculative.

SH_2 calls for temperatures that can only be obtained using LHe refrigeration systems (below 10 K). Even at pressures of a few atmospheres, the large-scale manufacture of HEDM propellants and their long-term stability pose a major challenge. It is has been found that at temperatures below the Lambda point, very high-energy density free radicals (such as atomic hydrogen) can be stabilized in concentrations of a few percent. Unfortunately, operations in large scale at those low temperatures become impractical due to the immense refrigeration systems that have to be available. A relief in logistics and economics can be met by adopting free radicals that can be kept at reasonable concentrations at temperatures ranging from 5 to 7 K for sufficiently long time. Atomic metals (Li, Al, B, Be) and metalloid clusters (B_2, C_2) fall in this category.

Rationale.

Regardless of whether SO_2 or SH_2 are selected as HEDM matrices, one must first undertake the challenge to design propulsion systems

that employ one or both of these condensates as propellants, as well as a launch vehicle and ground system that could be credibly demonstrated using present technology. Once the engineering elements of such a project have been identified and solved, it is a matter of extending those technologies to the utilization of free radical doped HEDMs using as matrices those condensate, and employing design elements, processes and operations that have been demonstrated in a propulsion system. This evolutionary concept is illustrated in Figure 1.

Anticipated Results.

The addition of free radicals can be thought of as an enhancement with its unique engineering schemes and enabling technologies. This proposed approach permits to:

(1) Disentangle the issues peculiar to the condensed propellants from those others raised by the utilization of free radical HEDM technology.

(2) Identify those HEDM schemes that can be readily implemented, providing thus a pathfinder to current HEDM programs.

(3) Focus and enhance objectivity to AFOSR R&D in the HEDM Program.

3. SOLID HYDROGEN AS A PROPELLANT.

Densification of LH_2

One of the problems for the utilization of hydrogen as a propellant is its low density. LH_2 has a density of 0.070 g/cc. Even if this propellant has been used extensively in the lunar program and also in various launch vehicles, its inherent low density leads to large tanks which, as mentioned above, can lead to unacceptable atmospheric drag losses during the ascent of the launch vehicle. This is also the reason that launch vehicles employing LH_2 operate at an oxidizer/fuel ratio higher than the optimum required for maximum specific impulse. Only the Orbiter main engines and the Japanese H-II launch vehicle employ LH_2/LO_2 for the first stage. The current launch vehicle design trend is to use more compact, lower specific impulse, solid rocket motors for the first stages, and reserve LH_2/LO_2 for the upper stages. Current tank mass factors for LH_2 range from 15-25% at moderate pressures.

The problem can be ameliorated by using densification of hydrogen and storing it as SH_2. With its higher density (0.086 g/cc), SH_2 already signifies a 19% savings in tank volume, and as much as 12% reduction in tank mass. In addition, adopting SH_2 as a propellant opens the path to its future utilization as a free radical trapping matrix.
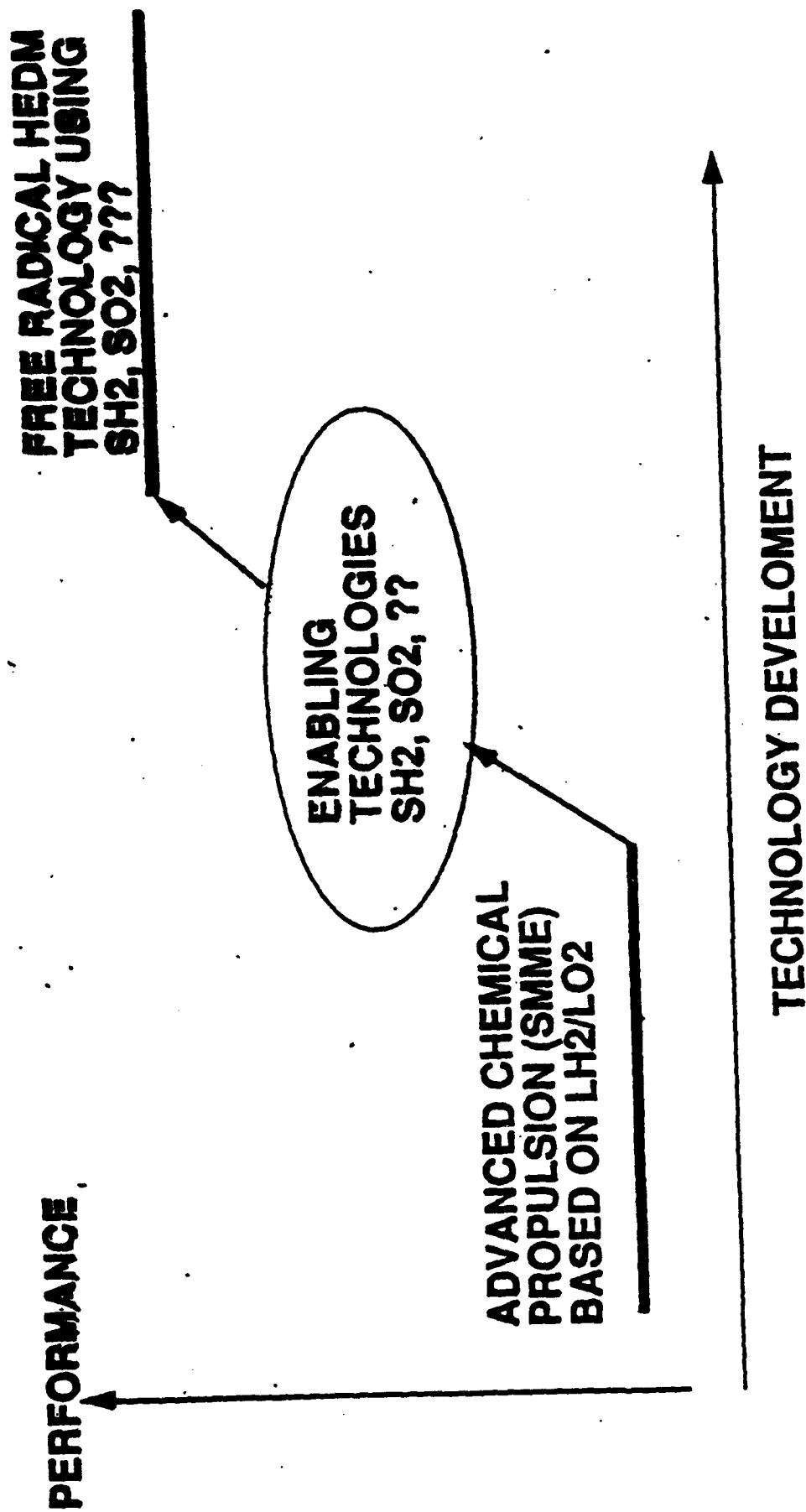
Figure 1. Rationale for the Development of SH2, SO2 Propulsion Systems.

Preparation and maintenance of large amounts of SH_2 call for additional developments given that SH_2 cannot be readily pumped into the combustion chamber, and it may be necessary to totally or partially melt it before its pumping into the chamber at high pressure. In short, switching from LH_2 to SH_2 will require new storage schemes, new pumping systems, and a yet unknown mass of super-insulation and heat sinks that will have to be installed on the LV.

Storage Schemes for Solid Hydrogen.

SH_2 can be stored as a slurry (introduced above as slush hydrogen) consisting of SH_2 dispersed in LH_2. This approach can be accomplished by installing separate tanks aboard the LV for SH_2 and LH_2, and arranging for a mixing reactor for the onboard production of SLH_2 (see Figure 2). Another scheme using a single tank loaded with SLH_2 is presented in Figure 3. The first approach may be more convenient in those cases where the slush is not stabilized sufficiently long before its utilization. It suffers from the drawback of necessitating a larger dry mass than the single tank scheme. Notice that low pressure and high pressure pumps are required to inject the hydrogen into the super-critical combustion chamber. Also, and in order to protect the high-pressure pump from erosion, it may be necessary to add a liquefier stage between the low and high pressure pumps to convert the SLH_2 into LH_2.

Another alternative that has been proposed in the past (Ref. 1) but which is somewhat speculative, is the storage of hydrogen as a solid with a certain amount of atomic hydrogen trapped in the matrix. The amount of atomic hydrogen needs to be only sufficient to release enough energy for melting the SH_2. In this manner, a melting front is achieved which can then be - with a propellant-management device - delivered to a low pressure pump. Following our rule of addressing only short-term technology, we will not elaborate this scheme at present.

Slush Hydrogen as a Fuel.

The requirement for densification of LH_2 is not unique to launch vehicles. It is shared by hypersonic airplanes using LH_2 as a fuel, such as the National Aerospace Plane (NASP), see Refs. 2-3. From the two techniques selected by NASP to densify LH_2, triple-point hydrogen (TPH) and slush hydrogen (SLH_2), only SLH_2 has been found an attractive possibility because of the simultaneous occurrence of two important properties: increased density, and increased heat capacity (see Figure 4). There are, however, certain areas in need of engineering solutions to carry forward the implementation of SLH_2 on a large scale, and these are:

1. Slush hydrogen production in a large scale.
2. Gelation of hydrogen and/or SLH_2.
3. Stability and storage of SLH_2.
4. Expulsion of SLH_2 from tank.
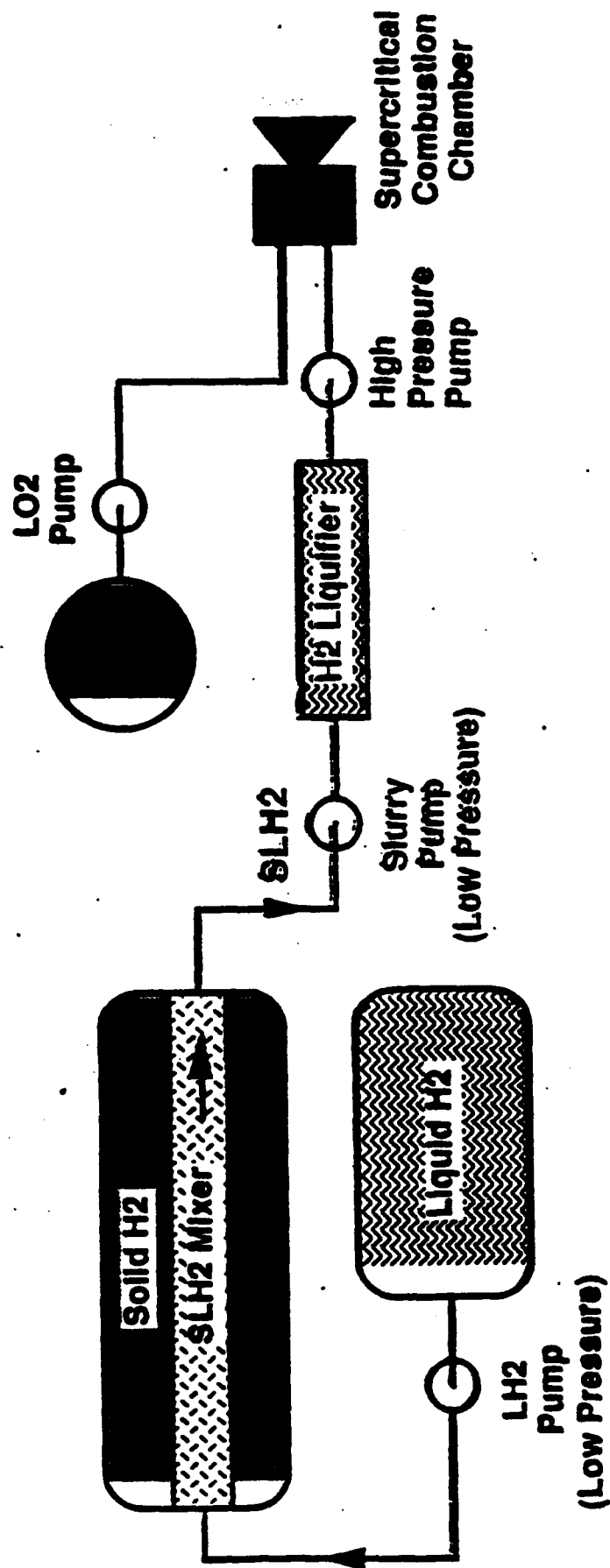5. Pumping and flow control.

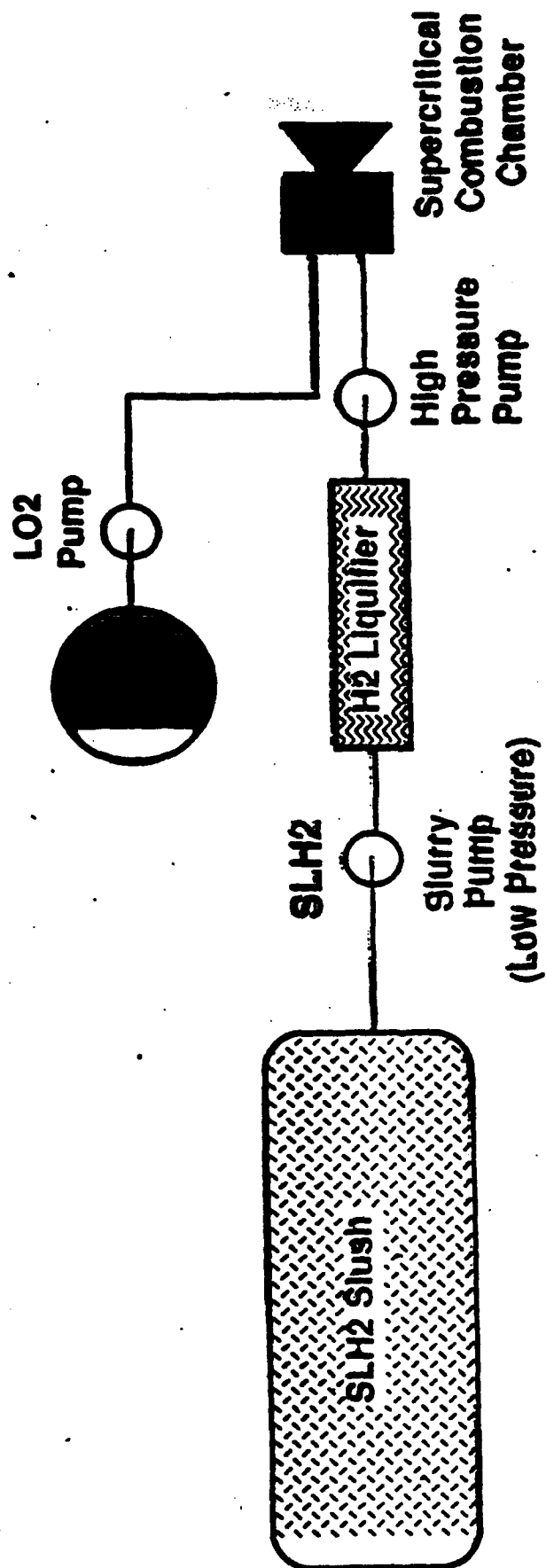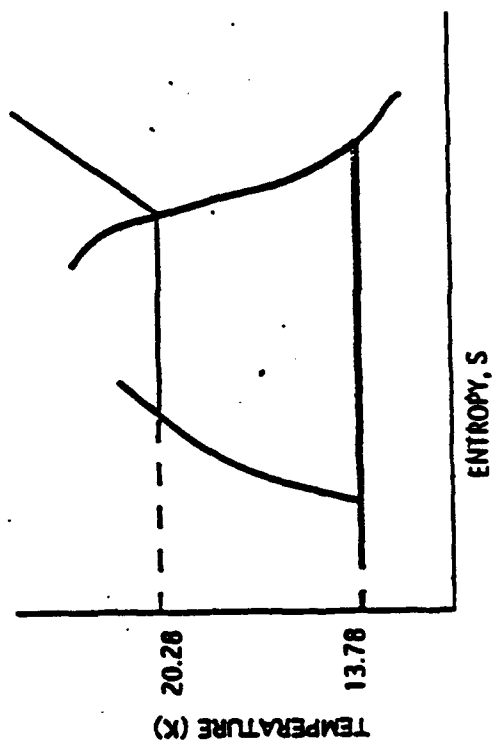Figure 2. SLH2 Slush/LO2 Scheme - Two Tank System with On-Board Mixing.

Figure 3. SLH2 Slush/LO2 Scheme – One Tank System with Pre-Mixed Slush.

	ENTHALPY GAIN	DENSITY GAIN
OPERATION AT THE TRIPLE POINT	11.5 %	9.1%
OPERATION WITH 50% SLUSH HYDROGEN	18.1%	15.9%

Figure 4. Comparison of Properties for TP Hydrogen and 50% Slush Hydrogen.

6. Liquefaction and injection.
7. Instrumentation.
8. Safety.

Large-Scale Production of SLH2.

From the enabling technologies outlined above, the most challenging is undoubtedly the large-scale production of LSH_2. Three methods have so far been considered by NASA/Lewis Research Center for the NASP program (Ref. 3). The freeze-thaw method, the auger method, and magnetic refrigeration. In the freeze-thaw method, SH_2 is obtained by evaporative cooling in a series of freeze-thaw cycles. Agitation is employed in the process to avoid the agglomeration of SH_2. The method is well characterized and documented. At present, this method is the most promising process for short-term implementation of large-scale production of SLH_2. In the auger method, SH_2 is trapped by a cold surface which is kept cold by a LHe refrigerator. The trapped SH_2 is mechanically removed by using an auger, and mixed with the LH_2. Process data exists for small-scale production only and the resulting SH_2 properties appear to be similar to those obtained by the freeze-thaw method. The magnetic refrigeration process is available only in its conceptual stage at present, but may become of value as an enhancing technology in the future.

The advanced stage of development of the SLH_2 makes it extremely attractive for our purposes, but it is not voided of some engineering issues that need to be overcome, among which are:

1. The onset of thermally driven acoustic oscillations (Ref. 4).
2. The sloshing of SH_2 in tank.
3. The dynamics of the thermal interface between the slush and the ullage gas.
4. The peculiar heat transfer phenomena due to thermal gradients within the tank and the mass of SLH_2.
5. The high pressure-drop in SLH_2 flow.
6. The difficulty in measuring and controlling the SLH_2 fraction history.

Slush SH_2 in LHe.

Because of its obviously favorable conditions for future free radical HEDM applications, there is serious consideration on whether lower operating temperatures can be achieved by making a slush of SH_2 with LHe. A slush, such as SH_2/LHe, can provide a medium to establish free radicals, not only for the energetic metallic atoms and metalloid clusters, but even for the most attractive free radical which is atomic hydrogen. If one would consider to employ helium instead of hydrogen as a fraction of the fuel, the performance penalty resulting for thermochemical equilibrium calculations is not large, and may in the end nearly be offset by the high density of LHe.

There are the necessary drawbacks, such as the open question on the stability of the slush, as well as to its suitability for transportation, storage, pumping, and SH_2 agglomeration in the slush due to the superfluidity of He II. There are indications of the possibility of forming such slush (see Ref. 5), but the feasibility of forming SH_2/LHe slush in large quantities remains to be demonstrated. What is most important, the large amounts of LHe, which would be lost to the atmosphere in LV boosters as He is injected into the combustion chamber, may signify a major challenge to the national capacity of LHe production.

As we shall see later, there is a potential application for this type of SH_2/LHe slush which may be most important and intriguing: LHe can be percolated out of the slush a few hours before launch, and recovered in a closed-loop refrigeration cycle for later utilization. The matrix of SH_2 could then be maintained and left within the LV at temperatures below the Lambda point, a most convenient arrangement for the implementation of HEDM.

4.   FEED AND INJECTION SCHEMES FOR SOLID HYDROGEN.

When operating the combustion chamber under sub-critical conditions, there is a substantial heritage for feed/injection systems derived from the Centaur and Apollo programs. Super-critical hydrogen pumping and injection, a superior performing scheme, is still considered to be a high technology, but it has the benefit of the Orbiter main engine heritage, and from this point of view, it can be considered a technology at hand. This scheme is also well suited for retaining regenerative cooling (only the low pressure segment), but requires the addition of a high-pressure pumping stage. Pumping of the SHL_2, even if in its embryonic stage, has been demonstrated in the NASP program. If one were to adopt the sub-critical injection, used by NASP, it is still possible to incorporate regenerative cooling in the low pressure segment and combine it with the liquefier stage discussed above and shown in Figures 2 and 3.

We have seen the difficulties which are incurred, even with undoped SH_2, if one were to adopt the common practice of splitting the processes of propellant production, storage in the LV tanks, pumping, and injection. Considerable simplification can be achieved if one were to consider the combustion chamber also as the propellant preparation reactor and the storage tank. This brings us to an altogether different approach which will be considered in the ensuing sections, and which does not require the "moving around" of the HEDM propellant.

5.   SOLID OXYGEN AS A PROPELLANT.

There is no information in the open literature in using solid oxygen as a propellant. The little experience existing on the handling of solid oxygen is derived from the accidental freezing of

oxygen when air comes in contact with liquid hydrogen or liquid helium. When SO_2 is formed at temperatures below 20 K, it appears to have a rough texture with jagged edges. At higher temperatures, however, there is work in progress that seems to indicate that it behaves as a plastic. Much work remains to be done in this area.

6. MERGING OF HYBRID ROCKET TECHNOLOGY WITH DENSIFIED CRYOGENIC PROPELLANTS.

A hybrid rocket motor is a rocket in which the fuel is stored in the combustion chamber in a manner similar to a solid propellant rocket motor. The oxidizer, however, is stored in liquid form and is kept in a tank. During operation, the oxidizer is fed into the chamber by means of a gas generator. The burning of solid propellant with the oxidizer vapor takes place along a series of ports longitudinally arranged (Figure 5). The oxidizer is injected into a pre-combustion chamber by means of a shower-head injector. Its length only needs to be sufficient for the propellant to become vaporized, before it is manifolded to each one of the fuel ports. In some designs, there is also a post-combustion chamber wherein the combustion comes to completion, and where there may or may not be further injection of oxidizer.
In an alternate arrangement (Figure 6), a solid oxidizer is encased in the combustion chamber, and liquid fuel is injected instead. This configuration is known as a reversed hybrid motor.

Hybrid motor technology has been known for a long time (see for example Ref. 6), but has recently acquired new impetus because of a Congressional mandate to NASA to eliminate HCl from SRM boosters because of its adverse environmental impact on the ozone layer. In FY93, NASA initiated, in conjunction with the rocket industry, an effort to develop and test large hybrid motors for launch vehicles. Demonstrations of large-scale motors have already been undertaken by the American Rocket Company, Ref. 7, and other motor manufacturers. Their findings and the current developments are most germane to our purposes, as we shall see in the following sections.

7.0. THE ALL-CRYOGENIC SH2/SO2 SOLID ROCKET MOTOR.

A third possibility is the encasing within the combustion chamber of both, the SH_2 and SO_2 matrices. The resulting agglomerate would consist in a mixture of fuel and oxidizer grains, as in a double base solid rocket motor. This approach would take advantage of the technology accumulated in high-performance solid rocket motors. The all-cryogenic solid rocket motor (Figure 7) constitutes a most intriguing approach, not only because of its simplicity, but because it also offers the possibility of very high burn rates. Present burn rates in solid propellants are about 1 in/sec for particle sizes of a few microns, and fine-to-coarse ratios of 50/50, when using 0.7% of burn additives. Hybrid motors show as much as 2 in/sec, and a cryogenic solid would most likely display
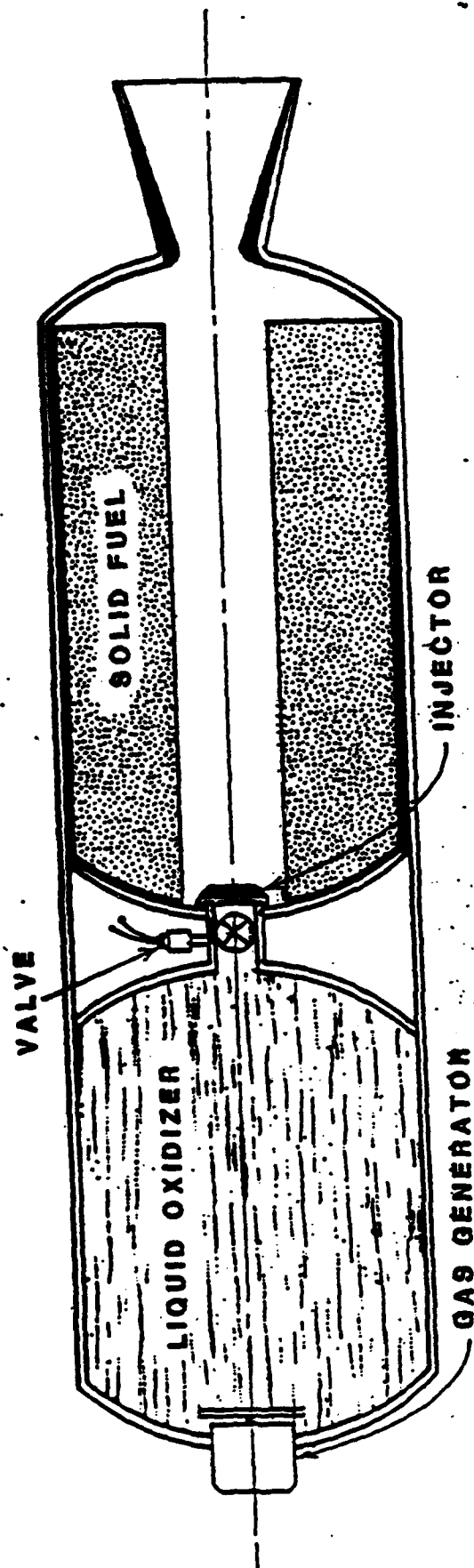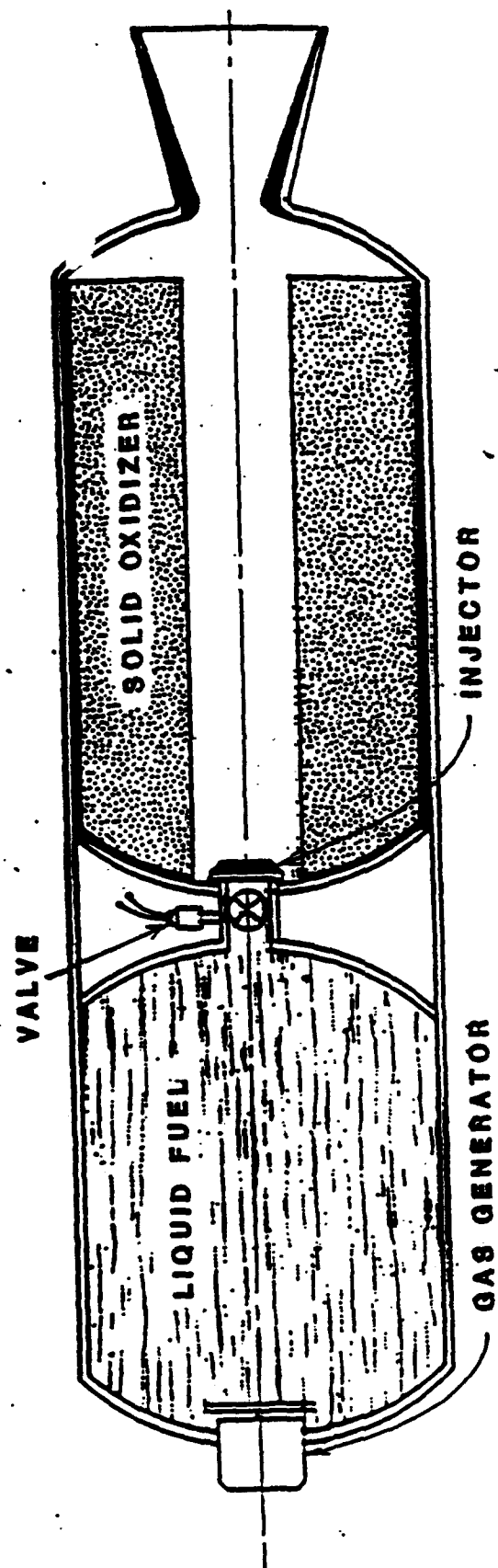
Figure 5. Hybrid Rocket Motor.
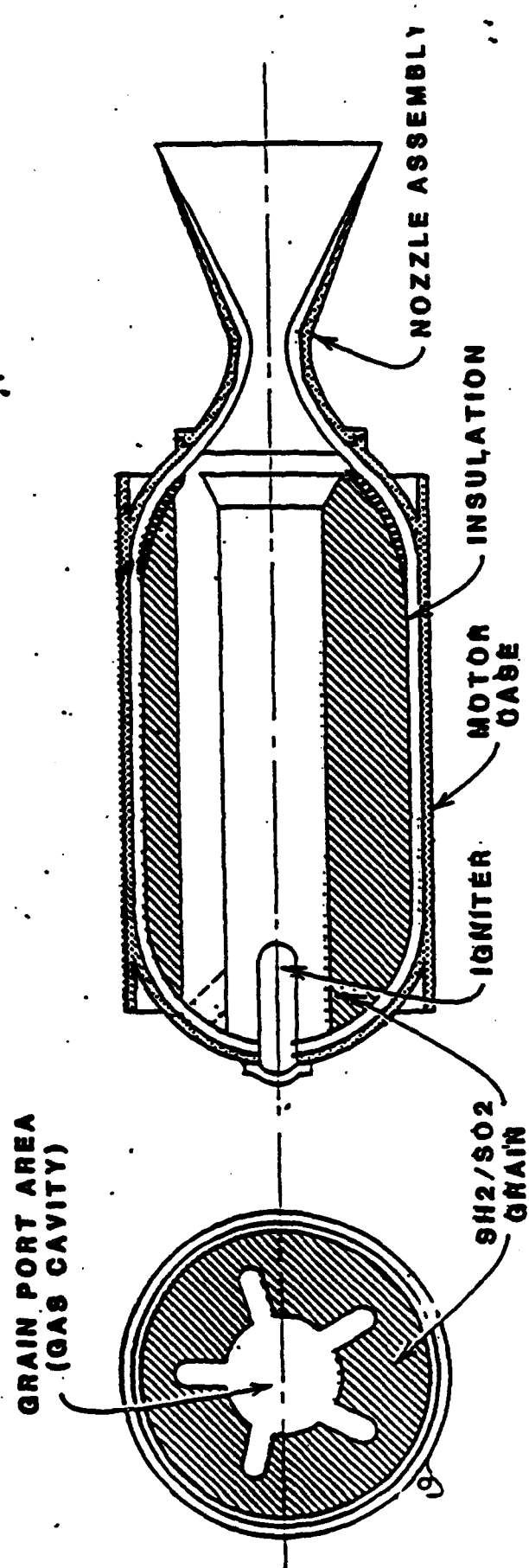
Figure 6. Reversed Hybrid Rocket Motor.

The figure is labeled with: SOLID OXIDIZER, INJECTOR, VALVE, LIQUID FUEL, GAS GENERATOR.

Figure 7. Cryogenic SH2/SO2 Solid Rocket Motor.

NOZZLE ASSEMBLY

INSULATION

MOTOR CASE

IGNITER

GRAIN PORT AREA
(GAS CAVITY)

SH2/SO2 GRAIN

324

10-20 in./sec. These high burn rates make these systems ideal for propelling fast interceptors (a sort of a Super-Patriot Interceptor), which could arrest the few missiles that may have penetrated the first line of defense. These fast interceptors would be employed for the terminal line of defense only, given that cryogenic SRM systems cannot be massively deployed due to economic constraints.

8. LARGE-SCALE INTEGRATION OF CRYOGENIC HEDM PROPELLED LAUNCH VEHICLES.

Design Requirements for Ground Facilities.

We have so far discussed propulsion system designs which would enable the utilization of SH_2 and/or SO_2 as propellants. Whether or not the solid matrices are doped with HEDM free radicals does not affect the discussed schemes, except in the issue of free-radical stability and propellant storage lead times. In what follows, we will proceed to integrate the technologies discussed above with the in-situ preparation and utilization of free radical HEDM propellants.

The nature of free radical HEDM propellants present unique challenges in the logistics of ground operations. The sites for propellant fabrication and loading, the facilities for integration of the LV and SV, and the launch pad site need to be in close proximity, if not within the same facility. One could in principle adopt the same site for all the aforementioned operations. This approach has its advantages in that enormous simplification is introduced in ground operations, resulting in lower costs, and assuring a prompt state of readiness. Furthermore, one cryogenic installation could service a cluster of launch vehicles. The approach has the obvious disadvantages of strategic vulnerability due to the loss of mobility. Its main application would be in LVs for cargo delivery to orbit and/or in terminal interception by fast ground-based AMB.

Launch Site Configuration.

A sketch of a facility for large-scale integration of a cluster of free radical HEDM launch vehicles based on SH_2 and using the cryogenic hybrid approach is shown in Figure 8. The selection of SH_2 does not exclude other approaches, and is made for the purposes of identifying the implementation issues. Notice that several sections of the LVs are clustered within the same cryogenic facility which is built underground and isolated from the environment by means of superinsulation and a LHe refrigeration system enclosed within a LN2 refrigerated liner. These sections are the HEDM portion of the vehicle, and are prepared and serviced in-situ.

The LVs are assembled and readied in separate silos. The HEDM section of the LV is extracted from the cluster facility and
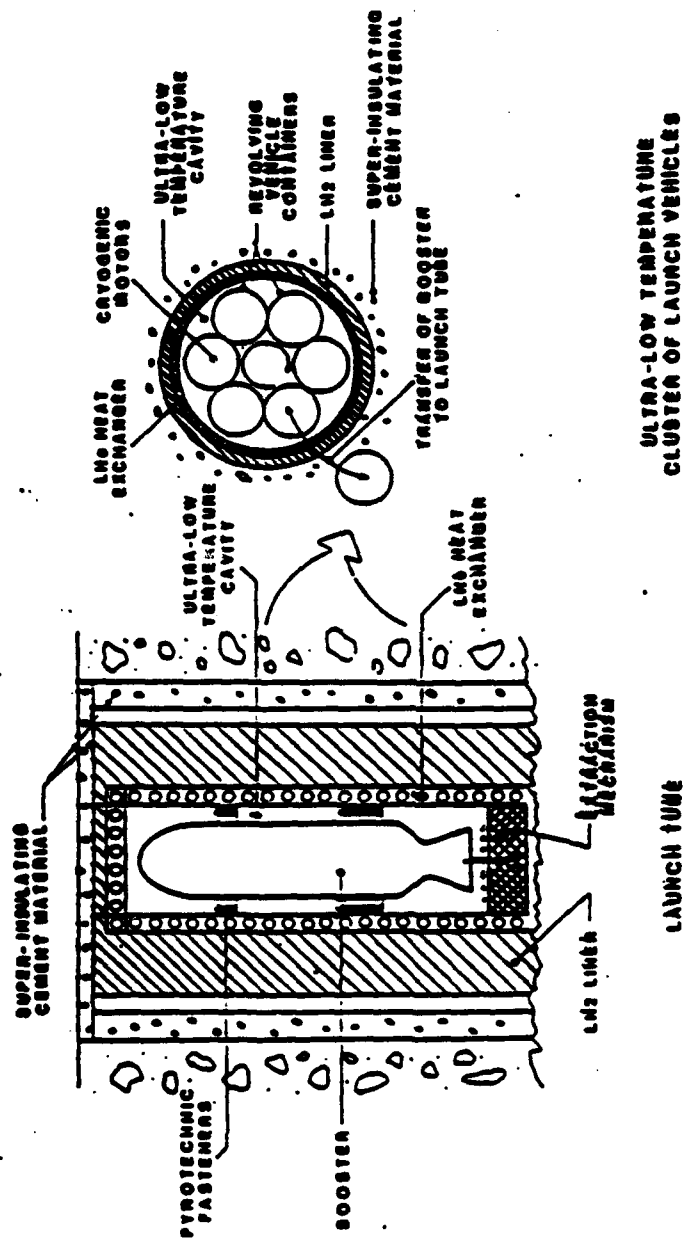
Figure 8. Example of Large-Scale Integration of a Cluster of Free-Radical/SH2 LVs.

introduced into the launch tube which is equipped with super-insulation and refrigeration scheme similar to the cluster facility. The SH_2 section is mated to the LO_2 tank section and integrated with the payload/fairing assembly within the launch tube of the silo (see Figure 9). When ready, the upper door of the silo opens a few seconds before the extraction mechanism impels the LV upwards, in a manner similar to the Poseidon mechanism. The launch tube is prolonged beyond the cryogenic door, and a fire-wall damper is quickly actuated in the launch tube extension, making it possible to ignite the hybrid motor seconds after the extraction without the hot exhaust gases impinging and damaging the silo's cryogenic structures.

HEDM Propellant Preparation.

The free radical HEDM propellant sections are assembled and loaded within the cluster facility. A viable HEDM propellant preparation process could be accommodated by adopting an arrangement as sketched in Figure 10. Six injector/combustion chamber shells are collocated within the cluster cryogenic facility. Note in Figure 9 that the propellant grain had a central port within which combustion is to take place in the hybrid motor (there will be in an actual motor a number of ports, but the central-port concept will suffice at present for discussion purposes).

Coannular with the port, and before propellant fabrication, an insert is introduced (see Figure 11) for injecting a mixture of hydrogen gas and free radicals. The process is shown in Figure 12, where one can see the free jet of hydrogen gas and radicals impinging on a growing matrix of SH_2; this matrix is formed on the shell wall and baffles, which are in turn refrigerated with LHe.

Techniques such as centrifugation of the condensate and/or electrophoretic processes may be required to densify the matrix. At the present, however, it appears that the best procedure is to form a slush of SH_2 and LHe. The agglomeration of SH_2 on the wall and baffles could be induced by the percolation of LHe. The LHe could then be collected from the bottom and circulated through the facility in a closed loop. Hence the value of exploring the properties of SH_2/LHe slush.

The insert tube (see Figure 12) has a dual function:

1. To manifold and inject into the shell jets of gaseous hydrogen mixed with free radicals.

2. To produce free radicals by microwave discharge of the parent molecules.

To this end, the insert has been designed as a bi-wall tube, with the inner tube perforated to provide a uniform plenum pressure along its length. The cavity between the tubes is in this manner kept at a constant temperature and can produce a uniform spray of gas. Upstream mixing of the hydrogen gas with, let us say borane

PAYLOAD FAIRING

LO$_2$ TANK

SH$_2$ TANK

CENTRAL PORT

LOW PRESSURE

HIGH PRESSURE
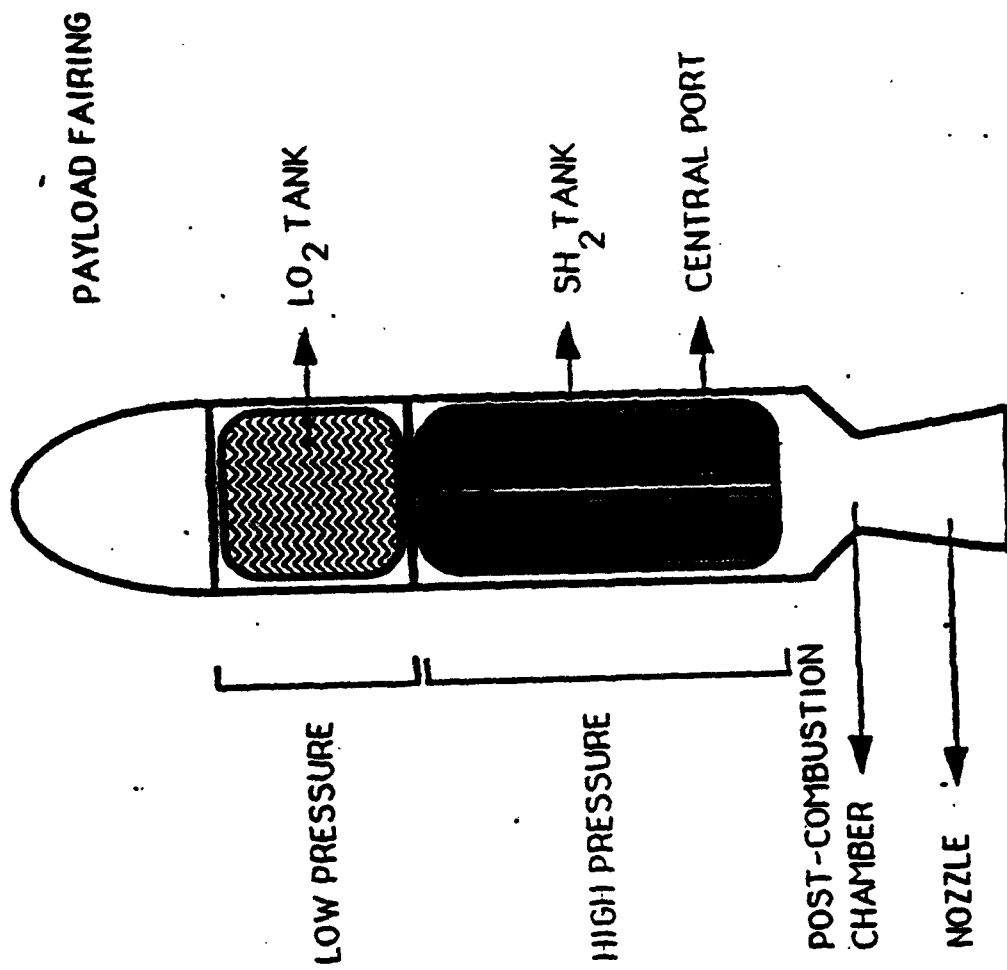
POST-COMBUSTION CHAMBER

NOZZLE

Figure 9. Hybrid Launch Vehicle: Single Stage.
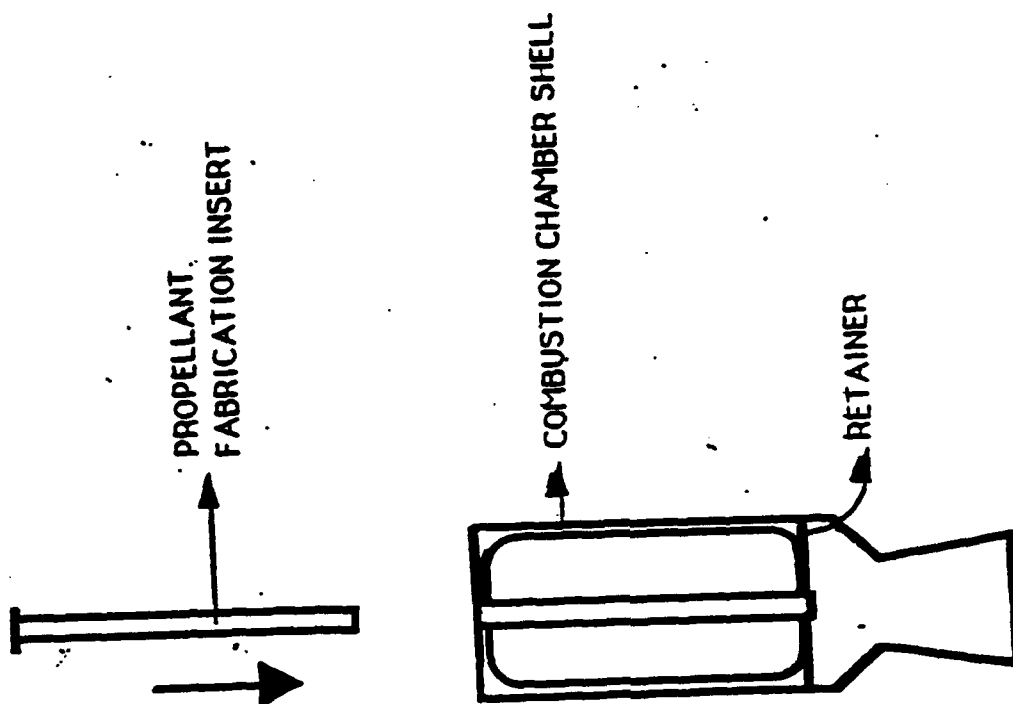
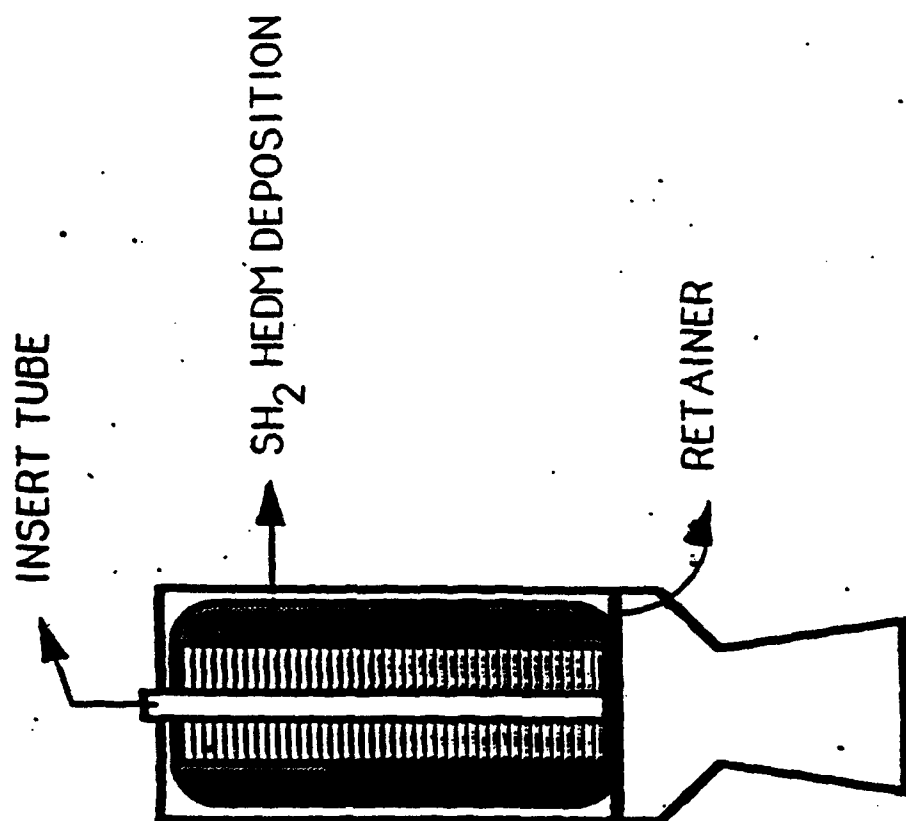Figure 10. Cryogenic Hybrid Motor Before Propellant Deposition.

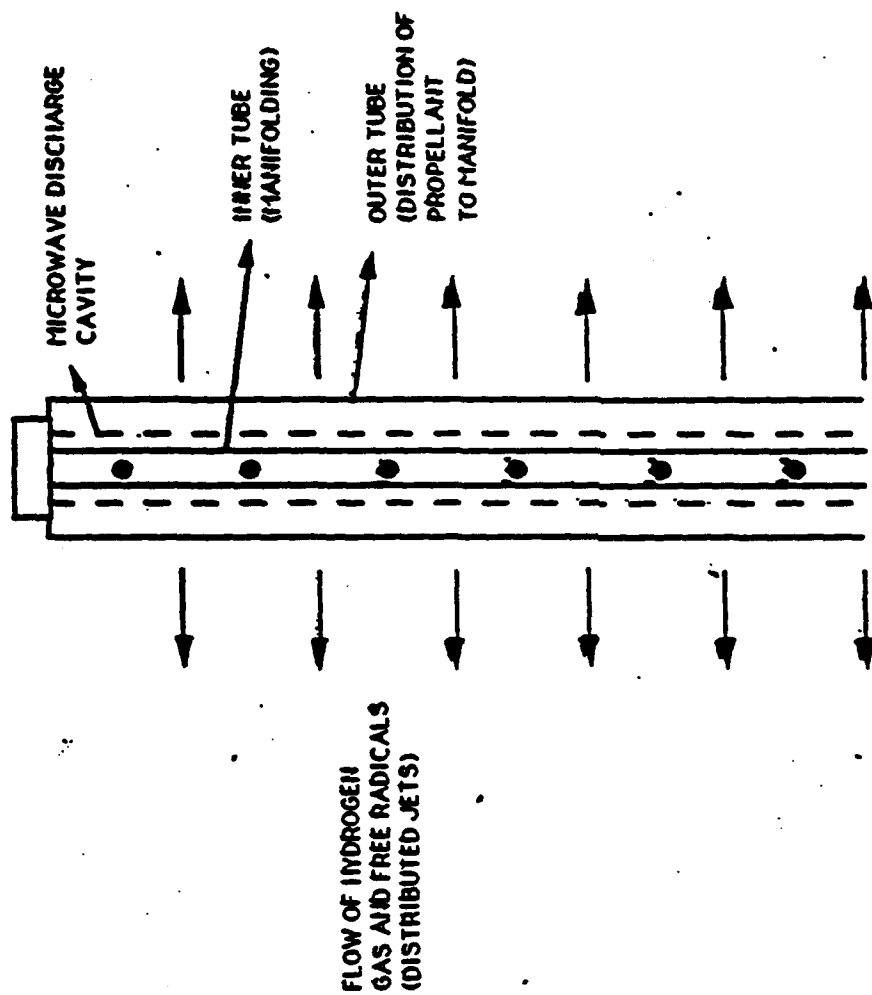Figure 11. Deposition of HEDM Propellant on Cryogenic Motor Shell.

MICROWAVE DISCHARGE
CAVITY

INNER TUBE
(MANIFOLDING)

OUTER TUBE
(DISTRIBUTION OF
PROPELLANT
TO MANIFOLD)

FLOW OF HYDROGEN
GAS AND FREE RADICALS
(DISTRIBUTED JETS)

Figure 12. Propellant Fabrication Insert.

or pentaborane, is performed if one determines that free radicals of boron are desired. The free radicals could be produced, for instance, by inducing a microwave discharge in the wave guide/resonator assembly after the gas mixture has been accelerated during the expansion to supersonic regime.

The concept described above, although relatively simple, is abundant with small but important engineering difficulties and uncertainties that need to be overcome. A fairly large gaseous flow rate of free radicals suspended in gaseous hydrogen need to be manufactured and impinged against a growing matrix of SH_2. In order to avoid the ever increasing threat of acoustic instabilities within the combustion chamber of high performance propellants, it is most important to control the uniformity of the grain distribution, as well as the homogeneity of the trapped free radicals. It is precisely in this step of the process where development is needed, and should received most serious consideration when addressing or proposing new techniques for free radical HEDM propellant preparation.

8. CONCLUSIONS.

1. On reviewing the technology of SH_2 as a propellant, it has been found that SLH_2 slush and triple point hydrogen (TPH) technology is well at hand and can be readily implemented in a large scale on a short-term basis.

2. There is hardly any data on the utilization of SO_2 as a propellant. Its physico-chemical and mechanical properties at low temperatures need to be investigated. The doping of SO_2 with free radicals has not been given the same attention than in SH_2.

3. The implementation of free radicals HEDM based on an SO_2 matrix is substantially easier to implement than it is in SH_2, but the resulting performance improvements cannot be estimated at present because of lack of data.

4. SH_2/LHe slush is technologically feasible, at least in a small scale. Only one scheme appears practical for this application: employing the slush to maintain SH_2 at temperatures below the Lambda point, by percolating LHe out of the SH_2/LHe slush and recovering the LHe in a closed loop refrigeration cycle.

6. SH_2/SO_2 mixture implemented in a solid rocket motor scheme is a most interesting and intriguing approach due to its potentials in propelling fast interceptors. Data to prove its feasibility, however, does not exist.

7. Large-scale integration of SH_2 and SO_2 hybrid systems appears to be the primary framework for the implementation of free radical HEDM propulsion systems.

Development of this concept as a test bed of HEDM propellants could become a most useful project to NASA/DoD since it would bring into focus the AFOSR and NASA HEDM technical programs.

8. The uniformity and homogeneity of a free radical HEDM propellant is to have an impact on the acoustic stability of combustion chambers using those propellants.

9. RECOMMENDATIONS.

The findings of this brief design study are summarized herein according to the three basic concepts which are recommended as test beds for Research and Development of free-radical HEDM properties.

1. SO_2 Reversed Hybrid Rocket Motors.

   (a) Investigate free-radical HEDM candidates in SO_2 which offer promising performance.

   (b) Determine the effects of temperature and pressure on the stability on such properties.

   (c) Investigate the physical properties of SO_2 aggregates at temperatures ranging from 10 K to LO_2 temperatures.

   (d) If the results from (a), (b), and (c) are justified, undertake an additives program to enhance propellant properties.

2. SH_2 Hybrid Rocket Motors.

   (a) Investigate techniques to obtain densified SH_2 as it grows on LHe cooled surfaces.

   (b) Determine the physico-chemical properties of SH_2 aggregates.

   (c) Determine the mechanical properties of SH_2 aggregates.

   (d) Undertake an additives program to enhance the stability of free-radical HEDM properties using SH_2 as a matrix.

   (f) Undertake a systematic investigation on the characteristics of SH_2/LHe slush. Specifically investigate:

      i.   Preparation.

      ii. Temperature and pressure effects.

iii. LHe percolation from the slush.

iv. Undertake an additives program to enhance the slush desirable properties.

3. SH_2/SO_2 Cryogenic Solid Rocket Motor.

(a) Develop methods for the preparation of stable polycrystalline mixtures of SH_2/SO_2. Investigate both:

i. Single-base propellant, that is a polycrystalline aggregate of H_2/O_2 mixed at the molecular level.

ii. Double-base propellant, that is an aggregate of SH_2 crystals intermixed with SO_2 crystals.

(b) Determine the physico-chemical properties of the resulting mixtures.

(c) Determine the mechanical properties of the solid mixtures.

(d) Investigate the stability of such mixtures and the need for an additives program to increase the stability if necessary.

(e) Conduct studies and experiments to determine performance projections and burning rates.

REFERENCES

(1) Frisbee, R.H.: "Systems-Level Implications of High Energy Density Matter (HEDM) Propulsion Concepts", Solid Hydrogen Workshop, Univ. of Hawaii, March 25-27, 1992.

(2) Hardy, T.L., and Whalen, M.V.: "Technology Issues Associated With Using Densified Hydrogen for Space Vehicles", 28th Joint Propulsion Conference and Exhibit, Nashville, TN, July 6-8, 1992.

(3) DeWitt, R.L., Hardy T.L., Whalen, M.V., and Richter, G.P.: "Slush Hydrogen (SLH2) Technology Development for Application to the National Aerospace Plane (NASP)", Cryogenic Engineering Conference, UCLA, July 24-28, 1989, Los Angeles, CA.

(4) Gu, Y.F., and Timmerhaus, K.D.: "Damping criteria for thermal acoustic oscillations in slush and liquid hydrogen systems", Cryogenics 1992, Vol. 32, No. 2, pp.194-198.

(5) Shirron, P.J., and Mochel, J.M.: "Atomically Thin Superfluid Helium Films on Solid Hydrogen", Physical Review Letters, Vol. 67, No. 9, 26 August 1991, pp. 1118-1121.

(6) Sutton, G.P., and Ross, D.M.: "Rocket Propulsion Elements", John Wiley & Sons, New York, 1976; pp. 418-421.

(7) Kniffen, R.J., McKinney, B., and Estey, P.: "Hybrid Rocket Development at the American Rocket Company", AIAA/SAE/ASME/ASEE 26th Joint Propulsion Conference, Orlando, FL; AIAA-90-2762, July 16-18, 1990.

Additives to Cryogenic Solid Propellants

Stephen Rodgers
Phillips Laboratory

See abstract from poster session by Pat Carrick

Mobilities of O Atoms and H Atoms in Cryogenic Solids

Dwayne LaBrake, E. Todd Ryan, and Eric Weitz

Department of Chemistry
Northwestern University
Evanston, IL 60208-3113

Introduction

The technique of matrix isolation spectroscopy[1] has served as a powerful tool for the study of reactive chemical species. The species of interest can be prepared in various ways. One common technique involves the photolysis of a precursor molecule in the matrix to produce a reactive species directly as a photoproduct. Another technique involves the production of an atom or radical by photolysis which subsequently reacts with some other radical or molecule in the matrix to produce the species of interest.[1,2]

In both of the above techniques, the rates for atomic and molecular mobility in the matrix are of prime importance. If the radical is produced by reaction of two species in the matrix, the timescale for its production will be effected by the diffusion time of reactant in the matrix. Once a radical is produced, its lifetime will be determined in part by the time that it takes for the radical to diffuse to some other reactant in the matrix.

It is also possible that the reactive species can absorb electromagnetic radiation. This radiation can then be degraded into energy in translational and/or internal degrees of freedom. If a significant amount of the initially absorbed energy eventually resides in translational degrees of freedom of the reactive species, the mobility of this species can be enhanced. This processes has been termed "photoinduced mobility"[3]. This is a particularly likely process when the reactive species can form an excited state or charge transfer complex with the host material. Under these circumstances relaxation of the complex will typically lead to a transition where the constituents of the complex are placed on the repulsive wall of the ground state potential energy surface leading to translational excitation of the species. We have observed such behavior for XeO complexes and have published results in this area [3,4]. We have also observed this behavior for H atoms and discuss initial results in this area in this report.

Clearly both diffusion and photoinduced mobility impact on the ability to "store" reactive chemical species in a matrix when these species are produced by photolysis. Indeed some of the reports of highly mobile atoms that exist in the literature may derive from the photoinduced mobility we have observed.

We also report on some recent data we have obtained on H atom thermal mobilities. By changing deposition conditions we can alter the rate for H atom loss in a xenon matrix. This change in loss rate as a function of deposition conditions is ascribed to a change in morphology of the matrix which in turn effects the thermal mobility of H atoms.

Finally, some recent results on the storage of O atoms in xenon matrices will be briefly discussed.

Experimental

The experimental apparatus used in these studies has been reported on in detail previously[3-5]. For H atom studies, the output of an ArF excimer laser is used to photolyze HBr.

The 193 nm output of this laser is also used to excite H atom - xenon exciplexes. These exciplexes have been reported to have an Xe_2H structure, analogous to the Xe_2X structure of rare gas - halogen exciplexes[6]. Pulses of approximately 10 mj/cm^2 are used to photolyze the samples while significantly reduced energy pulses are used to probe the H atom concentration via Xe_2H emission. For O atom experiments, the output of an excimer laser operating on either ArF (193 nm) or KrF (248 nm) with fluences typically in the range of 10.0 mj/cm^2 is used to irradiate an N_2O:Xe matrix. For both systems exciplex emission produced upon matrix irradiation, is viewed by a gated optical multichannel analyzer (OMA) (Princeton Instruments model IRY700) attached to an ISA HR-320 monochromator equipped with a 300 grooves/mm grating blazed at 600 nm. The gate width of the OMA is set to be significantly longer than the fluorescence decay time. The output from the OMA is thus the integrated fluorescence signal over the entire duration of fluorescence which is normalized by the excimer laser energy.

Results

The Xe_2H emission profile shown in Figure 1 was obtained subsequent to 193 nm excitation of a 1:800 HBr:Xe matrix which has been subjected to 7.0 mJ/cm^2 ArF photolysis pulses. This emission which peaks at 250 ± 0.25 nm with a full width at half maximum of 17.5 ± 0.25 nm is assigned to Xe_2H exciplex emission. The position and half width are in good agreement with published spectra for Xe_2H exciplex emission excited using a synchrotron beam source.[7] The data in Figure 2 are representative of the photoproduction of H atoms as a function of laser pulses. The H atom concentration is probed using the xenon hydride emission in figure 1 detected at $250 \pm .03$ nm. H atom production at 10 K is seen to rise rapidly to a steady state over 900 laser photolysis pulses. After 900 laser pulses the initial HBr concentration has been depleted to approximately 10% of its initial value. The amplitude of the H atom photoproduction plateau is observed to vary linearly with laser fluence. A production curve of the same shape is recorded for matrices deposited at 28 and 10 K.

For matrices deposited at either 28 or 10 K and held at 10 K no change in Xe_2H exciplex emission intensity is observed over the course of 5 days! At 40 K, the other extreme in temperature studied, the thermally induced loss rate of H atoms is on the time scale of minutes. The majority of H atom population in matrices deposited at 28 K decays in the first 30 minutes while the remainder decays more slowly changing only 15 % over the course of 3 hours. Eighty percent of the H atom population for matrices deposited at 10 K is lost over the first 20 minutes and the remaining 20 % remains unchanged over the next 4 hours. Figure 3 contains data for the thermal loss of H atoms at 40 K for matrices deposited at 10 K and at 28 K. In Figure 3 the linearity of the plots of 1/I(t) versus time demonstrates that the 40 K loss curves follow bimolecular kinetics. Interestingly the rate constant for bimolecular loss of H atoms at 40 K is approximately 5 times larger for the matrix deposited at 10 K versus the matrix deposited at 28 K.

Figure 4 displays photoproduction curves for O atoms that are analogous to those for H atoms and have been discussed in detail in other publications [3,4]. Curves are shown for three different concentration N_2O doped xenon matrices.

3

Discussion

The likely elementary kinetic processes occuring in this system subsequent to photolysis of HBr are indicated below. Attempts were made to fit the H atom photoproduction curve shown in Figure 2 by numerically integrating the following minimal set of kinetic equation.

$$HBr \xrightarrow{h\nu} H + Br \tag{1}$$

$$H + HBr \xrightarrow{k_2} H_2 + Br \tag{2}$$

$$H + H \xrightarrow{k_3} H_2 \tag{3}$$

$$H + Br \xrightarrow{k_4} HBr \tag{4}$$

While the rising portion of the curve could be fit using equations 1-4, we were unsuccessful at fitting the entire experimental curves unless we introduced a small population of HBr which underwent photolysis but where the H and Br atoms that were generated did not undergo subsequent reactions with other species in the matrix. This population could represent HBr molecules isolated in crystalline regions of the matrix. The existence of such a population was suggested by the shape of the H atom photoproduction curves at low HBr concentrations. Inclusion of the equation

$$HBr' \rightleftharpoons H' + Br' \tag{5}$$

leads to a kinetic curve generated from a numerical integration of equations 1-5 that can be superimposed on the data in Figure 2. Comparisons of the data obtained under a variety of conditions and the numerical solutions to these equations reveal other very interesting features of this system. We experimentally observe that the loss of HBr, which we probe via infrared spectroscopy and the appearance of Br atoms, which we probe via Xe_2Br exciplex emission both exhibit bimolecular kinetics. This implies a very efficient mobilization of H atoms and a very efficient consumption of H atoms by reaction 2. Using these experimental signals as inputs we can successfully generate curves from numerical integration of the above equations that adequately reproduce these experimental signals for H atoms, Br atoms and HBr.

The difference in the rate constants for thermal loss of H atoms as a function of matrix deposition temperature implies that H atom mobility can be effected by matrix morphology which can be altered by deposition temperature. Though annealing subsequent to deposition also can effect the rate constant for thermal diffusion and loss of H atoms, deposition temperature has a more profound effect on this process. The kinetic equations for the thermal loss of H atoms are expected to be the same as those listed above for photoinduced loss. Future experiments are planned to determine if the relative magnitudes of the rate constants are the same for thermal and photoinduced loss processes. An interpretation of these results in terms of diffusion coefficients and a comparison to measured diffusion coefficients for H atoms and O atoms under different conditions is presented in reference 5.

The signals in Figure 4 represent the dependence of the O atom concentration on laser pulses (photon dose) for three different concentration matrices. The observed dependance is representative of a competition between a first order production process, photolysis of N_2O, and a second order

depletion process, O atom recombination to form O_2. The kinetic model developed in reference 3 includes these process and can be used to replicate both the qualitative and quantitative shapes of the "production" curves for the two lowest concentrations shown in Figure 4. The fact that the model does not reproduce the curve for the highest concentration shown indicates that, under these circumstance, there is an additional loss process that is not accounted for in the model. We are in the process of trying to discern the nature of this process. We currently feel that it is likely due to the increased concentration of dimer and higher order multimers in the highest concentration curve. We have also been able to determine that it should be possible to exceed the approximately 20 mM concentration of stored O atoms that we have already achieved for the 1:101 N_2O doped xenon matrix shown in this figure.

Acknowledgments

References

1. M. E. Jacox in Chemistry and Physics of Matrix-Isolated Species, L. E. Andrews and M. Moskovits eds., (Elsevier, Amsterdam, 1989).
2. For example, B. Brocklehurst and G. C. Pimentel, J. Chem. Phys. 36, 2040 (1962); J. Fournier, C. Lalo, J. Deson and C. Vermiel, J. Chem. Phys. 66, 2656 (1977); R. N. Perutz, Chem. Rev. 85, 77 (1985).
3. E.T. Ryan and Eric Weitz, J. Chem. Phys. - in press
4. E.T. Ryan and Eric Weitz, J. Chem. Phys. - submitted
5. D. LaBrake and Eric Weitz, Chem. Phys. Letters - in press
6. M.E. Fajardo and V.A. Apkarian, J.Chem. Phys. 89, 4102 (1988)
7. M. Creuzburg and F. Wittl, J. Mol. Struct. 222, 127 (1990)

Figures

Figure 1. Xenon hydride exciplex emission spectrum recorded at 10 K. Excitation source was the 193 nm fundamental of an excimer laser operating on ArF. Spectral resolution is $\pm$ 0.25 nm.

Figure 2. H atom photoproduction as a function of laser pulses recorded at 10 K. H atom production was detected using Xe_2H emission at 250 $\pm$ 0.03 nm. Three laser pulses were averaged for each data point. The laser fluence was 7.0 mj/cm^2 pulse at 193 nm.

Figure 3. Bimolecular kinetic plot of the reciprocal Xe_2H emission intensity versus time. The Xe_2H emission intensity was recorded at 250 $\pm$ 0.03 nm using a laser fluence of 1 mj/cm^2 pulse at 193 nm.

Figure 4. Emission from XeO exciplexes following ArF photolysis of N_2O doped xenon matrices of the indicated composition. All photolysis was performed at 15 K.
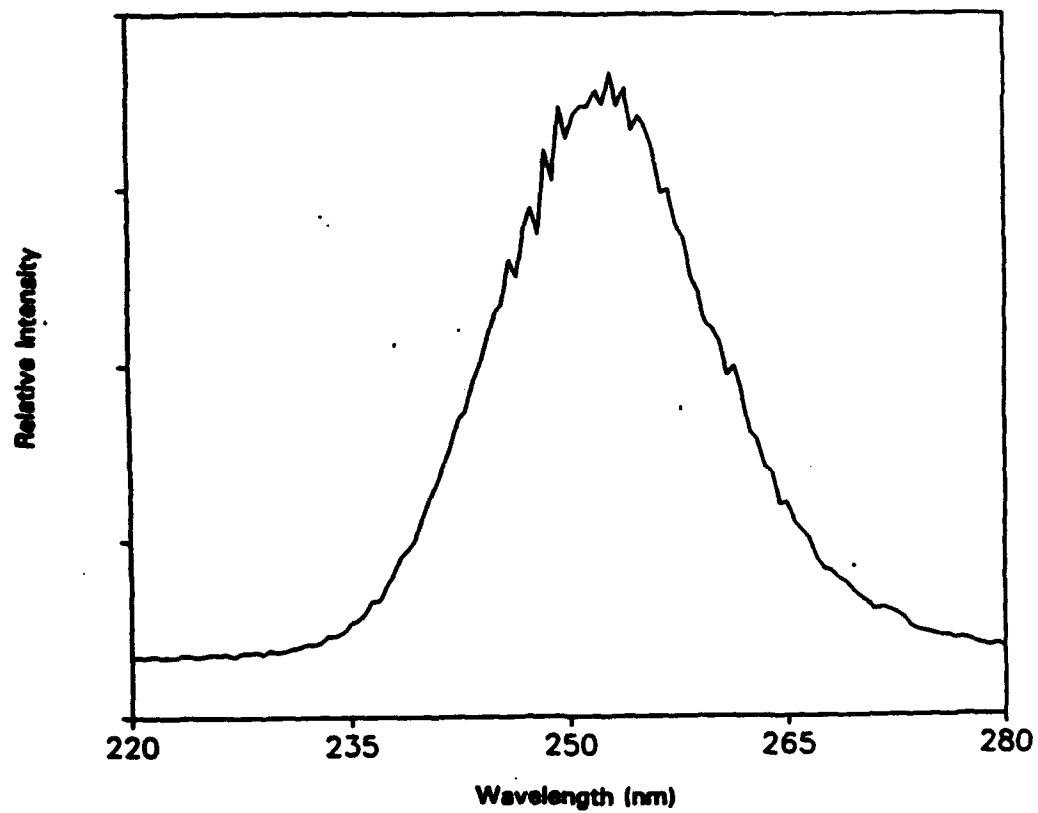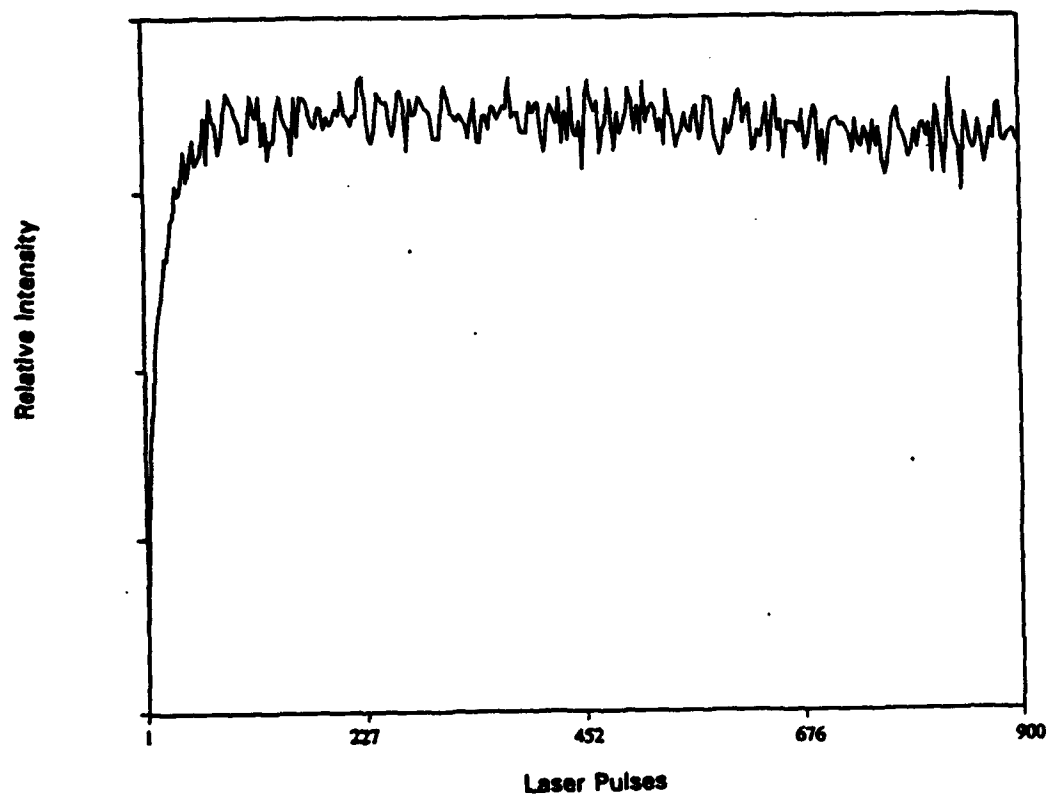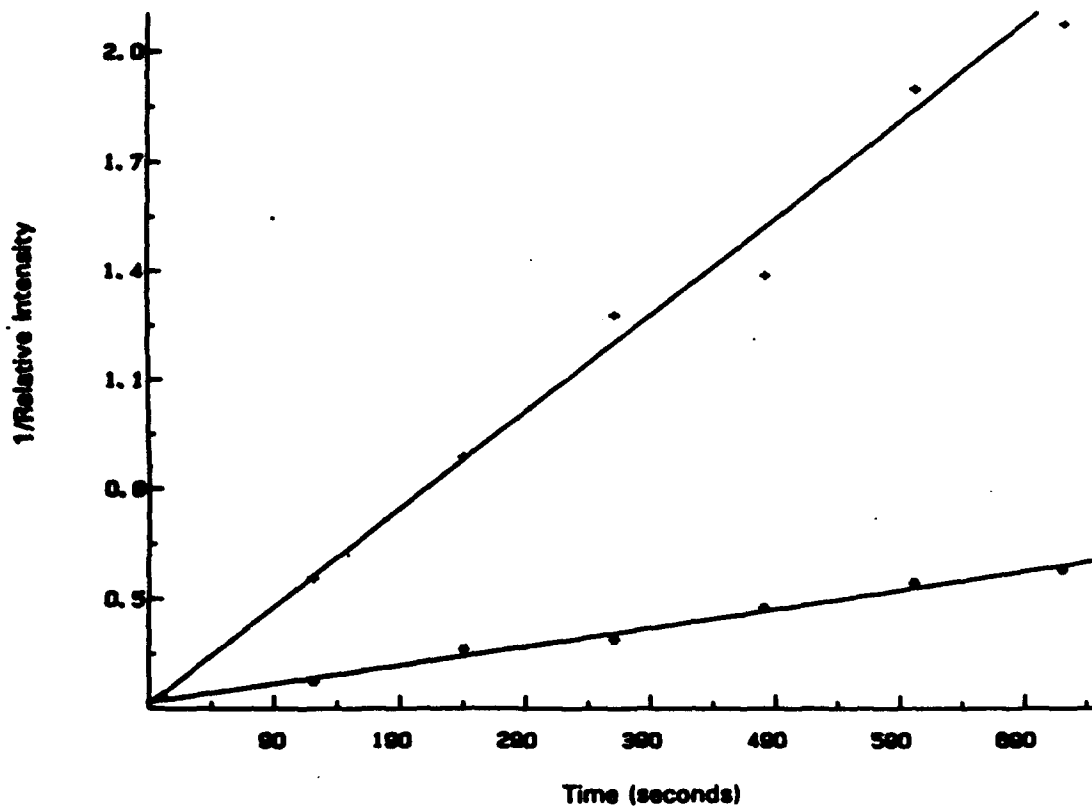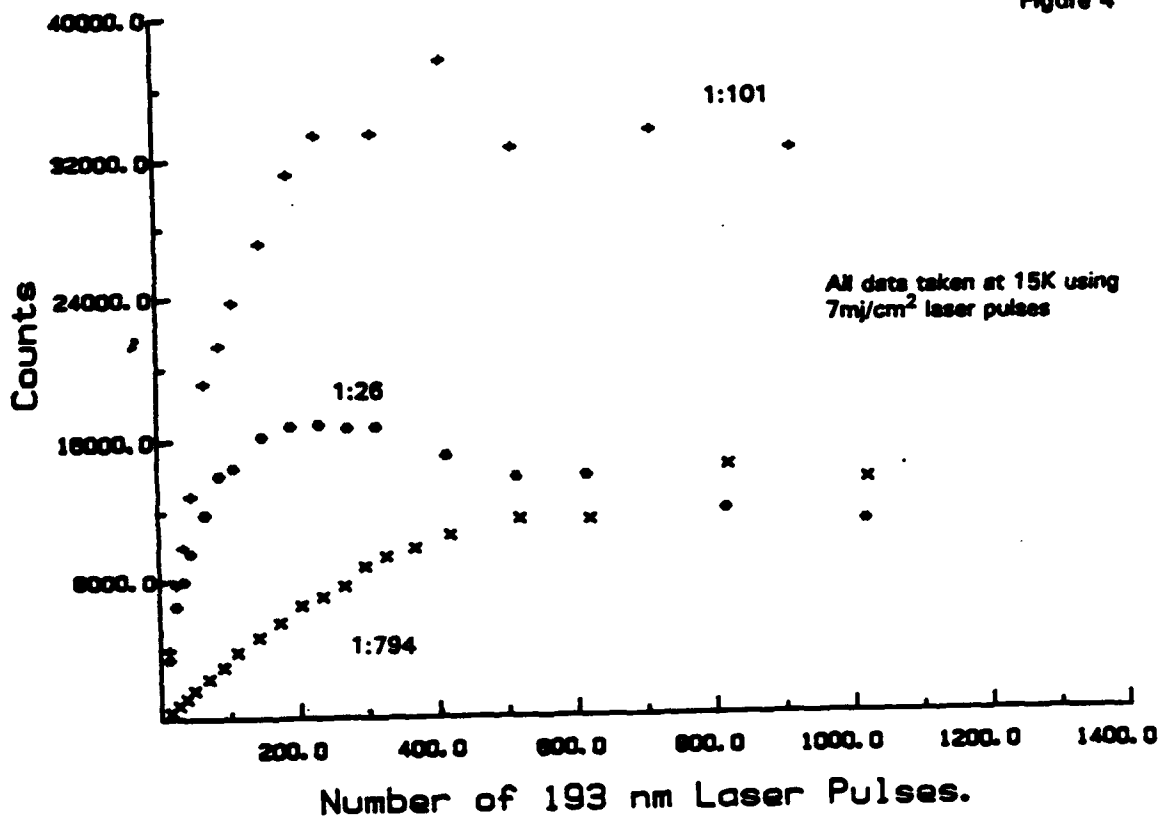
Figure 1

Figure 1

Figure 2

Figure 2

Figure 3

1/Relative Intensity vs. Time (seconds)

Figure 4

Counts vs. Number of 193 nm Laser Pulses.

1:101

1:26

1:794

All data taken at 15K using 7mj/cm² laser pulses

MODIFICATION OF NASCENT ENERGY DISTRIBUTIONS OF LASER ABLATED SPECIES USING TRANSVERSE MAGNETIC FIELDS.

MICHEL MACLER* AND MARIO E. FAJARDO
Emerging Technologies Branch, Propulsion Directorate, Phillips Laboratory,
OLAC PL/RKFE, 9 Antares Road, Edwards Air Force Base, CA 93524-7680.
*AFMC PL/NRC Post-doctoral Research Associate.

ABSTRACT

Results of experiments on Al and Li atomic beams produced by laser ablation using XeCl excimer laser pulses ($I \sim 10^7$ to 10^8 W/cm^2) are presented. Kinetic energy (KE) distributions of nascent Al ions were measured using an Electrostatic Energy Analyzer-Time of Flight Mass Spectrometer (ESA-TOFMS) system. Kinetic energy distributions for neutral species were measured using either transient absorption or photoionization-TOF mass spectroscopy. The results obtained for these various measurements are discussed.

INTRODUCTION

Recent successful efforts at isolating light metal atoms in cryogenic solid hydrogen have utilized a combination of pulsed laser ablation of the metal, and traditional matrix isolation spectroscopy techniques [1,2]. These experiments suggest that the incident KE of the metal atoms plays a key role in determining the atomic isolation efficiency of the matrix deposition process, and in the formation of novel metal atom trapping site structures. Unfortunately, little work has been done to measure the KE distributions of laser ablated species prior to matrix isolation. Thus, the immediate goals of this research effort are: (1) to characterize the chemical identity and KE distributions of laser ablated species under *our* specific experimental conditions, and (2) to examine the possibility of modifying the nascent metal atom KE distributions through a modification of the traditional laser ablation process.

EXPERIMENTAL

Fig. 1 depicts the experimental setup, configured for transient absorption measurements. The metal ablation targets are mounted on a rotatable rod within a vacuum chamber pumped directly by a small turbomolecular pump to $\sim 10^{-6}$ Torr. The ablated plumes are formed by focusing a XeCl excimer laser beam on the targets at an incident angle of 45° from the surface normal. The incident laser pulse energies were varied between 2 and 14 mJ; the pulses were focused onto a ~ 0.7 mm^2 area, resulting in incident intensities (I) of 10^7-10^8 W/cm^2.

To examine the directionality of the plume expansion, glass microscope slides were placed 1 cm from the target in order to collect the products of ablation. The thickness of the Al films deposited in this manner were assumed to be proportional to their optical density (O.D.) measured as a function of angle from the ablation target surface normal.

Emissions from the metal plumes were collected with a quartz lens, filtered to remove laser scatter, and recorded with an intensified, gated, optical multichannel analyzer (OMA) mounted on a 275 mm f.l. polychromator. The detection system was both wavelength and intensity calibrated using standard techniques. The observation region, a ~ 200 μm wide transverse slice of the plumes, was defined by a 100 μm wide aperture adjacent to the vacuum chamber and the 25 μm wide entrance slit of the polychromator. The entire mask/...polychromator assembly was mounted on a precision translator which was controlled manually by a micrometer positioner. Emission spectra were recorded at various distances, Z, from the target with a 10 μsec detector gate.

Transient absorption spectra were obtained as shown in Fig. 1. Short, polychromatic pulses were produced by using a second excimer laser (ArF) to pump a dielectric breakdown cell filled with ~ 1000 Torr of Xe gas, or a Xe:Ne mixture. A 50 mm f.l. quartz lens focused this emission through the metal atom plumes and onto the polychromator entrance slit. A digital delay generator was used to coordinate the arrival of the ablation and breakdown laser pulses, and the start of the 20 nsec wide OMA detector gate. As no metal atom emissions were detected with this experimental configuration, transmission spectra were calculated as the ratio between the OMA signals obtained with both ablation and breakdown
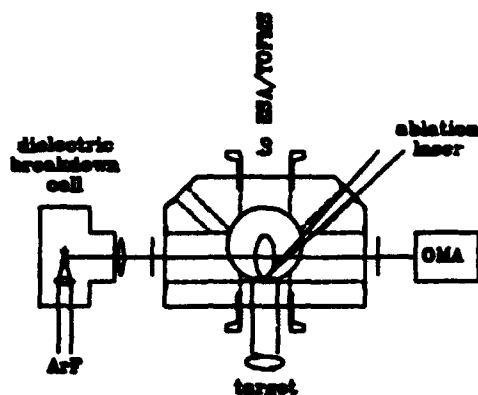
dielectric
breakdown
cell

ESA/TOFMS

ablation
laser

OMA

ArF

target

Fig. 1: *Schematic of the apparatus used for the transient absorption experiments. The ellipse extending from the target represents the ablated plume.*

laser pulses present (S), and that obtained with breakdown pulses only (S_0). Both S and S_0 signals were averaged over 100 pulses. As with emission spectra, the transient absorption spectra were obtained at various distances from the ablation target surface.

Kinetic energy distributions of nascent ions were measured using an Electrostatic Energy Analyzer-Time of Flight Mass Spectrometer (ESA-TOFMS) system (see Fig. 1). Ions traveling along the target surface normal were introduced in the ESA-TOFMS at various pass energies. The energy of the ions traveling inside the ESA was held at 10 eV. The voltages applied to the TOF tube and the microchannel plate detector depended on the gain necessary to record the signal. Under *our* conditions the resolution of the ESA was 0.272 eV FWHM. 2 mm diameter apertures were used to select particles traveling normal to the target surface. The mass resolution of the TOFMS was m/16. Integrated peaks corresponding to m/e=27 and 13.5 were used to generate KE distributions for Al(II) and Al(III) ions.

A transverse magnetic field was introduced in the ablation cell in order to deflect the ions. Its strength was typically 2100 G, applied on a 1/2 inch length in the path of the ablated species at 2.5 cm from the target. Al(II) were introduced in the ESA-TOFMS following photoionization of Al(I) at 193 nm. The experimental set up was similar to that used in the transient absorption experiment. The 193 nm laser pulse was focused through a quartz window on the Al(I) beam 1.5 cm ahead of the ESA, 21 cm from the target, resulting in ~10^8W/cm^2 laser intensity. The intensity of the integrated peak at m/e=27 was recorded as a function of the ablation laser-photoionization laser delay for a range of pass energies. The time integrations of these spectra were used to generate the KE distributions of Al(I).

RESULTS

The metallic Al deposit optical density data was fitted to O.D. $= k \cos^n(\theta - \theta_0)$, where θ is the angle with the surface normal, and θ_0 is the tilt of the axis of the plume. The fit yielded n = 9, and the tilt angle $\theta_0 \approx 5°$, indicative of a highly directional, near normal plume which justifies the simple, one-dimensional analysis of the TOF measurements on Al(I)/Al(II) plumes. No such measurements were attempted for Li plumes (*vide infra*).

The Al atomic and ionic emission spectra were used to characterize the properties of the plasma formed adjacent to the ablated aluminum surface. The use of a long detection gate (10 μsec) yielded fully time integrated spectra, as all emissions were finished on this time scale. Ionic emission peaks dominated near the target surface, but became barely noticeable for distances Z > 0.3 cm. Integrated emission intensities were extracted for a number of transitions. Electron temperatures (T_e) were extracted by assuming local thermodynamic equilibrium (LTE) [3,4]. Typically, for 0.08 < Z < 0.2 cm, the plasmas were dense enough for LTE to hold, and T_e was of order 20000 K (~ 2 eV). Electron densities (N_e) were also derived from emission spectra by measuring the Stark broadening of ionic lines [3]. For 0.08 < Z < 0.13 cm, N_e decreased rapidly from 7×10^{17} to < 8×10^{16} cm^{-3}, correlating strongly with the disappearance of the Bremsstrahlung continuum, and the decrease in Al(III) emissions.

Typical transient absorption spectra of Al plumes displayed the atomic doublet at 394.5 and 396.2 nm. For Al, no attempt to observe either excited or ionic state absorptions were made. However,
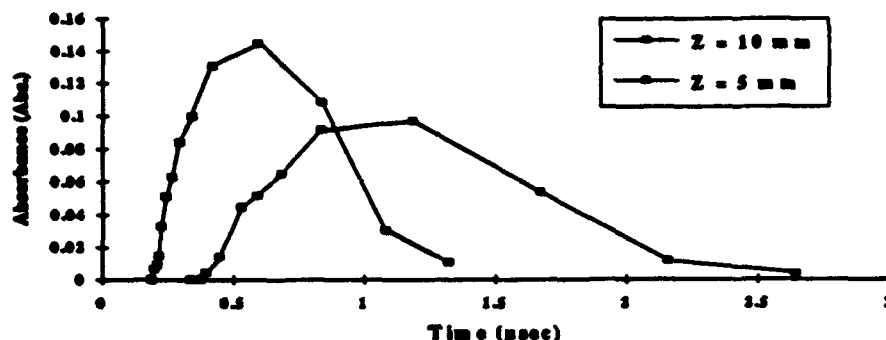
Fig. 2: *TOF spectrum of ground state Al atoms, recorded by monitoring the 4s←3p absorption doublet for ablation intensities ~10^8 W/cm².*

for Li, the 3d←2p absorption was observed at Z = 2.0 cm for delay times in the 0.6-1.6 µsec range. From this observation, the relative population of the Li 2p state was estimated to be ~ 10 % of that of the ground state. The time evolution of the absorption intensity following the ablation laser pulses gives the TOF distribution of the ground state atoms. For Al(I), TOF distributions were measured at Z = 0.5 and 1.0 cm; the raw data are displayed in Fig. 2. Raw TOF data were corrected for the velocity dependent detection probability. The transformation of the TOF distributions into velocity and KE distributions was done using the proper Jacobian expressions [5]. Al(I) velocity distributions are presented in Fig. 3.

Laser ablation transient absorption measurements of Li(I) yielded TOF distributions with a sharp, intense peak occurring for short delays, followed by a persistent "tail" at long delays (> 10 msec). This behavior was seen for the entire range of laser intensities used in these experiments. We suspect that these long delay tails are artifacts of our experimental geometry: the plume expansions for Li may be less directional than for Al, so Li atoms may enter the observation region at large angles from the surface normal. Also, slow Li(I) may be introduced into the observation region by evaporation from µm and sub µm size Li particles produced by the ablation process [6]. Because of these difficulties, only the short arrival time portions of the TOFs were converted in KE distributions. They are presented in Figs. 4.

Fig. 5 shows the nascent KE distributions for Al(II) and Al(III) for an ablation laser intensity of 9.5×10⁷W/cm². Fig. 6 displays the nascent Al(II) KE distributions for a range of laser intensities. 10^7W/cm² appeared to be the threshold intensity for plasma formation. The widths and maxima of these distributions increases with the laser intensity. This behavior is similar to that of the neutrals. Fig. 7 shows a typical photoionization TOF spectrum for KE>3 eV. The sharp feature corresponds to Al(I) formed within 100 ns of the ablation pulse. This feature becomes more prominent as KE increases. At low KE, only a broad band is observed. The delay between a 193 nm pulse centered on this broad feature and the actual detection of the signal corresponds to the TOF for m/e=27 particles. The signal detected for both broad and sharp features were saturated for ArF laser pulse energy in the 40-140 mJ range.Fig. 8 displays how the Al(I) KE distribution varies with I. Finally Fig. 9 shows KE distributions for nascent Al(I) at 1 cm from the target, photoionized Al(I), and Al(II) at 22.5 cm from the target, for I ~10^8W/cm². These distributions were integrated in the 2-50 eV range and subsequently normalized.
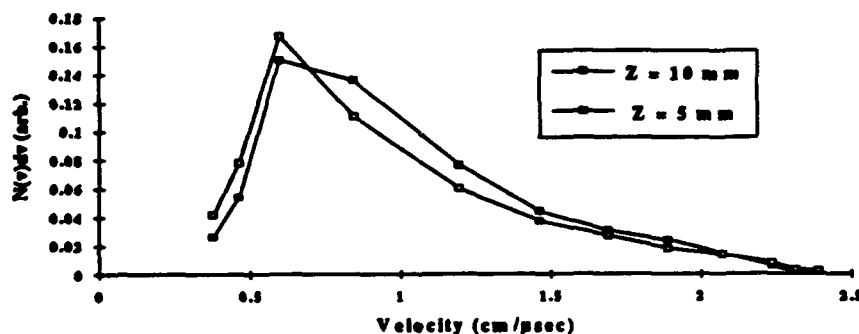

Fig. 3: *Velocity distribution for ground state Al atoms.*

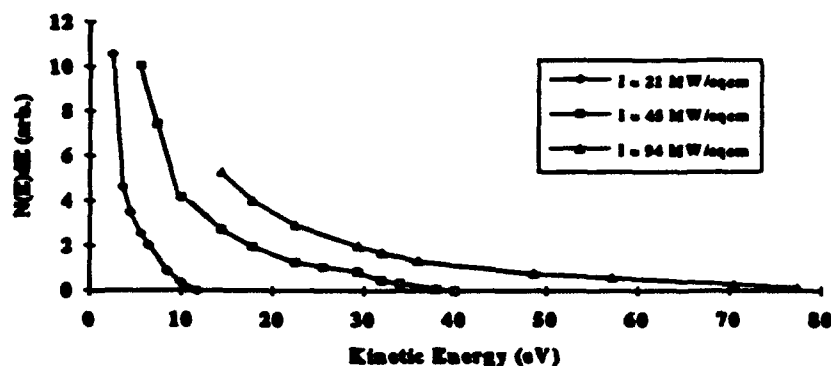**Fig. 4:** *Kinetic energy distributions for ground state Li atoms obtained from measurements made for Z = 1.0 cm, at laser intensities in the 2.1×10^7 to 9.4×10^7 W/cm² range.*
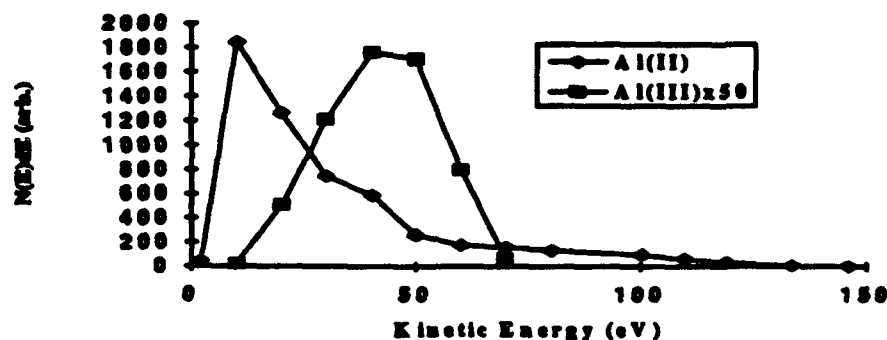

Fig. 5: *Kinetic energy distributions for nascent aluminum ions 22.5 cm from the target, I~10^8 W/cm².*
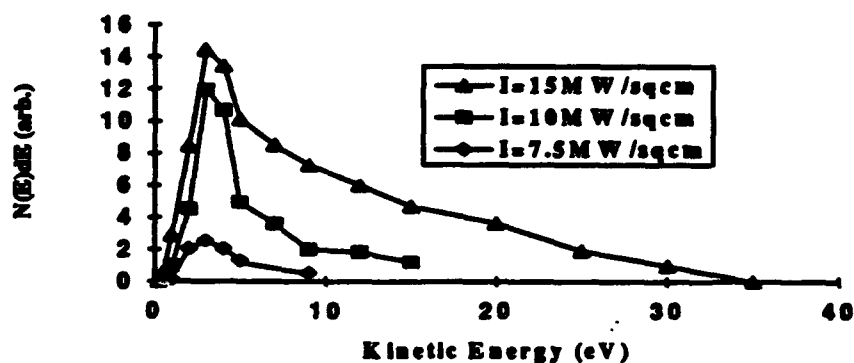

Fig. 6: *Kinetic energy distributions for nascent Al(II) 22.5 cm from the target, at various laser intensities.*

DISCUSSION

The emission data shows that near the target surface the plasma formed during ablation is very hot. Most of the vaporized aluminum is in ionized form. In this region, the ions are accelerated to high velocities, presumably by some "Coulomb Explosion" type mechanism [5]. For distances form the target between 0.08 and 0.15 cm, the decay of the Al(III) emission is accompanied by a sharp decrease in electron concentration, and a rise in the Al(I) emission, suggesting that electron-ion recombination may be producing excited neutrals. Yet, some of the ions survive and are detected 22.5 cm away from the target. At high enough ablation intensity, a bump in the KE distribution of Al(II) can be seen at ~ 40-50 eV. This region also corresponds to the peak of the Al(III) KE distribution, suggesting that electron-Al(III) recombination contributes to the formation of Al(II). Such effects have been reported [7]. One would then expect that the KE distributions of Al(I) and Al(II) would be fairly similar, if in fact most of the Al(I) population originates from Al(II). This holds true when comparing KE distributions of nascent

346
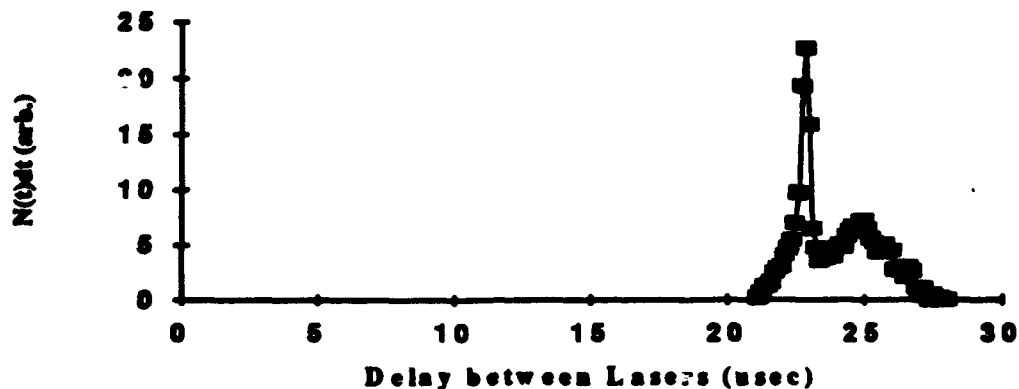
Fig 7: *Photoionization TOF spectrum for Al(I), at 21 cm from the target, with KE=12 eV, recorded for m/e = 27, I=8.6×10^{7}W/cm^2, ArF pulse energy ~140 mJ. The sharp feature corresponds to Al(I) leaving the target within 100 nsec after the arrival of the ablation pulse. Its FWHM results from the instrument broadening.*
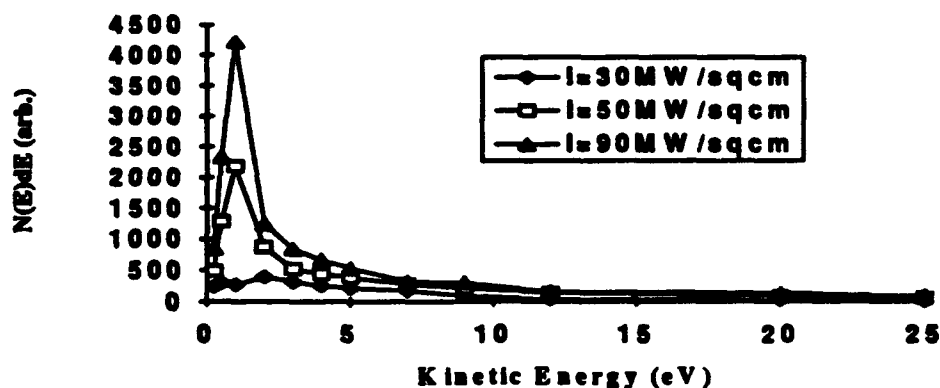
Fig. 8: *Kinetic energy distributions for Al(I) photoionized 21 cm from the target, at various ablation laser intensities, ArF pulse energy ~140 mJ.*
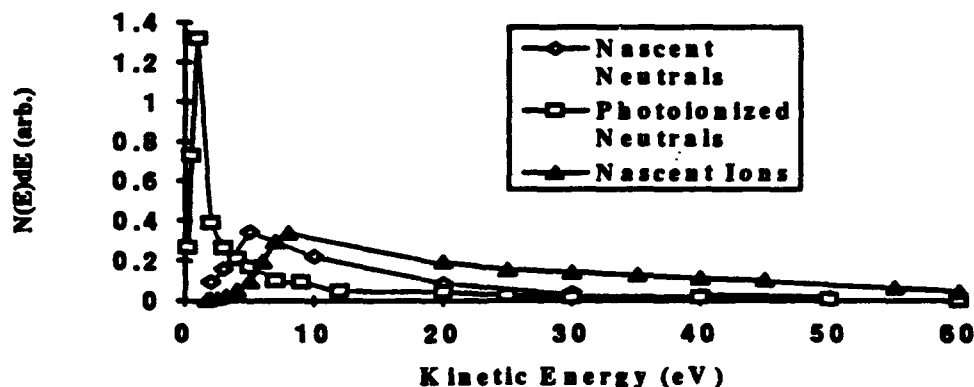
Fig. 9: *Kinetic energy distributions for ablated aluminum species at I~10^8 W/cm^2.*

Al(II) measured at 22.5 cm and of Al(I) measured at 1 cm. The differences between transient absorption measurements at 0.5 and 1.0 cm from the target are attributed to a finite production time for the Al atoms following the arrival of the ablation laser pulse. Simple stochastic computer simulations of our experiment suggest a ~ 100 nsec wide "window" for the establishment of an initial velocity distribution, followed by an essentially free expansion thereafter. The Al(I) distribution measured by transient absorption is shifted slightly toward lower energies and does not extend to energies above 80 eV. It is similar to those previously reported for similar laser intensities [8-10]. The photoionized Al(I)

347

distribution clearly peaks at 1 eV, where photoionization TOF spectra are very broad. At energies above 10 eV, there is no striking difference in KE distribution shape between the transient absorption data and the photoionization data. At high energy, the photoionization TOF spectra present a strong sharp feature, occurring at a delay corresponding to Al(I) leaving the target within 100 nsec of the ablation pulse arrival. This feature is the major contributor to the time integrated KE distribution for KE>10eV. We do not think that the differences between transient absorption and photoionization measurements is due to the presence of a magnetic field in the latter case. The spatial extent of the field was measured carefully. It was confined to the near vicinity of the magnets, at least 2.5 cm from the target surface, where the Al density was low. Al(I) with KE<2eV do not originate from the same process as the faster ones. They are not observed in transient absorption experiments, and there are no Al(II) detected at such energies. One possibility is that Al clusters/particles crossing the ArF laser path during firing dissociate and ionize, forming Al(II) with KE suitable to enter the ESA-TOFMS.

CONCLUSION

The laser ablation of Al has been characterized, using emission and transient absorption spectroscopies, as well as energy selected TOF mass spectroscopy. Laser ablation produces mostly Al(I) and Al(II). Electron-ion recombination seems to be the primary mechanism for the formation of fast Al(I). Al(I) and Al(II) fluxes and mean KE increase with ablation laser intensity. Typically, the lowest KE observed is ~1-2eV for both Al(I) (transient absorption) and Al(II). Al(I) and Al(II) leave the target within ~ 100 nsec of the ablation pulse arrival implying that there is a good one-to-one mapping of the initial velocities to distances traveled from the target after a delay of ~ 1 μsec. A static 2100 G transverse magnetic field can be used to deflect the ions away from the target surface normal without affecting the Al(I) formation process, provided it is placed at least 2.5 cm from the target surface. The effect of the magnetic field on the Al(I) production will be further investigated. For ablation laser intensities ~ $10^8 W/cm^2$, we have collected particles with diameter as large as 18μm, such particles might be responsible for the presence a large amount of 1 eV Al(II) following 193 nm photoionization of Al(I), 21.5 cm from the target. Photoionization experiments will be repeated with much lower ArF intensities.

REFERENCES

1. M.E. Fajardo, P.G. Carrick, J.W. Kenney III, J. Chem. Phys. 94, 5812 (1991).

2. M.E. Fajardo, J. Chem. Phys. 98, 110 (1993).

3. J.T. Knudtson, W.B. Green, D.G. Sutton, J. Appl. Phys. 61, 4771 (1987), and references therein.

4. R. Tambay, R. Singh, R. Thareja, J. Appl. Phys. 72, 1197 (1992).

5. J.C.S. Kools, T.S. Baller, S.T. De Zwart, J. Dielemann, J. Appl. Phys. 71, 4547 (1992).

6. Yu. A. Bykovskii, N.N. Degtyarenko, V.F. Elesin, Yu. P. Kozyrev, and S.M. Sil'nov, Sov. Phys. JETP 33, 706 (1971).

7. D.B. Geohegan, Appl. Phys. Lett. 62, 1463 (1993).

8. H. Wang, A.P. Salzberg, B.R. Weiner, Appl. Phys. Lett. 59, 935 (1991).

9. R.M. Gilgenbach and P.L.G. Ventzek, Appl. Phys. Let. 58, 1597 (1991).

10. R.W. Dreyfus, R. Kelly, R.E. Walkup, Appl. Phys. Lett. 49, 1478 (1986).

Structures, Relative Energies and Dissociation Barriers of N_2O_2 and N_2O_3 Isomers

Kiet A. Nguyen and Mark S. Gordon

Ames Laboratory, U. S. Department of Energy,
and Department of Chemistry
Iowa State University
Ames, IA 50011-3111

John A. Montgomery, Jr. and H. Harvey Michels
United Technologies Research Center
East Hartford, CT 06108

David R. Yarkony
Department of Chemistry
The Johns Hopkins University
Baltimore, MD 21218

I. N_2O_2

Due to their interest as possible new HEDM species[1] and the fascinating recent experiments,[2] the structures, energetics and dissociation barriers of the species listed in Figure 1 are investigated at several *ab initio* levels of electronic structure theory. Geometrical parameters of four N_2O_2 isomers—calculated at the SCF, MP2, and MCSCF(10,10) levels of theory with the 6-31G(d) basis set—are displayed in Figure 1. The calculated [MP4(SDTQ)/6-311G(d)//MP2/6-31G(d), G1, G2, MCSCF and MRCI with 6-311+G(2d) basis sets] relative energies—with reference to 2NO—of N_2O_2 isomers are listed in Table I. G2 relative energies are 41.7, 47.3, 63.8, and 69.3 kcal/mol for **1-4**, respectively. The corresponding G1 energetics are generally within 2.5 kcal mol^{-1} of G2 values. MP4(SDTQ)/6-311G(d) relative energies are about 6-12 kcal/mol higher that those predicted by G1 and G2. Except for the bond stretch bicyclodiazoxane (**2**), MRCI/6-311+G(2d)//MCSCF/6-31G(d) relative energies of all other isomers are within 6 kcal/mol of the G2 values. The large disagreement (15.8 kcal/mol for structure **2**) in relative energies between G2 and MRCI due (largely) to the poor description of reference configurations by single determinant based methods, since there is significant configurational mixing in structure **2**.

Structure **1-4** discussed above are high in energy (relative to 2NO) and thermodynamically stable (minima) on the singlet potential energy surface. The next step involves study of their kinetic stability for spin-allow (singlet) and spin-forbidden channels) starting with a-N_2O_2. On the singlet surface symmetric isomerization transition state (**5**) leading to a-N_2O_2 (**3**) in both directions is located at only 1.3

kcal/mol above the minimum a-N_2O_2. So structure 3 is non-rigid and can exchange the oxygen that links directly with the nitrogen end easily. The spin-forbidden decay channel a-N_2O_2 (^{1}A) → N_2O (X $^1\Sigma^+$ + O (^{3}P) is exoergic. The minimum energy crossing point for pre dissociation is only 2.1 kcal/mol above the minimum a-N_2O_2.[3a]

The next structure under consideration is the bicyclodiazoxane (4) and its bond stretch isomer (2). These two structures are connected by a bond stretch transition state calculated to be 40.2 kcal/mol at the MRCI/6-311+G(2d)//MCSCF(10,10)/6-31G(d) level.[3b] The bond stretch transition state (6) connecting 2 and 4 has a long N-N bond distance. At the MCSCF(10,10) level of theory, the N-N distance of this transition state structure lengthens to 1.893Å, 0.498Å longer than the N-N distance in bicyclodiazoxane and only 0.077Å shorter than the N-N bond in the long bond (2) bicyclodiazoxane; however, the 132.2° O-N-N-O dihedral angle of the transition state remains closer to that of (107.0°) bicyclodiazoxane (5). Work on other dissociation channels is in progress.

II N_2O_3

Preliminary calculations—using RHF/6-31G(d) for structure determination and MP2/6-31G(d)//RHF/6-31G(d) to predict relative energies—reveal several, potentially, HEDM species (see Figure 2 and Table II). We begin our investigation of decomposition pathways on the singlet surface, starting with 1,3-diaza-2,4,5-trioxabicyclo[1.1.1]pentane (1)—the highest in energy among the isomers in Figure 2. At the MP2/6-31G(d)//RHF/6-31G(d) level, the barrier for breaking one N-O bond is predicted to be only 7.4 kcal/mol. This barrier is reduced to 5.1 kcal/mol at the GVB-

PP(6)/6-31G(d)//GVB-PP(6)/6-31G(d) level. Work on decomposition barriers of other higher isomers (2 and 4) using GVB as well as CASPT2 to treat dynamic electron correlations in these species is in progress.

REFERENCES

1. a) Bardo, R. D. *J. Phys. Chem.* **1982**, 86, 4658. b) Bock, C.; Trachtman, M.; Schmiedekamp, A.; George, P.; Chin, T. S. *J. Comp. Chem.* **1983**, 4, 379. c) Neilin, C. J.; Bagus, P. S.; Behm, J.; Brundel, C. R. *Chem. Phys. Lett.* **1984**, 105, 58. d) Michels, H. H.; Montgomery, Jr. J. A. *J. Chem. Phys.* **1988**, 88, 7248.

2. a)Yang, X.; Kim, E. H.; Wodtke, A. M. *J. Chem. Phys.* **1992**, 96, 5111. b) Yang, Price, J. M.; Mack, J. A.; Morgan, C. G.; Rogaski, C. A.; McGuire, D.; X.; Kim, E. H.; Wodtke, A. M. *J. Chem. Phys.* **1993**, 97, 3944.

3. a) Nguyen, A. K.; Gordon, M. S.; Montgomery, Jr. J. A.; Michels, H. H.; Yarkony, D. R. *J. Chem. Phys.* **1993**, 98, 3845. b) Nguyen, A. K.; Gordon, M. S. Boatz, J. A. *J. Am. Chem. Soc.* Submitted

Table I. Enthalpies of formation, G1 and G2 relative energies of N_2O_2 isomers with reference to 2NO.

| Systems | 6-311+G(2d)//6-31G(d) | | | 6-311G(d)//6-31G(d) | |
	MCSCF	MRCI	MP4(SDTQ)	G1	G2
1	44.4	36.6	51.2	39.5	41.7
2	71.7	63.1	52.4	46.1	47.3
3	71.2	64.3	71.9	62.1	63.8
4	79.0	65.6	77.2	69.0	71.4
5	73.2	64.4	80.1	68.0	69.3

Table II. 6-31G(d) Relative Energies (kcal/mol) of N2O3 Isomers.

Systems	SCF	MP2
1	0.0	0.0
2	-23.2	-21.2
3	-69.9	-62.7
4	-26.8	-27.8
5	-41.5	-39.2
6	-141.6	-127.7
7	-138.0	-125.2
8	-130.1	-129.6
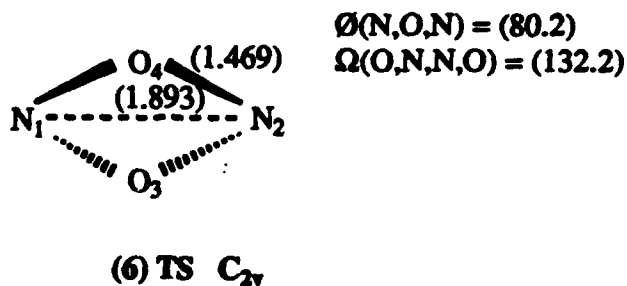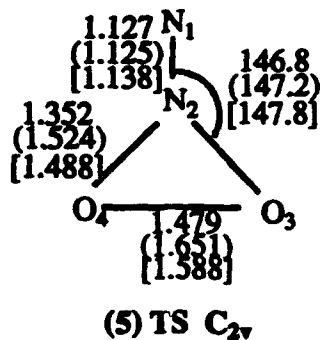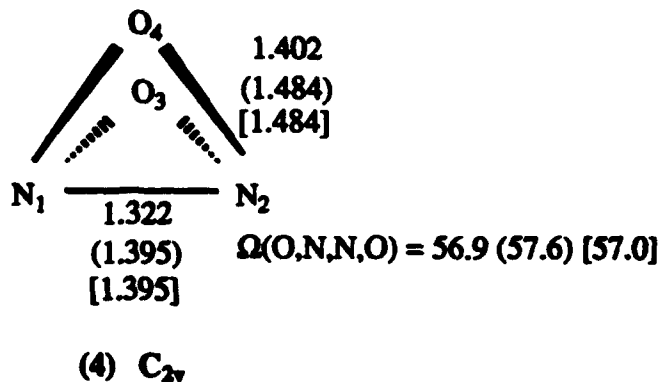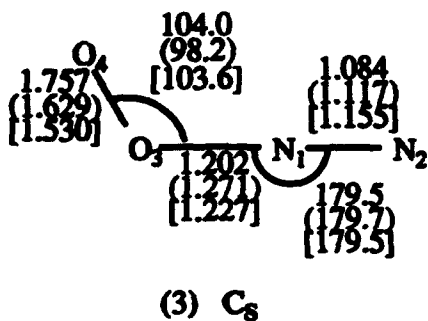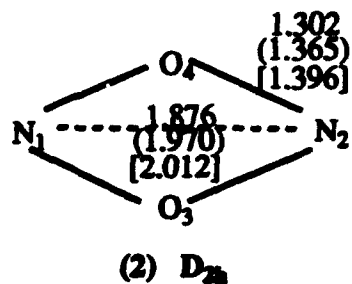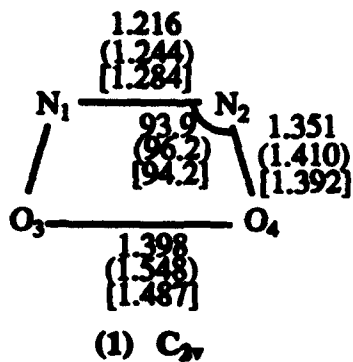
Figure 1. RHF, MCSCF(10,10) (in parentheses), and MP2 (in brackets) structures, calculated with 6-31G(d) basis set.
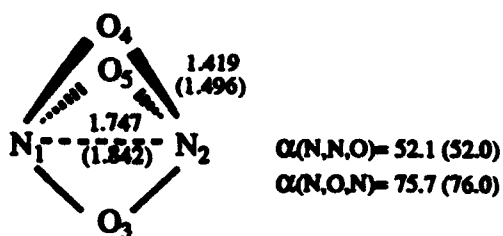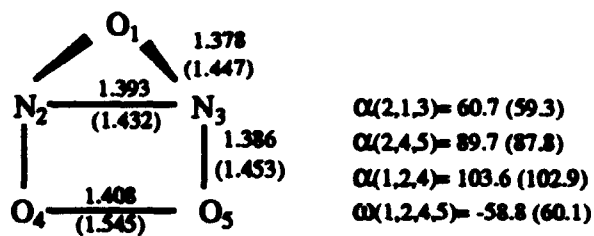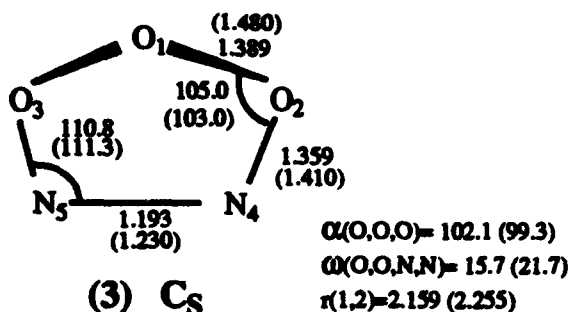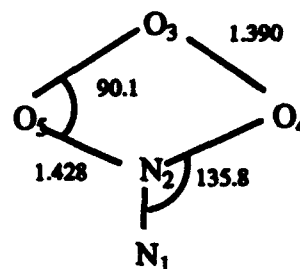
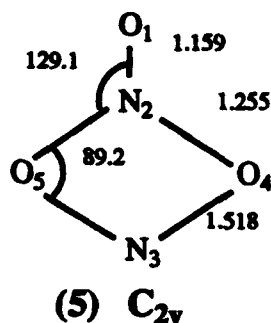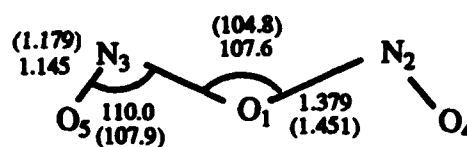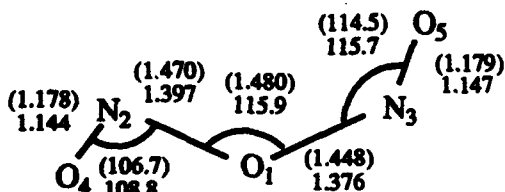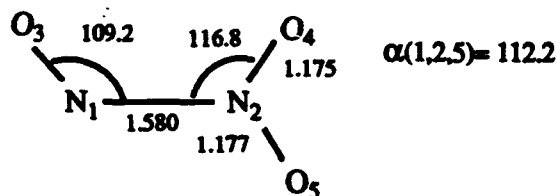Figure 2. RHF/6-31G (d) and 6 pair GVB-P(6)/6-31G(d) (values in parentheses) structures of N_2O_3. Bond lengths are in angstroms, angles are in degrees.

A Theoretical Study of High Energy
B-N Prismane

Nikita Matsunaga and Mark S. Gordon
Department of Chemistry
Iowa State University
Ames, IA 50011

Introduction

Our preliminary calculations have shown that the B-N analog of prismane is a high energy minimum on the potential energy surfaces (PES). The relative energy of the B-P prismane with respect to borazine, including zero-point energy correction, is 185.0 kcal/mol at the restricted Hartree-Fock (RHF) level of theory using effective core potential and basis sets of Stevens *et. al* (SBK(d))[1]. The relationship between the B-N prismane and borazine can be thought of as an intramolecular isomerization reaction, such that the bond between B_1 and N_1 breaks and followed by breaking two other bonds, *i.e.* B_2-B_2 and N_2-N_2 (**Scheme 1**) to obtain borazine.
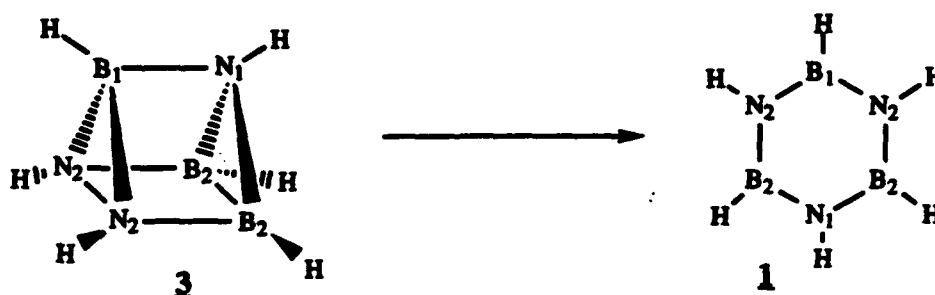
Scheme 1

In this abstract, a part of the PES of the B-N prismane and related molecules are explored in an attempt to achieve the isomerization reaction above. Also, the total electron density analysis was performed in order to shed light into the stabilities and the nature of bonding in the B-N primane.

Computational Approach

All calculations described here were performed with the GAMESS ab initio quantum chemistry program package[gamess]. These extensive calculations were facilitated by the recent implementation of a parallel version of the code for use on a CM5 and an iPSC/860. The geometries were optimized with the restricted Hartree-Fock (RHF) levle of theory using the Steven-Krauss-Jasien (SBKJ) effective core potentials (ECP) and basissets[1] for all heavy atoms and the -31G basis[2] for hydroen. All heavy atoms are augumeneted with d-polarizaiton functions[3]. The correlation energy is included by means of second-order Møller-Plesset perturbation theory (or MBPT)[7] for each stationary point found on the PES.

Recation path was followed for each transition state located with the RHF/SBKJ(d) level of theory by using Gonzalez-Schlegel method[4] in order to connect a transition state to corresponding two minima.

Bonding was analyzed by using localized molecular orbitals (LMO), constructed with the method of Mezey and Pipek[5]. The AIMPAC system of programs[6] was also used to elucidate the nature of bonding. A bond critical point exists between two atoms if there is a saddle point in the electron density between two atoms. At such a point the hessian of the electron density has one positive eigenvalue along the axis orthogonal to the bond axis. The existence of a bond critical point implies the existence of a bond path (path of maximum electron density passing through the bond critical point), and the two atoms are said to be bonded.

Results

Geometries of the B-N prismane and the related molecules along with the relative energies of each molecule with respect to the B-N prismane are shown in Figure 1. The normal modes correspoinding to the imaginary eigenvalue of the energy hessian for the transition state found are shown in Figure 2. The bond lengths of B-N bonds in prismane

form is substantially larger than that of the borazine. All the rectangular faces of the B-N prismane possess up to about 5° deviations from the ideal angle of 90°. The two triangular faces deviates less than 4° from the ideal angle, 60°, found in a prismane.

The bond critical points found for the bonds B_1-N_2 and N_1-B_2 (of Scheme 1) are located inside the ring. Especially, the bond critical points of the N_1-B_2 bond can be found close to the ring critical point associated with the ring N_1-B_2-B_2. It means that the ring has small ring strain. One could think of it as a "T-shaped" bond, though the total electron density contour map shows two distinct bond paths. The localized orbitals do not show such characteristics, either. On the other hand, prismane (carbon only) possesses the bond critical points associated with the triangular face are located outside the ring.

There seems to be some correlation between the bond strength of a given bond type and the value of electron density at the bond critical point. The graph below shows the values of electron density at the bond critical points plotted against the B-N bond distances.
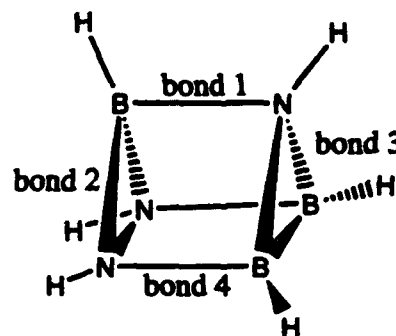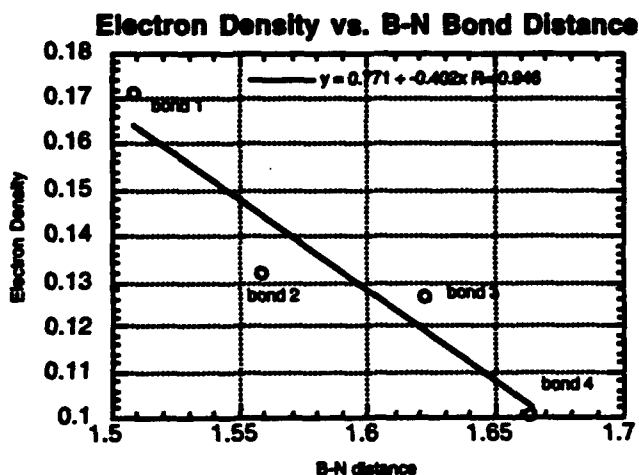
The bond between the N_1-B_1 (bond 1) possesses the highest electron density among B-N bonds, and the smallest value is assigned to the bond N_2-B_2 (bond 4). Then the reaction is likely to occur (or to initiate) by breaking the bond N_2-B_2 first. This implies that the

reaction shown in **Scheme 1** is not likely to occur, in which the strongest bond must be cleaved.

Substituents, chloro-, methyl- or sila- groups, are replaced on the hydrogen attached either to N_1 or $B1$. The relative energy of the substituted B-N prismanes with respect to the corresponding borazines are:

substituents	relative energy(kcal/mol)
H	185.0
Cl on N	182.2
Cl on B	187.8
Me on N	181.5
Me on B	184.5
SiH_3 on N	179.0
SiH_3 on B	183.4

Substituents on B_1 increases the relative energy. The substituted calculations on transition states and other related molecules are in progress in order to obtain informaions on the effect of substituents on the barrier height.

References

[1]   W. J. Stevens, H. Basch and M. Krauss *J. Chem. Phys.* **81** (1984) 6026
[2]   R. Ditchfield, W. J. Hehre and J. A. Pople *J. Chem. Phys.* **54** (1971) 724
[3]   We have used B=0.6 and N=0.8
[4]   C. Gonzales and H. B. Schlegel *J. Phys. Chem.***94** (1990) 5523
[5]   J. Pipek and P. G. Mezey *J. Chem. Phys.* **90** (1989) 4916
[6]   R. F. W. Bader *Atoms in Molecules--A Quantum Theory* (University of Oxford, Oxford, 1990)
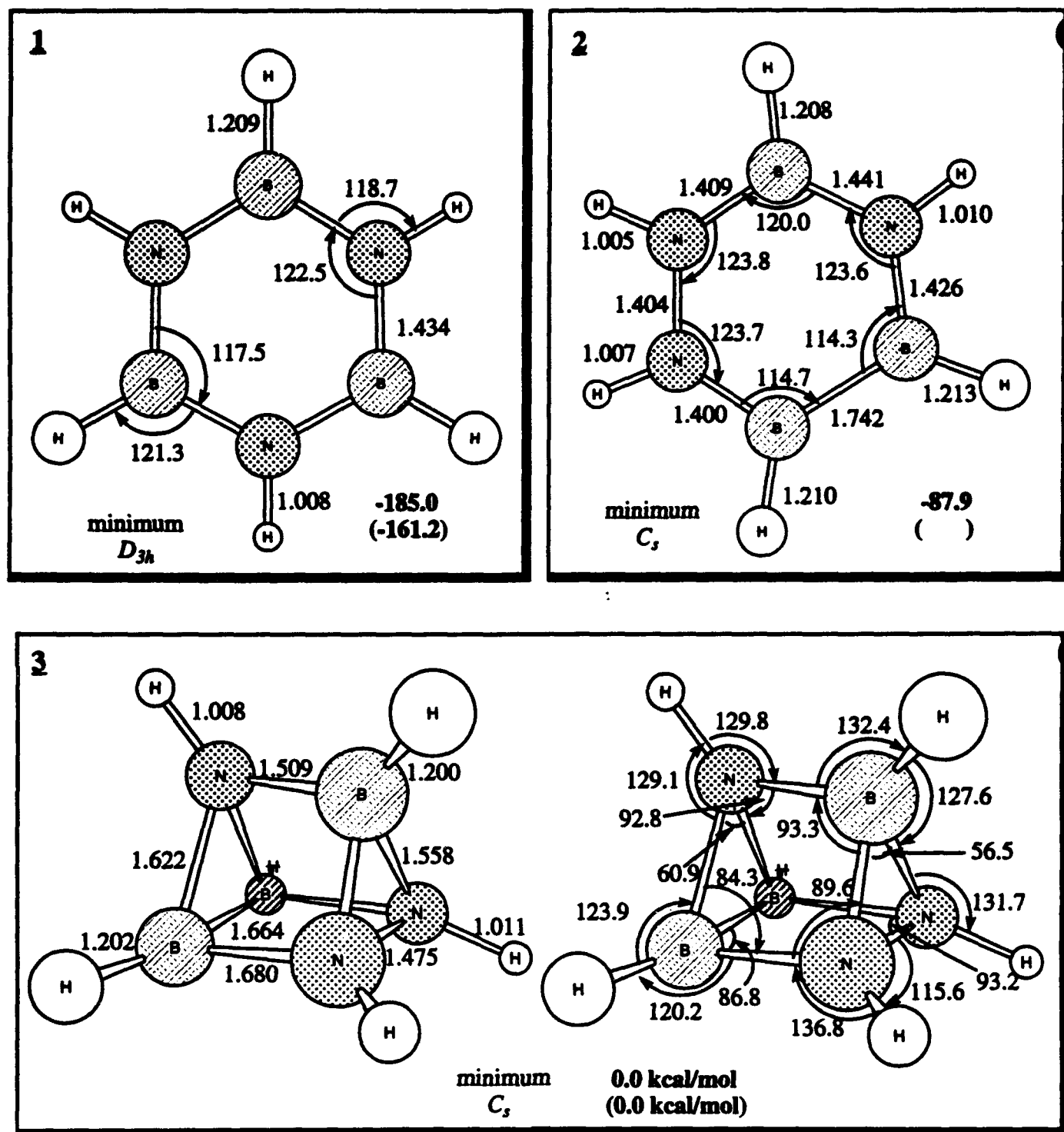[7]   C. Moller and M. S. Plesset *Phys. Rev.* **46** (1934) 618

Figure 1. RHF/SBKJ(d) optimized geometries and energetics of B-N prismane and related molecules. The energies are in kcal/mol. The numbers in parenthesis are of MP2/SBKJ(d)//RHF/SBKJ(d).
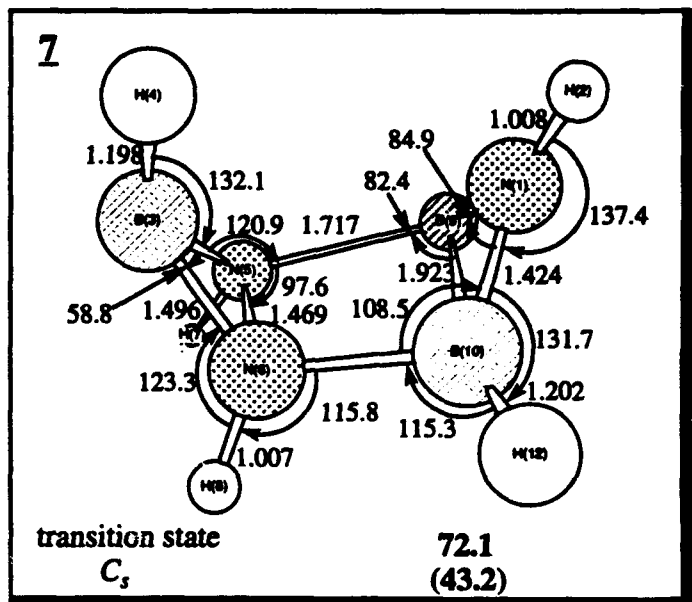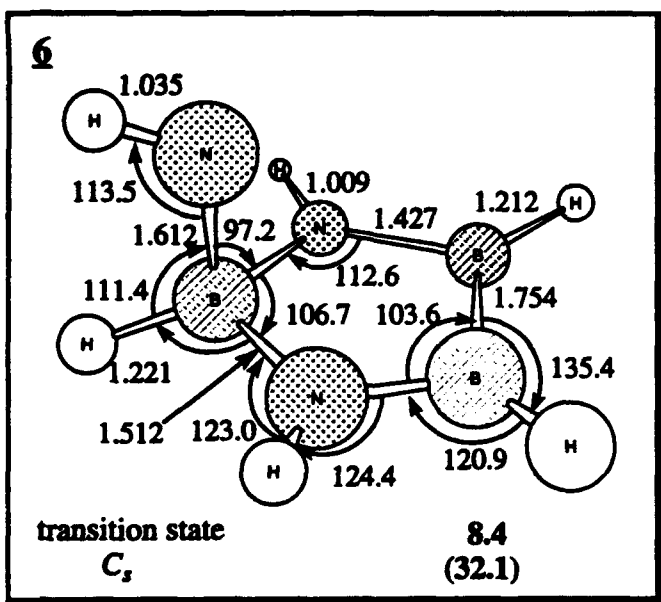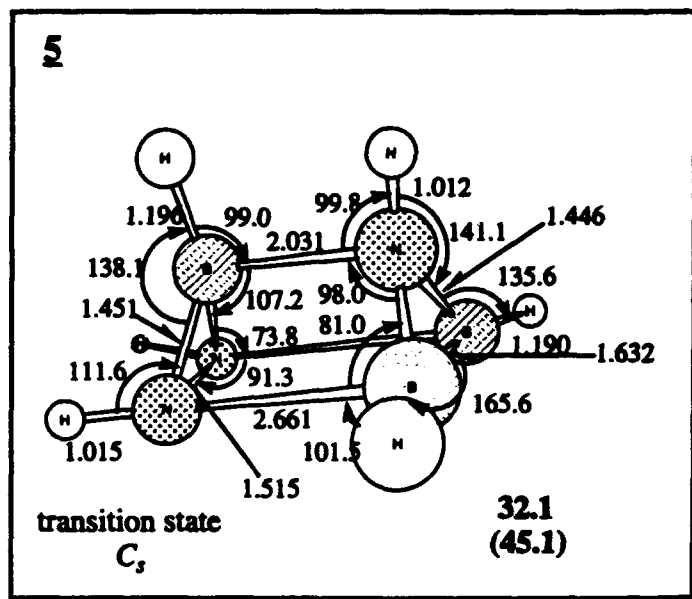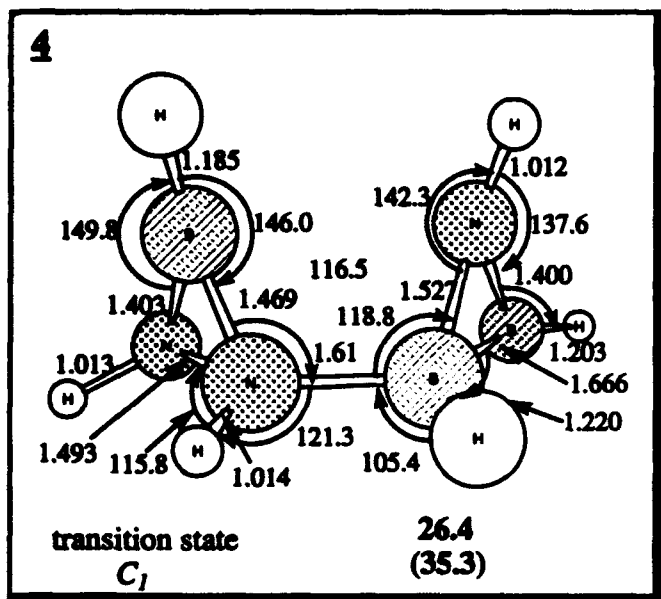
4

1.185

149.8 146.0

1.403 1.469 116.5

1.013 118.8 1.61

1.493 115.8 121.3 105.4

1.014

transition state
C_1

26.4
(35.3)

5

1.196 99.0 99.8 1.012

138.1 2.031 141.1 1.446

1.451 107.2 98.0 135.6

111.6 73.8 81.0 1.190 1.632

91.3

2.661 165.6

1.015 101.5

1.515

transition state
C_s

32.1
(45.1)

6

1.035

113.5

1.612 97.2 1.009 1.427 1.212

111.4 112.6

106.7 103.6 1.754

1.221

1.512 123.0 135.4

124.4 120.9

transition state
C_s

8.4
(32.1)

7

H(4) H(2)

1.198 84.9 1.008

132.1 82.4

120.9 1.717 N(1)

B(3) N(5) 137.4

58.8 97.6 1.923 1.424

1.496 1.469 108.5 B(10) 131.7

H(7)

123.3 115.8 115.3 1.202

1.007 H(12)

H(9)

transition state
C_s

72.1
(43.2)

Figure 1. continued

350e

Figure 1. continued

B3N3H6...RHF/SBK(d)
Imaginary Frequency   219.8 cm**-1

B3N3H6...RHF/SBK(d)
Imaginary Frequency   260.7 cm**-1

B3N3H6...RHF/SBK(d)
Imaginary Frequency   644.1 cm**-1

B3N3H6...RHF/SBK(d)
Imaginary Frequency   788.6 cm**-1
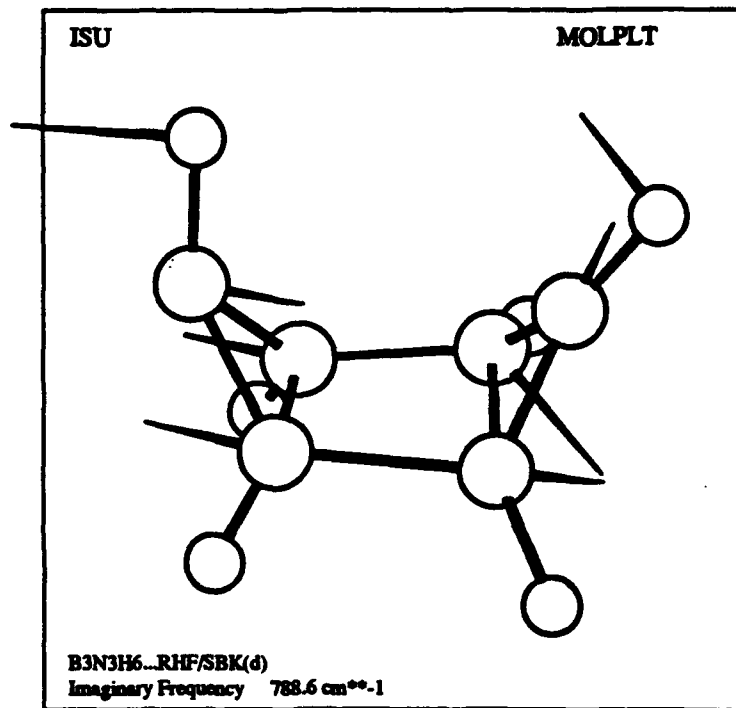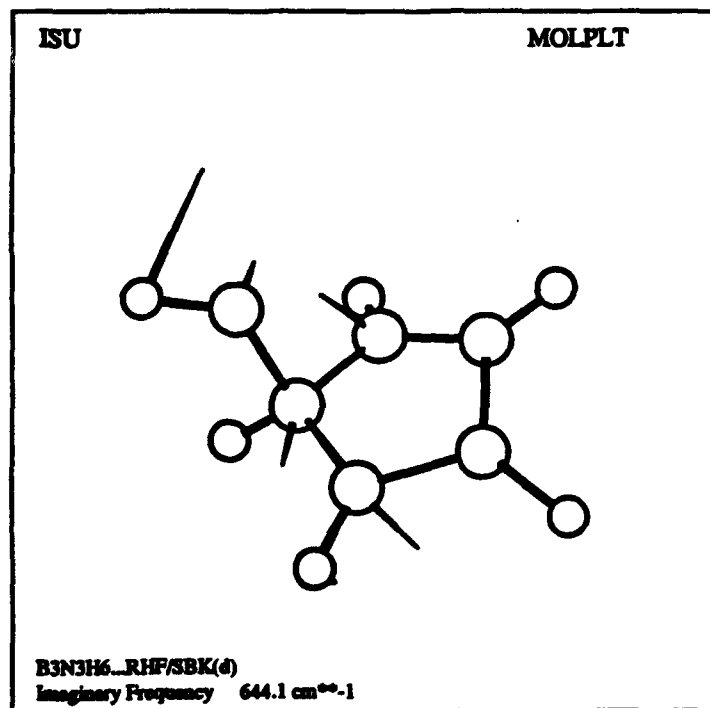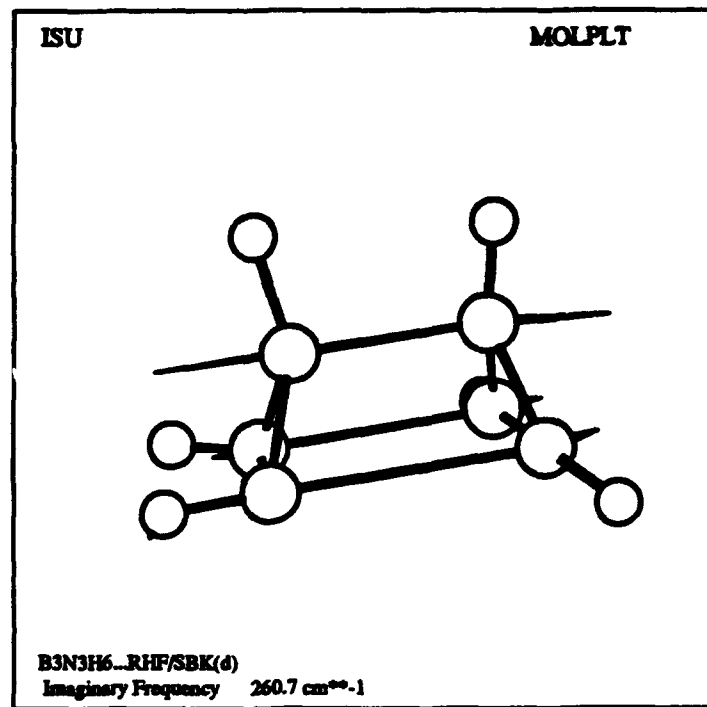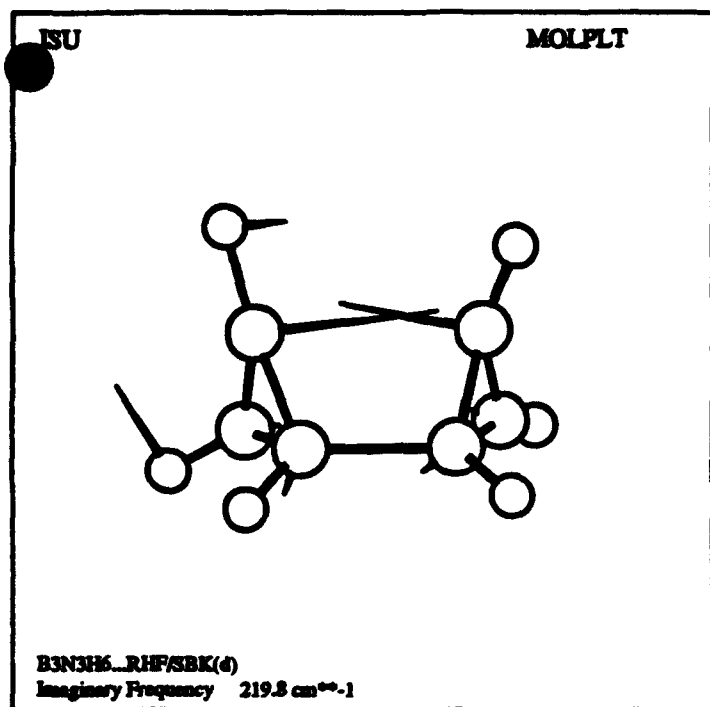
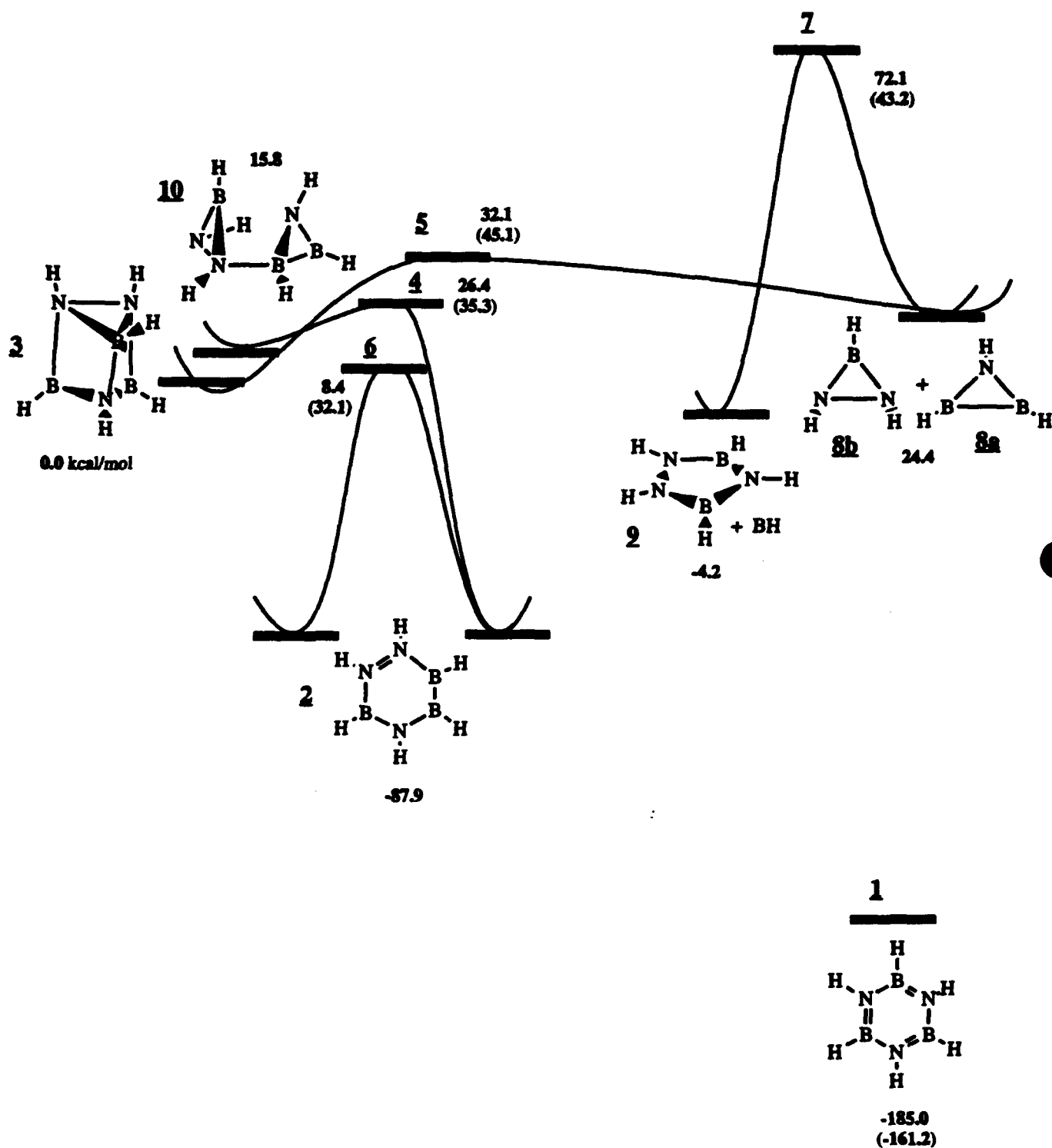**Figure 2. Normal Modes of Transition States**

350g

Figure 3. RHF/SBKJ(d) Potential Energy Surface of B-N Prismane
The values are in kcal/mol. The values in parentheses are of MP2 relative energies.

Monte Carlo Simulations of the Structures and Optical Absorption and Emission Spectra of Na/Ar and B/Ar Solids

Jerry A. Boatz and Mario Fajardo

Phillips Laboratory
OLAC PL/RKFE
9 Antares Road
Edwards AFB, CA 93524-7680

ABSTRACT

Classical Monte Carlo simulations of the structures and optical absorption and emission spectra of Na/Ar and B/Ar solids have been conducted in an effort to identify and characterize the trapping sites of light metal atoms embedded in rare-gas matrices. The optical absorption and emission spectra of the Na/Ar and B/Ar solids are predicted using the first-order degenerate perturbation theory method of Balling and Wright coupled with classical Monte Carlo calculations. The experimental absorption spectra of sodium atoms in argon (as observed by Tam and Fajardo) show the presence of three sets of "triplet" peaks, which are thought to arise from the $^2S \rightarrow {}^2P$ electronic transition of sodium atoms residing in structurally distinct sites in the argon matrix. Good qualitative agreement with the experimental triplet splittings and centroid shifts in sodium-doped solid argon is obtained using our model.

I. Introduction

The behavior of light atoms trapped in rare-gas matrices has long been a topic of interest in the study of condensed phases. These systems serve as classical prototypes to proposed HEDM systems such as boron-doped solid hydrogen. Of particular interest in these systems are the characteristics of the optical absorption and emission spectra of the embedded metal atoms,

since these spectra offer insights to the nature of the metal atom trapping sites.

A specific example of such a system is sodium-doped solid argon, for which both the experimental optical absorption[1,2] and emission spectra[1] have been obtained. The optical absorption spectrum, as observed in the laser ablation experiments of Tam and Fajardo,[2] shows the presence of three sets of "triplet" peaks, presumably arising from the $^2S \rightarrow {}^2P$ (i.e., 3s -> 3p) electronic transition of sodium atoms residing in structurally distinct sites in the argon matrix. The triplet feature is thought to arise from a breaking of the degeneracy of the excited-state p orbitals of the metal atom via either a dynamic Jahn-Teller effect and/or enhanced spin-orbit coupling in solid-state environments, or static asymmetry of the trapping site. The emission spectra of sodium-doped argon matrices has also been measured[1] for excitation energies corresponding to two of the three observed absorption triplets.

Another example of a condensed phase HEDM prototype is boron atoms embedded in solid argon. There is considerably less known about this system than for sodium-doped solid argon. However, optical absorption experiments on this system have been performed[3] and this poster presents preliminary results of simulations of the absorption and emission spectra of boron atoms in solid argon.

While condensed phase systems containing other types of light atoms are also of interest to the HEDM program, the nature of the ground and low-lying excited electronic states of sodium and boron atoms makes them particularly amenable to our methods of simulating their condensed-phase optical absorption and emission spectra. The purpose of the present study is to identify and characterize the metal-atom trapping sites being accessed experimentally in the laser-ablation deposition of sodium and boron atoms in solid argon and to elucidate the nature of the "matrix effects" responsible for the observed spectra.

II. Theoretical Methods

A crucial component of our Monte Carlo simulations is the
incorporation of the Balling and Wright[6] (B&W) model into our calculations.
This model, which assumes additivity of individual metal atom/rare gas atom
interactions, uses first-order degenerate perturbation theory to predict
the shifting and splitting of the three degenerate components of the ^2P Na
in the presence of multiple rare-gas perturbers. Evaluation of the
perturbation matrix elements requires only the A $^2\Pi$ and B $^2\Sigma^+$ Na-Ar excited
state potentials.[5] The B&W model not only enables the simulation of
absorption spectra arising from ns -> np electronic transitions, but a
straightforward generalization of the method[6] also permits three additional
types of spectral simulations; namely, simulations of np -> ns absorptions
and ns -> np and np -> ns emissions. In particular, the absorption and
emission spectra of boron atoms in solid argon can also be simulated within
this framework.

Trapping site structures: Classical Metropolis[7] Monte Carlo
simulations are used to predict the structures of solid Na/Ar and B/Ar.
Solid argon is modelled by imposing periodic boundary conditions in three
dimensions on a cubic "chunk" of an argon lattice containing 108 atoms. An
interstitial trapping site is simulated by placing a sodium or boron atom
in an octahedral hole in the Ar_{108} lattice. Various "n-atom"
substitutional trapping sites are modelled by replacing n adjacent argon
atoms (where n = 1, 2, 3, 4, 5, 6, or 13) with a single sodium or boron
atom. Both the interstitial and substitutional trapping sites are then
allowed to relax, subject to the constraint of constant volume, at the
specified temperature. Total energies are computed within the pairwise
additive approximation, using Ar-Ar,[8] Na-Ar,[5] and B-Ar[9] diatomic
potentials.

Spectral simulations: The method of B&W was originally used to predict
the absorption energies, arising from the 3s -> 3p electronic transition,
of a sodium atom surrounded by a static configuration of argon atoms,

although their method as originally derived can be used to predict the ns -> np transition energy of any ^{2}s ground-state atom in the presence of an arbitrary number and configuration of rare gas atoms. In the present work, this method is coupled with classical Monte Carlo simulations to incorporate the effect of the thermal motions of the atoms into the prediction of the absorption energies. Furthermore, we have extended the B&W method to simulate the emission spectra of solid Na/Ar as well as the absorption and emission spectra of solid B/Ar. With these extensions to the B&W model, it is possible to simulate the absorption or emission spectrum of any atom embedded in a rare-gas matrix, provided that the spectral simulations of interest involve electronic transitions of the type [core]ns -> [core]np, or [core]np -> [core]ns.

III. Results and Discussion

Figures 1 and 2 show the simulated absorption and emission spectra, respectively, for solid $NaAr_n$, where n=95, 102-108. Likewise, Figures 3 and 4 show the absorption and emission spectra for solid BAr_n. The most spacious trapping environment (n=95) corresponds to a 13-atom substitutional site and the tightest site (n=108) is initially interstitial. All simulations were performed at a temperature of 10 K.

Na/Ar Absorptions: The simulated optical absorption spectra of atomic sodium in solid argon are shown in Figure 1. The spectra corresponding to n=95, 102, 104, and 107 are symmetric and, with the exception of the spacious 13-atom substitutional site (n=95), all are triplets. The radial distribution functions (RDFs) for these 4 trapping sites (not shown) all indicate a high degree of symmetry (e.g., T_d or O_h)), as an average over the sampled configurations. Conversely, the four remaining spectra, which are all asymetric doublets or triplets, have RDFs indicative of trapping site symmetries less than T_d. The symmetric triplet spectra are in good qualitative agreement with the experimentally observed absorption spectra.[1,2] The most significant discrepancy between the observed and

354

simulated spectra is that the extent of the blue shift of the absorption centroid in the latter is approximately half of the experimentally observed "violet" triplet.[2]

Na/Ar Emissions: Figure 2 shows the simulated NaAr$_n$ emission spectra. All are singlets, in contrast to the experimentally observed doublet pattern.[1] All of the simulated spectra are red-shifted (in agreement with experiment) and, with the exception of the 5- and 6-atom substitutional trapping sites (n=103 and 102, respectively), the extent of red shifting increases with the tightness of the trapping environment. Since the sodium-argon interaction energies are computed "on the fly" using the B&W method rather than calculated as a pairwise sum over the X $^2\Sigma^+$ Na-Ar diatomic potential curve, analysis of this anomalous behavior in the magnitude of the red shift is difficult.

B/Ar Absorptions: The simulated BAr$_n$ absorption spectra are shown in Figure 3. For all eight trapping sites considered in this work, the predicted spectra are singlets and blue-shifted. Experimentally,[3] doublet absorptions are observed and the extent of blue shifting (7000 cm^{-1}) is much greater than in the simulations (2500 cm^{-1}). With the exception of the interstitial site (n=108), the magnitude of the blue shift increases as the size of the trapping site decreases.

B/Ar Emissions: Figure 4 shows the predicted BAr$_n$ emission spectra. These spectra are generally quite broad and show either singlet or doublet patterns. (Note that for each spectrum in Figure 4 there are three emission transitions which are individually shown in as light, dotted curves. The actual predicted spectrum is shown as a dark, heavy curve and is the sum of the three individual curves.) However, the predicted spectrum for the 13-atom substitutional site (n=95) shows a single, narrow peak. (There apparently has been no experimental measurement of the emission spectrum of atomic boron in solid argon.) This behavior can be understood in part by examination of the B-Ar diatomic potentials[9] used in these simulations (not shown). In particular, the B $^2\Sigma^+$ B-Ar potential, which is

used in calculating the boron-argon interaction energy, has two local minima. The deeper of the two minima is located at a B-Ar separation of 2.5 Å and is bound by approximately 450 cm^{-1} relative to the ^2S B ([core]3s) + Ar asymptote. The second well is much shallower (15 cm^{-1}) and has an R_e of about 7 Å. These two minima are separated by a barrier which is 180 cm^{-1} above the ^2S B + Ar asymptote. In the B/Ar emission simulations, the distance of the first nearest neighbor argon atoms from the boron atom determines if the spectrum is broad or sharp. If the nearest argon atoms are trapped within the deep well around R_e = 2.5 Å, then emission transitions will access the repulsive wall regions of the three underlying potential energy surfaces. This in turn implies that small fluctutations in the B-Ar internuclear distances in the excited state will lead to large fluctuations in the emission energies. However, if the nearest neighbor argon atoms are located within the shallow well centered at R_e= 7 Å, transitions to the underlying states will access a relatively "flat" portion of the underlying potential surfaces, thus leading to sharp emission peaks. Indeed, the RDFs for the B/Ar emission simulations (not shown) indicate that the nearest neighbor boron atoms for all trapping sites except the 13-atom substitutional site are in the region of the deeper B $^2\Sigma^+$ B-Ar well.

IV. Conclusions

The simulated Na/Ar absorption spectra show a variety of patterns which are primarily a function of the "average" symmetry of the sodium atom trapping site. Generally, highly symmetric trapping sites (such as T_d or O_h) have symmetric "triplet" absorptions while lower symmetry trapping sites are characterized by assymetric doublet or triplet absorption features. Since all experimentally observed Na/Ar absorptions attributed to atomic sodium have a triplet pattern, the present simulations are consistent with the notion that sodium atoms reside in symmetric trapping sites in the argon lattice.

Although the experimental Na/Ar emission and B/Ar absorption spectra both show "doublet" features, the corresponding simulated spectra contain a single peak. While the reason for the presence of the doublet pattern in the observed spectra remains unknown, it is possible in the case of B/Ar absorptions that the doublet arises from $^2P \to {}^2D$ boron atom transitions rather than $^2P \to {}^2S$ excitations.[10]

The simulated B/Ar emission spectra predict large red shifts and broad singlet or doublet emission patterns. Only for relatively spacious trapping environments (such as a 13-atom substitutional site) are sharp emission peaks predicted.

References

1. L.C. Balling, M.D. Havey, and J.F. Dawson, *J. Chem. Phys.* **69**, 1670 (1978).

2. S. Tam and M.E. Fajardo, *J. Chem. Phys.*, in press.

3. See, for example,
    a) W.R.M. Graham, W. Weltner, Jr., *J. Chem. Phys.* **65**, 1516 (1976).
    b) G. Jeong and K.J. Klabunde, *J. Am. Chem. Soc.* **1986**, 7103 (1986).
    c) G.H. Jeong, R. Boucher, and K.J. Klabunde, *J. Am. Chem. Soc.* **112**, 3332 (1990).

4. L.C. Balling and J.J. Wright, *J. Chem. Phys.* **79**, 2941 (1983).

5. R.P. Saxon, R.E. Olson, and B. Liu, *J. Chem. Phys.* **67**, 2692 (1977).

6. J.A. Boatz and M.E. Fajardo, manuscript in preparation.

7. N. Metropolis, A.W. Rosenbluth, M.N. Rosenbluth, A.H. Teller, and E. Teller, *J. Chem. Phys.* **21**, 1087 (1953).

8. R.A. Aziz and M.M. Slaman, *Mol. Phys.* **58**, 679 (1986).

9. E. Hwang, Y.-L. Huang, P.J. Dagdigian, and M.H. Alexander, *J. Chem. Phys.*, **98**, 1 (1993).

10. M.E. Fajardo, "Trapping of Light Metal Atoms in Hydrogen Matrices", these proceedings.
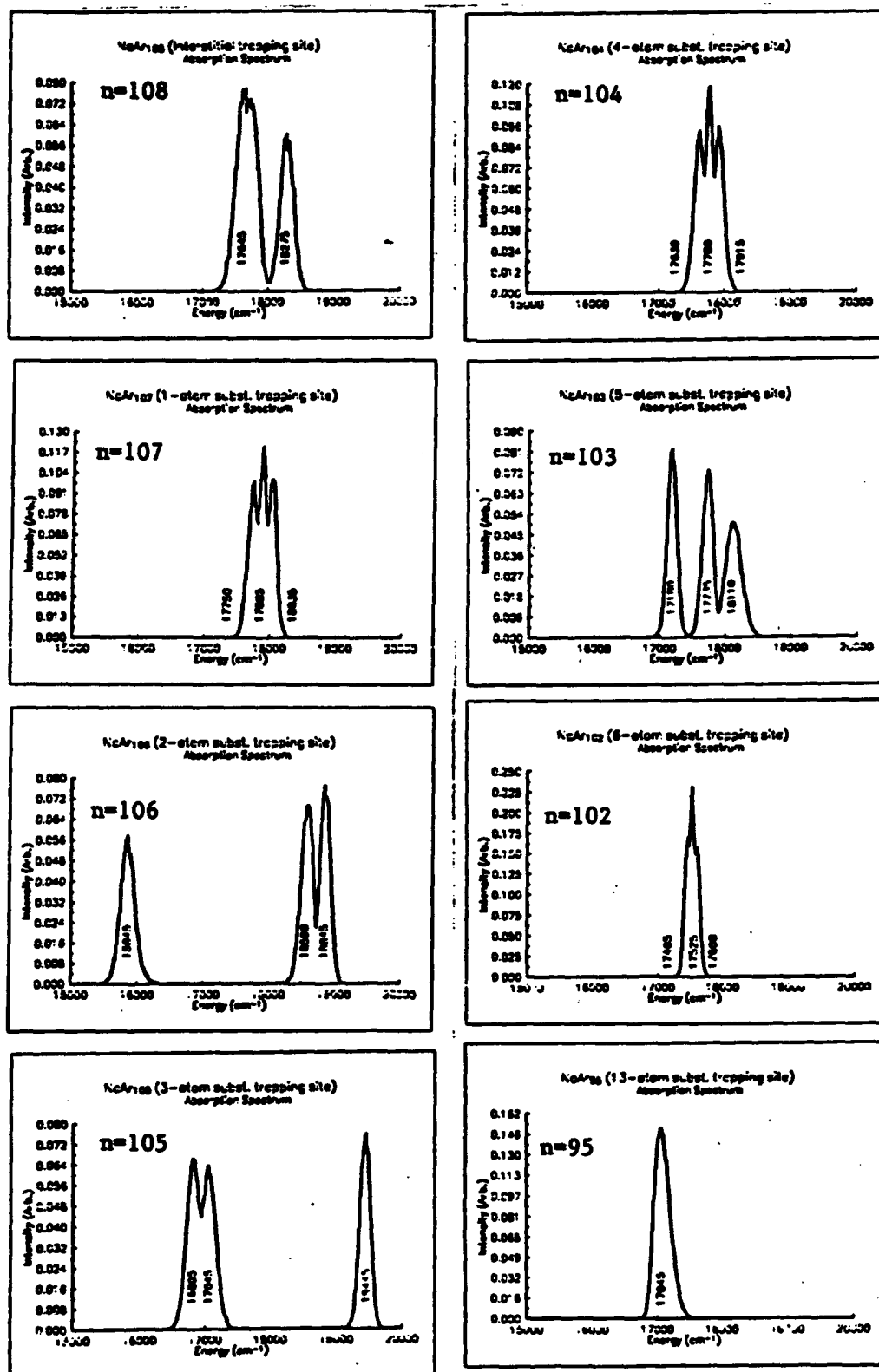
Figure 1

NaAr_n Absorption Spectra
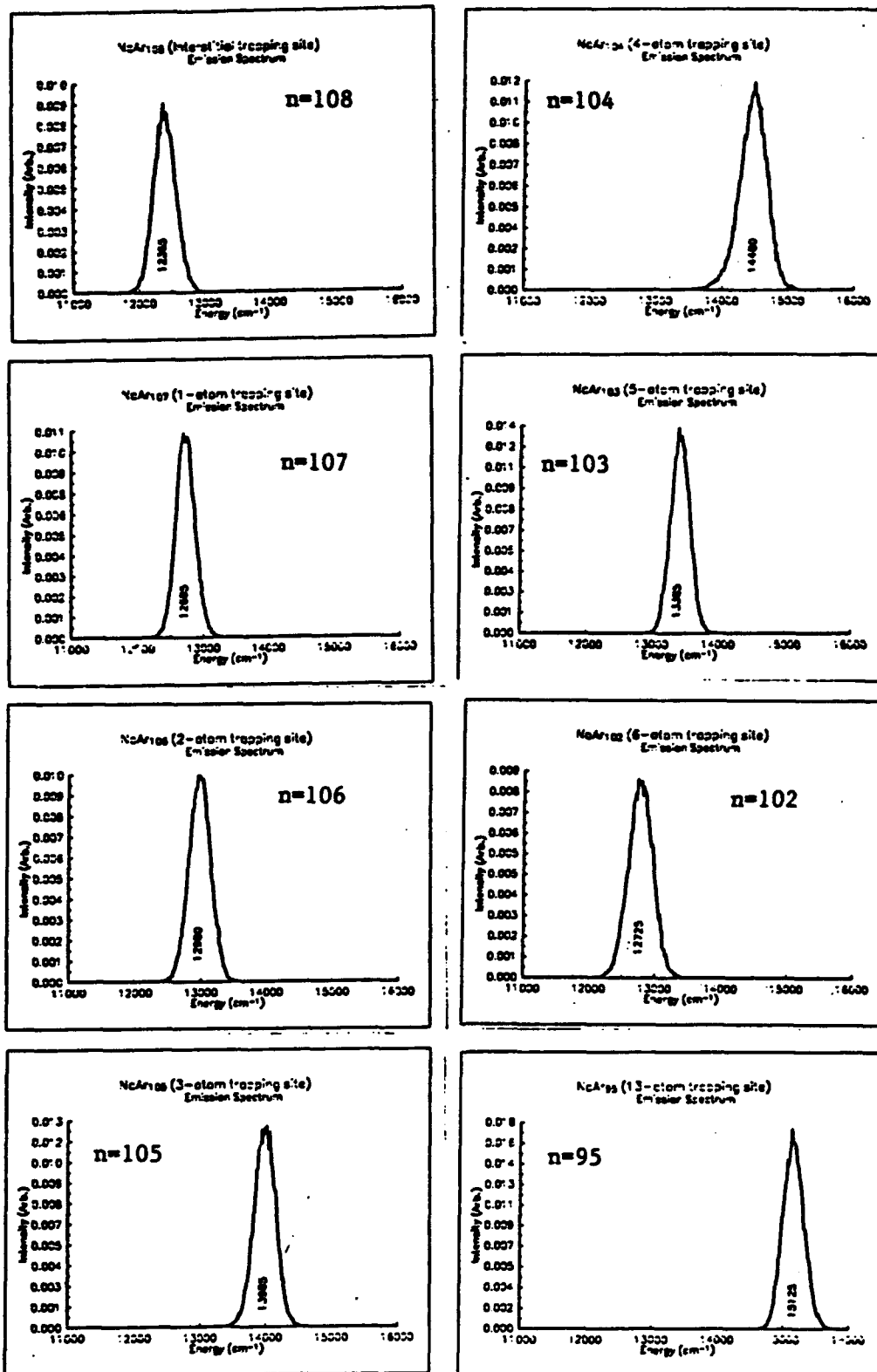
Figure 2

NaAr$_n$ Emission Spectra

Figure 3
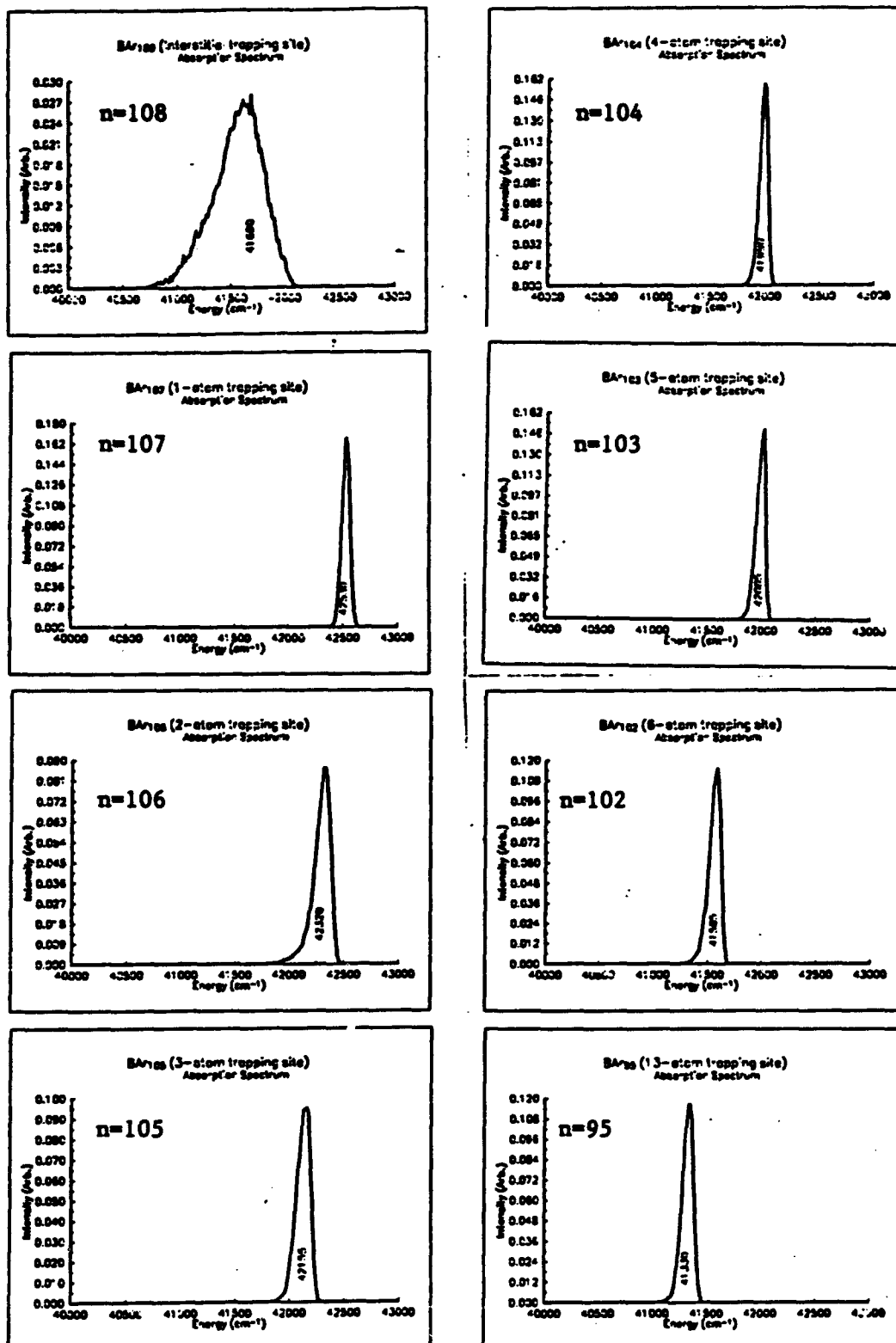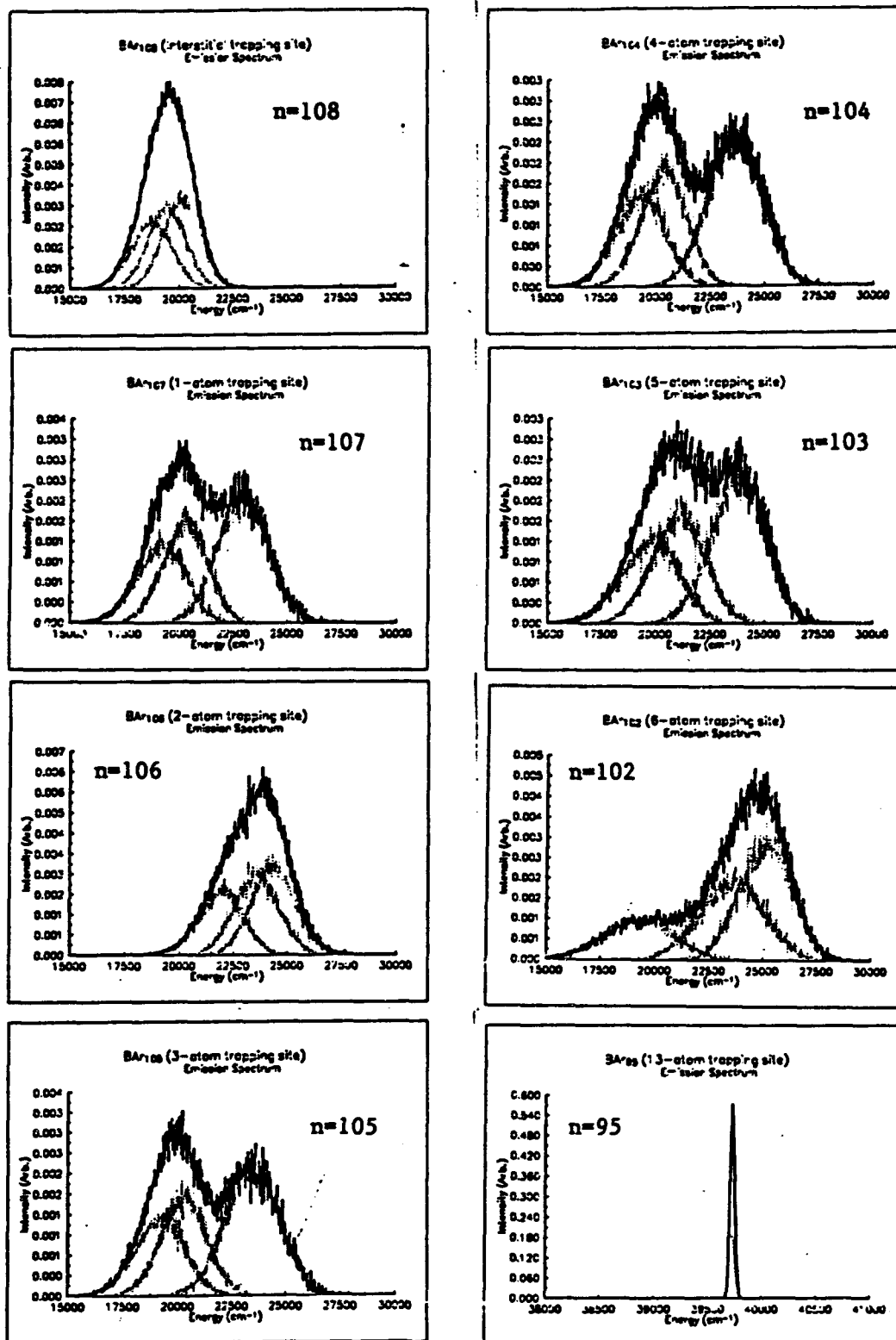
BAr_n Absorption Spectra

Figure 4

BAr_n Emission Spectra
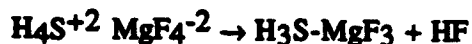
High Energy Materials that Coulomb Explode

Nick Gonzales, Mark Roberson, Alexander Boldyrev, and Jack Simons

Chemistry Department
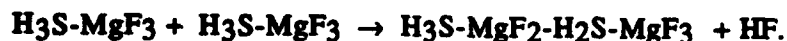University of Utah
Salt Lake City, Utah 84112

Our earlier work[1] on multiprotonated doubly charged cations MH_n^{+2} and work of others[2] on doubly charged anions involving MF_m^{-2} stoichiometry has lead us to examine compounds that use these ions as "building blocks". In particular, we consider in this paper the following species:

(i) "salts" such as H_4S^{+2} MgF_4^{-2} than might be formed by combining a pair[3] of double ions of opposite charge and which energy considerations cause to retain their +2/-2 charge separation, and

(ii) "chains" grown by covalently linking one or more pairs of such double ions and eliminating one or more HF molecule[4], for example, as in

$$H_4S^{+2} MgF_4^{-2} \rightarrow H_3S\text{-}MgF_3 + HF$$

or

$$H_3S\text{-}MgF_3 + H_3S\text{-}MgF_3 \rightarrow H_3S\text{-}MgF_2\text{-}H_2S\text{-}MgF_3 + HF.$$

In each of the doubly charged ions (e.g., see H_4S^{+2} and MgF_4^{-2} shown in Figs 1 and 2), there exists a great deal of pent up internal Coulomb energy as illustrated in Fig. 3.
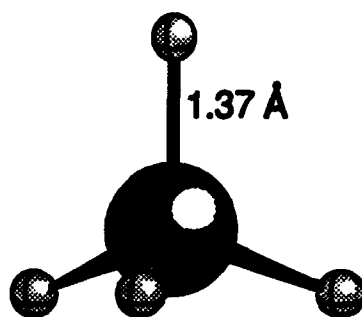
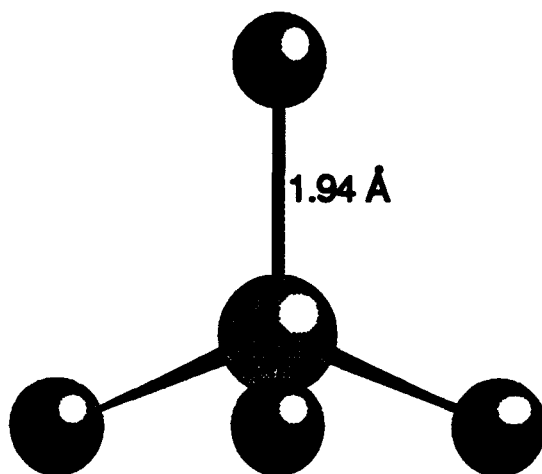Figure 1. Tetrahedral Equilibrium Geometry of The H_4S^{2+} Dication.

Figure 2. Tetrahedral Equilibrium Geometry of The F_4Mg^{2-} Dianion.
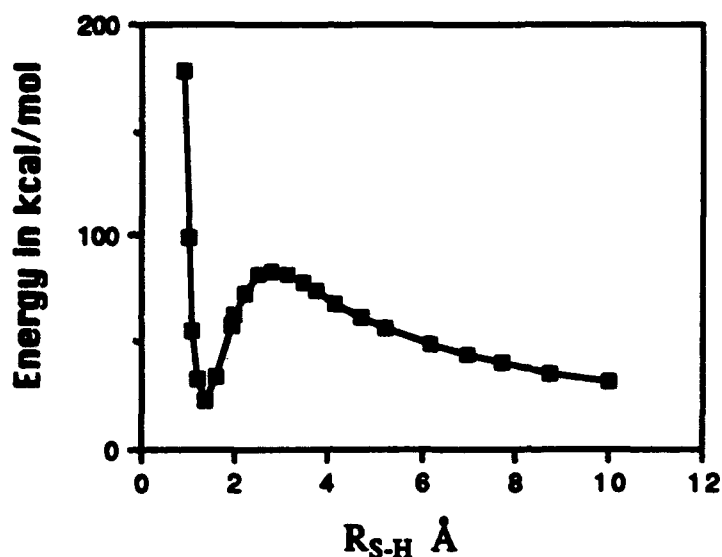
Figure 3. The SCF/6-31++G** ground-state electronic energy (including nuclear repulsion) of H_4S^{2+} as a function of <u>one</u> S-H bond length R(SH) with the remaining internal coordinates optimized to produce minimum energy.

The findings of our initial investigations on these two protoype ions are summarized below in Tables I and II. Of special importance are the (qualitatively accurate) predictions of the lowest energy optical transitions based on the highest occupied orbital (HOMO) to lowest unoccupied orbital (LUMO) energy gap, the internal atomic charges, and the fact that these ions are locally stable species.

Table I. Total and Relative Energies, Geometries, and Vibrational Frequencies for Species Relating to H_4S^{+2} Using a 6-311++G Basis Set**

Species	Point Group	Energy (Atomic Units)	Relative Energy (kcal/mol)	Distances (Å) & Angles (deg)	Vib. freq. (cm^{-1}) ZPE(kcal/mol)	$E_{(HOMO)}$- $E_{(LUMO)}$ (kcal/mol)	Atomic Charges
H_4S^{+2}	T_d	-399.120943	0	r=1.3784	T_2 1001 E 1209 T_2 2479 A_1 2484 /21.9	529	S= 0.70 H=0.33 H=0.33 H=0.33 H=0.33
$\{H_3S\cdots H_a\}^{+2}$	C_{3v}	-399.023887	56	r_{SHa} =2.8376 r_{SH} =1.3575 HSH_a=118.2 HSH=100.0	A_1 743i E 389 A_1 1029 E 1199 A_1 2638 E 2647 /17.4	229	S= 0.32 H_a=0.91 H=0.26 H=0.26 H=0.26
H_3S^+ + H^+	C_{3v}	-399.158895	-29	r=1.3465 HSH=95.9	A_1 1075 E 1233 A_1 2736 E 2746 /16.8	405	S= 0.44 H=0.19 H=0.19 H=0.19

Table II. Total and Relative Energies, Geometries, and Vibrational Frequencies for Species Relating to MgF_4^{-2} Using a 6-311++G** Basis Set

Species	Pt. Grp.	Energy (Atomic Units)	Relative Energy (Kcal)	Distances (Å) & Angles (deg)	Vib. freq. (cm^{-1}) /ZPE (Kcal)	$E_{(HOMO)}-E_{(LUMO)}$ (kcal/ mol)	Atomic Charges
MgF_4^{-2}	T_d	-598.612088	0	r=1.9483	E 137 T_2 223 A_1 382 T_2 492 /4.0	247	Mg=1.11 F=-0.78 F=-0.78 F=-0.78 F=-0.78
$\{F_3Mg\cdots F_a\}^{-2}$	C_{3v}	-598.573046	24	r_{MgFa} =3.817 r_{MgF} =1.8789 $FMgF_a$=101.5 FMgF=116.0	A_1 89i E 83 E 192 A_1 240 A_1 454 E 604 /3.5	195	Mg=1.11 F_a=-0.98 F=-0.72 F=-0.72 F=-0.72
F_3Mg^- + F^-	D_{3h}	-498.976324 + -99.684425	-31	r=1.8252	E' 182 A_2'' 249 A_1' 468 E' 655 /3.4	299	Mg=1.01 F=-0.67 F=-0.67 F=-0.67

The calculated barriers to dissociation and the energy release uppon fragmentation of several doubly charged ions are given below in Table III.

Table III. Calculated Dissociation Energies (ΔE) and
Dissociation Barriers ($E^{\dagger}$) (kcal/mol) for Doubly Charged Ions

Species	ΔE	$E^{\dagger}$
$H_4O^{2+} \rightarrow H_3O^+ + H^+$	-61	38
$H_3F^{2+} \rightarrow H_2F^+ + H^+$	-111	12
$H_4S^{2+} \rightarrow H_3S^+ + H^+$	-29	56
$H_3Cl^{2+} \rightarrow H_2Cl^+ + H^+$	-67	34
$H_2Ar^{2+} \rightarrow HAr^+ + H^+$	-115	5
$F_4Be^{2-} \rightarrow F_3Be^- + F^-$	-82	14
$F_4Mg^{2-} \rightarrow F_3Mg^- + F^-$	-31	24
$F_8Te^{2-} \rightarrow F_7Te^- + F^-$	-43	?
$Cl_8Te^{2-} \rightarrow Cl_7Te^- + F^-$	-69	?
$F_8Se^{2-} \rightarrow F_7Se^- + F^-$	-75	?

It is important to note that the dianions are not only geometrically metastable but are also electronically stable with respect to loss of a single electron to produce the mono-charged anion as shown in Table IV.

Table IV . Vertical Electron Detachment Energies DE (eV) at Koopmans' Theorem
and Correlated Levels of Theory

Species	Koopmans' DE	Correlated DE
F_4Be^{2-}	3.5	1.9
F_4Mg^{2-}	4.4	3.0
F_6Se^{2-}	5.4	3.8
F_8Te^{2-}	6.5	5.0
F_8Se^{2-}	5.5	?
Cl_8Te^{2-}	3.9	?
F_7Te^{2-}	11.9	?
F_7Se^{2-}	11.2	?
Cl_7Te^{2-}	8.0	?

Our initial calculations indicate that combining dianions with dications to produce "salts" which are locally metastable but which could fragment and release large

amounts of energy may be worth pursuing. As illustrated below, for example, MgF_4^{-2} and H_4S^{+2} can combine to form a salt, which, upon heating to overcome dissociation barriers, will release ca. 230 kcal/mol of energy to form F_2MgSH_2 + 2 HF. It is our intention to pursue such combinations of doubly charged ions further.
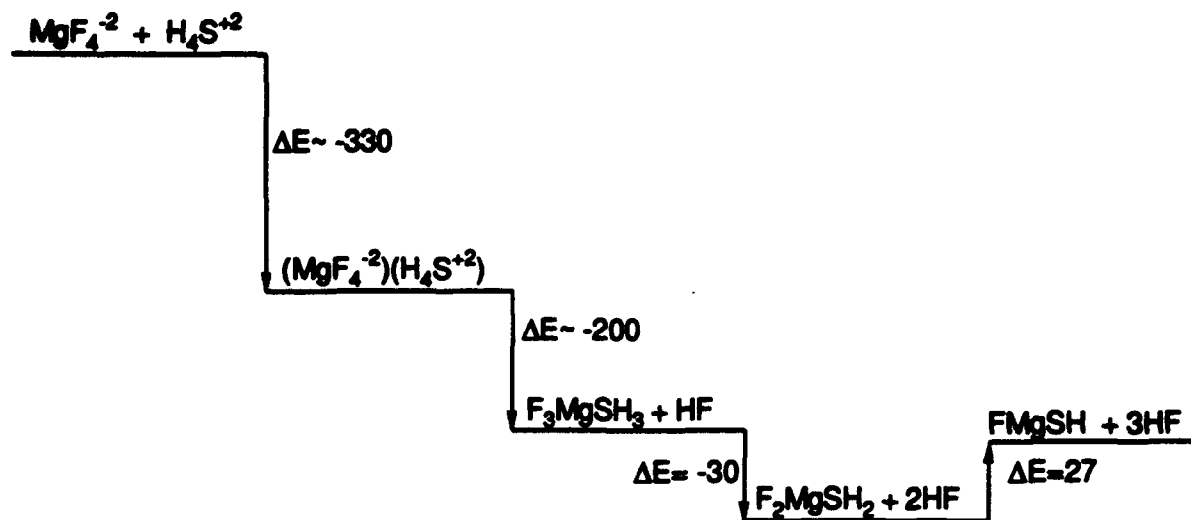

Figure 4. Thermochemistry Information for $(MgF_4^{2-})(H_4S^{2+})$ "salt" (energies in kcal/mol).

We also intend to pursue, using semi-empirical methods we are now reparameterizing to properly describe hypervalent species such as those discussed here, polymeric chain $F_3Mg\text{-}(SH_2\text{-}MgF_2)_n\text{-}SH_3$ and cross- linked polymers such as those shown below with an eye on geometrical stabilities and energy release upon decomposition.
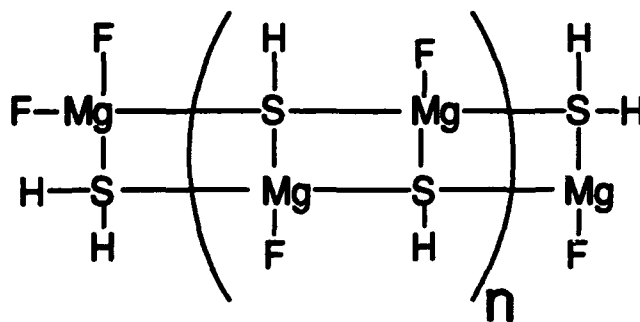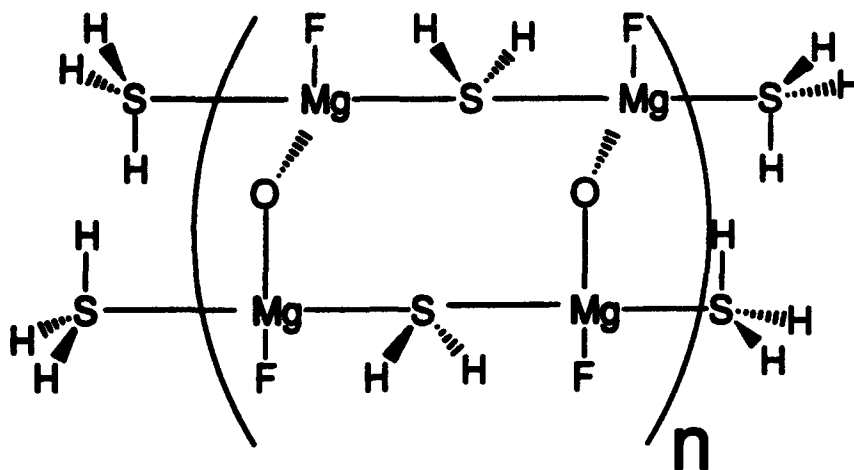
1. A. I. Boldyrev and J. Simons, J. Chem. Phys. **97**, 2826 (1992).

2. H. G. Weikert, L. S. Cederbaum, and A. I. Boldyrev, unpublished results; H. G. Weikert, L. S. Cederbaum, F. Tarantelli, and A. I. Boldyrev, Z. Phys. D. **18**, 299 (1991).

3. These species are viewed as prototypes for families of salts in which (i) the cation involves a multiply protonated species whose central atom is more electronegative than H and contains more than one lone pair of electrons (e.g. S, O, Se, F, Cl, etc.) and (ii) the anion's central atom is less electronegative than the ligands attached to it and contains two or more empty orbitals to act as Lewis acid sites for negatively charged ligands (e.g., Mg, Ca, B, Al, Ga, etc.). Which particular ion pairs are of most interest to examine will depend on the ionic radii of the positive and negative ions; only when these radii are proper will efficient packing into favorable crystal structures be possible.

4. The sizes of the positive MH_n^{2+} and negative $M'X_n'^{2-}$ ion moieties are also important here; if M and M' are too different in size, the M-M' bond will be weak, and if X is too large, steric crowding of the M-M' bond will occur.

"Chemistry and Propulsion: A Strained Relationship."

Mr. Robert Behdadnia, Dr. Dee Lange and Dr. E. J. Wucherer
Rocket Propulsion Directorate,
Phillips Laboratory,
Edwards AFB, CA 93524

The HEDM Synthesis Working Group focuses on preparation of new, high energy compounds. We have initiated several projects with both near-term and long-term goals. Our current efforts focus on the synthesis of three-member ring compounds as high energy additives to RP1/LOX systems. The additives are projected to increase the Isp of Atlas systems by 2 to 3 seconds. Both carbocyclic and heterocyclic systems are under study.

Construction of chains of spiro-connected cyclopropane rings is accomplished by a carbene addition to an exo-methylene compound and subsequent dehydrohalogenation of the resultant methyl-chloro cyclopropane. The resultant methylenecyclopropane can again be cyclopropanated. We are currently interested in compounds with two cyclopropanes tethered onto a larger hydrocarbon ring.

A second research effort is centered on the incorporation of aziridines and hydrazines into hydrocarbon molecules. Nitrene addition to olefins is used to generate aziridines which are can be further cyclized to strained aziridine-hydrazine cage molecules.

The long-term goal of these tasks is to develop synthetic pathways to polymeric energetic molecules and hetero atom cage structures.

Catenated Cyclopropyl Compounds. Methylchlororcarbene is generated from 1,1-dichloroethane and n-BuLi and immediately reacted with an olefin such as methylenecyclopentane. The resultant chlorocyclopropylcyclopentane is dehydrohalogenated to "5-3-ene". This product is being tested as a HEDM additive to RP1. The calculated $\Delta Hf = 31.4$kcal/mol and indicates that 5-3-ene would boost Isp by 1.7s if used as 20% additive in RP1. 5-3-ene can also serve as

a starting material for further cycles of chlorocyclopropanation or terminated with CH3N2 or similar alkyl carbene equivalents.

Aziridine Cage Hydrocarbons. The addition of a nitrene or diazenium ion to an olefin is used to generate an aziridine ring. Lead tetraacetate oxidation of N-aminophthalimide is used to generate a nitrene which subsequently reacts with either cyclohexa-1,4-diene or norbornadiene to form an aziridine. Treatment with hydrazine generates the N-amino-aziridine which can be further oxidized and closed to bis-aziridine cage compounds.

Alternatively, Br_2 can be used to oxidize UDMH in acidic solution to 1,1-dimethyldiazenium ion. This reacts *endo* with an active olefin such as norbornadiene to form an aziridine. In this case the dimethyl amine cannot be easily deprotected, so the mono-aziridine is the end product.

The nitrogen containing additives give a larger Isp boost (2.0 - 2.6 s) than the pure hydrocarbon additives. This is a consequence of the fact that most RP1/LOX systems are currently run fuel rich. The inclusion of non-combusting nitrogen in the fuel produces essentially the same amount of gas (N_2 vs. CO), but does not consume as much LOX, resulting in a more nearly optimized combustion.

Future Work. The molecules currently under study will provide us with information on the synthesis and utility of strained ring molecules in conventional combustion propulsion. Ideally we can discover or develop an additive which would boost the RP1/LOX system by at least 2% (6s) Isp and increase the fuel density by 5%. Ultimately, some of our results or observations may help lead to the synthesis of truly exotic strained ring propellants such as N_8.
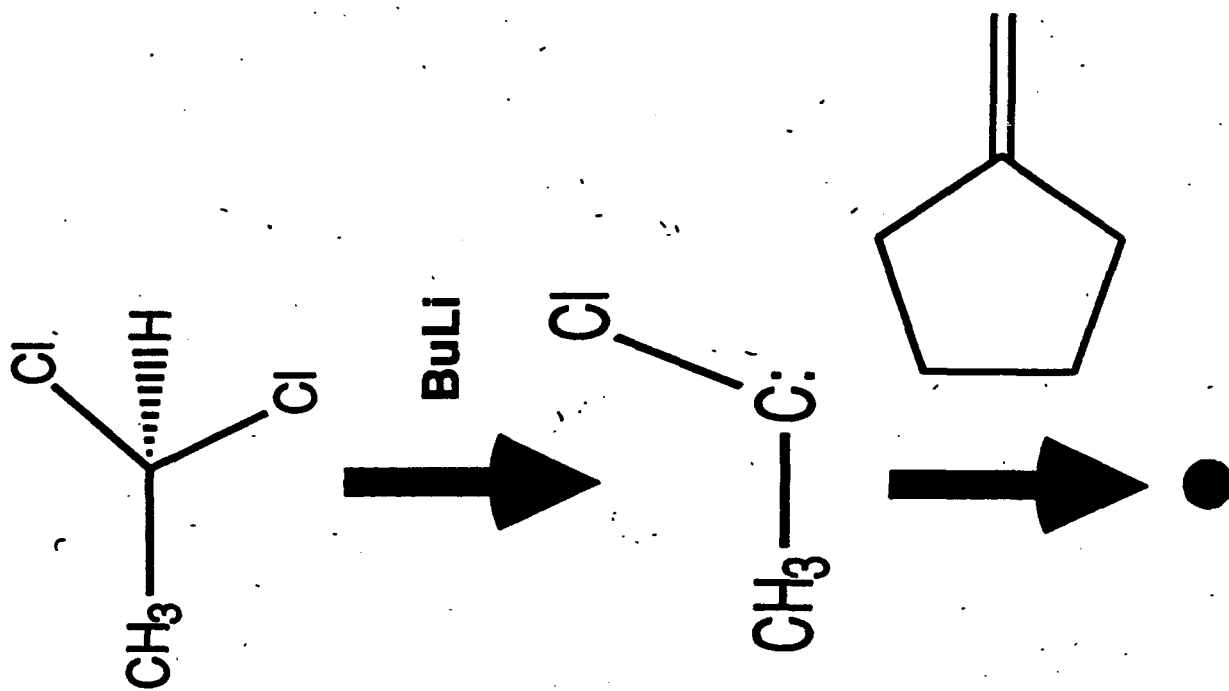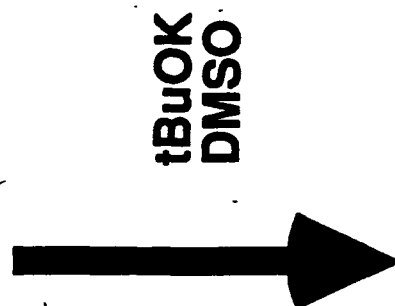
Objective

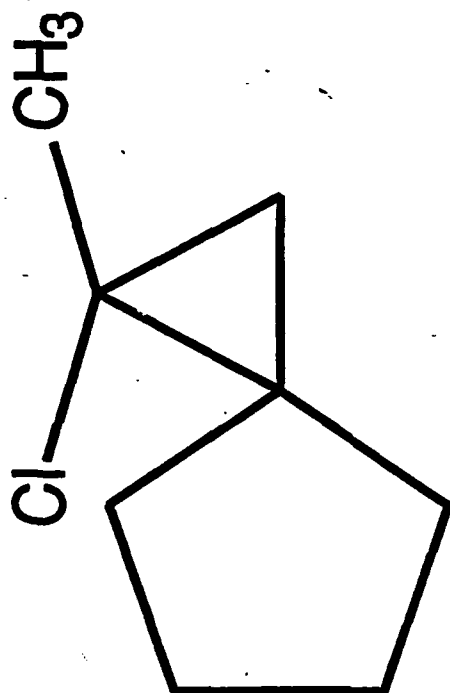**Near Term:**

Synthesize energetic strained-ring compounds for use as additives in RP1/LOX systems.

Long Term:

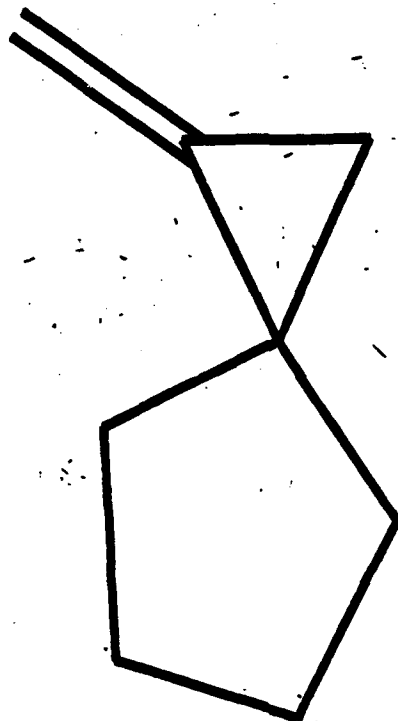**Develop synthetic pathways and methodology for synthesis of polymeric energetic molecules and hetero-atom cage structures.**

Spiro-cyclopropanes

$$\underset{\underset{CH_3}{\overset{Cl}{\mid}}}{\overset{Cl}{\overset{\mid}{C}}} H \quad \xrightarrow{\text{BuLi}} \quad \underset{\underset{CH_3}{\mid}}{\overset{Cl}{\overset{\mid}{C:}}} \quad \longrightarrow$$

$$\xrightarrow[\text{DMSO}]{\text{tBuOK}}$$

5-3-Ene
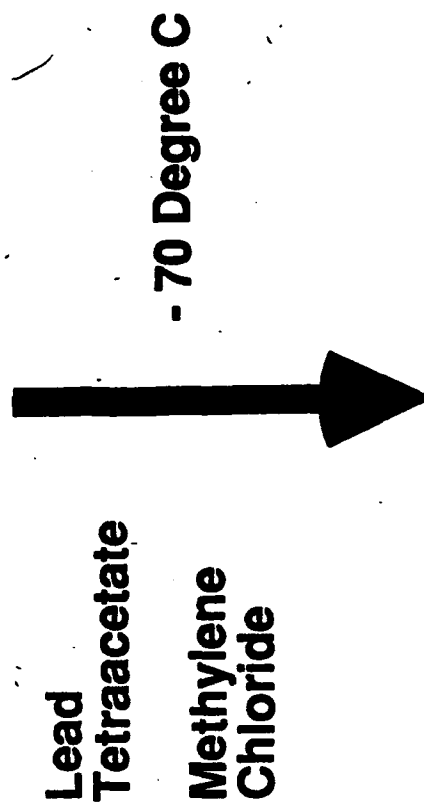
$\Delta Hf = +31.4$ kcal/mol (AM1)

Isp = 299.7s , 20% additive in RP1 w\ LOX

a 1.7s gain over RP1/LOX

Synthesis of Bis-Aziridines
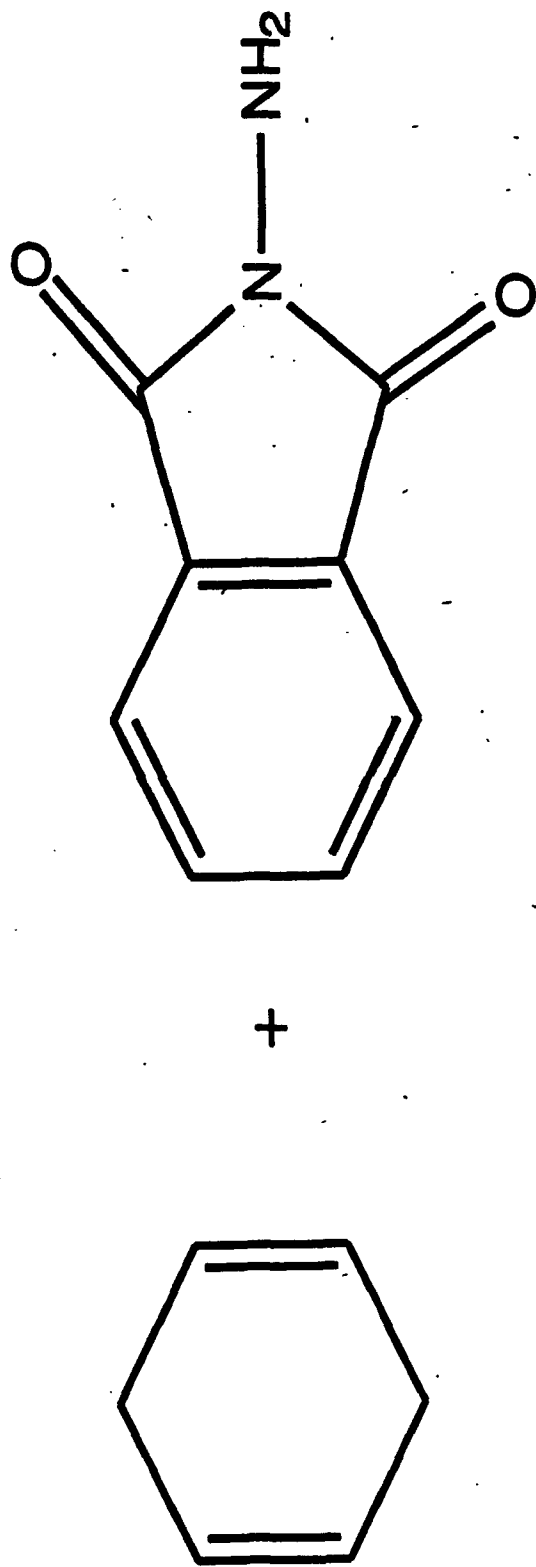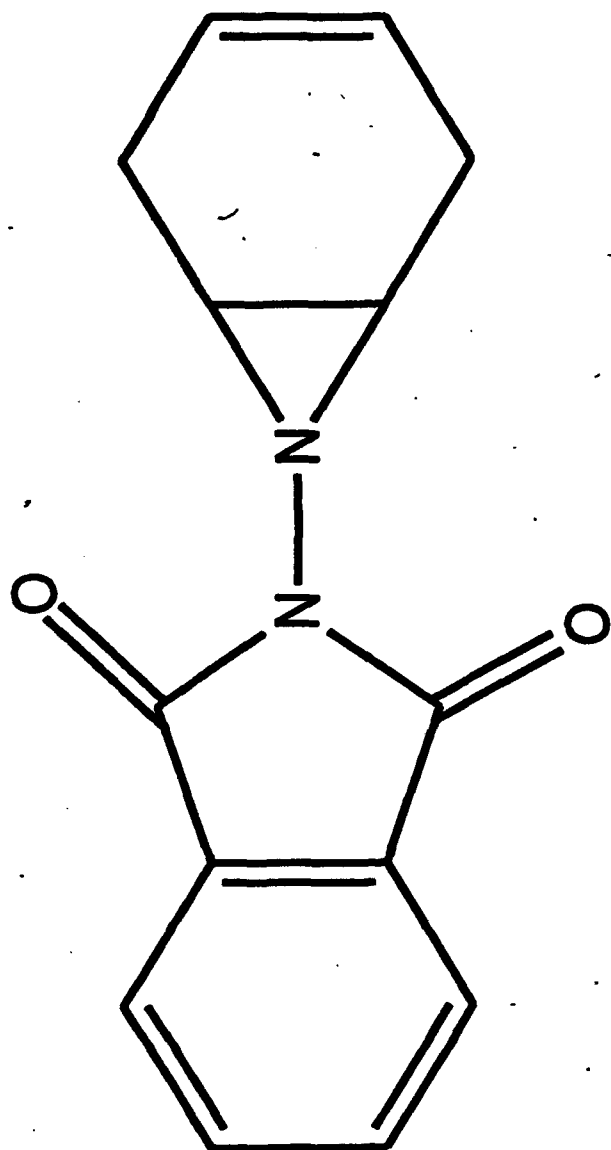
N-Phthalimido Aziridine $\xrightarrow{\text{Hydrazine}}$
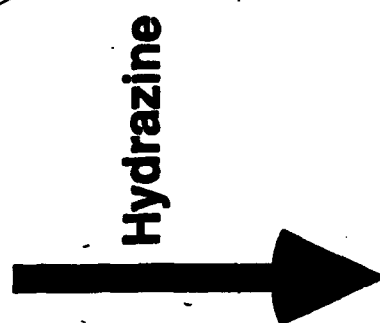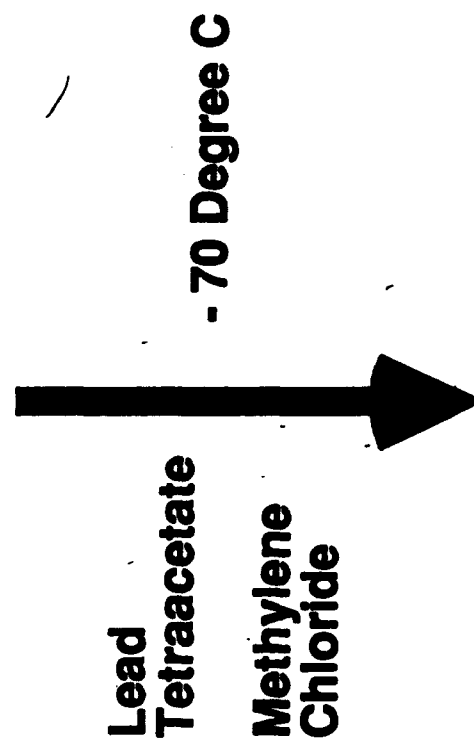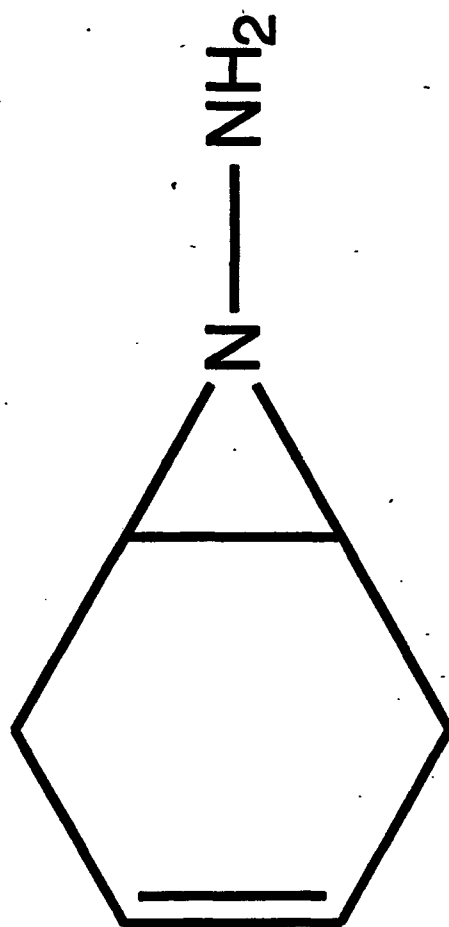
Bis-Aziridine C6
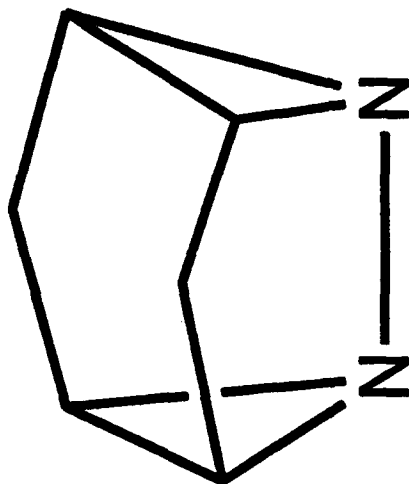
Hoesch et al. Helv. Chim. Acta 61, 1978, p. 795

$\Delta Hf = +72.9$ kcal/mol (MNDO)

Isp = 300s , 20% additive in RP1 w\ LOX

a 2s gain over RP1/LOX

Bis-Aziridine C7
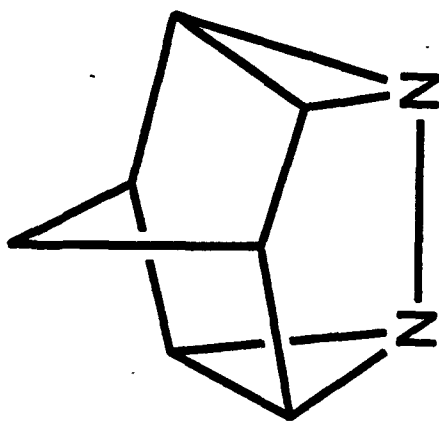
Hoesch et al. Helv. Chim. Acta 61, 1978, p. 795

Synthesis with Diazenium

$$H_3C - N(- NH_2) - CH_3 \xrightarrow{\text{Br2/HBr}}$$

Dimethyldiazenium
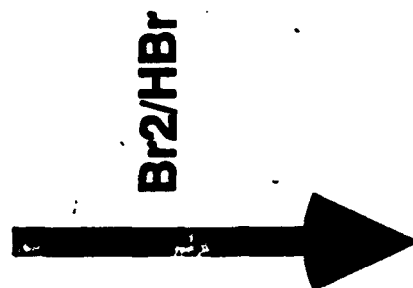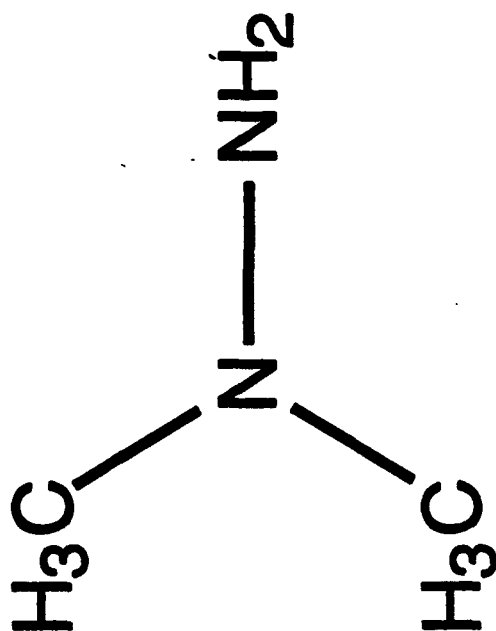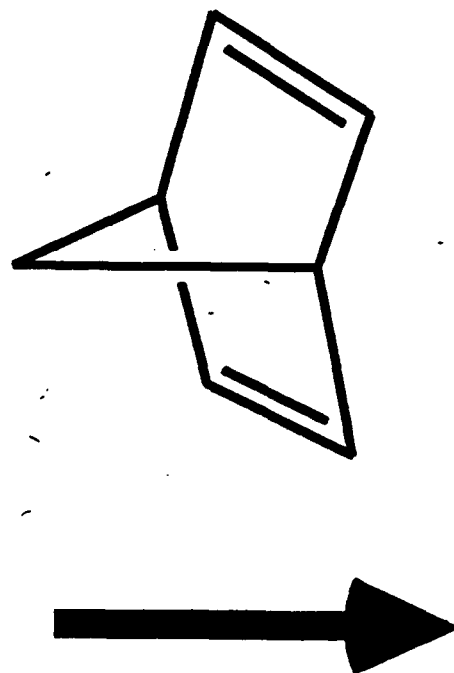
N-Dimethylamino Aziridine
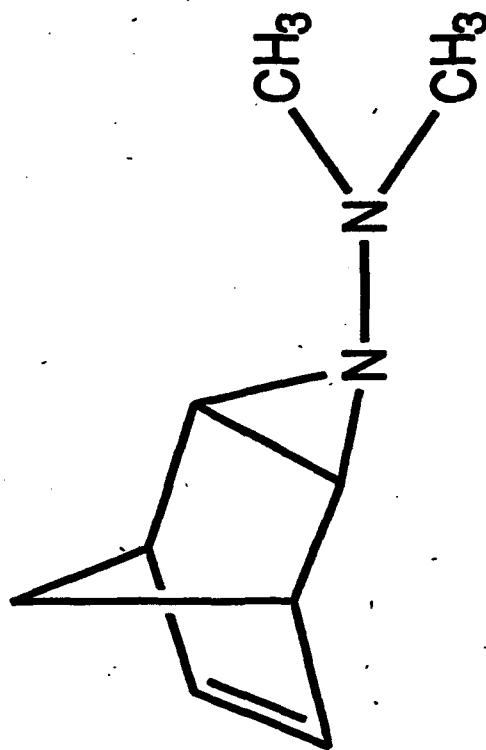
Urry *et al* JACS 13, 1973, p. 4338

ΔHf = +94.2 kcal/mol (PM3)

Isp = 300.6s , 20% additive in RP1 w\ LOX

a 2.6s gain over RP1/LOX

Pyrolysis of HEDM Materials

Angelo J. Alfano
The University of Dayton Research Institute
Air Force Phillips Laboratory
Edwards Air Force Base, CA

HEDM (high energy density) fuel molecules encompass a wide range of varieties. This includes the potential use of strained ring hydrocarbons as additives to conventional fuels (RP1). The specific impulse increases expected from these additives would result in larger deliverable payloads with significant economic benefits. Small scale testing of quadricyclane (C_7H_8) is already in progress and initial results are favorable.

To successfully recover the stored energy from a thermodynamically attractive HEDM system, an understanding of the available decomposition pathways is needed. This necessitates instrumentation with small sample size requirements and "universal" detection strategies. A well-stirred reactor (Figure 1) in conjunction with gas chromatography and mass spectrometric detection is being used to study pyrolysis/combustion mechanisms in the 298-1200 K range. Initially the pyrolysis products from quadricyclane/He in the gas phase from 80 to 600 C at a total pressure of 1 atmosphere were determined with gas chromatography/flame ionization detection. The results are detailed in Figures 2-4 and are interpreted with the mechanism outlined in Figure 5. The energies in Figure 5 are based upon the standard heats of formation and are referenced to a value of 80 Kcal/mole for gas phase quadricyclane. An unexpectedly low value for the energy of activation (10 kcal/mole) for the conversion of quadricyclane to norbornadiene between 150 and 250 C was obtained. This is in sharp contrast to the 40 kcal /mole activation energies typical of eight carbon strained rings. This is being investigated further along with the branching ratios for norbornadiene decomposition into cycloheptatriene and cyclopentadiene + acetylene. To clarify the role of surface effects on the mechanism in Figure 5, an infrared laser sensitized pyrolysis apparatus has also been constructed.

WELL-STIRRED REACTOR AND ANALYTICAL
INSTRUMENTATION FOR PYROLYSIS STUDIES

FIGURE 1

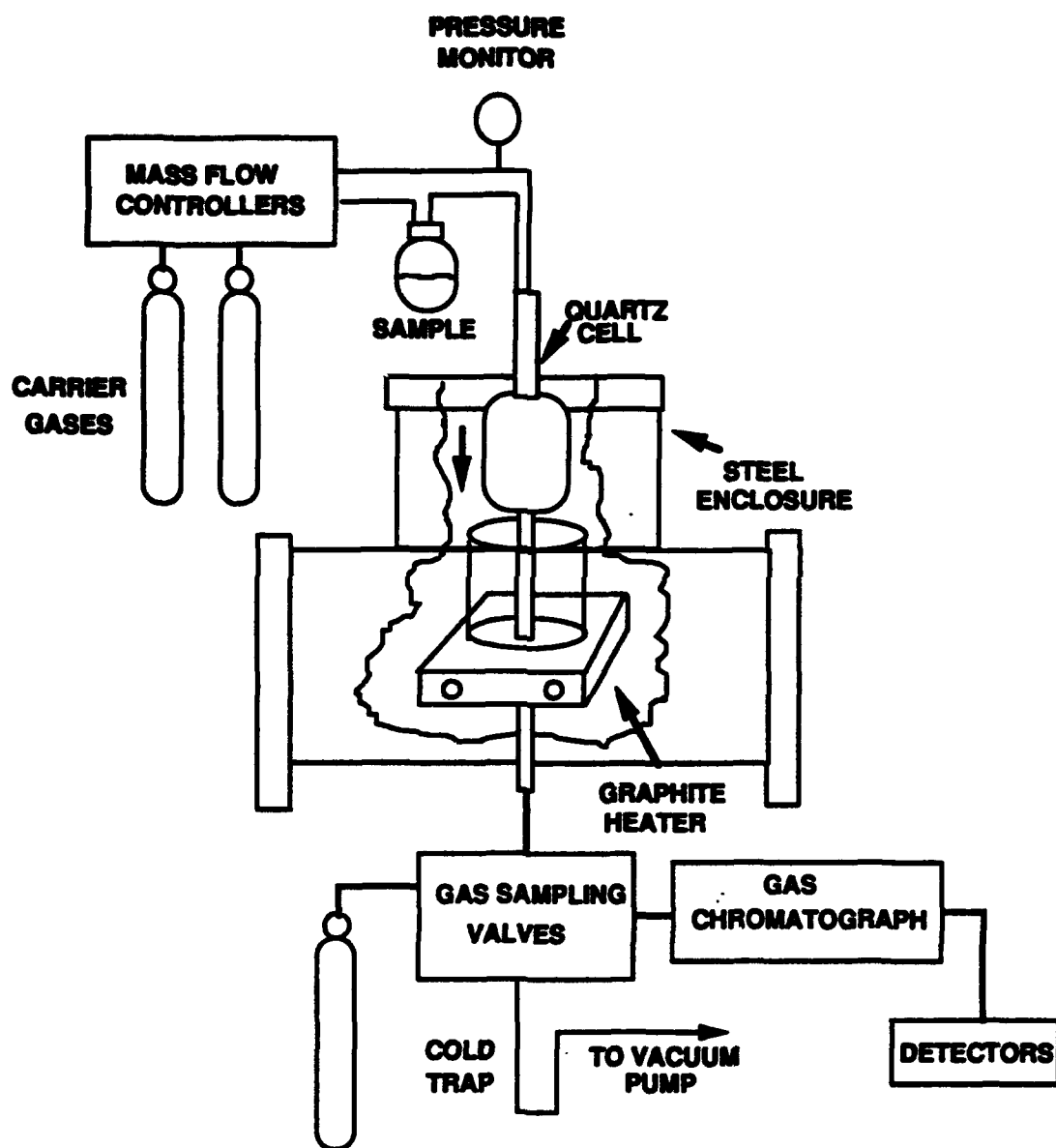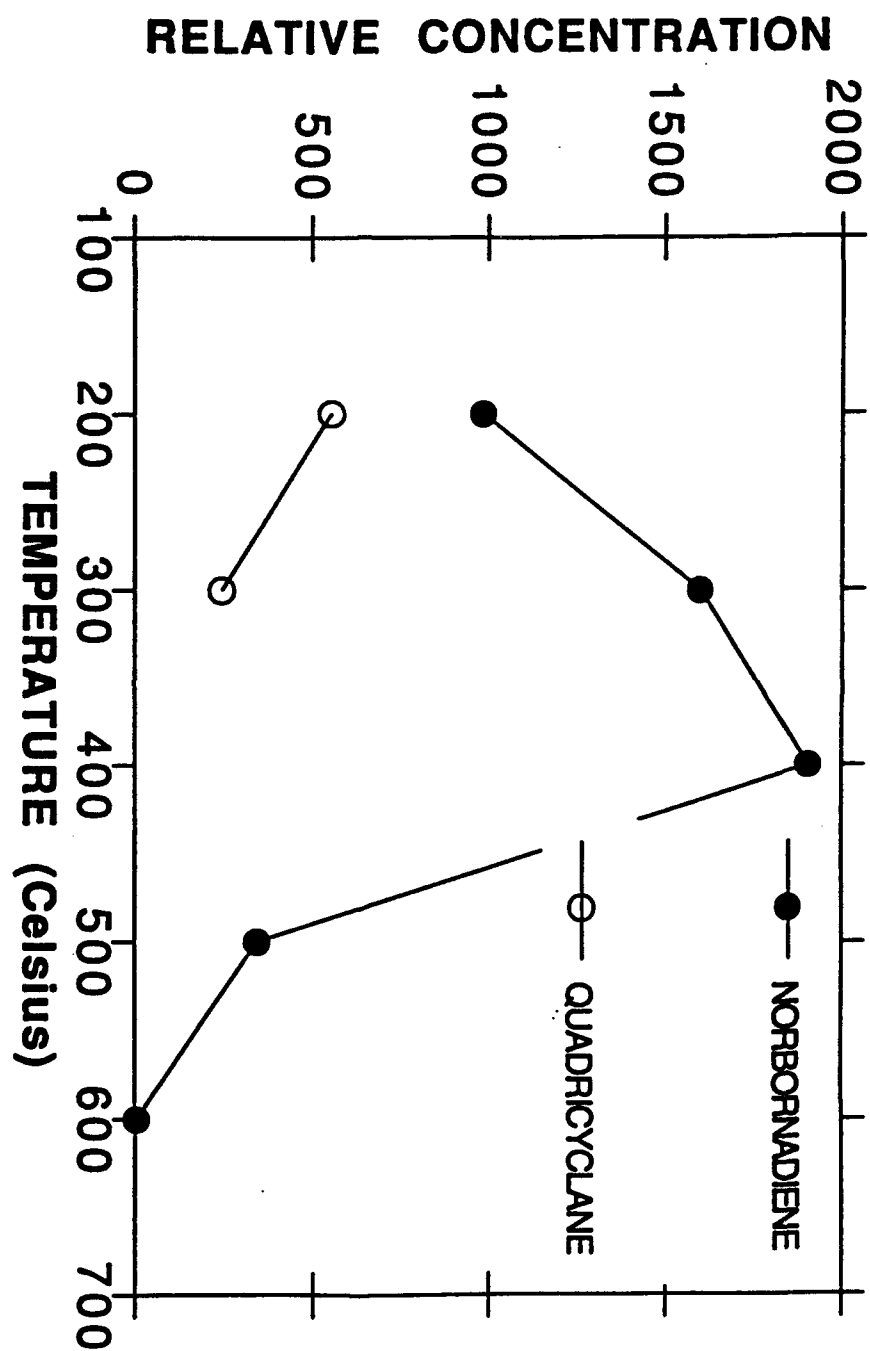QUADRICYCLANE THERMAL DECOMPOSITION

RELATIVE CONCENTRATION

TEMPERATURE (Celsius)

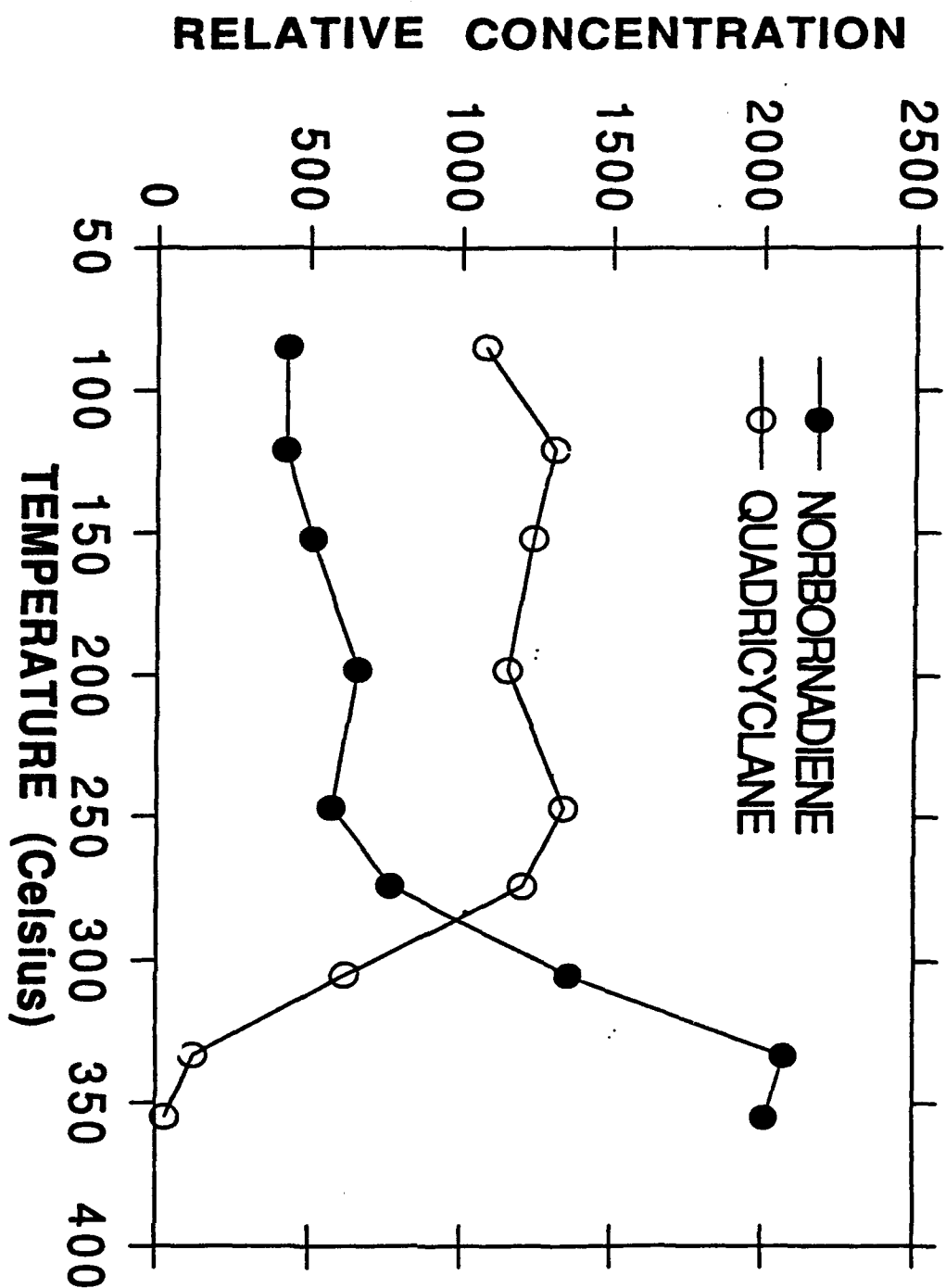○ — QUADRICYCLANE
● — NORBORNADIENE

FIGURE 2

387

QUADRICYCLANE THERMAL DECOMPOSITION

FIGURE 3
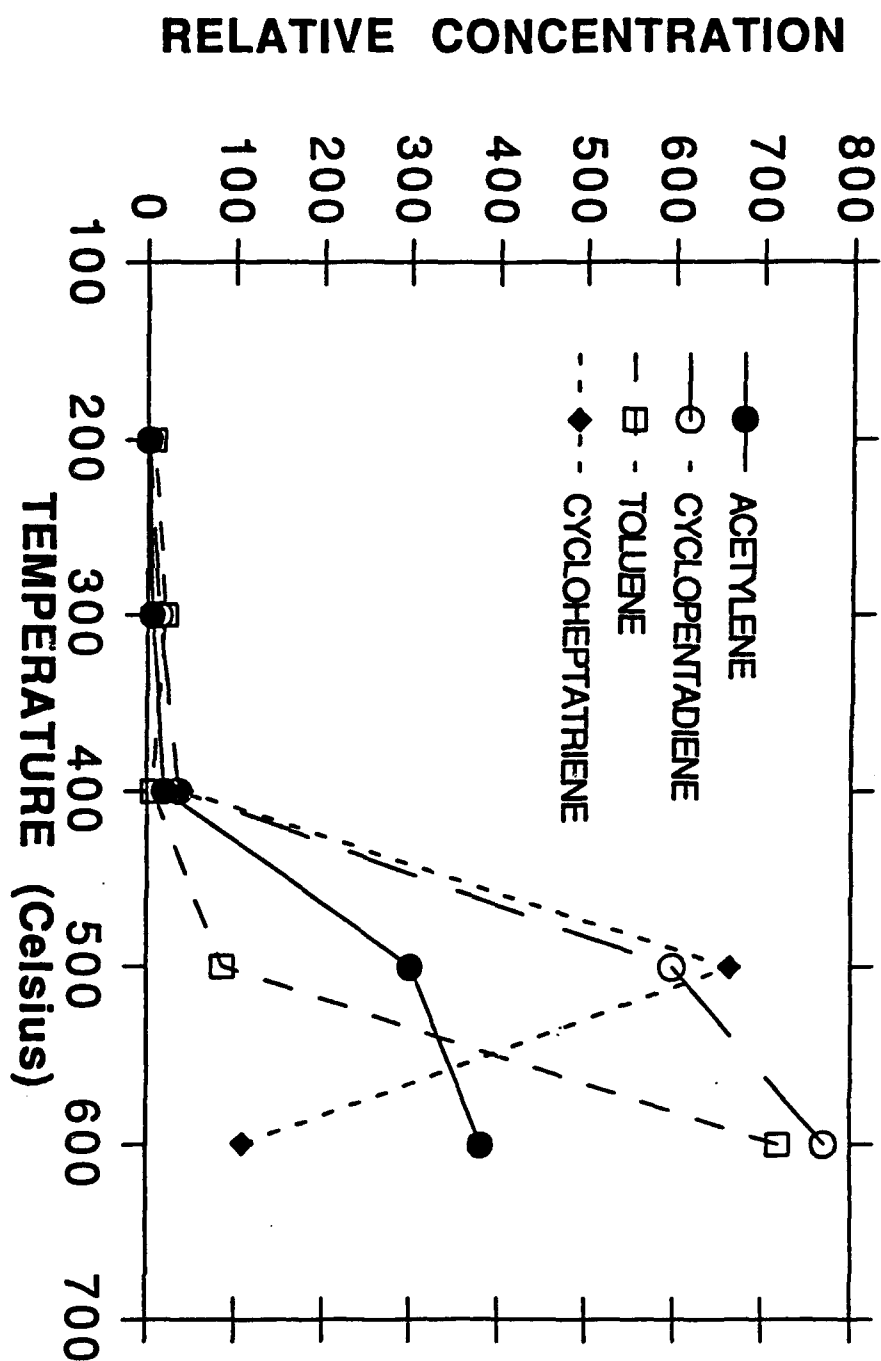
FIGURE 4

QUADRICYCLANE DECOMPOSITION MECHANISM
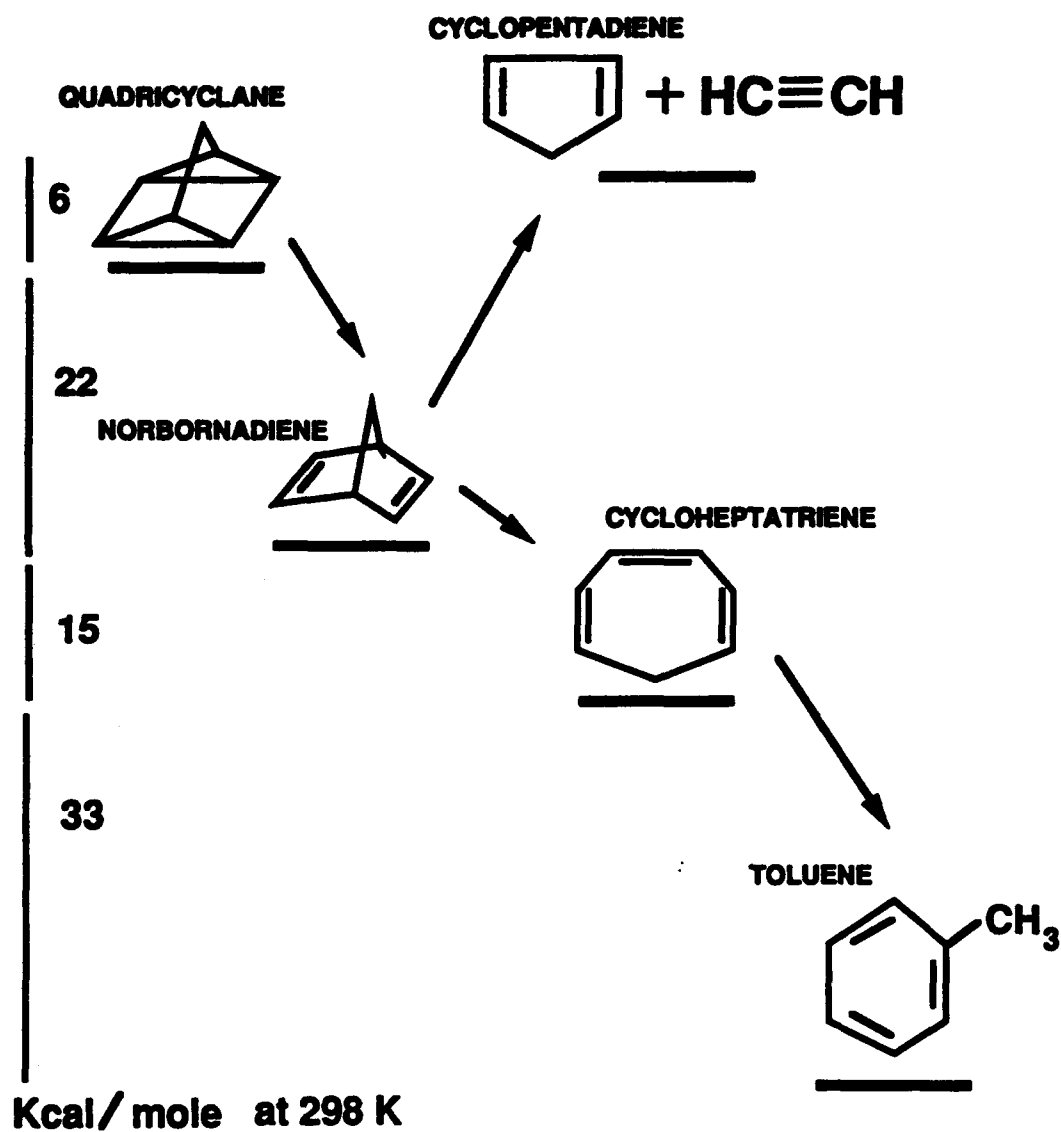
FIGURE 5

Trapped Electrons in Solid Hydrogen

G. W. Collins, F. Magnotta, E. R. Mapoles, H. E. Lorenzana

Lawrence Livermore National Laboratory

Livermore, Ca 94550

The discovery of trapped ions in tritiated solid hydrogen was made by P. C. Souers et. al. through the observation of stark shifted lines in the collision induced infrared absorption spectra of solid hydrogen[1]. One line was found 100 cm^{-1} below the $Q_1(1,0)$ line, and was assigned to a Stark shifted $Q_1(1,0)$ transition for molecules near a positive ion. Another line was found ~25 cm^{-1} below $Q_1(1,0)$ and was assigned to a Stark shifted $Q_1(1,0)$ transition for molecules near a negative ion. Thus the positive ion which tends to contract the neighboring molecules gives rise to a larger stark shift than negative ions which push away neighboring molecules due to the fermi interaction. There have also been weak absorptions found between these two stark shifted transitions that have been assigned to next nearest neighbors of the positive ion[2]. From timing experiments Brooks et. al. determined that there were two types of positive charges and negative charges. The most mobile was the negatively charged polaron, then a D_3^+ "small polaron hole", while a D_9^+ and an electron bubble were determined to be immobile over the period of hours[3]. After the discovery of these stark shifted lines, two broad absorptions, not related to the collision induced hydrogen spectra, were observed in tritiated solid hydrogen and in proton irradiated solid hydrogen[4,5,6,7]. In analogy with F-centers in Alkali Halides and from the time resolved data, it was postulated that these two absorptions were due to transitions of an electron bubble. From a simple spherical square well model, the electron bubble radius was determined to be 5.38 A, with a well depth of 3.81 eV, and it was estimated by Poll et. al. that an electron in the first excited state would dilate the lattice an additional 15%. The IR absorption band was assigned to the 1S to 1P transition and the UV absorption was assigned to the 1S to continuum

transition. There appeared to be an isotope shift in both the IR and UV transitions, and the UV band was broader in H_2 than in D_2 both doped with tritium, implying a broader conduction band in irradiated H_2. This result is similar to the work of Gedanken et al.[8] who studied trapped excitations in solid H_2 and D_2.

We then discovered an emission at 800 nm[9] in solid D-T that appeared to have the same temperature dependence as the hydrogen atoms in D-T as measured by electron spin resonance (ESR). This emission was confirmed by a group at the University of Guelph and the Riso Laboratory[10]. No assignment has been given to this emission, and correlation with previous absorption features seemed dubious since the timing data for this emission was very different than the timing data for the stark shifted collision induced lines and the UV line. Finally, unlike the UV and IR "bubble" absorptions, there appears to be no isotope shift in the 800 nm emission.

We report here a relatively large increase in emission of the integrated 800 nm line when pumping the UV absorption and a much smaller increase (by a factor of ~15) upon pumping the IR absorption band in solid D-T at 4.6 K. These data show the 800 nm emission is most likely the result of an electron bubble transition. We also present ESR data for electrons in D_2 and H_2 doped with 2% T_2 and pure T_2. We find there are two components to this absorption, a narrow line component which we attribute to trapped electrons and a broad line component which we attribute to delocalized electrons. The narrow ESR linewidth in the H_2 and D_2 samples are commensurate with the idea of electrons localized in vacancy seeded traps. In solid T_2 the broad line dominates, implying that most electrons are delocalized due to the large concentration of electrons and other impurities. We find that the temperature and time dependence of the electron concentration from the 800 nm line is similar to the unpaired atoms as measured previously with ESR[11].

Figure 1 shows the integrated emission intensity from 740 to 860 nm as a function of the wavelength of light incident onto solid D-T at 6K. Also plotted in Fig. 1a is the UV absorption data of solid D-T at 5 K of Fearon et. al.[6] and in Fig. 1b is

the 8 K T_2 IR absorption data of Richardson et. al.[4] The relative absorbance strength of the UV line to the IR line in solid DT is not known and the absolute frequency and shape of the IR line is also unknown. The shape of the UV enhancement follows closely the published UV absorption spectrum for solid D-T presumed to be due to the 1S to continuum transition of the electron bubble. The enhancement with IR pumping suggests that the response is related to the IR absorption band, presumed to be due to the 1S to 1P transition of the electron bubble, but due to the lack of data in the region around the emission itself (i.e. from 0.8 μm to 1.2 μm), the case is not as convincing as that for the UV response. Fig. 1a and 1b show that the 800 nm emission, the UV absorption and the IR absorption are related. Using a simple square well model with the previously published parameters (radius = 5.38A, depth = 3.81eV) it can be shown that there are 4 bound states, the 1S, 1P, 1D, and 2S states 3.0 eV, 2.2 eV, 1.2 eV, and .8 eV below the conduction band edge respectively. Obviously any excited state will severely increase the size of the well, but this simple example shows there are other bound states to the proposed bubble and one candidate for the emission is due to the 2S to 1P decay during bubble formation. Fig. 1a also shows an additional feature at about 425 nm not observed in the UV absorption spectra. This is close to the 1p->cont transition. Finally, we note that between 440 nm and the onset of the 800 nm emission there are no additional features.

The absorption shown in Fig 1b is that for solid T_2.[4] Based on the line shifts for H_2 and D_2 doped with small amounts of T_2, it is estimated that the IR absorption of DT should be close to that of T_2. It should be noted that the "steady state" time response of the enhancement is also somewhat different for UV vs IR enhanced emission. For both UV and IR pumping, the emission increases rapidly on a time scale of ~ 20 μs, however, the UV enhanced signal overshoots a steady state value by perhaps 5-10% whereas the IR enhanced signal overshoots by 50 to 75 % both having a settling time of ~25 seconds. We currently do not understand the nature of the overshoot but it is probably related to secondary heating of the sample. In figure 1b,

we plot both the instantaneous and steady state enhanced signal for IR pumping while in figure 1a, we only plot the final steady state enhanced signal for UV pumping.

Figure 2 shows that the temperature dependence of the 800 nm emission in solid D-T is very similar to the atom density in solid D-T and T_2. This implies that whatever process limits the recombination of atoms, also limits the recombination of centers responsible for the 800 nm line; possibly electron bubbles. It has been shown that at temperatures above half the triple point, the activation energy calculated from the hydrogen atom recombination data in solid H_2[12] and D_2[13], follows the vacancy diffusion model of Ebner and Sung[14] developed to describe the diffusion of molecules[15]. Recently in solid para H_2, the diffusion coefficient of electrons in solid parahydrogen has been measured and appears to follow the same temperature dependence as the atoms and molecules[16]. Moreover, the diffusion of the electrons appears to follow the temperature dependence of Ebner and Sung's model to temperatures well below half of the triple point, where NMR measurements of molecular motion are difficult. Therefore, the agreement for the temperature dependence of the atoms and the 800 nm emission agrees with the inference that the 800 nm line is due to trapped electrons and the speculation that atoms and electrons have the same vacancy diffusion mechanism.

The ESR spectrum of the middle line of the D atom hyperfine triplet in solid $D_2+2\%T_2$ at 1.4 K is shown in Fig. 3 at several different times during the experiment. This lineshape is near g=2 and shows a doublet structure not seen in the other hyperfine lines. The left absorption of this double peak is due to the middle D atom and the right absorption is assigned to trapped electrons. From top to bottom, Fig. 3a shows the electron and middle D atom lineshape after 4 min, 30 min, 54min, and a few minutes after a heat spike. The lineshape in Fig. 3b shows the same spectrum after 500 minutes at 1.4 K when no heat spikes are observed. During a "heat spike" when the atoms recombine en masse as described previously[17], the electon concentration also decreases. Moreover, when the sample is sitting in liquid

helium, the effective heat capacity and thermal conductivity of the sample is increased and the time between heat spikes is increased. When no heat spikes occure during the timescale of hours the narrow electron line is completely lost under the middle D atom line. We find that the electron linewidth in H_2 or D_2 is roughly 30% smaller than the linewidth of hydrogen atoms in the same matrix. That is for $D_2+2\%T_2$ sitting at 1.4K for 1 hour there are about 110 ppm of D atoms, 32% J=1 concentration, and 25 ppm electrons, the linewidth for atoms is about 2.2 ± .2 Gauss and the linewidth of the electron is about 1.7± .3 Gauss. $H_2+2\%T_2$ sitting at 1.7 K for 32 hours has about 15 % J=1 concentration, and 135 ppm atom concentration the linewidth for the H atom is 0.9+.2 Gauss and the linewidth of the electron is slightly less, but our signals were too noisy to make an accurate measurement. The J=1 concentration was calculated from the J=1 to J=0 conversion time constants reported previously of 30 hours in $D_2 +2\%T_2$ and 22 hours for $H_2+2\%T_2$ both at about 1.4 K. From these linewidths and a theoretical model for the linewidth we can estimate a nearest neighbor distance. Two models are typically used for analyzing the linewidth. For interacting dipoles with no wave function overlap we use the formalism described by Kittel and Abrahms[18], while when there is significant overlap of the electron wave function with neighboring molecules we use the formalism developed by Kip, Kittel, Levy and Portis[19] for analyzing F-centers. Hydrogen atoms are presumed to sit at vacancy like sites, producing a lattice dilation for the first shell of neighbors of about 6% in H_2 as calculated by Danilowitz and Etters. For D atoms in D_2 the lattice expansion will be reduced to roughly 4% due to the smaller zero point motion. From the ESR linewidths we can estimate the electron in D_2, located at a vacancy seeded site, has a lattice dilation of 8% larger than the atom, or about 12 %. This would give a bubble radius of about 0.4 nm.

Figures 4a and 4b show the ESR absorption's corresponding to electrons and the high field line of the T atoms in solid T_2 sitting at 6.3 K for 4 hours. The concentration of electrons here is roughly 50 ppm while the concentration of atoms is about 120 ppm. There is only a small signature of the narrow ESR "electron" line

seen in H_2 and D_2, because of the large, broad absorption feature. This broad feature at g~2 is much broader than the corresponding T atom lineshape. One possible explanation (mentioned above) for this broad line is that most of the electrons in solid T_2 are delocalized as compared to the localized electrons seen in H_2 and D_2 samples doped with only 2% T_2. There was also a broad underlying absorption component in the $H_2+2\%T_2$ and $D_2+2\%T_2$ samples but the signal to noise for this feature was very low. These data show that there are at least two different types of electrons in solid tritiated hydrogen, those localized in "bubbles" and those that are possibly delocalized.

We conclude with the following somewhat speculative picture. Solid Hydrogen containing tritium contains many neutral atoms, positive ions, and electrons. The concentration of electrons is typically about an order of magnitude lower than the concentration of atoms. The electrons, after being slowed well below the ionization threshold, form electron bubbles until the concentration of trapped electrons gets to several parts per million molecules. Afterwards, many of the electrons cannot form a bubble defect due to the large degree of radiation damage, and these electrons remain in the conduction band of the solid until inialation with a positively charged impurity. The electron bubbles have many bound states for the electrons which give rise to an IR absorption, a UV absorption, and an emission at 800 nm. Finally, these electron bubbles move through the lattice with the same vacancy diffusion mechanism as the atoms and molecules.
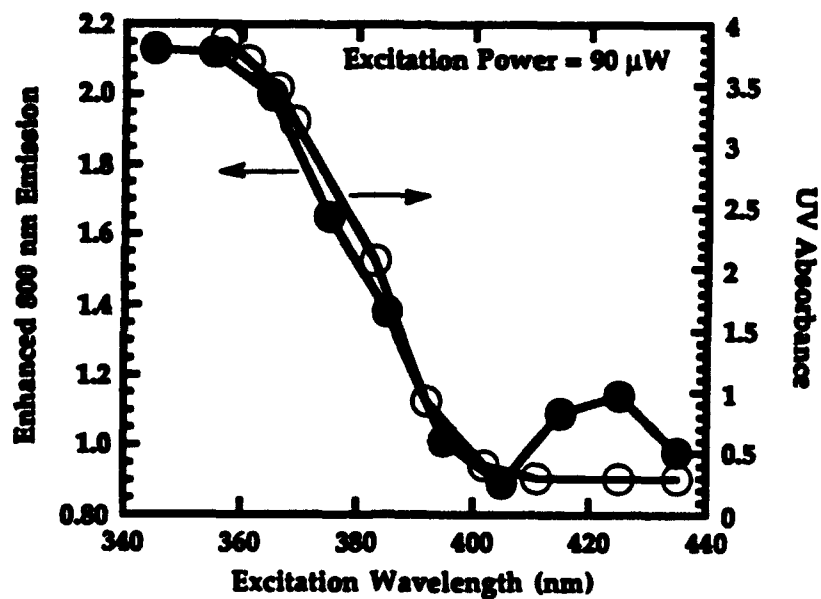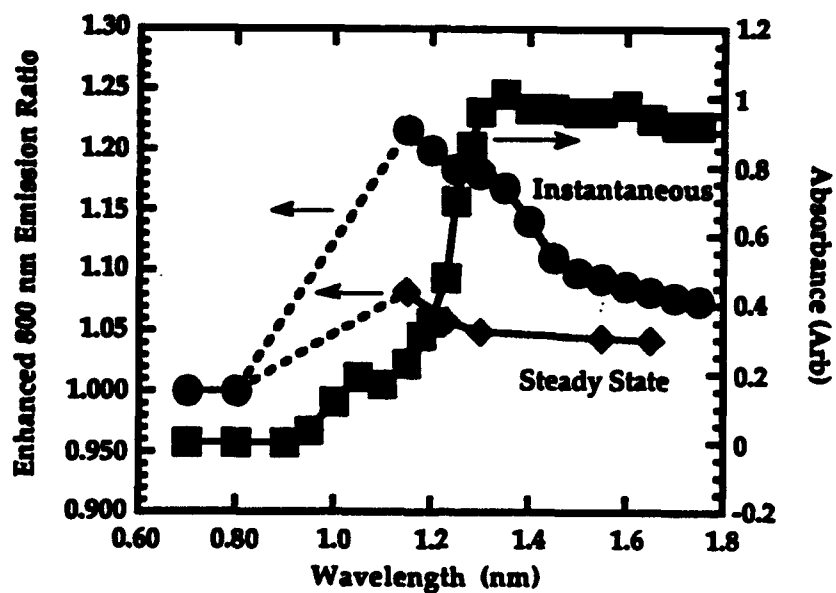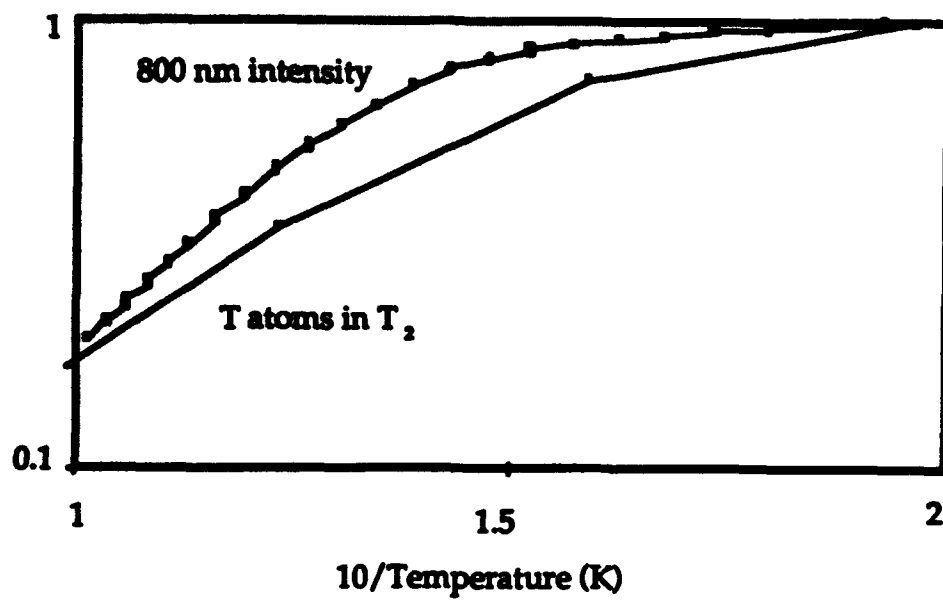
Fig. 1a

Fig 1b

Fig. 2
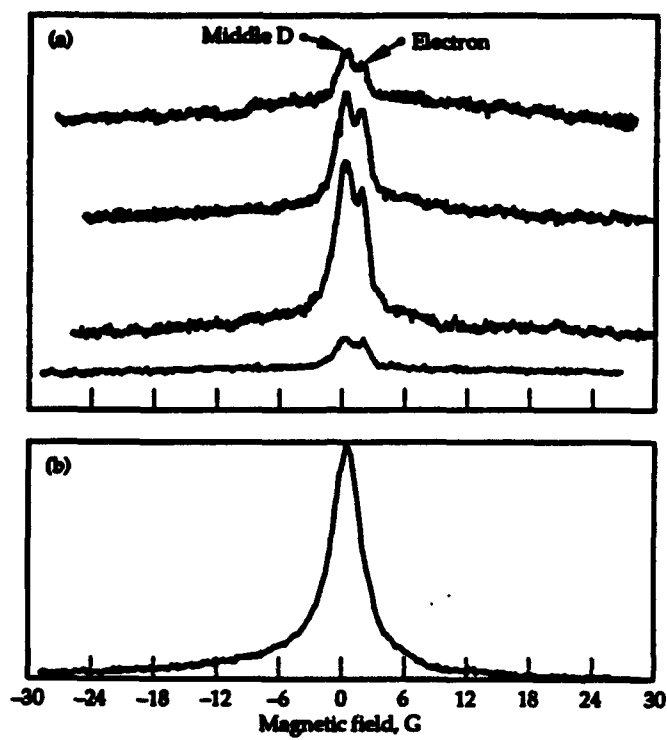
Fig. 3
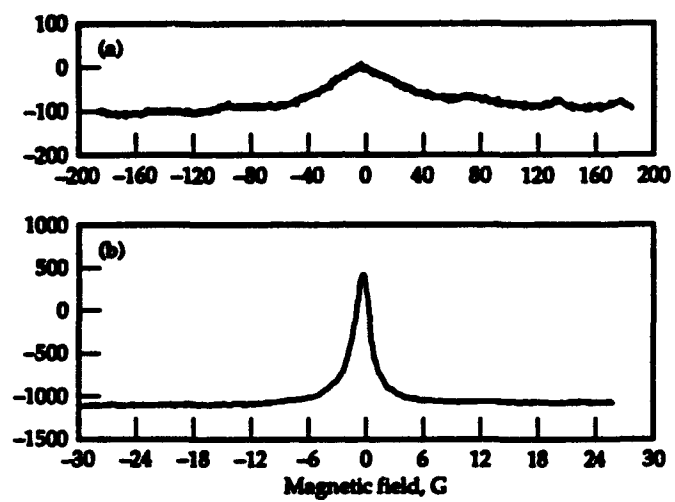
Fig. 4

[1]P. C. Souers, E. M. Fearon, R. L. Stark, R. T. Tsugawa, J. D. Poll, and J. L. Hunt, Can. J. Phys., **59**, 1408 (1981).

[2]S. K. Bose and J. D. Poll, Can. J. Phys. **63**, 67(1987).

[3]R. L. Brooks, S. K. Bose, J. L. Hunt, Jack R. MacDonald, J. D. Poll, and J. C. Waddington, Phys. Rev. B, **32**, 2478(1985)

[4]J. H. Richardson, S. B. Deutscher, P. C. Souers, R. T. Tsugawa, and E. M. Fearon, Chem. Phys. Lett., **81**, 26(1981).

[5]J. D. Poll, J. L. Hunt, P. C. Souers, E. M. Fearon, R. T. Tsugawa, J. H. Richardson, and G. H. Smith, Phys.Rev. A, **28**, 3147(1983).

[6]E. M. Fearon, R. T. Tsugawa, P. C. Souers, J. D. Poll, and J. L. Hunt, Fussin Tech. **8**, 2239(1985).

[7]J. A. Forrest, J. L. Hunt, and R. L. Brooks, Can. J. Phys., **68**, 1247(1990).

[8]A. Gedanken, B. Raz, and J. Jortner, Chem. Phys. Lett., **14**, 326(1972).

[9]E. R. Mapoles, F. Magnotta, G. W. Collins, and P. C. Souers, Phys. Rev. B. **41**, 11653, (1991).

[10]J. A. Forrest, R. L. Brooks J. L. Hunt, B. Stenum, J. Schou, H. Sorensen P. Gurtler, F. Magnotta, E. R. Mapoles, P. C. Souers, and G. W. Collins, Phys. Rev. B, **46**, 13820(1992).

[11]G. W. Collins, P. Cl Soers, J. L. Maienschein, E. R. Mapols, and J. R. Gaines, Phys. Rev. B, **45**, 549,(1992).

[12] R. Leach, _A Paramagnetic Resonance Study of Hydrogen Atom Production and Recombination in Solid Hydrogen From 1.4 to 8 Degrees K.,_ PhD thesis, University of Wisconsin (University Microfilms, Ann Arbor, MI., 1972). W. A. Fitzsimmons was the thesis advisor.

[13] A. S. Iskovskikh, A. Ya. Katunin, I. I. Lukashevich, V. V. Sklyarevskii, V. V. Suraev, V. V. Filippov, M. I. Filippov, V. A. Shevtsov, Soviet Phys JETP **64**, 1085 (1985).

[14]C. Ebner and C. C. Sung, Phys. Rev. A **5**, 2625 (1971).

[15] F. Weinhaus, H. ,Meyer, S. M. Myers, and A. B. Harris, Phys. Rev. B **7**, 2960, 1973: M. Bloom, Physica **23**, 767 (1957).

[16]A. A. Levchenko, L. P. Mezhov-Deglin, and I. E. Shtinov, JETP Lett., **54**, 234(1991).

[17]G. W. Collins, E. M. Fearon, J. L. Maienschein, E. R. Mapoles, R. T. Tsugawa, P. C. Souers, and J. R. Gaines, Phys. Rev. Lett., 65, 444(1990).

[18]C. Kittel and E. Abrahams, Phys. Rev. 90, 238 (1953).

[19]A. F. Kip, C. Kittel, R. A. Levy, and A. M. Portis, Phys. Rev. 91, 1066 (1953).

:

.·

RADIATIONLESS DECAY OF ENERGETIC MATERIALS

David R. Yarkony
Department of Chemistry
Johns Hopkins University
Baltimore, MD 21218

I. Radiationless decay: Relevance

The following figure illustrates a situation in which a potential HEDM can decay radiationlessly in an electronically nonadiabatic manner.
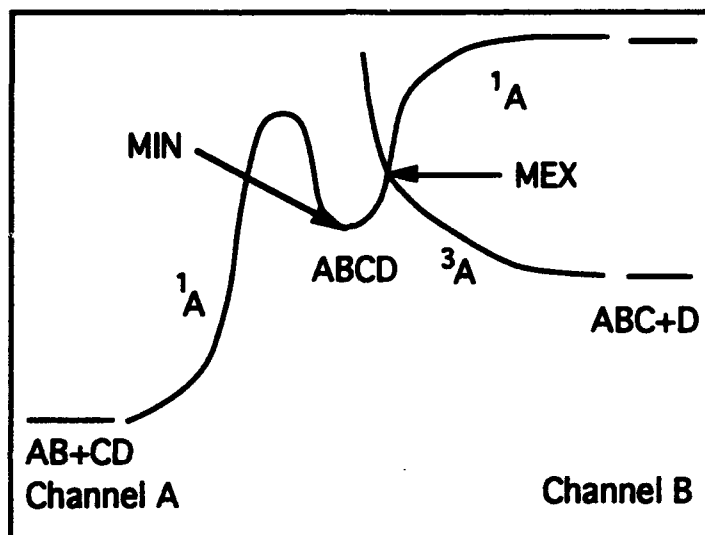
In the figure (i) adiabatic decay to channel A is improbable due to the high barrier, and (ii) adiabatic decay to channel B (an excited state of the ABC + D system) is energetically precluded. However nonadiabatic decay is energetically feasible to the ground state of channel B. The decay pictured above is a spin-forbidden however the capability to treat spin-allowed processes is also required.

II. Spin-forbidden Radiationless Decay of a-N_2O_2[1]

The system pictured below, denoted a-N_2O_2 has been suggested as a HEDM.[2]
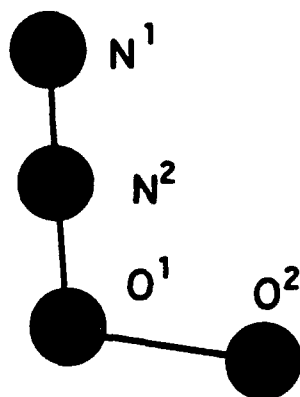
Theoretical calculations predicted this structure – a local minimum on the ground state potential energy surface– to be unstable by 102(62) kcal/mol relative to N_2+O_2 (NO+NO). Decay to the channel $N_2O + O(^1D)$ is energetically precluded whereas a decay to $N_2O + O(^3P)$ is energetically allowed but spin-forbidden. Although at the equilibrium geometry of a-N_2O_2 the lowest excited triplet state is approximately 24kcal/mol above the ground $^1A'$ potential energy surface [2,3] preliminary calculations reported at the 1992 HEDM meeting suggested that decay to $N_2O + O(^3P)$ (see channel B in the figure above) is possible. During the current performance period we extended those calculations and determined the rate of spin-forbidden predissociation.[1] This investigation is summarized below.

• Step 1: Locate minimum energy crossing point of lowest singlet and triplet surfaces in the vicinity of a-N_2O_2

a-N_2O_2: Energies, H^{so} and structures from MR-CISD wavefunctions[a]

Structure	MIN(^{1}A')(DZP)	MIN(^{1}A')(TZP)	MECP(DZP)	MECP(TZP)
R(N^1–N^2)	1.1115	1.0975	1.1143	1.1008
R(N^2–O^1)	1.2415	1.2324	1.2292	1.2190
R(O^1–O^2)	1.5639	1.5582	1.6720	1.6795
∠N^{1}N^{2}O^1	179.26	178.69	180.52	180.63
∠N^{2}O^{1}O^2	102.29	102.03	102.09	101.82
E(^{1}A')	-258.981267	-259.070881	-258.978869	-259.067517
E(^{3}A")	-258.943461	-259.028137	-258.978868	-259.067518
ΔE	23.72	26.82	1.51	2.11
$H_\perp^{so}$	12.4	12.0	11.1	10.9
$H_\parallel^{so}$	71.1	73.3	73.6	76.7

[a]Distances in Å, angles in degrees, total energies in atomic units, $\Delta E \equiv E[^3A"]-E[^1A'MIN(^1A')]$ in kcal/mol and spin-orbit couplings $H_\perp^{so}$ and $H_\parallel^{so}$ in cm^{-1}. For comparison using the QCISD/DZP approach MIN(^{1}A') corresponds to R(N^1–N^2)=1.1331Å, R(N^2–O^1)=1.2617Å, R(O^1–O^2) = 1.5475Å, ∠N^{1}N^{2}O^1=179.40° ∠N^{2}O^{1}O^2=103.31° with E(^{1}A')=-259.0754215, and ΔE= 23.0

kcal/mol. At the equilibrium structure of $N_2O(X^1\Sigma^+)$ R(N–N)=1.128Å and R(N–O)=1.184Å, from Ref. 4 .

From this table it is deduced that the minimum energy crossing point(MECP) is energetically accessible - only 1-2 kcal/mol above, and geometrically similar to, the a-N_2O_2 minimum. In addition an approximate reaction path on triplet surface leads to $N_2O+O(^3P)$. Thus it is concluded that a-N_2O_2 is likely to decay radiationlessly - but how rapidly.

• Step 2: Model for Predissociation

To address this question a simple pseudo diatomic - one dimensional - model was used in which O^2 dissociates from a frozen $N^1N^2O^1$ moiety with $\angle N^2O^1O^2$ fixed. The relevant one parameter potential energy curves obtained using the MR-CISD/DZP wavefunctions are presented in figure below as are the corresponding spin-orbit interactions $H_\perp^{so}$ and $H_\parallel^{so}$.

The spin-orbit interactions are defined as follows.

$$\Psi_{1A'}(^1A') = \Psi[^1A'(0)]$$

$$\Psi_{1A'}(^3A'') = i\,\Psi[^3A''(0)]$$

$$\Psi_{2A'}(^3A'') = i\,\{\Psi[^3A''(1)] - \Psi[^3A''(-1)]\}/\sqrt{2}$$

$$\Psi_{1A''}(^3A'') = i\,\{\Psi[^3A''(1)] + \Psi[^3A''(-1)]\}/\sqrt{2}$$

so that $H_\perp^{so} = \langle \Psi_{2A'}(^3A'') | H^{so} | \Psi_{1A'}(^1A') \rangle$ and $H_\parallel^{so} = \langle \Psi_{1A'}(^3A'') | H^{so} | \Psi_{1A'}(^1A') \rangle$ while $\langle \Psi_{1A''}(^3A'') | H^{so} | \Psi_{1A'}(^1A') \rangle = 0$ by symmetry.
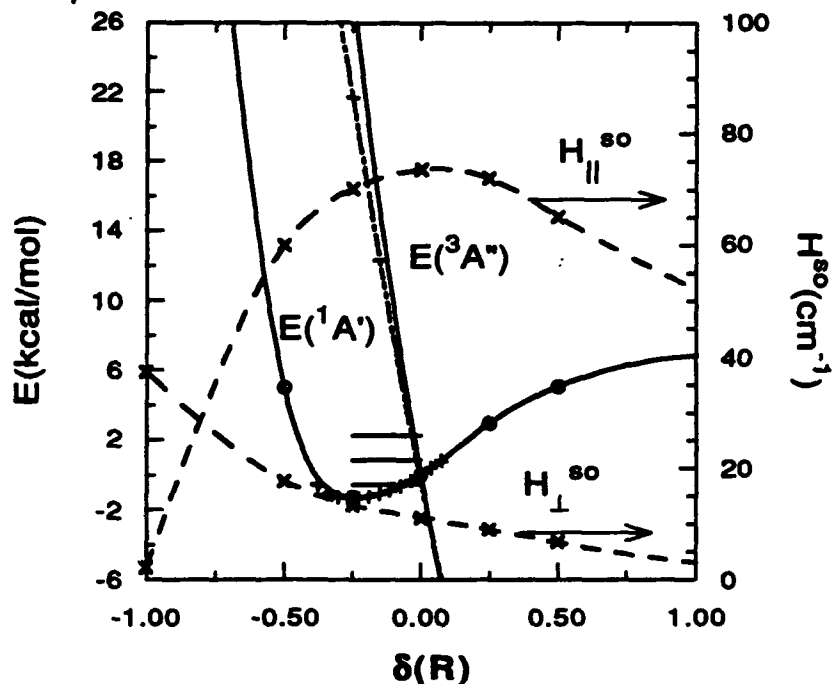
$H_\perp^{so}$ and $H_\parallel^{so}$ are seen to change little between MIN(^{1}A') and MECP with $H_\parallel^{so}$ achieving a maximum in this region. In computing these curves $\delta(R) \equiv R(O^1-O^2)(R) - R(O^1-O^2)(MECP)$ with the remainder of the geometrical parameters taken from the MECP structure. Note that the ^{3}A" potential energy curve decreases rapidly as $\delta(R)$ increases through MECP ($\delta(R)=0$). This is consistent with the small value of $\Delta E(MECP)$ reported in the table above.

• Step 3: Determination of a-N_2O_2 Lifetime

The lifetime of this pseudo–diatomic was determined using a standard Golden Rule lifetime formulation.[5] The effective one–dimensional system in the above figure has a fundamental frequency of ~500cm^{-1}. This is only in qualitative accord with the 706{652}cm^{-1} obtained at the MR-CISD/DZP {MP2} level for the normal mode of a-N_2O_2 identifiable as largely O-O stretch. To account for th lifetimes were computed using both the ^{1}A' potential energy curve in the figure above and model potential energy curves with fundamental frequencies of 600–700cm^{-1}. In each case the lifetime of the lowest vibrational levels are on the order of picoseconds. Raising the ^{3}A" potential energy curve by 5kcal/mol increased the lifetime of the lowest vibrational level by only a factor of 10. Thus although this type of estimate is likely to be a lower bound to the lifetime it is clear that a-N_2O_2 will be rapidly predissociated to $N_2O(X^1\Sigma^+) + O(^3P)$.

III. Stability of Additional Isomers of N_2O_2

Nguyen et al[3] have suggested additional isomers of N_2O_2 as potential HEDM. One such species is the D_{2h} isomer pictured below.
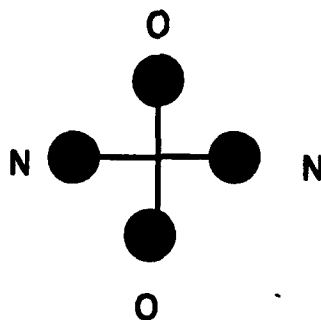
This species is isoelectronic and similar in structure to the O_4^{2+} dication considered by ONeil and co-workers.[6] The possibility of spin-forbidden decay in these systems was considered. The results are summarized in the figures below. For these calculations standard double zeta polarization basis sets, and state-averaged MCSCF(SA-MCSCF)/multireference CI(MRCI) wavefunctions of dimension 357389 configurations state functions (CSFs) and 794449 CSFs for ^{1}A' and ^{3}A" symmetry were used.

$$N_2O_2 \quad D_{2h} \quad \text{Isomer}$$
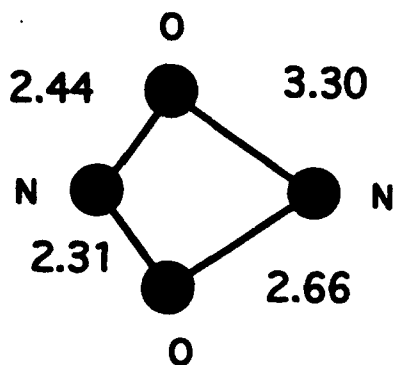
N_2O_2 MECP:$1^1A'$ - $1^3A''$

R(N-N)=3.84
R(O-O)=3.70

ΔE (MEX)= 61kcal/mol
(ΔE (vert)= ~75.kcal/mol)

Numbers in () from Nguyen et al
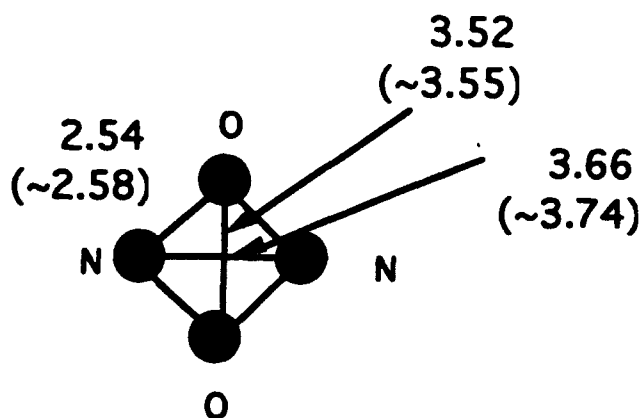
N_2O_2 equilibrium

(average of Nguyen et al data)

Frequencies
2085(1755)
1324(1129)
1246(1096)
1184(1022)
1102(957)
(MP2 of Nguyen et al)
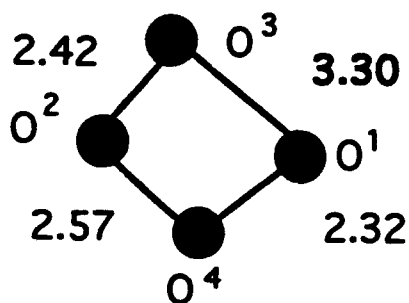
O_4^{2+} MECP:$1^1A'$ - $1^3A''$

R(O1-O2)=3.77
R(O3-O4)=3.75

O_4^{2+}

O_4^{2+} equilibrium

ΔE = 108.3kcal/mol
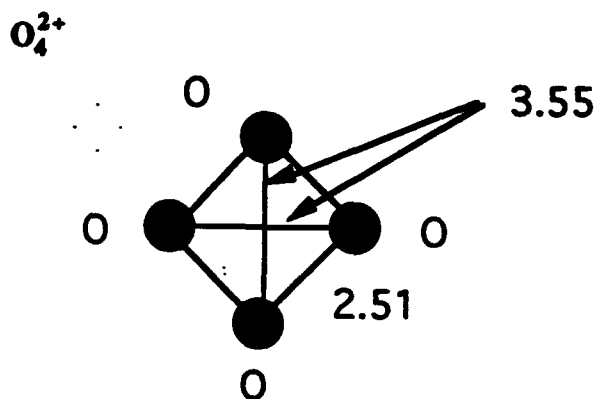
Several points should be emphasized.

D_{2h} N_2O_2:

407

The bond distances and to a lesser extend the frequencies of D_{2h} N_2O_2 are in good accord with the results of Nguyen et al. who used orbitals optimized individually for each state supporting the reliability of present MR-CISD (multireference CI single-double excitation) approach. The minimum energy crossing structure is 61kcal/mol above ground state. Consequently the low-lying vibrational levels of D_{2h} N_2O_2 is expected to be stable with respect to spin-forbidden radiationless decay.

• O_4^{2+} – D_{2h} N_2O_2 comparison

Equilibrium structures of O_4^{2+} and D_{2h} N_2O_2 are quite similar. However minimum energy crossing structures are less so . From the large ΔE it is concluded that spin-forbidden radiationless decay is not likely in this system either.

IV: New Tools for the Study of Radiationless Decay: Systematic Determination of Intersections of Potential Energy Surfaces of (i) the same overall symmetry (Conical Intersections)[7] and (ii) different spin-multiplicity(spin-allowed intersections)[8]

The goal of this methodological work is to enable determination of the (i) minimum energy crossing point for above classes of intersections and (ii) additional points on the surface of intersection for which a selected number of geometrical parameters have been fixed and the remainder are optimized to minimize the energy of the crossing point. The motivation for this aspect of our research program is the fact that the minimum energy crossing point may not be sufficient to understand mechanism of nonadiabatic process and that more precise treatments of predissociation dynamics than that used for a–N_2O_2 require more than just a single point on the crossing surface.

These methodological goals are achieved through the use of Lagrange multiplier constrained minimization procedures. A minimum of the Lagrangian function $L_{IJ}(\mathbf{R}, \xi, \lambda)$ defined as:

$$L_{IJ}(\mathbf{R}, \xi, \lambda) = E_I(\mathbf{R}) + \xi_1 \Delta E_{IJ}(\mathbf{R}) + \xi_2 H_{IJ}(\mathbf{R})/2 + \sum_{k=1}^{M} \lambda_k C_k(\mathbf{R})$$

is sought where $E_I(\mathbf{R}) - E_J(\mathbf{R}) \equiv \Delta E_{IJ}(\mathbf{R})$, $H_{IJ}(\mathbf{R}) = \langle \Psi_I(r;\mathbf{R}) | H(r,R) | \Psi_J(r;\mathbf{R}) \rangle$ and the $C_i(\mathbf{R})$ are a set of geometrical constraints, for example, $C_i(\mathbf{R}) = R_{MN(i)}^2 - a_i^2$ with $R_{MN}^2 = (\mathbf{R}^M - \mathbf{R}^N) \bullet (\mathbf{R}^M - \mathbf{R}^N)$. In words we minimize $E_I(\mathbf{R})$ subject to the constraints $\Delta E_{IJ}(\mathbf{R}) = 0$ and $H_{IJ}(\mathbf{R}) = 0$ and if desired additional geometric constraints. We distinquish between two cases (i) spin-allowed crossing: $H_{IJ}(\mathbf{R}) \equiv 0$ for all $\mathbf{R}$ so that $\xi_2 \equiv 0$ and (ii) conical intersections: $H_{IJ}(\mathbf{R}) \neq 0$ so that $\xi_2 \neq 0$

Minimization $L_{IJ}(\mathbf{R})$ at second order gives:

$$
\begin{bmatrix}
Q^{U}(R,\xi,\lambda) & g^{U}(R) & h^{U}(R) & K(R) \\
g^{U}(R)^{\dagger} & 0 & 0 & 0 \\
h^{U}(R)^{\dagger} & 0 & 0 & 0 \\
K(R)^{\dagger} & 0^{\dagger} & 0^{\dagger} & 0
\end{bmatrix}
\begin{bmatrix}
\delta R \\
\delta \xi_{1} \\
\delta \xi_{2} \\
\delta \lambda
\end{bmatrix}
= -
\begin{bmatrix}
g^{I}(R)+\xi_{1}g^{U}(R)+\xi_{2}h^{U}(R)+\sum_{i=1}^{M}\lambda_{i}K^{i}(R) \\
\Delta E_{IJ}(R) \\
0 \\
C(R)
\end{bmatrix}
$$

where $g_{\alpha}^{I}(R) = \dfrac{\partial E_{I}(R)}{\partial R_{\alpha}}$, $g_{\alpha}^{U}(R) = \dfrac{\partial \Delta E_{IJ}(R)}{\partial R_{\alpha}}$ and $h_{\alpha}^{U}(R) = \dfrac{\partial H_{IJ}(R)}{\partial R_{\alpha}}$ and the constraint gradients

are given by $K_{w_{\alpha}}^{i}(R) = 2R_{w}^{MN(i)}(\delta_{\alpha,M(i)} - \delta_{\alpha,N(i)})$ w=x,y,z. At convergence the right hand side of

these Newton-Raphson equations are zero so that

$$
g^{I}(R)+\xi_{1}g^{U}(R)+\xi_{2}h^{U}(R)+K(R)^{\dagger}\cdot\lambda = 0
$$

and constraints are satisfied. The intellectual content of the above equation is seen as follows:

(i) Same Symmetry Case: $\xi_{2} \neq 0$

Energy gradient is zero except along M+2 directions defined by tangents to (i)$\Delta E_{IJ}(R)$,
(ii) $H_{IJ}(R)$ and (iii) geometric constraints. Consequently the crossing surface has dimension at most N–2.

(ii) Distinct Spin Symmetry Case: $\xi_{2} = 0$

Since $\xi_{2} = 0$ the energy gradient is zero except along M+1 directions defined by tangents to
(i) $\Delta E_{IJ}(R)$ and (ii) the geometric constraints. Consequently the crossing surface has dimension at most N–1.

Two final comments are appropriate. In the distinct symmetry case all derivatives exist. However in the 'same symmetry' case the intersection point is a singular point. This limits the accuracy with which the crossing point can be determined. The accuracy with which the minimum energy crossing point can be determined is considered in the computational example given below. The algorithms described above are predictive in the following sense. Given $g_{\alpha}^{I}(R)$, $g_{\alpha}^{U}(R)$ and if appropriate $h_{\alpha}^{U}(R)$ at R and constraints corresponding to a new point the Newton-Raphson equations 'predict' a new starting geometry. It will be seen in the table below this predictive capablity can reduce the amount of work required to determine subsequent points on the crossing surface.

In the following a seam of conical intersections is determined for the $1,2^{2}A'$ states of the formyl radical(HCO). The following figure serves to motivate the choice of system. Herzberg[4] reported an observation by Johns et al [9] that the avoided crossing pictured below exists in the HCO system. The algorthm discussed above was used to see if in fact the avoided crossing might be a conical intersection.

$B\ ^2A'$ 　　　　　　　$^2S + ^3\Pi$

$^2A''$

$^2S + ^1\Sigma$

$^2A'$ 　　　　　　　$H + CO$
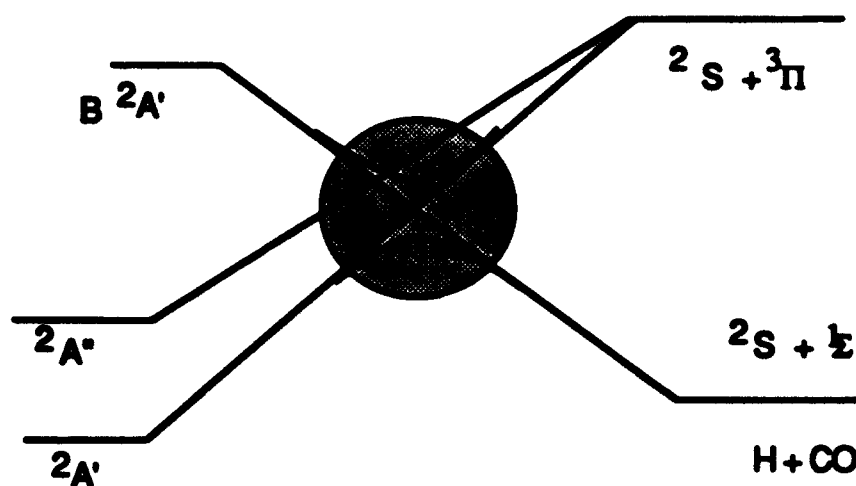
Conical Intersection Determination:Algorithm Performance:HCO $1,2\,^2A'$ Crossing Surface

Iter	$E(1\,^2A')$	$E(2\,^2A')$	R_{CO}	R_{HC}	R_{OH}	Norm
		Minimum Energy Crossing - $q(R,\xi) = 1$				
0	-113.324919	-113.292215	2.432412	3.019385	2.592188	
1	-113.316466	-113.314633	2.333579	3.049433	2.410928	.816(-02)
2	-113.315543	-113.315527	2.335198	3.047688	2.419480	.155(-02)
3	-113.315541	-113.315541	2.334160	3.046533	2.418513	.976(-03)
4	-113.315542	-113.315541	2.333537	3.045782	2.417905	.627(-03)
5	-113.315542	-113.315542	2.333136	3.045301	2.417518	.402(-03)
6	-113.315543	-113.315542	2.332879	3.044992	2.417270	.257(-03)
		Additional Points with Prediction				
		$a_{CO} = 2.433479$				
0	-113.311507	-113.311314	2.435598	3.168592	2.516925	
2	-113.311544	-113.311544	2.433478	3.165083	2.514148	
		$a_{CO} = 2.233479$				
0	-113.312085	-113.311298	2.241702	2.938017	2.330708	
2	-113.310678	-113.310677	2.233479	2.924388	2.319816	
		$a_{CO} = 2.283479$				
0	113.314503	-113.314424	2.284035	2.986235	2.369992	
2	-113.314423	-113.314422	2.283479	2.985298	2.369108	
		$a_{CO} = 2.183479$				
0	-113.304416	-113.304111	2.185669	2.866629	2.273271	
1	-113.303810	113.303809	2.183477	2.862963	2.269795	
		$a_{CO} = 2.383479$				
0	-113.314861	-113.313564	2.392640	3.120988	2.480851	
2	-113.314461	-113.314460	2.383479	3.105640	2.466167	

[a]Atomic units used throughout. Each constrained minimization was begun from 'prediction' based on final geometry of preceding optimization.

410

The minimum energy point on the surface of conical intersections is pictured below. It is occurs for a nuclear configuration more appropriate to COH than to the HCO system noted above.
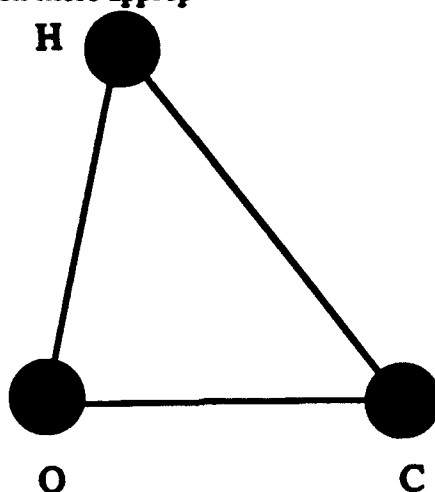
References

1. K. A. Nguyen, M. S. Gordon, J. A. Montgomery, H. H. Michels, and D. R. Yarkony, J. Chem. Phys. 98, 3845 (1993).

2. H. H. Michels and J. J. A. Montgomery, J. Chem. Phys. 88, 7248 (1988).

3. K. A. Nguyen, N. Matsunaga, M. S. Gordon, J. A. Montgomery, and H. H. Michels, in preparation.

4. G. Herzberg, *Electronic Spectra and Electronic Structure of Polyatomic Molecules*, (Van Nostrand Reinhold, New York, 1966) .

5. O. K. Rice, Phys. Rev. 33, 748 (1929).

6. W. C. Lineberger, S. R. Leone, and S. V. ONeil *Abstracts of the High Energy Density Materials Contractors Meeting*, 1992, .

7. M. R. Manaa and D. R. Yarkony, J. Chem. Phys. submitted for publication.

8. D. R. Yarkony, J. Phys. Chem 97, 4407 (1993).

9. Johns, Pridle, and Ramsay, Disc. Far. Soc. 35, 90 (1963)..

Theoretical Performance of Atomic and Molecular HEDM Additives to Solid H_2

Patrick G. Carrick

Phillips Laboratory, Propulsion Directorate
Edwards Air Force Base, CA 93524-7680

The potential for advanced rocket propellants composed of additives to cryogenic solid hydrogen has been under investigation by the HEDM program for a number of years. Most of the studies have focused on atomic additives composed of H, Li, B, C, Mg, and Al. Previous studies reported the limitations for storage of atoms in solid hydrogen[1], the expected specific impulse (I_{sp}) for these atoms[2], and the first observation of isolated energetic atoms composed of these elements in hydrogen[3]. The study of the limitations of storage for atoms in solid hydrogen concluded that molecular clusters will form a significant proportion of the additive for concentrations on the order of a few percent. In addition, the report of the isolation of lithium in solid hydrogen concluded that the lithium atoms must be deposited with sufficient kinetic energy to overcome surface recombination. Both of these studies point to the distinct probability that small molecular systems may form a significant fraction of any "real" additive to cryogenic solid hydrogen propellants.

The energetics under which lithium atoms have been deposited into solid hydrogen point to two potential mechanisms for the formation of small molecules trapped in the hydrogen. One likely mechanism is the reaction of the energetic atom with the solid hydrogen to form a small hydrogen containing molecule. For instance, lithium atoms with a kinetic energy of about 10 eV could dissociate molecular hydrogen and eventually form LiH. The other possible mechanism is the recombination of the deposited atom with a like atom or a different species "metal" atom. For example, a co-deposition of lithium atoms and boron atoms could result in a small amount of LiB molecules. These mechanisms are currently under investigation.

Different deposition processes (such as ovens or electric discharges) may also result in the formation of diatomic or polyatomic species in the hydrogen.

The specific impulse[2] values for a variety of atomic and small molecular additives to solid hydrogen are presented in Table 1. Values for 5% of the additive and for the amount of additive resulting in the maximum specific impulse are listed. Note that the majority of the atomic concentrations for the maximum specific impulse values are greater than 10% and that all of the maximum concentration values are greater than 5%.

The potential specific impulse of a "real" system of atom additives to solid hydrogen will be effected by the amount of the molecular components. The overall effect of the molecular components in the additive is dependent on several factors, but primarily on the total concentration of the additive and the heat of formation of the particular molecular component. Consider, for example, the case of 5% boron atoms in solid hydrogen. The optimum concentration for boron to give the maximum specific impulse is 23%, so increasing the boron atom concentration to greater than 5% will result in a gain in I_{sp}. The substitution of 5% B_2 molecules in effect *doubles* the boron *atom* concentration, and therefore the specific impulse for B_2 (at the 5% level) is greater than boron atoms, despite the loss of energy due to the boron-boron bond. Therefore, a certain fraction of boron diatomic molecules in a 5% boron atom in hydrogen sample will actually *add* to the specific impulse. Note that this is not the case for carbon atoms and C_2 molecules since the bond strength in C_2 is large enough to overcome the advantage of greater effective atom concentration.

The largest I_{sp} values for atoms at the 5% level are for boron and carbon, both giving specific impulse gains (over LOX-LH$_2$) of about 80 seconds. The largest I_{sp} values for the diatomic molecules at the 5% level (disregarding beryllium compounds) are for LiB and B_2, with specific impulse gains of greater than 100 seconds, and BC, with a specific impulse gain of over 90 seconds. From these specific impulse values, it appears that additives containing boron or carbon are the most promising candidates for energetic additives to solid hydrogen.

Table 1: Calculated Atomic and Diatomic I$_{sp}$

Species	ΔH$_f$	5% I$_{sp}$	% LOX	Opt. I$_{sp}$	% M	% LOX	% sH$_2$
H$_2$ (s)	-2.21	----	----	360	0	20.6	79.4
H	52.1	407	19.0	1478	100.0	0	0
LiH	34.2	399	13.1	478	20.4	5.1	79.6
BeH	82.4	455	2.8	551	15.2	7.6	84.8
BH	109.3	449	3.8	563	28.3	0	71.7
CH	143.2	433	2.2	809	24.8	0	75.2
MgH	55.7	406	14.9	438	14.0	7.0	86.0
AlH	61.2	415	10.1	445	11.1	8.4	88.9
Li	38.1	401	12.2	481	19.9	5.0	80.1
Li$_2$	53.6	417	5.8	461	11.6	5.8	88.4
LiBe	109.8	482	3.9	512	15.0	7.6	85.0
LiB	159.6	494	5.0	527	29.0	0	71.0
LiC	159.9	465	1.3	523	30.0	0	70.0
LiMg	69.3	414	5.8	432	8.3	6.2	91.7
LiAl	97.4	448	5.0	458	7.3	7.4	92.7
Be	77.4	452	2.5	544	14.4	7.2	85.6
Be$_2$	153.1	525	5.0	545	7.8	7.8	92.2
BeAl	147.4	481	6.3	485	6.2	7.7	93.8
B	135.0	472	3.8	607	23.0	0	77.0
B$_2$	207.2	492	7.4	550	14.3	0	85.7
BC	201.6	482	3.7	542	14.2	0	85.8
C	171.3	469	0.0	645	20.0	0	80.0
C$_2$	199.3	462	0.0	533	15.3	0	84.7
CAl	174.5	458	3.8	464	6.8	5.1	93.2
N	113.0	414	15.0	581	34.2	0	65.8
Mg	35.2	398	16.8	417	13.8	7.1	86.2
Mg$_2$	68.8	408	8.9	416	7.4	7.6	92.6
Al	78.9	425	7.5	456	10.2	7.7	89.8
Al$_2$	125.1	445	7.5	445	5.6	8.4	94.4
Si	107.6	432	5.1	451	8.2	8.2	91.8
Ti	113.2	404	11.5	414	9.0	7.9	91.0

Conditions: Chamber Pressure = 1000 psi, Exhaust Pressure = 14.7 psi

Specific impulse calculations over the complete range of interesting concentration values for the additives were also completed. The resulting 3D grid of data (mole % additive vs. mole % LOX vs. I_{sp}) can be plotted in the form of a contour map by projecting the specific impulse values onto the plane formed by the additive and LOX mole percents. The resulting contour maps can then be used to determine the optimum operating conditions for any concentration of additive in the solid hydrogen.

The 3-dimensional contour plots for the atomic species that result in the largest specific impulse gains (boron and carbon) are given in Figures 1 and 2. Similar contour plots for the other elements in Table 1 (except for Si and Ti) are contained in reference 2. An inspection of the carbon atom graph reveals that above about 4 mole % atoms, addition of LOX *decreases* the I_{sp} and therefore at 5 % this system should be run as a monopropellant. These same conditions occur for boron atoms near 11% and therefore the 5% boron atom system requires LOX to obtain the maximum I_{sp}.
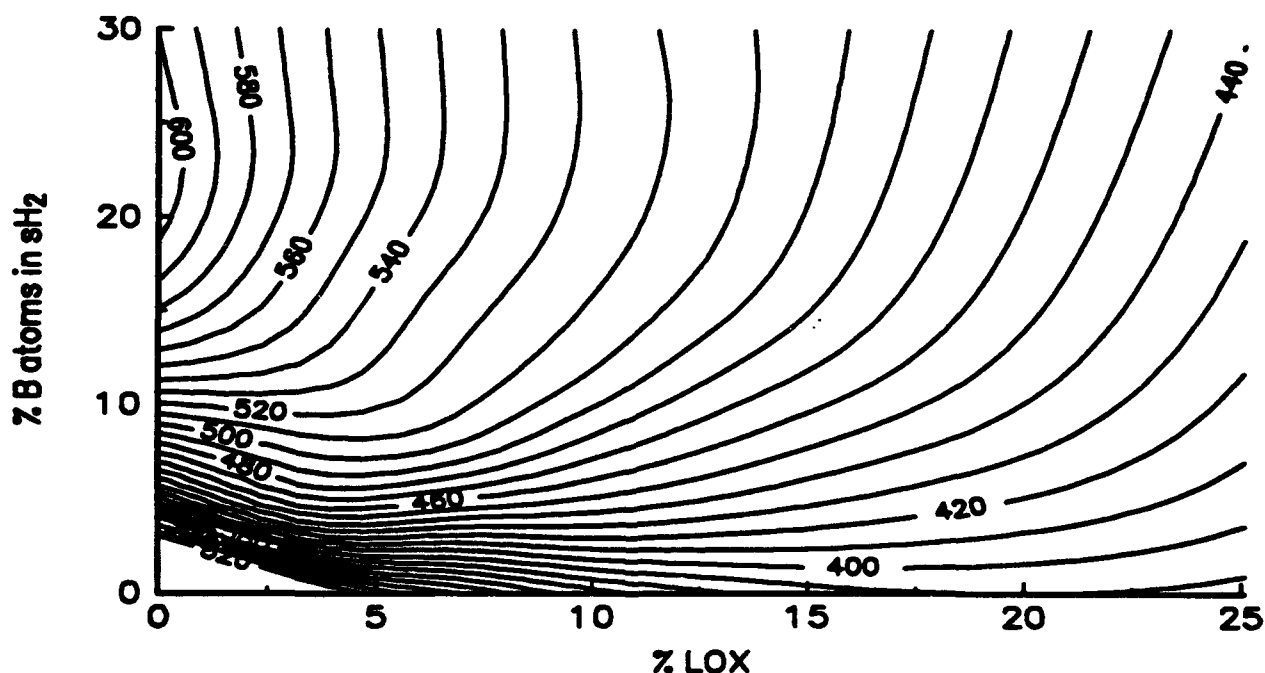

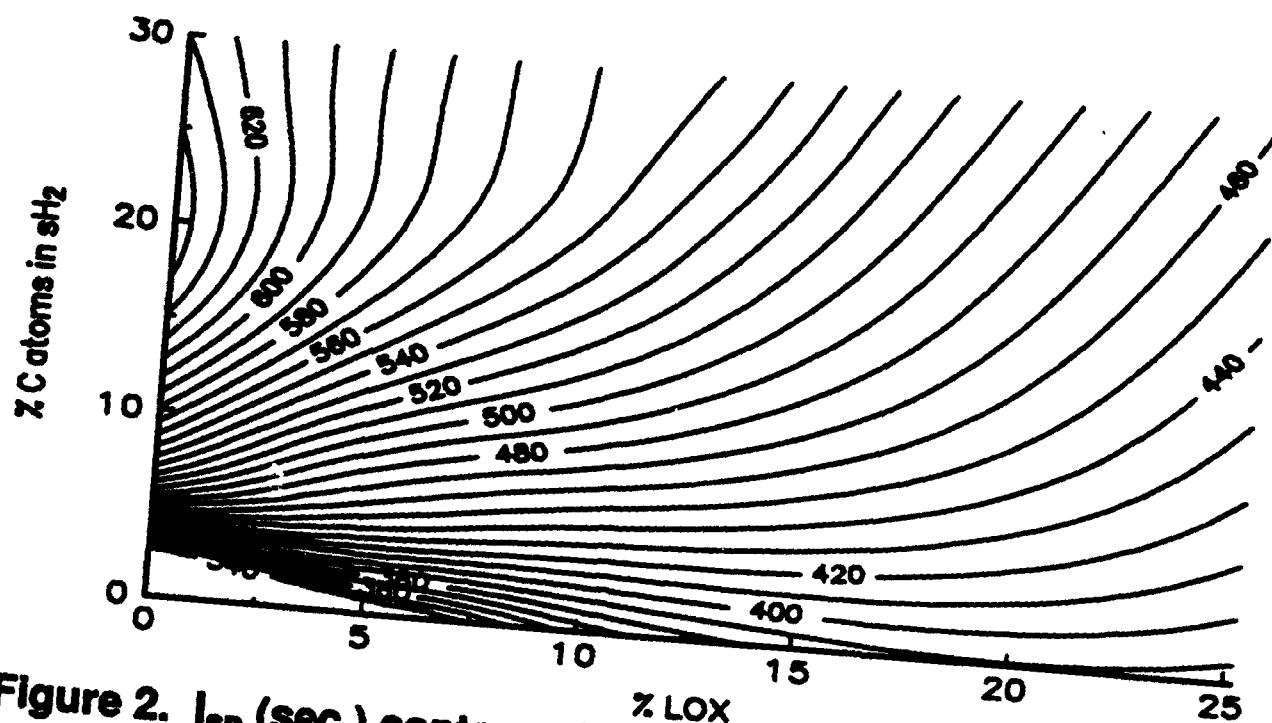Figure 1. I_{sp} (sec.) contour plot of boron atoms in solid H_2.

Figure 2. I_{sp} (sec.) contour plot of carbon atoms in solid H_2.

The 3-D contour plots for B_2 and LiB are given in Figures 3 and 4. The boron diatomic graph shows the point at which the system becomes a "monopropellant" to be about 8 mole percent. This points to the possibility that even boron trimers may significantly contribute to the available specific impulse at 5% total loading.

The contour plot for LiB shows an interesting "compression" of specific impulse increase at lower concentrations and much less gain at higher concentrations, even though the concentration at the maximum I_{sp} is about 28 mole %. Therefore most of the potential gain in performance can be obtained at moderate additive concentrations.

These calculations show that an increase in diatomic molecules in a reasonably concentrated sample of atoms in solid hydrogen can have a positive effect, in most cases. The result of the calculations for mixed atoms in solid hydrogen shows that, in some cases, larger specific impulse gains can be obtained than from just the individual atoms.
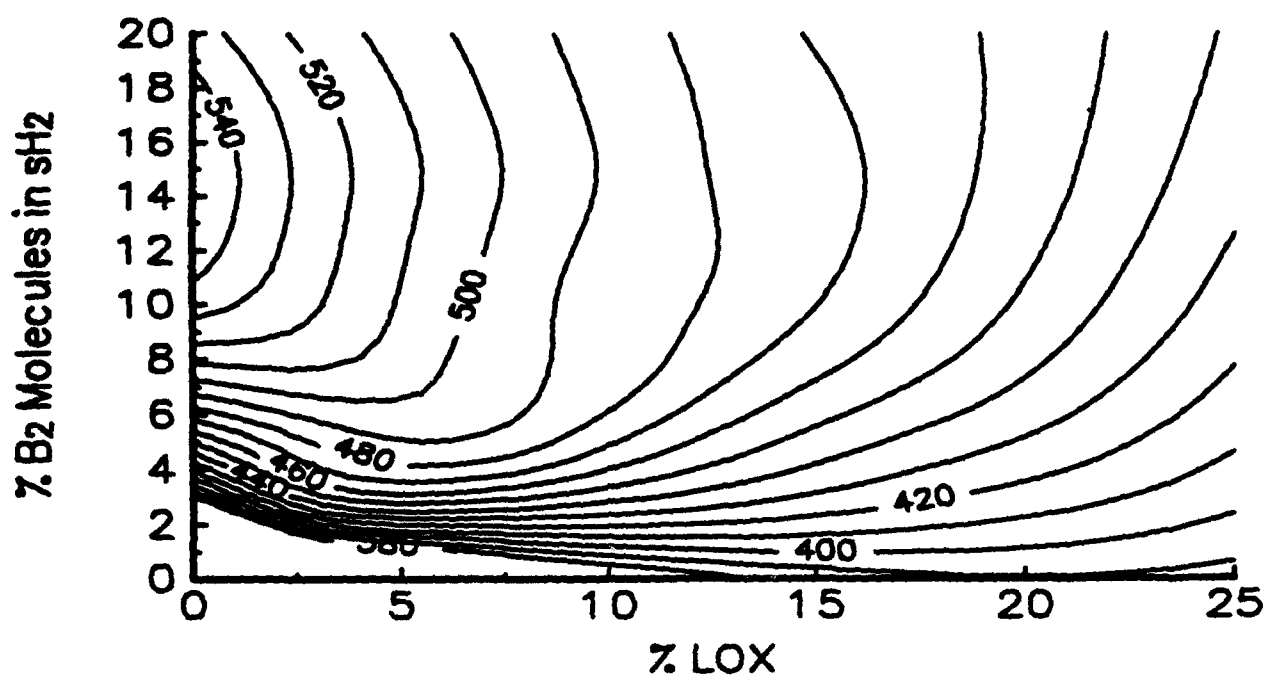
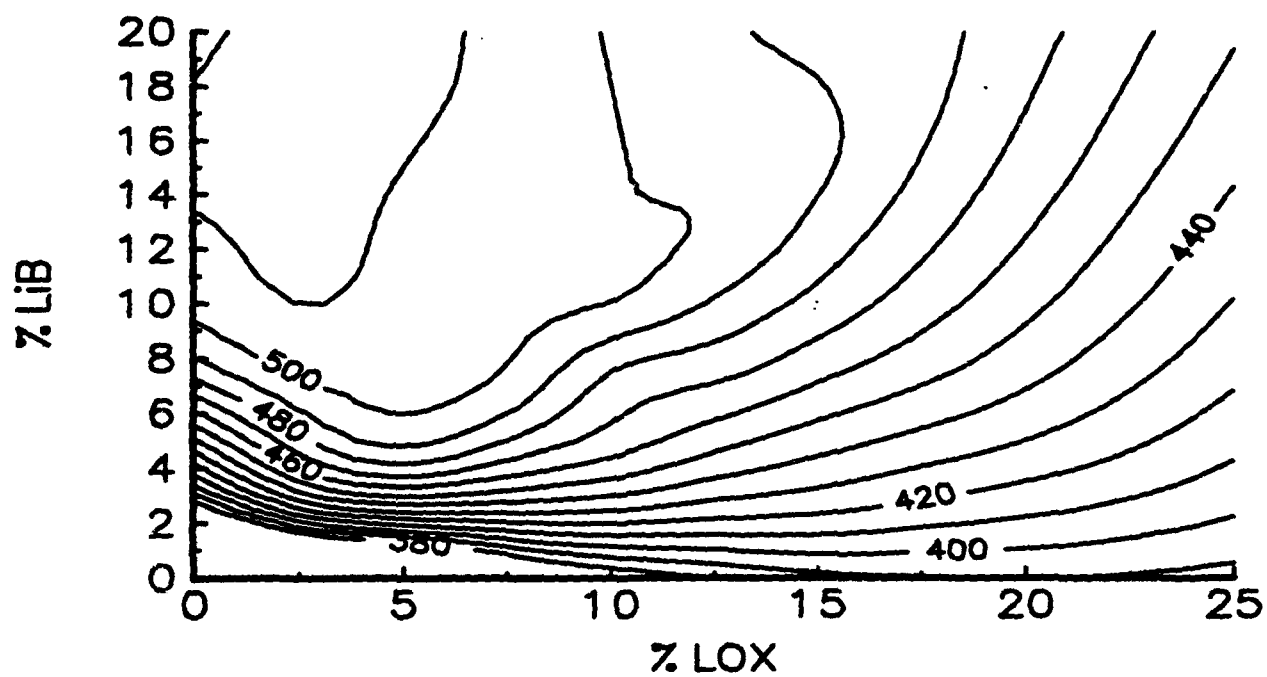**Figure 3.** I_{sp} (sec.) contour plot of B_2 Molecules in solid H_2.

Figure 4. I_{sp} (sec.) contour plot of LiB Molecules in solid H_2.

417

SUMMARY

Specific impulse calculations on a variety of atomic and diatomic additives to solid hydrogen resulted in the identification of 18 species (at the 5 mole % level) which increase the I_{sp} by 10 % or greater over LOX/LH_2. Some of these energetic additives contain beryllium and are therefore probably not of interest for ground based rocket propulsion. The best candidate species contain boron or carbon.

It has been shown that, in most cases, the effect of diatomic species in the additive can lead to an increase in the specific impulse. For several diatomic molecules, the specific impulse gains at the 5% level are greater than the corresponding atoms that comprise the molecules. This is due to the need for greater concentrations of the atom to obtain the maximum specific impulse, which overcomes the energy lost to the molecular bond. An investigation of the possible effects from triatomic and larger molecules is underway.

REFERENCES

1. Pritt, A. T., Jr., Presser, N. and Herm, R. R., "Limitations on the Atom Densities in Cryogenic Matrices," *Proceedings of the High Energy Density Matter (HEDM) Conference* (AL-CP-89-002), pp. 245 - 249, T. G. Wiley and R. A. van Opijnen, eds., 1989 .

2. Carrick, P. G., "Specific Impulse Calculations of High Energy Density Solid Cryogenic Rocket Propellants 1: Atoms in Solid H_2," Air Force Technical Report PL-TR-93-3014, 1993.

3. Fajardo, M. E., "Metal Atoms in Solid Rare Gases," *Proceedings of the High Energy Density Matter (HEDM) Conference* (PL-CP-91-3003), pp. 61 - 66, M. E. Cordonnier, ed., 1991.

Photochemistry of Solid Ozone[a]

Charles A. Wight

Department of Chemistry
University of Utah
Salt Lake City, UT 84112

High energy density materials formed by trapping of impurity atoms, free radicals or ions in cryogenic solids have attracted considerable attention recently.[1,2] Aside from fundamental interests in determining the nature of condensed phase reaction dynamics, these systems are of potential use as advanced propellants. For example, several groups have investigated the properties of metal atoms trapped in solid hydrogen.[3,4,5] This is a challenging field, especially from an experimental standpoint, because solid hydrogen is stable only at temperatures below about 4 K.

In our research group, we have been interested in the spectroscopic, photochemical and photophysical properties of solid ozone and mixtures of ozone with inert or reactive solids.[6,7] In this paper, we describe recent results aimed at characterizing photochemical pathways and quantum yields for destruction of ozone molecules in thin solid films of this type.

Experimental Details

Thin films of ozone and its mixtures with argon or nitrogen have been prepared by vapor deposition of the gaseous mixtures directly onto the surface of an optical window at 10 K (see Figure 1). The window is mounted in a copper retainer at the cold tip of a closed-cycle helium refrigerator. Typical sample thicknesses are from 1-500 microns, depending on the concentration of ozone. The ozone is prepared by electric discharge of O_2 in a glass vacuum manifold. The ozone is continuously removed from the gas discharge by condensation at the bottom of the vessel, which is immersed in a liquid nitrogen bath.

Apparatus

Figure 1

Samples are subjected to pulsed UV laser photolysis at 266 nm (4th harmonic output of a Nd:YAG
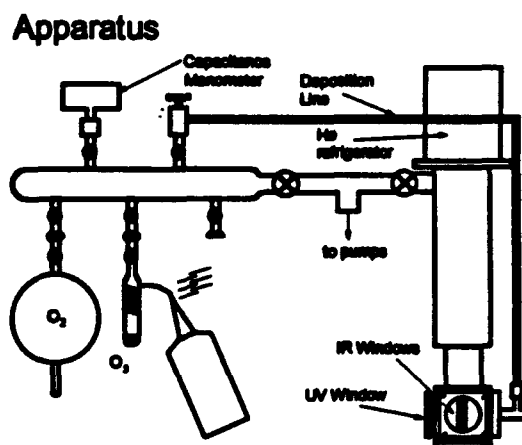
laser). Typical conditions are 10 laser pulses per second at 100 µJ/cm²/pulse. The extent of photolysis is measured either by UV absorption spectroscopy (as a measure of total ozone concentration) or by transmission FTIR spectroscopy (which is useful for distinguishing monomers from dimers and larger clusters).

Results and Discussion

Deposition of dilute mixtures of ozone in argon produces films that exhibit two distinct spectral bands in the region of the v_3 fundamental vibrational mode of ozone (asymmetric stretch). Typical spectra are shown in Figure 2. The band near 1040 cm^{-1} increases in relative intensity (at the expense of the 1022 cm^{-1} feature) as the concentration of ozone is increased. On this basis, we have assigned the lower frequency band to the isolated monomer species. The higher frequency band is composed of dimer, trimer and larger clusters of ozone. Similar results have been obtained for mixtures of ozone with nitrogen except that the monomer band is split into two features

Figure 2

UV laser photolysis at 266 nm (in the intense Hartley band of ozone) results in complete destruction of the ozone clusters, as shown by the disappearance of the feature at 1040 cm^{-1}. However, the monomers are left largely undisturbed.[b] Our interpretation of this observation is that in clusters, photodissociation of an ozone molecule generates a hot O atom that is cages in the local site of photolysis. The atom can either recombine with the original O_2 partner or react with another O_3 molecule of the cluster. The overall reaction sequence is

$$O_3 + hv \rightarrow O_2 + O$$
$$O + O_3 \rightarrow 2 O_2$$

net reaction: $2 O_3 + hv \rightarrow 3 O_2$
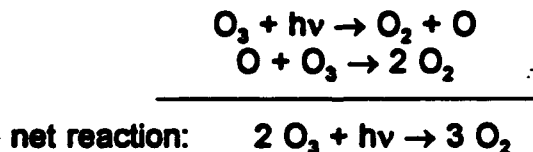
Interestingly, the quantum yield for photodissociation of the clusters depends on the bulk concentration of ozone in the sample. At the lowest concentrations investigated (O_3:Ar = 1:1000) the quantum yield for photodestruction of ozone clusters is 0.3 ± 0.1 (see Figure 3). The yield increases with increasing concentration to 2.0 ±
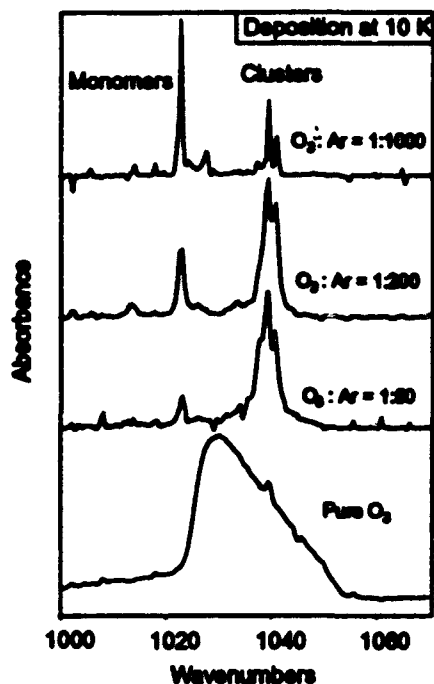
---

[b] The 1022 cm^{-1} band decreases somewhat in intensity during the initial stages of photolysis, but most monomers (more than 80% in samples of O_3:Ar at 1:1000) remain undisturbed, even after extended photolysis periods. Tthe small extent of photolysis may be due to pairs of O_3 molecules that are next-nearest neighbors in the argon lattice.

0.1 in pure ozone.

The concentration dependence of the quantum yield may be a result of changes in the surface area/volume ratio of the clusters. In small clusters (i.e., in dilute samples), the hot O atom produced in the initial photolysis step is more likely to encounter an argon atom than another O_3 molecule. This kind of event favors cage recombination of $O + O_2$ to regenerate the original O_3 molecule (no net reaction). On the other hand, in large clusters formed at high O_3 concentrations, the hot O atom is likely to first encounter another O_3 molecule, leading to reaction and net destruction of the ozone.

Figure 3

Similar results have been obtained for mixtures of O_3 with N_2, except that in this case, a reactive channel involving the host matrix can also occur:

$$O_3 + h\nu \rightarrow O_2 + O$$
$$O + N_2 \rightarrow N_2O$$

net reaction: $O_3 + N_2 + h\nu \rightarrow O_2 + N_2O$
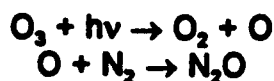
Formation of N_2O has been observed directly by its characteristic absorption in the ν_3 fundamental region, but this product accounts for only about 10-20% of the photodestructive yield of O_3, even at high dilution. Both of the other channels, recombination and reaction with another O_3 molecule, are more efficient than reaction with the matrix host.

References

1.   H. Kunttu, E. Sekreta, and V. A. Apkarian, J. Chem. Phys. 94, 7819 (1991).
2.   R. Alimi, V. A. Apkarian, and R. B. Gerber, J. Chem. Phys. 98, 331 (1993).
3.   M. E. Fajardo, J. Chem. Phys. 98, 110 (1993).
4.   M. E. Fajardo, P. G. Carrick, and J. W. Kenney, III, J. Chem. Phys. 94, 5812 (1991).
5.   D. H. Li and G. A. Voth, J. Chem. Phys. 96, 5340 (1992).
6.   A. J. Sedlacek and C. A. Wight, J. Phys. Chem., 93, 509 (1989).
7.   T. J. Tague, Jr., M. R. McCarthy and C. A. Wight, "Desensitization of Solid Ozone with Respect to Pulsed UV Laser Detonation", manuscript in preparation.
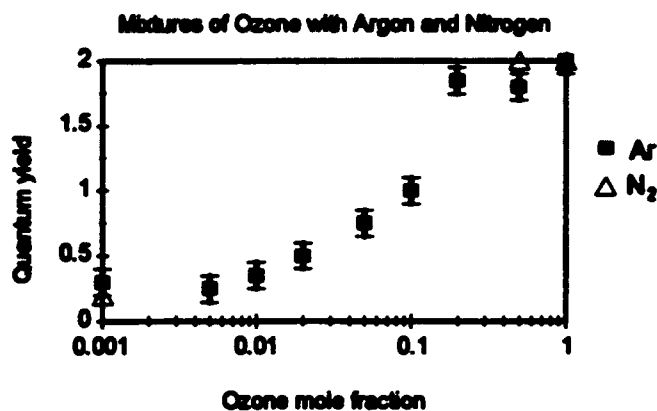
421

Excited State Products of Electron-Ion Recombination

Nigel G. Adams, B. Lachele Foley and Lucia M. Babcock
Department of Chemistry, University of Georgia,
Athens, GA 30602.

Dissociative electron-ion recombination

$$XY^+ + e \rightarrow X + Y$$

is extremely important in ionized media (such as planetary atmospheres, interstellar gas clouds, the space shuttle environment and combustion flames) both in controlling ionization density and in producing reactive neutral radical species. The rate coefficients have been determined for quite a large number of reactions[1], however, very few studies have been made of the products.[2] The atoms H, N, and O have been detected from the recombinations of H_2O^+, N_2^+, NO^+ and O_2^+.[3-5] Recently, H-atoms and OH radicals have been detected from the recombinations of N_2H^+, HCO^+, HCO_2^+, N_2OH^+, $OCSH^+$, H_2CN^+, H_3O^+, H_3S^+, NH_4^+ and CH_5^+.[6,7] Recombination reactions are sufficiently energetic to populate electronically excited states in addition to ground states. Indeed, the observed ground state OH may to some degree result from the radiative decay of electronically excited states produced directly in the recombination. In addition, identification of excited state products may provide insight into which ground state species will be produced, although it must be emphasized that these different recombination channels will occur along different repulsive potential curves. Excited state products that have previously been detected have been Ne from Ne_2^+ [8] and $CO(A^1\Pi)$, $CO(d^3\Delta_i)$ and $CO(a^3\Pi_r)$ from CO_2^+.[9-11] Recently, $N_2(C^3\Pi_u)$ emissions have been detected from the recombination of N_4^+.[12]

In the present study, a flowing afterglow coupled with emission spectroscopy has been used to detect emissions from electronically excited states in the wavelength range 190 to 800 nm for the recombinations of O_2H^+, N_2H^+, N_2OH^+, CO_2^+, HCO_2^+, OCS^+, $OCSH^+$, H_3O^+, H_3S^+ and the cluster ions N_4^+ and N_4H^+. For maximum sensitivity this requires that the emissions be observed in the region where the recombining ions are being produced and, as such, the spectra may be contaminated by other emissions such as those from the ion-molecule reactions producing the ions, as well as other sources. To overcome this problem, a technique has been developed to distinguish between the different sources of the emissions that uses a gas which rapidly attaches electrons to quench the electron-ion recombination process.

The flowing afterglow used for these measurements has been described in detail previously.[13] He^+ ions and He metastables, He^m, were created in helium in a microwave discharge and at the pressures used in these experiments (~1.8 Torr), the He^+ is rapidly

Table 1. Energetics (in eV) and accessible electronic states for the recombination reactions indicated.

Recombining Ion	Possible Products	Accessible Electronic States
O_2H^+	$H + O_2 +9.2$	O_2(states up to $d^1\Pi_g$)
	$O + OH + 8.5$	$OH(A^2\Sigma^+)$
	$H + 2O + 4.1$	-
N_2OH^+	$H + N_2O + 7.7$	N_2O(states up to $\tilde{B}$)
	$H + N+ NO +2.7$	-
	$H + O + N_2 + 6.6$	-
	$NH + NO + 6.6$	$NH(A^3\Pi_i;$ states up to $c^1\Pi)$
	$OH + N_2 + 10.5$	$OH(A^2\Sigma^+;$ states up to $D^2\Sigma)$
CO_2^+	$O + CO + 8.3$	$CO(a^3\Pi_r, a'^3\Sigma^+, d^3\Delta_i, e^3\Sigma^-, A^1\Pi, I^1\Sigma, D^1\Delta)$
	$C + O_2 + 2.2$	$O_2(a^1\Delta_g, b^1\Pi_g^+)$
HCO_2^+	$H + CO_2 + 7.9$	$CO_2(\tilde{A}^1B_2(\Delta_u))$
	$H + O + CO + 2.4$	$CO(a^3\Pi_r)$
	$OH + CO + 6.8$	$OH(A^2\Sigma^+)$
	$HCO + O + 3.2$	$HCO(\tilde{A}^2A''\Pi)$
N_2H^+	$H + N_2 + 8.5$	N_2(states up to $a^1\Sigma_g)$
	$NH + N + < 2.2$	$NH(a^1\Delta)$
N_4^+	$N_2 + N_2 + 14.6$	N_2(states up to $c_5'^1\Sigma_u^+)$
	$2N + N_2 + 4.8$	-
	$N + N_3 + < 9.4$	-
N_4H^+	$H + 2N_2 + 7.8$	$N_2(A^3\Sigma_u^+, B^3\Pi_g, w^3\Delta_u)$
	$NH + N + N_2 + <1.5$	-
	$NH + N_3 + < 6.0$	$NH(a^1\Delta)$
	$N + H +N_3 + \sim 2.6$	?
	$H + N_4$	?

converted to He_2^+. Ar was then added and this reacted with the He_2^+ and He^m to produce an Ar^+/electron plasma. Other gases such as H_2 and the gas, XY, from which the recombining ions were produced, were added further downstream at an upstream facing port located directly in front of a 0.66m optical spectrometer so that the emissions from electronically excited recombination products could be detected. Sufficient gases were added to ensure that the ions were vibrationally relaxed before recombination.

The technique for distinguishing between emissions due to recombination and from other sources is illustrated in Fig. 1. An "origin" spectrum (a) of the wavelength region of interest containing all emissions is first recorded. A gas, AB, which very rapidly attaches electrons is

423

then added upstream with the Ar to remove electrons and thus quench electron-ion recombination. Since upper limit attachment rate coefficients are about two orders of magnitude larger than the equivalent ion-neutral reaction rate coefficients, the ion chemistry is only slightly affected. A "background" spectrum (b) is then taken which contains all emissions other than those from electron-ion recombination. If the amount of attaching gas is sufficient to attach all of the electrons then the difference (c) between these two spectra will give the spectrum due to recombination alone with any ion-ion (mutual neutralization) contribution being negative. A great deal of additional information can be obtained by taking the ratio of the origin to the background spectrum (d) (in this case somewhat less attaching gas needs to be added so that the electron-ion recombination emissions are not completely quenched). The peaks on this plot will be approximately square with the features originating from a given process having the same amplitude independent of the intensity of the emission. Thus very low intensity emissions can be detected. The ratios associated with ion-neutral and neutral-neutral reactions are somewhat greater than one because even with rapidly attaching gases there is some reaction and thus a reduction in the emissions.

The techniques are illustrated in Fig. 2 for the recombination of N_2OH^+. Reaction energetics and accessible electronically excited states are given in Table 1. To confirm the sources of the emissions, the variations of the intensities of the spectral features with SF_6 flow were determined. Very different forms of the variations were obtained for emissions arising from different sources[13] and establish very clearly which emissions result from electron-ion recombination. Details of all of the emissions from recombination that we have, so far, identified are given in Table 2.

Now that it has been established which emissions are due to recombination, their relative contributions to the product distribution can be assessed by integrating under the emission bands and accounting for the differing transition probabilities. The populations of the vibrational levels of the OH A-state deduced in this manner for the O_2H^+ and N_2OH^+ recombinations are given

Table 2. Optical emissions (190 to 800 nm), so far identified, from the recombination reactions indicated.

Recombining Ion	Optical Emissions
O_2H^+	$OH(A{\to}X)$
N_2H^+	$OH(A{\to}X)$, $NH(A{\to}X)$
CO_2^+	$CO(d{\to}a)$, $CO(a{\to}X)$, $CO(e{\to}a)$, $O_2(B{\to}X)$
HCO_2^+	$OH(A{\to}X)$, $HCO(\tilde{A}^2A''{\to}X^2A')$
$OCSH^+$	many lines, now being assigned.
N_2H^+	$N_2(B{\to}A)$
N_4H^+	$N_2(B{\to}A)$, $NH(A{\to}X)$

Table 3. Vibrational state population distributions for the OH($A^2\Sigma^+$) electronic state (v' = 0,1,2) resulting from the electron recombinations of N_2OH^+ and O_2H^+.

Recombining Ion	v' = 0	v' = 1	v' = 2
O_2H^+	62 ± 15%	26 ± 15%	12 ± 12%
N_2OH^+	59 ± 15%	28 ± 15%	13 ± 13%

in Table 3. In addition for N_2OH^+, the relative contributions of the OH A-state and the NH A-state are 4 to 1.

In the case of the spectral emissions from CO_2^+ recombination, there are previous data available[9] which are in good agreement with the present data. This gives added confidence in the validity of our measurements. Very recently, emission spectra have been recorded from the recombinations of N_4^+ and N_4H^+. In these cases there is the possibility of forming N_3 and also N_4 for the N_4H^+ recombination (see Table 1) and these products will be observable if they have appropriate excited states. In particular tetrahedral N_4 may be detected even if the N_4H^+ recombining ion does not have a tetrahedral structure (this is not known and thus a calculation would be useful), since depending on the available potential surfaces there could be significant structural rearrangement. Our experimental studies are continuing.

Acknowledgements

References

1. J. B. A. Mitchell, *Phys. Repts. 186*, 215 1990.
2. N. G. Adams, In *Advances in Gas Phase Ion Chemistry, Vol.1*. Eds. N. G. Adams and L. M. Babcock, JAI Press, Greenwich Connecticut, 1992 p.271.
3. D. Kley, G. M. Lawrence and E. J. Stone, *J. Chem. Phys. 66*, 4157 1977.
4. E. C. Zipf, *J. Geophys. Res. 85*, 4232 1980.
5. B. R. Rowe and J. L. Queffelec, In *Dissociative Recombination: Theory, Experiment and Applications* Eds. J. B. A. Mitchell and S. L. Guberman, World Scientific, Singapore, 1989 p.151.
6. N. G. Adams, C. R. Herd and D. Smith, *J. Chem. Phys. 91*, 963 1989.
7. N. G. Adams, C. R. Herd, M. Geoghegan, D. Smith, A. Canosa, J. C. Gomet, B. R. Rowe, J. L. Queffelec and M. Morlais, *J. Chem. Phys. 94*, 4852 1991.
8. L. Frommhold and M. A. Biondi, *Phys. Rev. 185*, 244 1969.
9. T. S. Wauchop and H. P. Broida, *J. Chem. Phys. 56*, 330 1972.
10. R. A. Gutcheck and E. C. Zipf, *J. Geophys. Res. 78*, 5429 1973.
11. F. Vallee, B. R. Rowe, J. C. Gomet, J. L. Queffelec, and M. Morlais, *Chem. Phys. Letts.*

124, 317 1986.

12. Y. S. Cao and R. Johnsen, *J. Chem. Phys.* **95**, 7356 1991.

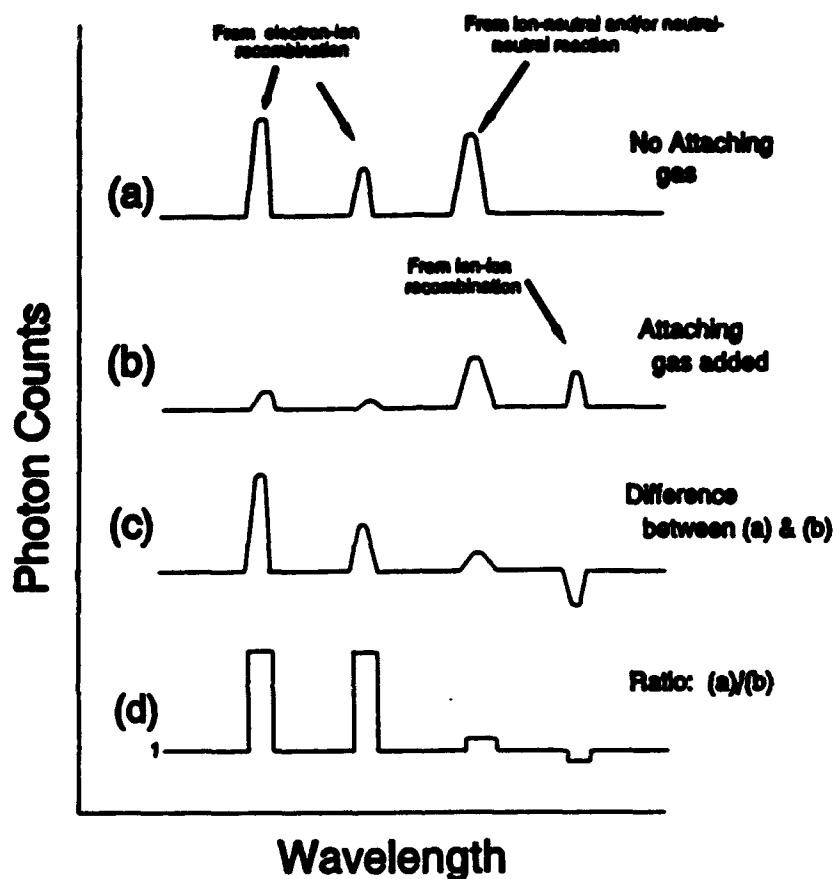13. B. L. Foley, N. G. Adams and H. S. Lee, *J. Phys. Chem.* **97**, 5218 1993.

Fig. 1. Schematic optical spectra to illustrate techniques for identifying emissions due to recombination. The spectra are: a) an origin spectrum with emissions originating from electron-ion recombination, ion-neutral reactions and neutral-neutral reactions; b) a background spectrum in which electron-ion recombination emissions have been greatly reduced by addition of an attaching gas, AB; c) a difference plot, (a - b), exhibiting emissions primarily from recombination; d) a ratio plot ; .., in which the emissions appear as square topped peaks with the height depending on the process giving rise to the emission. For case d) it is essential that the amount of attaching gas added is less than that for complete removal of the recombination emissions.

Fig. 2. Spectral emissions from a recombining N_2OH^+/electron afterglow: a) without, and b) with SF_6 attaching gas added at a level which is not quite sufficient to remove the recombination emissions. c) is the ratio of the plots, a/b, with the magnitudes of the ratios expected for emissions originating from electron-ion recombination (e-i) and ion-neutral plus neutral-neutral (i-n and n-n) reactions indicated. The spectra have been corrected for variations in the optical efficiency of the monochromator and detection system. Note that all emissions are not quenched by the addition of SF_6. Inspection reveals that the OH and NH emissions originate from electron-ion recombination, whereas the N_2O^+ emissions (not from recombination) are from ion-neutral and neutral-neutral reactions. The square topped peaks at wavelengths less that 280 nm show that there are emissions (not visible on the intensity scale of a) and b)) which result from recombination.
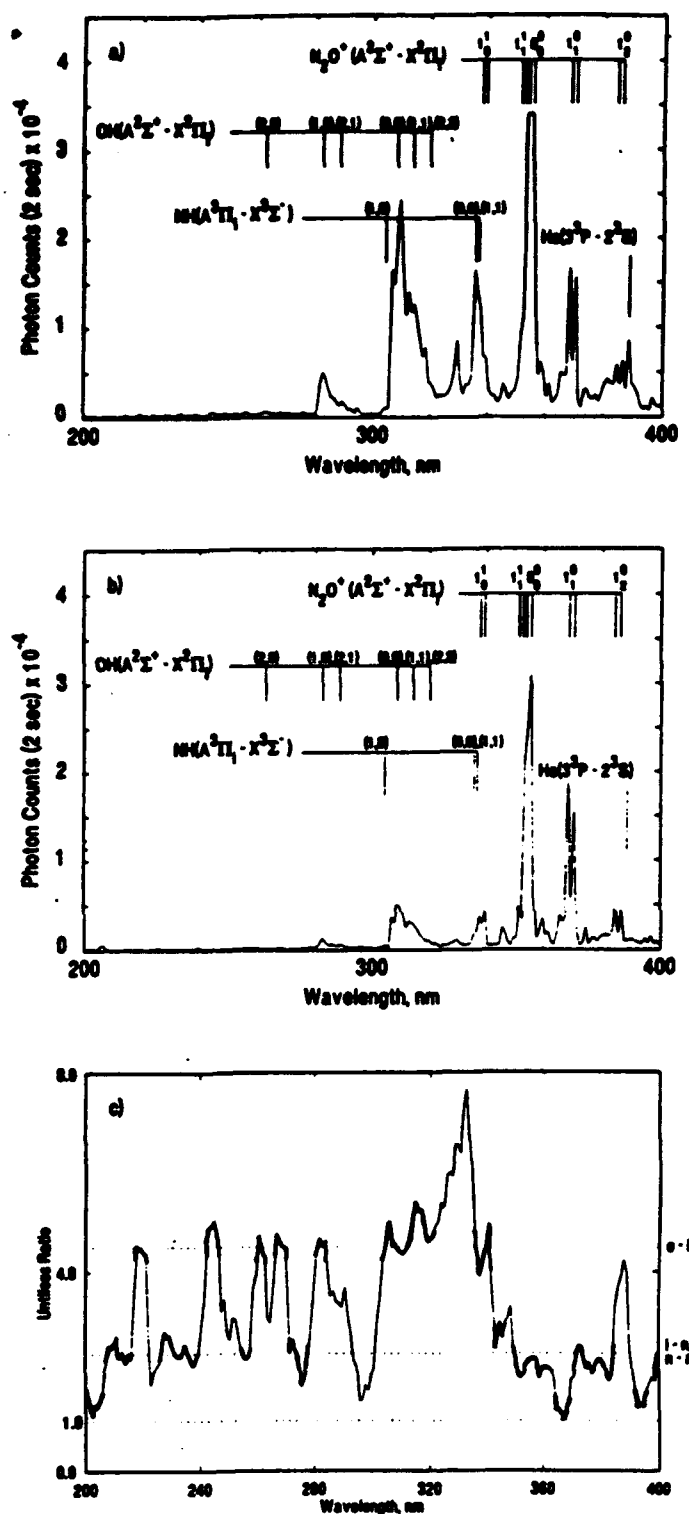
BORON ATOM REACTIONS WITH ACETYLENE. AB INITIO CALCULATED AND OBSERVED ISOTOPIC INFRARED SPECTRA OF THE BORIRENE RADICAL BC$_2$H$_2$. A FINGERPRINT MATCH.

Lester Andrews and Parviz Hassanzadeh
Department of Chemistry
University of Virginia
Charlottesville, VA 22901
and
Jan M. L. Martin and Peter R. Taylor
San Diego Supercomputer Center
P. O. Box 85608
San Diego, CA 92186-9784

ABSTRACT

Pulsed laser evaporated boron atoms react with C$_2$H$_2$ to produce several new organoboron species. The strongest absorption at 1170.6 cm^{-1} in the B-C$_2$ stretching region exhibits ^{10}B, ^{13}C and D shifts for 7 isotopic molecules in agreement with MP2/DZP calculations for a BC$_2$H$_2$ borirene radical species. This agreement provides a "fingerprint" match for identification of the BC$_2$H$_2$ ring species. Calculated bond lengths are appropriate for delocalized bonding in the BC$_2$ ring system.

INTRODUCTION

Boron atom reactions with small molecules such as O$_2$, H$_2$O, N$_2$, CO and CH$_4$ have produced new boron species for matrix infrared spectroscopic characterization.[1-7] The boron-acetylene reaction is of particular interest because theoretical calculations suggest that both C-H insertion and C≡C addition reactions will proceed readily.[8] The addition product borirene radical BC$_2$H$_2$ is expected to be a novel 2π electron aromatic system like predicted for borirene (HBC$_2$H$_2$)[9-11] and observed for substituted borirene species.[12,13] The infrared spectrum and MP2/DZP calculations on the borirene radical will be presented here.

EXPERIMENTAL

Mixtures of argon/acetylene (200/1 to 800/1) were codeposited at 12±1 K with pulsed laser evaporated boron atoms (^{n}B: 80% ^{11}B, 20% ^{10}B and ^{10}B: 94% ^{10}B, 6% ^{11}B) using Q-switched 1064 nm radiation with 40 mJ/pulse at the target as described previously.[1,3] Spectra for reaction of each boron sample with C$_2$H$_2$, ^{13}C$_2$H$_2$ and C$_2$D$_2$ were collected at 0.5 cm^{-1} resolution. Samples were also subjected to UV photolysis and to annealing cycles.

RESULTS AND DISCUSSION

Two spectral regions are of interest: the 2100-1900 cm^{-1} region shows 3 species with strong C=C stretching modes, which will be the subject of a full paper,[14] and the 1200-1100 cm^{-1} region reveals two sharp product absorptions at 1175.3, 1170.6 cm^{-1} (E) and 1122.7 cm^{-1} (F), which will be considered here. The E doublet and F band are decreased 40% by $\lambda > 290$ nm photolysis, and further $\lambda > 254$ nm irradiation almost destroyed the E and F bands. Annealing to 18 ± 1 K to allow diffusion and reaction of trapped boron atoms restored some of the 1170.6 cm^{-1} band, and acetylene absorptions did not change. Further annealing to 28 ± 1 K reproduced the 1170.6 cm^{-1} E band, sharpened the F band, and increased acetylene cluster absorptions.

Isotopic data for the E bands are given in Table I. The 1170.6 cm^{-1} band exhibits 26.4 cm^{-1} boron-10, 22.9 cm^{-1} carbon-13, and 1.2 cm^{-1} deuterium shifts and as such defines a symmetric B-C$_2$ stretching vibration. The natural boron isotopic 4:1 doublet demonstrates the presence of a single boron atom, and the observation of a single mixed carbon-12,13 peak in carbon-13 enriched samples characterizes two equivalent carbon atoms. Species E thus contains one B atom, two equivalent C atoms, and hydrogen.

Calculations were done at the MP2 level with the DZP (double ζ plus polarization) basis set using the GAUSSIAN 92 program. Calculated vibrational frequencies and intensities show that the strong calculated 1214.9 cm^{-1} band dominates the spectrum. Table I also lists the calculated harmonic isotopic fundamentals; multiplying by the average scale factor 0.964 gives calculated bands in agreement within a 1.0 cm^{-1} average for 7 isotopic E band frequencies. (The fit for the 5 hydrogen isotopes with similar anharmonicities is much better.) This excellent agreement between calculated and observed isotopic frequencies confirms the identification of BC$_2$H$_2$. Large basis set coupled cluster calculations[14] predict BC$_2$H$_2$ to be 74 kcal/mol more stable than B+C$_2$H$_2$.

On the other hand, the F bands are assigned to the cyclic HBC$_2$ species; the different 28.7 cm^{-1} boron-10, 16.5 cm^{-1} carbon-13, and 47.0 cm^{-1} deuterium isotopic shifts are matched (±1.7 cm^{-1}) by quantum chemical calculations for HBC$_2$.[14] Calculations for the similar borirene molecule HBC$_2$H$_2$ reveal still different isotopic shifts for the strong B-C$_2$ fundamental calculated at 1215.8 cm^{-1}: 26.3 cm^{-1} boron-10, 22.3 cm^{-1} carbon-13 and 50.2 cm^{-1} deuterium. Clearly, each molecule has a unique arrangement of atoms and unique normal vibrational modes, which can be characterized by *isotopic substitution at all atomic positions*. The important conclusion reached here is that agreement between scaled calculated and observed isotopic frequencies for *one vibrational fundamental with substitution at all atomic positions* constitutes *a fingerprint match* for identification of the molecule, which is demonstrated for BC$_2$H$_2$.

It is clearly seen that the C=C bonds in BC_2H_2 and HBC_2H are longer than in C_2H_4. Likewise the B-C bonds are shorter than typical single bonds (1.558 Å in $B(C_2H_5)_3$).[13] Similar evidence has been offered to support delocalization of the two pi electrons over the 3-membered ring and aromatic character for the BC_2 ring in trimesitylborirene.[12,13] Furthermore, the BC_2 rings in BC_2H_2 and HBC_2H_2 are seen to be virtually identical. Thus, the sigma radical site in BC_2H_2 has no effect on the delocalized bonding in the BC_2 ring.

The photolysis of BC_2H_2 at 254-290 nm indicates a strong absorption band in this region, in agreement with trimesitylborirene.[13] The photolysis behavior also provides evidence for delocalized bonding as acetylene and ethylene absorb at shorter wavelengths.

The appearance of BC_2H_2 on diffusion and reaction of B atoms at 17 K in solid argon follows similar behavior for BO_2.[1] These reactions proceed without activation energy. The BC_2H_2 radical is the simplest borirene species yet observed and characterized. Further studies are in progress in this laboratory to prepare substituted borirene radicals.

ACKNOWLEDGEMENT

REFERENCES

1.   T. R. Burkholder and L. Andrews, *J. Chem. Phys.* 95, 8697 (1991).
2.   L. Andrews and T. R. Burkholder, *J. Phys. Chem.* 95, 8554 (1991).
3.   P. Hassanzadeh and L. Andrews, *J. Phys. Chem.* 96, 9177 (1992).
4.   Y. M. Hamrick, R. J. Van Zee, J. T. Godbout, W. Weltner, Jr., W. J. Lauderdale, J. F. Stanton, and R. J. Bartlett, *J. Phys. Chem.* 95, 2840, 5366 (1991).
5.   T. R. Burkholder and L. Andrews, *J. Phys. Chem.* 96, 10195 (1992).
6.   G. H. Jeong, R. Boucher, and K. L. Klabunde, *J. Am. Chem. Soc.* 112, 3332 (1990).
7.   P. Hassanzadeh and L. Andrews *J. Am. Chem. Soc.* 114, 9239 1992.
8.   J. R. Flores and A. Largo, *J. Phys. Chem.* 96, 3015 (1992).
9.   K. Krogh-Jespersen, D. Cremer, J. D. Dill, J. A. Pople, and P. v. R. Schleyer, *J. Am. Chem. Soc.*, 103, 2539 (1981).
10.   P. H. M. Budzelaar, S. M. van der Kerk, K. Krogh-Jespersen, and P. v. R. Schleyer, *J. Am. Chem. Soc.* 108, 3960 (1986).
11.   Y.-G. Byun, S. Saebo, and C. U. Pittman, Jr. *J. Am. Chem. Soc.* 113, 3689 (1991).
12.   J. J. Eisch, B. Shafii, and A. L. Rheingold *J. Am. Chem. Soc.* 109, 2526 (1987).

13. J. J. Eisch, B. Shafii, J. D. Odom, and A. L. Rheingold, *J. Am. Chem. Soc.* 112, 1847 (1990).
14. L. Andrews, P. Hassanzadeh, J. M. L. Martin, and P. R. Taylor, *J. Phys. Chem.*, to be published.

Table I. Calculated and observed isotopic frequencies (cm^{-1}) for the strongest E band.

	$^{11}B^{12}C_2H_2$	$^{10}B^{12}C_2H_2$	$^{11}B^{12}C^{13}CH_2$	$^{11}B^{13}C_2H_2$
v(B-C$_2$)obs	1170.6	1197.4	1161.9	1147.3
v(B-C$_2$)calc	1214.9	1242.8	1206.3	1190.8
v(scaled 0.964)	1171.2	1198.1	1162.8	1147.9
Δ(obs-scaled)	-0.6	-0.7	-0.9	-0.6

Table I. continued

	$^{10}B^{13}CH_2$	$^{11}B^{12}C_2D_2$	$^{10}B^{12}C_2D_2$
	1172.0	1169.4	1196.0
	1216.4	1211.0	1239.2
	1172.6	1167.4	1194.6
	-0.6	2.0	1.4

MCD SPECTROSCOPY OF LASER ABLATED ALKALI METALS IN MIXED RARE GAS MATRICES

Robert A. Corbin
John W. Kenney, III

Chemical Physics Laboratory
Department of Physical Sciences-Chemistry
Eastern New Mexico University
Portales, New Mexico 88130

Introduction:

The sharp $^2S \rightarrow {}^2P$ ($ns^1 \rightarrow np^1$) atomic transition of a gas phase alkali metal emerges as one or more broad "triplets" when the alkali metal is trapped in a solid rare gas matrix of Ar, Kr, or Xe.[1] Laser ablation studies by Fajardo et al. have demonstrated that the triplet absorption pattern blue shifts as the alkali metal atoms are deposited in progressively tighter trapping sites in the rare gas matrix.[2] Moreover, Fajardo and Corbin recently discovered that this triplet structure persists even when the alkali metal atoms are deposited by laser ablation into mixed rare gas solid matrices comprised of Ar and Xe in varying proportions.[3]

MCD Spectra of Li/Rg:Rg' Systems Prepared by Laser Ablation

This study represents an extension of the MCD technique into an area of virtually untrammeled spectroscopic ground where the laser ablation technique is used for metal atom deposition onto mixed rare gas matrices. All of the published MCD studies are on metal/pure rare gas systems in which the Knudsen effusion technique was used to generate the metal atom vapors.[4] Only red triplet sites in M/Rg systems have been investigated in detail. The UV-visible and MCD studies we report below utilize the laser ablation technique (308 nm excimer pulses) to generate metal atom vapors. Matrices were deposited on at $0°$ sapphire window held at cryogenic temperatures (~13-20 K) in a closed-cycle liquid He refrigerator. MCD spectra were detected by the standard photoelastic modulator/lock-in amplifier technique. All MCD spectra are repeatedly reproducible, change sign when magnet polarity is reversed, and disappear when the magnet is turned off.

Li/Xe: Fajardo et al. showed that the UV-visible spectra of Li/Xe generated by laser ablation and by the Knudsen oven method are identical.[2] In this particular system, the excess kinetic energy afforded by laser ablation does not force the metal atoms into a tighter binding sites in the Xe matrix. As such, Li/Xe provides a convenient benchmark for our MCD studies since we

can compare our MCD spectra directly to the Schatz et al. MCD spectra for this particular system. In Figure 1, we present our UV-visible and MCD spectra of Li/Xe generated by the laser ablation technique. Both the UV-visible and MCD spectra are virtually identical to the UV-visible and MCD spectra reported by Schatz et al.[4] in the ~15-20 K temperature range. These results give us confidence that our magnet, cryostat, and circular dichroism detection instrumentation are indeed working properly.

Li/Ar: In Figure 2, we present UV-visible and MCD spectra of Li/Ar prepared by laser ablation. The three lowest peaks in the UV-visible transmission spectrum in the 600-650 nm region correspond to the Li/Ar blue triplet previously reported by Fajardo et al.[2] The corresponding MCD spectrum in Figure 2, comprised of two up peaks and one down peak in the 600-650 nm region, represents a distinctly different MCD pattern than found in Li/Xe. Interestingly enough, this MCD pattern is somewhat like the pattern found in the Schatz et al. MCD spectrum of Li/Ar generated by the Knudsen oven technique.[4] The Schatz et al. UV-visible spectrum of the Li/Ar sample clearly shows it to be a mixture of red and blue triplet sites. Schatz et al. did not subject their Li/Ar spectra to detailed analysis because they realized that they were dealing with more than one Li/Ar site. Here we see clearly the significant advantage of the laser ablation technique in allowing us to control access to red or blue triplet sites by adjusting laser power, repetition rate, and matrix gas deposition rate. Even though the particular Li/Ar matrix represented in Figure 2 is not a pure blue triplet matrix, it represents a significant enhancement of Li/Ar blue triplet sites over the percentage of blue sites available to Schatz et al. using Knudsen oven generated matrices. We certainly have the potential to do much better than we have done in Figure 2 in producing pure blue triplets in Li/Ar.

Li/Ar;Xe: In Figures 3 and 4, we present the UV-visible and MCD spectra of Li atoms deposited in mixed Ar;Xe matrices with two different Ar;Xe ratios. In Figure 3, a 50% Ar;50% Xe mixture, we see an exceedingly broad triplet in the UV-visible spectrum in the 630-700 nm region. The corresponding MCD spectrum is comprised of one up peak and two down peaks analogous to the Li/Xe MCD spectrum shown in Figure 1. In Figure 4, a 90% Ar;10% Xe mixture, the MCD spectrum consists of two up peaks and one down peak in the 625-675 nm region. This pattern is analogous to the Li/Ar MCD pattern shown in Figure 2. The Li/Ar;Xe MCD spectra have the same overall structure as the pure Li/Ar and pure Li/Xe MCD spectra but stretch out over a greater spectral range along with their corresponding UV-visible spectra. The MCD activity of the triplet is definitely preserved in these M/Rg;Rg' systems. The MCD pattern of one up peak and two down peaks (pure Li/Xe, Figure 1) persists even up to a Li/50% Ar;50% Xe mixture (Figure 2). However, the MCD pattern of two up peaks and one down peak in pure Li/Ar

(Figure 2) is preserved in Li/90% Ar;10% Xe (Figure 4). These results suggest that the gross MCD pattern may, with further refinements, be able to serve as a simple diagnostic that can be used to tell us what kinds of sites are present in a given M/Rg system.
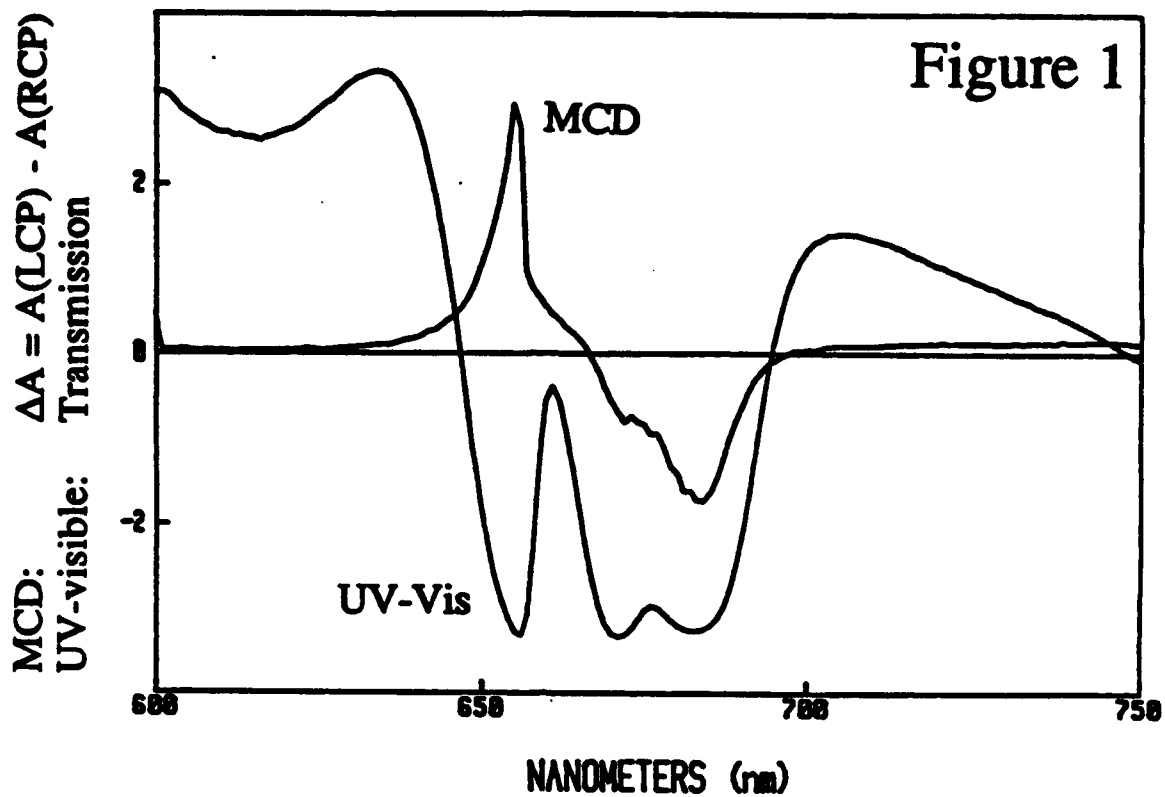
---

[1]Andrews, L.; Pimentel, G. C. *J. Chem. Phys.* 1967, 47, 2905-2910.

[2]Fajardo, M. E.; Carrick, P.; Kenney, J. W., III *J. Chem. Phys.* 1991, 94, 5812.
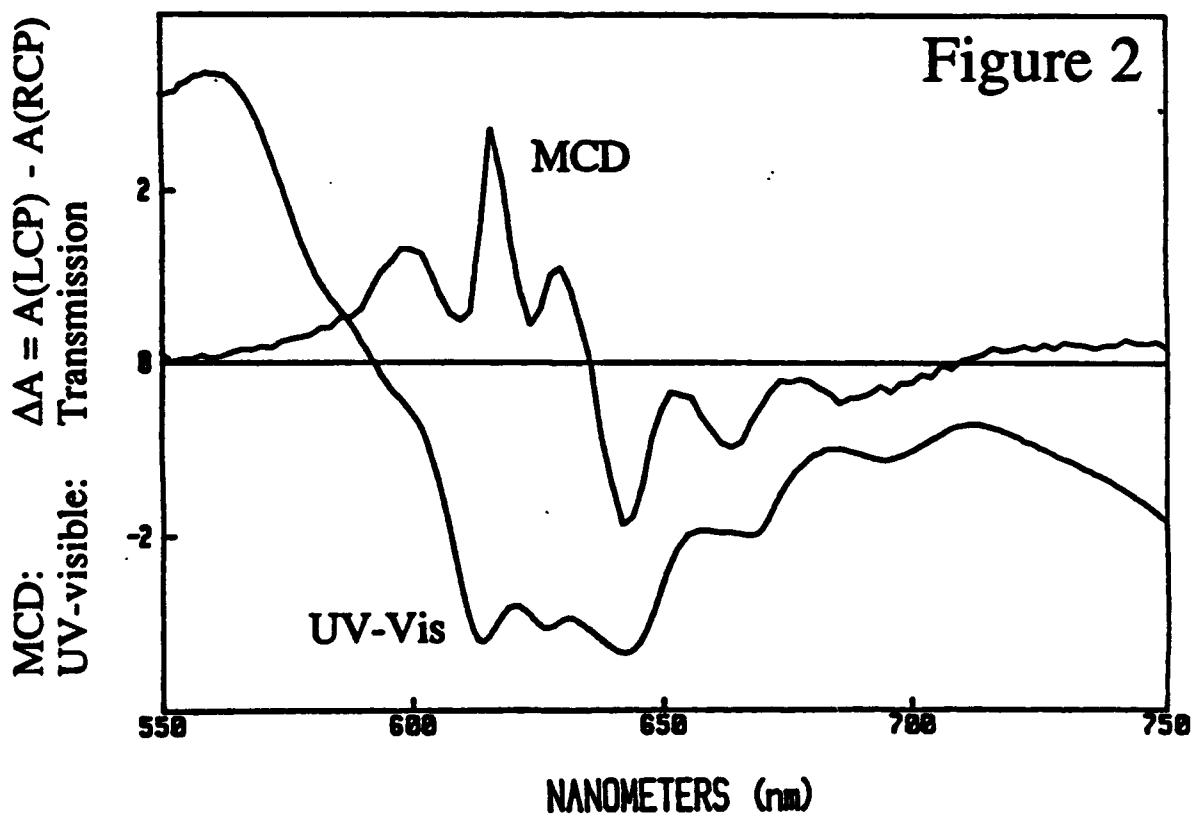
[3] Fajardo, M. E.; Corbin, R. A., to be published.

[4] (a) Lund, P.A.; Smith, D.; Jacobs, S. M.; Schatz, P. N. *J. Phys. Chem.* 1984, 88, 31-42. (b) Rose, J.; Smith, D.; Williamson, B. E.; Schatz, P. N. *J. Phys. Chem.* 1986, 90, 2608-2615. (c) Samet, C.; Rose, J. L.; Williamson, B. E.; Schatz, P. N. *Chem. Phys. Lett.* 1987, 142, 557-561.
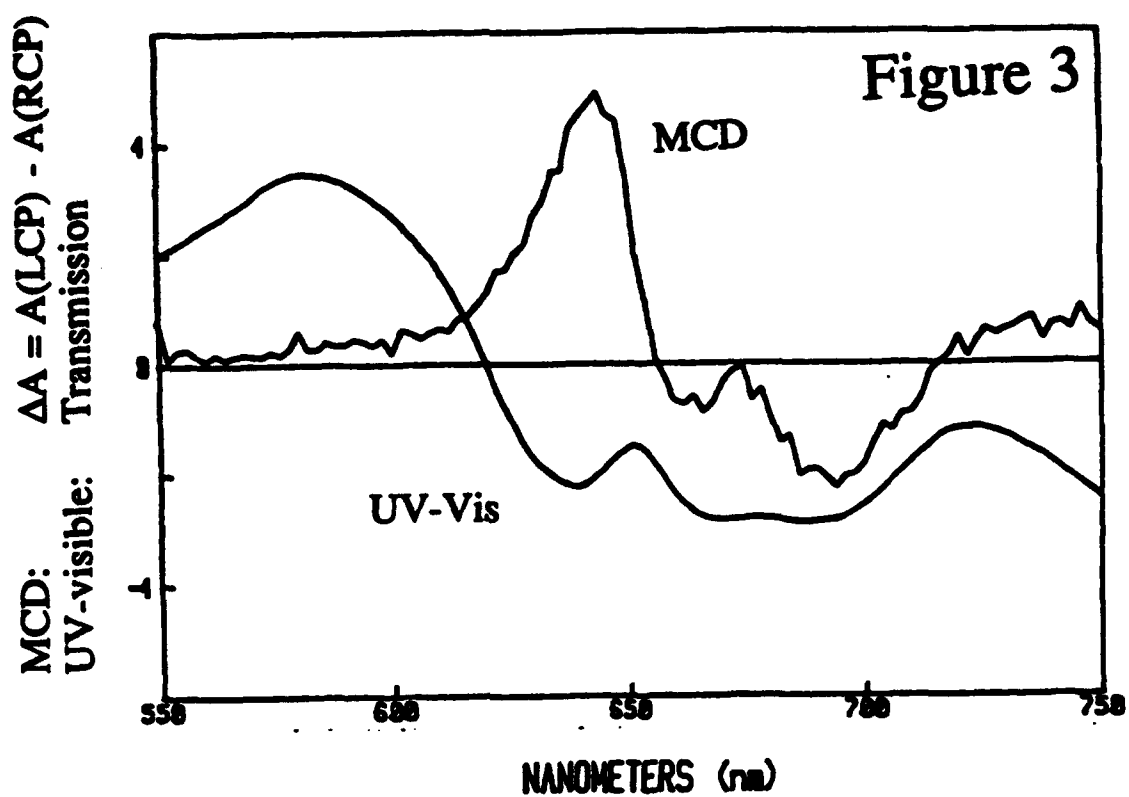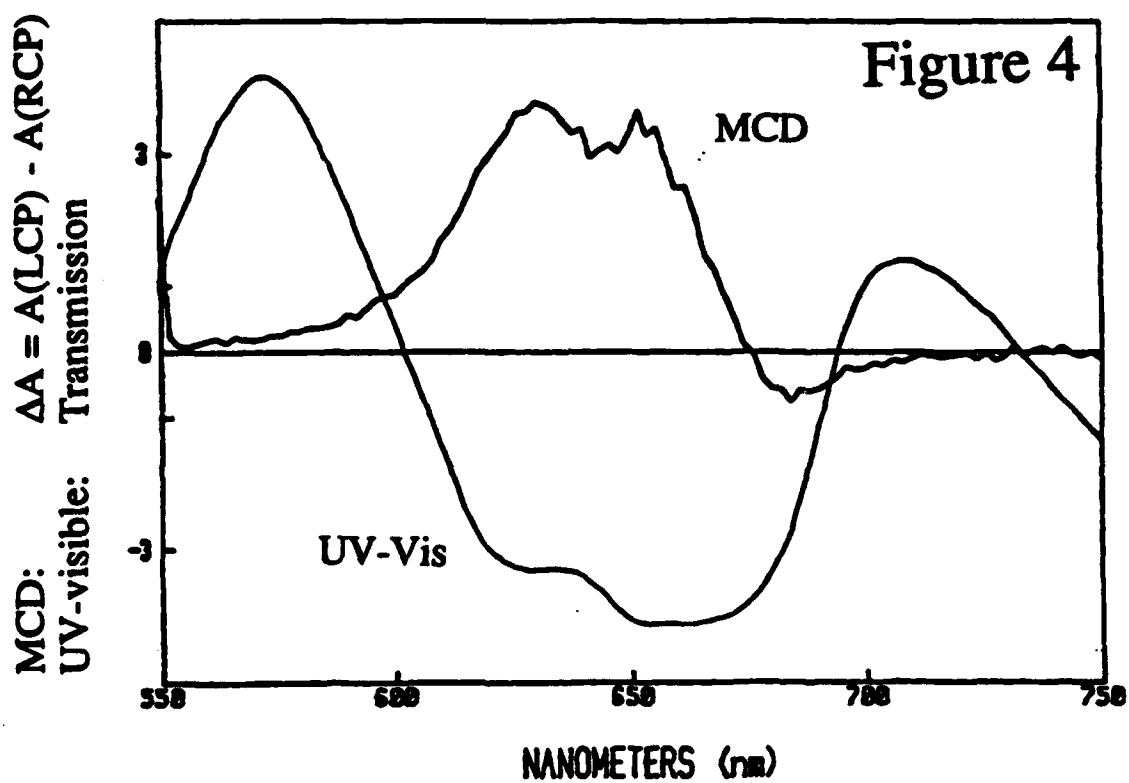
Li/0%Ar;100%Xe

Figure 1

Li/100%Ar;0%Xe

Figure 2

Li/50%Ar;50%Xe

Figure 3

MCD

UV-Vis

Li/90%Ar;10%Xe

Figure 4

MCD

UV-Vis

436

Ion Chemistry of Boron Hydride Species:

Small and Large

Robert Damrauer , Michele Krempp, Martin Stephan, and Veronica. M. Bierbaum

Chemistry Departments, University of Colorado in Denver and Boulder, Colorado

Many insights into the chemical bonding of boron hydrides have resulted from structure and reactivity studies over the last eighty years. Much of the initial practical interest in such boranes arose in evaluating their potential as rocket propellants. More recently, the use of other boron compounds to protect high-performance carbon-carbon composites has helped reinvigorate boron chemistry.

Despite such activities, no comprehensive effort to study the gas phase ion chemistry of boron-containing anions has been reported. We have undertaken such an investigation using tandem selected ion flowing afterglow techniques. Our initial efforts are based on observations that a complex array of boron hydride anions can be prepared by reaction of B_2H_6 with either HO^- or H_2N^- in the source region of our tandem flowing afterglow instrument. Subsequent mass selection of various boron hydride anions allows further study. Some of these anions exhibit unusual reaction chemistry and collision-induced dissociation (CID) behavior. One particularly important aspect of such studies is that they often allow indirect probing of unusual oxidation states of the neutral molecules related to the anions under study.

This poster will focus on the preparation and reactivity studies of boron hydride anions, both large and small. It will report on detailed studies of the reaction chemistry of $B_2H_3{}^-$ as well as various aspects of the CID and reaction chemistry of larger anions.

LOW TEMPERATURE THERMAL DECOMPOSITION OF NH₄N(NO₂)₂ - THE IR MATRIX ISOLATION SPECTRUM AND UV PHOTOLYSIS OF HN(NO₂)₂

A. J. Tulis and A. Snelson, IIT Research Institute, Chicago, IL 60616

D. Patel, Belvoir RD&E Center, Fort Belvoir, VA 22060

Abstract

The vapor species over ammonium dinitramide heated in a Teflon Knudsen cell (55-110°C) have been examined using IR matrix (argon) isolation spectroscopy. Some twenty-two "unknown" absorption bands were identified in the matrix spectra that appeared to be associated with a single trapped species, most likely hydrogen dinitramide $HN(NO_2)_2$. UV irradiation of the unknown absorption bands resulted in their disappearance, and the appearance of new absorptions bands assignable to trans-HNO_2, N_2O, NO and $(NO)_2$. A tentative assignment of the 22 "unknown" vibrational frequencies to $HN(NO_2)_2$ has been made assuming C_s symmetry (18 IR active frequencies) and is in reasonable agreement with a recent theoretical calculation of these vibration frequencies by Michels et al.[1] No evidence was obtained in this study for the existence of structural isomers of hydrogen dinitramide, notably the aci-form $N(NO_2)(NOOH)$, which recent theoretical calculations[1] suggest is only slightly less stable than the secondary amine structure.

Ammonium Dinitramide $NH_4N(NO_2)_2$ - An Energetic Oxidizer

$$\Delta H^\circ_f\ (298K)\ =\ -36\ kcal\ mol^{-1},\ Density\ 1.8\ g\ cm^{-3},\ Mp \approx 95°C$$

Potential replacement for ammonium perchlorate in rocket motors. Eliminates environmentally undesirable plume of HCl.

Objective of Study

(1) Characterize the low temperature vaporization behavior of $NH_4N(NO_2)_2$.
(2) Determine if parent acid hydrogen dinitramide, $HN(NO_2)_2$, exists.
(3) Obtain evidence for existence of isomers of hydrogen dinitramide.

Theoretical Studies on Hydrogen Dinitramide

Ab initio calculations by Michels and Montgomery have identified five stable isomers of hydrogen dinitramide:
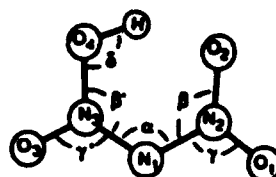
---

[1] H. H. Michels and J. A. Montgomery, Jr. Preprint of paper to appear in J. Physical Chemistry, June, 1993.

- The most stable has secondary amine structure, $HN(NO_2)_2$, ΔH°_f (O K) = 28.4 kcal mol^{-1}.

- The remaining four isomers have acid structures $N(NO_2)(NOOH)$ some 7.9-9.7 kcal mol^{-1} less stable than the secondary amine isomer.

- Vibration frequencies of amine and acid isomers were calculated.

Secondary Amine and Acid Structures of Hydrogen Dinitramide
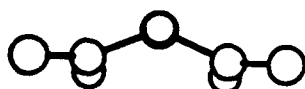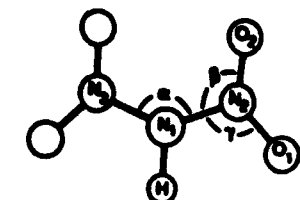
Secondary amine-form	Aci-form
Non-Planar (C_s) 18 IR Active Frequencies	Planar (C_s) 18 IR Active Frequencies
Planar (C_{2v}) 16 IR Active Frequencies	Non Planar (C_1) 18 IR Active Frequencies

IR Matrix Studies on $NH_4N(NO_2)_2$

1. Samples of $NH_4N(NO_2)_2$ obtained from SRI and Thiokol Corporation. Stated purities >99%.

2. Samples vaporized from all Teflon Knudsen cells:

   - Vaporization temperature 55-110°C

   - Argon matrices formed at 10K over periods of 2-40 hours.

   - Argon matrix spectra of NH_3, HNO_3, NO, NO_2, N_2O and cis and trans HNO_2 recorded under conditions of good isolation for comparison purposes.

   - Matrices containing $NH_4N(NO_2)_2$ vaporization products irradiated in UV (medium pressure Hg Arc) and visible (1,000 W tungsten lamp).

   - IR spectra obtained in the 4,000-200 cm^{-1} range.

Vaporization Behavior of NH₄N(NO₂)₂ Based on Matrix Studies

In the temperature range investigated:

(1)   NH$_3$ and HNO$_3$ were always present as major vaporization products.

(2)   N$_2$O was found at levels varying from almost non-existent to major.

(3)   Absorption bands not attributable to any "known" molecular specie(s) were present that varied in intensity from almost non-existent to major.

(4)   Relative amounts of the above species in the vaporization products were highly variable and not related to the temperature of vaporization. Attempts to purify the NH$_4$N(NO$_2$)$_2$ by recrystallization did not stabilize the vaporization product distribution. Both samples (SRI and Thiokol) of NH$_4$N(NO$_2$)$_2$ showed the same erratic vaporization behavior.

(5)   Stabilization of the product distribution over NH$_4$N(NO$_2$)$_2$ was finally achieved by prolonged heating in which approximately 50% of the sample was vaporized from the Knudsen cell.

(6)   After stabilitization of NH$_4$N(NO$_2$)$_2$ sample's vaporization behavior:

   (a)   NH$_3$ and HNO$_3$ were always present as major vaporization products.

   (b)   The amounts of N$_2$O and the unknown molecular specie(s) in the vaporization products appeared to increase with temperature, becoming comparable to those of HNO$_3$ and NH$_3$ at the high end of the temperature range studied.

IR Matrix Spectra of the NH₄N(NO₂)₂ Vaporization products

(1)   Typical spectra of as deposited NH$_4$N(NO$_2$)$_2$ vaporization products are shown in Figure 1 (Curves [a] and [b]). "Unknown" absorption bands are indicated by (X).

(2)   Spectra resulting from the UV photolysis of the as "deposited" NH$_4$N(NO$_2$)$_2$ are shown in Figures 1 (Curve [c]) and 2.

(3)   A spectrum of ammonium nitrate vaporization products (HNO$_3$ and NH$_3$) are shown in Figure 1 (Curve [d]) for references purposes.

(4)   Some 22 "unknown" absorption bands are identified in the spectra shown in Figure 1. Qualitatively:

(a) These absorption bands always appeared with similar relative intensities to each other regardless of vaporization temperature.

(b) UV photolysis of matrices containing the "unknown" absorption bands resulted in their "bleaching out" at a uniform rate (Figures 1 and 2).

Tentative Assignment of IR Spectrum to $HN(NO_2)_2$

The above behavior suggests that the "unknown" absorption bands may be reasonably attributed to a single molecular species, most probably hydrogen dinitramide. Frequencies of the "unknown" absorption bands are shown in Table 1, together with a tentative partial vibrational mode assignment to $HN(NO_2)_2$. The amine structure is suggested based solely on the magnitude of the hydrogen stretching frequency appearing at 3341 cm^{-1} which is characteristic of an N-H stretching mode. Frequencies for N-H stretching modes are found at 3359, 3478, 3350 and 3290 cm^{-1} in NH_2NO_2 and NH_2OH, respectively.

If hydrogen dinitramide was present with the acid structure, an O-H stretching mode might be expected to appear at a frequency >3500 cm^{-1} based on values of 3635 and 3570 cm^{-1} found in NH_2OH and $t-HNO_2$, respectively, though the latter are probably poor analogues for the aci-structure of $N(NO_2)NOOH$.
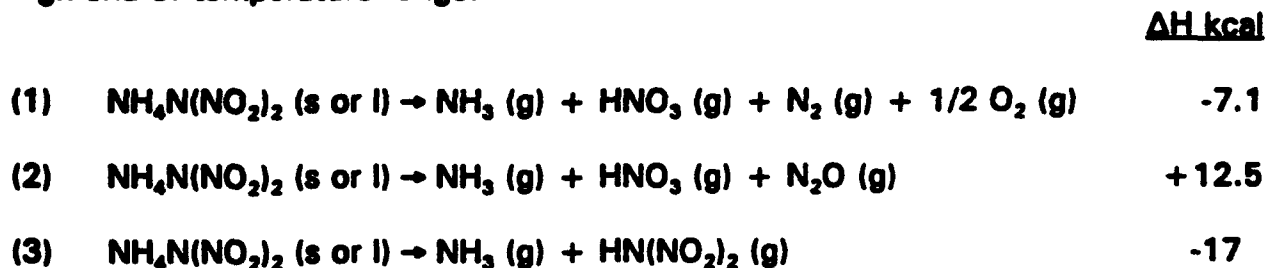
Data are presented in Table 2 allowing comparison of the observed hydrogen dinitramide frequencies with those values calculated for the amine and aci forms (H. H. Michels et al.). The overall "fit" between the observed and calculated frequencies for the amine and aci forms is equally good. The calculated frequency for the O-H stretching mode of the aci-form of hydrogen dinitramide is substantially lower than that observed experimentally and attributed in this study to the amine isomer $HN(NO_2)_2$, possibly lending some support to the current assignment.

Identification of UV Photolysis Products of $HN(NO_2)_2$

Data are provided in Table 3 to support the conclusion that UV photolysis of hydrogen dinitramide results in the formation of trans-nitrous acid, nitrous oxide, nitric oxide monomers and dimers. The form of the spectra suggest that matrix cage effects perturb the vibrational levels of the trapped photolysis products, particularly $t-HNO_2$ and $NO/(NO)_2$. There were no indications that NO_2, HNO, cis-HNO_2 or isomeric forms of hydrogen dinitramide, namely $N(NO_2)NOOH$, were formed as a result of UV or visible photolysis of $HN(NO_2)_2$.

Conclusions

After stabilization of the sample, $NH_4N(NO_2)_2$ appears to vaporize according to equations shown below in the temperature range 55-110°C. At lower temperatures, process (1) is favored with processes (2) and (3) becoming of equal importance at the high end of temperature range.

$$\underline{\Delta H \; kcal}$$

(1) $NH_4N(NO_2)_2$ (s or l) → NH_3 (g) + HNO_3 (g) + N_2 (g) + $1/2$ O_2 (g)   -7.1

(2) $NH_4N(NO_2)_2$ (s or l) → NH_3 (g) + HNO_3 (g) + N_2O (g)   +12.5

(3) $NH_4N(NO_2)_2$ (s or l) → NH_3 (g) + $HN(NO_2)_2$ (g)   -17

In the IR matrix spectra of the vaporization products over $NH_4N(NO_2)_2$, twenty-two absorption bands have been identified that may reasonably be assigned to a single vaporizing species, namely, $HN(NO_2)_2$, having a secondary amine structure.

No evidence was found for the existence of structural isomers of hydrogen dinitramide, specifically $N(NO_2)(NOOH)$.

Further matrix studies using isotopically substituted ammonium nitramide precursors could lead to a definitive characterization of $HN(NO_2)_2$. The dissociation mechanism of $HN(NO_2)_2$ and possible existence of structural isomers of hydrogen dinitramide could be investigated by superheating the vapor species over $NH_4N(NO_2)_2$.

TABLE 1. TENTATIVE VIBRATIONAL ASSIGNMENT FOR THE IR MATRIX ABSORPTION FREQUENCIES ATTRIBUTED TO HYDROGEN DINITRAMIDE, HN(NO₂)₂

Frequency, cm⁻¹	Apparent Intensity	Mode[a] Assignment	Frequency, cm⁻¹	Apparent Intensity	Mode Assignment
3347	s	N-H (str)	1194	vw	?
2933	vw	3347 · 400	1158	vw	400 + 790
2966	vw	1670 + 1218	1047	vw	1670 · 623
2674	vw	1282 + 1324	1012	m	N-N(str)
1670	vs	NO₂ (a-str)	946[b] 930	vs	NO₂ (bend)
1666	vw	1282 + 400	820[b] 818	s	NO₂ (bend)
1648	m	NO₂ (a-str)	790[b] 778	m	
1324	w	N-N (bend)	730	w	
1282[b] 1248	vs	NO₂ (s-str)	714	w	
1218	w	NO₂ (s-str)	623	m	
			618	ms	
			400	m	Probable Fundamental Modes Not Assigned

[a] Combination and difference modes as indicated.
[b] Shoulder.

TABLE 2. CALCULATED[a] HARMONIC FREQUENCIES (cm⁻¹) AND IR INTENSITIES[b] FOR HN(NO₂)₂ AND NH(NO₂)₂ AND ASSIGNED EXPERIMENTAL VALUES FROM THIS STUDY

Mode	HN(NO₂)₂ Calculated		Experimental Values		HN(NO₂)₂ Calculated	
	Frequency (Int)		Frequency (Int)	Mode	Frequency (Int)
ν₁ (A')	36 (6)		-	A'	67 (9)
ν₂ (A')	110 (11)		-	A'	169 (3)
ν₃ (A')	283 (3)		-	A'	342 (39)
ν₄ (A')	428 (3)		400 (63)	A'	440 (19)
ν₅ (A')	463 (1)		618 (78)	A'	601 (9)
ν₆ (A')	647 (69)		632 (47)	A'	718 (9)
ν₇ (A')	757 (78)		714 (9)	A'	749 (29)
ν₈ (A')	774 (2)		730 (9)	A'	767 (96)
ν₉ (A')	812 (1129)		778 (67)	A'	962 (1112)
ν₁₀ (A')	949 (89)		818 (129)	A'	819 (37)
ν₁₁ (A')	1037 (126)		960 (439)	A'	934 (39)
ν₁₂ (A')	1046 (269)		1012 (49)	A'	1094 (22)
ν₁₃ (A')	1362 (509)		1218 (49)	A'	1144 (953)
ν₁₄ (A')	1412 (334)		1249 (943)	A'	1370 (218)
ν₁₅ (A')	1442 (29)		1304 (34)	A'	1664 (280)
ν₁₆ (A')	1711 (1146)		1648 (82)	A'	1663 (1000)
ν₁₇ (A')	1789 (1000)		1670 (1000)	A'	1778 (304)
ν₁₈ (A')	3419 (1134)		3347 (166)	A'	3035 (941)

[a] Data provided by H. H. Michels et al.[20] from ab initio calculations (HF/6-31 G**) at level of theory[20] on two structural isomers of hydrogen dinitramide. The computed frequencies are scaled by a factor of 0.8929 to better reflect experimental values.[20]

[b] Intensities are reported relative to the strongest absorption band for each species having an arbitrarily assigned value of 1,000.
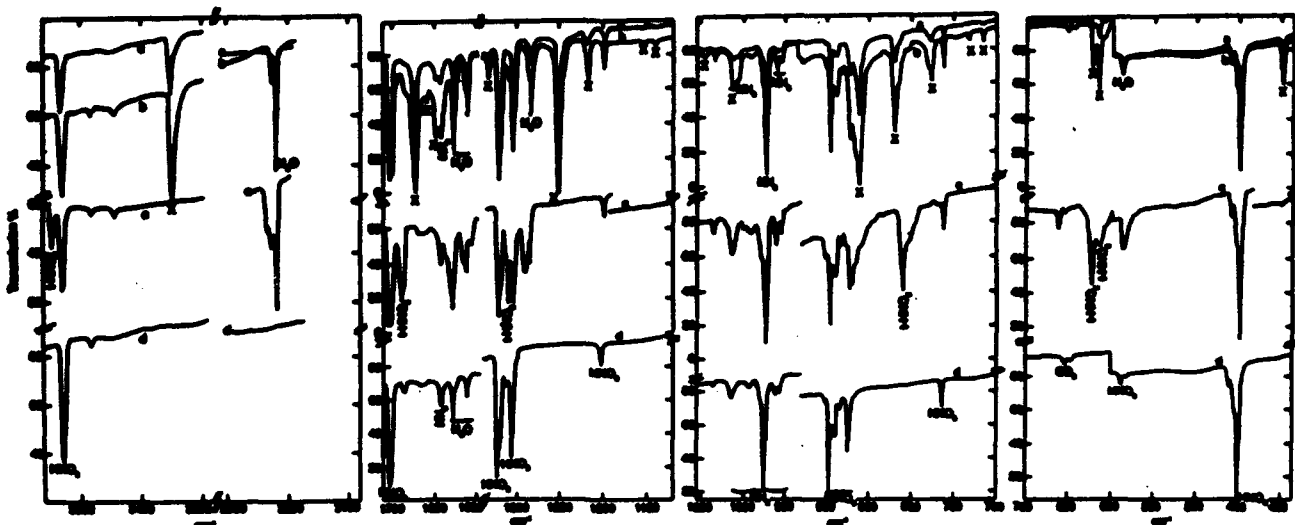
TABLE 3. FREQUENCIES AND ASSIGNMENTS FOR ABSORPTION BANDS THAT APPEAR ON UV IRRADIATION OF MATRICES CONTAINING VAPORIZATION PRODUCTS FROM NH₄N(NO₂)₂

Frequency, cm⁻¹[a]	Species Assignment	Frequency, cm⁻¹	Species Assignment
3346 (m)[a]	t-HNO₂ (3570)[d]	1312 (m)	t-HNO₂ (1326)[d]
2227 (m) 2220 (m)	N₂O (2219)[d]	1290 (m)	N₂O (1285)[d]
1904 (m) 1881 (m) 1873 (m) 1849 (m)	NO (1700)[c]	908 (s) 906 (s)	t-HNO₂ (1796)[d]
1202 (s)	(NO)₂ (1866)[c]	880 (w)	t-HNO₂ (993)[d]
1789 (s)	(NO)₂ (1776)[c]	820 (s)	t-HNO₂ (517)[d]
1764 (m)		812 (m)	
1724 (m)		986 (m) 982 (m)	N₂O (1866)[d]
1696 (s) 1653 (m)	t-HNO₂ (1690)[d]		

[a] Approximate intensity.
[b] As matrix frequencies recorded in this study under conditions of good isolation.
[c] Frequencies reported in literature for species isolated in Ar matrix.[n]

443

Figure 1. Argon matrix IR spectra of vaporization products over $NH_4N(NO_2)_2$ heated at 102°C. Curve (a) 1.5 hrs deposition; curve (b) 5.25 hrs deposition; curve (c) matrix in (b) photolyzed for 1 hr with Hg arc lamp; and curve (d) Argon matrix IR spectrum of vapor species above NH_4NO_3 heated at 80°C and deposited for 2.8 hrs.
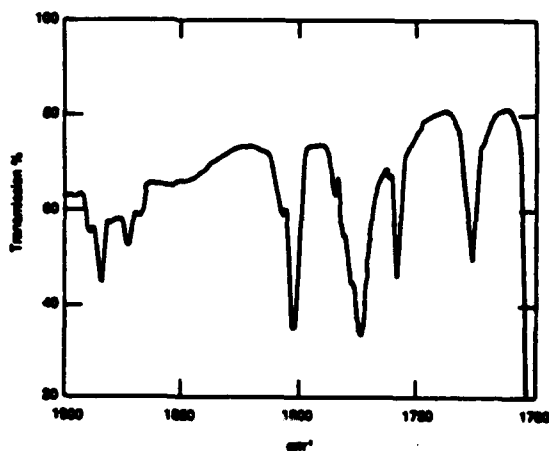

Figure 2. Argon matrix IR spectra showing absorption bands that appear (1900-1700 cm⁻¹) on UV photolysis of a matrix containing isolated vaporization products over $NH_4N(NO_2)_2$ heated at 102°C and deposited for 5.25 hrs.

444

1+1 Resonant Multiphoton Ionization of HI Through the First UV Continuum

Mark A. Young

Department of Chemistry
University of Iowa
Iowa City, IA 52242

Introduction

Resonance enhancement of multiphoton ionization (MPI) results when the energy of one, or more, of the incident photons matches that of an intermediate level in the system under study. An interesting situation is encountered in a molecule if the intermediate state is purely repulsive in nature, engendering rapid dissociation. We have studied such a process in the hydrogen halide, HI, by employing a 1+1 MPI process that is one-photon resonant with the first ultraviolet continuum. The structureless continuum absorption, due to a $n \rightarrow \sigma^*$ transition, begins near 300 nm and has a maximum at 220 nm. The accessible states that comprise the continuum are known to be repulsive and a diagram of the relevant potential energy curves is shown in Figure 1. Despite the fast photodissociation which occurs, we are still able to observe the parent ion, HI^+, using conventional nanosecond laser sources. Sharp features in the wavelength resolved spectrum of HI^+ are recorded and are assigned to two-photon transitions to autoionizing Rydberg states with a finite lifetime. Differences in the two-photon spectra compared to data obtained by single-photon VUV photoionization have been noted. A simple kinetic analysis of the data can be employed to illuminate the mechanism of ionization and to explain the observed laser flux dependence of the parent ion signal.
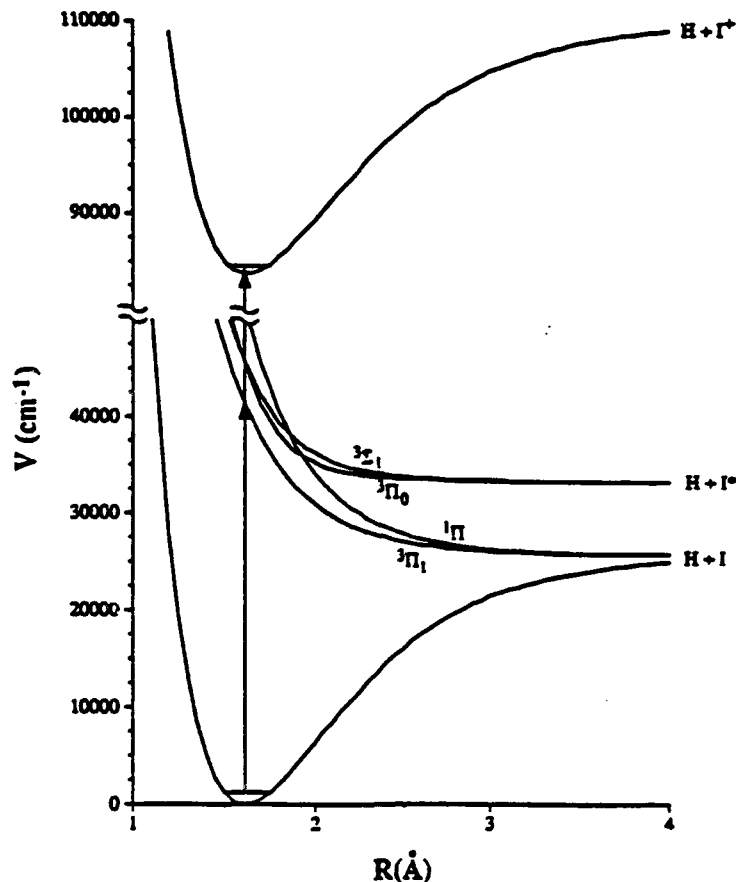

Figure 1.

An analogous situation has been addressed by various investigations of MPI in the polyatomic species, CH_3I. Bernstein and co-workers[1] studied methyl iodide using a 2+1 REMPI process resonant with the dissociative $\tilde{A}$ state continuum. Excitation with several millijoules of radiation from a nanosecond laser yielded no parent ion, CH_3I^+, while fragment ions, I^+ and CH_3^+, were readily observed. Danon et. al.[2] excited a sample of CD_3I prepared by expansion of the neat gas from a narrow bore capillary using a similar laser source. In contrast to the previous results, CD_3I^+ was observed with a quadratic intensity dependence which decreased as higher intensities were used. It was proposed[3] that the discrepancy in these results was due to the sample conditions employed by Danon et. al. which may have promoted the formation of clustered species. The formation of the parent ion was thought to be facilitated by cluster induced caging which inhibits the dissociation of the initially excited molecule.

Experimental

Samples of hydrogen iodide and helium carrier gas were expanded at pressures of 1-40 psig through a commercial pulsed valve. The supersonic jet source was coupled to a time-of-flight (TOF) mass spectrometer equipped with a reflectron. The laser source was an excimer pumped dye laser combination using C480 and C460 dyes and a BBO crystal to yield radiation tunable over the 255 nm - 225 nm region with an approximate UV bandwidth of ≤ 0.4 cm^{-1}. Photoions were detected with a dual microchannel plate (MCP) detector. Mass resolved scans were recorded with a digital oscilloscope and wavelength resolved spectra employed a boxcar integrator to selectively monitor the signal due to the desired mass.

Results

Irradiation of a dilute (0.2% HI in helium) expansion at a total stagnation pressure of 1 psig at 238.4 nm manifests I^+ and HI^+ mass peaks. Under these expansion conditions monomeric species are expected to dominate and no other mass peaks, which would be evidence of cluster formation, were observed. The boxcar gate was set to integrate the HI^+ signal and the wavelength of the dye laser scanned to produce the extended spectrum contained in Figure 2, plotted as a function of the two-photon energy. Sharp, well resolved features were observed overlapping a weaker continuous signal and the onset of the spectrum, $\approx$ 239 nm, was very near the 2-photon energetic threshold for the production of HI^+ (I.P. = 10.386 eV). The HI^+ mass signal decreases significantly at higher energies until eventually, beyond $\approx$ 88,700 cm^{-1}, no distinct signal was observed.

The threshold of the spectrum was found to be a sensitive function of the applied extraction voltage of the TOF, shifting to lower energies as the electric field was increased. An external electric field can reduce the measured I.P. of molecular species by field ionizing highly excited Rydberg levels. The zero-field threshold of our data was calculated to be 83,755 cm^{-1}, very near the accepted I.P. of HI (83,771 cm^{-1}). We also examined the intensity dependence of the HI^+ signal with the laser tuned to resonance with the strong feature at 83,904 cm^{-1}. The maximum flux was estimated to be approximately 1-2 x 10^{26} photons/s·cm^2 and the dependence was measured over a range slightly greater than one order of magnitude. The overall trend can be fit reasonably well to a straight line with a slope of unity.

Discussion

Hydrogen iodide excitation at 239 nm is resonant with the first UV continuum (Figure 1), which consists of several excited states correlating with ground state H-atoms and I-atoms in either the ground, $I(^2P_{3/2})$, or excited, $I^*(^2P_{1/2})$, state. Molecular beam photodissociation studies[4,5] indicate that these states are purely repulsive in nature, with a

quantum yield for dissociation of unity. Conservation of momentum dictates that virtually all of the released energy is deposited into the kinetic energy of the departing H-atom and dissociation is rapid on the time scale of our 20 nsec laser pulse

It is possible to analyze the multiphoton absorption process as two sequential steps with real, as opposed to virtual, intermediate states. In that light, the ionization rate achieved with our laser source is apparently sufficient to compete with dissociation of HI and yield a measurable parent ion signal. The linear intensity dependence recorded for HI$^+$ indicates that one of the steps is saturated, or nearly so. We propose that a simple rate equation model may be instructive in considering the data presented here. We have constructed a three level model, depicted in Figure 3, with the ground state, X, the repulsive intermediate states, R, and the final ionized state, C. The state, P, represents the fragment products of HI photodissociation. The stimulated absorption/emission and ionization rates are $\alpha = \sigma F$ and $\beta = \gamma F$, respectively, with associated cross-sections σ and γ with a photon flux, F. The dissociation rate of the repulsive intermediate states is k_D. The set of coupled rate equations can be readily solved by applying the method of Laplace transforms. An insightful limiting case is reached when all of the HI molecules in the laser interaction region sampled by the mass spectrometer are either dissociated or ionized. Such saturation is likely in our experiments with the result for the ionized state, C:

$$C = \frac{\beta}{\beta + k_D} X_0$$

and likewise for the fragment species, P:

$$P = \frac{k_D}{\beta + k_D} X_0$$

The number of ions produced is seen to be some fraction of the initial number of ground state HI molecules determined by the ratio of the ionization rate to the total loss rate of the intermediate state due to irreversible processes. The fraction can be considered as the quantum yield for ion production. Similarly, the product of a quantum yield for dissociation and the ground state number density yields the number of fragment species produced. These results clearly indicate the competition between dissociation and ionization from the intermediate repulsive states.

The dissociation rate is expected to be quite large relative to the ionization rate maintained by the nanosecond dye laser so that, $k_D \gg \beta$. The ion concentration is then given by

$$C \approx \frac{\beta}{k_D} X_0 = F\left(\frac{\gamma X_0}{k_D}\right)$$

and the laser flux dependence of HI$^+$ will be linear, the result determined through experimentation. We estimate from our experimental parameters that $\beta/k_D \approx 2\text{-}10 \times 10^{-10}$. Clearly, our ability to monitor the production of HI$^+$ from the MPI process is a tribute to the sensitivity of our instrument.

We can estimate the effective fragmentation rate from a simple, classical consideration of the dissociation process to be, $k_D \approx 1.5 \times 10^{14}$ sec^{-1}. Using our estimate for k_D with a peak flux of 10^{26} photons/s·cm^2, the cross-section for ionization originating from the repulsive intermediate states is calculated to be $\gamma = 3\text{-}15 \times 10^{-22}$ cm^2. In contrast,
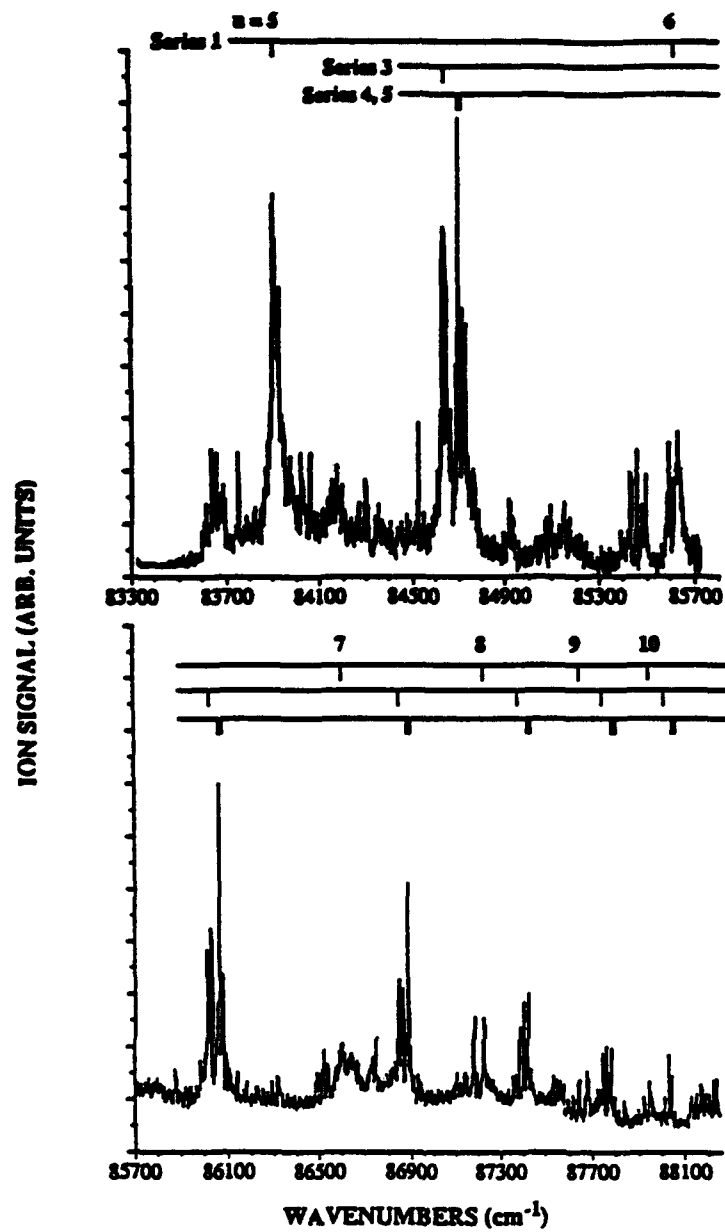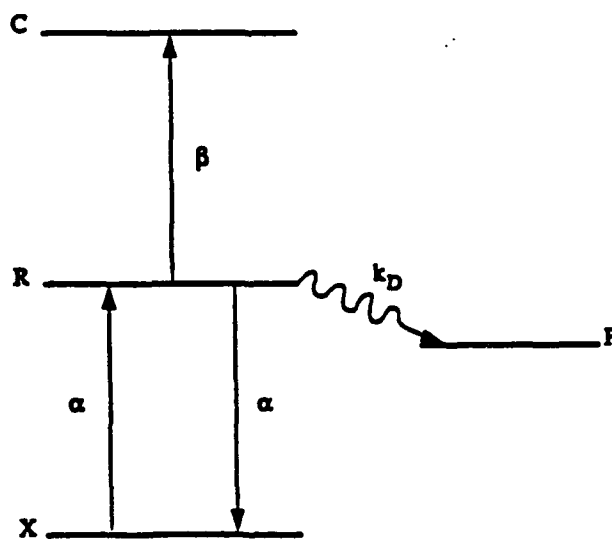
FIGURE 2.

Figure 3.

448

the cross-section for single photon ionization from the ground state is in the range of 10-75 x 10^{-18} cm^2,[6] much larger than our estimate.

The identities of the autoionizing Rydberg states that appear in the HI$^+$ spectrum remain to be clarified. Several investigators[7,8] have employed nonlinear four-wave mixing techniques to conduct high resolution ($\Delta\tilde{v} \approx 0.5$ cm^{-1}) VUV photoionization studies of HI and several Rydberg series have been identified. The appearance of our spectrum is qualitatively different from the results but we have been able to plausibly identify several features as members of the Rydberg series detected in the single-photon work. Using the series labels of Mank et. al.,[8] we have assigned peaks in Figure 2 due to Series 1,3,4 and 5. The single photon studies were able to record well resolved spectral features up to the $^2\Pi_{1/2}$ ($v = 0$) threshold of HI$^+$ at 89,122 cm^{-1}, much higher in energy than the observed limit of the 2-photon spectrum, $\approx 88,700$ cm^{-1}. The overall decrease in the HI$^+$ signal in the 2-photon spectrum at shorter wavelengths may be due to the general decrease in the ionization cross-section concurrent with an increase in the HI dissociation rate as the first step terminates on steeper portions of the repulsive potential. The ion quantum yield, $\approx \beta/k_D$, decreases and an insufficient number of ions are produced to be detected even with the very sensitive MCP detector. In addition, resonance requirements for each transition in the 2-photon excitation mechanism may result in a constriction of the Franck-Condon accessible region relative to single photon absorption.

Noticeably absent from our spectrum are peaks due to Series 2 and Series 6, which are clearly observed in the one-photon studies. In fact, the strong, broad peaks of Series 2 are the most prominent spectral features in the one-photon studies. Such different behavior may be a result of the two-photon process operative in our study versus the one-photon transitions recorded in the VUV investigations.

Conclusion

We have excited HI, isolated in a supersonic expansion, with UV light from a tunable nanosecond dye laser. The parent ion, HI$^+$, is observed due to a 1+1 REMPI process, resonant with the repulsive states that comprise the first UV continuum of hydrogen iodide. The wavelength resolved spectrum reveals sharp features which arise due to autoionizing Rydberg levels converging to the HI$^+$ ground state. Comparison with spectra obtained by other investigators using one-photon excitation shows that specific Rydberg series are suppressed in the two-photon spectrum. A kinetic analysis indicates that the initial excitation step is saturated and that the ionization cross-section, due to a free-bound transition, is relatively small. While the dissociation rate of the excited HI is extremely rapid, the flux from a nanosecond laser is still sufficient to ionize a small fraction prior to fragmentation.

References

(1) Jiang, Y.; Giorgi-Amazzi, M. R.; Bernstein, R. B. *Chem. Phys.* **1986**, *106*, 171.
(2) Danon, J.; Zacharias, H.; Rottke, H.; Welge, K. H. *J. Chem. Phys.* **1982**, *76*, 2399.
(3) Sapers, S. P.; Vaida, V.; Naaman, R. *J. Chem. Phys.* **1988**, *88*, 3638.
(4) van Veen, G. N. A.; Mohamed, K. A.; Baller, T.; de Vries, A. E. *Chem. Phys.* **1983**, *80*, 113.
(5) Clear, R. D.; Riley, S. J.; Wilson, K. R. *J. Chem. Phys.* **1975**, *63*, 1340.
(6) Carlson, T. A.; Gerard, P.; Krause, M. O.; Wald, G. V.; Taylor, J. W.; Grimm, F. A. *J. Chem. Phys.* **1986**, *84*, 4755.
(7) Hart, D. J.; Hepburn, J. W. *Chem. Phys.* **1989**, *129*, 51.
(8) Mank, A.; Drescher, M.; Huth-Fehre, T.; Bowering, N.; Heinzman, U.; Lefebvre-Brion, H. *J. Chem. Phys.* **1991**, *95*, 1676.

Preliminary Investigation of a Graded Interface Between Solid Rocket Motor Propellant and Insulation

Joseph D. Lichtenhan, Tommy W. Hawkins, Kevin P. Chaffee. Phillips Laboratory, Rocket Propulsion Directorate, Edwards AFB, CA 93524

Inadequate control over the material properties of the insulation and propellant interface has been a traditional problem for solid rocket motors.[1] Deficiencies along this structurally critical region can result in catastrophic motor failure through over-pressurization or case burn through. The ramification from such an event may include substantial financial setbacks from lost vehicles, vehicle payloads, facilities, delayed launch schedules, and increased insurance and operational costs due to decreased system confidence and reliability.

The insulation/propellant interface problems stem from the necessity to form a bond between these two materials. This is necessary in order for the propulsion system to withstand various operational stresses, and to control the amount of burnable propellant surface area.[1] Traditional propellants and insulations are composite like in nature. This not only hinders the manufacturability of these materials, but also limits the extent of bonding that can be achieved between the two material surfaces. The conventional insulation-propellant interface (called a bondline) is two-dimensional and requires the use of a third material to function as an adhesive liner (Figure 1).
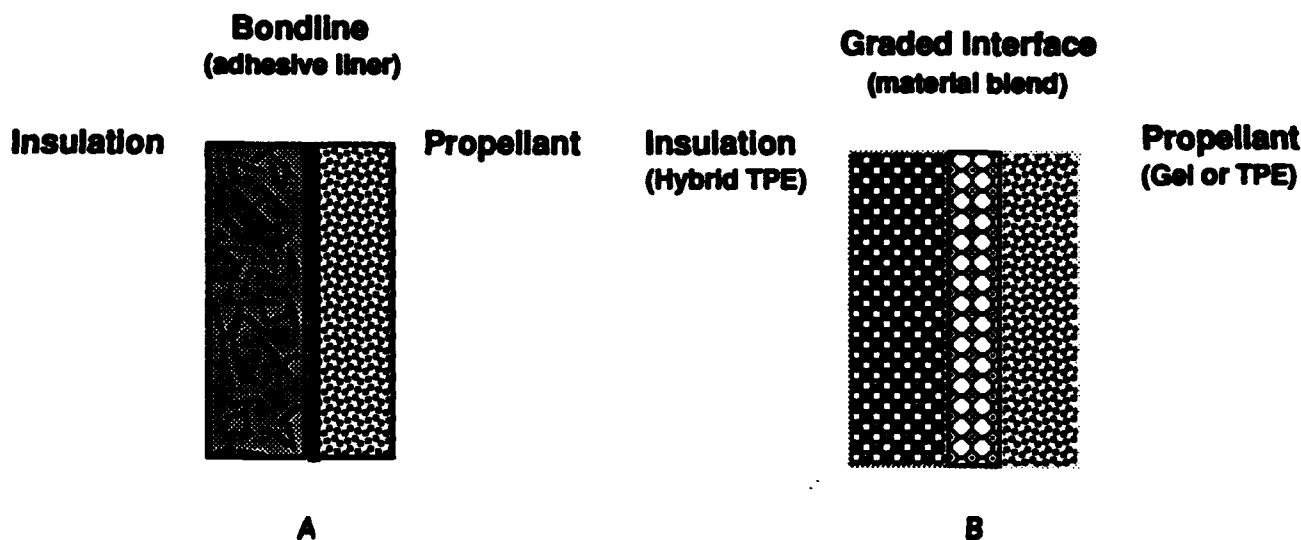

Figure 1. (a) Conventional bondline approach and (b) Graded insulation-propellant concept.

The degree of bonding between the two materials in the bondline approach is sensitive to surface preconditioning since the presence of particulate, dirt, moisture, and oils create regions of reduced or nonexistent bonding. The bondline approach is further plagued by a material compatibility problem. This arises from the necessity to plasticize composite propellants in order to achieve acceptable mechanical properties at low temperatures. Migration of these plasticizing agents across the propellant-insulation interface (during system manufacture) can

---

[1] For example see: H.L. Schreuder-Stacer, R.G. Stacer in Bonded Interface Technology Development for Solid Rocket Motors AL-TR--89--082 September 1991.

severely alter the material properties of the bondline and create mechanically weakened boundary areas.[2] It is interesting to note that for over 20 years and after numerous studies and patents, the problem of bondline integrity still persists while the overall design approach to this critical interface has not seen significant change.

Future solid propulsion systems can potentially avoid many drawbacks of current systems by taking advantage of new generations of propellants and insulations. The Phillips Laboratory (Rocket Propulsion Directorate) is pursuing the design of propulsion systems possessing a graded insulation / propellant interface. This approach differs from the bondline method through the formation of an interfacial region which is composed of a physical blend (or alloy) of both the insulation and the propellant. This type of approach will allow for intermediate (or graded) material properties to be achieved across the interfacial region and will promote three-dimensional cohesive bonding between the insulation and propellant.

The successful design of a graded insulation / propellant interface requires the consideration of several key issues. A primary concern is chemical compatibility between the two material compositions. Incompatibilities may result in material segregation, undesirable chemical reactivity, or the transport / diffusion of species across the interface. It also desirable to match the physical properties (such as tensile, melt, and viscosity) of the two bulk materials. This level of control would allow the properties profile (from bulk insulation to bulk propellant) to approach that of a uni-material (Figure 2).
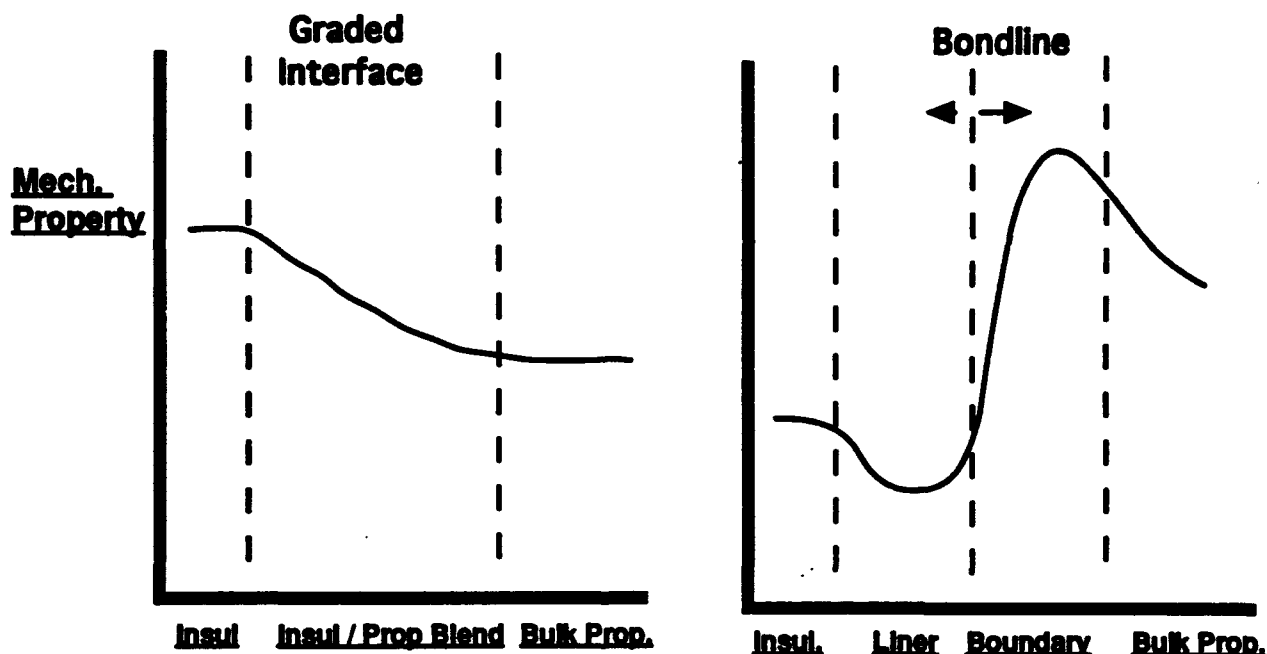

Figure 2. Mechanical properties profile for a insulation / propellant interface.

This figure shows the contrast in the mechanical properties between the graded interface concept and the traditional bondline approach.[2b] Note that mechanical failure for the latter typically occurs at the low point on the profile.

Development and evaluation of the graded insulation / propellant interface requires that non-composite (uncured) insulations and propellants be developed and utilized. Along these lines the Phillips Laboratory currently has programs focused on the development low cost,

---

[2] For example see: (a) F.E. Oberth in Principles in Solid Propellant Development CPIA 469, September 1987. (b) Propellant Case Interface Technology Program Status Report F296001-91-C-004, CDRL A001 Thiokol Corp. May 1992.

environmentally friendly propellants and insulations which are highly processable and do not required cure processing. Two promising technologies are the Gel Propellants and the Hybrid Insulations. The preparation of acrylate based gel propellants and acrylate derived hybrid insulations will be discussed.

Gel Propellant Synthesis

Gel propellant technology is a radically different and innovative approach to producing solid propellants which are environmentally acceptable and processable. Conventional solid propellant is composed of solid oxidizer particulates suspended in a matrix of rubber (e.g. polybutadiene) which is crosslinked with highly toxic curatives. This structure makes propellant waste reclamation or disposal environmentally difficult. Gel propellant is produced from a combination of liquid oxidizer and ionophilic, uncrosslinked polymer (requires no toxic curatives). Such a combination produces a solid propellant with environmentally enhanced reclaimability and processability.

Recent work on gel propellant is focused on developing acrylic based, ionophilic polymers capable of gelling with liquid oxidizers at high liquid oxidizer phase volumes. One such polymer which has recently demonstrated this capability is poly(hydroxamic acid) which can be produced from polyacrylamide (Figure 3).[3]
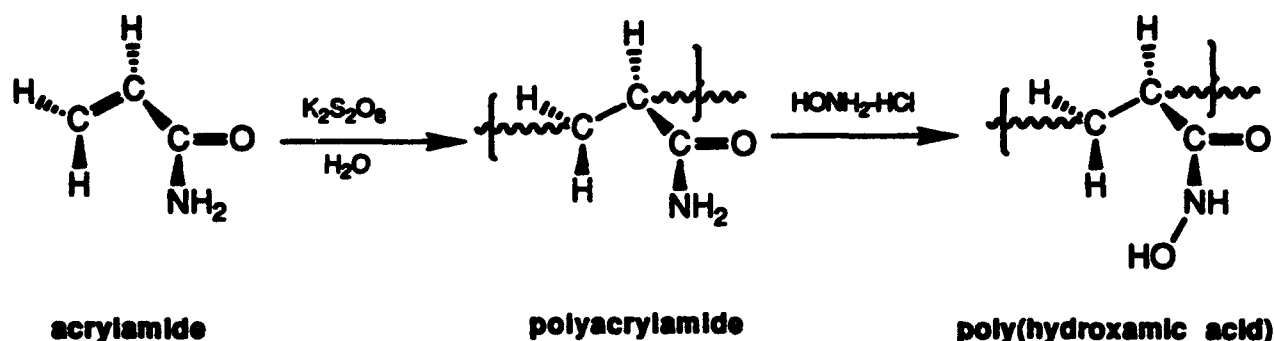

Figure 3. Synthesis of the (polyhydroxamic acid) gel propellant polymer.

Work is continuing on the synthesis and properties of ionophilic acrylic polymers and their performance in gel propellant formulations.[3]

Hybrid Insulation Synthesis

Recent advances in the synthesis of preceramic polymers (or Hybrids) provides an opportunity to take advantage of a unique class of evolving materials which combine the favorable properties of both organic and inorganic substances.[4] Hybrid materials show excellent potential as ablative materials because upon pyrolysis they can be converted into an erosion resistant ceramic which is more resistant to oxidation and mechanical erosion than current char forming organic based ablative systems.

In attempt to produce hybrid insulations that would be chemically compatible with acrylate based gel propellants we have undertaken the synthesis of acrylate derived hybrid polymers (Figure 4). Monomers for these materials are produced by a corner capping reaction which places a polymerizable acrylate functionality on a polyhedral oligosilsesquioxane

[3] Hawkins, T. W.; Fuller, D. L. work in progress.
[4] Lichtenhan, J. D.; Vu, N. Q.; Carter, J. A.; Gilman, J. W.; Feher, F. J. *Macromolecules* 1993, 26, 2141-2142.

(POSS).[5] This molecule can then be polymerized to afford polymers which contain the desired acrylate functionality and the preceramic POSS group for ceramic char formation.

Mwt. = 230K, T_{dec} = 327 °C

Figure 4. Synthesis of an acrylate based monomer and hybrid polymer.

Properties of these materials can be manipulated further through copolymerizations with alternate monomers or through the formation of blends with other materials.[5, 6]
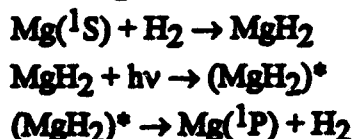
Future Directions

Investigations are underway to further the development of gel propellants and compatible hybrid insulations. We are also exploring a variety of manufacturing and processing conditions that will allow for optimal formation of the graded insulation / propellant interface.[7] For example, the simultaneous extrusion (coaxial-coextrusion) of propellant and insulation is a particularly attractive method for system manufacture. Similar plastics processing methods are used for the manufacture of automotive parts (such as bumpers, moldings) and in the packaging industry (bottles, containers). One advantage of extrusion processing may be the benefit of shear mixing aiding formation of the graded interface during processing. Other manufacturing techniques under investigation include blow-molding/diffusion processing and compression/diffusion molding.

[5] Lichtenhan, J. D.; Otonari, Y. A.; Carr, M. J. work in progress.
[6] Lichtenhan, J. D.; Bolf, A. G.; Noel, C. J. work in progress.
[7] Lichtenhan, J. D.; Chaffee, K. P.; Noel, C. J. work in progress.

Ab Initio Calculations of the Mg + H$_2$ and MgH + H Potential Energy Surfaces

Marcy E. Rosenkrantz
University of Dayton Research Institute
OLAC PL/RKFE
9 Antares Road
Edwards AFB, CA 93524-7680

We are interested in using H atoms for rocket propulsion. In the laboratory we would like to be able to trap H atoms in a solid H$_2$ matrix. The H atoms would have to be trapped with low kinetic energy to prevent their migration and recombination. Kleiber, and coworkers [J. Chem. Phys. 85, (1986)] have shown that in the gas phase magnesium atoms can react with H$_2$ according to the following set of reactions:

$$Mg(^1S) + H_2 \rightarrow MgH_2$$
$$MgH_2 + h\nu \rightarrow (MgH_2)^*$$
$$(MgH_2)^* \rightarrow Mg(^1P) + H_2$$

or

$$(MgH_2)^* \rightarrow MgH(v'',J'') + H$$

In the matrix we are interested in further dissociating the MgH as well to obtain the following overall reaction:

$$Mg + H_2 + h\nu + h\nu' \rightarrow Mg^* + H_{lke} + H_{lke'}$$
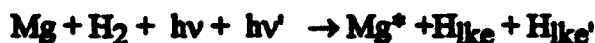
where H$_{lke}$ is a hydrogen atom with low kinetic energy.

These calculations were designed to help us understand the method by which the excited Mg atom mediates the dissociation of H$_2$. I employed a state averaged multiconfiguration self-consistent field (SAMC) calculation to obtain orbitals for a multi-reference configuration interaction (MRCI) calculation of the low lying singlet states of MgH$_2$ and those of MgH(X$^2\Sigma^+$, A$^2\Pi$) + H.

The calculations were performed in the region of the C$_{2v}$ interaction of Mg + H$_2$ where the ground ^{1}A$_1$ and the ^{1}B$_2$ states cross. This region, which I call the "transition state" region, is shown in Figure 1. Note that there is no real transition state for the reaction Mg+H$_2$ $\rightarrow$ MgH$_2$ that I could determine, even though in the search for the transition state I did not confine my attention to the C$_{2v}$ symmetry. It is obvious from fig. 1 that there is a ridge where the two potential energy surfaces cross. The oscillations along the ridge are probably a result of the spacing of the points at which I have calculated results. I believe that a denser grid of points would eliminate these oscillations. Figure 2

shows a different view of this region and includes the difference potential. Note the maximum in the difference potential where the energy difference approaches zero.
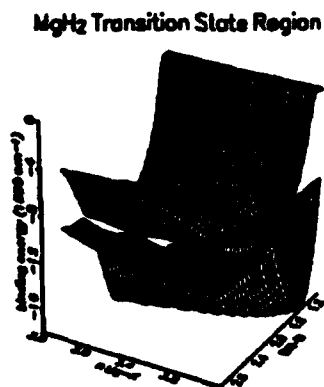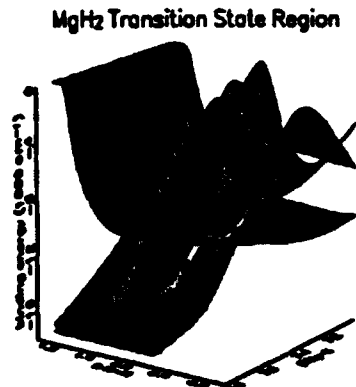
MgH₂ Transition State Region

MgH₂ Transition State Region

Fig. 1

Fig. 2

To begin to map the rest of the reaction I investigated the MgH($X^2\Sigma^+$, $A^2\Pi$) + H interaction potentials. Here I use Jacobi coordinates according to the cartoon in Fig. 3.
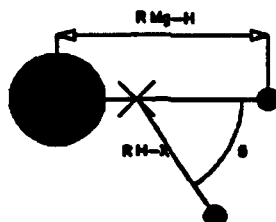
Fig. 3

A series of these potential surfaces are shown in Figs. 4-9. Note that the two surfaces are of the same symmetry and that the surfaces are very close together for $\theta=60^\circ$. A better view of this is given in Fig. 10. Also note that the scale used in fig. 9 is different from the rest of the series. This is due to the fact that the jacobi coordinates require the H-center of mass distance quite large to avoid having the two H atoms lie on top of each other. The avoided curve crossing is very obvious in the data, which page limitations and good taste forbid me to show.
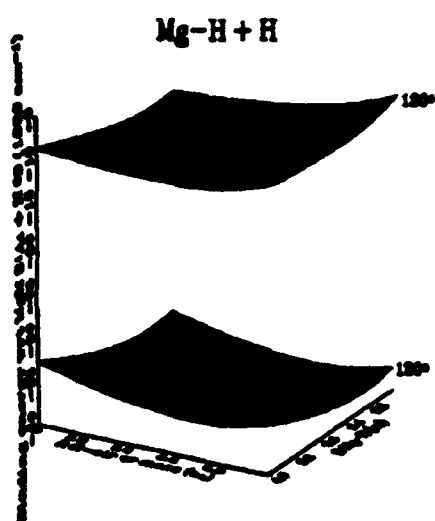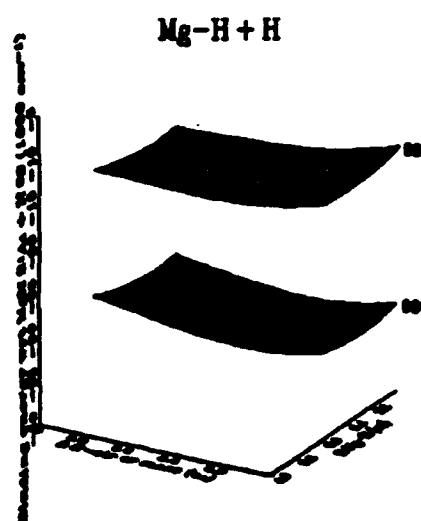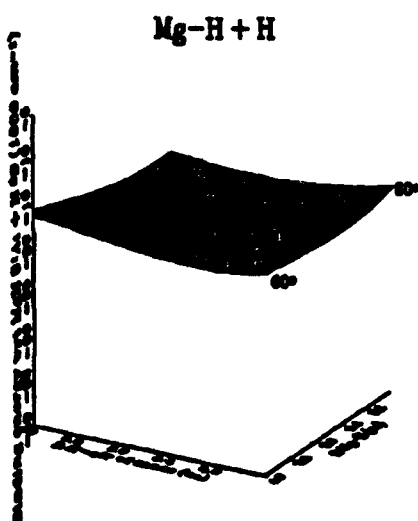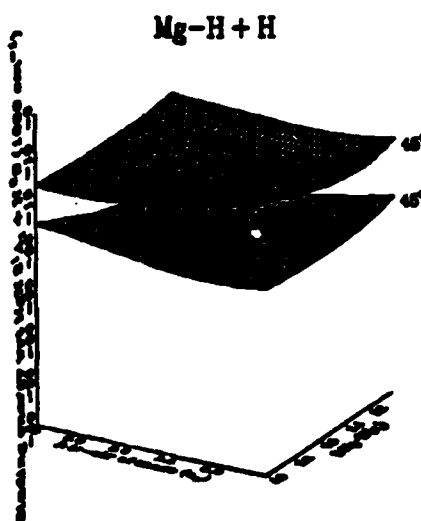
Mg–H + H

Fig. 4

Mg–H + H

Fig. 5

Mg–H + H

Fig. 6

Mg–H + H

Fig. 7

456

Mg–H + H

Fig. 8

Mg–H + H

Fig. 9

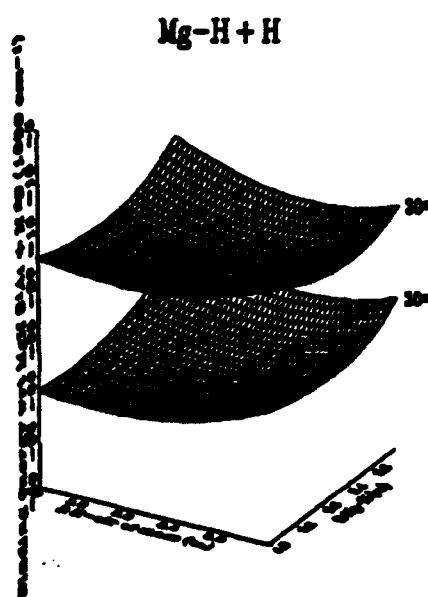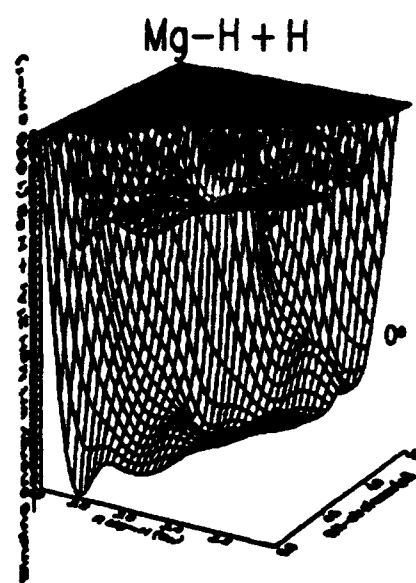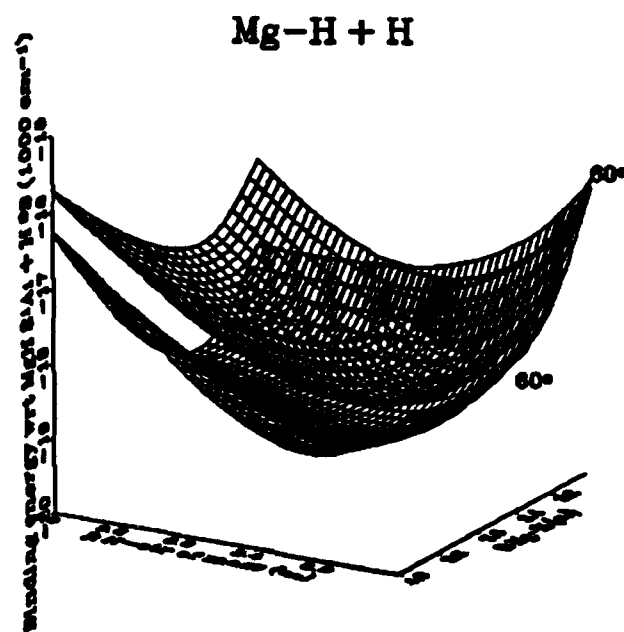Mg–H + H

Fig. 10

457

Finally in fig. 11 the energy levels of the states considered in this study are given. Here, the energy level of the ground state Mg (^1S) + H_2 $(X^1\Sigma_g{}^+)$ is considered to be the zero of energy. The excitation energy Mg $(^1S)\leftarrow Mg$ (^1P) is within 3 cm^{-1} of the accepted value. The T_e of the $A^2\Pi$ state of MgH is within 1 cm^{-1} of the value determined by Saxon, Kirby and Liu [J. Chem. Phys. 69, 5301(1978)]. The heights of the barriers between the various levels have still to be determined. The geometries of the local minima have been determined and are given in table 1. The minima of the two A' states of MgH +H do not lie directly above each other. The minimum in the excited state is located on the 60° curve while that for the ground state is located on its 120° curve. When the MgH + H system becomes linear with an H-x-H angle of 180° we have the ground state of the linear H-Mg-H molecule. This is the global minumum. However, the minimum of its excited state ($^1B_2$) occurs when the molecule is bent.

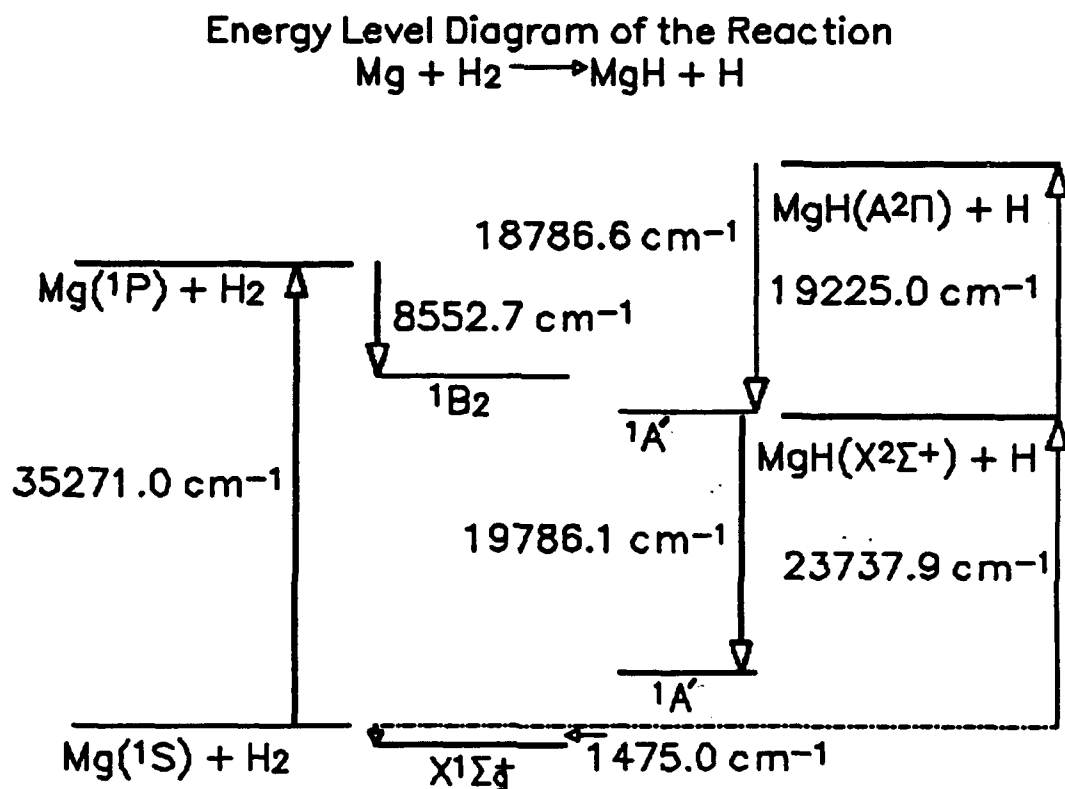## Energy Level Diagram of the Reaction
Mg + H₂ ⟶ MgH + H

Fig. 11

Table 1. Geometric parameters of the levels arising from the reaction $Mg + H_2 \rightarrow$ MgH + H.

State	R Mg-H (a_0)	R H-H (a_0)	angle H-Mg-H	method
$X^1\Sigma_g^+$	3.25	6.50	180.00°	MCSCF geometry opt.
$^1B_2$	3.49	2.13	35.59°	bi-cubic spline interpolation
$1^1A'^*$	3.20	5.61	118.11°	minimum estimated from data
$2^1A'^*$	3.40	3.33	57.40°	minimum estimated from data

* Note that the geometric parameters have been converted from the Jacobi coordinates for the sake of consistency.